

REPORT DOCUMENTATION PAGE

AFRL-SR-BL-TR-98-

d
188

Public reporting burden for this collection of information is estimated to average 1 hour per response, and maintaining the data needed, and completing and reviewing the collection of information. Send information, including suggestions for reducing this burden, to Washington Headquarters Services, Directorate for Information Operations and Reports, 1204, Arlington, VA 22202-4302, and to the Office of Management and Budget, Paperwork Reduction Project (0704-0188).

sources, gathering
this collection of
is Highway, Suite

0795

1. AGENCY USE ONLY (Leave Blank)	2. REPORT DATE December, 1994	3. Final
4. TITLE AND SUBTITLE USAF Summer Research Program - 1994 Summer Faculty Research Program Final Reports, Volume 4, Rome Laboratory		5. FUNDING NUMBERS
6. AUTHORS Gary Moore		
7. PERFORMING ORGANIZATION NAME(S) AND ADDRESS(ES) Research and Development Labs, Culver City, CA		8. PERFORMING ORGANIZATION REPORT NUMBER
9. SPONSORING/MONITORING AGENCY NAME(S) AND ADDRESS(ES) AFOSR/NI 4040 Fairfax Dr, Suite 500 Arlington, VA 22203-1613		10. SPONSORING/MONITORING AGENCY REPORT NUMBER
11. SUPPLEMENTARY NOTES Contract Number: F49620-93-C-0063		
12a. DISTRIBUTION AVAILABILITY STATEMENT Approved for Public Release		12b. DISTRIBUTION CODE
13. ABSTRACT (Maximum 200 words) The United States Air Force Summer Faculty Research Program (USAF- SFRP) is designed to introduce university, college, and technical institute faculty members to Air Force research. This is accomplished by the faculty members being selected on a nationally advertised competitive basis during the summer intersession period to perform research at Air Force Research Laboratory Technical Directorates and Air Force Air Logistics Centers. Each participant provided a report of their research, and these reports are consolidated into this annual report.		
14. SUBJECT TERMS AIR FORCE RESEARCH, AIR FORCE, ENGINEERING, LABORATORIES, REPORTS, SUMMER, UNIVERSITIES		15. NUMBER OF PAGES
		16. PRICE CODE
17. SECURITY CLASSIFICATION OF REPORT Unclassified	18. SECURITY CLASSIFICATION OF THIS PAGE Unclassified	19. SECURITY CLASSIFICATION OF ABSTRACT Unclassified
20. LIMITATION OF ABSTRACT UL		

UNITED STATES AIR FORCE
SUMMER RESEARCH PROGRAM -- 1994
SUMMER FACULTY RESEARCH PROGRAM FINAL REPORTS

VOLUME 4

ROME LABORATORY

RESEARCH & DEVELOPMENT LABORATORIES

5800 Uplander Way

Culver City, CA 90230-6608

Program Director, RDL
Gary Moore

Program Manager, AFOSR
Major David Hart

Program Manager, RDL
Scott Licoscas

Program Administrator, RDL
Gwendolyn Smith

Program Administrator, RDL
Johnetta Thompson

Submitted to:

AIR FORCE OFFICE OF SCIENTIFIC RESEARCH

Bolling Air Force Base

Washington, D.C.

December 1994

19981204 040

PREFACE

Reports in this volume are numbered consecutively beginning with number 1. Each report is paginated with the report number followed by consecutive page numbers, e.g., 1-1, 1-2, 1-3; 2-1, 2-2, 2-3.

This document is one of a set of 16 volumes describing the 1994 AFOSR Summer Research Program. The following volumes comprise the set:

<u>VOLUME</u>	<u>TITLE</u>
1	Program Management Report
	<i>Summer Faculty Research Program (SFRP) Reports</i>
2A & 2B	Armstrong Laboratory
3A & 3B	Phillips Laboratory
4	Rome Laboratory
5A & 5B	Wright Laboratory
6	Arnold Engineering Development Center, Frank J. Seiler Research Laboratory, and Wilford Hall Medical Center
	<i>Graduate Student Research Program (GSRP) Reports</i>
7	Armstrong Laboratory
8	Phillips Laboratory
9	Rome Laboratory
10	Wright Laboratory
11	Arnold Engineering Development Center, Frank J. Seiler Research Laboratory, and Wilford Hall Medical Center
	<i>High School Apprenticeship Program (HSAP) Reports</i>
12A & 12B	Armstrong Laboratory
13	Phillips Laboratory
14	Rome Laboratory
15A&15B	Wright Laboratory
16	Arnold Engineering Development Center

SFRP FINAL REPORT TABLE OF CONTENTS

i-xxi

1. INTRODUCTION	1
2. PARTICIPATION IN THE SUMMER RESEARCH PROGRAM	2
3. RECRUITING AND SELECTION	3
4. SITE VISITS	4
5. HBCU/MI PARTICIPATION	4
6. SRP FUNDING SOURCES	5
7. COMPENSATION FOR PARTICIPANTS	5
8. CONTENTS OF THE 1994 REPORT	6

APPENDICIES:

A. PROGRAM STATISTICAL SUMMARY	A-1
B. SRP EVALUATION RESPONSES	B-1

SFRP FINAL REPORTS

SRP Final Report Table of Contents

Author	University/Institution Report Title	Armstrong Laboratory Directorate	Vol-Page
Dr. James L Anderson	University of Georgia , Athens , GA Determination of the Oxidative Redox Capacity of	AL/EQC	2- 1
Dr. Hashem Ashrafiuon	Villanova University , Villanova , PA ATB Simulation of Deformable Manikin Neck Models	AL/CFBV	2- 2
DR Stephan B Bach	Univ of Texas-San Antonio , San Antonio , TX Pre-Screening of Soil Samples Using a Solids Inser	AL/OEA	2- 3
Dr. Suzanne C Baker	James Madison University , Harrisonburg , VA Rat Pup Ultrasonic Vocalizations: A Sensitive Indi	AL/OER	2- 4
DR Alexander B Bordetsky	Univ of Texas - Dallas , Richardson , TX Knowledge-Based Groupware for Geographically Distr	AL/HRGA	2- 5
DR. Michael J Burke	Tulane University , New Orleans , LA An Empirical Examination of the Effect of Second-O	AL/HRMI	2- 6
DR Yu-Che Chen	University of Tulsa , Tulsa , OK A Study of the Kinematics, Dynamics and Control AI	AL/CFBS	2- 7
DR Shashikala T Das	Wilmington College , Wilmington , OH The Benchmark Dose Approach for Health Risk Assess	AL/OET	2- 8
DR. Donald W DeYoung	University of Arizona , Tucson , AZ Noise as a Stressor: An Assessment of Physiologic	AL/OEBN	2- 9
DR Judy B Dutta	Rice University , Houston , TX Memory for Spatial Position and Temporal Occurence	AL/CFTO	2- 10
DR Paul A Edwards	Edinboro Univ of Pennsylvania , Edinboro , PA Fuel Identification by Neural Network Analysis of	AL/EQC	2- 11

SRP Final Report Table of Contents

Author	University/Institution Report Title	Armstrong Laboratory Directorate	Vol-Page
Dr. Daniel L Ewert	North Dakota State University , Grand Forks , ND Regional Arterial Compliance and Resistance Change	AL/AOCN	2- 12
Dr. Bernard S Gerstman	Florida International Universi , Miami , FL Laser Induced Bubble Formation in the Retina	AL/OEO	2- 13
DR Robert H Gilkey	Wright State University , Dayton , OH Relation Between Detection and Intelligibility in	AL/CFBA	2- 14
Dr. Kenneth A Graetz	University of Dayton , Dayton , OH Using Electronic Brainstorming Tools to Visually R	AL/HRGA	2- 15
Dr. Donald D Gray	West Virginia Unicersity , Morgantown , WV Improved Numerical Modeling of Groundwater Flow an	AL/EQC	2- 16
Dr. Pushpa L Gupta	University of Maine , Orono , ME Regression to the Mean in Half-Life Studies	AL/AOEP	2- 17
Dr. Thomas E Hancock	Grand Canyon University , Phoenix , AZ An Expanded Version of the Kulhavy/Stock Model of	AL/HR2	2- 18
DR. Alexis G Hernandez	University of Arizona , Tucson , AZ Preliminary Results of the Neuropsychiatrically En	AL/AOCN	2- 19
DR P. A Ikomi	Central State University , Wilberforce , OH A Realistic Multi-Task Assessment of Pilot Aptitud	AL/HRMI	2- 20
Dr. Arthur Koblasz	Georgia State University , Atlanta , GA Distributed Sensory Processing During Graded Hemod	AL/AOCI	2- 21
DR Manfred Koch	Florida State University , Tallahassee , FL Application of the MT3D Solute Transport Model to	AL/EQC	2- 22

SRP Final Report Table of Contents

Author	University/Institution Report Title	Armstrong Laboratory Directorate	Vol-Page
Dr. Donald H Kraft	Louisiana State University , Baton Rouge , LA An Exploratory Study of Weighted Fuzzy Keyword Bo	AL/CFHD	2- 23
Dr. Brother D Lawless	Fordham University , New York , NY Apoptosis Advanced Glycosylated End Products, Auto	AL/OER	2- 24
Dr. Tzesan Lee	Western Illinois University , Macomb , IL A Statistical Method for Testing Compliance	AL/OEM	2- 25
DR Robert G Main	California State Univ-Chico , Chico , CA A Study of Interaction in Distance Learning	AL/HRTT	2- 26
Dr. Augustus Morris	Central State University , Wilberforce , OH A Novel Design Concept for a Small, Force Reflecti	AL/CFBS	2- 27
DR Mark A Novotny	Florida State University , Tallahassee , FL Computer Calculation of Rate Constants for Biomole	AL/EQS	2- 28
Dr. Joseph H Nurre	Ohio University , Athens , OH A Review of Parameter Selection for Processing Cyl	AL/CFHD	2- 29
DR Edward L Parkinson	Univ of Tennessee Space Inst , Tullahoma , TN Improving the United States Air Force Environmenta	AL/EQS	2- 30
DR Malcom R Parks	University of Washington , Seattle , WA Communicative Challenges Facing Integrated Product	AL/AOE	2- 31
DR David R Perrott	California State Univ-Los Ange , Los Angeles , CA Aurally Directed Search: A Comparison Between Syn	AL/CFBA	2- 32
Dr. Edward H Piepmeier	University of South Carolina , Columbia , SC Dose Response Studies for Hyperbaric Oxygenation	AL/AOHP	2- 33

SRP Final Report Table of Contents

Author	University/Institution Report Title	Armstrong Laboratory Directorate	Vol-Page
DR Miguel A Quinones	Rice University , Houston , TX The Role of Experience in Training Effectiveness	AL/HRTE	2- 34
Dr. Ramaswamy Ramesh	SUNY, Buffalo , Buffalo , NY AETMS: Analysis, Design and Development	AL/HRAU	2- 35
DR Gary E Riccio	Univ of IL Urbana-Champaign , Urbana , IL REPORT NOT AVAILABLE AT PRESS TIME	AL/CFHP	2- 36
DR Kandasamy Selvavel	Claflin College , Orangeburg , SC Sequential Estimation of Parameters of Truncation	AL/AOEP	2- 37
DR David M Senseman	Univ of Texas-San Antonio , San Antonio , TX Multisite Optical Recording of Evoked Activity in	AL/CFTO	2- 38
DR Wayne L Shebilske	Texas A&M University , College Station , TX Linking Laboratory Research and Field Applications	AL/HRTI	2- 39
Dr. Larry R Sherman	University of Scranton , Scranton , PA Using The Sem-EDXA System at AL/OEA for Analysis o	AL/OEA	2- 40
Dr. Richard D Swope	Trinity University , San Antonio , TX Regional Arterial Compliance and Resistance Chang	AL/AOCI	2- 41
DR Steven D Tripp	The University of Kansas , Lawrence , KS Representing and Teaching a Discrete Machine: An	AL/HRTC	2- 42
DR Ryan D Tweney	Bowling Green State University , Bowling Green , OH Automated Detection of Individual Response Charact	AL/CFHP	2- 43
Dr. Brian S Vogt	Bob Jones University , Greenville , SC A Multiplexed Fiber-Optic Laser Fluorescence Spect	AL/EQW	2- 44

SRP Final Report Table of Contents

Author	University/Institution Report Title	Armstrong Laboratory Directorate	Vol-Page
DR Janet M Weisenberger	Ohio State University , Columbus , OH Investigation of the Role of Haptic Movement in Ta	AL/CFBA	2- 45

SRP Final Report Table of Contents

Author	University/Institution Report Title	Phillips Laboratory Directorate	Vol-Page
DR Behnaam Aazhang	Rice University , Houston , TX High Capacity Optical Communication Networks	PL/VTPT	3- 1
DR Nasser Ashgriz	SUNY-Buffalo , Buffalo , NY On The Mixing Mechanisms in a Pair of Impinging Je	PL/RKFA	3- 2
Dr. Raymond D Bellem	Embry-Riddle Aeronautical Univ , Prescott , AZ Radiation Characterization of Commerically Process	PL/VTET	3- 3
DR Gajanan S Bhat	Tennessee , Knoxville , TN Polyetherimide Fibers: Production Processing and	PL/RKFE	3- 4
DR Ronald J Bieniek	University of Missouri-Rolla , Rolla , MO Practical Semiquantal Modelling of Collisional Vib	PL/GPOS	3- 5
DR Jan S Brzosko	Stevens Institute of Tech , Hoboken , NJ Conceptual Study of the Marauder Operation in the	PL/WSP	3- 6
DR Ping Cheng	Hawaii at Manoa , Honolulu , HI Determination of the Interfacial Heat Transfer Coe	PL/VTPT	3- 7
DR Meledath Damodaran	University of Houston-Victoria , Victoria , TX Concurrent Computation of Aberration Coefficients	PL/LIMI	3- 8
Dr. Ronald R DeLyser	University of Denver , Denver , CO Analysis to Determine the Quality Factor of a Comp	PL/WSA	3- 9
DR Jean-Claude M Diels	University of New Mexico , Albuquerque , NM Unidirectional Ring Lasers and Laser Gyros with Mu	PL/LIDA	3- 10
Dr. David M Elliott	Arkansas Technology University , Russellville , AR REPORT NOT AVAILABLE AT PRESS TIME	PL/RKFE	3- 11

SRP Final Report Table of Contents

Author	University/Institution Report Title	Phillips Laboratory Directorate	Vol-Page
DR Vincent P Giannamore	Xavier University of Louisiana , New Orleans , LA An Investigation of Hydroxylammonium Dinitramide:	PL/RKA	3- 12
DR James E Harvey	University of Central Florida , Orlando , FL A New Mission for the Air Force Phillips Laborator	PL/LIM	3- 13
DR Stan Heckman	Massachusettes Inst of technol , Cambridge , MA REPORT NOT AVAILABLE AT PRESS TIME	PL/GPAA	3- 14
DR. James M Henson	University of Nevada , Reno , NV High Resolution Range Doppler Data and Imagery for	PL/WSAT	3- 15
Dr. San-Mou Jeng	University of Cincinnati , Cincinnati , OH Can Design for Cogging of Titanium Aluminide Alloy	PL/RKFA	3- 16
MR. Gerald Kaiser	University of Mass/Lowell , Lowell , MA Physical Wavelets fo Radar and Sonar	PL/GPOS	3- 17
MR Dikshitulu K Kalluri	University of Mass/Lowell , Lowell , MA Backscatter From a Plasma Plume Due to Excitation	PL/GP	3- 18
Lucia M Kimball	Worcester Polytechnic Inst. , Worcester , MA Investigation of Atmospheric Heating and Cooling B	PL/GPOS	3- 19
MR. Albert D Kowalak	University of Massachusetts/Lo , Lowell , MA Investigations of Electron Interactions with Molec	PL/GPID	3- 20
MR. Walter S Kuklinski	University of Mass/Lowell , Lowell , MA Ionspheric Tomography Using a Model Based Transfor	PL/GP	3- 21
Dr. Min-Chang Lee	Massachusetts Institute , Cambridge , MA Studies of Plasma Turbulence with Versatile Toroid	PL/GPSG	3- 22

SRP Final Report Table of Contents

Author	University/Institution Report Title	Phillips Laboratory Directorate	Vol-Page
DR Kevin J Malloy	University of New Mexico , Albuquerque , NM REPORT NOT AVAILABLE AT PRESS TIME	PL/VTRP	3- 23
Dr. Charles J Noel	Ohio State University , Columbus , OH Preparation and Characterization of Blends of Orga	PL/RKA	3- 24
DR Hayrani A Oz	Ohio State University , Columbus , OH A Hybrid Algebraic Equation of Motion-Neural Estim	PL/VTSS	3- 25
DR Sudhakar Prasad	University of New Mexico , Albuquerque , NM Focusing Light into a Multiple-Core Fiber: Theory	PL/LIMI	3- 26
DR Mark R Purtill	Texas A&M Univ-Kingsville , Kingsville , TX Static and Dynamic Graph Embedding for Parallel Pr	PL/WSP	3- 27
DR Krishnaswamy Ravi-Chandar	University of Houston , Houston , TX On the Constitutive Behavior of Solid Propellants	PL/RKAP	3- 28
Dr. Wolfgang G Rudolph	University of New Mexico , Albuquerque , NM Relaxation Processes In Gain Switched Iodine Laser	PL/LIDB	3- 29
DR Gary S Sales	Univof Massachusetes-Lowell , Lowell , MA Characterization of Polar Patches: Comparison of	PL/GPIA	3- 30
DR I-Yeu Shen	University of Washington , Seattle , WA A Study of Active Constrained Layer Damping Treatm	PL/VTSS	3- 31
DR Melani I Shoemaker	Seattle Pacific University , Seattle , WA Frequency Domain Analysis of Short Exposure, Photo	PL/LIMI	3- 32
DR Yuri B Shtessel	University of Alabama-Huntsvil , Huntsville , AL Topaz II Reactor Control Law Improvement	PL/VTPC	3- 33

SRP Final Report Table of Contents

Author	University/Institution Report Title	Phillips Laboratory Directorate	Vol-Page
Dr. Alexander P Stone	University of New Mexico , Alburquerque , NM Impedances of Coplanar Conical Plates in a Uniform	PL/WSR _____	3- 34
DR Charles M Swenson	Utah State University , Logan , UT Reflected Laser Communication System	PL/VTRA _____	3- 35
Dr. Y. C Thio	University of Miami , Coral Gables , FL A Mathematical Model of Self Compression of Compac	PL/WSP _____	3- 36
DR Jane M Van Doren	College of the Holy Cross , Worcester , MA Investigations of Electron Interactions with Molec	PL/GPID _____	3- 37
DR Daniel W Watson	Utah State University , Logan , UT A Heterogeneous Parallel Architecture for High-Spe	PL/VTEE _____	3- 38
Dr. Wayne J Zimmermann	Texas Woman's University , Denton , TX Determination of Space Debris Flux Based on a Fini	PL/WS _____	3- 39

SRP Final Report Table of Contents

Author	University/Institution Report Title	Rome Laboratory Directorate	Vol-Page
DR Valentine A Aalo	Florida Atlantic University , Boca Raton , FL A Program Plan for Transmitting High-Data-Rate ATM	RL/C3BA	4- 1
DR Moeness G Amin	Villanova University , Villanova , PA Interference Excision in Spread Spectrum Using Ti	RL/C3BB	4- 2
Richard G Barakat	Tufts University , Medford , MA REPORT NOT AVAILABLE AT PRESS TIME	RL/EROP	4- 3
DR David P Benjamin	Oklahoma State University , Stillwater , OK Designing Software by Reformulation Using Kids	RL/C3CA	4- 4
DR Frank T Berkey	Utah State University , Logan , UT The Application of Quadratic Phase Coding to OTH R	RL/OCDS	4- 5
DR Joseph Chaiken	Syracuse University , Syracuse , NY A Study of the Application of Fractuals and Kineti	RL/ERDR	4- 6
Dr. Pinyuen Chen	Syracuse University , Syracuse , NY On Testing the Equality of Covariance Matrices Use	RL/OCTS	4- 7
DR. Julian Cheung	New York Inst. of Technology , New York , , NY On Classification of Multispectral Infrared Image	RL/OCTM	4- 8
DR Ajit K Choudhury	Howard University , Washington , DC Detection Performance of Over Resolved Targets wit	RL/OCTS	4- 9
Dr. Eric Donkor	University of Connecticut , Stroes , CT Experimental Measurement of Nonlinear Effects in	RL/OCPA	4- 10
DR. Frances J Harackiewicz	So. Illinois Univ-Carbondale , Carbondale , IL Circular Waveguide to Microstrip Line Transition	RL/ERA	4- 11

SRP Final Report Table of Contents

Author	University/Institution Report Title	Rome Laboratory Directorate	Vol-Page
DR Joseph W Haus	Rensselaer Polytechnic Inst , Troy , NY Simulation of Erbium-doped Fiber Lasers	RL/OCP	4- 12
DR Yolanda J Kime	SUNY College-Cortland , Cortland , NY A Macroscopic Model of Electromigration: Comparis	RL/ERDR	4- 13
DR. Phillip G Kornreich	Syracuse University , Syracuse , NY Semiconductor Cylinder Fibers for Fiber Light Ampl	RL/OCP	4- 14
DR Guifang Li	Rochester Institute of Tech , Rochester , NY Self-Pulsation and Optoelectronic Feedback-Sustain	RL/OCP	4- 15
Dr. Beth L Losiewicz	Colorado State University , Fort Collins , CO Preliminary Report on the Feasibility of Machine S	RL/IR	4- 16
DR. Mohamad T Musavi	University of Maine , Orono , ME Automatic Extraction of Drainage Network from Di	RL/IR	4- 17
DR John D Norgard	Univ of Colorado-Colorado Sprg , Colorado Springs , CO Infrared Images of Electromagnetic Fields	RL/ERPT	4- 18
DR Michael A Pittarelli	SUNY Institute of Technology , Utica , NY Anytime Inference and Decision Methods	RL/C3CA	4- 19
DR Dean Richardson	SUNY Institute of Technology , Utica , NY Ultrafast Spectroscopy of Quantum Heterostructures	RL/OCP	4- 20
DR. Daniel F Ryder, Jr.	Tufts University , Medford , MA Synthesis and Properties of B-Diketonate-Modified	RL/ERX	4- 21
DR Gregory J Salamo	University of Arkansas , Fayetteville , AR Photorefractive Development and Application of InP	RL/ERX	4- 22

SRP Final Report Table of Contents

Author	University/Institution Report Title	Rome Laboratory Directorate	Vol-Page
Dr. Scott E Spetka	SUNY, Institute of Technology , Utica , NY The TkWWW Robot: Beyond Browsing	RL/IR	4- 23
DR James C West	Oklahoma State University , Stillwater , OK Polarimetric Radar Scattering from a Vegation Can	RL/ERC	4- 24
DR Rolf T Wigand	Syracuse University , Syracuse , NY Transferring Technology Via the Internet	RL/XP	4- 25
Dr. Xi-Cheng Zhang	Rensselaer Polytechnic Institu , Troy , NY Temperature Dependence of THz Emission for <111> G	RL/ERX	4- 26

SRP Final Report Table of Contents

Author	University/Institution Report Title	Wright Laboratory Directorate	Vol-Page
DR Sunil K Agrawal	Ohio Univeristy , Athens , OH A Study of Preform Design Problem for Metal Deform	WL/MLIM _____	5- 1
DR Michael E Baginski	Auburn University , Auburn , AL Calculation of Heating and Temperature Distributio	WL/MNMF _____	5- 2
Dr. William W Bannister	Univ of Massachusetts-Lowell , Lowell , MA Anomalous Effects of Water in Fire Firefighting:	WL/FIVC _____	5- 3
Mr. Larry A Beardsley	Athens State College , Athens , AL RFSIG Target Model Intergrated With the Joint Mode	WL/MNSH _____	5- 4
DR Thomas L Beck	McMicken Coll of Arts & Sci , , OH Multigrid Method for Large Scale Electronic Struct	WL/MLPJ _____	5- 5
DR Victor L Berdichevsky	Wayne State University , Detroit , MI Diffusional Creep in Metals and Ceramics at High T	WL/FIB _____	5- 6
DR. Steven W Buckner	Colullmbus College , Columbus , GA Quantitation of Dissolved O2 in Aviation Fuels by	WL/POSF _____	5- 7
DR. James J Carroll	Clarkson University , Potsdam , NY Development of an Active Dynamometer System	WL/POOC- _____	5- 8
Dr. Ching L Chang	Cleveland State University , Cleveland , OH Least-Squares Finite Element Methods for Incompres	WL/FIMM _____	5- 9
Dr. David B Choate	Transylvania University , Lexington , KY A New Superposition	WL/AAWP _____	5- 10
DR Stephen J Clarson	University of Cincinnati , Cincinnati , OH Synthesis of Novel Second and Third Order Nonlinea	WL/MLBP _____	5- 11

SRP Final Report Table of Contents

Author	University/Institution Report Title	Wright Laboratory Directorate	Vol-Page
Dr. Milton L Cone	Embry-Riddel Aeronautical Univ , Prescott , AZ The Sensor Manager Puzzle	WL/AAAS- _____	5- 12
DR Robert W Courter	Louisiana State University , Baton Rouge , LA A Research Plan for Evaluating Wavegun as a Low-Lo	WL/MNAA _____	5- 13
DR Vinay Dayal	Iowa State University , Ames , IA Longitudinal Waves in Fluid Loaded Composite Fiber	WL/MLLP _____	5- 14
DR Jeffrey C Dill	Ohio University , Athens , OH Discrete Wavelet Transforms for Communication Sign	WL/AAW _____	5- 15
DR Vincent G Dominic	University of Dayton , Dayton , OH Electro-Optic Characterization of Poled-Polymer Fi	WL/MLPO _____	5- 16
DR Franklin E Eastep	University of Dayton , Dayton , OH Influence of Mode Complexity and Aeroelastic Con	WL/FIBR _____	5- 17
DR Georges M Fadel	Clemson University , Clemson , SC A Methodology for Affordability in the Design Proc	WL/MTR _____	5- 18
Dr. Joel R Fried	University of Cincinnati , Cincinnati , OH Computer Modeling of Electrolytes for Battery Appl	WL/POOS- _____	5- 19
DR Paul D Gader	University of Missouri-Columbi , Columbia , MO Scanning Image Algebra Networks for Vehicle Identi	WL/MNGA _____	5- 20
DR Philip Gatt	University of Central Florida , Orlando , FL Laser Radar Performance Modelling and Analysis wit	WL/MNGS _____	5- 21
Dr. Richard D Gould	North Carolina State Univ , Raleigh , NC Analysis of Laser Doppler Velocimetry Data	WL/POPT _____	5- 22

SRP Final Report Table of Contents

Author	University/Institution Report Title	Wright Laboratory Directorate	Vol-Page
Dr. Raghava G Gowda	University of Dayton , Dayton , OH Issues Involved in Developing an Object-oriented S	WL/AAAS- _____	5- 23
DR Guoxiang Gu	Louisiana State University , Baton Rouge , LA Gain Scheduled Missile Autopilot Design Using Obse	WL/MNAG _____	5- 24
Dr Venkata S Gudimetla	OGI , Portland , OR Thermal Modeling of Heterojunction Bipolar Transis	WL/ELMT _____	5- 25
Dr. Raimo J Hakkinen	Washington University , St. Louis , MO Further Development of Surface-Obstacle Instrument	WL/FIMN _____	5- 26
DR Russell C Hardie	Univisity of Dayton , Dayton , OH Adaptive Quadratic Classifiers for Multispectral T	WL/AARA _____	5- 27
DR Larry S Helmick	Cedarville College , Cedarville , OH Effect of Humidity on Friction and Wear for Fombli	WL/MLBT _____	5- 28
DR Alan S Hodel	Auburn University , Auburn , AL Automatic Control Issues in the Development of an	WL/MNAG _____	5- 29
DR Vinod K Jain	University of Dayton , Dayton , OH Can Design for Cogging of Titanium Aluminide Alloy	WL/MLLN _____	5- 30
DR Jonathan M Janus	Mississippi State University , Mississippi State , MS Multidemensional Algorithm Development and Analysi	WL/MNAA _____	5- 31
DR Iwona M Jasiuk	Michigan State University , East Lansing , MI Characterization of Interfaces in Metal Matrix Com	WL/WLL _____	5- 32
Dr. Jack S Jean	Wright State University , Dayton , OH Reed-Solomon Decoding on Champ Architecture	WL/AAAT- _____	5- 33

SRP Final Report Table of Contents

Author	University/Institution Report Title	Wright Laboratory Directorate	Vol-Page
Dr. Ismail I Jouny	Lafayette College , Easton , PA Modeling and Mitigation of Terrain Scattered Inter	WL/AARM	5- 34
DR Tribikram Kundu	University of Arizona , Tucson , AZ Lamb Wave Scanning of a Multilayed Composite Plate	WL/MLLP	5- 35
DR. Jian Li	University of Florida , Gainesville , FL High Resolution Range Signature Estimation	WL/AARA	5- 36
DR. Chun-Shin Lin	University of Missouri-Columbi , Columbia , MO Prediction of Missile Trajectory	WL/FIPA	5- 37
Dr. Paul P Lin	Cleveland State University , Cleveland , OH Three Dimensional Geometry Measurement of Tire Def	WL/FIVM	5- 38
Dr. Juin J Liou	University of Central Florida , Orlando , FL A Model to Monitor the Current Gain Long-Term Inst	WL/ELRD	5- 39
Dr. James S Marsh	University of West Florida , Pensacola , FL Numerical Reconstruction of Holograms in Advanced	WL/MNSI	5- 40
DR Rajiv Mehrotra	Univ. of Missouri-St. Louis , St. Louis , MO Integrated Information Management for ATR Research	WL/AARA	5- 41
DR Douglas J Miller	Cedarville College , Cedarville , OH A Review of Nonfilled Intrinsically Conductive Ela	WL/MLBP	5- 42
DR Nagaraj Nandhakumar	University of Virginia , Charlottesville , VA Thermophysical Affine Invariants from IR Imagery	WL/AARA	5- 43
Dr. M. G Norton	Washington State University , Pullman , WA Surface Outgrowths on Laser-Deposited YBa2Cu3O7 Th	WL/MLPO	5- 44

SRP Final Report Table of Contents

Author	University/Institution Report Title	Wright Laboratory Directorate	Vol-Page
DR. James F O'Brien	Southwest Missouri State Univ. , Springfield , MO The Importance of Lower Orbital Relaxations in Po	WL/MLBP _____	5- 45
DR Krishna M Pasala	University of Dayton , Dayton , OH Performance of Music and Monopulse Algorithms in t	WL/AARM _____	5- 46
DR Robert P Penno	University of Dayton , Dayton , OH An Assessment of the WL/AAAI-4 Antenna Wavefront S	WL/AAAI- _____	5- 47
DR Marek A Perkowski	Portland State University , Portland , OR A Survey of Literature on Function Decomposition	WL/AAAT- _____	5- 48
DR Ramachandran Radharamanan	Marquette University , Milwaukee , WI A Study on Virtual Manufacturing	WL/MTI _____	5- 49
DR Ramu V Ramaswamy	University of Florida , Gainesville , FL Annealed Proton Exchanged (APE) Waveguides in LiTa	WL/MNG _____	5- 50
DR Stanley J Reeves	Auburn University , Auburn , AL Superresolution of Passive Millimeter-Wave Imaging	WL/MNGS _____	5- 51
Dr. William K Rule	University of Alabama , Tuscaloosa , AL <RESTRICTED DISTRIBUTION - CONTACT LABORATORY>	WL/MNM _____	5- 52
DR Arindam Saha	Mississippi State University , Mississippi State , MS Evaluation of Network Routers in Real-Time Paralle	WL/AAAT- _____	5- 53
DR John J Schauer	University of Dayton , Dayton , OH Turbine Blade Film Jet Cooling with Free Stream Tu	WL/POTT _____	5- 54
DR Carla A Schwartz	University of Florida , Gainesville , FL Neural Networks Identification and Control in Meta	WL/FIGC _____	5- 55

SRP Final Report Table of Contents

Author	University/Institution Report Title	Wright Laboratory Directorate	Vol-Page
DR. James P Seaba	University of Missouri-Columbi , Columbia , MO Multiple Jet Mixing and Atomization in Reacting an	WL/POSF _____	5- 56
DR Sivanand Simanapalli	University of NC-Charlotte , Charlotte , NC HRR Radar Based Target Identification	WL/AARA _____	5- 57
DR. Terrence W Simon	University of Minnesota , Minneapolis , MN Documentation of Boundary Layer Characteristics Fo	WL/POTT _____	5- 58
DR Marek Skowronski	Carnegie Melon University , Pittsburgh , PA Mechanism for Indium Segregation In InxGa1-xAs Str	WL/ELRA _____	5- 59
DR Joseph C Slater	Wright State Univesity , Dayton , OH QFT Control of an Advanced Tactical Fighter Aeroel	WL/FIGS _____	5- 60
DR John A Tague	Ohio University , Athens , OH Performance Analysis of Quadratic Classifiers for	WL/AARA _____	5- 61
Dr. Barney E Taylor	Miami Univ. - Hamilton , Hamilton , OH Electroluminescence Studies of the Rigid Rod Polym	WL/MLBP _____	5- 62
DR Krishnaprasad Thirunarayan	Wright State University , Dayton , OH VHDL-93 Paser in Prolog	WL/ELED _____	5- 63
DR Robert B Trelease	University of California , Los Angeles , CA Developing Qualitative Process Control Discovery S	WL/MLIM _____	5- 64
DR. Chi-Tay Tsai	Florida Atlantic University , Boca Raton , FL A Study of Massively Parallel Computing on Epic Hy	WL/MNM _____	5- 65
DR James M Whitney	University of Dayton , Dayton , OH Stress Analysis of the V-Notch (Iosipescu) Shear T	WL/MLBM _____	5- 66

SRP Final Report Table of Contents

Author	University/Institution Report Title	Arnold Engineering Development Center Directorate	Vol-Page
DR Ben A Abbott	Vanderbilt University , Nashville , TN The Application Challenge	Sverdrup	6- 1
DR Theodore A Bapty	Vanderbilt University , Nashville , TN Development of Large Parallel Instrumentation Syst	Sverdrup	6- 2
Dr. Csaba A Biegl	Vanderbilt University , Nashville , TN Univeral Graphic User Inteface for Turbine Engine	Sverdrup	6- 3
DR Steven H Frankel	Purdue University , West Lafayette , IN Towards The Computational Modeling of Postall Gas	Sverdrup	6- 4
Dr. Peter R Massopust	Sam Houston State University , Huntsville , TX A Wavelet-Multigrid Approach To Solving Partial Di	Calspan	6- 5
DR Randolph S Peterson	University of the South , Sewanee , TN Infrared Imaging Fourier Transform Spectrometer	Sverdrup	6- 6
DR Roy J Schulz	Univ of Tennessee Space Inst , Tullahoma , TN Design of Soot Capturing Sample Probe	Sverdrup	6- 7
DR S A Sherif	College of Eng-Univ of Florida , Gainesville , FL A Model For Local Heat Transfer & Ice Accretion In	Sverdrup	6- 8
DR. Michael Sydor	University of Minnesota-Duluth , Duluth , MN Dimensional Analysis of ARC Heaters	Calspan	6- 9
Dr. John T Tarvin	Samford University , Birmingham , AL Ultraviolet Flat-Field Response of an Intensified	CALSPAN	6- 10

SRP Final Report Table of Contents

Author	University/Institution Report Title	Frank J Seiler Research Laboratory Directorate	Vol-Page
Dr. Gene O Carlisle	West Texas State University , Canyon , TX REPORT NOT AVAILABLE AT PRESS TIME	FJSRL/ NC	6- 11
DR John R Dorgan	Colorado School of Mines , Golden , CO Fundamental Studies on the Solution and Adsorption	FJSRL/NE	6- 12
DR Mary Ann Jungbauer	Barry University , Miami , FL Non-Linear Optical Properties of a Series of Linea	FJSRL/NC	6- 13
DR. Lawrence L Murrell	Pennsylvania State University , University Park , PA Catalytic Gasification of Pitch Carbon Fibers with	FJSRL/NE	6- 14
DR David E Statman	Allegheny College , Meadville , PA Charge Transport and Second Harmonic Generation in	FJSRL/NP	6- 15

SRP Final Report Table of Contents

Author	University/Institution Report Title	Wilford Hall Medical Center Directorate	Vol-Page
DR Walter Drost-Hansen	University of Miami , Coral Gables , FL Effects of Temperature on Various Hematological Pa	WHMC/RD	6- 16

1. INTRODUCTION

The Summer Research Program (SRP), sponsored by the Air Force Office of Scientific Research (AFOSR), offers paid opportunities for university faculty, graduate students, and high school students to conduct research in U.S. Air Force research laboratories nationwide during the summer.

Introduced by AFOSR in 1978, this innovative program is based on the concept of teaming academic researchers with Air Force scientists in the same disciplines using laboratory facilities and equipment not often available at associates' institutions.

AFOSR also offers its research associates an opportunity, under the Summer Research Extension Program (SREP), to continue their AFOSR-sponsored research at their home institutions through the award of research grants. In 1994 the maximum amount of each grant was increased from \$20,000 to \$25,000, and the number of AFOSR-sponsored grants decreased from 75 to 60. A separate annual report is compiled on the SREP.

The Summer Faculty Research Program (SFRP) is open annually to approximately 150 faculty members with at least two years of teaching and/or research experience in accredited U.S. colleges, universities, or technical institutions. SFRP associates must be either U.S. citizens or permanent residents.

The Graduate Student Research Program (GSRP) is open annually to approximately 100 graduate students holding a bachelor's or a master's degree; GSRP associates must be U.S. citizens enrolled full time at an accredited institution.

The High School Apprentice Program (HSAP) annually selects about 125 high school students located within a twenty mile commuting distance of participating Air Force laboratories.

The numbers of projected summer research participants in each of the three categories are usually increased through direct sponsorship by participating laboratories.

AFOSR's SRP has well served its objectives of building critical links between Air Force research laboratories and the academic community, opening avenues of communications and forging new research relationships between Air Force and academic technical experts in areas of national interest; and strengthening the nation's efforts to sustain careers in science and engineering. The success of the SRP can be gauged from its growth from inception (see Table 1) and from the favorable responses the 1994 participants expressed in end-of-tour SRP evaluations (Appendix B).

AFOSR contracts for administration of the SRP by civilian contractors. The contract was first awarded to Research & Development Laboratories (RDL) in September 1990. After completion of the 1990 contract, RDL won the recompetition for the basic year and four 1-year options.

2. PARTICIPATION IN THE SUMMER RESEARCH PROGRAM

The SRP began with faculty associates in 1979; graduate students were added in 1982 and high school students in 1986. The following table shows the number of associates in the program each year.

Table 1: SRP Participation, by Year

YEAR	Number of Participants			TOTAL
	SFRP	GSRP	HSAP	
1979	70			70
1980	87			87
1981	87			87
1982	91	17		108
1983	101	53		154
1984	152	84		236
1985	154	92		246
1986	158	100	42	300
1987	159	101	73	333
1988	153	107	101	361
1989	168	102	103	373
1990	165	121	132	418
1991	170	142	132	444
1992	185	121	159	464
1993	187	117	136	440
1994	192	117	133	442

Beginning in 1993, due to budget cuts, some of the laboratories weren't able to afford to fund as many associates as in previous years; in one case a laboratory did not fund any additional associates. However, the table shows that, overall, the number of participating associates increased this year because two laboratories funded more associates than they had in previous years.

3. RECRUITING AND SELECTION

The SRP is conducted on a nationally advertised and competitive-selection basis. The advertising for faculty and graduate students consisted primarily of the mailing of 8,000 44-page SRP brochures to chairpersons of departments relevant to AFOSR research and to administrators of grants in accredited universities, colleges, and technical institutions. Historically Black Colleges and Universities (HBCUs) and Minority Institutions (MIs) were included. Brochures also went to all participating USAF laboratories, the previous year's participants, and numerous (over 600 annually) individual requesters.

Due to a delay in awarding the new contract, RDL was not able to place advertisements in any of the following publications in which the SRP is normally advertised: *Black Issues in Higher Education*, *Chemical & Engineering News*, *IEEE Spectrum* and *Physics Today*.

High school applicants can participate only in laboratories located no more than 20 miles from their residence. Tailored brochures on the HSAP were sent to the head counselors of 180 high schools in the vicinity of participating laboratories, with instructions for publicizing the program in their schools. High school students selected to serve at Wright Laboratory's Armament Directorate (Eglin Air Force Base, Florida) serve eleven weeks as opposed to the eight weeks normally worked by high school students at all other participating laboratories.

Each SFRP or GSRP applicant is given a first, second, and third choice of laboratory. High school students who have more than one laboratory or directorate near their homes are also given first, second, and third choices.

Laboratories make their selections and prioritize their nominees. AFOSR then determines the number to be funded at each laboratory and approves laboratories' selections.

Subsequently, laboratories use their own funds to sponsor additional candidates. Some selectees do not accept the appointment, so alternate candidates are chosen. This multi-step selection procedure results in some candidates being notified of their acceptance after scheduled deadlines. The total applicants and participants for 1994 are shown in this table.

Table 2: 1994 Applicants and Participants

PARTICIPANT CATEGORY	TOTAL APPLICANTS	SELECTEES	DECLINING SELECTEES
SFRP	600	192	30
(HBCU/MI)	(90)	(16)	(7)
GSRP	322	117	11
(HBCU/MI)	(11)	(6)	(0)
HSAP	562	133	14
TOTAL	1484	442	55

4. SITE VISITS

During June and July of 1994, representatives of both AFOSR/NI and RDL visited each participating laboratory to provide briefings, answer questions, and resolve problems for both laboratory personnel and participants. The objective was to ensure that the SRP would be as constructive as possible for all participants. Both SRP participants and RDL representatives found these visits beneficial. At many of the laboratories, this was the only opportunity for all participants to meet at one time to share their experiences and exchange ideas.

5. HISTORICALLY BLACK COLLEGES AND UNIVERSITIES AND MINORITY INSTITUTIONS (HBCU/MI)s

In previous years, an RDL program representative visited from seven to ten different HBCU/MI's to promote interest in the SRP among the faculty and graduate students. Due to the late contract award date (January 1994) no time was available to visit HBCU/MI's this past year.

In addition to RDL's special recruiting efforts, AFOSR attempts each year to obtain additional funding or use leftover funding from cancellations the past year to fund HBCU/MI associates. This year, seven HBCU/MI SFRPs declined after they were selected. The following table records HBCU/MI participation in this program.

Table 3: SRP HBCU/MI Participation, by Year

YEAR	SFRP		GSRP	
	Applicants	Participants	Applicants	Participants
1985	76	23	15	11
1986	70	18	20	10
1987	82	32	32	10
1988	53	17	23	14
1989	39	15	13	4
1990	43	14	17	3
1991	42	13	8	5
1992	70	13	9	5
1993	60	13	6	2
1994	90	16	11	6

6. SRP FUNDING SOURCES

Funding sources for the 1994 SRP were the AFOSR-provided slots for the basic contract and laboratory funds. Funding sources by category for the 1994 SRP selected participants are shown here.

Table 4: 1994 SRP Associate Funding

FUNDING CATEGORY	SFRP	GSRP	HSAP
AFOSR Basic Allocation Funds	150	98 ^{*1}	121 ^{*2}
USAF Laboratory Funds	37	19	12
HBCU/MI By AFOSR (Using Procured Addn'l Funds)	5	0	0
TOTAL	192	117	133

*1 - 100 were selected, but two canceled too late to be replaced.

*2 - 125 were selected, but four canceled too late to be replaced.

7. COMPENSATION FOR PARTICIPANTS

Compensation for SRP participants, per five-day work week, is shown in this table.

Table 5: 1994 SRP Associate Compensation

PARTICIPANT CATEGORY	1991	1992	1993	1994
Faculty Members	\$690	\$718	\$740	\$740
Graduate Student (Master's Degree)	\$425	\$442	\$455	\$455
Graduate Student (Bachelor's Degree)	\$365	\$380	\$391	\$391
High School Student (First Year)	\$200	\$200	\$200	\$200
High School Student (Subsequent Years)	\$240	\$240	\$240	\$240

The program also offered associates whose homes were more than 50 miles from the laboratory an expense allowance (seven days per week) of \$50/day for faculty and \$37/day for graduate students. Transportation to the laboratory at the beginning of their tour and back to their home destinations at the end was also reimbursed for these participants. Of the combined SFRP and GSRP associates, 58% (178 out of 309) claimed travel reimbursements at an average round-trip cost of \$860.

Faculty members were encouraged to visit their laboratories before their summer tour began. All costs of these orientation visits were reimbursed. Forty-one percent (78 out of 192) of faculty associates took orientation trips at an average cost of \$498. Many faculty associates noted on their evaluation forms that due to the late notice of acceptance into the 1994 SRP (caused by the late award in January 1994 of the contract) there wasn't enough time to attend an orientation visit prior to their tour start date. In 1993, 58 % of SFRP associates took orientation visits at an average cost of \$685.

Program participants submitted biweekly vouchers countersigned by their laboratory research focal point, and RDL issued paychecks so as to arrive in associates' hands two weeks later.

HSAP program participants were considered actual RDL employees, and their respective state and federal income tax and Social Security were withheld from their paychecks. By the nature of their independent research, SFRP and GSRP program participants were considered to be consultants or independent contractors. As such, SFRP and GSRP associates were responsible for their own income taxes, Social Security, and insurance.

8. CONTENTS OF THE 1994 REPORT

The complete set of reports for the 1994 SRP includes this program management report augmented by fifteen volumes of final research reports by the 1994 associates as indicated below:

Table 6: 1994 SRP Final Report Volume Assignments

LABORATORY	VOLUME		
	SFRP	GSRP	HSAP
Armstrong	2	7	12
Phillips	3	8	13
Rome	4	9	14
Wright	5A, 5B	10	15
AEDC, FJSRL, WHMC	6	11	16

AEDC = Arnold Engineering Development Center
 FJSRL = Frank J. Seiler Research Laboratory
 WHMC = Wilford Hall Medical Center

APPENDIX A -- PROGRAM STATISTICAL SUMMARY

A. Colleges/Universities Represented

Selected SFRP and GSRP associates represent 158 different colleges, universities, and institutions.

B. States Represented

SFRP - Applicants came from 46 states plus Washington D.C. and Puerto Rico. Selectees represent 40 states.

GSRP - Applicants came from 46 states and Puerto Rico. Selectees represent 34 states.

HSAP - Applicants came from fifteen states. Selectees represent ten states.

C. Academic Disciplines Represented

The academic disciplines of the combined 192 SFRP associates are as follows:

Electrical Engineering	22.4%
Mechanical Engineering	14.0%
Physics: General, Nuclear & Plasma	12.2%
Chemistry & Chemical Engineering	11.2%
Mathematics & Statistics	8.1%
Psychology	7.0%
Computer Science	6.4%
Aerospace & Aeronautical Engineering	4.8%
Engineering Science	2.7%
Biology & Inorganic Chemistry	2.2%
Physics: Electro-Optics & Photonics	2.2%
Communication	1.6%
Industrial & Civil Engineering	1.6%
Physiology	1.1%
Polymer Science	1.1%
Education	0.5%
Pharmaceutics	0.5%
Veterinary Medicine	0.5%
TOTAL	100%

Table A-1. Total Participants

Number of Participants	
SFRP	192
GSRP	117
HSAP	133
TOTAL	442

Table A-2. Degrees Represented

Degrees Represented			
	SFRP	GSRP	TOTAL
Doctoral	189	0	189
Master's	3	47	50
Bachelor's	0	70	70
TOTAL	192	117	309

Table A-3. SFRP Academic Titles

Academic Titles	
Assistant Professor	74
Associate Professor	63
Professor	44
Instructor	5
Chairman	1
Visiting Professor	1
Visiting Assoc. Prof.	1
Research Associate	3
TOTAL	192

Table A-4. Source of Learning About SRP

SOURCE	SFRP		GSRP	
	Applicants	Selectees	Applicants	Selectees
Applied/participated in prior years	26%	37%	10%	13%
Colleague familiar with SRP	19%	17%	12%	12%
Brochure mailed to institution	32%	18%	19%	12%
Contact with Air Force laboratory	15%	24%	9%	12%
Faculty Advisor (GSRPs Only)	--	--	39%	43%
Other source	8%	4%	11%	8%
TOTAL	100%	100%	100%	100%

Table A-5. Ethnic Background of Applicants and Selectees

	SFRP		GSRP		HSAP	
	Applicants	Selectees	Applicants	Selectees	Applicants	Selectees
American Indian or Native Alaskan	0.2%	0%	1%	0%	0.4%	0%
Asian/Pacific Islander	30%	20%	6%	8%	7%	10%
Black	4%	1.5%	3%	3%	7%	2%
Hispanic	3%	1.9%	4%	4.5%	11%	8%
Caucasian	51%	63%	77%	77%	70%	75%
Preferred not to answer	12%	14%	9%	7%	4%	5%
TOTAL	100%	100%	100%	100%	99%	100%

Table A-6. Percentages of Selectees receiving their 1st, 2nd, or 3rd Choices of Directorate

	1st Choice	2nd Choice	3rd Choice	Other Than Their Choice
SFRP	70%	7%	3%	20%
GSRP	76%	2%	2%	20%

APPENDIX B -- SRP EVALUATION RESPONSES

1. OVERVIEW

Evaluations were completed and returned to RDL by four groups at the completion of the SRP. The number of respondents in each group is shown below.

Table B-1. Total SRP Evaluations Received

Evaluation Group	Responses
SFRP & GSRPs	275
HSAPs	116
USAF Laboratory Focal Points	109
USAF Laboratory HSAP Mentors	54

All groups indicate near-unanimous enthusiasm for the SRP experience.

Typical comments from 1994 SRP associates are:

"[The SRP was an] excellent opportunity to work in state-of-the-art facility with top-notch people."

"[The SRP experience] enabled exposure to interesting scientific application problems; enhancement of knowledge and insight into 'real-world' problems."

"[The SRP] was a great opportunity for resourceful and independent faculty [members] from small colleges to obtain research credentials."

"The laboratory personnel I worked with are tremendous, both personally and scientifically. I cannot emphasize how wonderful they are."

"The one-on-one relationship with my mentor and the hands on research experience improved [my] understanding of physics in addition to improving my library research skills. Very valuable for [both] college and career!"

Typical comments from laboratory focal points and mentors are:

"This program [AFOSR - SFRP] has been a 'God Send' for us. Ties established with summer faculty have proven invaluable."

"Program was excellent from our perspective. So much was accomplished that new options became viable "

"This program managed to get around most of the red tape and 'BS' associated with most Air Force programs. Good Job!"

"Great program for high school students to be introduced to the research environment. Highly educational for others [at laboratory]."

"This is an excellent program to introduce students to technology and give them a feel for [science/engineering] career fields. I view any return benefit to the government to be 'icing on the cake' and have usually benefitted."

The summarized recommendations for program improvement from both associates and laboratory personnel are listed below (Note: basically the same as in previous years.)

- A. Better preparation on the labs' part prior to associates' arrival (i.e., office space, computer assets, clearly defined scope of work).
- B. Laboratory sponsor seminar presentations of work conducted by associates, and/or organized social functions for associates to collectively meet and share SRP experiences.
- C. Laboratory focal points collectively suggest more AFOSR allocated associate positions, so that more people may share in the experience.
- D. Associates collectively suggest higher stipends for SRP associates.
- E. Both HSAP Air Force laboratory mentors and associates would like the summer tour extended from the current 8 weeks to either 10 or 11 weeks; the groups state it takes 4-6 weeks just to get high school students up-to-speed on what's going on at laboratory. (Note: this same argument was used to raise the faculty and graduate student participation time a few years ago.)

2. 1994 USAF LABORATORY FOCAL POINT (LFP) EVALUATION RESPONSES

The summarized results listed below are from the 109 LFP evaluations received.

1. LFP evaluations received and associate preferences:

Table B-2. Air Force LFP Evaluation Responses (By Type)

Lab	Evals Recv'd	How Many Associates Would You Prefer To Get ?								(% Response)			
		SFRP				GSRP (w/Univ Professor)				GSRP (w/o Univ Professor)			
		0	1	2	3+	0	1	2	3+	0	1	2	3+
AEDC	10	30	50	0	20	50	40	0	10	40	60	0	0
AL	44	34	50	6	9	54	34	12	0	56	31	12	0
FJSRL	3	33	33	33	0	67	33	0	0	33	67	0	0
PL	14	28	43	28	0	57	21	21	0	71	28	0	0
RL	3	33	67	0	0	67	0	33	0	100	0	0	0
WHMC	1	0	0	100	0	0	100	0	0	0	100	0	0
WL	46	15	61	24	0	56	30	13	0	76	17	6	0
Total	121	25%	43%	27%	4%	50%	37%	11%	1%	54%	43%	3%	0%

LFP Evaluation Summary. The summarized responses, by laboratory, are listed on the following page. LFPs were asked to rate the following questions on a scale from 1 (below average) to 5 (above average).

2. LFPs involved in SRP associate application evaluation process:
 - a. Time available for evaluation of applications:
 - b. Adequacy of applications for selection process:
3. Value of orientation trips:
4. Length of research tour:
5.
 - a. Benefits of associate's work to laboratory:
 - b. Benefits of associate's work to Air Force:
6.
 - a. Enhancement of research qualifications for LFP and staff:
 - b. Enhancement of research qualifications for SFRP associate:
 - c. Enhancement of research qualifications for GSRP associate:
7.
 - a. Enhancement of knowledge for LFP and staff:
 - b. Enhancement of knowledge for SFRP associate:
 - c. Enhancement of knowledge for GSRP associate:
8. Value of Air Force and university links:
9. Potential for future collaboration:
10.
 - a. Your working relationship with SFRP:
 - b. Your working relationship with GSRP:
11. Expenditure of your time worthwhile:

(Continued on next page)

12. Quality of program literature for associate:
 13. a. Quality of RDL's communications with you:
 b. Quality of RDL's communications with associates:
 14. Overall assessment of SRP:

Laboratory Focal Point Responses to above questions							
	<i>AEDC</i>	<i>AL</i>	<i>FJSRL</i>	<i>PL</i>	<i>RL</i>	<i>WHMC</i>	<i>WL</i>
= <i>Evals Recv'd</i>	10	32	3	14	3	1	46
<i>Question =</i>							
2	90 %	62 %	100 %	64 %	100 %	100 %	83 %
2a	3.5	3.5	4.7	4.4	4.0	4.0	3.7
2b	4.0	3.8	4.0	4.3	4.3	4.0	3.9
3	4.2	3.6	4.3	3.8	4.7	4.0	4.0
4	3.8	3.9	4.0	4.2	4.3	NO ENTRY	4.0
5a	4.1	4.4	4.7	4.9	4.3	3.0	4.6
5b	4.0	4.2	4.7	4.7	4.3	3.0	4.5
6a	3.6	4.1	3.7	4.5	4.3	3.0	4.1
6b	3.6	4.0	4.0	4.4	4.7	3.0	4.2
6c	3.3	4.2	4.0	4.5	4.5	3.0	4.2
7a	3.9	4.3	4.0	4.6	4.0	3.0	4.2
7b	4.1	4.3	4.3	4.6	4.7	3.0	4.3
7c	3.3	4.1	4.5	4.5	4.5	5.0	4.3
8	4.2	4.3	5.0	4.9	4.3	5.0	4.7
9	3.8	4.1	4.7	5.0	4.7	5.0	4.6
10a	4.6	4.5	5.0	4.9	4.7	5.0	4.7
10b	4.3	4.2	5.0	4.3	5.0	5.0	4.5
11	4.1	4.5	4.3	4.9	4.7	4.0	4.4
12	4.1	3.9	4.0	4.4	4.7	3.0	4.1
13a	3.8	2.9	4.0	4.0	4.7	3.0	3.6
13b	3.8	2.9	4.0	4.3	4.7	3.0	3.8
14	4.5	4.4	5.0	4.9	4.7	4.0	4.5

3. 1994 SFRP & GSRP EVALUATION RESPONSES

The summarized results listed below are from the 275 SFRP/GSRP evaluations received.

Associates were asked to rate the following questions on a scale from
1 (below average) to 5 (above average)

1. The match between the laboratories research and your field:	4.6
2. Your working relationship with your LFP:	4.8
3. Enhancement of your academic qualifications:	4.4
4. Enhancement of your research qualifications:	4.5
5. Lab readiness for you: LFP, task, plan:	4.3
6. Lab readiness for you: equipment, supplies, facilities:	4.1
7. Lab resources:	4.3
8. Lab research and administrative support:	4.5
9. Adequacy of brochure and associate handbook:	4.3
10. RDL communications with you:	4.3
11. Overall payment procedures:	3.8
12. Overall assessment of the SRP:	4.7
13. a. Would you apply again?	Yes: 85%
b. Will you continue this or related research?	Yes: 95%
14. Was length of your tour satisfactory?	Yes: 86%
15. Percentage of associates who engaged in:	
a. Seminar presentation:	52%
b. Technical meetings:	32%
c. Social functions:	03%
d. Other	01%

16. Percentage of associates who experienced difficulties in:

- | | |
|---------------------|-----|
| a. Finding housing: | 12% |
| b. Check Cashing: | 03% |

17. Where did you stay during your SRP tour?

- | | |
|----------------------|-----|
| a. At Home: | 20% |
| b. With Friend: | 06% |
| c. On Local Economy: | 47% |
| d. Base Quarters: | 10% |

THIS SECTION FACULTY ONLY:

18. Were graduate students working with you? Yes: 23%

19. Would you bring graduate students next year? Yes: 56%

20. Value of orientation visit:

- | | |
|-----------------|-----|
| Essential: | 29% |
| Convenient: | 20% |
| Not Worth Cost: | 01% |
| Not Used: | 34% |

THIS SECTION GRADUATE STUDENTS ONLY:

21. Who did you work with:

- | | |
|-----------------------|-----|
| University Professor: | 18% |
| Laboratory Scientist: | 54% |

4. 1994 USAF LABORATORY HSAP MENTOR EVALUATION RESPONSES

The summarized results listed below are from the 54 mentor evaluations received.

1. Mentor apprentice preferences:

Table B-3. Air Force Mentor Responses

		How Many Apprentices Would You Prefer To Get ?			
		<i>HSAP Apprentices Preferred</i>			
<i>Laboratory</i>	<i># Evals Recv'd</i>	<i>0</i>	<i>1</i>	<i>2</i>	<i>3+</i>
AEDC	6	0	100	0	0
AL	17	29	47	6	18
PL	9	22	78	0	0
RL	4	25	75	0	0
WL	18	22	55	17	6
Total	54	20%	71%	5%	5%

Mentors were asked to rate the following questions on a scale from 1 (below average) to 5 (above average)

2. Mentors involved in SRP apprentice application evaluation process:
 - a. Time available for evaluation of applications:
 - b. Adequacy of applications for selection process:
3. Laboratory's preparation for apprentice:
4. Mentor's preparation for apprentice:
5. Length of research tour:
6. Benefits of apprentice's work to U.S. Air force:
7. Enhancement of academic qualifications for apprentice:
8. Enhancement of research skills for apprentice:
9. Value of U.S. Air Force/high school links:
10. Mentor's working relationship with apprentice:
11. Expenditure of mentor's time worthwhile:
12. Quality of program literature for apprentice:
13.
 - a. Quality of RDL's communications with mentors:
 - b. Quality of RDL's communication with apprentices:
14. Overall assessment of SRP:

	<i>AEDC</i>	<i>AL</i>	<i>PL</i>	<i>RL</i>	<i>WL</i>
<i># Evals Recv'd</i>	6	17	9	4	18
<i>Question #</i>					
2	100 %	76 %	56 %	75 %	61 %
2a	4.2	4.0	3.1	3.7	3.5
2b	4.0	4.5	4.0	4.0	3.8
3	4.3	3.8	3.9	3.8	3.8
4	4.5	3.7	3.4	4.2	3.9
5	3.5	4.1	3.1	3.7	3.6
6	4.3	3.9	4.0	4.0	4.2
7	4.0	4.4	4.3	4.2	3.9
8	4.7	4.4	4.4	4.2	4.0
9	4.7	4.2	3.7	4.5	4.0
10	4.7	4.5	4.4	4.5	4.2
11	4.8	4.3	4.0	4.5	4.1
12	4.2	4.1	4.1	4.8	3.4
13a	3.5	3.9	3.7	4.0	3.1
13b	4.0	4.1	3.4	4.0	3.5
14	4.3	4.5	3.8	4.5	4.1

5. 1994 HSAP EVALUATION RESPONSES

The summarized results listed below are from the 116 HSAP evaluations received.

HSAP apprentices were asked to rate the following questions on a scale from
1 (below average) to 5 (above average)

1. Match of lab research to you interest:	3.9
2. Apprentices working relationship with their mentor and other lab scientists:	4.6
3. Enhancement of your academic qualifications:	4.4
4. Enhancement of your research qualifications:	4.1
5. Lab readiness for you: mentor, task, work plan	3.7
6. Lab readiness for you: equipment supplies facilities	4.3
7. Lab resources: availability	4.3
8. Lab research and administrative support:	4.4
9. Adequacy of RDL's apprentice handbook and administrative materials:	4.0
10. Responsiveness of RDL's communications:	3.5
11. Overall payment procedures:	3.3
12. Overall assessment of SRP value to you:	4.5
13. Would you apply again next year?	Yes: 88%
14. Was length of SRP tour satisfactory?	Yes: 78%
15. Percentages of apprentices who engaged in:	
a. Seminar presentation:	48%
b. Technical meetings:	23%
c. Social functions:	18%

**A PROGRAM PLAN FOR TRANSMITTING
HIGH-DATA-RATE ATM/SONET SIGNALS OVER THE ACTS**

**Valentine Aalo
Assistant Professor
Electrical Engineering Department
Florida Atlantic University
500 North West 20th Street
Boca Raton, FL 33431**

**Okechukwu Ugweje
Electrical Engineering Department
Florida Atlantic University
500 North West 20th Street
Boca Raton, FL 33431**

**Final Report For:
Summer Research Program
Rome Laboratory**

**Sponsored By:
Air Force Office of Scientific Research
Bolling Air Force Base, Washington, D.C.**

and

U.S. Air Force Rome Laboratory

September 1994

**A PROGRAM PLAN FOR TRANSMITTING
HIGH-DATA-RATE ATM/SONET SIGNALS OVER THE ACTS**

**Valentine Aalo
Assistant Professor
Electrical Engineering Department
Florida Atlantic University**

**Okechukwu Ugweje
Electrical Engineering Department
Florida Atlantic University**

Abstract

The feasibility, desirability and usefulness of Asynchronous Transfer Mode and Synchronous Optical Network transmission protocols over the Advanced Communications Technology Satellite (ACTS) was studied. A program plan for the transmission of Asynchronous Transmission Mode and Synchronous Optical Network signals at high data rates via the ACTS satellite was developed for the U. S. Air Force Rome Laboratory. The high data rate terminals will transmit and receive signals at DS-3 (45 Mbps) and OC-3 (155 Mbps) over the NASA's ACTS.

A PROGRAM PLAN FOR TRANSMITTING HIGH-DATA-RATE ATM/SONET SIGNALS OVER THE ACTS

Valentine Aalo
Okechukwu Ugweje

1 INTRODUCTION

Communication systems have developed at a very rapid pace over the last decade. One of the outcomes of this development is in the area of broadband packet switching. In the last few years, research activities in this field have been very active. Hardly any publication presently on switching networks can be opened without the mention of ATM. ATM is now regarded as the communication protocol of the future and all efforts are being made by researchers to find more effective use of this new technology.

The objective of this program plan is to study the feasibility, desirability and usefulness of using ATM/SONET transmission protocols over the NASA's Advanced Communication Transmission Satellite (ACTS) for multimedia application at HDR. This objective is a subset of a proposed high speed network under development which will link the assets of the Air Force at Rome Laboratory (RL), the Army at Communications Electronic Command (CECOM), and the Navy at Naval Research and Development (NRaD). This network has the potential of becoming a world wide broadband network connecting a large number of remote tactical sites (i.e. U.S. Navy ships) with voice, video and data. This objective will then be integrated into the Technical Technology Cooperation Program (TTCP) network in which RL will communicate via the satellite with the Canadians at the Communication Research Centre (CRC), NRaD will communicate with the Australians and CECOM with Great Britain [1].

The proposed experiment will consist of two phases. Under phase I experiment, the transmission of ATM cells will be performed at 45 Mbps between RL and CRC. Phase II experiment will be performed between RL and the Joint Interoperability Test Center (JITC), Ft. Huachuca, Arizona at 155 Mbps.

This report describes the program plan necessary to achieve these objectives. It documents the equipment and satellite requirements, data requirements, test procedures and all relevant mathematical calculations.

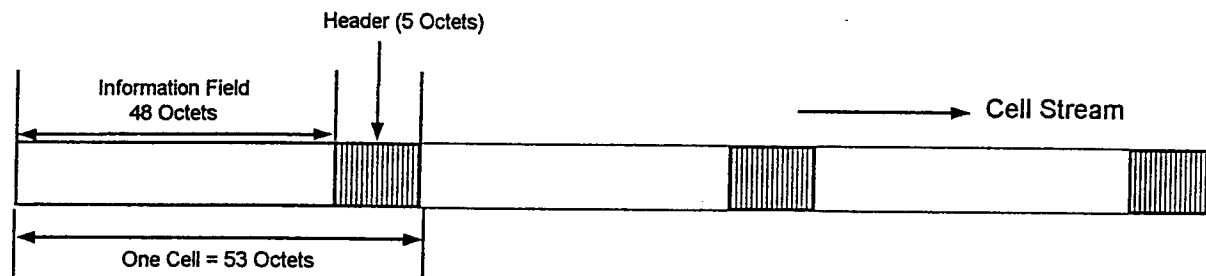
2 PRELIMINARIES

2.1 Asynchronous Transfer Mode (ATM)

ATM is a broad-bandwidth, low delay, packet-like switching and multiplexing protocol. It is a technique that uses constant-length packets as the basic units whereby the user information is carried in cells and is transferred asynchronously when it appears at the input of a communication system. It is essentially connection oriented whereby information is buffered as it arrives and inserted into an ATM cell when there is enough to fill the cell, and is then transported asynchronously across the network.

2.1.1 Basic Principles of ATM

Cell Structure:



1 octet = 1 byte;

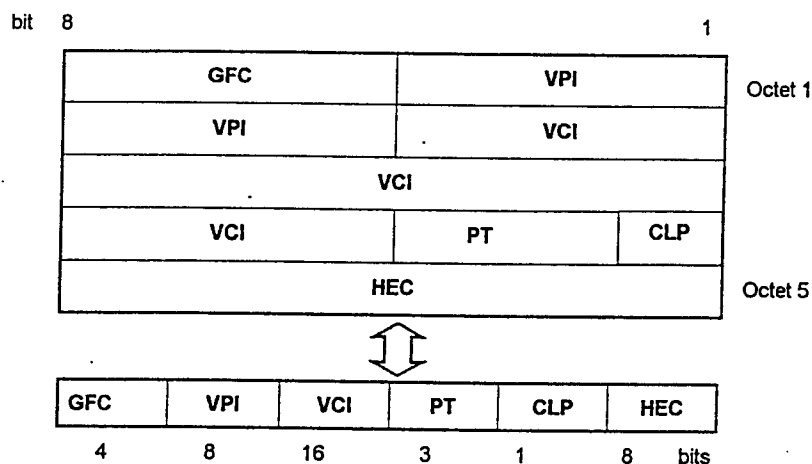
1 cell = 53 octets = 424 bits;

Header = 5 octets = 40 bits.

Two header cell formats have been specified.

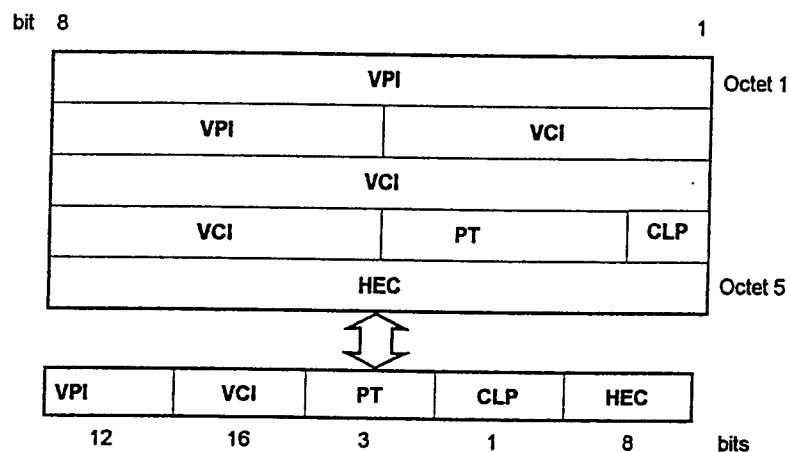
1. User-Network Interface (UNI)

This header format is used for user-to-ATM connections.



2. Network-Node Interface (NNI)

NNI is used for ATM-to-ATM connections.



where GFC: Generic Flow Control
VCI: Virtual Channel Identifier
CLP: Cell Loss Priority

VPI: Virtual Path Identifier
PT: Payload Type
HEC: Header Error Control

In ATM, cells from more than one connection are multiplexed together, and at the receiving end the cell sequence is preserved. The information field (payload) is transported transparently (i.e. no error correction done) across the network by the ATM. Because it is a connection-oriented technique, a path must be established between the users before any information can be exchanged.

ATM Layers:

The ATM layer is concerned with transporting information across the network. It uses virtual connections for information transport and is divided into the virtual path and the virtual channel. The ATM layer performs functions such as generic flow control, cell header generation and extraction, cell virtual identifier translations and cell multiplexing and demultiplexing.

Due to the statistical behavior of the ATM network and the fact that a theoretical unlimited number of virtual connections can share the same link, it is required that an ATM switch synchronize to the incoming cell stream and examine the header field of each cell in order to identify the virtual connection and derive routing and control information for the switch network.

Another important aspect of the ATM protocol is the ATM Adaptation Layer (AAL). The ATM layer is independent of the services it carries and it relies on the AAL to adapt higher level data into a format that it can handle. AAL performs the necessary mapping between the ATM layer and the higher layers. Also, due to the payload independence, all the functions specific to the services are provided at the boundary of the ATM network and are performed by the AAL. Within the AAL, data flow can be corrupted by errors in transmission or it can suffer cell delay variation as a result of variable delay in buffers or through congestion in the network, thereby leading to cell loss or misdelivery of cells [2]. Since the services are dependent on the AAL type, it supports multiple protocols to fit the needs of the user.

2.1.2 Properties of ATM

Merits

- 1 ATM has the flexibility to match the rate of transmission to the rate of reception (i.e. variable bit rate). ATM can transport constant-bit-rate information at the same time as a variable-bit-rate bursty data. It does this by using a different ATM adaptation layer for each service being carried. Information can be transmitted through existing copper wire as well as through optical fibers.
- 2 The transmission of cells is matched to the generation of information such that it does not

transmit wasted cells during period of low multiplexing. This is known as statistical multiplexing.

- 3 ATM offers the ability of integrating various sources or media into one link. It can be applied to data, voice and video and may be used to integrate these applications.

Demerits

- 1 Cell delay variations (CDV)

This arises from the variable delays introduced into the network by the queues at the switches and multiplexers. This delay leads to a change in the expected gap between cells and is most acute in delay sensitive services such as speech transmission.

2. Cell Assembly Delay (CAD)

This arises because information from the source is buffered until there is sufficient information to fill a cell. The waiting time in the buffer depends on the arrival rate. This delay is also acute in delay sensitive services.

2.1.3 Theoretical Considerations and Practical Limitations

The theoretical analysis of the ATM systems is beyond the scope of this report. However, we will mention some important active research issues in ATM networks.

One of these issues is the cell loss performance of ATM networks. Cell loss probability has been estimated by model simulations using Monte Carlo and Importance Sampling simulation methods. The problem with these types of analysis is that the statistical behavior of the input and output queuing properties of the ATM switch has additional restrictions imposed on them. This is because the changes imposed by ATM queuing system introduces nonlinearity, large memory with random length, and complex traffic conditions. Thus a more suitable model (other than the conventional queuing theory) needs to be developed whereby the bias is applied to the conditional arrival probabilities.

Some of the practical aspects of ATM include the issue of generating and collecting ATM traffic using the adapter cards, the vulnerability of ATM signals to burst errors, and link BER characterization variation as a function of transmit power on the uplink.

2.2 Advanced Communication Technology Satellite (ACTS)

Spectrum congestion resulting from increased demand for telecommunications services have forced satellite system planners to consider operating at very high frequencies. ACTS is NASA's latest experimental communication satellite which was developed in order to research on how to accommodate this

projected increase in telecommunications demand in the future by effective utilization of the frequency spectrum. ACTS operates in the Ka-band (30/20 GHz) where atmospheric distortions, especially rain attenuation, are severe.

The on-orbit configuration of ACTS is shown in Figure 1 [3]. ACTS employs several elements not found in conventional bent-pipe transponders. Among many features of ACTS, the following are more profound:

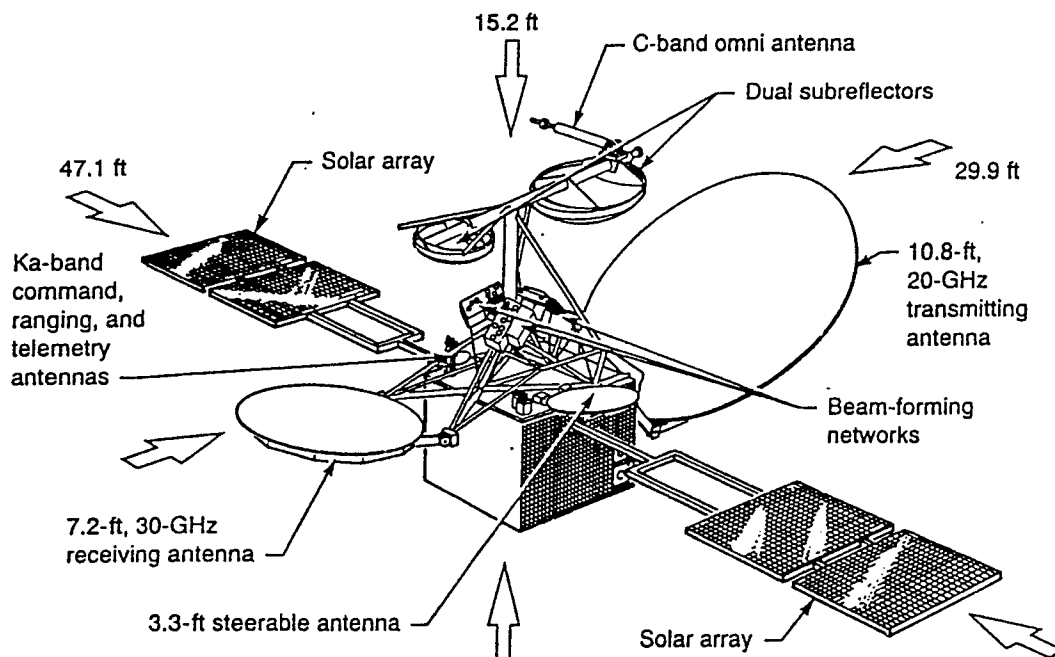


Figure 1: ACTS On-orbit Configuration

Multibeam Antenna (MBA)

ACTS employs multiple dynamically hopping spot beams. The MBA consists of two high-gain offset-feed Cassegrain antenna systems: one for uplink reception at 30 GHz band (2.2 m) with nominal gain of 60.2 dB, and the other for downlink transmission at 20 GHz band (3.3 m) with nominal gain of 56.7 dB.

Each antenna has five ports, two Baseband Forming Network (BFN) ports and three fixed-beam ports. Any part of the port can be connected to the Baseband Processor through the waveguide switches. These BFN ports are the East and West hopping beams receiving families. The operation of these two families are similar. Also connected to the West beam family is the steerable antenna which can be connected to any point in U.S.A. and Canada. It is possible to transmit and receive simultaneously through the steerable antenna, but it can only access one ground location at a time. If experiments are not co-located, using the steerable beam for uplink and downlink will not be possible. Also, its main reflector is smaller and thus smaller gain is achieved when the steerable antenna is used.

On-board Switching and Processing System

There are two radiofrequency communication modes: Baseband Processor mode (BBP) and the Microwave Switch Matrix mode (MSM). In the BBP mode the received signal is demodulated, encoded or decoded if necessary, routed, and remodulated by the baseband processor and then retransmitted. Modulation for BBP must be serial MSK. BBP can receive modulated signal at two different transmission rates but output is limited to 100 mega symbols per second. It can accommodate 15 dB of uplink fade and 6 dB of downlink fade and still achieve bit error rate of 10^{-6} [3].

For the MSM mode of operation, the received signal are transmitted back without processing. The MSM is a programmable 4X4 switch that can connect a maximum of three transmitters to three receivers. It can operate in two modes: the static mode or the dynamic mode. The static mode is equivalent to the conventional "bent pipe" satellite mode of operation in which the switch configuration is fixed. In this mode, traffic can be FDMA or very high-burst-rate TDMA and bandwidth is limited to one GHz. In the dynamic mode, traffic is switched around rapidly, and the modulation method is limited to digital modulation schemes, such as BPSK or QPSK. MSM mode can support 12 dB (8 dB) of uplink (downlink) fades and still achieve bit error rate of 10^{-6} .

3 TEST OBJECTIVE

Rome Laboratory is part of the Secure Survivable Communications Network (SSCN) program which has the objective (among others) of determining the feasibility, desirability and usefulness of ATM protocol as the communication backbone in a tactical environment. To accomplish this objective, RL will conduct series of tests over satellite links carrying ATM cells.

Satellites provide fast, low cost communication infrastructure deployable in a tactical environment where terrestrial network does not exist. ATM allows access to all types of media (voice, data, video). A combination of ATM and satellite provide an improved quality of service. This test will be an investigative test with the objective of verifying the above assertions. Each phase of this test will be further subdivided into two subtests.

3.1 Subtest I

Subtest I will be for the characterization of the satellite channel. Its purpose will be to establish the operating points of the channel and for link budget analysis. To specify the transmission quality of ATM cells over the ACTS at the rate of interest, the transmission performance obtained in conjunction with the Earth Station Terminals (EST) must be determined. In order to determine this, the carrier-to-noise ratio and the receiving system noise temperature in the presence and absence of rain is considered. This is because the most limiting factor in the Ka-band satellite transmission is rain fade.

Using the information on ACTS and the EST parameters, link budget calculations were made. These calculations include the uplink and downlink budget for RL node, the estimated uplink and downlink budget for CRC and the uplink and downlink budget for JITC.

3.2 Subtest II

Subtest II will be concerned with the application of ATM protocol over the satellite. To determine to what extent ATM cells can be transmitted over the ACTS, file transfer, video teleconferencing (VTC) and/or both will be used. Files (data files only) will be created and transmitted over the link. A copy of the transmitted files will be kept for comparison with the received files. Using the assets of the network group at RL and presumably at CRC and JITC, VTC will be established between any two nodes. The success or failure of the VTC will be noted and participating members will be asked to evaluate the quality of the services.

File transfer and video teleconferencing will be carried out simultaneously and if possible a voice transmission will be integrated. The objective is to determine the multimedia capabilities of ATM transmissions.

3.3 Data Acquisition and Analysis of Result

During link characterization, the cell loss rate, cell error rate and the link bit error rate will be determined or computed from measured data. The data collecting forms are given in Appendix B.

The transferred files are compared with the received files in order to determine the following:

- a. Percent of transferred files without error and the percent of errored files.
- b. For the errored files, the severity of the error.
- c. Any correlation of error with the properties of the transmission data.

All relevant information must be recorded on data collection sheet.

For the VTC case, the quality of the video transfer must be determined. The participants are asked to subjectively evaluate the quality of service and record their observations.

An important objective in any experiment is to collect some information. A more important objective is to be able to interpret accurately the meaning of the collected data. In this experiment, we expect ATM cells to be lost, files to be corrupted and link BER to rise above expectations. This experiment must try to answer why these errors occur so that subsequent experiments will prevent or minimize the occurrence of these errors.

To achieve this objective, the results will be discussed with reference to, a) BER, b) causes of cell loss, c) discussion of limiting factors, and d) the correlation of data to error. The issue of generating enough data to fully load the channel should be discussed. And if the channel is not fully loaded, the exact rate at which experiment was performed must be specified.

4 SETUP AND CONFIGURATION

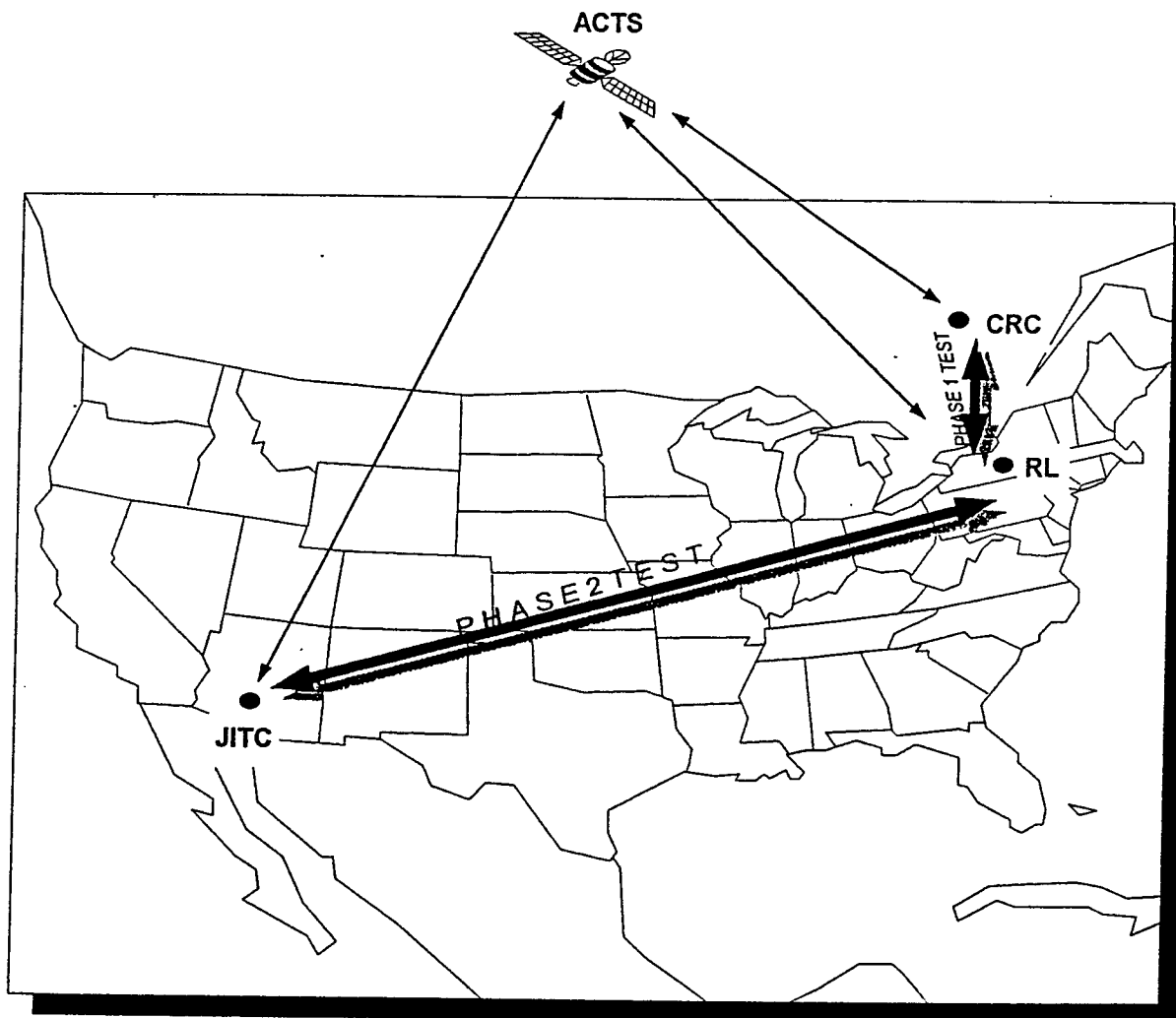
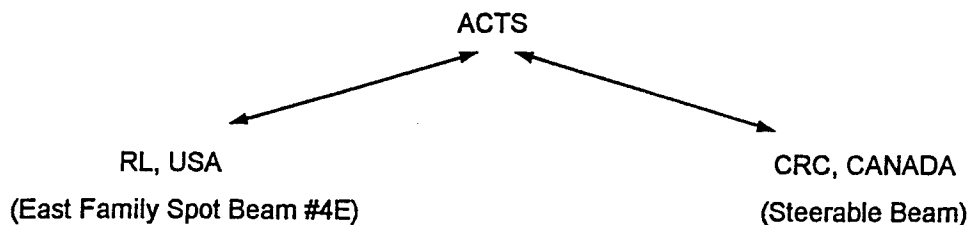


Figure 2: Experiment Setup (USA and Canada)

4.1 Experiment Description

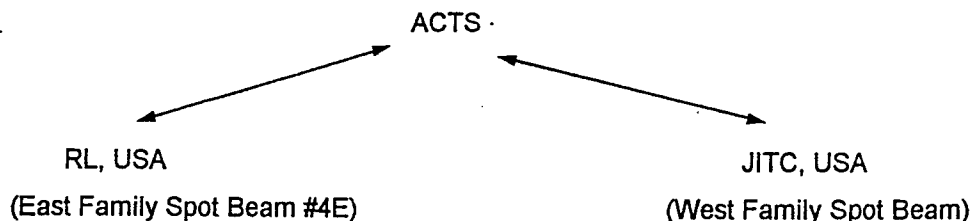
Phase I experiment will link RL to CRC. The terminals at RL and CRC will transmit and receive ATM signal at DS-3 rates over the ACTS. CRC will provide the two terminals for this experiment. RL has a commitment from CRC to upgrade two of their old terminals (originally used with the Olympus satellite at DS-1 rate) to be able to operate at DS-3 rates. It is our understanding that these two terminals are upgradable to be compatible with the ACTS. For this experiment, we suggest the following scenario.



RL: Latitude: 43° 13' 13.176" N
 Longitude: 75° 24' 34.003" W
 Spot Beam 4E: Latitude: 42° 75' N
 Longitude: 74° 86' W

CRC: Latitude: 46.05° N
 Longitude: 77.20° W

Phase II experiments will link RL to JITC. The transmission rate for this experiment will be at OC-3 rates. The terminals (two required) will be provided by NASA. These are the HDR earth terminals offered by NASA to experimenters in conjunction with the ACTS. For this experiment, we suggest the following scenario.



RL: Latitude: 43° 13' 13.176" N
 Longitude: 75° 24' 34.003" W

JITC: Latitude: 31° 134' 17" N
 Longitude: 110° 20' 38" W

Spot Beam 4E: Latitude: 42° 75' N
 Longitude: 74° 86' W

West Scan Beam centered at Phoenix, AZ.
 Latitude: 30° 30' N
 Longitude: 112° W

4.2 Phase I Experiment

The proposed end-to-end block diagram of phase I experiment is shown in Figure 3. As was indicated earlier, the satellite transmission equipments and the terminals will be provided by the Canadians. CRC is still working on the upgrade of these equipments and full information is not yet available. In the

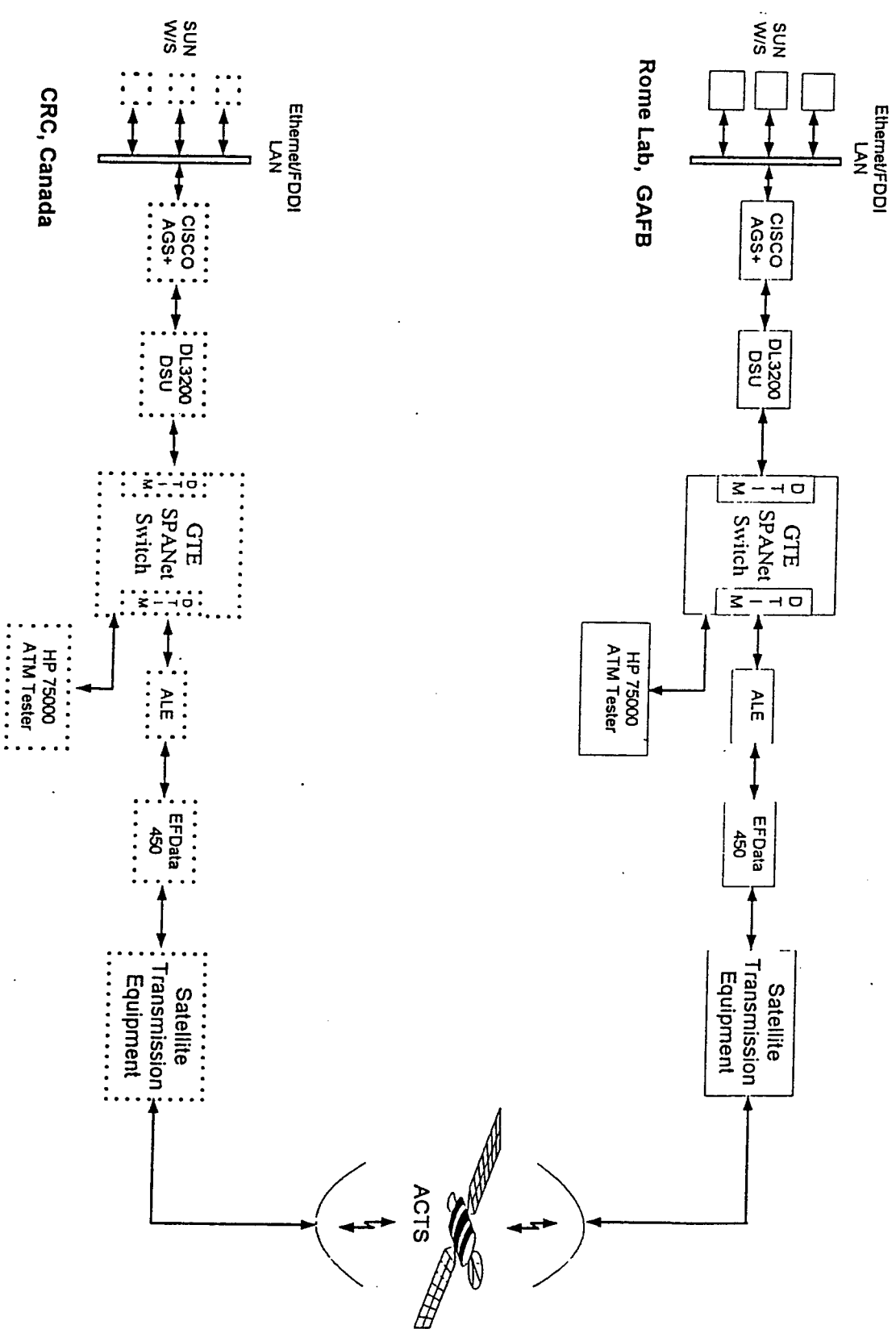


Figure 3: Phase I Experiment

absence of specific information on the terminals, we will assume the components shown in the Figure. The dotted boxes signify assumed components. Satellite data and application will be provided via the GTE SPANet ATM switch for the RL node. The SPANet switch at RL is already fully functional and equipped with DS-3 modules. No information is available on the ATM switch at CRC. Since full information is not available on the proposed Canadian terminals, we will assume a mirror image of RL equipments for CRC until such times when specific information will be made available.

4.2.1 ATM Switching Equipment

At RL the ATM generation and switching equipments shown in Figure 3 is the responsibility of the Network Group RL/C3BC. These components consist of the GTE SPANet switch, Device Service Units, Routers, LANs, and Workstations. These components are already installed and operable. These equipments are described below.

1. ATM Interface Hardware

The SUN workstations (W/S) at RL is equipped with ATM interface hardware to generate ATM cells. Each W/S is equipped with ATM adapter card.

2. GTE SPANet Switch

The GTE SPANet switch is the major ATM switching equipment at RL. The configuration of this switch is as follows [4]:

- DS-3 Trunk Interface Module (DTIM-3) with three 45 Mbps ports. Each port can access the Ethernet LAN and/or FDDI LAN.
- DS-1 Interface Module (DIM) with four 1.544 Mbps ports. Each port is access for T-1 carrier or TRI-TAC circuit switch through DTGI.
- Low-Rate Trunk Interface Module (LTIM) with variable rate port. Each port can access TRI-TAC radio and switches, satellite, T-1 carrier, and "Generic Low-Rate" devices.
- SONET Interface Module (SIM). The port is access to the Fiber Optic cable or the FDDI LAN at a transmission rate of 155 Mbps.
- Workstation Interface Module (WIM). This module provides access to workstations at a maximum speed of 100 Mbps.

3. Switch Accessories

The other accessories used in conjunction with the SPANet switch are the Device Service Units (DL3200), CISCO Router AGS+, and ATM cell converters.

4.2.2 Satellite Transmission and Communication Equipments

An ATM Link Enhancer (ALE) is recommended for this experiment. At high data rate, the ALE implements selective interleaving which significantly improves the performance of ATM traffic over satellite links. The ALE is capable of bit interleaving of the ATM header which improves the performance of the header error correction, thereby providing an acceptable "cell discard probability" [5].

The modem and other terminal equipments will be provided by CRC, Canada. Meanwhile, we will assume the equipment configuration as shown in Figure 3 for the Canadian terminals. The modem is assumed to be EFDATA 450 which has the capability of handling up to 45 Mbps. The satellite transmission equipment is assumed to be standard EHF satellite equipment.

4.2.3 Test Equipments

The HP 75000 Broadband analyzer is identified as the ideal test equipment and is recommended for this experiment. This piece of equipment is capable of generating ATM cells and monitoring the performance of the switch as well as the satellite channel. Different data on the ATM cells, the switch and the link can be collected with this equipment. This equipment is also vital for link characterization.

4.2.4. Test Procedure

Subtest I

1. Set up the equipment as shown in Figure 3.
2. Align the earth station antenna at both test nodes to the ACTS and set the frequencies and power levels as specified in the satellite access approval.
3. Initialize the test equipments HP 75000, and the ATM cell generating/switching equipments in accordance to the instructions contained in the operations manual or in accordance to the direction of the network branch.
4. Observe and record the status of all the equipment at time $t=0$ (initial point). Calibrate the equipment if necessary.
5. GTE SPANet switch setup instructions:
 - Please consult the network branch for setup and operation instructions.
6. Use the HP 75000 to generate and send ATM sample data for the subtest I. To do this, follow the procedure as specified below. Select "OK" or "Close Window" at the end of your selection.
 - Open the Test Session Manager and configure the system as follows:
 - Set Adaptation: AAL-1
 - All Others: Default values
 - Configure the test procedure
 - Set the active port by activating the DS-3 interface.

- Open the Configure Interface window and set the following parameters:
Select type of connection such that signal travel to and from the system under test (SUT) via the transmitter and receiver independently.

Framing Format:	C-bit
Interface:	UNI
Cell Scrambler/Discrambler:	OFF
Line Scrambler/Discrambler:	OFF
Header Correction:	ON
All Others:	Default Values

◆ Cell Generation

- Open the PDU sequence builder under the Builders window
Under this window, select Create and give the PDU name as "Test_phase1"
Select edit if necessary to edit your selection.
- Open the LIF sequence builder and create sequence from the ATM cells.
- Open the Foreground Cell Generation window.

Open Set Content window (under Cell Access) and set the following:

VPI:	1
VCI:	1
PT:	0
Cell Loss Priority:	1
Defined Sequence:	Test_Phase1
Sequence Length	1500*
AAL Type:	1
All Others:	Default values

- * This equipment can only generate a maximum of 1500 cells per second in the foreground condition and 16 cells per second in the background condition. This is not enough for 45 Mbps data. At this rate, the required number of cells is 106,132.08 cells per second. This is a problem that is still to be resolved. Filling the pipe with the HP 75000 is not possible!!!

- Open the ATM Cell Selector under Receiver window and set the following:

VPI:	1
VCI:	1
PT:	0
SN Correction:	OFF
AAL Type:	1

All Others:

Default values

- ◆ Activate the monitor and capture cell stream in the Capture Memory window.
 - Open the Foreground Channel Generator and activate the transmit button.Select the display icon to view the captured PDUs. Store these PDUs for comparison with the received PDUs.

7. Data Collection

- Use appropriate data sheets for data collection. Please indicate and record all observations. Use extra sheets if necessary.

Subtest II

To demonstrate the extent by which ATM can be transmitted over ACTS, high speed file transfer, VTC or both should be used to test the usefulness of ATM. For this demonstration set up the experiment as shown in Figure 4.

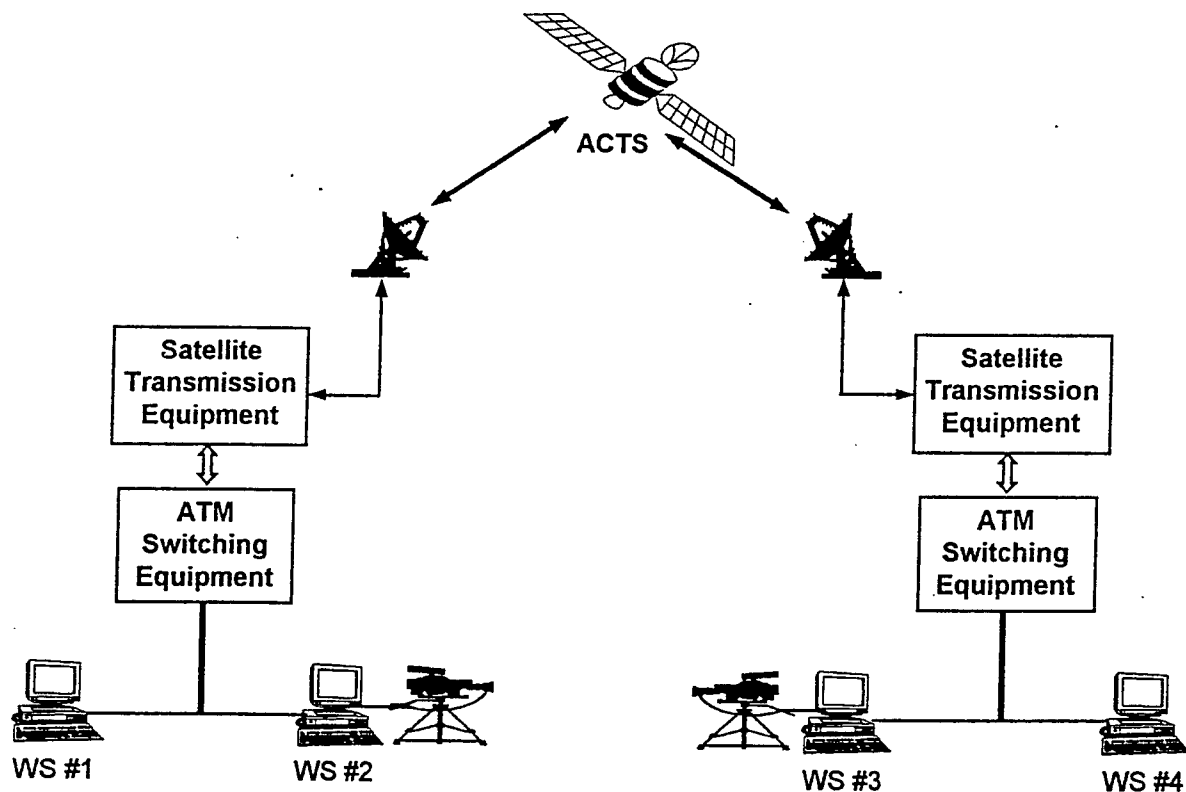


Figure 4: Application Experiment Setup

Workstations #2 and #3 should run a point to point VTC between RL and CRC. Setup and operation of the VTC is the responsibility of the Network Branch. Consult with the network group for direction on the VTC setup. Workstations #1 and #4 should be pre-loaded with a data intensive file (any file or combinations of files at least 45 magabyte). These files will be transferred between the two nodes.

4.2.5 Phase I Equipments

RL Node:

Description	On-Site Availability	Obtainable
Sun Sparc 10 Workstation	Yes	
ATM Computer Interface @ 45 Mbps	Yes	
GTE SPANet Switch & Accessories	Yes	
Video Teleconference Components - Camera with accessories - Tripod Stand - Speakers - Amplifier and Microphone	Yes	
ATM Link Enhancer	No	Yes (COMSAT)
Ka-band antenna with up/down converters, feed systems and accessories.	No	Yes (CRC)
EFDData modem, SDM-450	No	Yes (COMSAT)
EFDData Buffer EB-450	No	Yes (COMSAT)
HP 75000 Broadband Analyzer	No	Yes (Mitre)
Firebird Communication Analyzer MC6000	Yes	

CRC Node:

Description	On-Site Availability	Obtainable
Sun Sparc 10 Workstation	Yes ?	
ATM Computer Interface @ 45 Mbps	Yes ?	
GTE SPANet Switch & Accessories	Yes ?	
Video Teleconference Components - Camera with accessories - Tripod Stand - Speakers - Amplifier and Microphone	Yes ?	
ATM Link Enhancer	No ?	Yes (COMSAT)
Ka-band antenna with up/down converters and feed systems and accessories.	Yes	
EFDData modem, SDM-450	No ?	
EFDData Buffer EB-450	No ?	
HP 75000 Broadband Analyzer	?	Yes (Mitre) ?
Firebird Communication Analyzer MC6000	?	Yes (RL) ?

Note: ? is used to indicate unanswered questions regarding the equipments

4.3 Phase II Experiment

Figure 5 shows the setup of the test configuration for the phase II experiment. As we previously indicated, the experiment will be conducted between RL and JITC.

4.3.1 ATM Switching Equipments

As the block diagram indicates, both RL and JITC already have fully functional ATM switching equipments. Both sites have the GTE SPANet switch equipped with SONET Interface Module (SIM) operating at OC-3 rates. This switch has been described in section 4.2.1.

4.3.2 Satellite Transmission and Communication Equipments

The terminals for this phase of the experiment will be provided by NASA. This terminal is the 3.4m Ka-band transmit/receive HDR transportable terminal system assembled by BBN Systems and Technologies. These terminals will transmit and receive ATM signals at OC-3 rates via the ACTS between RL and JITC.

On the recent ACTS HDR experimenters meeting held in Cambridge Massachusetts at the BBN Systems & Technology complex, on July 6-7, 1994, the issues concerning the HDR experiment were outlined. These issues include the HDR Earth Station site requirement, HDR safety handling procedure, HDR terminal distribution allocation, ACTS time allotment, availability and acquisition of the HDR terminals. NASA, in conjunction with BBN Systems and Technologies, will provide all the necessary components and software to run the terminal. Also, the transportation of the terminals to and from the sites will be provided by NASA. However, the sites (RL & JITC) will respectively be responsible for the terminals site preparation, approval and the operation of the terminal after it is installed.

4.3.3 Testing Equipments

Since the connectivity of the terminal is not available at this time, we will assume that the HP 75000 and Firebird MC6000 will be compatible with the HDR terminal system.

4.3.4 Test Procedure

To stipulate the test procedure, we will assume that no extra-ordinary procedure is required for the HDR operation. If this is true, the test procedure will be identical to the procedure outlined in section 4.2.4 for the phase I experiment. The only difference is that this experiment will be performed at 155 Mbps as opposed to 45 Mbps. In other words, the terminals will be equipped with ATM/SONET user interfaces modules. Through these interfaces, this experiment will be performed via the ACTS.

In this phase of the experiment, we also encounter the problem of generating enough data for OC-3 transmission rate. At this rate, we require to generate 365,566.04 cells per second. The generation and testing of cells big enough to file the pipe is the bottleneck to this experiment. To the best of our knowledge, no equipment currently exist for the generation of such cells per second.

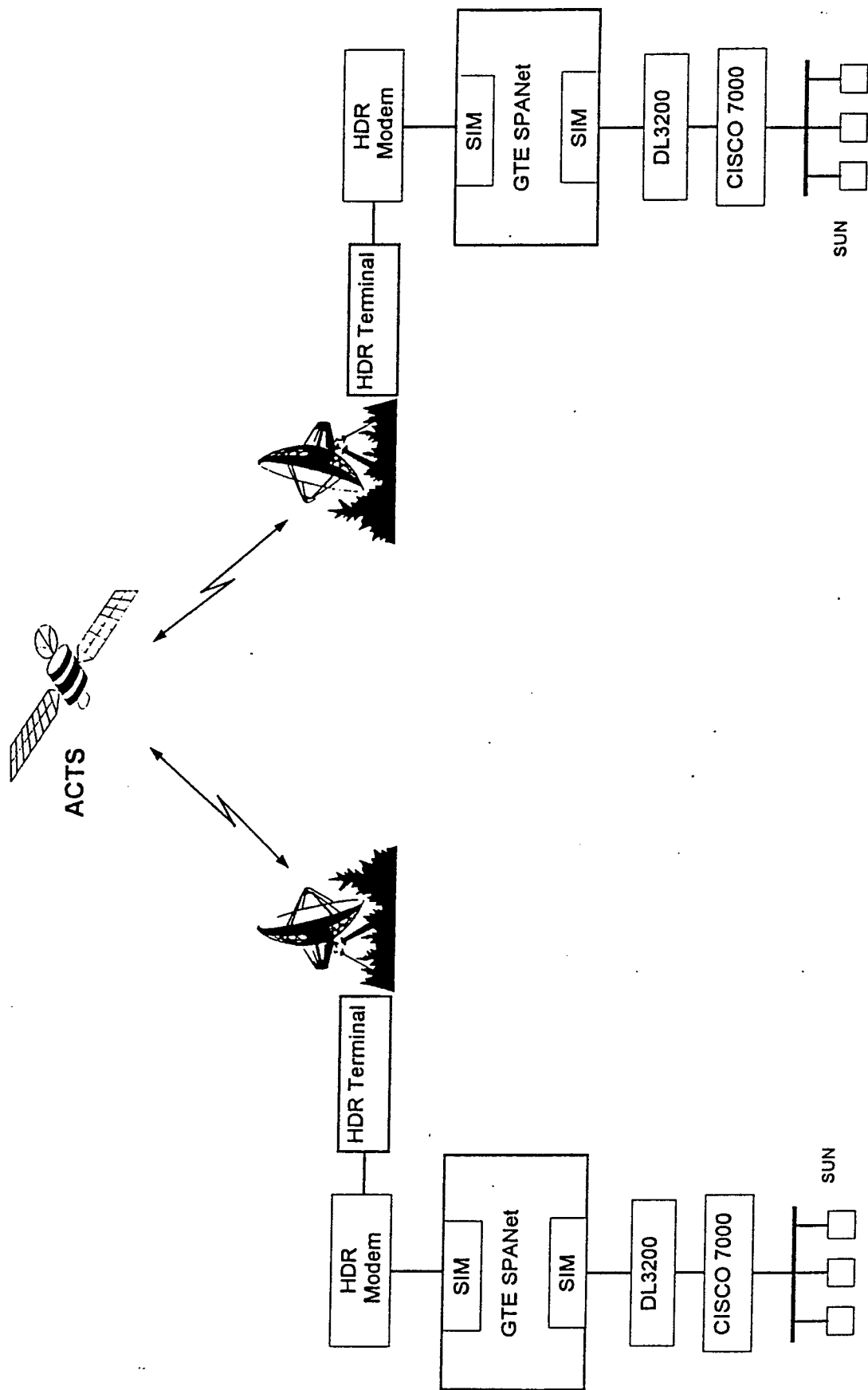


Figure 5: Phase II Experiment

1-19

4.3.5 Phase II Equipments

RL/JITC Nodes:

Description	On-Site Availability	Obtainable
Sun Sparc 10 Workstation	Yes	
ATM Computer Interface @ 155 Mbps	?	?
GTE SPANet Switch & Accessories	Yes	
Video Teleconference Components - Camera with accessories, Tripod Stand, Speakers - Amplifier and Microphone	Yes	
HDR Terminal with all the accessories	No	Yes (NASA)
ATM Link Enhancer	No	Yes (COMSAT)
HP 75000 Broadband Analyzer	No ?	Yes (Mitre) ?
Firebird Communication Analyzer MC6000	Yes	

5 SUMMARY

In this paper, we have described a program plan for transmitting high data rate ATM/SONET data over the ACTS. This plan is described based on the available information during the summer research program at the Rome Laboratory.

The execution of this plan is contingent upon several factors. Phase I experiment depends on the ability of CRC to upgrade their terminal to ACTS specification. Phase II depends on the availability of the HDR terminal from NASA.

6 REFERENCES

- [1] G. A. Bivens, "Satellite Networking Research in Scalable Networking Technology, Rome Laboratory Technology Demonstration with NASA ACTS Satellite - (proposal)", May 1994.
- [2] L. G. Cuthbert and J-C. Sapanel, *ATM The Broadband Telecommunications Solution*, England, Short Run Press Ltd., 1993.
- [3] NASA Lewis Research Center, *Systems Handbook - Advanced Communications Technology Satellite*, Technical Report TM-101490
- [4] N. Kowalchuk, "Secure Survivable Communications Network (SCCN), RL Project Report, 10/93
- [5] COMSAT, *Demonstration of Asynchronous Transfer Mode (ATM) via Commercial Satellite*, Technical Report 10/25/93, COMSAT Technology Services.
- [6] R. Manning, "A Unified Statistical Rain Attenuation Model for Communication Link Fade Predictions and Optimal Stochastic Fade Control Design Using Location Dependent Rain Statistics Data Base", *International Journal of Satellite Communications*, vol. 8, pp. 11-30, 1990

INTERFERENCE EXCISION IN SPREAD SPECTRUM USING TIME-FREQUENCY DISTRIBUTIONS

Moeness G. Amin
Professor
Department of Electrical and Computer Engineering

Villanova University
Villanova, Pa 19085

Final Report for:
Summer Faculty Research Program
Rome Laboratory

Sponsored by
Air Force Office of Scientific Research
Bolling Air Force Base, DC

September 1994

INTERFERENCE EXCISION IN SPREAD SPECTRUM USING TIME-FREQUENCY DISTRIBUTIONS

Moeness G. Amin
Professor
Department of Electrical and Computer Engineering
Villanova University

Abstract

This report deals with the application of time-frequency distributions(TFD) to direct sequence spread spectrum(SS) communication systems. The case studied is that of a jammer with time-varying characteristics. The capability of the newly devised TFDs to properly localize a single as well as multiple component signals in time and frequency permit unbiased low variance estimation of the interference instantaneous frequency under abrupt as well as evolutionary rapidly changing conditions. This estimate is then used to construct a finite impulse response filter which substantially reduces the interference power with a minimum possible distortion of the desired signal. This two step mechanism for interference excision can be viewed as a case of an open loop adaptive filtering. However contrary to the existing techniques of close loop self-tuning linear predictors or open loop adaptive filtering based on fast Fourier transforms, the filter coefficients in the proposed technique are obtained via *time-varying spectral analysis*. Closed form expressions of the improvement of SNR at the receiver correlator output using TFD-based adaptive filtering are derived. Results show that time-frequency representations of signals should be considered as an important tool to immune the SS systems to smart jamming.

INTERFERENCE EXCISION IN SPREAD SPECTRUM USING TIME-FREQUENCY DISTRIBUTIONS

Moeness G. Amin

Introduction

Spread spectrum (SS) systems are widely used in communications in a variety of applications including suppression of a strong interfering signal due to jamming or multipath propagation and in low probability of intercept communications. The spread spectrum system is characterized by 1) The signal occupies a bandwidth much in excess of the minimum bandwidth necessary to send the information. 2) Spreading is accomplished by means of spreading signal, often called a code signal, which is independent of the data. 3) At the receiver, despreading for recovering the original data is accomplished by the correlation of the received spread signal with a synchronized replica of the spread signal used to spread the information.

The most commonly used type of SS is the direct sequence (DS) in which modulation is achieved by superimposing a pseudo random (PN) sequence upon the data bits. In the receiver, the cross correlation with the replica of the PN sequence transfers the information signal back to its original bandwidth, while reducing the level of a narrow-band interference by spreading it across the bandwidth occupied by the PN sequence.

The performance of a PN SS system can be further improved, with respect to its immunity to narrow-band interference, by applying an excision filter prior to despreading. This filter suppresses the interference and thus increases the signal to noise ratio (SNR) at the output of the correlator. Excision can be performed in the following domains:

- 1) *Frequency Domain* : The (FFT) of the data over one information bit is weighted by appropriate values and then transformed back to the time domain[1]. This is an effective method for stationary narrow-band interference. Sidelobes may present a problem in removing the interference without losing some of the signal energy.
- 2) *Time domain* : This includes adaptive linear predictors and smoothers(LMS, RLS) [2,3]. Tracking is highly dependent on the SNR and often fails under rapidly time-varying interference.

- 3) *Wavelet domain:* The discrete wavelet transform (DWT) is applied to the data and the coefficients of high energy are removed prior to the inverse transform[4]. The DWT is appropriate for cases of pulse jamming or interference with burst characteristics.
- 4) *Time and frequency domains :* Non-parametric spectral techniques are first employed. Then, a time-domain transversal filter is designed from the spectral information of the data[1]. Spectral estimation methods combined with open loop adaptive filtering were shown to suffer from the same drawbacks as frequency-domain techniques.

None of the above methods is capable of properly incorporating the time-varying nature of the interference frequency characteristics. Fig.1 shows that frequency and wavelet excision, in essence, respectively remove all desired signal information over the frequency band ΔF and time duration ΔT . As such, we maintain that in the case of a chirp as well as other time-varying interfering signals, frequency-domain methods ignore the fact that only few frequency bins are contaminated by the jammer at a given time. Wavelet-domain excision techniques, on the other hand, do not account for the interference characteristics where only few time samples may be contaminated by the jammer for a given frequency. Applying either method will eliminate the interference, but unnecessarily reduce the desired signal energy.

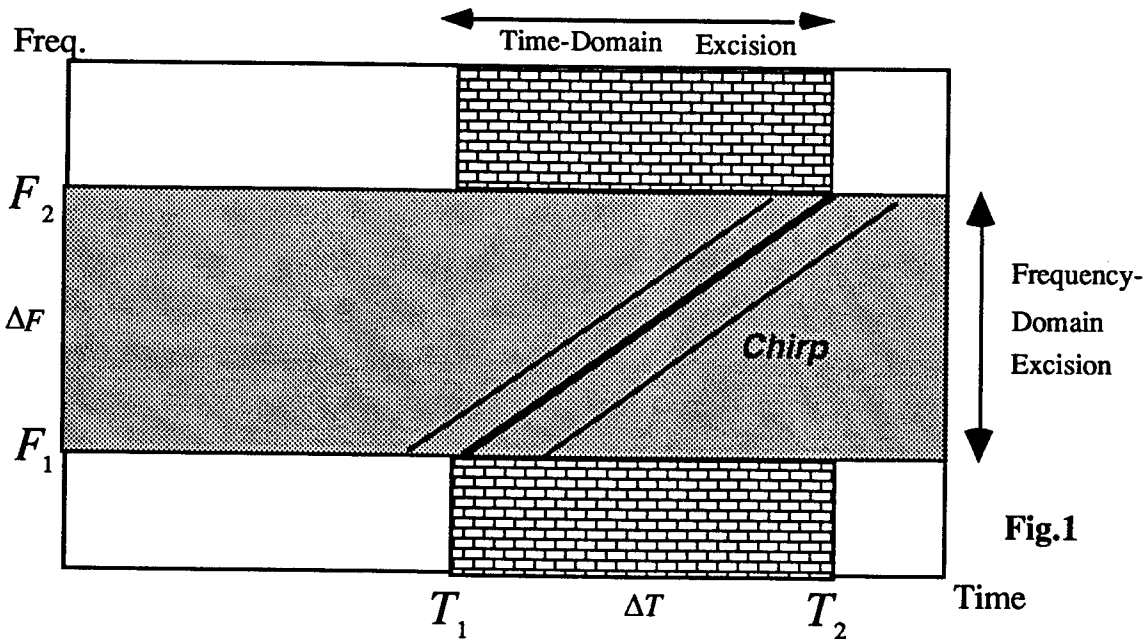


Fig.1

Contributions

In this report, time-frequency (t-f) distributions are employed for performing time-varying spectral analysis on the received signal (see Fig.2). On the basis of the instantaneous frequency estimate, three and five coefficients linear phase open loop adaptive filter can be formed to annihilate the time-varying interference with minimum possible loss of signal energy.

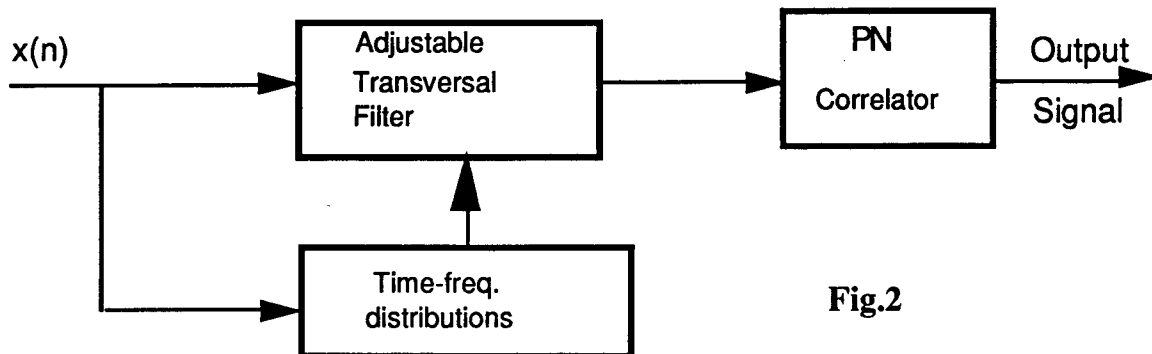


Fig.2

The objective of the proposed technique is to highly attenuate the received signal in those *time-frequency regions* which contain strong interference, as depicted by the region in between the dashed lines in Fig.1. The effectiveness of the t-f based interference suppression algorithm is assessed by evaluating the performance of the receiver with and without the interference suppression filter. Analysis and simulations clearly show reduction in the probability of error using t-f techniques over time/frequency only methods.

Time-Frequency Distributions

Time-frequency distributions (TFDs) have been shown to be a powerful tool in signal analysis and processing. They properly depict the time-varying characteristics of nonstationary signals. TFDs allow separation between signals overlapping in time and in frequency, which could not be done using windowing or filtering techniques. TFDs are characterized by a two dimensional function. This function is referred to as a "kernel" and can be designed such that the corresponding TFD satisfies several desired properties. For a full discussion of the TFDs and kernel design methods, we refer the reader to references [5,6]. Among the desired t-f properties is the capability to satisfy the instantaneous frequency condition. Generally, this property allows the TFD to encounter peaks at the derivative of the phase of each signal component, irrespective of their time-varying nature.

In this report, we use TFD methods to localize a rapidly time-varying interferer in the time-frequency domain and excise it, yielding a higher SNR at the receiver output than that obtained using other excision methods. Below, we present the general class of TFDs defined by Cohen[5] and discuss its relation with both the Wigner distribution (WD) [7] and the ambiguity function. The kernel role in uniquely characterizing the TFD is highlighted. Let $R_f(t, \tau)$ be the instantaneous autocorrelation of the complex signal $f(t)$

$$R_f(t, \tau) = f(t + \tau/2) f^*(t - \tau/2) \quad (1)$$

then

$$W_f(t, \omega) = \int R_f(t, \tau) e^{-j\omega\tau} d\tau \quad (2)$$

and the ambiguity function is

$$A_f(\theta, \tau) = \frac{1}{2\pi} \int R_f(t, \tau) e^{j\theta t} dt \quad (3)$$

with

$$W_f(t, \omega) = \iint A_f(\theta, \tau) e^{-j(\theta t + \omega\tau)} d\theta d\tau \quad (4)$$

This establishes the relationship between the ambiguity function and Wigner distribution. Smoothing in both the time and frequency directions is often carried out.

$$W'_f(t, \omega) = \frac{1}{4\pi^2} \iint W_f(v, \zeta) \Phi(t - v, \omega - \zeta) dv d\zeta. \quad (5)$$

By the 2-D convolution theorem, we have

$$W'_f(t, \omega) = \frac{1}{4\pi^2} \iint A_f(\theta, \tau) \Phi(\theta, \tau) e^{-j(\theta t + \omega\tau)} d\theta d\tau = C_f(t, \omega; \Phi), \quad (6)$$

which is the Cohen class of time-frequency distributions[5,6]. $C_f(t, \omega; \Phi)$ can also be expressed as the Fourier transform of the generalized autocorrelation function

$$C_f(t, \omega; \Phi) = \int R'_f(t, \tau) e^{-j\omega\tau} d\tau \quad (7)$$

where

$$R'_f(t, \tau) = \frac{1}{2\pi} \int R_f(u, \tau) \varphi(t - u, \tau) du$$

The autocorrelation domain kernel $\varphi(t, \tau)$ is defined as

$$\varphi(t, \tau) = \int \Phi(\theta, \tau) e^{-j\theta t} d\theta$$

The generalized class of t-f distributions $C_f(t, \omega; \Phi)$ can also be obtained from the IFT of the generalized spectral correlation R'_F

$$C_f(t, \omega; \Phi) = \frac{1}{2\pi} \int R'_F(\omega, \theta) e^{j\theta t} d\theta, \quad R'_F(\omega, \theta) = \frac{1}{2\pi} \int R_F(\zeta, \theta) \Psi(\omega - \zeta, \theta) d\zeta \quad (8)$$

with R_F and Ψ representing the instantaneous spectral correlation and the spectral correlation domain kernel

$$R_F(\omega, \theta) = F(\omega + \theta/2)F^*(\omega - \theta/2) \quad \Psi(\omega, \theta) = \int \Phi(-\theta, \tau)e^{-j\tau\omega}d\tau$$

respectively. The following relations follow from equations (1-8)

$$R_F(\omega, \theta) = \iint R_f(t, \tau)e^{-j(\theta t + \tau\omega)}dtd\tau, \quad W_F(\omega, t) = \int R_F(\omega, \theta)e^{-j\theta t}d\theta = 2\pi W_f(-t, \omega)$$

$$A_F(\tau, \theta) = \frac{1}{2\pi} \int R_F(\omega, \theta)e^{j\omega\tau}d\omega = 2\pi A_f(-\tau, \theta)$$

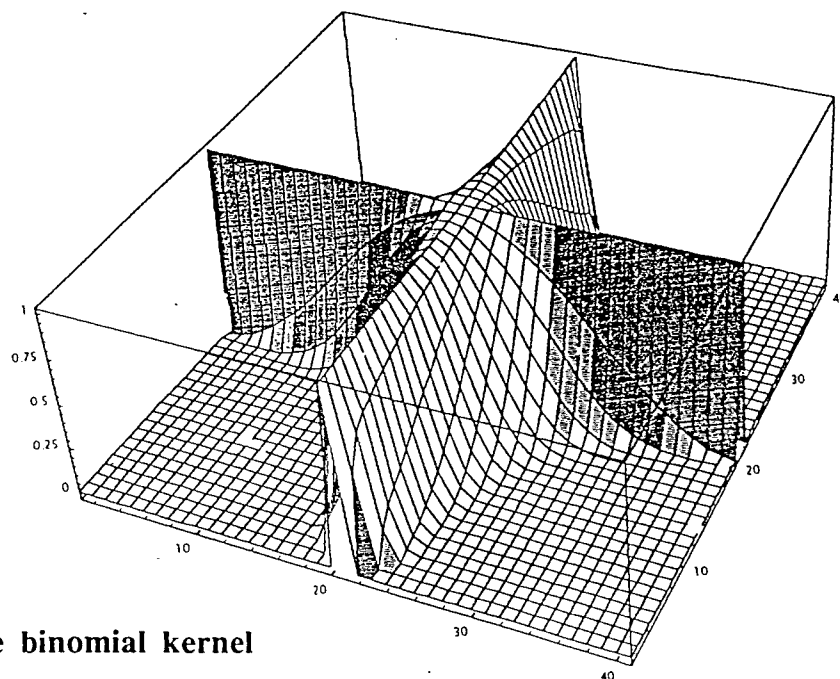
Thus the generalized time-frequency distribution can be viewed in four ways 1) The 2-D convolution of the WD with the time-frequency domain kernel. 2) The 2-D FT of the product between the ambiguity function and the kernel. 3) The 1-D FT(with respect to the lag variable) of the convolution(in the time direction) between the instantaneous autocorrelation and the temporal correlation domain kernel. 4) The 1-D IFT(with respect to the Doppler shift variable) of the convolution(in the frequency direction) between the instantaneous spectral autocorrelation and the spectral correlation domain kernel.

Table 1 depicts the desired properties which any devised t-f distribution should satisfy. Each property translates into a condition on the employed kernel. All conditions are compatible and can be satisfied simultaneously. In this report, we emphasize property 6. The ability to estimate the instantaneous frequency is the key for using the t-f distribution in SS communication problems. Two commonly used kernels, namely the binomial and Born Jordan, which satisfy all constraints are shown in Fig.3 in the ambiguity domain. The unit values at the center axes are necessary to satisfy the time and frequency marginal constraints. The low-pass filter characteristics lead to reduced cross-terms, which are positioned away from the origin. Cross-terms are undesired components and are produced from the data bilinear properties of the distributions, evident in the above equations.

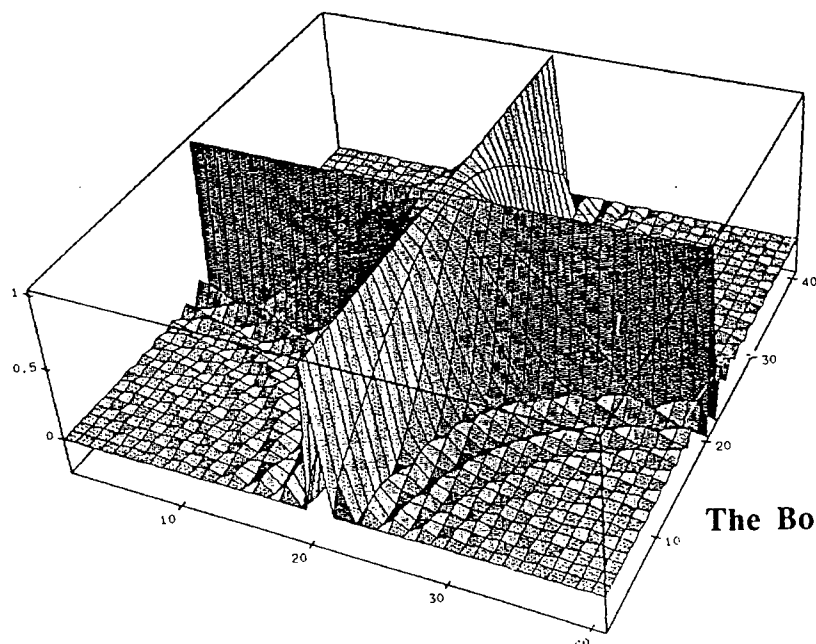
Figure 4 illustrates the time and time-frequency plots of a burst of a single sinusoid with SNR=20dB. The time-frequency distribution was generated using the binomial kernel. The mesh and contour plots clearly show the starting and ending times of the sinusoid. Fig.5 depicts the case of a chirp signal in noise. The chirp signal exists over the period[200-264]. In addition to the signal duration, the WD in Fig.5 shows a peak positioned at the instantaneous frequency of the chirp, irrespective of its rate of variation.

Table 1. Distribution properties and associated kernel requirements.

P0. nonnegativity : $C_f(t, \omega; \phi) \geq 0 \forall t, \omega$
Q0. $\phi(\theta, \tau)$ is the ambiguity function of some function $w(t)$.
P1. realness : $C_f(t, \omega; \phi) \in R$
Q1. $\phi(\theta, \tau) = \phi^*(-\theta, -\tau)$
P2. time shift : $g(t) = f(t - t_0) \Rightarrow C_g(t, \omega; \phi) = C_f(t - t_0, \omega; \phi)$
Q2. $\phi(\theta, \tau)$ does not depend on t .
P3. frequency shift : $g(t) = f(t)e^{j\omega_0 t} \Rightarrow C_g(t, \omega; \phi) = C_f(t, \omega - \omega_0; \phi)$
Q3. $\phi(\theta, \tau)$ does not depend on ω .
P4. time marginal : $\frac{1}{2\pi} \int W_f(t, \omega) d\omega = f(t)f^*(t)$
Q4. $\phi(\theta, 0) = 1 \forall \theta$
P5. frequency marginal : $\int C_f(t, \omega; \phi) dt = F(\omega)F^*(\omega)$
Q5. $\phi(0, \tau) = 1 \forall \tau$
P6. instantaneous frequency : $\frac{\int \omega C_f(t, \omega; \phi) d\omega}{\int C_f(t, \omega; \phi) d\omega} = \omega_i(t)$
Q6. Q4 and $\frac{\partial \phi(\theta, \tau)}{\partial \tau} \Big _{\tau=0} = 0 \forall \theta$
P7. group delay : $\frac{\int t C_f(t, \omega; \phi) dt}{\int C_f(t, \omega; \phi) dt} = t_g(\omega)$
Q7. Q5 and $\frac{\partial \phi(\theta, \tau)}{\partial \theta} \Big _{\theta=0} = 0 \forall \tau$
P8. time support : $f(t) = 0$ for $ t > t_c \Rightarrow C_f(t, \omega; \phi) = 0$ for $ t > t_c$
Q8. $\psi(t, \tau) \triangleq \int \phi(\theta, \tau) e^{-j\theta t} d\theta = 0$ for $ \tau < 2 t $
P9. frequency support : $F(\omega) = 0$ for $ \omega > \omega_c \Rightarrow C_f(t, \omega; \phi) = 0$ for $ \omega > \omega_c$
Q9. $\int \phi(\theta, \tau) e^{j\omega \tau} d\tau = 0$ for $ \theta < 2 \omega $
P10. Reduced Interference
Q10. $\phi(\theta, \tau)$ is a 2-D low pass filter type.



The binomial kernel



The Born-Jordan kernel

Fig.3 Commonly used time-frequency kernels

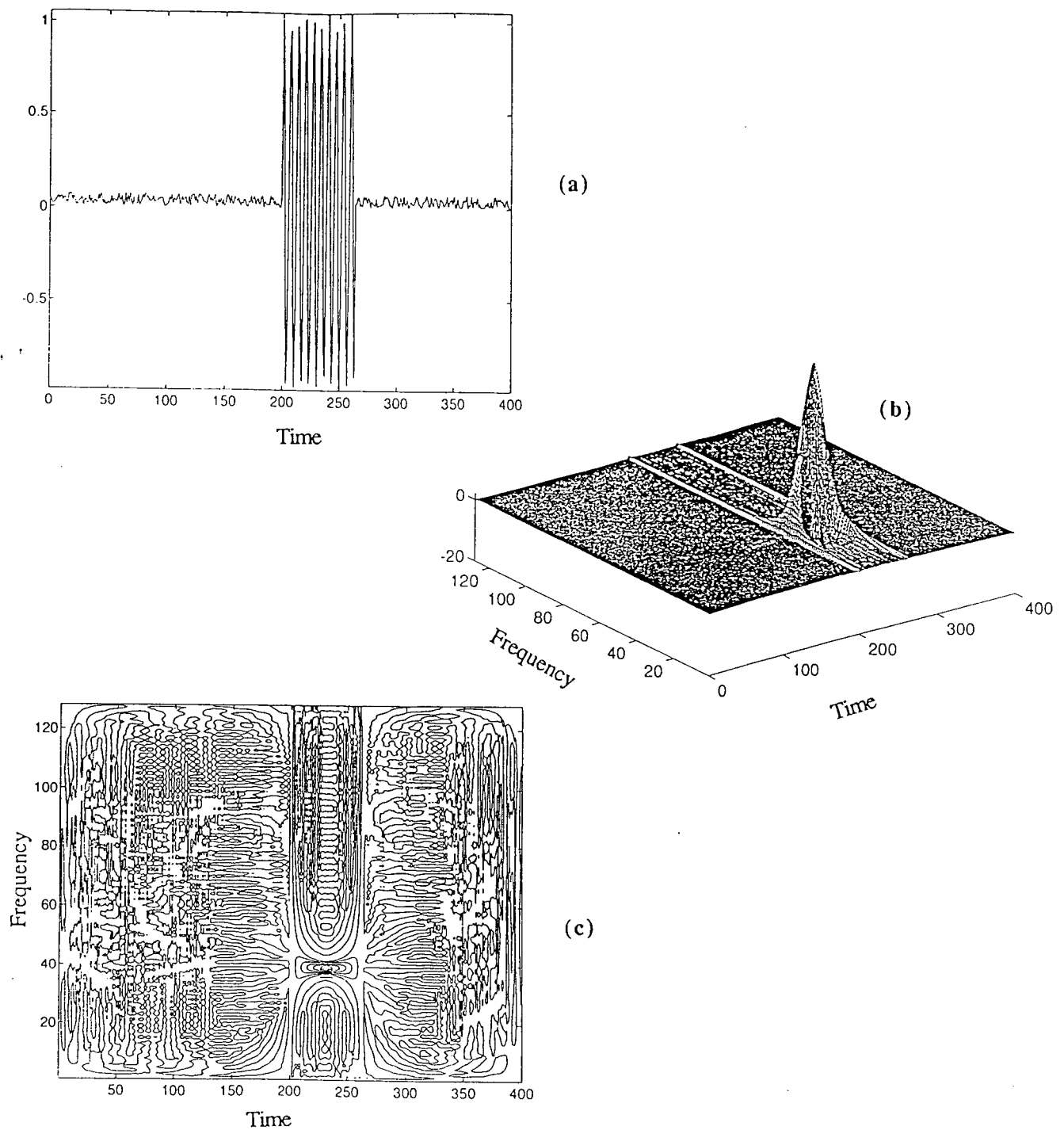


Fig.4 A single sinusoid in noise (a) the signal, (b) the mesh plot, (c) the contour plot

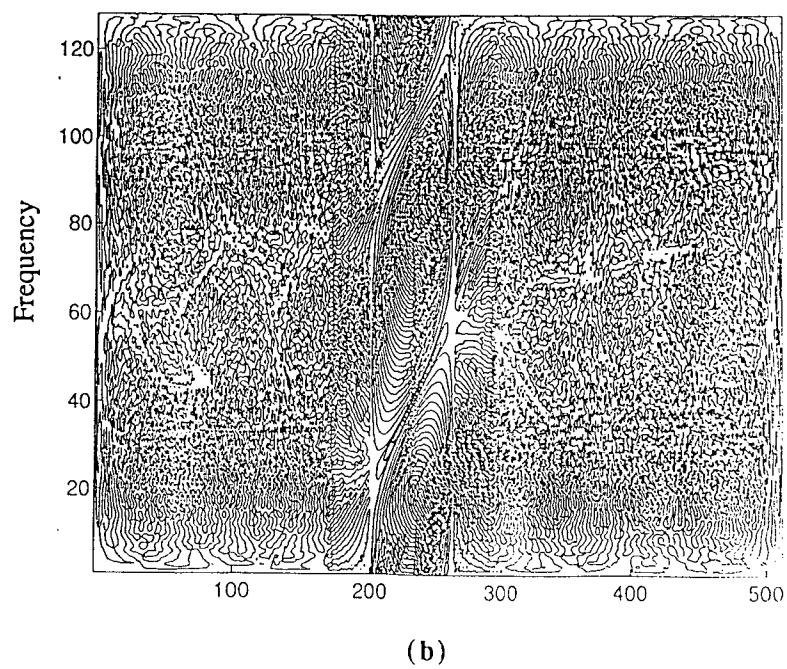
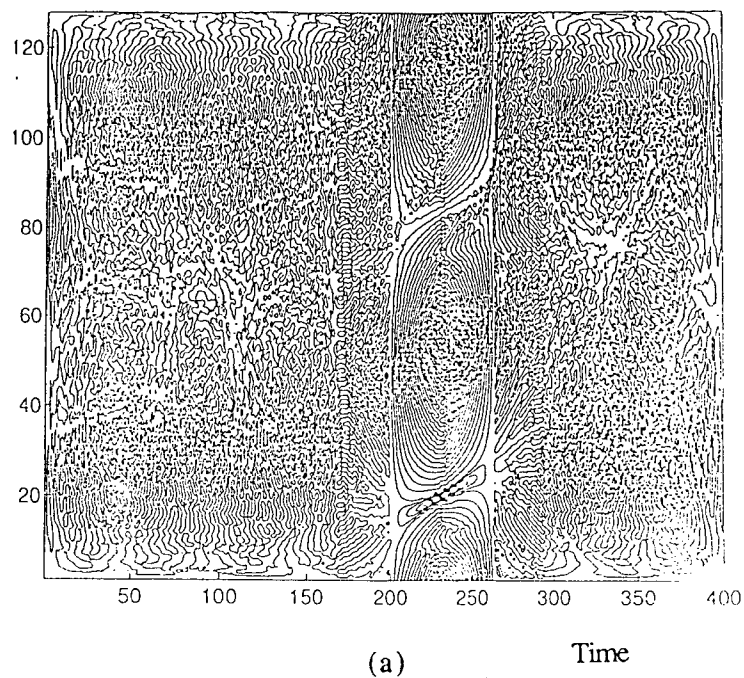


Fig.5 Contour plots of a chirp in noise (a) low rate (b) high rate

Analysis

In the transmitted signal generation, the number of PN chips per information bit is L , i.e.,

$$b_k(t) = \sum_{j=1}^L p_{kj} q(t - j\tau_c) \quad (9)$$

where p_{kj} represent the output sequence from the PN code generator for the k th information bit and $q(t)$ is a rectangular pulse of duration τ_c and unit energy. The total transmitted signal may be expressed in the form

$$s(t) = \sum_k I_k b_k(t - kT_b) \quad (10)$$

where $\{I_k\}$ represents the binary information sequence and $T_b = L\tau_c$ is the bit interval (reciprocal of the bit rate). The received signal has the form $r(t) = s(t) + i(t) + n(t)$, where $w(t)$ is the uncorrelated white noise process, $s(t)$ is the desired signal, and $i(t)$ the interference. In the following, we present three different cases of excision filters based on TFDs. Under the assumption of highly rapidly-varying environment, the length of the excision filter should be kept to a minimum. Since nulling a cosinusoidal function requires at least three coefficient filter, we consider in Case 1 the application of a linear phase 3-coefficient filter whose zero lies on the unit circle with the phase equal to the instantaneous frequency (obtained from the TFD). We maintain that a zero on a unit circle implies perfect nulling. However, due to problems cited in case 1, two other cases are considered which we advocate for use in TFD-based excision SS systems.

Case 1: Three coefficient excision Filter

Let $h(n)$ represent the impulse response of the linear phase excision filter with coefficients $h(0)=h(1)=1$, $h(2)=-2 \cos(\omega_n)$, where ω_n is the instantaneous frequency of the time-varying interference obtained using TFD. The filter input is the received signal $x(n)$ and the output is $y(n)$

$$y(n) = \sum_{m=-1}^1 h(m)x(n-m)$$

By linearity, the output can be written as

$$y(n) = p_o(n) + i_o(n) + w_o(n)$$

where the subscript "o" denotes output. The output signal is fed into the PN correlator yielding the decision variable U .

$$U = \sum_{n=1}^L p_o(n)p(n) + \sum_{n=1}^L i_o(n)p(n) + \sum_{n=1}^L w_o(n)p(n)$$

It is assumed that the interference is eliminated by filtering. Then,

$$U = \sum_{n=1}^L p_o(n)p(n) + \sum_{n=1}^L w_o(n)p(n) = U_1 + U_2$$

The first term U_1 can be detailed as

$$\begin{aligned} U_1 &= \sum_{n=1}^L \sum_{m=-1}^1 h(m)p(n-m) = \sum_{n=1}^L (p(n-1) + p(n+1) - 2\cos(\omega_n)p(n))p(n) \\ &= \sum_{n=1}^L p(n)p(n-1) + \sum_{n=1}^L p(n)p(n+1) - 2\sum_{n=1}^L \cos(\omega_n)p^2(n) \end{aligned}$$

The following assumptions are invoked to simplify analysis and gain preliminary insights into the performance of the proposed method under rapidly time-varying environments.

- 1) The PN sequence is identically distributed random variables such that $p(n)=1,-1$ with equal probability.
- 2) The instantaneous radian frequency is a random variable uniformly distributed over $[0, 2\pi]$.

With the above two assumptions, the expected value and mean square values of U can be determined as follows

$$E[U_1] = \sum_{n=1}^L E[p(n)p(n-1)] + \sum_{n=1}^L E[p(n)p(n+1)] - 2\sum_{n=1}^L E[\cos(\omega_n)] \quad (11)$$

But since

$$E[\cos(\omega_n)] = \frac{1}{2\pi} \int_0^{2\pi} \cos(\omega_n) d\omega_n = 0, \quad (12)$$

then

$$E[U_1] = 0.$$

Further, it can easily be shown that $E[U_2] = 0$. The SNR of the correlator is defined as the ratio of the square of the mean to the variance of the correlator output y_{peak} (peak value)

$$SNR = \frac{\{E[y_{peak}]\}^2}{Var\{y_{peak}\}} \quad (13)$$

Accordingly,

$$E[y_{peak}] = E[U_1 + U_2] = 0 \quad (14)$$

Equation (14) implies that under the above two assumptions, the SNR becomes $-\infty$, which is highly undesired.

Case 2: Five coefficient excision filters

Next we try a five coefficient linear phase FIR filter with

$$h(n) = [1 \quad -4\cos(\omega_n) \quad 2 + 4\cos^2(\omega_n) \quad -4\cos(\omega_n) \quad 1] \quad (15)$$

Which is obtained by convolving the impulse response of the 3-coefficient filter in case 1 with itself. It is clear that the middle term in the impulse response is no longer a cosinusoidal function, but rather includes the square value of the cosinusoid. As a result, the expected value of the correlator output will no longer be zero, forbidding the SNR to be negative infinity, as in case 1. Using the new filter,

$$U_1 = \sum_{n=1}^L [p(n-2) - 4p(n-1)\cos(\omega_n) + (2 + 4\cos^2(\omega_n))p(n) - 4p(n+1)\cos(\omega_n) + p(n+2)]p(n) \quad (16)$$

The expected values of the first, second, forth and fifth terms in the above summation are all zeros due to the uncorrelatedness of the PN and the instantaneous frequency as well as the zero mean property of both the PN sequence and the cosinusoidal function. The expected value of the middle term is given by

$$E[U_1] = \sum_{n=1}^L E[2 + 4\cos^2(\omega_n)] = 2L + \frac{4}{2\pi} \int_0^{2\pi} \cos^2(\omega_n) d\omega_n = 4L \quad (17)$$

Because the noise is uncorrelated with the PN sequence, $E[U_2] = 0$. Therefore the numerator in equation (13) is given by

$$E[y_{peak}] = E^2[U_1] = 16L^2 \quad (18)$$

The variance of U can be computed as

$$\begin{aligned}
E[U_1^2] = & \sum_{k=1}^L \sum_{n=1}^L E\{p(n)p(n-2)p(k)p(k-2)\} + \sum_{k=1}^L \sum_{n=1}^L E\{p(n)p(n+2)p(k)p(k+2)\} \\
& + 16 \sum_{k=1}^L \sum_{n=1}^L E\{p(n)p(n-1)p(k)p(k-1)\cos(\omega_n)\cos(\omega_k)\} \\
& + 16 \sum_{k=1}^L \sum_{n=1}^L E\{p(n)p(n+1)p(k)p(k+1)\cos(\omega_n)\cos(\omega_k)\} \\
& + \sum_{k=1}^L \sum_{n=1}^L E\{(2+4\cos(\omega_n))(2+4\cos(\omega_k))\} \\
& + \sum_{k=1}^L \sum_{n=1}^L p(n)p(n-2)p(k)p(k+2) + \sum_{k=1}^L \sum_{n=1}^L p(k)p(k-2)p(n)p(n+2)
\end{aligned} \tag{19}$$

The rest of the terms in the mean square value of U_1 represent the cross products of the individual terms. These products are zeros, due to the PN and the instantaneous frequency characteristics.

The only non-zero terms in the first and second double summations of equation (19) are those corresponding to $n=k$. These terms take unit values. As such, the first two double summations are L . The third and forth double summations take the value $8L$. This is due to the fact that the only nonzero terms are those corresponding to $n=k$. Each of these terms has an expected value of $1/2$. In the last two double summations there are $L-2$ nonzero terms corresponding to $n=k+2$ and $n=k-2$, respectively. The fifth double summation can be simplified to

$$\begin{aligned}
& \sum_{n=1}^L \sum_{k=1}^L E\{(4+8\cos^2(\omega_n)+8\cos^2(\omega_k)+16\cos^2(\omega_n)\cos^2(\omega_k))\} \\
& = 4L^2 + 4L^2 + 4L^2 + 16 \sum_{n=1}^L E\{(0.5(1+2\cos(2\omega_n)))^2\} + 16 \sum_{n=1}^L \sum_{k \neq n, k=1}^L \cos^2(\omega_n)\cos^2(\omega_k) \\
& = 12L^2 + 4 \sum_{n=1}^L E\{(1+2\cos(2\omega_n)+\cos^2(\omega_n))\} + 4(L^2 - L) = 12L^2 + 6L + 4L^2 - 2L \\
& = 16L^2 + 2L
\end{aligned} \tag{20}$$

By adding the values of the different terms constituting $E[U_1^2]$, we obtain

$$E[U_1^2] = 16L^2 + 22L - 2 \tag{21}$$

Now we focus on the mean square value of the correlator output due to noise, which is denoted by U_2

$$U_2 = \sum_{n=1}^L [w(n-2) - 4w(n-1)\cos(\omega_n) + (2 + 4\cos^2(\omega_n))w(n) - 4w(n+1)\cos(\omega_n) + w(n+2)]p(n) \quad (22)$$

Applying the expectation operator to the square value of the above equation, we obtain

$$\begin{aligned} E[U_2^2] = & \sum_{k=1}^L \sum_{n=1}^L E\{p(n)w(n-2)p(k)w(k-2)\} + \sum_{k=1}^L \sum_{n=1}^L E\{p(n)w(n+2)p(k)w(k+2)\} \\ & + 16 \sum_{k=1}^L \sum_{n=1}^L E\{p(n)w(n-1)p(k)w(k-1)\cos(\omega_n)\cos(\omega_k)\} \\ & + 16 \sum_{k=1}^L \sum_{n=1}^L E\{p(n)w(n+1)p(k)w(k+1)\cos(\omega_n)\cos(\omega_k)\} \\ & + \sum_{k=1}^L \sum_{n=1}^L E\{(2 + 4\cos(\omega_n))(2 + 4\cos(\omega_k))w(n)p(n)w(k)p(k)\} \end{aligned} \quad (23)$$

Each of the first two double summations yields $L\sigma^2$. The value of the third and the forth double summations is $8L\sigma^2$. The last double summation is $14L\sigma^2$. All of the above values were obtained based on the assumption that the PN sequence and the white noise sequence are uncorrelated, and the noise is a white random stationary process. Since

$$E[U_1] = 16L^2, \quad E[U_2] = 0, \quad (23)$$

then

$$\text{var}[U_1] = 22L - 2, \quad \text{var}[U_2] = 32L\sigma^2 \quad (24)$$

Substituting (23) and (24) in (13), we obtain

$$SNR_o = \frac{16L^2}{22L - 2 + 32L\sigma^2} \quad (25)$$

For reasonably high value of L , the above expression can be simplified to

$$SNR_o = \frac{L}{\frac{22}{16} + 2\sigma^2} \quad (26)$$

Case 3: Two three-coefficient excision filters

Next, we apply the same 3-coefficient filter of Case 1 to both the input sequence and the receiver PN sequence. In this case, the correlator output is

$$U = \sum_{n=1}^L p_o(n)p_o(n) + \sum_{n=1}^L i_o(n)p_o(n) + \sum_{n=1}^L p_o(n)w(n) \quad (27)$$

Assuming that the interference is completely excised, then the second term in the above summation is zero. The mean value of the correlator output is

$$E[U] = E[U_1] + E[U_2] \quad (28)$$

where the first term is due to the signal and the second term is due to the noise. It is easily shown that

$$E[U_1] = E\left[\sum_{n=1}^L (p(n-1) + p(n+1) - 2\cos(\omega_n)p(n))(p(n-1) + p(n+1) - 2\cos(\omega_n)p(n))\right] \quad (29)$$

$$E[U_2] = E\left[\sum_{n=1}^L (w(n-1) + w(n+1) - 2\cos(\omega_n)w(n))(p(n-1) + p(n+1) - 2\cos(\omega_n)p(n))\right] \quad (30)$$

Using the uncorrelatedness of the PN sequence and the noise sequences, the mean value of the correlator output signal is $4L$, whereas the correlator output noise is zero.

$$\begin{aligned} E[U_1^2] &= \sum_{k=1}^L \sum_{n=1}^L 4 + 4 \sum_{k=1}^L \sum_{n=1}^L E\{p(n-1)p(n+1)p(k-1)p(k+1)\} \\ &\quad + 16 \sum_{k=1}^L \sum_{n=1}^L E\{p(n)p(n+1)p(k)p(k+1)\cos(\omega_n)\cos(\omega_k)\} \\ &\quad + 16 \sum_{k=1}^L \sum_{n=1}^L E\{p(n)p(n-1)p(k)p(k-1)\cos(\omega_n)\cos(\omega_k)\} \\ &\quad + 16 \sum_{n=1}^L \sum_{k=1}^L E\{\cos^2(\omega_n)\cos^2(\omega_k)\} + 16 \sum_{n=1}^L \sum_{k=1}^L E\{\cos^2(\omega_n)\} \\ &= 4L^2 + 4L + 8L + 8L + 4L^2 + 2L + 8L^2 = 16L^2 + 22L \end{aligned} \quad (31)$$

Similarly, it can be shown that

$$E[U_2^2] = 20L\sigma^2 \quad (32)$$

$$\text{So,} \quad \text{SNR}_o = \frac{16L^2}{22L - 2 + 22L\sigma^2} \quad (33)$$

For a reasonable high value of L , the above expression can be approximated by

$$\text{SNR}_o = \frac{L}{\frac{22}{16} + \frac{20}{16}\sigma^2} \quad (34)$$

Comparing the results in Case 1, Case 2, and Case 3, it is clear that :

- 1) A three-coefficient filter should not be used alone under the stated assumptions.
- 2) If the three coefficient filter is used, then a similar filter should be applied to the receiver PN sequence.
- 3) Using two three-coefficient filters applied to the received signal and the receiver PN sequence yields a higher SNR than using a five-coefficient filter applied to the received signal. This is due to the fact that a longer filter encompasses more samples of the white noise sequence and as such provides a higher noise power level at the correlator output.

Conclusions

A combined time-frequency distribution and adaptive filtering approach for interference excision is presented. The ability of the TFD to localize the time-varying frequency is utilized to estimate the instantaneous frequency of the jammer. Based on this estimate, an FIR filter is designed which places an infinite null at the jammer frequency every time sample. Three different cases are considered. In the first two cases, the received signal is processed by a three- and a five-coefficient filter, respectively. In the third case, a three-coefficient filter is applied to both the received signal and the receiver PN sequence. In each case, closed form expressions for the improvement of the SNR are derived. The analytical results show that the third case yields the highest SNR.

References

- [1] J. Ketchum and J. Proakis, " Adaptive algorithms for estimating and suppressing narrow band interference in PN spread spectrum systems", IEEE Transactions on Communications, May 1982.
- [2] S. Theodoridis, N. Kalouptsidis, J. Proakis and G. Koyas, " Interference rejection in PN spread spectrum systems with linear phase FIR filters", IEEE Transactions on Communications, vol. 37, no. 9, September 1989.
- [3] R. Iltis, J. Ritcey ,and L. Milstein, "Interference rejection in FFH systems using least squares estimation techniques", IEEE Transact. on Communications, vol. 38, Dec. 1990.
- [4] M. Medley, G. Saulnier, and P. Das, "Applications of the wavelet transform in spread spectrum communications systems", SPIE, Wavelet Applic., Orlando, Florida, April 1994.

[5] Methods and Applications of Time-Frequency Signal Analysis, Ed. B. Boashash, Longman Cheshire, Melbourne, Australia, 1991.

[6] T.A.C.M. Claasen and W.F.G. Mecklenbrauker, "The Wigner distribution -- a tool for time-frequency signal analysis; part II: discrete time signals," Phillips Jour. of Research., vol. 35, pp. 276-300, 1980.

[7] F. Hlawatsch and G.F. Boudreaux-Bartels, "Linear and quadratic time-frequency signal representations," IEEE SP Magazine, pp. 21-67, April 1992.

DESIGNING SOFTWARE BY REFORMULATION USING KIDS

D. Paul Benjamin
Assistant Professor
Computer Science Department

Oklahoma State University
219 Math Sciences Building
Stillwater, Oklahoma, 74078-0599 USA
dpb@a.cs.okstate.edu

Final Report for:
Summer Faculty Research Program
Rome Laboratory

Sponsored by:
Air Force Office of Scientific Research
Bolling Air Force Base, DC

and

Rome Laboratory

August, 1994

DESIGNING SOFTWARE BY REFORMULATION USING KIDS

D. Paul Benjamin
Assistant Professor
Computer Science Department
Oklahoma State University

Abstract

In recent years, much attention has been paid to designing software by formal methods. Such an approach has been shown to facilitate the design of correct software. The KIDS system utilized at Rome Laboratory is an example of a software design system based entirely on a formal approach - the theory of institutions developed by Joseph Goguen and his coworkers. KIDS combines a theory of problem solving with a domain theory to derive a high-level program, which can then be transformed to improve efficiency. Frequently, the problem solving theory is a theory of global search, as it is in the KTS transportation scheduling system. Unfortunately, although global search through the space of possible solutions may be suitable for some problems, it is extremely inefficient for many others. In many problems, the search space is far too large for such an approach. Rather, it is desirable to decompose the space into independent components, so that partial solutions can be found in each piece and combined to give a global solution. KIDS does support problem space decomposition, but does not provide methods for finding useful decompositions for specific problems. This paper describes how a theory of decomposition and reformulation can be used in conjunction with KIDS to derive efficient programs.

DESIGNING SOFTWARE BY REFORMULATION USING KIDS

D. Paul Benjamin

Introduction

In recent years, much attention has been paid to designing software by formal methods. Such an approach has been shown to facilitate the design of correct software. KIDS (Kestrel Institute Development System) is an example of a software design system based entirely on a formal approach - the theory of institutions developed by Joseph Goguen and his coworkers. Two of the research groups at Rome Labs, the KBSA (Knowledge-Based Software Assistant) group and the KBP (Knowledge-Based Planning) group, use KIDS as the environment within which to develop software.

The emphases of planning and software engineering differ in many ways, e.g., software engineering in a formal environment is concerned with developing a program that is provably correct with respect to a given specification, while planning is concerned more generally with developing a program that has a high probability of producing a specified behavior. However, despite the many different emphases between planning and software engineering, both possess extremely large spaces of possible designs. Thus, designers in both fields are faced with the difficult task of finding efficient designs. A system such as KIDS helps the designer to make clear specifications, to write correct programs, and to refine existing code to improve its efficiency. However, no existing system helps the designer find efficient designs in the first place.

KIDS combines a theory of problem solving with a domain theory to derive a high-level program, which can then be transformed to improve efficiency. Frequently, the problem solving theory is a theory of global search, as it is in the KTS transportation scheduling system. Unfortunately, although global search through the space of possible solutions may be suitable for some problems, it is extremely inefficient for many others. In many problems, the search space is far too large for such an approach. Rather, it is desirable to decompose the space into independent components, so that partial solutions can be found in each piece and combined to give a global solution. KIDS does support problem space decomposition, but does not provide methods for finding useful decompositions for specific problems. This paper

describes how a theory of decomposition and reformulation can be used in conjunction with KIDS to derive efficient programs.

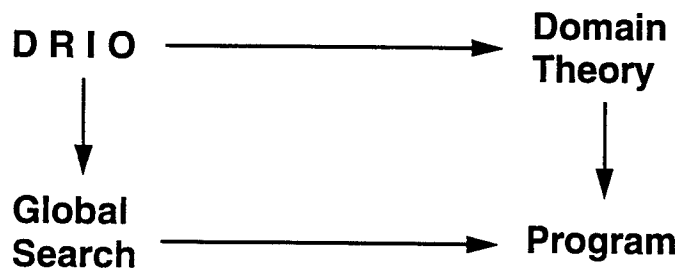
Example: n-Queens

The following brief review of KIDS is intended for the reader with some working knowledge of the system. Other readers are urged to read Smith(1990) and related papers to understand how KIDS works. This example is drawn from Smith(1990).

The n-Queens task is to place n queens on an nxn chessboard so that no two queens are on the same row, column, or diagonal. We are posed the task of enumerating all solutions for a given value of n.

1		Q		
2				Q
3	Q			
4			Q	
	1	2	3	4

The KIDS user must develop a theory of this domain that specifies the legal solutions. A direct way to do this is to specify a solution as satisfying a predicate that is the conjunction of the goal conditions: no-two-queens-on-same-row & no-two-queens-on-same-column & no-two-queens-on-same-up-diagonal & no-two-queens-on-same-down-diagonal. In Smith (1990), it is shown how KIDS combines this domain theory with a theory of global search to derive a correct high-level program. KIDS provides optimizations that the user can apply to this program. The process of theory combination can be viewed as forming the pushout of the domain theory with the global search theory. DRIO stands for the domain and range of the function to be synthesized, and the input and output conditions that specify legal inputs and outputs.



The goal conditions are used as filters to reduce the search space. However, even with these filters, the search space grows exponentially with the size of the problem. For example, in the 4-queens problem shown above, there is no solution if we place the first queen in the upper left-hand corner or lower-left hand corner, but the system cannot know this until it has searched all ways of placing the remaining queens. This exponential growth in the number of possibilities is the well-known Achilles' heel of problem solving, as it precludes the efficient solution of very large problems. Global search cannot be used to enumerate the solutions to the million-queens problem.

Effective search heuristics are known for finding a single solution to a problem of that magnitude, but they cannot efficiently enumerate all solutions. This prevents consideration of the space of solutions, and in particular prevents optimal problem solving. More seriously, the heuristic approach requires engineering a new heuristic for each problem class. This does not even partially solve the designer's problem of finding an efficient algorithm; it merely transforms it into the problem of finding an efficient heuristic.

What the designer needs is a method for finding good decompositions of the problem. A good decomposition of the problem has at least the following two properties: it splits the problem into components such that solutions within the components compose to form solutions to the whole problem, and it applies to all problems in the class.

KIDS does support decomposition, with its split and combine operations. However, the only two forms of decomposition implemented are first-rest decomposition and half-half decomposition. In first-rest decomposition, the first part of the problem description is solved and its solution is combined with the solution of the rest (this constituting a recursive call to first-rest decomposition.) In half-half decomposition, the problem description is split roughly in half, and solutions of each half are combined (again leading to recursive calls.) Mergesort is a typical example of half-half decomposition, while bubble sort is an example of first-rest decomposition.

These forms of decomposition are not generally applicable. For example, neither of these forms of decomposition applies to the n-queens problem. In first-rest decomposition, we would place one queen, then place the remaining n-1 queens. But as we saw above, if we place the first queen in the wrong place (a corner), the 1-queen solution will not compose with any solution to the n-1 queens to give a valid n-queen solution. Similarly, half-half decomposition would find any solution for placing 2 queens, and compose it with another 2-queen solution (which could be a copy of itself.) This need not be a solution to the 4-queen problem.

The next section briefly describes a domain-independent theory for finding domain-dependent decompositions. The reader is referred to Benjamin(1993) and Benjamin(1992) for further detail.

Automatic Decomposition of Theories

The remainder of this paper presents a method for automatically reformulating a domain theory. This method finds the local symmetries and invariants of a theory and uses them in two ways:

- to reformulate the theory in terms of the composition of independent subtheories, thereby generating a hierarchy for synthesis by decomposition;
- to inductively construct the class of problems in which this decomposition is guaranteed to work.

The decomposition method yields a set of components that are associated with independent features of the problem.

By analyzing the local symmetries and invariants of the theory, the system can relate local and global properties. In particular, it can derive how local solutions can be composed to give valid global solutions. By computing how these symmetries can be transformed into each other, the system inductively defines the class of tasks in which these properties are guaranteed to hold, i.e., it determines how the solutions scale up.

We are considering a task theory $M = (Q, A, \delta)$ consisting of a set A of actions defined as partial functions on a state space Q , together with a mapping $\delta: Q \times A \rightarrow Q$ that defines the state transitions. We are not concerned with the syntactic details of the encoding of A , but rather with which actions should be labeled the same and should therefore be considered instances of a common abstraction. In other words, we are concerned with the algebraic structure of A . A task is specified by a pair (i, g) , where $i: 1 \rightarrow Q$ maps a one-element set into Q identifying an initial state, and $g: 1 \rightarrow Q$ identifies a desired state. Further details are given in Benjamin et al.(1990). Without loss of generality, we can restrict our attention to semigroups of partial 1-1 functions on the state space Q (Howie, 1976).

The description of a system for the synthesis of a plan (or control) for M differs from the description of M in at least one essential way: the process of planning an action is reversible whether or not the action itself is reversible (assuming the synthesizing system can back-track.) Thus, the process of synthesizing plans for a given $M_1 = (Q, A_1, \delta_1)$ can be described by an automaton whose actions form an appropriate inverse semigroup containing A_1 ,

together with newly added inverse corresponding to backtracking. To define this automaton properly it is necessary to avoid the situation where a new inverse is applied (an action is retracted) when that action was not previously applied, e.g., moving a pawn backwards when the last action was not moving it forwards. To do so, we define the synthesizing automaton as a pushdown automaton M_2 defined as follows:

The state set of M_2 is $Q \times B_2^*$,

The action set of M_2 is $A_2 = A_1$ augmented by inverses for the non-invertible actions in A_1 ,

The pushdown alphabet $B_2 = A_1$,

The state transition map δ_2 pushes actions on which it is defined onto the stack. δ_2 is defined to act like δ_1 on actions in A_1 , and to invert a non-invertible action in A_1 only when that action is on top of the pushdown store. Otherwise, δ_2 is undefined.

In the remainder of this paper, we will consider pushdown automata for plan synthesis.

To analyze the structure of such a semigroup of transformations, a natural step is to examine Green's relations (Lallement, 1979). Green's equivalence relations are defined as follows: given any semigroup S :

$$\begin{aligned} aRb &\text{ iff } aS^1 = bS^1 & aLb &\text{ iff } S^1a = S^1b & aJb &\text{ iff } S^1aS^1 = S^1bS^1 \\ H &= R \cap L & D &= R \vee L \end{aligned}$$

where S^1 denotes the monoid corresponding to S (S with an identity element 1 adjoined) and \vee denotes the join of two relations. Intuitively, we can think of these relations in the following way: aRb iff for any plan that begins with "a", there exists a plan beginning with "b" that yields the same behavior; aLb iff for any plan that ends with "a", there exists a plan ending with "b" that yields the same behavior; aHb indicates functional equivalence, in the sense that for any plan containing an "a" there is a plan containing "b" that yields the same behavior; two elements in different D -classes are functionally dissimilar, in that no plan containing either can exhibit the same behavior as any plan containing the other. Utilizing Green's relations, Lallement defines a coordinate system for a semigroup:

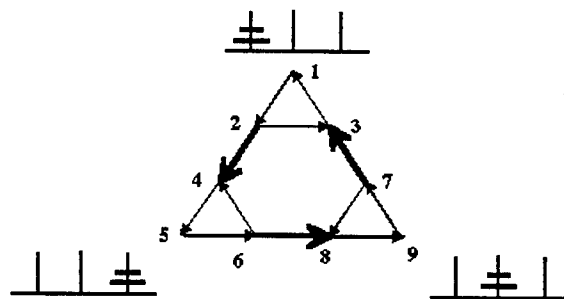
Definition. Let D be a D -class of a semigroup, and let $H_{\lambda\rho}$ ($\lambda \in \Lambda, \rho \in P$) be the set of H -classes contained in D (indexed by their L -class and R -class). A coordinate system for D is a selection of a particular H -class H_0 contained in D , and of elements $q_{\lambda\rho}, q'_{\lambda\rho}, r_{\lambda\rho}, r'_{\lambda\rho} \in S^1$ with $\lambda \in \Lambda, \rho \in P$ such that the mappings $x \rightarrow q_{\lambda\rho}xr_{\lambda\rho}$ and $y \rightarrow q'_{\lambda\rho}yr'_{\lambda\rho}$ are bijections from H_0 to $H_{\lambda\rho}$ and from $H_{\lambda\rho}$ to H_0 , respectively. A coordinate system for D is denoted by $[H_0; \{(q_{\lambda\rho}, q'_{\lambda\rho}, r_{\lambda\rho}, r'_{\lambda\rho}) : \lambda \in \Lambda, \rho \in P\}]$.

Each coordinate system gives a Rees matrix representation in much the same way that a coordinate system in a vector space gives a matrix representation, permitting us to change coordinates within a semigroup by performing a similarity transformation (inner automorphism) in the usual way (the reader is referred to Lallement for details). Each local coordinate system within the semigroup expresses a distinct structuring of a subtask, as we can choose a point in Q to be the "origin", and label points in Q according to the actions that map the origin to them. As we vary the coordinate system, each action varies through an equivalence class of actions. Any local property that is invariant under all local coordinate transformations is a property of the subtask itself, and hence is an abstract property. Any property that is not invariant under coordinate transformation is an implementation property. In particular, the abstract names for actions, which should not reflect implementation distinctions, can be determined by factoring a given automaton by its group of local coordinate transformations. The quotient semigroup thus obtained is the abstract language implemented in the given automaton.

The morphism from the D-class of the original semigroup to its abstract quotient is a partial morphism. The inverse of this morphism specifies the implementation of each abstract action in terms of sets of sequences of actions of the original semigroup.

Example: The Towers of Hanoi

Let us number the nine states of the 2-disk Towers of Hanoi as follows:



Let the two possible actions be denoted by "x" and "y".

x = 1 2 3 4 5 6 7 8 9 y = 1 2 3 4 5 6 7 8 9
 2 3 1 5 6 4 8 9 7 4 8 3

"x" moves the small disk right one peg (wrapping around from peg 3 to peg 1), and "y" moves the large disk one peg to the left (wrapping around from peg 1 to peg 3). In the figure, "x" is shown by narrow, counterclockwise arrows, and "y" is shown by thick, counterclockwise arrows. These two actions generate a semigroup of 31 distinct partial functions on the

states. Green's relations for this semigroup are:

D0

0

D1

x, xx, xxx

D2	xyx xyxxyx xyxxxyxx	xy xyxxy xyxxxyxy	xyxx xyxxxyxx xyxxxyxxxyxx
	xxyx xxyxxxyx xxyxxxyxxxyx	xxy xxyxxy xxxyxxxyxy	xxyxx xxyxxxyxx xxyxxxyxxxyxx
	yx yxxxyx yxxxyxxxyx	y yxxxy yxxxyxxxy	yxx yxxxyxx yxxxyxxxyxx

There are three D classes, shown as the three separate large boxes. In each D class, the R classes are rows and the L classes are columns, and they intersect in the small boxes, which are H classes. Note that D0 and D1 consist of only one R class and one L class, and hence one H class. The idempotents are in bold type.

There are no nontrivial inner automorphisms of D0 and D1. The group of inner automorphisms of D2 is a cyclic group of order three. These coordinate transformations are global within D2, but are local in the semigroup. These inner automorphisms are calculated by the matrix techniques explained by Lallement (1979). A generator for this group is the automorphism that maps xyx to xxy , xxy to yxx , and yxx to xyx . Factoring D2 by this map gives:

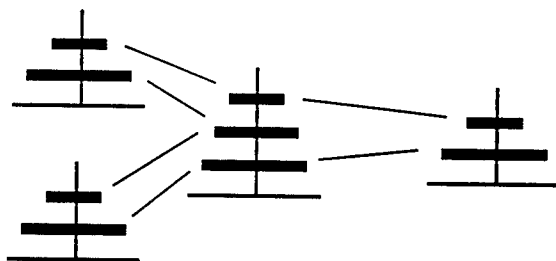
Define $z = \text{case } \{ \text{little disk left of large disk: } xxy$
 little disk on large disk: xyx
 little disk right of large disk: $yxx \}$

where z is a new symbol.

x is as before, and z moves both disks left one peg. z is a macro-action, which is implemented as a disjunction of sequences of actions. x and z are independent controls; x solves the position of the small disk, and z solves the big disk. x does not change the position of the big disk, and z does not change the relative positions of the disks. The disks can be solved in either order, as the new representation is an abelian group. This new representation cap-

tures the important property of the Towers of Hanoi task: the disks can be solved in any order. In the original theory, this property was obscured by details of the implementations of the disk moves.

This decomposition applies not only to the two-disk problem, but to all Towers of Hanoi problems. This is seen by forming free products of the semigroup with itself, amalgamating the coordinate axes in all possible ways. There are three free products of this semigroup with itself that amalgamate coordinates: D2 can be identified with itself, D1 with itself, and D2 with D1 (by mapping xyx , xyx , and yxx to x). These correspond to identifying the moves of the larger disk of one copy of the semigroup with the moves of the larger disk in another copy, identifying the moves of the smaller disk with the moves of the smaller disk, and identifying the moves of the larger disk with the moves of the smaller disk, respectively. The result of this construction is the three-disk Towers of Hanoi, which is viewed as three copies of the two-disk task running concurrently.



From the logical perspective, this can be viewed as composing three copies of a theory for the two-disk Towers of Hanoi, to yield a valid theory for the three-disk problem. Copies of the theory are joined by unifying variables between theories. Two copies joined at the middle disk will not suffice, as then the largest disk could be placed on the smallest disk. A third copy of the theory prohibits this. The purpose of computing a coordinate system is that the coordinate axes determine what to unify.

The interaction of these three smaller tasks yields a set of relations. For example, consider moving the middle disk one peg to the right. When considering this disk as the larger disk in the task consisting of the upper two disks, this move is $xyxy$ (in the state when all disks are on the left peg), $yxyx$ (when the smallest disk is to the right of the middle disk), or $xyxyxx$. On the other hand, when considering this disk as the smaller disk in the task consisting of the lower two disk, this move is x (in the other copy of the semigroup). This means that we add the relation $xyxy = yxyx = xyxyxx$ to the presentation of the semigroup.

This method of composing larger tasks from smaller ones guarantees that this decompo-

sition generalizes to any Towers of Hanoi problem with n disks, by considering a coordinate system for the three-disk task, and forming free products with amalgamation in the same manner as before. These free products with amalgamation will always reduce to free products with amalgamation of coordinate systems of the two-disk task, so that by induction the properties of the two-disk task determine the properties of all Towers of Hanoi tasks.

Example: Robot Path Planning

Let us consider a simple robot that moves on a hexagonal grid. Each grid point is labeled by its row and column. The robot's orientation can be north (N), northeast (NE), southeast (SE), south (S), southwest (SW), or northwest (NW). It has six basic motions: forward (F), forward right (R), forward left (L), backwards (b), backwards right (r), and backwards left (l). These motions are shown in Figure 1.

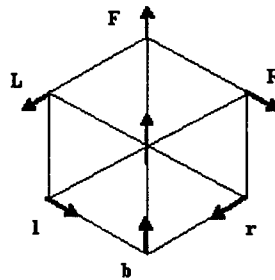


Figure 1.

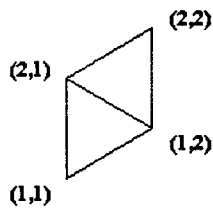


Figure 2.

The states of this robot split into two disjoint sets: any position with orientation N, SE, or SW, and any position with orientation S, NE, or NW. No state in either set is reachable from the other. We will examine only the first set, as the other is isomorphic. Let us examine the motion of this robot on a 2×2 grid, shown in Figure 2. There are twelve states in Q . The transformation semigroup A consists of all distinct state mappings generated by $\{F, R, L, b, r, l\}$, together with 0 (the empty mapping). Green's relations in this semigroup are

shown below.

0		
Fb F	Rr R	LI L
b bF	r rR	I IL
FbRr Rb Fr	LLL LL LLLL	FbLI FI Lb
FrF FrR FbR		FIL FIF FbL
bRb bFr bRr	RRR RR RRRR	bFI bLb bLI
bFrR Rb rF		IF bL bFIL

FRrb	RIFL	FRRF	FRr	RbLI	RIF	RbL	FR	Ri	RbLb	RIL	FRR
rrb	FrLbI	rRF	Fbrr	FrLI	FrFIF	FrL	Fbr	FrFI	FrLb	rrbR	FbrR
FILr	LbI	LIR	Rbrr	RrLI	LbII	RrL	Rbr	FrRI	RrLb	FrRIL	RbrR
lbLr	LFbI	LFIR	lbLrF	LFi	lbF	LF	LFIRbr	lb	LFb	lbL	LFIRb
brrb	rLbI	brRF	brr	rLI	rFIF	rL	br	rFI	rLb	rFIL	brR
ILr	IFL	bLIR	rFRr	bRrLI	rRIF	bRrL	rFR	rRI	IFLL	rRIL	rFRR
Rrb	bRIFL	RRF	bFRr	RRFr	bRIF	bRbL	bFR	bRI	bRbLb	bRIL	bFRR
bLr	bFL	bLbR	bLrF	LLFI	bFLI	LLF	bLrFR	Llb	bFLL	bLrR	bLbRb
lFr	bl	IR	lFrF	IRr	bII	bILF	IRbr	bIIb	bIL	lFrR	IRb
rb	RFrLbI	RF	rbF	RFr	rbRIF	RFrL	RFbr	rbRI	RFrLb	rbR	RFb
Lr	FL	LbR	LrF	LbRr	FLI	FLLF	LrFR	FLlb	FLL	LrR	LbRb
FIFr	FbI	FIR	FIFrF	FIRr	FbII	ILF	FIRbr	IIb	FbIL	IIbL	FIRb

Green's relations are used to construct a Rees matrix representation for the semigroup, and for the global and local inner automorphisms (the coordinate transformations.) These details are omitted here, due primarily to space considerations. Factoring this semigroup by its local coordinate transformations gives the familiar decomposition of path planning into planning changes in position and then planning changes in orientation. (More precisely, the semigroup is the normal extension of the subsemigroup that holds orientation invariant by

a group of orientation changes that holds position invariant.)

Now let us see how this decomposition scales up to all path planning on any such grid.

There are twelve free products of this semigroup with itself that amalgamate local coordinates.

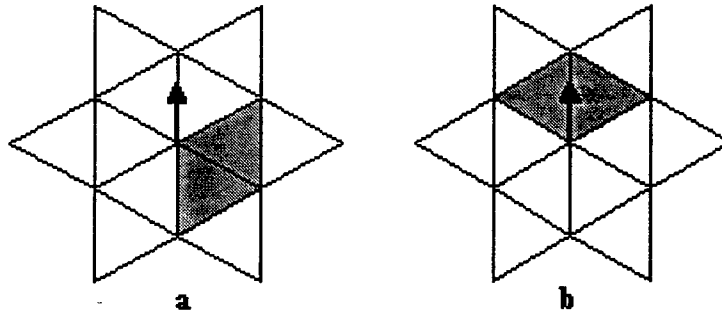


Figure 3. The twelve ways of composing 2x2 grids. This "flower" shape contains twelve 2x2 grids, each of which intersects every other in at least one point, the center point.

For example, the state (2,1,N) of the bold grid in Figure 3a corresponds to a different state in each of the other eleven 2x2 grids in the figure. For example, it corresponds to the state (2,1,SE) in the bold 2x2 grid in Figure 3b. In this way, each state in the 2x2 grid can potentially correspond to any of the other eleven states in another 2x2 grid. For example, the motion $RRFrLbll$, which maps (2,1,N) to (2,1,SW) must be given the same relabeling as $LbllbLrF$, which maps (2,1,SE) to (2,1,N). Continuing in this way, we derive the following: $FRRF = rLbll = lbLr = RFrL = bllb = LrFR = RRRFrLbll = bLrFRRfr = LbllbLrF = FrLbllbL = rFRRFrLb = llbLrFRR$. These twelve strings are the motions that rotate the robot counter-clockwise one turn, while holding the grid position invariant. Similarly, the clockwise motions, and the motions that hold the orientation invariant while changing position map together.

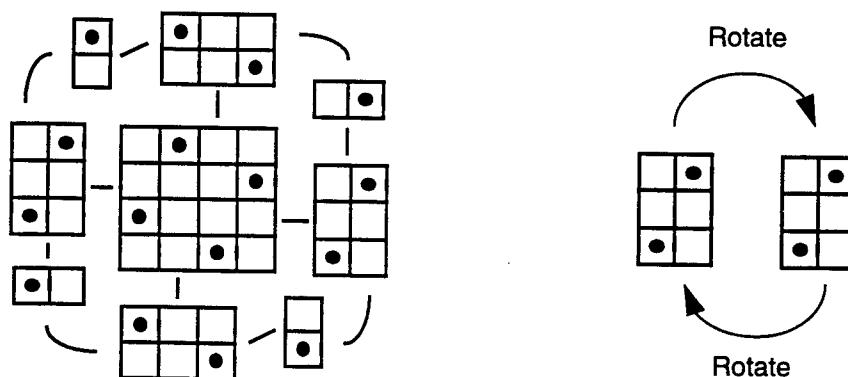
This can be viewed as composing twelve copies of a theory for the 2x2 grid to yield a valid theory for moving on a larger grid. Copies of the theory are joined by unifying variables between theories. The purpose of computing a coordinate system is that the coordinate axes identify what to unify. When the small grid is a subtask of a larger grid, the actions on the small grid must be able to be formulated as actions on the large grid. So, when considering all ways of composing grids to make larger grids, we are considering all ways of formulating small grid actions as larger grid actions, i.e., all ways of transforming coordinates within the small grid.

Thus, this method of composing larger tasks from smaller ones guarantees that the abstract properties of the small grid scale up to any grid composed from small grids, and in particular that the decomposition of the small grid generalizes to this infinite class of grids. This justifies the use of this path planning algorithm on any such grid. If any of the component semigroups resulting from this reformulation are too large, then the method is applied recursively, yielding a hierarchical decomposition. The method is terminated when the semigroups at the leaf nodes are considered sufficiently small to be searched, or are recognized as previously solved subtasks.

Example: N-Queens

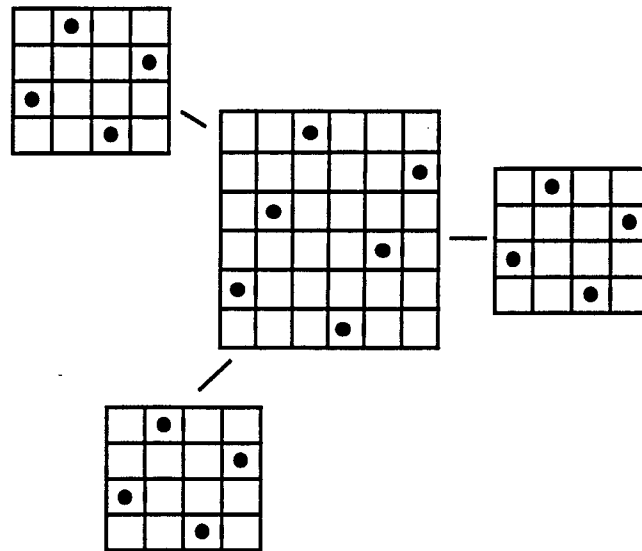
We now return to the n-Queens problem, to show how the reformulation method leads to a program for enumerating the solutions to the problem without considering any non-solutions. In this section, we will not show the computation of Green's relations, as this is repetitive. Instead, we will show the local and global symmetries pictorially.

The next figure shows a solution to the 4-queens problem. (The other solution is obtained by a flip symmetry of this one.) This solution has a hierarchy of local symmetries. The top-level local symmetry is that of the 3×4 subproblems, but the four 3×4 subproblems in the 4×4 are mapped to each other only by the cyclic global symmetry of order 4. The first new local symmetries arise from considering the 2×3 subproblem that contains 2 queens. The four instances of this subproblem are of course also mapped to each other by the cyclic global symmetry, but also map to themselves by a local symmetry of order 2. The next figure shows these four instances, together with the 1×2 subproblems that arise from intersecting the 2×3 subproblems:



As in the other problems considered, we construct larger instances of the n-queens problem from copies of the 4x4 solution, amalgamating the local symmetries. For example, the 6-

queens solution can be constructed from four copies of the 4-queens solution by amalgamating 2x3 subproblems:



The 6-queens solution can be viewed as three 4-queens solutions in this way.

Stated another way, the construction of the 6-queens solution from multiple 4-queens solutions can be thought of as follows: take 2 copies of the 4-queens solution and amalgamate a 2x3 subproblem in one copy with a 2x3 in the other. There are 6 distinct queens. The four queens in the first copy are guaranteed to be on their own rows, columns, and diagonals, and the four queens in the second copy are similarly guaranteed to satisfy the solution conditions. But we are not guaranteed that the two non-amalgamated queens in one copy are on distinct rows, columns, or diagonals from the two non-amalgamated queens in the other copy. It is necessary that those four queens also satisfy the solution conditions, i.e., we need them to be a 4-queens solution by themselves. Therefore, composing three 4-queens solutions in this way is both necessary and sufficient to give a 6-queens solution, which implies that all 6-queens solutions are constructed in this way.

Thus, we can construct n -queens solutions from smaller solutions. It is not necessary to search a space containing non-solutions. Instead, analysis of the structure of the base case reveals both the decompositions of the base case and the inductive definition of the class of problems with the same structure. Ideally, a system such as KIDS should have the capability to perform this analysis, to synthesize programs that construct the solution space directly in this fashion whenever possible.

Summary

The analysis of the structure of a representation can lead to both a greater understanding of the task and to techniques for system design and implementation. Identification of the invariants and symmetries of a representation yields decompositions of the representation. The definition of coordinate systems for transformation semigroups gives a method for automatic design of a representation for a class of tasks.

KIDS supports the divide-and-conquer approach to problem solving, but needs a technique for automatic identification of useful decompositions. This work has completed a theory of decomposition, and demonstrated how it can be used to reformulate KIDS domain theories to find effective algorithms.

REFERENCES

- Benjamin, D. Paul, (1993). Formulating Patterns in Problem Solving, *Annals of Mathematics and Artificial Intelligence*, special issue on Mathematics in Pattern Recognition (forthcoming).
- Benjamin, D. Paul, (1992a). Towards an Effective Theory of Reformulation, in *Proceedings of the Workshop on Change of Representation and Problem Reformulation*, Michael R. Lowry (ed.), NASA Ames Research Center Technical Report FIA-92-06, pp.13-27, April, 1992.
- Benjamin, D. Paul, (1992). Reformulating Path Planning Problems by Task-preserving Abstraction, *Journal of Robotics and Autonomous Systems*, **9**, pp. 1-9.
- Howie, J. M., (1976). An Introduction to Semigroup Theory, Academic Press.
- Lallement, Gerard (1979). Semigroups and Combinatorial Applications, Wiley & Sons.
- Smith, Douglas R., (1990). KIDS: A Semi-Automatic Program Development System, *IEEE Transactions on Software Engineering*, Vol. 16, No. 9, Special Issue on Formal Methods, pp.1024-1043, September, 1990.

THE APPLICATION OF QUADRATIC PHASE CODING TO OTH RADAR SIGNALS

Frank T. Berkey
Research Professor
Center for Atmospheric and Space Sciences

Utah State University
Logan, UT 84322-4405

Final Report for:
Summer Faculty Research Program
Rome Laboratory

Sponsored by:
Air Force Office of Scientific Research
Bolling Air Force Base, DC

and

Rome Laboratory/OCDS
26 Electronic Parkway
Griffiss AFB, NY 13441-4514

September 1994

THE APPLICATION OF QUADRATIC PHASE CODING TO OTH RADAR SIGNALS

Frank T. Berkey
Research Professor
Center for Atmospheric and Space Sciences
Utah State University
Logan, UT 84322-4405

ABSTRACT

High-frequency radio waves reflected from the Earth's ionosphere can be used to illuminate targets that are several thousand kilometers from the transmitter. Much of the early research and development of this over-the-horizon (OTH) technique was conducted during the 1950s at the Air Force Rome Laboratory (then called the Rome Air Development Center) and at the Naval Research Laboratory. Today, OTH radar technologies play a central role in the DoD Counterdrug Program, where the primary mission is the detection of small targets with relatively low radial velocity. The ionosphere, however, is a highly variable medium containing a wide range of irregularities, whose structure and behavior is dependent on many factors. In many situations, these irregularities can have a deleterious effect on the signals received by HF OTH radar systems. Although ionospheric plasma irregularities are present to some degree at all latitudes, they are most prevalent at night and in the equatorial and auroral regions. Their effect is to broaden the Doppler spectrum of the backscattered clutter which in turn masks the signature of low-velocity targets with small radar cross section. Several strategies have been proposed to mitigate the effect of these irregularities but no satisfactory solution has yet been adopted for operational systems. One possible solution to this problem is the application of phase encoding of the transmitted signal and the appropriate decoding of the received backscatter echoes. The implementation of this solution was carried out by Decision-Science Applications, Inc. under contract to Rome Laboratory and the first experimental field tests were carried out in June and July of 1994 using in-house facilities. This report discusses some of the initial results obtained during these field tests.

THE APPLICATION OF QUADRATIC PHASE CODING TO OTH RADAR SIGNALS

FRANK T. BERKEY

Introduction

For several decades, high-frequency (HF) radio waves have been used to study the ionosphere using vertical incidence ionospheric radars known as ionosondes [e.g. *Davies*, 1991]. These instruments transmit vertically into the ionosphere and sweep through the HF spectrum at frequencies from ≈ 1 to 20 MHz, recording the time-of-flight of echoes reflected from the various ionospheric layers as a function of frequency. The time-of-flight can be converted to the "virtual" height of the ionosphere and the frequency at which wave retardation occurs directly interpreted as the critical plasma density of the particular ionospheric layer through the relation $N_e = f^2 / 81$, where N_e is the electron density per cubic meter and f is the probing frequency in Hertz. The measurements from these instruments, distributed in a loose-knit network of global stations, have been (and currently are) used to infer a wide variety of information about the morphology of the ionosphere. Since the ionospheric plasma density is a function of many variables, such as latitude, time-of-day, season and solar cycle, it is not easily characterized by mathematical functions except on a very coarse time scale. Thus, synoptic measurements from the global ionosonde network have been used to determine the ionospheric "weather" on both micro- and macro-scales

To obtain information about the ionosphere at locations other than overhead, the technique of oblique sounding was developed, which provided data at the ionospheric mid-point between transmitter and receiver [see e.g. *Croft*, 1972]. Subsequently, it was recognized within the defense community that targets beyond the horizon could be illuminated using high power HF radio waves that have been reflected one or more times from the ionosphere. This technique, known as over-the-horizon (OTH) radar, was developed in the United States at the Air Force Rome Laboratory (RL) and the Naval Research Laboratory starting in the 1950s [*Stebbins*, 1992]. The research and development carried out under the auspices of these laboratories led to the deployment of operational OTH systems [*Headrick*, 1974, 1990a,b]. The same technique was also employed by the former Soviet Union [*Kolosov*, 1987; *Estravkov*, 1994] and more recently in Australia [*Anderson*, 1986, 1992; *Earl and Ward*, 1987]. OTH radar systems were initially utilized for the detection and early warning of long-range bomber and/or cruise missiles launched in hostile attacks against the United States. To that end, the first two operational OTH systems, deployed on the east and west coasts, were intended to monitor the ionosphere above the former Soviet Union. After the end of the Cold War in 1989, the Soviet threat disappeared as did the primary mission of the OTH-B radars. In place of more conventional airborne radar systems, OTH radar technology has recently been utilized in the DoD/ARPA Counterdrug program to detect the small, low speed, maneuvering aircraft that are typically used to transport contraband drugs from South and Central America into the U.S.

Two OTH radar systems are currently operational within the U.S. The Air Force OTH radar, designated AN/FPS-118, is sited near Bangor, Maine and has been in operation since 1985 [*Boutacoff*, 1985]. The field-of-view (FOV) of this OTH radar encompasses look angles over the South American continent although this was not the

intended function of the system. In 1992, the U.S. Navy deployed an OTH radar (designated AN/TPS-71) at a location near Chesapeake, Virginia (this system is also referred to as ROTH). The primary FOV of this radar is directed over South America; ten angular cones of $\approx 12^\circ$ HPBW are illuminated by the transmitter, each of which is sampled using 16 narrow receive beams. Two additional AN/TPS-71 radars are to be installed, one in Texas and the other at a site yet to be determined. The deployment of an advanced OTH (AOTH) radar in an offshore theater is currently under consideration.

The range window sampled by an OTH radar is governed to a large extent by the propagation conditions existing at the time of transmission, but generally covers between 900 and 3700 km via a single ionospheric reflection. Targets at relatively short ranges are illuminated by HF radio wave propagation via the ionospheric *E*-layer (at ≈ 120 km), whereas *F*-layer (≈ 250 km) propagation enables target detection at greater distances. The radar cross section (RCS) of the target is also important since it is a function of the frequency transmitted by the radar. At night, for example, the ionosphere supports HF propagation at lower frequencies than during the day when ionospheric densities are higher. Hence, the same target will have a smaller RCS when illuminated at night because of the longer wavelengths that are needed to sustain long distance propagation. A further advantage of HF OTH technology is its effectiveness against stealth aircraft.

The OTH radar systems deployed in the U.S. transmit a frequency modulated, continuous wave (FMCW) wave form at power outputs ranging from 200-1200 kW. The transmitter and receiver sites are spatially separated, typically by distances on the order of ≈ 200 km, since a continuous wave form is transmitted. Note that co-sited OTH systems have recently been advocated for the proposed French NOSTRADUMUS OTH system [Casamayou, 1991; Saillant, 1992]. Large aperture arrays with narrow, steerable beams have been developed for receiving [e.g. Washburn and Sweeney, 1976]. For example, the wide aperture research facility (WARF) operated by Stanford Research Institute (SRI), employs a linear receiving antenna array 2.5-km in length containing 256 vertical monopole elements, each 5.5m tall. MITRE Corporation has recently constructed a 3-km diameter array of 96 short (6m) vertical monopole elements near Odessa, Texas [e.g. Rastogi *et al.*, 1994]. Each of the monopole elements in this sparse array is connected to a digital receiver and numerical beamforming is carried out.

In most OTH applications the Doppler frequency spectrum of the backscattered signal is the fundamental data product. Ionospherically reflected backscatter is received from both land and sea surfaces and is typically 30-70 dB stronger than an aircraft target [Barnum, 1993]. Land reflections have zero Doppler shift and are often characterized by echoes from mountain ranges, large urban areas, and long, elevated power lines. Backscatter from the ocean has a characteristic Doppler spectrum due to surface waves which generate the so-called Bragg lines at ± 0.38 Hz [Crombie, 1955; Wyatt, 1990]. Such spectra have been utilized to derive surface wind maps over a wide area of the ocean [Georges and Harlan, 1992; Atlas and Weinman, 1992] but generally require long radar dwell times. The difference in reflectance at the land-sea boundary also produces a unique backscatter signature. A moving target with sufficient radial velocity will produce a spectral signature in the Doppler regime that is distinguishable from other sources of clutter.

To a first approximation, the ionosphere can be considered as a perfectly reflecting mirror in which case the backscattered signals undergo little Doppler "smearing" and have relatively narrow peaks in the Doppler frequency regime. In practice, however, the ionosphere is frequently both in motion and highly structured which has the effect of broadening the backscatter signal in the Doppler regime. The occurrence of backscatter echoes with a broad Doppler spectrum is termed spread Doppler clutter (SDC) by the OTH radar community and it has a deleterious effect on operational systems. The ionospheric irregularities (generally referred to as "spread- F ") responsible for this clutter are most prevalent in the auroral and equatorial regions but also occur at mid-latitude, particularly at night.

The backscattered OTH echoes undergo several forms of signal contamination and distortion that can be identified with known physical processes occurring in the ionosphere [Anderson, 1992]. These processes result in errors of up to ± 20 km in the location of aircraft targets. The primary sources are:

- Slow phase path variations caused by traveling ionospheric disturbances and other large-scale phenomena;
- Discrete multi-mode propagation via E, F₁, F₂ and hybrid paths to and from the target area;
- Spectral broadening due to small-scale plasma turbulence;
- High angle rays, with strongly range-dependent Doppler shifts;
- Impulsive noise from thunderstorms in the lower atmosphere;
- Man-made radio frequency interference;
- Echoes from meteors, auroras, field-aligned plasma striations and equatorial plasma instabilities;
- Ground clutter received through sidelobes, back lobes and two-hop contributions.

Ionospheric spread- F in the equatorial region is a major source of SDC for OTH systems in both the U.S. and Australia. The equatorial region is broadly defined as that region within $\pm 20^\circ$ of the geomagnetic equator where anomalously large electron densities are observed (i.e. the Appleton anomaly). On the 75°W meridian, the magnetic equator occurs at $\approx 10^\circ\text{S}$ latitude, or ≈ 6000 km down range from the RL transmitter at Ava, NY. The Doppler spectrum of backscattered echoes passing through these irregularities (or reflected by them) can be broadened to such an extent ($\approx \pm 10$ Hz) that targets with low Doppler velocity are undetectable. Although equatorial spread- F has been studied rather extensively, no satisfactory theory can address such questions as to why it occurs on some nights and not on others or why it is more prevalent during particular seasons of the year at certain locations [Kelley, 1989]. Structures with spatial scale sizes between 0.1 and 10^5 m have been detected in the equatorial ionosphere and various hypotheses have been put forth to explain the generation of the observed irregularities [Kelley, 1992]. These are:

- Gravity wave seeding and electrodynamic uplift ($\lambda > 200$ km),
- Shear effects ($200 \text{ km} > \lambda > 20$ km),
- The generalized Rayleigh-Taylor instability ($0.1 \text{ km} < \lambda < 20$ km),
- Low-frequency drift wave ($1 \text{ m} < \lambda < 100$ m),
- Lower hybrid drift waves ($\lambda < 1$ m).

In an attempt to predict the effect of ionospheric irregularities on HF propagation [see e.g. Elkins, 1990], several approaches to developing a model of SDC have been undertaken, several of which utilized phase screens [Basler et al., 1988]. Another approach extended a statistical model of clutter in the auroral ionosphere to the equato-

rial regions [Elkins, 1987; Elkins and Providakes, 1992]. Recently, Coleman [1993] has combined the statistics of irregularities with ray tracing and an ionospheric model to predict the characteristics of SDC. This model shows that the upward motion of the ionosphere at sunset leads to a negative Doppler which accumulates to produce a negative tilt to the clutter. When the equatorial F2 peak is very high, the model suggests that rays spending a considerable time in regions of strong irregularities are those returning from the far side of the Appleton anomaly. In the early morning, as the F2 peak falls, an overall positive tilt in the clutter develops.

Clutter Mitigation Techniques

Because SDC can mask targets of interest, there is considerable motivation to find solutions which will mitigate these effects. However, the problem becomes complex because of the ambiguities associated in selecting the radar parameters. The wave form repetition frequency (WRF) determines the range over which backscatter echoes can occur without range aliasing. For example, at a WRF of 10 Hz, the unambiguous range extent is 15,000 km but the unambiguous velocity extent is only 200 meters/sec. Increasing the WRF to 50 Hz increases the Doppler resolution (to 1450 meters/sec), but decreases the unambiguous range extent to only 3000 km. At the higher WRFs, backscatter echoes from more distant ranges will be aliased into the range window; an example of such aliasing is discussed below.

Several clutter mitigation strategies have been proposed; one recent suggestion has been the deployment of "stereo" OTH radars that view a common ionospheric volume from different azimuths [Barnum, 1991]. As there is some evidence that equatorial clutter has a different temporal evolution at different azimuths, the fusion of the two OTH data sets could be used to mitigate against strong SDC observed by one or the other of the radars. Another proposal has been to take advantage of the parallax that exists as a result of the separation between transmitter and receiver [Sievers, 1991] in system siting. This solution also takes into consideration the azimuthal dependence of the growth of irregularities in the equatorial ionosphere.

A third approach to the problem, proposed by Decision-Science Applications (DSA), Inc., is the utilization of non-recurrent wave form (NRWF) coding of the transmitted signal. This technique has the desired effect of suppressing the range ambiguous clutter by means of modifying the ambiguity diagram. Various NRWF codes were evaluated (adaptive, random binary, Frank and quadratic) with regard to their suppression of range ambiguities and the degree of subclutter visibility. The quadratic NRWF was selected because it modifies the classical "bed of nails" ambiguity surface such as to fold the range ambiguous clutter to "unused" negative (positive) Doppler frequencies. The capability of moving the SDC to either positive or negative frequencies can enable OTH operators to selectively search for targets which are moving toward (away from) the radar. In order to implement the quadratic phase code (QPC), it was necessary to acquire a frequency agile signal simulator (FASS) manufactured by Hewlett-Packard that is used to encode the transmitted FM wave form of the Ava transmitter. The backscattered signal is decoded using matched filter techniques. The DSA receiving system consists of six Watkins-Johnson receivers which interface with the VXI bus and are controlled by an embedded 80486 DOS-based computer. The quadrature output of the receivers is digitized under the control of a 68020 CPU (operating under OS-9) which hosts three DSP boards each containing three TMS320C30 CPUs on a VME bus. Communication between the CPUs is effected with ethernet.

The implementation of the QPC wave form was carried out by DSA under contract to RL and the first experimental field tests were conducted in June and July of 1994 using in-house RL facilities.

The ambiguity function is defined as the absolute value of the envelope of the output of a matched filter when the input to the filter is a Doppler-shifted version of the original signal, to which the filter was matched [Levanon, 1988]. If the complex envelope of the signal is $u(t)$, the ambiguity function can be expressed by

$$|X(\tau, \nu)| = \left| \int_{-\infty}^{\infty} u(t) u^*(t - \tau) \exp(j2\pi\nu t) dt \right|,$$

where τ is a time delay and ν is the Doppler shift. A linear FM pulse has a complex envelope which is written

$$u(t) = \frac{1}{\sqrt{t_p}} \text{rect}\left(\frac{t}{t_p}\right) \exp(j\pi k t^2),$$

where t_p denotes the pulse duration. By replacing ν with $\nu + k\tau$, the ambiguity function of the linear FM pulse can be written

$$|X(\tau, \nu)| = \left| \left(1 - \frac{|\tau|}{t_p}\right) \frac{\sin\left[\pi t_p (1 - |\tau|/t_p)(\nu + k\tau)\right]}{\pi t_p (1 - |\tau|/t_p)(\nu + k\tau)} \right|, \quad |\tau| \leq t_p.$$

The ambiguity functions for a single pulse and pulse trains are discussed in detail in the monograph by *Rihaczek* [1977]. Detailed modeling of the ambiguity function for the QPC has been carried out in MATLAB® by DSA [Clancy, private communication].

Experimental Program

A series of tests were begun June 28, 1994 utilizing the RL Verona receiving facility and the Ava transmitter site. Due to software problems in the receiving hardware, no measurements were acquired on either June 28 or June 29. However, these initial problems were overcome and data were recorded during the evening hours of June 30. Additional measurements were made during three nights beginning July 11, 1994. During this series of tests, three different wave forms were tested: 1) a WRF of 48.8 Hz using the QPC to effect both positive and negative off-set; 2) a WRF of 48.8 Hz with no coding, and; 3) a WRF of 10 Hz with no coding. Details of the wave forms are given in Table 1. Transmissions at several frequencies were used, dependent on the propagation conditions and the

WRF (Hz)	48.828	48.828	10
Wave form	LFM +QPC	LFM	LFM
Doppler Resolution (Hz)	0.375	0.375	0.5
Unambiguous Range (km)	3072	3072	15,000
Number of range bins	128	128	625

Table 1. Details of transmitted wave forms used during the July 1994 Ava-Verona experiments.

channel occupancy; the signal bandwidth was 4 kHz and a transmitted power of 100 kW was used. A rhombic antenna (azimuthal HPBW $\approx 7.5^\circ$) directed at 184° from true north was used for transmitting; a Beverage array having a 10° HPBW was employed at the Verona site for receiving. This array has 12 elements, not all of which were functional during the field tests.

For the purposes of this report, only data acquired on July 14/15, 1994 will be discussed. The data shown here were acquired over an interval of ≈ 30 min, between 0500 UT and 0530 UT on 15 July 1994. Figure 1 shows a Doppler-range plot where the unambiguous range is 15,000 km (wave form 3) and the number of samples was 20 (Doppler resolution = 0.5 Hz). Three distinct regions of backscatter echoes are present at ranges of 1824-3400 km, 4250-6600 km and 8780-9400 km. The same data are shown in a three-dimensional format in Figure 2. In Figure 3, the WRF was increased to 48.828 Hz (unambiguous range of 3072 km) and 128 samples were digitized (wave form 2). In this case, range aliasing occurs and clutter (backscatter echoes) from longer ranges is folded over the whole range window. As a result of the higher WRF, the spectra shown in Figures 3, 4, 5 and 6 cover a frequency range of ± 24 Hz. The results shown in Figure 4 and 5 were obtained when QPC coding was applied to the FMCW signal using a WRF of 48.828 Hz (wave form 1). In these Figures, the first range window (0-3072 km) is centered at 0 Hz; echoes from longer ranges appear at integer multiples of negative Doppler offsets of 48.828 Hz/10. For example, echoes between 3073 and 6144 km are centered at -4.8828 Hz. Taking into account the Doppler frequency at which the echoes occur, these data can be compared with the unambiguous backscatter data shown in Figure 1. Doing so indicates that backscatter echoes occur between 2470-3650 km, 4700-7200 km and 8850-10,800 km. These ranges are in general agreement with the three groups of echoes observed using a WRF of 10 Hz; any disagreement can presumably be accounted for by the fact that the two soundings were acquired 30 minutes apart, during which time the height of the F2 region increased. Clutter introduced by echoes from what is possibly ionization created by a meteor can be seen at a slant range of 500 km. In each of the three examples discussed here, the transmissions occurred at 16.5 MHz at a power level of 100 kW and a bandwidth of 4 kHz.

The Doppler spectra derived from the data shown in Figure 1 (10 Hz WRF) are presented in Figure 6 and those from Figure 4 (48.8 Hz WRF) in Figure 7. Spectra from 12 successive range gates at 24 km intervals, starting with the closest range in the upper left-hand corner and continuing to the farthest of the 12 range gates in the lower right-hand corner, are depicted. In panel (a) of Figure 6, data from range gates between 1920 and 2184 km are shown. These data have a relatively narrow spectral peak (≈ 2 Hz) which shifts from positive to slightly negative Doppler values with increasing range. The spectra from the second hop ground backscatter (i.e. 4824-5088 and 6024-6288 km) exhibit approximately the same Doppler width and the peak also moves from positive to negative Doppler values. Although the clutter detected at ranges > 9000 km has a somewhat broader spectra, none of these data are suggestive of the spread Doppler clutter observed in sector 7 by the ROTH system during the January 1994 SDC campaign [Boak, 1994; Rastogi and Providakes, 1994].

In Figure 7, spectra acquired when the QPC wave form was transmitted are shown. These spectra correspond to range gates between (a) 2112 and 2376 km, (b) 2616 and 2880 km and (c) 144 and 408 km are depicted. The spectra in Fig. 7(a) are dominated by a single peak near -5 Hz and a weak secondary maxima near -10 Hz. A

peak near 0 Hz develops at ranges beyond ≈ 2200 km. The Doppler offset of ≈ 5 Hz indicates that the dominant peak occurs at a range of > 5200 km. Two spectral peaks occur in Fig. 7(b), the largest near 0 Hz and a secondary peak at ≈ -4.8 Hz indicative of echoes at ≈ 2600 km and ≈ 5700 km. In Figure 7(c), showing spectra between 144-404 km, four distinct peaks occur corresponding to echoes at ranges of 144, 3216, 6288 and 9360 km. The echo at 144 km is the ground wave signal from the Ava transmitter.

Ionospheric ray tracing programs can be used as a tool to predict or model HF propagation paths. One such program [Argo *et al.*, 1990] was implemented by the author on a Sun Workstation at RL and employed to model the path of a 16.5 MHz radio wave transmitted from the Ava site. On July 15, the effective sunspot number was 35 and the geomagnetic field was at minor storm levels ($K_p=4^+$) at the time of the backscatter soundings. Results from the LANL Tracker program are shown in Figure 8a,b where a path due south from the Ava field site (43.5°N , 75.1°W) was specified. For a sunspot number of 35, no HF propagation at 16.5 MHz is sustainable (panel a); when the *F*-region density is increased using a sunspot number of 100, rays with elevation angles of $4\text{--}7^\circ$ are propagated. The entire 24 hr interval (at two hour increments) has been simulated, the results of which are shown in Appendix A (not included in this final report). At local noon (16 UT), the *E*-region is present and nearly all the low angle rays are propagated by reflection from that region, although some higher angle rays undergo reflection from the *F*-layer. The first hop Earth reflection occurs approximately 1600 km down range. The propagation conditions do not change drastically until 1800 LT, when ionization in the *E*-region decreases and *F*-layer reflections begin to dominate. By 2000 LT, all propagation occurs via the *F*-region and the first hop Earth reflection is at a range of ≈ 2000 km. As the *F*-region peak increases in height, the distance at which the first Earth reflection occurs also increases, and is ≈ 2500 km down range at 0530 UT. This result is generally consistent with the observed backscatter ionograms. The *E*-region begins to form again at 0400 LT and short range propagation is possible at some elevation angles. At this time, many of the rays propagate through the ionosphere and there is a time near 0600 LT when only long distance propagation can occur. Presumably, ionospheric tilts associated with sunrise are responsible for this chaotic interval of propagation. As the Sun ionizes the *E*-region, it again becomes the dominant layer and sustains most of the low angle propagation.

Conclusions

The initial series of field experiments conducted at RL has demonstrated that the QPC wave form can be successfully applied to OTH backscatter radar systems, shifting the range-folded backscatter echoes to higher or lower frequencies in Doppler space. What has not yet been demonstrated is the application of this method under conditions when equatorial clutter was known to have occurred. In this context, it should be noted that no prior experiments have demonstrated that SDC from the equatorial ionosphere can be detected using the Ava-Verona facilities. It is certainly possible that the relatively small receiving array at Verona does not have enough gain to detect SDC, which is often 20-30 dB weaker than the normal ground clutter. Certainly, none of the spectra acquired thus far exhibit the broad Doppler frequency extent that have been reported by operational OTH radar systems [Boak, 1994; Rastogi and Providakes, 1994; Coleman and Ward, 1994]. Backscattered echoes from the Ava transmitter should undergo Doppler broadening at ranges between ≈ 4300 and 7600 km, which more-or-less coincides with the second group of

echoes in Figure 1. In addition, the performance of the wave form in an operational (i.e. tracking) mode has also not been studied and the question of how targets might be aliased in Doppler space remains open.

Future experiments ought to focus on the following aspects:

- 1) Apply only the uncoded 10 Hz WRF and the coded 48.8 WRF with short time intervals (≈ 5 min) between the two formats;
- 2) Test codes that enable larger frequency offsets in Doppler space;
- 3) Utilize longer coherent integration times to obtain sea backscatter spectra so as to verify system performance;
- 4) Test higher WRFs in the range 60 to 100 Hz [*Clancy*, private communication];
- 5) Conduct extended operations to acquire data during the day-night and night-day transition in the equatorial region;
- 6) Document the occurrence of spread Doppler clutter in the appropriate ROTH beam;
- 7) Acquire time-contiguous data to demonstrate tracking capability;
- 8) Incorporate improvements to the receiving antenna array, such as modifying the VALAR array to look south instead of north;
- 9) Utilize additional receivers, perhaps for impulsive noise reduction (thus far, only one of six has been used);
- 10) Employ more modern spectral analysis techniques in the data analysis process [e.g. *Bourdillion et al.*, 1987; *Cooley et al.*, 1987].

References

- Anderson, S.J., Adaptive remote sensing with HF skywave radar, *IEE Proc.*, **139**(2), 182-192, 1992.
- Anderson, S.J., Remote Sensing with the JINDALEE Skywave Radar, *IEEE J. Ocean. Eng.*, OE-11, 158, 1986.
- Argo, P.E., T.J. Fitzgerald, J.H. Wolcott, D.J. Simons, S. Warshaw, and R. Carlson, HF Propagation Through Actively Modified Ionospheres, Proc. 1990 Ionospheric Effects Symposium, May 1-3 1990.
- Atlas, R. and J.A. Weinman, White Paper on the meteorological impact of surface wind directions measured by over-the horizon radar (OTHR), Proc. OTH Radar Technology Conference 5-7 November 1991, Vol. IV, January 1992.
- Barnum, J.R., Stereo OTH Radar Development and Evaluation, Vol. IV ESD/RADC OTH Radar Symposium, Hanscom AFB, 5-7 November 1991.
- Barnum, J.R., Long-range surveillance of private aircraft by OTH radar, with CD applications, ONDCP/CTAC Tactical Technologies and Wide Area Surveillance Intl. Symp., Chicago, IL, Nov. 1993.
- Basler, R.P., G.H. Price, R.T. Tsunoda and T.L. Wong, Ionospheric distortion of HF signals, *Radio Sci.*, **23**(4), 569-579, 1988.
- Boak, S.J., Relocatable Over the Horizon Radar (ROTHR), American Sector Measurements of Equatorial Spread-Doppler Clutter, 11 to 15 January 1994, Quick Look Report, Raytheon Company, January 1994.
- Bourdillon, A., F. Gauthier and J. Parent, Use of maximum entropy spectral analysis to improve ship detection by over-the-horizon radar, *Radio Sci.*, **22**(2), 313-320, 1987.
- Boutacoff, D.A., Backscatter radar extends early warning times, *Defense Electronics*, 71-83, May 1985.
- Bucknam, J.N., OTH Technology Analysis III, RL-TR-91-236, Final Tech. Rep., Raytheon Company, October 1991.
- Casamayou, J.-P., The French Over-the Horizon Radar is Created, *Air and Cosmos*, **1330**, 20-21, May 1991.
- Coleman, C.J. and B.D. Ward, The effect of irregularities on radar clutter, Peaceful Valley Conference, June 1994.
- Coleman, C.J., A Model of Doppler Spread Clutter, p. 37, 1993 Ionospheric Effects Symposium, Ed. J.M. Goodman, 1993.
- Cooley, D.W., J.M. Lletsky, D.M. Bubenik, D.S. Seaton, W.F. Marshall and J.R. Barnum, Modern Spectral Analysis Techniques for Enhanced Detection and Resolution of OTH-Radar Targets in Spatial and Doppler Domains, Contract N00014-84-C-0436, SRI Project 7259, Tech. Rep. 75, SRI Intl., June 1987.
- Croft, T.A., Sky-wave Backscatter: A Means for Observing Our Environment at Great Distances, *Rev. Geophys.*, **10**(1), 73-155, 1972.
- Crombie, D.D., Doppler Spectrum of Sea Echo at 13.56 Mc/s, *Nature*, **175**, 681-682, 1955.
- Davies, K., **Ionospheric Radio Propagation**, NBS monograph #80, Dept. Commerce, 1965.
- Earl, G.F. and B.D. Ward, The frequency management system of the Jindalee over-the-horizon backscatter HF radar, *Radio Sci.*, **22**, 2, 1987.
- Elkins, T.J., Ionospheric Clutter Model for OTH Radar, MITRE Report MTR10299, August 1987.
- Elkins, T.J., OTH Radar Performance Estimation, MITRE Report MTR10938, July 1990.
- Elkins, T.J. and J.F. Providakes, A Revised Global OTH Clutter Model, Proc. OTH Radar Technology Conference 5-7 November 1991, Vol. II, January 1992.

- Evstratov, F.F., A.A. Kolossov, A.A. Kuzmin, E.I. Shustov, V.A. Yakunin, Yu.I. Abramovich and V.A. Alebastrov, Over-the-horizon radiolocation in Russia and Ukraine (The history and achievements), *L'Onde Électrique*, **74**(3), 29-33, 1994.
- Georges, T.M. and J.A. Harlan, Environmental Monitoring Applications of OTH-B, Proc. OTH Radar Technology Conference 5-7 November 1991, Vol. IV, January 1992.
- Headrick, J.M., Looking over the horizon, *IEEE Spectrum*, 36-39, 1990.
- Headrick, J.M. and M.I. Skolnik, Over-the-horizon Radar in the HF Band, *Proc. IEEE*, **62**, 664-673, 1974.
- Headrick, J.M., HF Over-the-horizon Radar, in **Radar Handbook**, ed. M.I. Skolnik, 2nd Edition, McGraw-Hill, New York, 1990.
- Jones, R.M. and J.J. Stephenson, A versatile three dimensional ray tracing computer program for radio waves in the ionosphere, U.S. Department of Commerce, Washington, D.C., Report OT 75-76, October 1975.
- Kelley, M.C., **The Earth's Ionosphere**, Academic Press, New York, 1989.
- Kelley, M.C., Recent Advances in mid-latitude Spread-F, Proc. OTH Radar Technology Conference 5-7 November 1991, Vol. II, January 1992.
- Kolosov, A.A., **Over the Horizon Radar**, Artech House, Boston, MA, 1987.
- Levanon, N., **Radar Principles**, John Wiley & Sons, New York, 1988.
- Providakes, J., T.J. Elkins, R.B. Godwin and M.C. Kelley, An OTH Radar Clutter Simulation, Mitre M91-114, ESD/RADC OTH Radar Symposium, Hanscom AFB, 5-7 November 1991.
- Providakes, J.F., T.J. Elkins, L. Giandomenico, K.R. Overfield and P. Josephson, The Clutter Environment of the ROTH in Virginia, MITRE Rept. MTR 93W0000189, October 1993.
- Rastogi, P.K., J. Providakes, J.P. Flaherty and K. Overfield, MITRE Texas Facility: Results of Midlatitude Over-the-Horizon Radar Clutter Experiments, MTR Rept. 93B0000163, May 1994.
- Rastogi, P.K. and J. Providakes, American Sector OTH Radar Clutter Experiments: January 11-15, 1994, Mitre Rept. MP 94B0000028, March 1994.
- Rihaczek, A.W., **Principles of High-Resolution Radar**, Mark Resources, Marina del Rey, CA, 1977.
- Saillant, S., NOSTRADAMUS Over the Horizon Radar - First sub-array experimentation, Proc. Radar 92, IEE Electronics Division, 12-13 October 1992.
- Sievers, W.E., Next Generation Over-the-horizon Radar Technology (OTH-X), Vol. IV ESD/RADC OTH Radar Symposium, Hanscom AFB, 5-7 November 1991.
- Stebbins, D.M., History of OTH Radar at Rome Laboratory, RL-TM-92-24, In-House-Report, Rome Laboratory, October 1992.
- Washburn, T.W. and L.E. Sweeney, Jr., An On-Line Adaptive Beamforming Capability for HF Backscatter Radar, *IEEE Trans. Ant. Prop.*, **AP-24**(5), 721-732, 1976.
- Wyatt, L.R., Progress in the interpretation of HF sea echo: HF radar as a remote sensing tool, *IEE Proc.* **137**(2), 139-147, 1990.

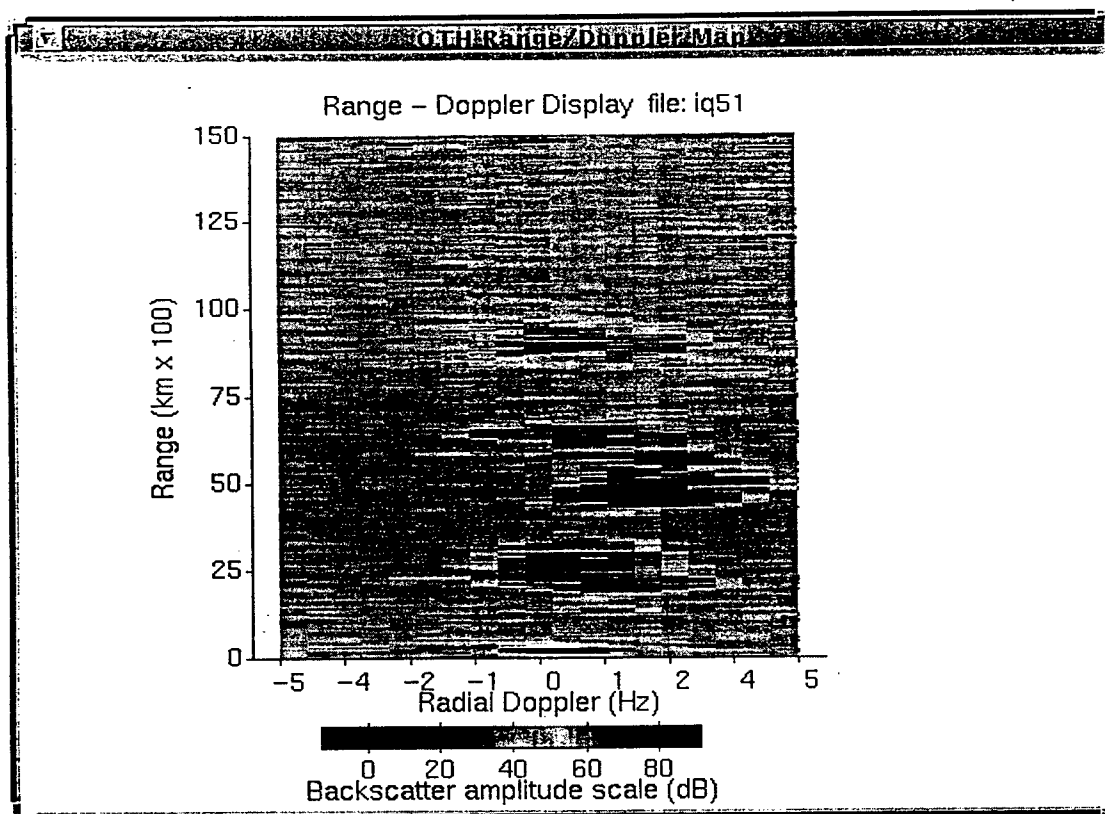


Figure 1

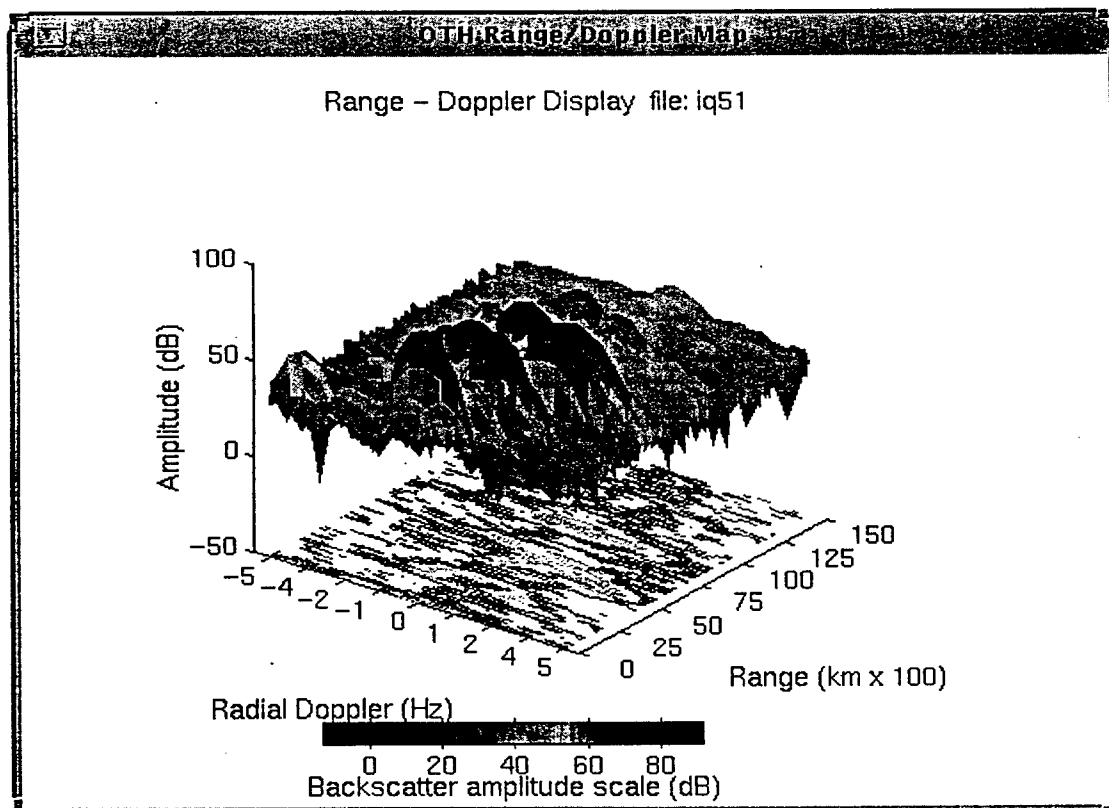


Figure 2

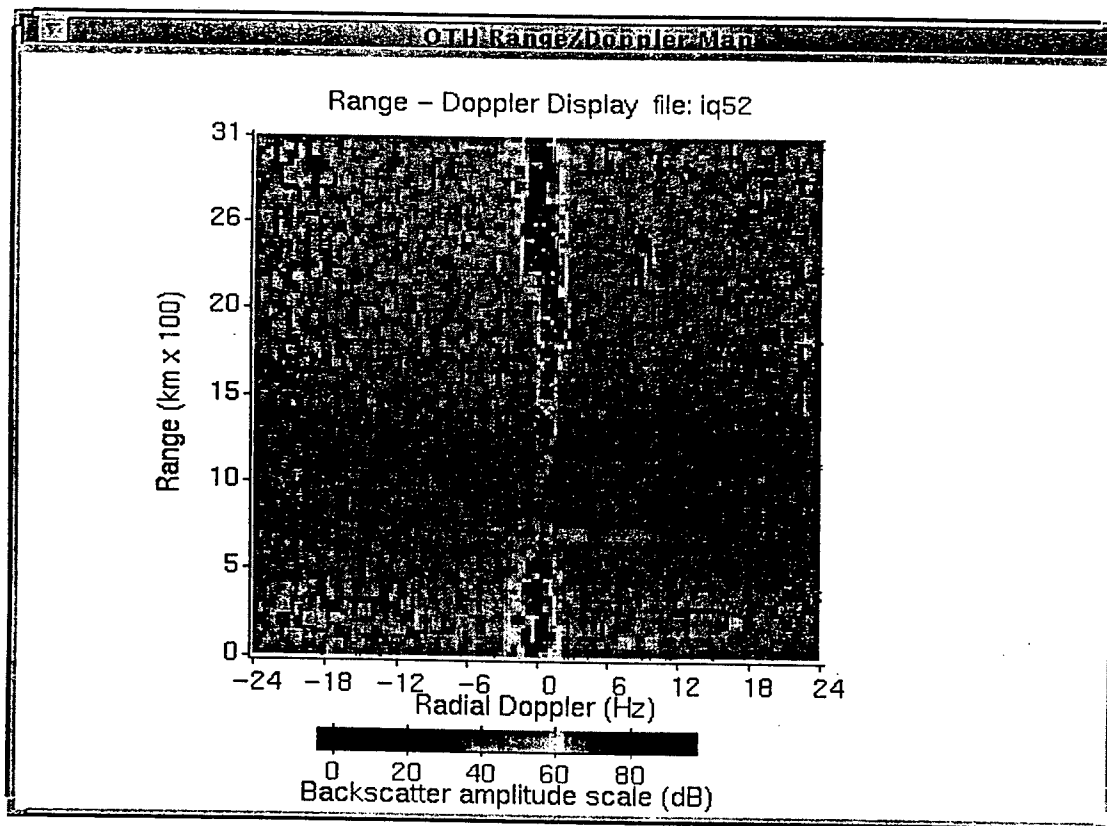


Figure 3

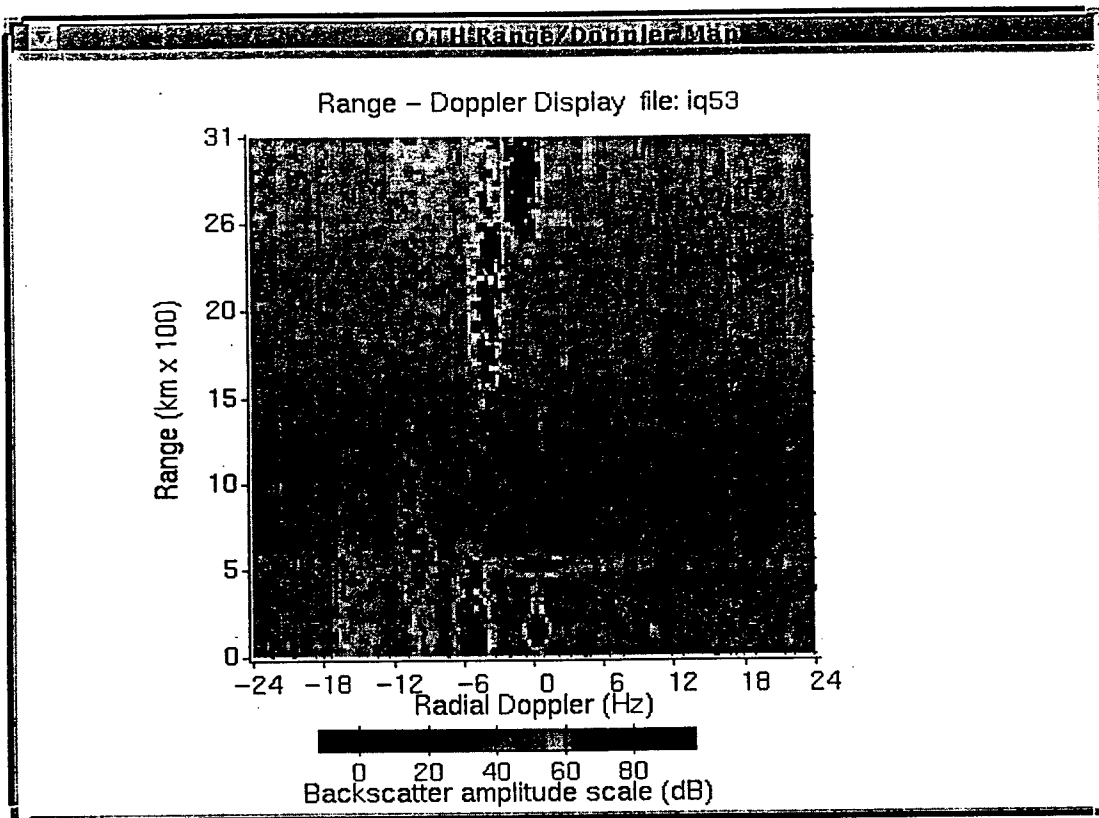


Figure 4

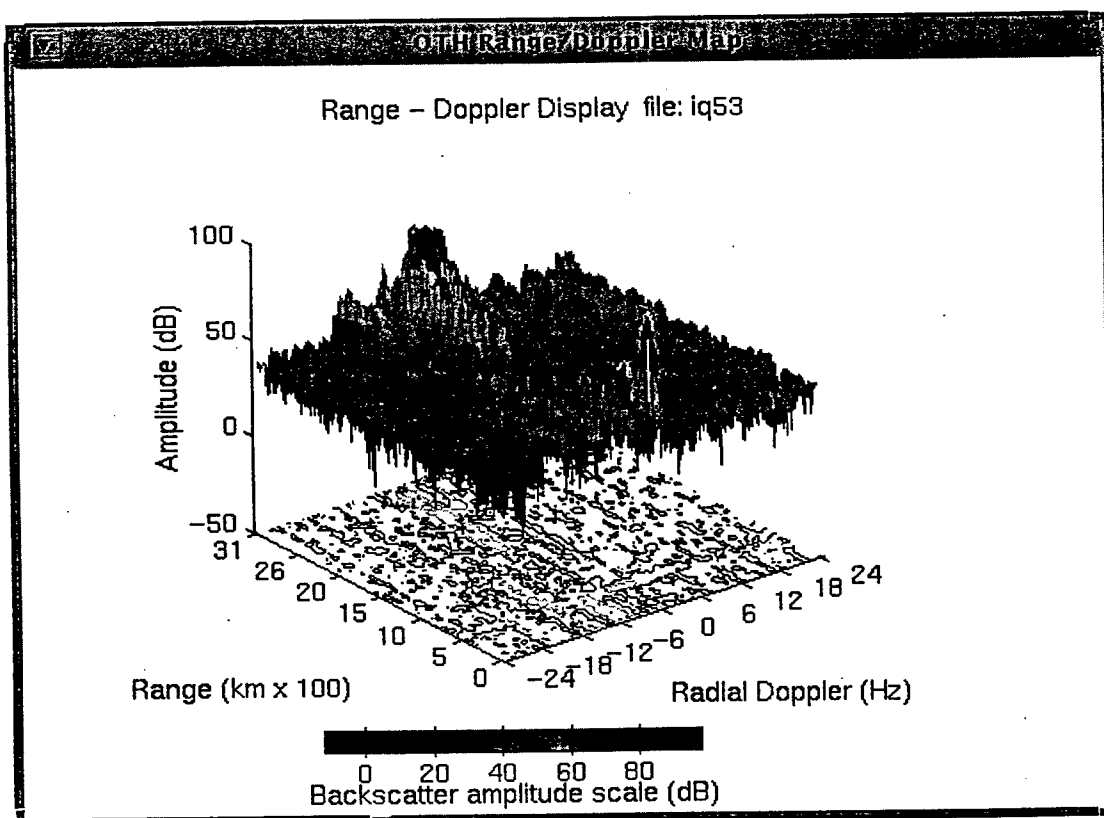


Figure 5

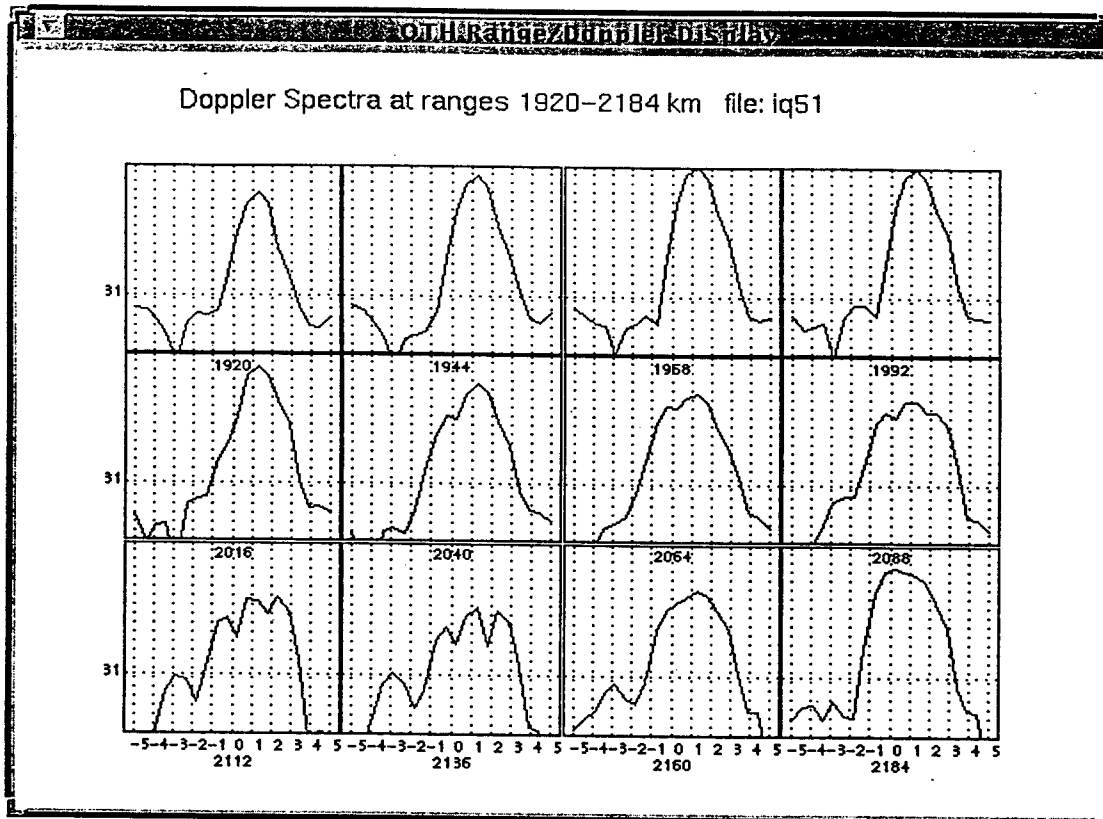


Figure 6(a)

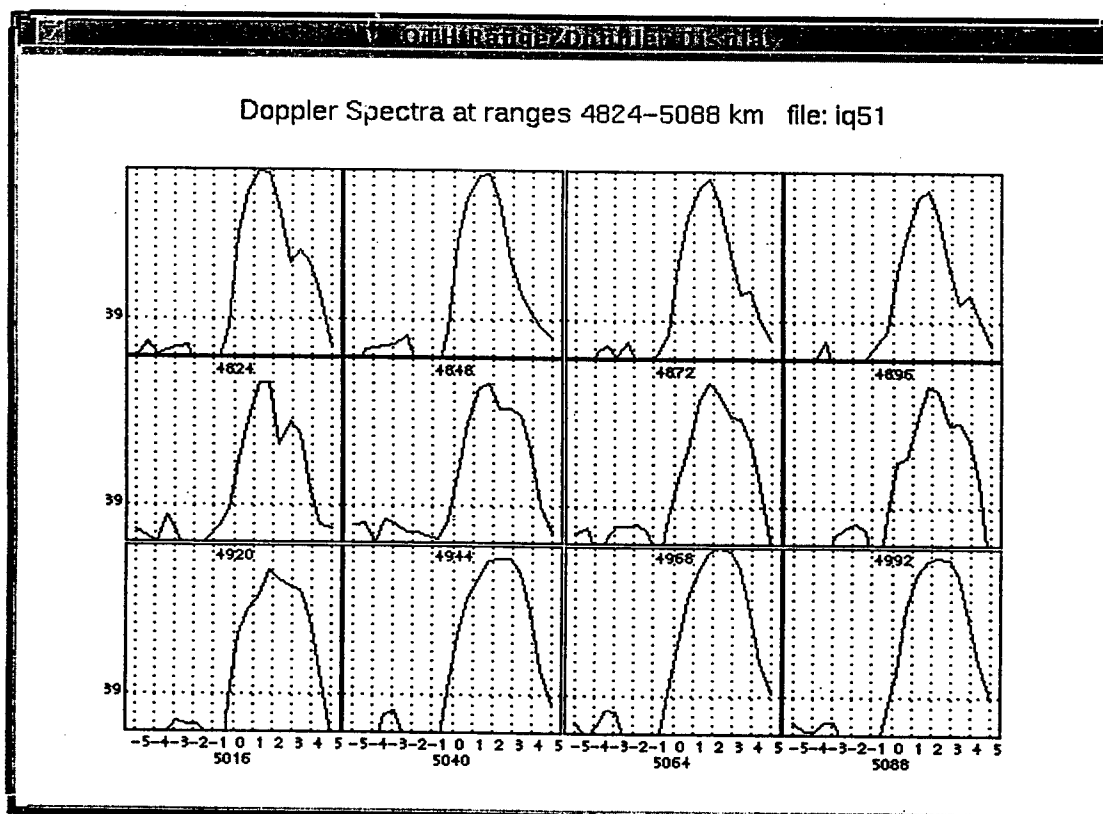


Figure 6(b)

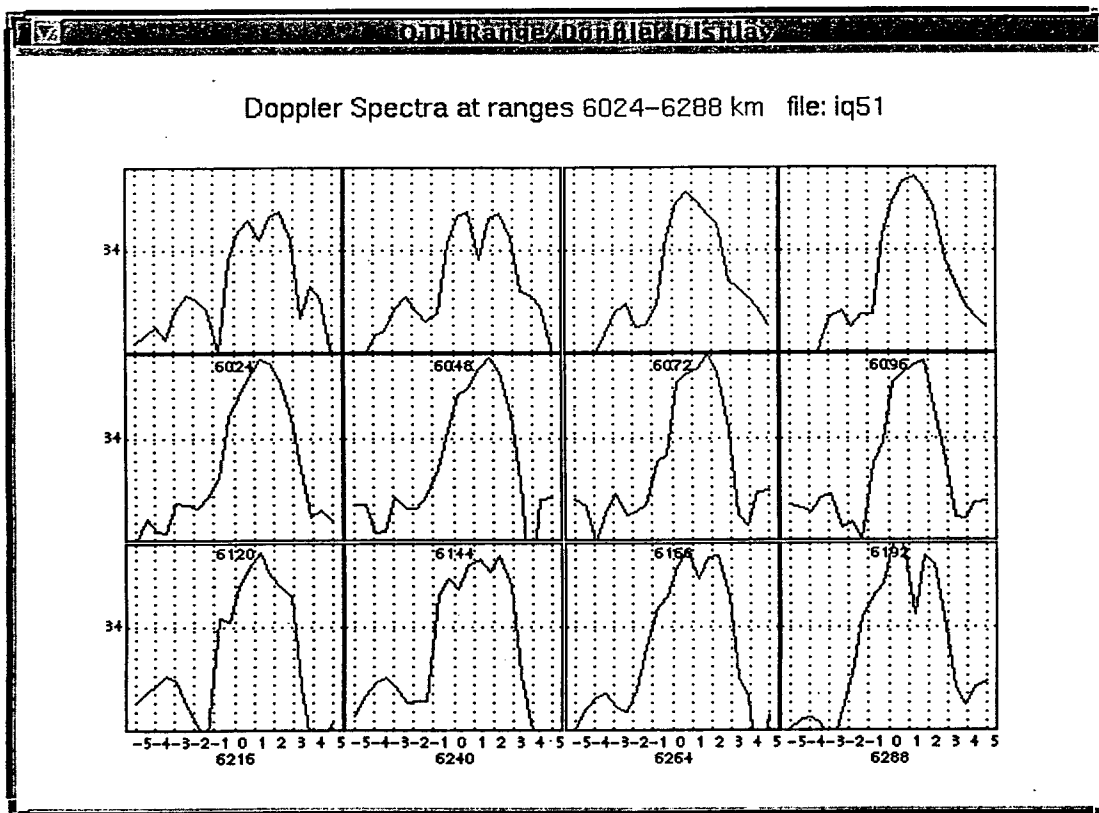


Figure 6(c)

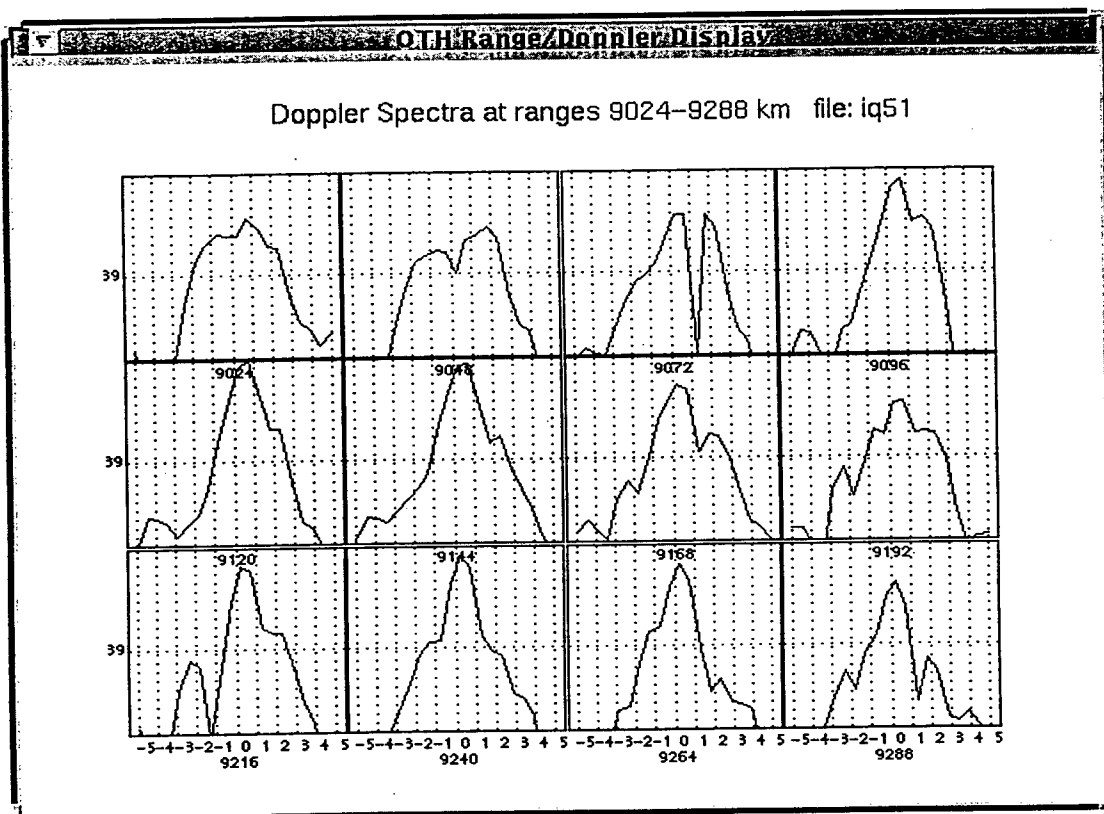


Figure 6(d)

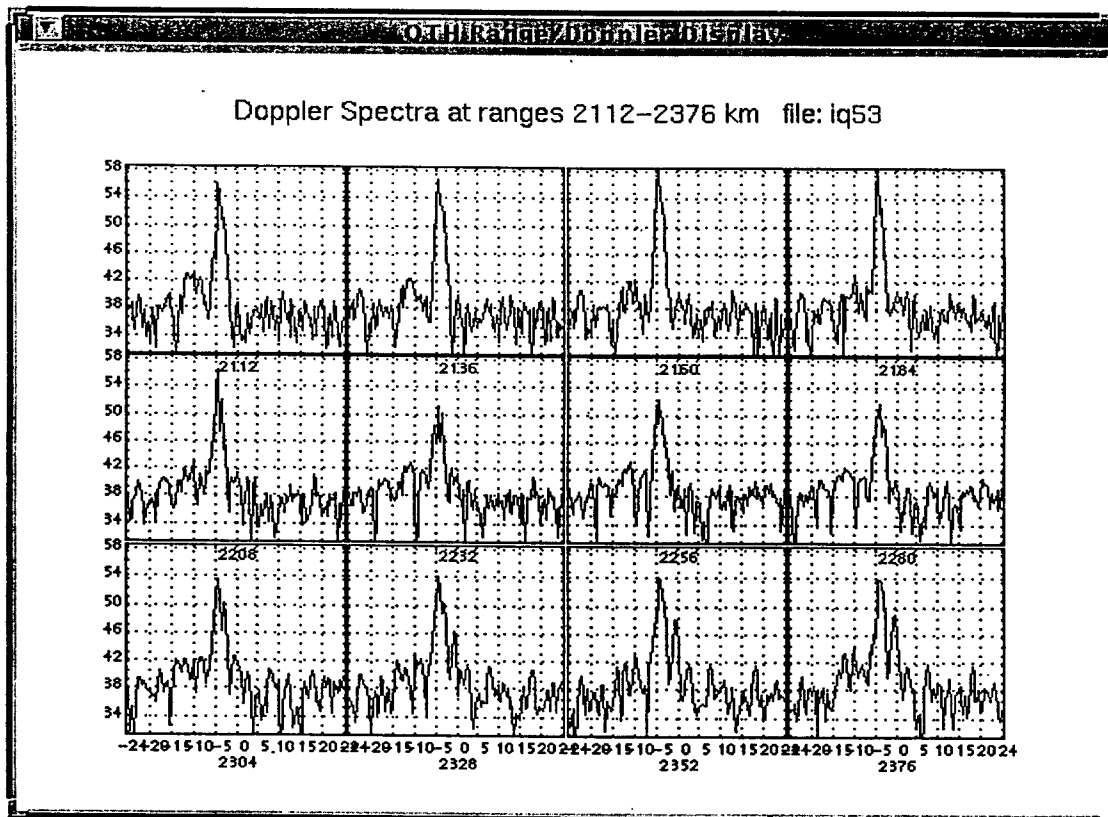


Figure 7(a)

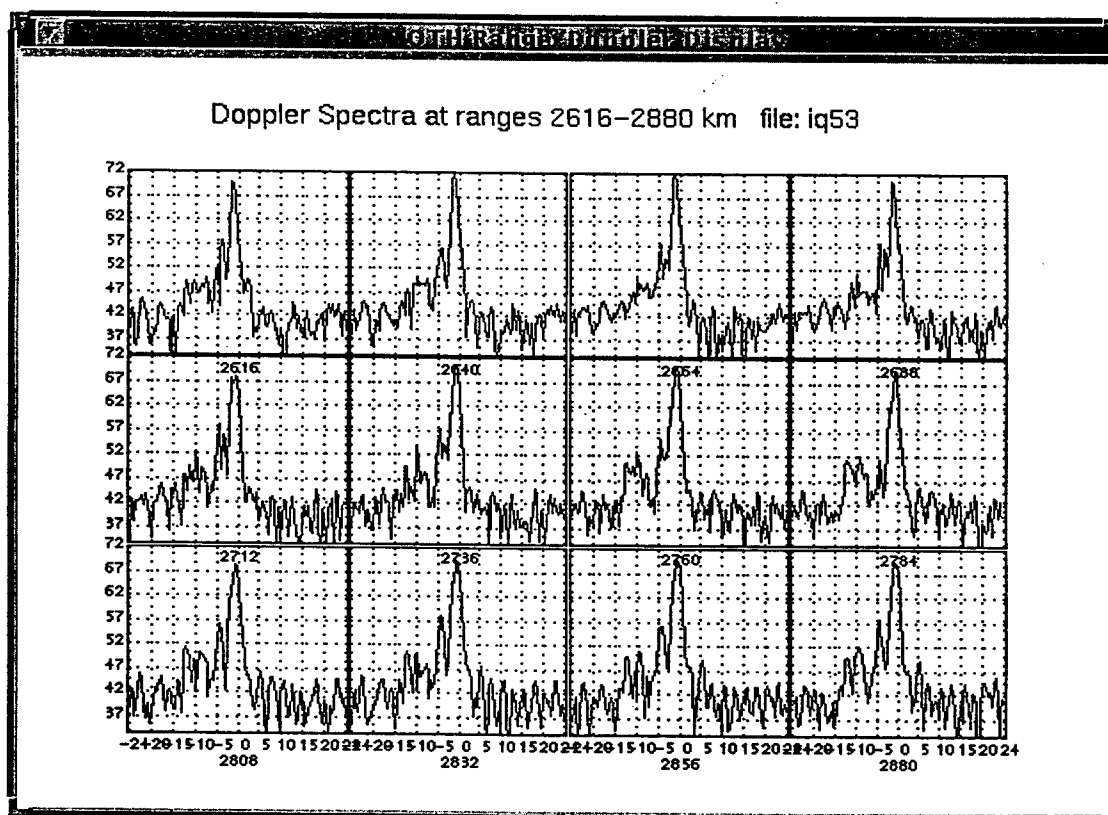


Figure 7(b)

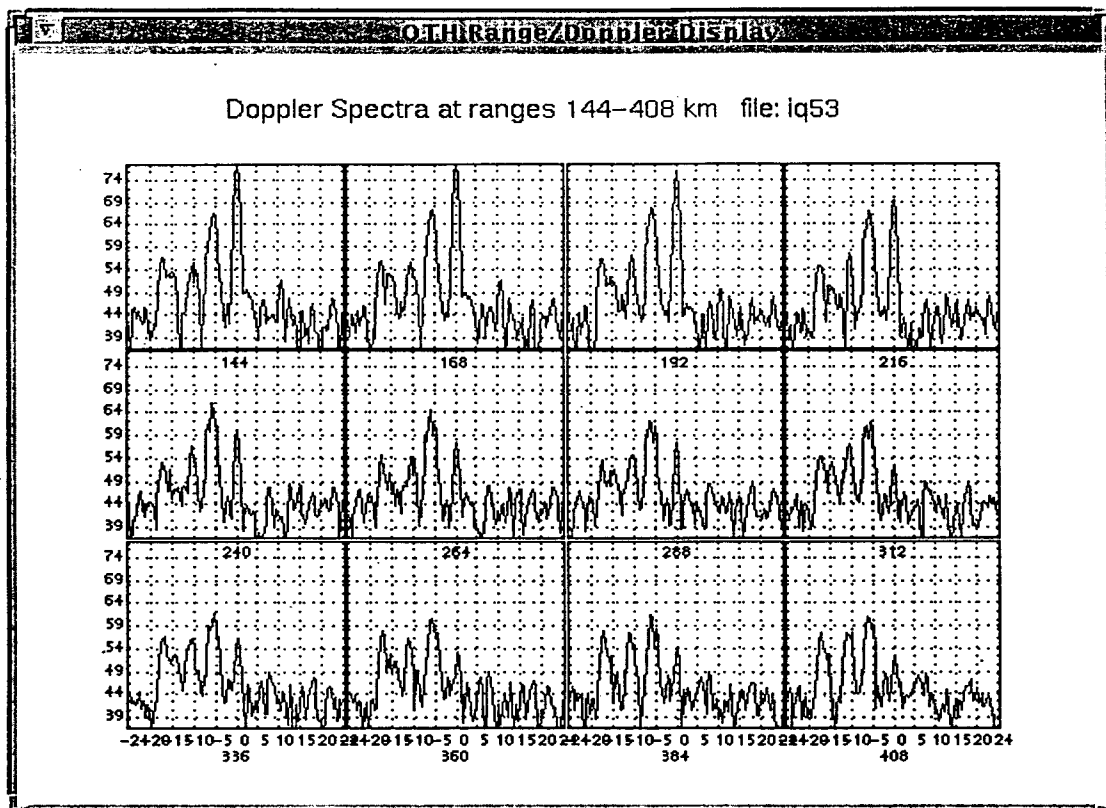


Figure 7(c)

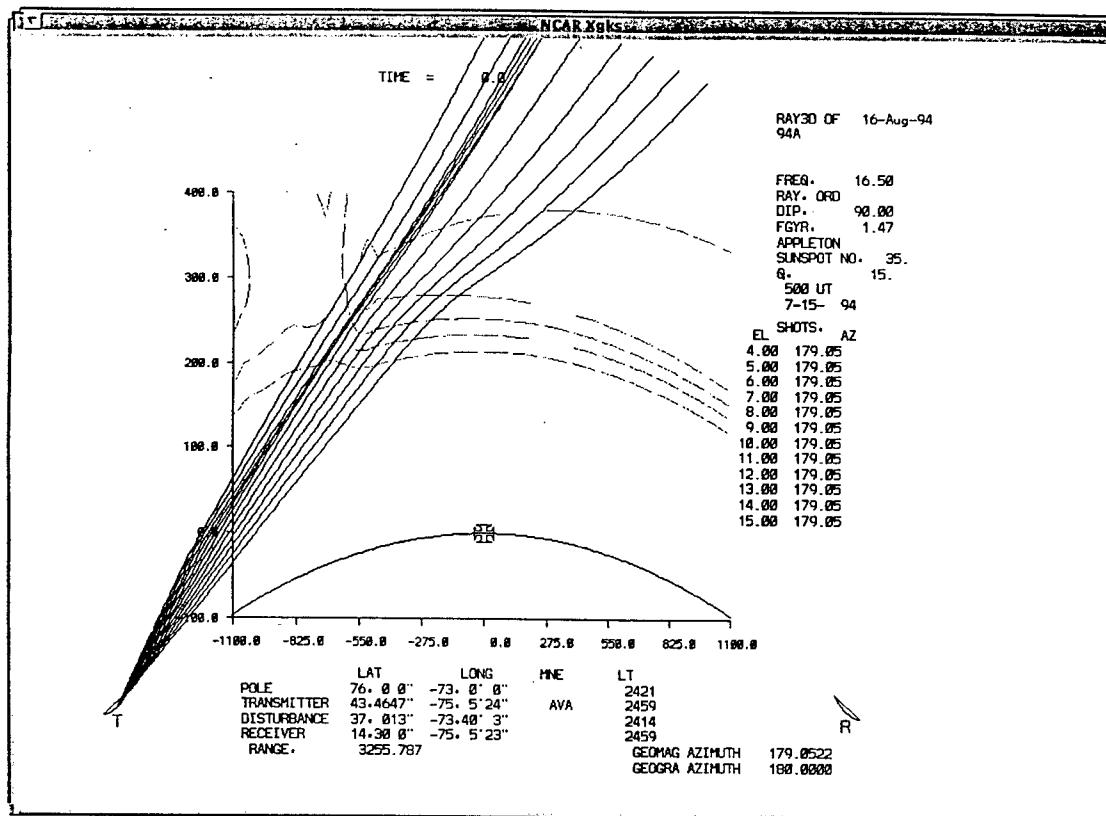


Figure 8(a)

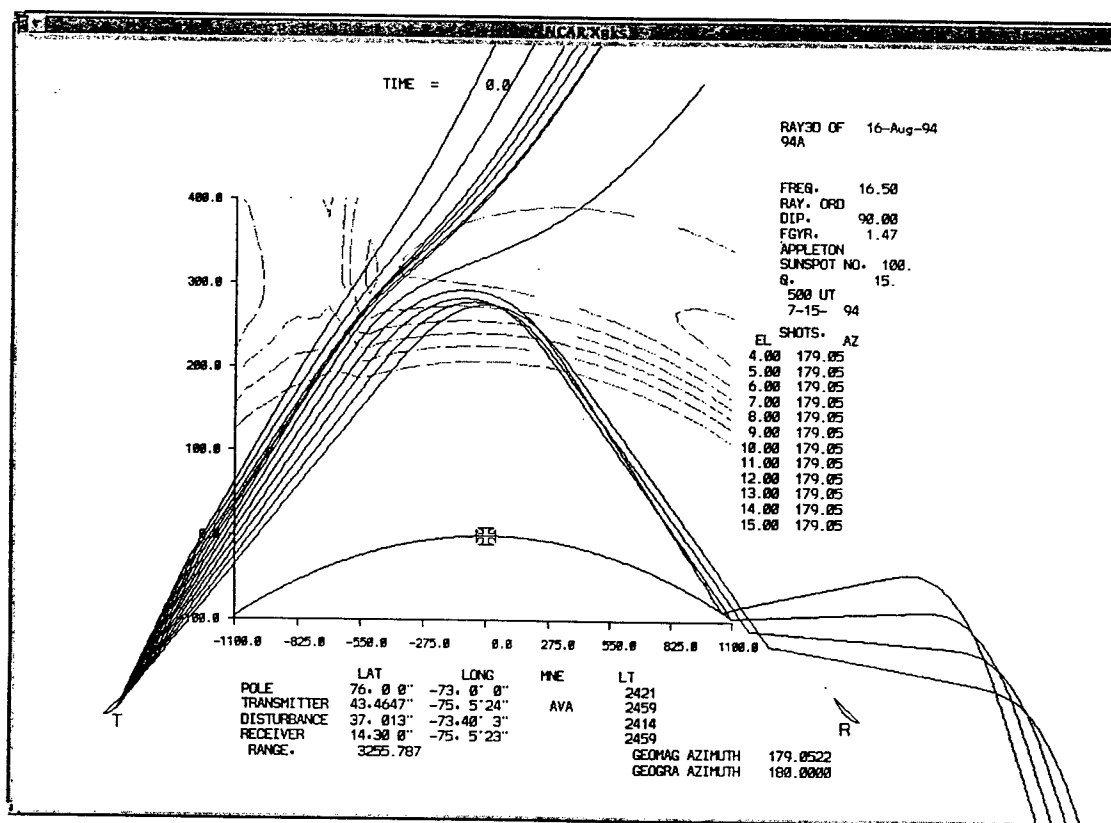


Figure 8(b)

A STUDY OF THE APPLICABILITY OF FRACTALS AND KINETIC EQUATIONS TO
ELECTROMIGRATION AND THERMALLY INDUCED HILLOCK AND VOID EVOLUTION

Joseph Chaiken*
Associate Professor
Department of Chemistry

and

Martin Villarica
Graduate Research Assistant
Department of Chemistry

Syracuse University
Department of Chemistry
1-014 Center for Science and Technology
Syracuse, New York 13244-4100

Final Report for:
Summer Faculty Research Program
Rome Laboratory

Sponsored by:
Air Force Office of Scientific Research
Bolling Air Force Base, DC

and

Rome Laboratory

August 1994

A STUDY OF THE APPLICABILITY OF FRACTALS AND KINETIC EQUATIONS TO
ELECTROMIGRATION AND THERMALLY INDUCED HILLOCK AND VOID EVOLUTION

Martin Villarica, Graduate Research Assistant
Joseph Chaiken*, Associate Professor
Department of Chemistry
Syracuse University

Abstract

The growth of hillocks and voids in metal films was studied. The applicability of a model involving fractals and kinetic equations was examined on the basis of whether there is independent justification for using scaling arguments in the model and for whether there is reason to connect the evolution of hillocks with that of voids. Hillocks and voids were found to be self-similar across about three orders of magnitude of variation in spatial scale with the same fractal dimension. Voids and hillocks were found to have the same fractal dimension whether studied using atomic force microscopy (AFM) or scanning electron microscopy (SEM). The parameters obtained from these fractal analyses demonstrate quantitative internal consistency with an earlier time dependent study of thermal annealing effects on hillock distributions. Remarkably, area-perimeter data obtained from either a long-time study of a single void or a spatial average of a large number of different voids both yield quantitatively identical results.

A STUDY OF THE APPLICABILITY OF FRACTALS AND KINETIC EQUATIONS TO ELECTROMIGRATION AND THERMALLY INDUCED HILLOCK AND VOID EVOLUTION

Martin Villarica and Joseph Chaiken*

Introduction

We recently reported¹ the very encouraging results of our first attempt at applying a kinetic model² to the time evolution of the growth of hillocks in metal films. These results raise various questions requiring satisfactory exploration before we can confidently form conclusions regarding any possible relationship between the assumptions and parameters of the model and actual physical structures and interactions. Fundamental to the model are assumptions and parameters derived from the scaling behavior of the microscopic parameters describing the entities responsible for hillock and void growth. Additional relationships between the spatial, temporal and mass scaling of the equations describing the interactions between those entities also require exploration. In what follows we describe our attempt to obtain independent evidence justifying the scaling assumptions of the model and their application to electromigration.

First, we will briefly review the model and the results of our application of the model to data obtained independently by Vook and coworkers^{3,4}. Naturally, the questions we hoped to address this summer are articulated in the succeeding section. We then present the results of atomic force microscopy (AFM) and scanning electron microscopy (SEM) experiments on aluminum films which provide some answers or at least insights into these questions. It should be clearly noted from the outset that what we seek is a general model for rearrangement of thin film matter when subjected to thermal and/or electromigration stress and so much work will be needed to establish the reality of the physical picture suggested by any model. We believe the potential empirical use of the model for reliability and failure prediction will be clear in any case. Whereas the log normal distribution has been applied to electromigration in various ways, our model employs the Poisson distribution which usually fits experimental data equally well or better. Our model assigns physically meaningful quantities to the microscopic parameters of the Poisson distribution which, at worst, could be the basis for a semi-empirical parameterization. The log normal distribution cannot offer the same opportunity for connection with microscopic causes and effects.

The Model

The model has been described in detail in the literature^{2,5} and is based on the Smoluchowski equations (1) with Jullien's asymptotic solution⁶ (2) giving the time dependent concentration, n_k , of a cluster, hillock or some other association or entity having k monomers units, i.e. a k -mer. The model assumes that k -mers are only produced by coalescence of smaller clusters and are only destroyed when they coalesce with another cluster to form a still larger cluster. If there was a population of monomers at $t=0$, say metal atoms impinging on a substrate from the gas phase, the formation of a film would commence by the formation of associations between the atoms. These "associations" might be thought of as islands, hillocks or some other name depending on their specific properties.

$$\frac{dn_k}{dt} = \frac{1}{2} \sum_{j=1}^{k-1} K_{j,k-j} n_j n_{k-j} - n_k \sum_{j=1}^{\infty} K_{j,k} n_j \quad (1)$$

$$n_k \rightarrow C k^a e^{-bk} \quad (2)$$

Although this model seems to contain much of the physical nature of the hillock/void formation and growth process, realistically, we know there are at least a few potential processes which could lead to fragmentation of some islands or clusters. Although both unimolecular⁷ and bimolecular processes⁸ can be imagined, we will group them all together under the heading of "evaporation". There is no explicit term for evaporation at this point except to note that the rate constants used in (1) implicitly relate the fact that not all encounters between i -mers and j -mers result in coalescence. The greater the probability of evaporation occurring on some time scale related to the averaged time before the next collision occurs, the smaller the crosssections or rate constants used in (1). Since in this model the presence of a buffer system, e.g. buffer gas in gas phase systems or codeposition gas in matrix isolation, does not appear explicitly, these rate constants contain this information implicitly when the equations are fit to real data. The asymptotic solution, (2), can be interpreted in terms of the scaling of the bimolecular rate constants, $K_{i,j}$, relating the interaction of individual agglomerating entities, e.g. i -mers and j -mers, with increasing numbers of monomers in the clusters. Under certain situations⁹, it is thought that the rate constants could scale smoothly with increasing the number of monomer units, and if (3) is satisfied they are termed "homogeneous".

$$K_{\lambda i, \lambda j} = \lambda^{2\omega} K_{i,j} \quad (3)$$

The most empirical mathematical implications of homogeneity and scaling are best summarized by noting that they allow the rate constants, the $K_{i,j}$, to be written explicitly in terms of i and j . This allows analysis of the equations and the possibility of discovering rigorous closed form mathematical connections between microscopic parameters defining the $K_{i,j}$ and actual measurements of hillock or cluster size distributions.

Although we shall choose not to do so in this work, it is possible¹⁰ to factor the $K_{i,j}$ into a product of two functions. The first involves only those factors which calculate the probability of a hard sphere(or other generic shape) encounter. The second is a probability factor relating the likelihood of an encounter ending in a certain action, e.g. coalescence. The first factor is essentially the collision frequency, i.e. related to overall mass transfer conditions, while the second contains information related to appropriately averaged trajectories and so contains the chemistry of the each reaction system in the agglomeration process. For very small clusters and entities, the observation of quantum effects is expected in the form of discontinuities in the variation of the $K_{i,j}$ with size.

In the absence of the above factoring of the $K_{i,j}$, the model's results, e.g. a distribution of cluster sizes produced in the long time limit, show what would happen if the distribution function was determined purely by kinetics. These kinetics would be determined entirely by mass transfer as if there were no preferred pathways for the formation or destruction of any size satisfying the homogeneity condition. The Stockmayer formula¹¹ from polymer chemistry relating the number of independent kinetic pathways producing a given size cluster to the number of monomers in that product cluster plays a prominent role in the rigorous proof of the validity of (2). We assume that neither the total number of monomers, whether free or in clusters, nor the temperature, varies with time. The model is a so-called "mean value" model in that there is assumed to be no spatial correlation between the locations of the various reactants and products.

These scaling laws⁹ are consistent with specific limits of attainable reaction conditions. They are based on rigorous calculation of things like how the mass of a cluster increases with increasing number of monomer units while the velocity of the clusters decreases. The scaling of mass transfer and energy transfer, in addition to reaction rates, depends on such quantities. The scaling of surface area of a cluster with increasing number of monomers is another such quantity. The distribution of the mass of the clusters with increasing monomer size is yet

another. Assumptions of Jullien^{6,9} and others applying the Smoluchowski equation embrace specific ways of mathematically representing these quantities so as to make the equations describe systems which are "self-similar" across spatial and temporal scales. We shall define the term "self-similar" in this connection more precisely a little later.

We assert that the more often a given cluster encounters other clusters, the more rapidly it coalesces with other clusters. As a cluster gets larger, it becomes more massive, therefore moving more slowly, thereby exploring space more slowly and encountering fewer potential coalescence partners per unit time. The result is a slower growth rate. Balanced against this effect is the fact that as monomers or other size clusters are added to a cluster, it must get larger so its cross section increases. Because of this, more space is explored per unit time and so a faster growth rate obtains. The overall effect depends on whether a cluster becomes spatially larger faster than they become slower due to becoming more massive. The validity or importance of this physical picture in determining size distributions and other observable characteristics of coalescence growth systems is one of the fundamental questions regarding the entities responsible for hillock and void growth mentioned in the Introduction.

It is possible to show⁶ that these effects, as well as the scaling of concentrations with varying spatial scales, are connected by (4). This equation can be shown valid in a variety of commonly attainable sets of reaction conditions.

$$2\omega = \alpha + (d - d_w)/D \quad (4)$$

(4) is obtained by considering the relationship between the spatial, temporal and mass scaling of the Smoluchowski equations. Mathematically, one considers a microscopic collision frequency or rate constant and the effect of increasing(or decreasing) each length which enters into the microscopic calculation of the rate constant or in expressing the concentrations. Calculating the reciprocal temporal scale change needed to make the terms of the Smoluchowski equations invariant to the net effect of the two scale changes, one encounters (4) as a necessary condition. We do not know whether other forms of the kernels exist which also produce self-similar distributions. What is important for this effort is that Jullien's solution does⁶.

The first parameter, α , is obtained due to the scaling of velocity with increasing cluster mass. It will usually be negative. For an isothermal system at thermodynamic equilibrium, heavy objects move more slowly than light ones.

$$V_{rms} = \sqrt{\frac{3kT}{m}} \quad (5)$$

(5) is simply the root mean square speed of an ideal gas molecule of mass m at temperature T . V_{rms} obviously scales as $m^{-1/2}$ so when the mass transfer is limited by the molecular speeds and not the concentration gradient, i.e. the ballistic regime and not the diffusive, $\alpha = -0.5$. The parameter d_w , the "fractal dimensionality of the cluster trajectories", results from the scaling of the mean square displacement between collisions with increasing cluster mass. When motion is diffusive, $d_w=2$, when ballistic, $d_w=1$. The dimensionality of the space in which the coalescence occurs is d . For clusters formed in bulk gases, $d=3$. For islands formed on single crystal surfaces by interaction of adsorbates diffusing along the surface, $d=2$. The fractal dimensionality of the clusters, defined in terms of a mass fractal, is D . These parameters define, and provide quantitation of, energy and mass transfer properties of the reacting system and chemical properties of the clusters.

When the shape of an experimentally produced cluster size distribution can be quantitatively calculated, based on scaling properties and the assumption that the kernels are homogeneous, we accomplish an enormous decrease in the number of variables needed to model the system. There are physical implications as well. For cluster or hillock sizes corresponding to homogeneous kernels, there are no special structures or interactions that occur as the clusters become larger. Alternatively, it may also be true that a given sized cluster occurs in various equivalent structures. This is consistent with the idea that the Smoluchowski equations produce self-similar cluster size distributions. It has been stated¹² that surfaces produced from distributions of self-similar hillocks and voids are self-similar, i.e. fractal.

Application to Vook's Data

Vook and coworkers allowed us access to several hillock size distributions that they produced using evaporated aluminum and aluminum-copper films on silicon substrates. Obtained using SEM, these distributions corresponded to a nominal magnification of 10,000x. The films systematically surveyed a range of deposition conditions, i.e. substrate temperature and deposition rate. The data were well fit using any of a few different distributions. Overall, the Poisson distribution usually fit best for pure aluminum films while alloys were often fit slightly better by a log normal distribution. Based on the quality of the fits it could certainly be said that homogeneous kernels could correspond to the physical situation represented by these

films. Vook approximated the hillocks as non-overlapped hemispheres; his raw data consisted of lists of diameters.

Vook's data suggested that SEM at 10,000x magnification is not adequate to discern the smallest and most mobile participants in the coalescence process. The distributions therefore poorly reflected the value of a from (4) that could be obtained from the fits to (2). The value of b from (4) should be reasonably well determined. In fact, the b parameter is valuable because a plot of $\ln(b)$ vs $\ln(\text{time})$ for the time evolution of a given system should be linear with slope $1/(2\omega-1)$. Since $a=-2\omega$, having such data allows a test of internal consistency for the application of the model to a given system. In the case of Vook's data, the value of a obtained from the plot of $\ln(b)$ vs $\ln(\text{time})$ was -0.25 and comparable to the average value obtained from all the fits to the Poisson distribution directly, -0.21. On the basis of this and other results the application of the model was very encouraging.

The Summer of '94

There were many potential goals which we could have pursued this summer that would have been intelligent extensions of our work with Vook's data. We decided to proceed along a few different tracks in order to hedge against the possibility that various potential difficulties would defeat one or more of our efforts.

We hoped to be able to duplicate Vook's time dependent annealing experiment using a pure metal film, preferably Al, with greater resolution. We were able to obtain a time dependent data set on a pure aluminum film. The magnification was only 5,000x and the number of hillocks found was in fact less than the number obtained by Vook. Our statistics cannot be as good as Vook's data and we will still have a poorly determined a parameter from the direct fit of the Poisson distribution function to the experimental data, but we will be able to obtain a plot of $\ln(b)$ vs $\ln(\text{time})$. When completed, we will have an a value which can be compared with that obtained by us using Vook's data. There is a real possibility that we can combine this data collected by Dr. Walsh with some data collected by Jennifer Synowczynski which will improve our statistics. This data is still being analyzed and the results cannot be discussed further. There is no question that we will ultimately want to apply this model to films of various metals on a variety of different substrates.

It would clearly be useful to obtain data at much higher resolution so that an accurate and precise a value can be determined directly from the fit to the Poisson distribution. We hoped to

be able to obtain independent evidence that scaling arguments and scaling based models have relevance to hillock and void evolution in thermal and electromigration stressed films. It would also be important if we could establish any quantitative and preferably analytic, direct correlation between hillock evolution, to which our kinetic model pertains, and void evolution which is clearly of central importance in electromigration induced device failure.

We decided to attempt to establish the proposition that voids and hillocks in metal films are self-similar. Establishing this as fact would establish the relevance of scaling in the analysis of hillock and void distributions. Using atomic force microscopy (AFM), it would be possible to establish self-similarity and to examine the hillock distributions at much higher resolution than is possible using SEM on these types of samples. It should be pointed out that SEM studies cannot be performed using conductive paints or other approaches to keep charging effects from limiting the resolution since any approach which contaminates the surface is not compatible with time dependent studies.

Self-Similarity

The question of exactly what physical meaning, if any, the term "self-similarity" denotes is deserving of some attention at this point. Within the context of having limited space, we begin with an example of a generic mathematical definition paraphrased from Korvin¹². We consider a physical structure, perhaps a hillock in a metal film, the Nile river, or the Andromeda galaxy. It is possible, for whatever reason, to consider various ways to characterize the object's shape. In the effort to do so, we might consider a single object or set of objects, that for independent reasons we suppose might have something to do with each other, and the set's distinguishing characteristics as compared with other sets of objects.

Attempting to be exhaustive in our considerations, we ask whether there exists a relationship between the area of an object, or a 2-dimensional projection of the object, and the perimeter of the object. The comparison is based on the idea that a perimeter increases linearly as larger objects in a self-similar set are considered, whereas the area increases quadratically as larger members of the set are considered. "Larger" might be based on any convenient measure such as the largest distance across the interior of the object, the perimeter, or the area. Since we have been careful to make no assumptions regarding the actual shape of any objects we may consider, the ratio of these two quantities might be sensitive to the shape of the objects.

We can express the idea of considering the value of one measure of size and shape, say w , in terms of the simultaneous value of some other measure of size and shape, say L in terms of the equation below.

$$w = W(L)$$

Now if this relationship holds for all the members of the set, then it may be possible to write an equation which connects the members of the set in terms of the scaling of perimeter or area, i.e. L . Furthermore, if it is possible to write (6) below in which f is an unknown function which depends on the shape of the objects. This form amounts to a very significant assumption because if a set of objects can be found which satisfy (6), then (7) can also be shown to be true and the objects form a self-similar set.

$$w_2/w_1 = W(L_2)/W(L_1) = f(w_2/w_1) \quad (6)$$

$$f(ab) = f(a)f(b) \quad (7)$$

It is then possible to apply Cauchy's treatment of functional forms to write that the function f connecting values of the two measures must be

$$w = w_0 L^p \quad (8)$$

of the form above. At first, this may seem like a real leap forward in that we have a functional form which at the very least allows us to classify sets of objects. The use of group theory to classify various matrix elements by their behavior with respect to their behavior under various point and space group transformations seems analogous. Empirically, self-similarity and point group symmetry are analogous in that they allow a reduction in the number of variables needed to specify the state of a given system but in the case of self-similarity we presently have very little with which to satisfy our intuition as to why the classification should be physically meaningful.

First, there is nothing in the definition of self-similarity, i.e. satisfying the equations above, which pretends to allow a general first principles calculation of the prefactor f or p . Each case must be considered as an isolated situation. The significance and physical interpretation of the exponent p , known in the vernacular as a variety of different kinds of

fractal dimension depending on the specific case under consideration, beyond the idea that area or perimeter increases as an object gets larger, is usually difficult to clearly discern. The fact that we have chosen to express these measures of size and shape in terms of each other and examine their scaling behavior is not guaranteed to have any particular significance. To state one overall benefit of using self-similarity we directly quote H. E. Stanley¹³.

"If you are an experimentalist, you try to measure the fractal dimension of things in nature. If you are a theorist, you try to calculate the fractal dimension of models chosen to describe experimental situations; if there is no agreement then you try another model."

In addition to having discovered an empirical measure that a correct theory of whatever processes being considered must correctly reproduce, if one has a theory which predicts self-similar objects, then discovering that they exist in reality clearly supports the model. If a model *assumes* self-similarity and makes predictions which turn out to be true, then this is good but we are still not guaranteed that the model is unique. There could be another model not based on self-similarity which also accounts for the empirical data. However, discovering that the objects are actually self-similar clearly supports the theory which makes that assumption. Our hillock model expresses the mass distribution in terms of a mass fractal, i.e. self-similarity is assumed. Another important benefit is that self-similarity allows construction of a models having relatively few adjustable parameters. Therefore we attempted to find out whether hillocks and voids under thermal annealing or electromigration conditions are self-similar.

Again, following Korvin¹⁴ and Stanley: "The numerical determination of fractal dimension of an object embedded into the d -dimensional Euclidean space is generally based on the following simple rule: Suppose we plot on log-log paper some quantity that can be interpreted as 'number of objects' or 'mass' against a characteristic length scale L . If there is an asymptotic ($L \rightarrow \infty$) region in which this plot becomes straight, then the slope is termed the fractal dimension d_q characterizing the distribution of the quantity q . Alternately, we can keep the size of the object, L , fixed and determined q for different resolutions, l . If we plot q against l , and the plot is a straight line in a range ($l < l_0 \ll L$), the fractal dimension will be the negative slope of this line. For example, if q is the area of a square of side L , it scales with L as L^2 , if q is the number of squares of side $l \ll L$ contained in the large square, it scales as:"

$$q=(L/l)^2 \propto l^{-2}$$

Of course, this all follows from (6-8) above.

When examining surfaces, there is considerable latitude in defining hillocks and voids. The AFM data consists of a set of points, x, y, z defining the surface contour of the sample. We choose to view the surface as a collection of hillocks and voids because we believe the evolution of hillocks parallels the evolution of voids. The fractal dimension of a set of hillocks is conveniently calculated using a so-called "area-perimeter plot". Using (6-8) above it is easy to show that a plot of the logarithm of the area of a set of hillocks as a function of the logarithm of the perimeter is linear with slope D when the hillocks are a self-similar set. D is the fractal dimension of the projection of the hillock on 2 dimensions. The fractal dimension of the surface composed of the hillocks or voids is commonly taken as $D+1$ although, according to Korvin¹⁵, the rigorous proof of this has not been given. Given AFM data, one need only choose some plane of reference in order to designate all the surface structures contained in the image as either hillocks or voids.

The choice of reference plane requires some discussion of thresholding. The basic fact of scanning probe microscopy is that some type of small probe is brought into close proximity to an object under study. As the probe, which is a very fine tip of one sort or another, approaches the the object to within a distance on the order of molecular dimensions, a variety of forces between the surface and the tip become measurable. By sensing one of the processes driven by these forces, e.g. electrical conduction, van der Waals attraction or repulsion, it is possible to sense how close the tip is to the object. This allows the mapping of the surface contours of the object as the tip is rastered across the region of interest at constant height. Balancing these forces allows assignment of a z value to each x,y point on the surface. "Thresholding" refers to construction of iso- z contours in the x,y plane. The contiguous regions of x and y that have larger or lower z than the threshold are designated as hills or voids respectively.

A useful analogy is that of visualizing the flooding with water of a hilly region. The depth of the water determines the number of visible hills and lakes. A high threshold corresponds to deep water. Figures 1a-b are AFM images showing that metal films are very rough at all scales. For the $1\mu\text{m}$ square region (resolution of 500×500 lines) scans, the lateral resolution could approach 20\AA but we suspect the tips are much wider. The z resolution is on the order of 1\AA . The smallest features are on the order of 500\AA in the xy plane and most of the voids(lakes)

have the same shape near their bottom. Since it is arbitrary how we define the zero point level for the z direction, we can create hills or voids arbitrarily by our choice of $z=0$ elevation. Some hills are not of higher z than the water level. Analyzed from this point of view, the question of thresholding becomes a percolation problem involving the formation of a single contiguous flooded region or land region. The number of voids and hills is a strong function of threshold although it is thought that the fractal dimension calculated for a particular choice is much less sensitive if chosen far from the percolation threshold.

Figure 2 shows a graph of the number of hills and lakes found as a function of z threshold for a particular AFM image which is typical of those studied. The film was 7000Å of evaporated aluminum on silicon. Both substrate and film were passivated so we suspect that our images are obtained through a conformal oxide layer on the order of 20-30Å thick. The thresholding is normalized such that the limits of the abscissa are 0-100% of the maximum z found for that image. Figures 3a-c show graphs of the surface fractal dimension calculated for a range of thresholds for a few different films. Figure 4 shows a series of typical area-perimeter plots based on either lakes or hills obtained from another image. These results reveal much about the structure of these films.

Figure 2 suggests that a cut into a film, along a plane perpendicular to its surface would reveal a profile like that shown in Figure 5a in which hillocks are taken as spherical. The point here is whether the bases of different sets of adjacent hillocks make contact at different z values or whether a picture more like Figure 5b is appropriate in which there are very flat regions separating isolated hemispherical hillocks. The situation depicted in Figure 5b would go from zero hills to the maximum found within the smallest z increment instrumentally possible and then decline in numbers monotonically for increasing z thereafter. When there are hillocks on top of hillocks, increasing certain z thresholds will cover more hills than they will separate. This results in the number of hills or voids found not immediately being a maximum value at the lowest z value for which hills are found.

In the midwestern United States, a favorite country witicism is: "For every hill there's a hole." The land is so flat that the statement is very often true in actual fact. For every film studied there was always a choice of z threshold possible for which the number of hills was equal to the number of voids. This was always very close to the percolation threshold. It is clear that there is not perfect symmetry between the number of hills or voids as a function of threshold. It is also clear that the fractal dimension is a function of z threshold and that it

sometimes seems as if there is a systematic variation occurring. This deserves more study as does a more quantitative study of the variation of the number of hills and voids with choice of z threshold.

The variability may be unfortunate if we eventually want to establish a reproducible protocol for thresholding that will allow calculation of fractal dimension that can be compared from sample to sample, as a function of electromigration or thermal annealing or perhaps after various other types of film processing. While unfortunate, it still must be admitted that the entire range of surface fractal dimensions found for the AFM images of aluminum was roughly $2.57 \pm .11$ regardless of whether voids or hillocks were used in the area-perimeter plots. If a systematic part of the variability exists and can be quantitatively analyzed then we suspect that the uncertainty on the fractal dimension measurement could be reduced by an order of magnitude or more. This would greatly increase the potential utility the observable fractal dimension for various applications. Although we were only able to obtain a few usable images, it should be noted that for laser deposited platinum films on quartz, the fractal dimension found from area-perimeter plots was $2.55 \pm .09$.

Graphs illustrating the other type of analysis mentioned by Stanley involving changing the size of the region observed and counting the number of objects are shown in Figure 6. The slopes of these graphs for the aluminum films give a surface fractal dimension of ≈ 2.55 while for the platinum film we obtain 2.9. Why the aluminum films seem to give better agreement with the value obtained from area-perimeter plots compared with the agreement displayed using platinum film we cannot say. The fact that the fractal dimension obtained using hills is not distinguishable from the value obtained from voids supports our hope that we may be able to connect the behavior of hills predicted using our model with that of the voids.

These fractal dimension measurements can be used as a check of the quantitative consistency of our coalescence growth model. To utilize (4), we assign $\alpha = -.5$ and $d_w = 2$. This follows from assuming that hillock growth occurs by diffusive motion of very small clusters and that the velocity of the mass transfer scales as the inverse square root of the mass of the cluster, consistent with the usual simple kinetic theory. The fractal dimension of the surface of the of the films, which may be where most of the material involved in coalescence growth can be found just before coalescence events occur, is $d \approx 2.55$. This number therefore corresponds to the dimension of the space in which the coalescence growth is occurring. Finally, the dimensionality of the hillocks themselves is also obtained by adding unity to the slope of the

area-perimeter plots giving $D = 2.57$. Using (4) we predict $\omega \approx -0.29$ which can be compared quite favorably with $\omega \approx -0.24$ from Vook's $\ln(b)$ vs $\ln(t)$ plots.

We obtained perimeter-area plots using SEM data for comparison with the same kinds of plots based on AFM data. Vook's data was not available for this purpose since he only reported diameters as his raw data. For this purpose, Professor Kime¹⁶ allowed us to analyze the data she had obtained last summer. She obtained area-perimeter data on over 1000 voids of similar passivated aluminum films. The plot obtained from this data is in Figure 7 and, remarkably, over 900 voids form a reasonable line giving a surface fractal dimension of 2.71 in good agreement with the values obtained from AFM data. Many of the voids which deviated significantly from the line shown were in fact on the lower limit of the resolution of the instrument. This is a common pitfall causing the measured areas to depend of the instrumental resolution and that data would have had to be discarded on that basis regardless of any other considerations.

Finally, we utilized the remarkable data of Thomas and Calabrese¹⁷ involving the evolution of a single void under electromigration conditions. A single void was observed under nominally constant conditions for a period of hours with images being obtained every few minutes or so. This data was converted to a standard area-perimeter data set as shown in Figure 8 except that all the areas and perimeters correspond to the *exact same void*. The plot yields a reasonably straight line giving a surface fractal dimension of 2.67. It appears that the long time average behavior of a single microscopic void can be replaced by a spatial average of a large number of voids at a single time. We believe this to be a singular result in science. One of the basic precepts of statistical mechanics is explicitly confirmed by direct observation.

This final result is profound. It again shows that the fractal dimension of voids and hills are nearly equal, that AFM and SEM data are comparable, that the fractal dimension of the voids, and therefore probably hillocks, *remains constant throughout their evolution*. Despite the fact that the void changes its exact shape repeatedly in their data, the fractal dimension could be used in (4) to follow the growth of a distribution of such hillocks(voids).

Summary and Conclusions

At the precision available to us, voids and hillocks are self similar across spatial scales spanning greater than three orders of magnitude and they appear to have the same fractal dimensionality. Fractal exponents obtained from either AFM or SEM images can be inserted into

the equation governing the scaling parameter ω from our kinetic model of hillock evolution. Direct observation shows that the fractal dimensionality of an electromigration driven void does not vary with time during its growth. The fractal exponent for passivated aluminum metallization patterns is $2.57 \pm .22(2\sigma)$.

Acknowledgements

I would like to acknowledge the beneficial interaction and assistance provided by Profs. Yolanda Kime and Herbert F. Helbig, Drs. Joe Beasock, Lois Walsh, Tom Renz, and G. Ramseyer, and the summer students Jennifer Synowczynski and Nathan Terry.

References

- 1 J. Goodisman, J. Chaiken, Thin Solid Films, manuscript accepted with major revisions
- 2 M. Villarica, M. J. Casey, J. Goodisman, J. Chaiken, J. Chem. Phys. 98 (1993) 4610-4625
- 3 S. Aceto, C. Y. Chang, R. W. Vook, Thin Solid Films, 219 (1992) 80-86
- 4 R. W. Vook, Materials Chemistry and Physics, 36(1994) 199-216
- 5 J. Goodisman, J. Chaiken, J. Photochem Photobio. A.
- 6 R. Botet and R. Jullien, J. Phys. Math. A: Math. Gen. 17 (1984) 2517-2530
- 7 John W. Brady, Jimmie D. Doll, Donald L. Thompson, J. Chem. Phys. 74(1981)1026-1028 and earlier papers referenced therein
- 8 I. Langmuir, J. Meteorol., 5 (1948) 175-192
- 9 R. Jullien, New J. Chem. 14 (1990) 239
- 10 R. C. Srivastava, J. Atmos. Sci. 45 (1988) 1091-1092
- 11 W.H. Stockmayer, J. Chem. Phys. 11 (1943) 45
- 12 G. Korvin in "Fractal Models in the Earth Sciences" (Elsevier, New York, 1992) page 193 in connection with discussion of equation (3.1.7)
- 13 H.E. Stanley, Form: An introduction to self-similarity and fractal behavior. In: H. E. Stanley and N. Ostrowsky(Editors), "On Growth and Form. Fractal and Non-Fractal Patterns in Physics." Martin Nijhoff Publ., Dordrecht-Boston-Lancaster, pp. 21-53
- 14 G. Korvin in "Fractal Models in the Earth Sciences" (Elsevier, New York, 1992) page 171
- 15 G. Korvin in "Fractal Models in the Earth Sciences" (Elsevier, New York, 1992) page 66
- 16 Yolanda J. Kime and Peter Grach, accepted Proc. Mat. Res. Soc.(Spring 1994 Meeting)
- 17 Robert W. Thomas and Donald W. Calbrese, Phenomenological Observations of Electromigration, 21st annual meeting proceedings, Reliability Physics, 1983, pp. 1-9

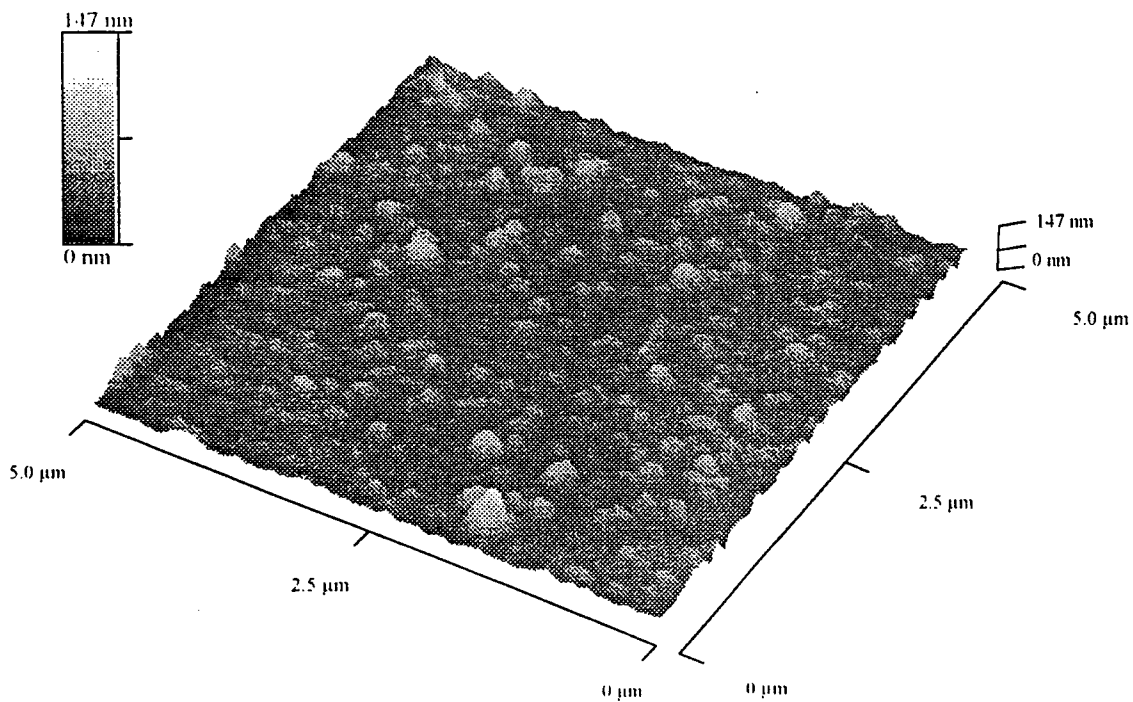


Figure 1a: 5μx5μ AFM image, lowest resolution (100x100 points).

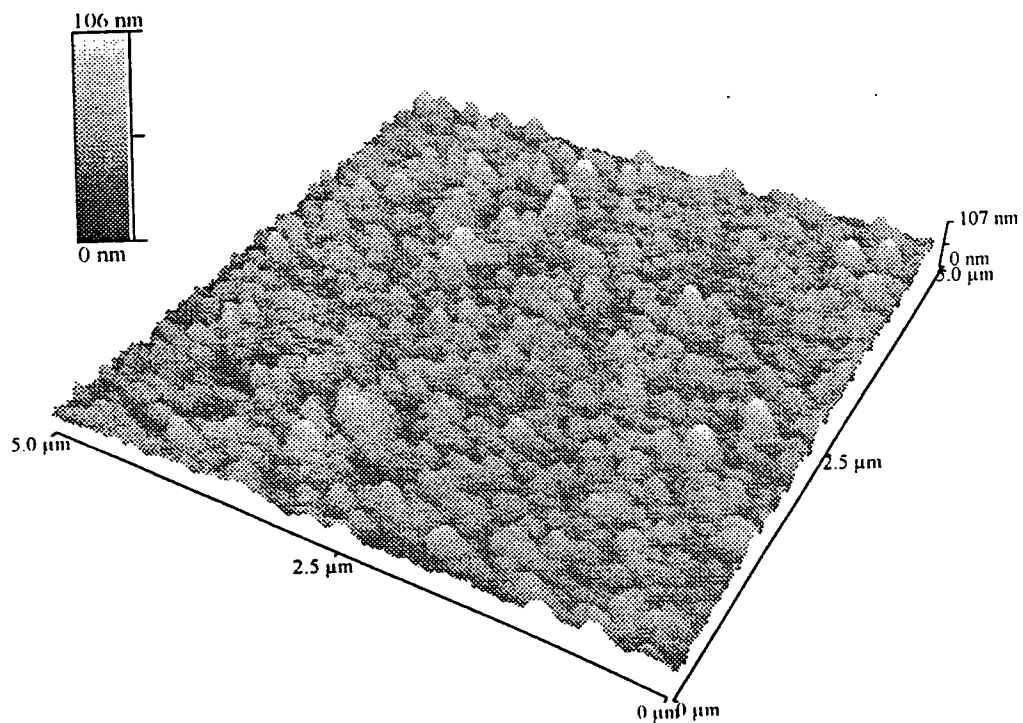


Figure 1b: 5μx5μ AFM image, highest resolution (500x500 points).

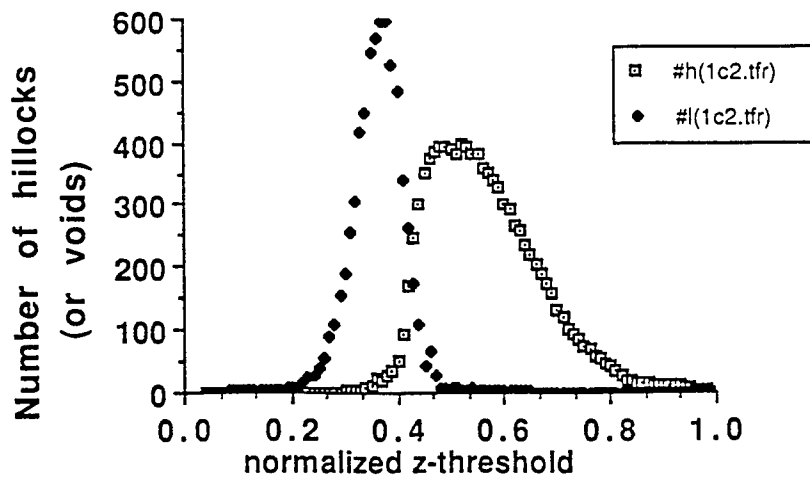


Figure 2: Number of hillocks (or voids) found as a function of z-threshold.

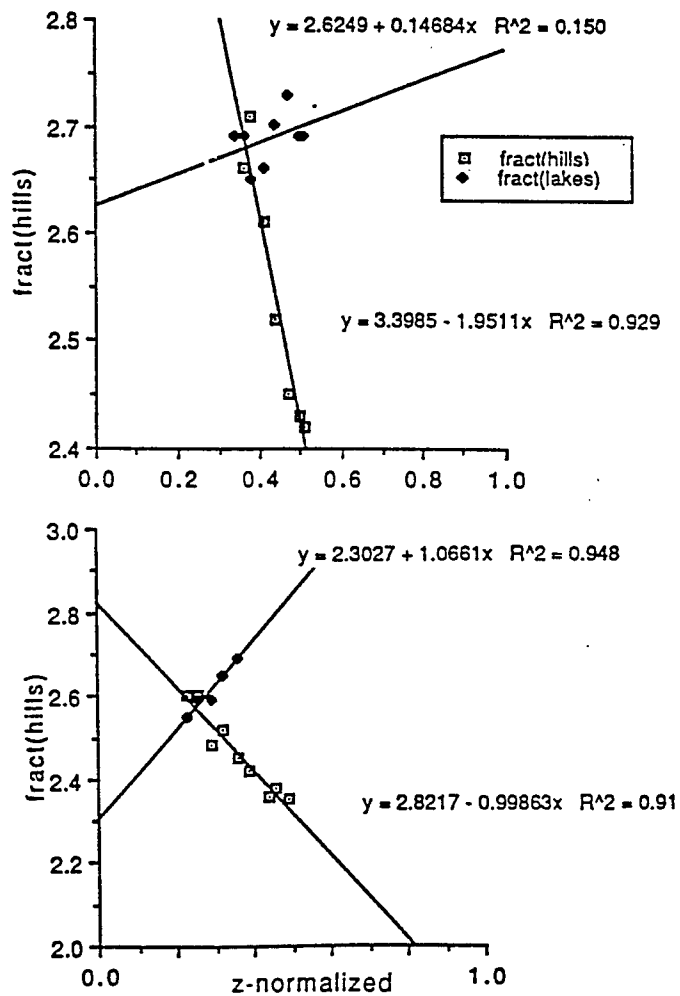


Figure 3a-b: Fractal dimension found as a function of z-threshold for 2 typical films. Some systematic variation seems apparent.

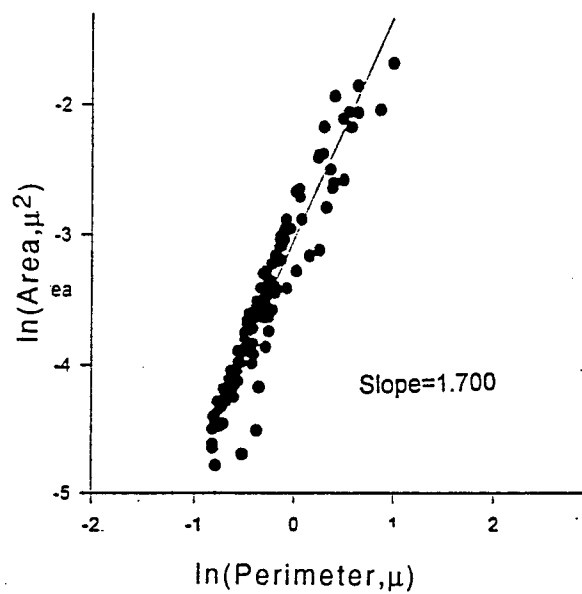


Figure 4: Typical area-perimeter plot of hillocks obtained from an AFM image.



Figure 5: Surface profile for close packed hillocks (a) and non-overlapping hillocks (b).

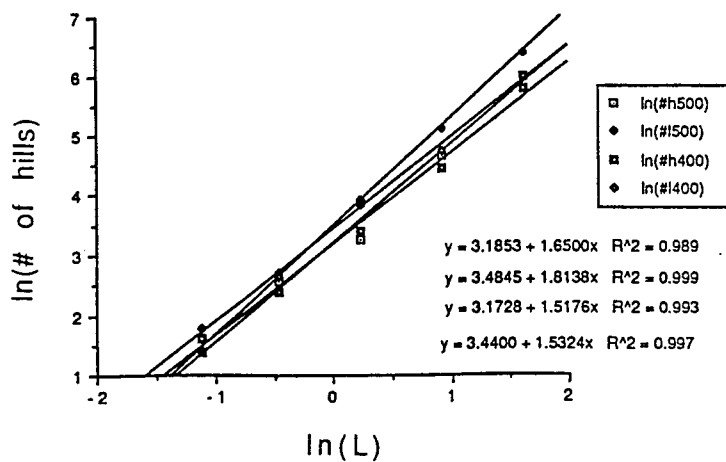


Figure 6: Number of hillocks (lakes) found for a particular z-threshold as a function of size of the region (L) examined. 500x500 and 400x400 point resolution data are used. Ordering of the fits matches the ordering of the legend.

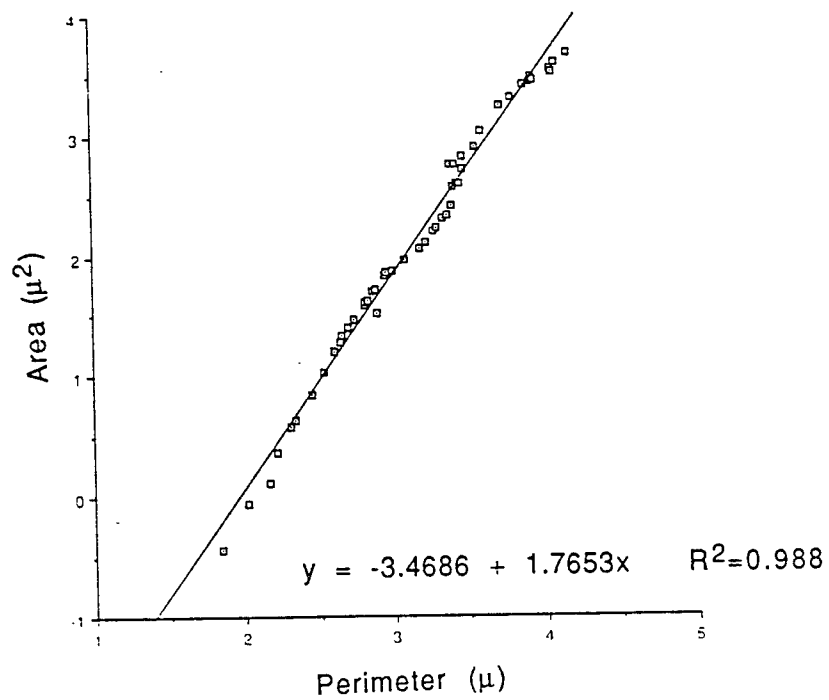


Figure 7: Area perimeter plot obtained from Professor Kime's data (see text).

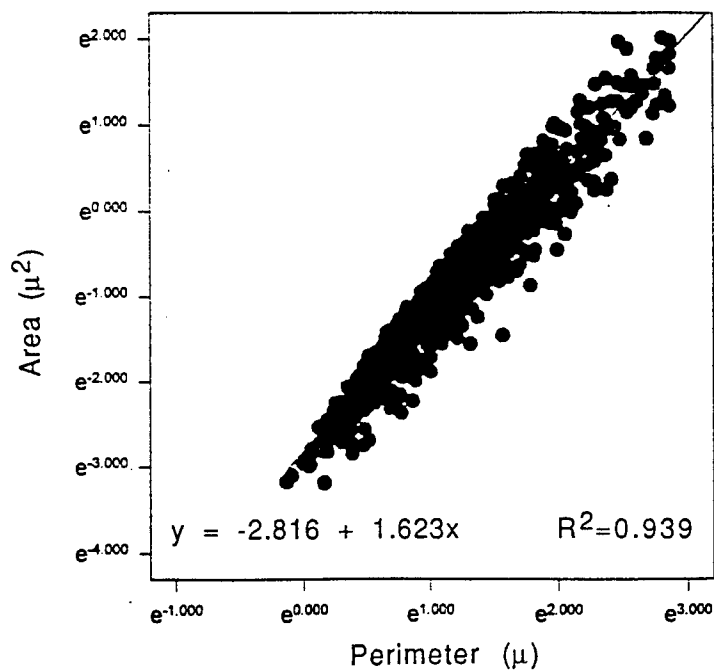


Figure 8: Area perimeter plot obtained from Thomas and Calabrese data (see text).

ON TESTING THE EQUALITY OF COVARIANCE MATRICES UNDER SINGULARITY

Pinyuen Chen
Professor
Department of Mathematics

Syracuse University
215 Carnegie
Syracuse, NY 13224-1150

Final Report for:
Summer Faculty Research Program
Rome Laboratory

Sponsored by:
Air Force Office of Scientific Research
Bolling Air Force Base, DC
and
Rome Laboratory

August 1994

ON TESTING THE EQUALITY OF COVARIANCE MATRICES UNDER SINGULARITY

Pinyuen Chen

Professor

Department of Mathematics

Syracuse University

Abstract

This report considers the problem of statistically testing the equality of two covariance matrices from complex multivariate normal distributions. The underlying distribution is assumed to be singular in the sense that one of the two sample covariance matrices has rank one and the other is of full rank. A test procedure is proposed and its distributions under null and alternative hypotheses are derived. Two interesting properties of the test procedure, invariance and monotonicity properties of the power function are studied for a general setting, and then apply to the special case studied in this project. The test procedure is also shown to be equivalent to several other well-known test procedures which were previously studied only for the regular case, that is, when both sample covariance matrices are of full rank. Some suggestions for further research are given in the last two sections of this report.

ON TESTING THE EQUALITY OF COVARIANCE MATRICES UNDER SINGULARITY

Pinyuen Chen

1. Introduction

A signal detection problem is usually described in terms of a model $X = s + n$ where s is a fixed signal, $n \sim CN_p(0, R_1)$ is an noise variable, and X is the received message. A signal is said to be detected if the received message X contains the signal s . In statistical terms, a signal is claimed to be present if the null hypothesis that $s=0$ is rejected versus the alternative hypothesis that $s=a$ (specified). The above testing procedure is based on two independent random variables X and S_1 where $X \sim CN_p(s, R_1)$ and $S_1 \sim CW_p(k, R_1)$. In this report, we study a hypothesis testing problem on the equality of the covariance matrix of X (denoted by R_2) and the expectation of S_1 (denoted by R_1). Instead of testing if the mean vector of X is null-vector against that it is a given non-null vector, we are interested in testing if the distribution of the statistic X comes from the same family that induces the statistics S_1 . This is a meaningful step taken prior to the testing problem on s as we mentioned before because almost all the inferences in signal detection are based on the assumption that the covariance matrix of X is the same as the expectation of S_1 . An earlier inference on the equality of R_1 and R_2 may be helpful in identifying an outlier or a contaminated sample in the background environment. A detection of a violation in the model (that is, an acceptance of $H_1: R_1 \neq R_2$) will certainly impose investigation on the robustness of the original procedures in testing $s = 0$. The violation in the model will also guide the experimenters to use a different procedure. The procedure may be less powerful than the ones that were derived under the assumption of $R_1 = R_2$. But it certainly will give better detection probability when the assumption of $R_1 = R_2$ is not true.

The classical likelihood ratio criterion in testing the equality of two covariance matrix is not appropriate here as we can argue as follows. It is clear from the literature (see formula (8) on page 406, Anderson [1]) that the likelihood criterion can be written as $\lambda = \frac{|S_1|^{\frac{1}{2}n_1} |S_2|^{\frac{1}{2}n_2}}{|S_1 + S_2|^{\frac{1}{2}(n_1+n_2)}}$ where S_1 and S_2 are the respective sample covariance matrices, and n_1 and n_2 are respective degrees of freedom. In our application to signal detection, S_1 has rank 1 and thus is singular when $p > 1$. This implies that the above test statistic λ is identically 0. So the likelihood ratio approach is not valid here.

In Section 2, we introduce the notation, describe the problem in a formal manner, make the necessary assumptions on the samples and populations, and introduce the proposed test statistic and acceptance criterion. We also give the distributions of the proposed test statistic under both null and non-null hypotheses. All the results are given in both the real and the complex cases. Most of those distributions are derived theoretically. Only one of them is argued heuristically. In Section 3, we study two important

properties, namely the invariance and the monotonicity property of the power function, of the proposed test statistic. Concluding remarks and acknowledgments are made in the Section 4.

2. The problem and the proposed test procedure

We assume that X_1, X_2, \dots, X_k are k independent random vectors from a p -variate complex normal distribution $CN_p(0, R_1)$. The random vector X_{k+1} is distributed, independently of X_1, X_2, \dots, X_k , according to a p -variate complex normal distribution $CN_p(0, R_2)$. Here both R_1 and R_2 are unknown. Our goal is to perform a statistical hypothesis testing on

$$(2.1) \quad H_0: R_1 = R_2 \text{ versus } H_1: R_1 \neq R_2.$$

Our proposed test statistic is

$$(2.2) \quad T = X_{k+1}^H S_1^{-1} X_{k+1} \text{ where } S_1 \text{ is the sample variance-covariance matrix of } \{X_1, X_2, \dots, X_k\}.$$

Now we consider the distributions of T for the following cases:

Case 1: When the sample size k is large, the application of the law of large number to each element in the covariance matrix implies that S_1 is a consistent estimate of R_1 . So S_1 converges to R_1 in probability. In this case, we can use S_1 to estimate R_1 and thus consider R_1 is known.

Under $H_0: R_1 = R_2$, $T \sim$ Chi-square with $2p$ degrees of freedom.

Proof: We refer now to Theorem 3.3.3 in Anderson [1] which considers the distribution of T for the real elements case. To extend his result in real elements case to our complex elements case, we change all the Y', v', c', z' , and λ' to Y^H, v^H, c^H, z^H , and λ^H respectively. Then we will get $Y^H T^{-1} Y = Z^H Z$ which can be considered as the sum of squares of the components of Z . Since $Y^H T^{-1} Y \sim \sum_{i=1}^m Z_i^H Z_i \sim$ Chi-square with $2p$ degrees of freedom with non-centrality parameter $v^H T^{-1} v$. Thus we have $T \sim$ Chi-square with $2p$ degrees of freedom.

Under $H_1: R_1 \neq R_2$:

Let $Z = R_1^{-1/2} X_{k+1}$. Then $Z^H Z \sim CW_p(R_1^{-1/2} R_2 R_1^{-1/2}, I)$ which does not have a regular Wishart density if $p > 1$. However $T = X_{k+1}^H R_1^{-1} X_{k+1}$ is a quadratic form in normal variates whose distribution has been approximated by many authors. Here we suggest the following approach.

We wish to find the distribution of T , that is $P(T < a)$. We first show that the distribution of T is the same as that of $W^H A W = \sum_{i=1}^p \lambda_i (W_{ii}^2 + W_{2i}^2)$ where $\lambda_1 \geq \lambda_2 \geq \dots \geq \lambda_p$ are the eigenvalues of $R_2 R_1^{-1}$, A is the diagonal matrix of $\lambda_1, \lambda_2, \dots, \lambda_p$, and $W_{11}, W_{12}, \dots, W_{1p}, W_{21}, W_{22}, \dots, W_{2p}$ are i.i.d. standard normal random variables. Any quadratic form in X_1, X_2, \dots, X_p may be written as $Q(X) = X^H A X$ where A is a p by p

symmetric matrix. Let $q = R_2^{-1/2}y$, then $q^H q = y^H R_2^{-1} y$, and $|R_2| = |R_2^{-1/2}| |R_2^{-1/2}|$, we obtain

$$(2.3) \quad P(T < a) = P(Q(X) < a) = \pi^{-p} \int_{q^H ((R_2^{-1/2})^H R_1 (R_2^{-1/2})) q < a} \exp(-q^H q) dq.$$

If Λ is the diagonal matrix of eigen values of $R_2 R_1^{-1}$, and P the associated orthogonal matrix of eigen vectors, then $P^H (R_2^{-1/2})^H R_1 R_2^{-1/2} = \lambda P^H (R_2^{-1/2})^H R_1 R_2^{-1/2} P = \Lambda$. Making another transformation $W = Pq$, we obtain

$$(2.4) \quad P(T < a) = P(Q(X) < a) = \pi^{-p} \int_{w^H \Lambda w < a} \exp(-w^H w) dw.$$

Thus the distribution of T is the same as of $W^H \Lambda W = \sum_{i=1}^p \lambda_i (W_{ii}^2 + W_{2i}^2)$ where $W_{11}, W_{12}, \dots, W_{1p}, W_{21}, W_{22}, \dots, W_{2p}$ are i.i.d. standard normal random variables.

Now we consider Ruben's [2] (Theorem 1, page 550) approximation to the probability $P(T < a)$.

For $\lambda_1 = \alpha_1, \lambda_2 = \alpha_2, \lambda_3 = \alpha_3, \dots, \lambda_p = \alpha_{2p-1} = \alpha_{2p}$ we have

$$(2.5) \quad P(T < a) = P\left(\sum_{i=1}^p \lambda_i (W_{ii}^2 + W_{2i}^2) < a\right) = P\left(\sum_{j=1}^{2p} \alpha_j Z_j^2 < y\right) = \sum_{l=0}^{\infty} c_l F_{2p+2l}(y/\alpha)$$

where F_{2p+2l} is the distribution of central Chi-square random variable with $(2p+2l)$ degrees of freedom, p is an arbitrary constant, and

$$(2.6) \quad c_j = (2j)^{-1} \sum_{r=0}^{j-1} g_{j-r} c_r \quad (j > 0), c_0 = \prod_{j=1}^{2p} (\alpha / \alpha_j)^{1/2}$$

where $g_m = \sum_{j=1}^{2p} (1 - \alpha / \alpha_j)^m, m = 1, 2, \dots$

Another possible approach to the distribution of T under $H_1: R_1 \neq R_2$ is to use simulation on $\sum_{i=1}^p \lambda_i (W_{ii}^2 + W_{2i}^2)$ to calculate the power at different values of λ 's.

Case 2: For the case where k is any integer such that $k \geq p$:

Under the null hypothesis $H_0: R_1 = R_2$:

First we state a theorem which deals with the distribution of T in the real case.

Theorem 2.1 (Anderson [1], page 163): Let $T = Y^H S^{-1} Y$, where Y is distributed according to $N(v, \Sigma)$ and nS is independently distributed as $\sum_{\alpha=1}^n Z_{\alpha} Z_{\alpha}^H$ with Z_1, Z_2, \dots, Z_n independent, each with distribution $N(0, \Sigma)$. Then $(T/n)[(n-p+1)/p]$ is distributed as a noncentral F with p and $n-p+1$ degrees of freedom and noncentrality parameter $v^H \Sigma^{-1} v$. If $v = 0$, the distribution is central F.

To prove an analogous result for the complex case, we can proceed in a similar manner as in the proof of the theorem (see Anderson [1], page 163). We need only to change the transpose Z^H to the conjugate transpose Z^H , $N(v, \Sigma)$ to $CN(v, \Sigma)$, and orthogonal matrix to unitary matrix and the following result will follow.

Corollary 2.2: Let $T = Y^H S^{-1} Y$, where Y is distributed according to $CN(v, \Sigma)$ and nS is independently distributed as $\sum_{\alpha=1}^n Z_{\alpha} Z_{\alpha}^H$ with Z_1, Z_2, \dots, Z_n independent, each with distribution $CN(0, \Sigma)$.

Then $(T/n)[(n-p+1)/p]$ is distributed as a noncentral F with $2p$ and $2(n-p+1)$ degrees of freedom and noncentrality parameter $\nu' \Sigma^{-1} \nu$. If $\nu = 0$, the distribution is central F.

Thus in our notation,

$$T \sim \left(\frac{kp}{k-p+1} \right) F_{2p, 2(k-p+1)}.$$

Under the alternative hypothesis $H_1: R_1 \neq R_2$:

Now $T = X_{k+1}^H S_1^{-1} X_{k+1} = \text{tr}(X_{k+1}^H S_1^{-1} X_{k+1}) = \text{tr}(X_{k+1} X_{k+1}^H S_1^{-1}) = \text{tr}(S_2 S_1^{-1})$ where $S_2 = X_{k+1} X_{k+1}^H$.

First we consider the case that all the variables are real normal random variables. Since S_2 has rank 1 and S_1 has full rank p , the rank of $S_2 S_1^{-1}$ is 1. Thus

$$(2.7) \quad T = \text{tr}(S_2 S_1^{-1}) = \text{the largest eigen value of } S_2 S_1^{-1}.$$

For non-singular case where both S_2 and S_1 have full rank p and orders n_1 and n_2 respectively, formula (16) of Khatri [3] gives the density of f_p , the largest eigenvalue of $S_2 S_1^{-1}$ (we are considering the real case now), as follows:

$$(2.8) \quad c |\Lambda|^{-\frac{1}{2}n_1} f_p^{\frac{1}{2}pn_1-1} |I + f_p \Lambda^{-1}|^{-\frac{1}{2}(n_1+n_2)} {}_3F_2\left(\frac{1}{2}n_1 + \frac{1}{2}n_2, \frac{1}{2}p+1, \frac{1}{2}p - \frac{1}{2}; \frac{1}{2}p, \frac{1}{2}(n_1+p+1); f_p(\Lambda + f_p I)^{-1}\right)$$

where

$$c = \Gamma\left(\frac{1}{2}\right) \Gamma_p\left(\frac{1}{2}n_1 + \frac{1}{2}n_2\right) \Gamma_{p-1}\left(\frac{1}{2}p+1\right) \left\{ \Gamma\left(\frac{1}{2}p\right) \Gamma\left(\frac{1}{2}n_1\right) \Gamma_p\left(\frac{1}{2}n_2\right) \Gamma_{p-1}\left(\frac{1}{2}n_1 + \frac{1}{2}p + \frac{1}{2}\right) \right\}^{-1},$$

$$\Gamma_p(t) = \pi^{\frac{1}{2}p(p-1)} \prod_{j=1}^p \Gamma\left(t - \frac{1}{2}j + \frac{1}{2}\right), \quad \Lambda = \text{diag}(\lambda_1, \lambda_2, \dots, \lambda_p),$$

here λ 's are the eigen values of $R_2 R_1^{-1}$, and ${}_3F_2$ is the hypergeometric function in matrix argument as defined in James [4]. Since the derivation of the distribution of T for our case involves the simplification of ${}_3F_2$, we need to write down the complete definition of the hypergeometric function in matrix argument. We consider the partition $\mathbf{k} = (k_1, k_2, \dots, k_m)$, $k_1 \geq k_2 \geq \dots \geq k_m \geq 0$, $k_1 + k_2 + \dots + k_m = k$, of k into not more than m (the number of variables in each vector) parts. Then from page 477 of James [4], we have

Definition 2.1

$$(2.9) \quad {}_pF_q(a_1, \dots, a_p; b_1, \dots, b_q; S) = \sum_{k=0}^{\infty} \sum_{\mathbf{k}} \frac{(a_1)_{\mathbf{k}} \cdots (a_p)_{\mathbf{k}}}{(b_1)_{\mathbf{k}} \cdots (b_q)_{\mathbf{k}}} \frac{C_{\mathbf{k}}(S)}{k!}$$

$a_1, \dots, a_p, b_1, \dots, b_q$ are real or complex constants and the multivariate hypergeometric coefficient

$$(2.10) \quad (a)_k = \prod_{i=1}^m (a - \frac{1}{2}(i-1))_{k_i}$$

where $(a)_k = a(a+1)(a+2)\dots(a+k-1)$.

It is clear from the arguments made in Anderson [1], Section 13.2.4 that, in order to obtain the density function of the roots of $|A - f(A+B)|$ for the singular case (that is, when the rank of A is less than p), we only need to make the changes in the density function of the roots of $|A - f(A+B)|$ by replacing p by the new n_1 , n_1 by the new p , and $n_2 - p - 1$ by the new $n_2 - p - 1$ (that is, replace n_2 by the new $n_1 + n_2 - p$). Thus in formula (2.8) by changing (n_1, n_2, p) to $(p, n_1, n_1 + n_2 - p)$, we obtain

$$(2.11) \quad d|\Lambda|^{-\frac{1}{2}p} f_p^{\frac{1}{2}pn_1-1} |I + f_p \Lambda^{-1}|^{-\frac{1}{2}(n_1+n_2)} {}_3F_2(\frac{1}{2}n_1 + \frac{1}{2}n_2, \frac{1}{2}n_1 + 1, \frac{1}{2}n_1 - \frac{1}{2}; \frac{1}{2}n_1, \frac{1}{2}(n_1 + p + 1); f_p(\Lambda + f_p I)^{-1})$$

where
 $d =$

$$\Gamma(\frac{1}{2})\Gamma_{n_1}(\frac{1}{2}n_1 + \frac{1}{2}n_2)\Gamma_{n_1-1}(\frac{1}{2}n_1 + 1)\{\Gamma(\frac{1}{2}n_1)\Gamma(\frac{1}{2}p)\Gamma_{n_1}(\frac{1}{2}(n_1 + n_2 - p)\Gamma_{n_1-1}(\frac{1}{2}n_1 + \frac{1}{2}p + \frac{1}{2})\}^{-1}$$

$$=$$

$$\Gamma(\frac{1}{2})\Gamma_{n_1}(\frac{1}{2}n_1 + \frac{1}{2}n_2)\{\Gamma(\frac{1}{2}n_1)\Gamma(\frac{1}{2}p)\Gamma_{n_1}(\frac{1}{2}(n_1 + n_2 - p)\Gamma_{n_1-1}(\frac{1}{2}n_1 + \frac{1}{2}p + \frac{1}{2})\}^{-1}$$

and Λ is the diagonal matrix with n_1 elements $\lambda_1 > \lambda_2 > \dots > \lambda_{n_1}$.

Now we replace n_1 by 1 in the ${}_3F_2$ function in (2.10). The third argument in the first 3-vector becomes 0.

For any $k > 0$, since $k_1 > 0$, we have

$$(2.12) \quad (a_3)_k = (0)_k = (0)_{k_1} (-\frac{1}{2})_{k_2} \dots = 0$$

For $k = 0$, by Formula (17) in James [4], we get

$$(2.13) \quad (a)_k = 1 \quad \text{for all } a.$$

Thus we obtain, in (2.11) above, ${}_3F_2$ function becomes

$$(2.14) \quad {}_3F_2(\frac{1}{2}n_1 + \frac{1}{2}n_2, \frac{1}{2}n_1 + 1, \frac{1}{2}n_1 - \frac{1}{2}; \frac{1}{2}n_1, \frac{1}{2}(n_1 + p + 1); f_p(\Lambda + f_p I)^{-1})$$

$$= {}_3F_2(\frac{1}{2} + \frac{1}{2}n_2, \frac{3}{2}, 0; \frac{1}{2}, \frac{1}{2}(p + 2); f_p(\Lambda + f_p I)^{-1})$$

$$= \sum_k C_k (f_p(\Lambda + f_p I)^{-1})$$

where \mathbf{k} is the partition for $k=0$. Moreover by (17) in James [4],

$$(2.15) \quad (\text{tr} S)^k = \sum_k C_k(S).$$

Thus the ${}_3F_2$ function in (2.10) is equal to 1. Now by letting $n_1 = 1$ in the density function (2.11), we finally obtain the density of $T = f_p$:

$$(2.16) \quad f(f_p) = \frac{\Gamma(\frac{l}{2} + \frac{k}{2})}{\Gamma(\frac{l}{2})\Gamma(\frac{k}{2})} \left(\frac{f_p}{\lambda_1}\right)^{\frac{l}{2}p-1} \left(1 + \frac{f_p}{\lambda_1}\right)^{\frac{l}{2}(n_2+p)} (1/\lambda_1).$$

Thus $f_p / \lambda_1 \sim$ Pearson Type VI distribution with p and $n_2 - p + 1$ degrees of freedom.

That is

$$(2.17) \quad \frac{n_2 - p + 1}{p} \left(\frac{f_p}{\lambda_1}\right) \sim \text{F distribution with } p \text{ and } n_2 - p + 1 \text{ degrees of freedom.}$$

Now we consider the complex case by a heuristic argument. The analogous theory for the density function of the largest eigen value of the matrix $S_2 S_1^{-1}$ does not exist as for the largest eigen value of the matrix $S_2 S_1^{-1}$ in the above real case. However, based on the facts that (1) since both S_2 and S_1 are positive Hermitian and thus their eigen values are positive real, so are the eigen values of $S_2 S_1^{-1}$, (2) the F distribution can usually be considered as the ratio of two Chi-square random variables, and (3) most of the Chi-square random variables involved in the complex case have twice as many degrees of freedom as in the analogous real case, we conjecture that the density function of the complex case has the following property:

$$(2.18) \quad \frac{n_2 - p + 1}{p} \left(\frac{f_p}{\lambda_1}\right) \sim \text{F distribution with } 2p \text{ and } 2(n_2 - p + 1) \text{ degrees of freedom.}$$

Here we suggest two methods to verify the above conjecture on the distribution of T .

Method 1: Simulation method.

First generate from a normal variates generator k independent complex normal samples from $X_1, X_2, \dots, X_k \sim CN_p(0, R_1)$ and an independent complex normal sample from $X_{k+1} \sim CN_p(0, R_2)$ where both R_1 and R_2 are given. Calculate the statistic $T = X_{k+1}^H S_1^{-1} X_{k+1}$ where S_1 is the sample variance-covariance matrix of $\{X_1, X_2, \dots, X_k\}$. Use Kolmogorov test (see for example, Lehmann[6]) to test the null hypothesis that $\frac{n_2 - p + 1}{p} \left(\frac{T}{\lambda_1}\right) \sim \text{F distribution with } 2p \text{ and } 2(n_2 - p + 1) \text{ degrees of freedom where } \lambda_1 \text{ is the largest eigen value of the known matrix } R_2 R_1^{-1}.$

Method 2: Theoretical proof.

Goodman [5] has studied distributions derived from a sample of k independent observations from a complex p -variate normal distribution. However, the distribution of the largest eigen value of the matrix $S_0^H S_1^{-1}$ was not derived in Goodman [5]. Khatri's [3] results, which deals with real normal random vectors, may be generalized to complex case. In order to extend the results of the

density function of the largest eigenvalue of the matrix $S_0 S_1^{-1}$ which was given in Khatri [3], we need to prove the lemmas similar to those in Khatri [3] for the complex case by using the hypergeometric functions ${}_pF_q$ in matrix argument for the complex case. Thus we need to define the hypergeometric functions ${}_pF_q$ in matrix argument for the complex case appropriately. James [4] has some definitions and some properties of ${}_pF_q$ in matrix argument for the complex case. But it is clear that not all of them are useful in our research, and in our research we need more properties as given in James [4].

It can be seen from the description of the two methods, the verification of (2.18) is interesting and important for both theoreticians and practitioners. The author proposes to study these two methods in a follow-up research.

3. Invariance and monotonicity properties

Invariance is a mathematical property for symmetry and in practice many statistical testing problems exhibit symmetries. It is a widely accepted principle that if a hypothesis under consideration is invariant under a transformation, then a good test statistic or the critical region should also be invariant under the same transformation. The reason for the intuitive appeal of an invariant test procedure is the desire for a unique best way to analyze a collection of data. A well-known invariant test in multivariate statistical analysis (see, for example, Anderson [1], page 181) is the Hotelling T- test for testing the mean vector of a normal random vector. It is uniformly most powerful among all tests of μ (mean vector) = 0 based on the sufficient statistics $(\bar{X}, A = \sum (X_\alpha - \bar{X})(X_\alpha - \bar{X})')$ that are invariant with respect to transformations $\bar{X}^* = C\bar{X}, A^* = CAC'$, where C is a non-singular matrix. For a general treatment of invariance, see Lehmann [6]. For the invariant properties of some testing procedures in multivariate statistical analysis, refer to Anderson [1]. These texts do not deal the exact problem that is considered in this research. However, in the following we will review the background of invariance and apply the invariance idea to our problem.

Definition 3.1:

- (1) A function $T(x)$ defined on the sample space X is invariant under the group of transformations G if $T(x) = T(gx)$ for all x in X and g in G .
- (2) An invariant function is a maximal invariant under the group of transformation G if $T(x) = T(y)$ for all x, y in X implies that there exists a g in G such that $y = gx$.

Our problem of testing $H_0: R_1 = R_2$ versus $H_1: R_1 \neq R_2$ is invariant under the group of transformations G of $p \times p$ nonsingular complex matrices which transform x to gx for g in G since for $X \sim CN_p(0, R)$, $CX \sim CN_p(0, CRC^H)$ which is in the same class of distributions as x , and $gR_1g^H = gR_2g^H$ implies $R_1 = R_2$. We are now ready to show that the set of eigenvalues of $R_2R_1^{-1}$ is a maximal invariant under the group of transformation G .

Theorem 3.1: A set of maximal invariants under the group G comprises the eigen values of $R_2R_1^{-1}$, that is, the roots of

$$(3.1) \quad |R_2R_1^{-1} - \lambda I| = |R_2 - \lambda R_1| = 0.$$

Proof: Since $|g(R_2R_1^{-1} - \lambda I)g^H| = |R_2R_1^{-1} - \lambda I|$, the roots of equation (3.1) are invariant under G . To show that they are maximal invariant, we suppose that $|R_2R_1^{-1} - \lambda I| = 0$ and $|A - \lambda I| = 0$ have the same roots where A is a hermitian positive definite matrix. We want to show that there exists a g in G such that $A = g(R_2R_1^{-1})g^H$.

Since both A and $R_2 R_1^{-1}$ are Hermitian and positive definite, there exist unitary matrices $g_1, g_2 \in G$ such that

$$g_1(R_2 R_1^{-1})g_1^H = \Lambda = g_2 B g_2^H$$

where Λ is a diagonal matrix whose elements are the roots of the equation (3.1). Thus we get $B = g_2^H g_1(R_2 R_1^{-1})g_1^H g_2$ where $g = g_2^H g_1 \in G$.

Similarly the maximal invariants in the sample space are the roots of

$$(3.2) \quad |S_2 S_1^{-1} - \lambda I| = |S_2 - \lambda S_1| = 0.$$

Any invariant test statistic or invariant critical region can be expressed in terms of the roots of the equation (3.2). The null hypothesis is rejected if the smaller roots are too small or if the larger roots are too large, or both. In terms of the eigen values $R_2 R_1^H$, the null hypothesis can be written as

$$(3.3) \quad H_0: \lambda_1 = \lambda_2 = \dots = \lambda_p.$$

Any useful invariant test of H_0 has a rejection region in the space of $f_1 \leq f_2 \leq \dots \leq f_p$ that includes the points that in some sense are far from $f_1 = f_2 = \dots = f_p = 0$. The power of an invariant test depends on the parameters through the roots $\lambda_1 \geq \lambda_2 \geq \dots \geq \lambda_p$. It is clear from (2.7) that the critical region of our test depends only on the trace of $S_2 S_1^H$ which is equivalent to the largest eigen value in our case. Thus it is an invariant test. Therefore, the power function should depend on the parameters only through the roots $\lambda_1 \geq \lambda_2 \geq \dots \geq \lambda_p$.

We now discuss another interesting property of the test. It is based on the following theorem and corollary of Anderson and Das Gupta [7].

Consider two independent random matrices U_1 of dimension $p \times n_1$ and U_2 of dimension $p \times n_2$, such that the column vectors of U_1 are independently and normally distributed with mean 0 and covariance matrix Σ_1 and the column vectors of U_2 are independently and normally distributed with mean 0 and covariance matrix Σ_2 . Then we have

Theorem 3.2 (due to Anderson and Das Gupta [7]):

Let ω be a set in the space of (R_1, R_2, \dots, R_p) , the characteristic roots of $(U_1 U_1') (U_2 U_2')^{-1}$ such that when a point $(r_1, r_2, \dots, r_p) \in \omega$, so is every point $(\bar{r}_1, \bar{r}_2, \dots, \bar{r}_p)$ for which $\bar{r}_i \leq r_i, i = 1, \dots, p$. Then the probability of the set ω depends on Σ_1 and Σ_2 only through $(\lambda_1, \dots, \lambda_p)$ and is a monotonically decreasing function of each λ_i .

Corollary 3.3 (due to Anderson and Das Gupta [7]):

If an invariant test with respect to G has an acceptance region ω' such that if $(r_1, r_2, \dots, r_p) \in \omega'$, so is $(\bar{r}_1, \bar{r}_2, \dots, \bar{r}_p)$ for which $\bar{r}_i \leq r_i, i = 1, \dots, p$, then the power function of the test is a monotonically increasing function of each λ_i .

The above theorem and corollary were shown for the case of real multivariate normal populations. To the author's best knowledge, the results have not been shown for the complex multivariate normal case yet. However, it is conjectured that both the theorem and the corollary are still true for the complex case.

Since our test is an invariant test from Theorem 3.1, the power function should have the monotonicity property as described in the corollary of Theorem 3.2.

4. Concluding remarks

Let $\mathbf{X}_1(p \times n_1)$ and $\mathbf{X}_2(p \times n_2)$ be independent matrix variates, columns of \mathbf{X}_1 being independently distributed as $CN(0, R_1)$ and those of \mathbf{X}_2 independently distributed as $CN(0, R_2)$. In testing the equality of R_1 and R_2 , Various test criteria have been proposed and studied in the literature. Let $f_1 \leq f_2 \leq \dots \leq f_p$ be the eigen values of $|\mathbf{X}_1 \mathbf{X}_1' - f \mathbf{X}_2 \mathbf{X}_2'| = 0$ and $\lambda_1 \geq \lambda_2 \geq \dots \geq \lambda_p$ be the eigen values of $|\mathbf{R}_1 - f \mathbf{R}_2| = 0$. These test criteria can be summarized as follows:

- (1) Wilks criterion (Wilks [8]), $W = \prod_{i=1}^p (1 + f_i)^{-1}$
- (2) Roy's largest root (Roy [9]) : f_p ,
- (3) Hotelling's trace (Hotelling [10]), $U = \sum_{i=1}^p f_i$,
- (4) Pillai's trace (Pillai [11]), $V = \sum_{i=1}^p f_i / (1 + f_i)$,
- (5) Modified likelihood ratio (see Anderson [1]), $\lambda = \frac{|\mathbf{X}_1 \mathbf{X}_1'|^{1/2 n_1} |\mathbf{X}_2 \mathbf{X}_2'|^{1/2 n_2}}{|\mathbf{X}_1 \mathbf{X}_1' + \mathbf{X}_2 \mathbf{X}_2'|^{1/2 (n_1 + n_2)}}$,
- (6) Nagao's criterion (Nagao [12]), $N = \frac{1}{2} \sum_{i=1}^2 n_i \text{tr} \left[\frac{\mathbf{X}_i \mathbf{X}_i'}{n_i} (\mathbf{X}_1 \mathbf{X}_1' + \mathbf{X}_2 \mathbf{X}_2')^{-1} - \mathbf{I} \right]^2$.

It is clear that tests (1) to (4) are all functions of the roots of $|\mathbf{X}_1 \mathbf{X}_1' - f \mathbf{X}_2 \mathbf{X}_2'| = 0$. So by Theorem 3.1 in the last section, they are all invariant tests. It can also be shown that the test criteria (5) and (6) are also invariant for the group G of transformations defined in Section 3 (see page 408, Anderson [1]). It is readily verify that tests (1) to (4) satisfy the conditions of Theorem 3.2. Thus they all possess the monotonicity property for their respective power functions. It is not trivial that test (5) satisfies the condition required by Theorem 3.2. But test (5) certainly has its own attractive properties as described in Anderson [1]. Chu and Pillai [13] made some numerical power comparisons for the tests (1) to (5) for the regular case, that is, for both $n_1, n_2 \geq p$, only. Their results, however, are for the real case only. Due to the complications of the computation, their comparisons are limited to $p = 2$ and 3 . Even for the limited cases considered by them, they made no general conclusion on which test is uniformly better than the others. So far no attempt has been made by anyone to compare the powers of the test criterion (6) to any other criterion on testing the equality of covariance matrices. As we have mentioned earlier in Section 1, test (5) is inappropriate for the singular case that we are considering. The motivation behind Nagao's test (6) can be briefly summarized as follows. Nagao [12] showed that the variance of the limiting distribution of $-2 \log \lambda$ (λ = likelihood ratio criterion) can be expressed as

$$(4.1) \quad \tau^2 = \sum_{i=1}^2 (n_i / n) \text{tr} [R_i (n_i R_i + n_2 R_2)^{-1} - \mathbf{I}]^2$$

Thus for testing the equality of two covariance matrices R_1, R_2 , we replace the population covariance matrices in (4.1) by the sample covariance matrices and obtain the test criterion (6).

From the above discussion, only test (5) is not appropriate for the singular case. Thus comparing tests (1), (2), (3), (4), (6) for the complex case as well as for the real case for the singular case, both theoretically and numerically, could be an important and challenging task.

As for our problem described in Section 2, $n_1 = 1$. Thus $f_1 = f_2 = \dots = f_{p-1} = 0 < f_p$, the Wilks test statistic is $W = 1/(1 + f_p)$ whose critical region is equivalent to our test T . The Roy's test statistic f_p is exactly the same as our test statistic T . Hotelling's test statistic, in our case, is $U = \sum_{i=1}^p f_i = f_p$ which is again exactly the same as our T . Pillai's test statistic can be rewritten, in our case, as $V = \sum_{i=1}^p f_i / (1 + f_i) = f_p / (1 + f_p) = 1 - 1/(1 + f_p) = 1 - W$. It is also equivalent to our test T . Thus all the tests (1) to (4) are either exactly the same as our test T or can be considered equivalent to our test T . Test (6) is derived from the limiting distribution of test (5) whose original form can not be used in singular case. Thus it is meaningful to compare the performances of our test T and test (6) in both real and complex cases.

Acknowledgement:

First I wish to express my gratitude to Professor Hong Wang, University Resident Researcher at RL/OCTS from the Department of Electrical and Electronic Engineering at Syracuse University, for his initial suggestions on this research topic and valuable discussions. I am also grateful to Michael Wicks and Russell Brown who gave me their constructive comments leading to considerable improvement in the final draft. The realization of this report was made possible through generous support from the offices of AFOSR, RL/OCTS, and RDL.

REFERENCES

- [1] Anderson, T. W. (1984) *An introduction to multivariate statistical analysis*, second edition, Wiley, New York.
- [2] Ruben, H. (1962) Probability content of regions under spherical normal distributions, IV: the distribution of homogeneous and non-homogeneous quadratic functions of normal variates, *Ann. Math. Statist.* 33, 542-570.
- [3] Khatri, C. G. (1967) Some distribution problems connected with the characteristic roots of $S_1 S_2^{-1}$, *Ann. Math. Statist.* 38, 944-948.
- [4] James, A. T. (1964) Distributions of matrix variates and latent roots derived from normal samples, *Ann. Math. Statist.*, 35, 475-501.
- [5] Goodman, N. R. (1963) Statistical analysis based on a certain multivariate complex Gaussian distribution (an Introduction), *Ann. Math. Statist.*, 34, 152-177.
- [6] Lehmann, E. L. (1986) *Testing Statistical Hypotheses*, second edition, Wiley, New York.
- [7] Anderson, T. W. and Das Gupta, S. (1964) A monotonicity property of the power functions of some tests of the equality of two covariance matrices, *Ann. Math. Statist.*, 35, 1059-1063.
- [8] Wilks, S. S. (1932) Certain generalizations in the analysis of variance, *Biometrika*, 24, 417 - 494.
- [9] Roy, S. N. (1945) The individual sampling distribution of the maximum, the minimum and any intermediate of the p-statistics on the null hypotheses, *Sankhya*, 7, 133-158.
- [10] Hotelling, H. (1951) A generalized T test and measure of multivariate dispersion, *Proceedings of the Second Berkeley Symposium on Mathematical Statistics and Probability* (edited by Neyman, J.), University of California, Los Angeles and Berkeley, 23-41.
- [11] Pillai, K. C. S. (1955) Some new test criteria in multivariate analysis, *Ann. Math. Statist.*, 26, 117-121.
- [12] Nagao, H. (1973) On some test criteria for covariance matrix, *Ann. of Statistics*, vol. 1, 700-709.

**ON CLASSIFICATION OF
MULTISPECTRAL INFRARED IMAGE DATA**

Julian Cheung
Assistant Professor
Department of Electrical Engineering

New York Institute of Technology
1855 Broadway
New York, NY 10023

Final Report for:
Summer Faculty Research Program
Rome Laboratory

Sponsored by:
Air Force Office of Scientific Research
Bolling Air Force Base, DC

and

Rome Laboratory

August 1994

ON CLASSIFICATION OF MULTISPECTRAL INFRARED IMAGE DATA

JULIAN CHEUNG

Assistant Professor

Department of Electrical Engineering

New York Institute of Technology

ABSTRACT

In this work we analyze a detector on the basis of a model whereupon each signal component consists of the radiant thermal energy contributed by the emissivity and the blackbody radiation reference (BBRR) of either the small low-observation target or the intense, highly structured background. A low-order power series is employed to approximate the BBRR. A sufficient statistic, when the underlying sensor noise and spectral emissivities are normally distributed, is derived. It is shown that the new detector is effective in enhancing the target and suppressing cluttered background on a pixel-by-pixel basis. It is also shown that under more regular conditions, the new detector represents other classes of detectors, including the constant emissivity detector and the maximum *a posteriori* type detector. This suggests that the new class of detectors performs at least as well as other classes of detectors and yields better performance when some restrictive conditions are relaxed. Numerical computations demonstrate the superior performance of the proposed detector.

ON CLASSIFICATION OF MULTISPECTRAL INFRARED IMAGE DATA

Julian Cheung

I. INTRODUCTION

The detection of small low-intensity observable target in high intensity clutter is a difficult task and is of growing importance due to numerous applications, including, to name a few, geological remote sensing, mineralogic exploration, environmental monitoring, and ground/airborne target identification. These applications are characterized by spatial resolution sufficient to barely resolve the target imbedded in intense, highly structured background clutter. Classical spatial filtering techniques of single band infrared (IR) imagery do not provide high probability of detection with a low false alarm rate. One way to achieve satisfactory results for these demanding cases is to apply multi-spectral signal processing techniques which exploit spectral differences between the target signature and the background. In fact, several recent studies [1]-[4] indicate that on the basis of multispectral emissivity differences between the target and the background, the detectability of small man-made objects viewed in a natural background clutter may be improved dramatically. Research work in this area has been stimulated primarily by the development of imaging sensors capable of collecting high-quality spectral data in the thermal IR region, such as the NASA Thermal Infrared Multispectral sensor (TIMS) and the DARPA-sponsored Multispectral Infrared Camera (MUSIC).

However, the effective radiance incident upon the detectors of the sensors, after it has been compensated for noise effects, and, for any particular bandwidth, is a nonlinear function of emissivity and temperature of the emitting target/background. The sensor system simply cannot separate the contribution from the emissivity and temperature that constitute the radiance value. Since detection has to be made based on spectral radiances, it becomes necessary to accurately specify temperatures of the targets and backgrounds in order to characterize the emissivities properly. One approach is to assume that the temperatures of the target and the background are the same, so that the difference of the scene data in one band with respect to the scene data in the other spectral band, on a pixel-by-pixel basis, is the target residual in the output image because of the coloring between spectral bands [5],[6].

In real applications, temperature of the target (e.g., engine plume) may be drastically different from the temperature of the background, or the temperature may deviate from information at hand. Also, sensor noise may be correlated for various color bands. Furthermore, prior knowledge regarding emissivities of the target and the background may be very limited. However, if the parameters for the target and background used to generate the radiance statistics for detection are not the same as encountered in the real world, the detector may suffer enormous losses. To overcome these problems, a new approach is presented in this paper.

Section II introduces a radiance signal model including the effects of both temperature and emissivity for the target and the background. This is followed by the approximation of $L_i(T)$, the sensor response to the black body radiance reference. Section III presents a derivation of a sufficient statistic of an optimal likelihood ratio detector based on the assumption of a Gaussian distribution for sensor noise and emissivity. Section IV indicates the generality of the proposed detector and some of its relevant properties. Section V compares performance of the proposed detector relative to others via numerical computations. Further suggestions and conclusions are given in Section VI.

II. PRELIMINARIES

Let the N -variate $\mathbf{x} = [x_1 \dots x_N]'$ be the multiband radiant energy observable to a multispectral sensor with N channels. Each component of the observation $x_i = x(\lambda_i)$ is an additive sum of radiant energy $s_i(\epsilon, T)$ and sensor (channel) noise w_i for a specific wavelength region $(\lambda_i - 1/2 \Delta \lambda_i, \lambda_i + 1/2 \Delta \lambda_i]$. The radiant energy component $s_i(\epsilon, T)$ is generated by integrating the blackbody spectral radiation from a thermally emitting source attenuated by the spectral responsivity of an infrared (IR) filter over its spectral bandwidth, and multiplying the result by the emissivity of the source (random emissivity of the source over $(\lambda_i - 1/2 \Delta \lambda_i, \lambda_i + 1/2 \Delta \lambda_i]$), i.e., $s_i(\epsilon, T) = \epsilon_i L_i(T)$, where $\epsilon_i = \epsilon(u \mid u \in (\lambda_i - 1/2 \Delta \lambda_i, \lambda_i + 1/2 \Delta \lambda_i])$,

$$L_i(T) = \int_{\lambda_i - 1/2 \Delta \lambda_i}^{\lambda_i + 1/2 \Delta \lambda_i} L(u, T) r_i(u) du \quad (1)$$

and $r_i(\lambda)$ is the spectral response or the so-called point spread function (psf) of the i th sensor characterized by the center wavelength λ_i and bandwidth $\Delta \lambda_i$, $L(\lambda, T)$ is Planck's function of the black body radiation

$$L(\lambda, T) = \frac{c_1}{\pi \lambda^5} (\exp(c_2/\lambda T) - 1)^{-1} \quad (2)$$

and $c_1 = 3.7415 \times 10^4 \text{ W cm}^{-2} \mu\text{m}^{-1}$, $c_2 = 1.43879 \times 10^4 \mu\text{m} \cdot \text{K}$ [7]. Therefore the N -variate observable is

$$\mathbf{x} \equiv \begin{bmatrix} x_1 \\ \vdots \\ x_N \end{bmatrix} = \begin{bmatrix} s_1(\epsilon, T) \\ \vdots \\ s_N(\epsilon, T) \end{bmatrix} + \begin{bmatrix} w_1 \\ \vdots \\ w_N \end{bmatrix}, \quad s_i(\epsilon, T) \equiv \epsilon_i L_i(T) \quad (3)$$

where bold letters represent vectors, underlined bold letters represent matrices, and prime denotes the transposition. As is evident from (2), the blackbody IR filter output $L_i(T)$ is nonlinear. This poses many theoretical and implementation problems. However, because the temperature range is usually known, we may approximate it by a power series. This is addressed by the theorem below.

Theorem I. Suppose $\int_{T_r - \frac{1}{2}\Delta T_r}^{T_r + \frac{1}{2}\Delta T_r} L_i(T)^2 dT < \infty$, then within the interval $I_r = (T_r - \frac{1}{2}\Delta T_r, T_r + \frac{1}{2}\Delta T_r]$ $L_i(T)$ may be approximated arbitrarily close by a power series of finite order

$$L_i(T) \approx a_{i0} + a_{i1}T + a_{i2}T^2 + \dots + a_{iM}T^M, \quad M \in \mathbb{N}^* \quad (4)$$

and approximation is in the integral square error (ISE) sense.

In addition, for reasons that will become apparent, this approach requires a very low order power series and incurs a negligible error. This observation is confirmed in [8,9], which considered the approximation of $L_i(T)$ using a second order power series. The uniform convergence of the power series approximation implies the convergence in the mean square sense and with probability 1 [11]. Consequently, we may assume the blackbody filter output $L_i(T)$ is known (almost) exactly. The estimation of the temperature coefficient vector $\mathbf{a}_i = [a_{i0} \dots a_{iM}]'$ will be considered later.

When there is no target, the signal components (thermal radiant energy) $s_i(\epsilon, T)$ depend solely on the naturally occurring backgrounds, which may be composed of natural scenes such as water, soil, sand, etc. This is indicated by the subscripted letter b (*background*). In the presence of a target that fills an entire pixel, then the signal components depend solely on the multispectral emissivity of the target and the corresponding blackbody filter response. This is marked by a subscripted letter t (*target*).

The detection of the target imbedded in background clutter is our main concern and can be formulated as a composite hypothesis testing problem

$$\begin{aligned} H_0: \quad \mathbf{x} &= \begin{bmatrix} s_{b,1}(\epsilon, T) \\ \vdots \\ s_{b,N}(\epsilon, T) \end{bmatrix} + \begin{bmatrix} w_1 \\ \vdots \\ w_N \end{bmatrix}, \quad s_{b,i}(\epsilon, T) = \epsilon_{b,i} L_i(T_b), \quad i=1, \dots, N \\ H_1: \quad \mathbf{x} &= \begin{bmatrix} s_{t,1}(\epsilon, T) \\ \vdots \\ s_{t,N}(\epsilon, T) \end{bmatrix} + \begin{bmatrix} w_1 \\ \vdots \\ w_N \end{bmatrix}, \quad s_{t,i}(\epsilon, T) = \epsilon_{t,i} L_i(T_t), \quad i=1, \dots, N. \end{aligned} \quad (5)$$

It is well known that the Neyman-Pearson test statistics for above model is [10]

$$\mathcal{L}(\mathbf{x}; \epsilon_b, T_b, \epsilon_t, T_t) = \frac{f_{X|H_1}(\mathbf{x}|H_1)}{f_{X|H_0}(\mathbf{x}|H_0)} = \frac{\int \dots \int f_{X|s_t, H_1}(\mathbf{x}|s_t, H_1) f_{s_t}(s_t) ds_t}{\int \dots \int f_{X|s_b, H_0}(\mathbf{x}|s_b, H_0) f_{s_b}(s_b) ds_b} \underset{H_0}{\overset{H_1}{>}} \tau \quad (6)$$

where τ is the threshold for a prespecified type-I error α , $f(\cdot)$ the probability density function (pdf) of \mathbf{X} . Evidently, the specific form of the test statistics $\mathcal{L}(\cdot)$ is a function of the probability distributions

of the sensor noise field $w = [w_1 \dots w_N]'$, the multispectral emissivity fields $\epsilon_\gamma = [\epsilon_{\gamma,1} \dots \epsilon_{\gamma,N}]'$, and the temperatures T_γ , $\gamma = b$ (background clutter), t (target), respectively.

III. OPTIMAL MULTISPECTRAL DETECTORS

For general development, the following assumptions are made:

- i) The blackbody radiation flux $L_\gamma = [L_1(T_\gamma) \dots L_N(T_\gamma)]'$, $\gamma = b, t$ is known or can be approximated reasonably close;
- ii) The multispectral emissivity field $\epsilon_\gamma = [\epsilon_\gamma(\lambda_1) \dots \epsilon_\gamma(\lambda_N)]' = [\epsilon_{\gamma,1} \dots \epsilon_{\gamma,N}]'$ is normally distributed $N(\mu_{\epsilon_\gamma}, \underline{\Psi}_{\epsilon_\gamma})$, i.e.,

$$f_{\epsilon_\gamma}(y) = \left((2\pi)^N |\underline{\Psi}_{\epsilon_\gamma}| \right)^{-1/2} \exp \left\{ -1/2 (y - \mu_{\epsilon_\gamma})' \underline{\Psi}_{\epsilon_\gamma}^{-1} (y - \mu_{\epsilon_\gamma}) \right\}, \quad \gamma = b, t, \quad (7)$$

where $|\cdot|$ denotes the determinant of;

- iii) The sensor noise field $w = [w_1 \dots w_N]'$ is also normally distributed $N(\mu_w, \underline{\Psi}_w)$ and is statistically independent of the emissivity field.

Combining i), ii), and eq.(3) we get

- iv) The multispectral signal field $s_\gamma = [\epsilon_{\gamma,1} L_1(T_\gamma) \dots \epsilon_{\gamma,N} L_N(T_\gamma)]'$ is normally distributed $N(\mu_{s_\gamma}, \underline{\Psi}_{s_\gamma})$, with the mean vector $\mu_{s_\gamma} = [\mu_{s_\gamma,1} \dots \mu_{s_\gamma,N}]'$, $\mu_{s_\gamma,ii} = E \{ \epsilon_{\gamma,ii} L_i(T_\gamma) \} = \mu_{\epsilon_\gamma,ii} L_i(T_\gamma)$, and the covariance matrix $\underline{\Psi}_{s_\gamma} = \{ cov(s_{\gamma,ii}, s_{\gamma,jj}) \}$, each element is

$$cov(s_{\gamma,ii}, s_{\gamma,jj}) = E \{ (s_{\gamma,ii} - \mu_{s_\gamma,ii})(s_{\gamma,jj} - \mu_{s_\gamma,jj}) \} = cov(\epsilon_{\gamma,ii}, \epsilon_{\gamma,jj}) L_i(T_\gamma) L_j(T_\gamma), \quad i, j = 1, \dots, N; \quad \gamma = b, t. \quad (8)$$

The probabilities of the observation vector X conditional on H_j are

$$f_{X|H_j}(x|H_j) = \int \dots \int \left((2\pi)^{2N} |\underline{\Psi}_w| |\underline{\Psi}_{s_\gamma}| \right)^{-1/2} \exp \left\{ -1/2 (x - s_\gamma - \mu_w)' \underline{\Psi}_w^{-1} (x - s_\gamma - \mu_w) \right\} \\ \times \exp \left\{ -1/2 (s_\gamma - \mu_{s_\gamma})' \underline{\Psi}_{s_\gamma}^{-1} (s_\gamma - \mu_{s_\gamma}) \right\} ds_\gamma, \quad \gamma = b \text{ for } H_0, \quad t \text{ for } H_1. \quad (9)$$

Since the covariance matrix $\underline{\Psi}$ is symmetric, so is its inverse $\underline{\Psi}^{-1}$, and, together with the identity

$(ABC)' = C' B' A'$, we have

$$(x - s_\gamma - \mu_w)' \underline{\Psi}_w^{-1} (x - s_\gamma - \mu_w) = x' \underline{\Psi}_w^{-1} x - 2x' \underline{\Psi}_w^{-1} \mu_w + \mu_w' \underline{\Psi}_w^{-1} \mu_w - 2x' \underline{\Psi}_w^{-1} s_\gamma + s_\gamma' \underline{\Psi}_w^{-1} s_\gamma + 2s_\gamma' \underline{\Psi}_w^{-1} \mu_w,$$

$$(s_\gamma - \mu_{s_\gamma})' \underline{\Psi}_{s_\gamma}^{-1} (s_\gamma - \mu_{s_\gamma}) = s_\gamma' \underline{\Psi}_{s_\gamma}^{-1} s_\gamma - 2s_\gamma' \underline{\Psi}_{s_\gamma}^{-1} \mu_{s_\gamma} + \mu_{s_\gamma}' \underline{\Psi}_{s_\gamma}^{-1} \mu_{s_\gamma}.$$

Summing the above two equations, we obtain

$$Q(x, s_\gamma) = (x - \mu_w)' \underline{\Psi}_w^{-1} (x - \mu_w) + \mu_{s_\gamma}' \underline{\Psi}_{s_\gamma}^{-1} \mu_{s_\gamma} + s_\gamma' (\underline{\Psi}_w^{-1} + \underline{\Psi}_{s_\gamma}^{-1}) s_\gamma - 2s_\gamma' \{ \underline{\Psi}_w^{-1} (x - \mu_w) + \underline{\Psi}_{s_\gamma}^{-1} \mu_{s_\gamma} \}. \quad (10)$$

Substituting (9) into (6), the optimum detector is

$$\mathcal{L}(x) = \frac{\int \dots \int K_t \exp \{ -\frac{1}{2} Q(x, s_t) \} ds_t}{\int \dots \int K_b \exp \{ -\frac{1}{2} Q(x, s_b) \} ds_b} \underset{H_0}{\overset{H_1}{>}} \tau \quad (11)$$

with the normalizing constant $K_\gamma = \left((2\pi)^{2N} |\underline{\Psi}_w| |\underline{\Psi}_{s_\gamma}| \right)^{-1/2}$, $\gamma = b, t$, and $Q(x, s_\gamma)$ defined in (10).

We proceed to evaluate each of the multi-dimensional integrals.

Since $\underline{\Psi}_w$, $\underline{\Psi}_{s_\gamma}$, $\underline{\Psi}_{s_\gamma}$ are covariance matrices, they are symmetric and positive definite [11],[12].

These properties extend to their inverses and sum of their inverses. There exist two sets of $N \times 1$ orthonormal eigenvectors $\{v_{\gamma j}\}$ and corresponding eigenvalues $\{\lambda_{\gamma j}\}$ such that [13]

$$(\underline{\Psi}_w^{-1} + \underline{\Psi}_{s_\gamma}^{-1}) v_{\gamma j} = \lambda_{\gamma j}^{-1} v_{\gamma j}, \quad v_{\gamma i}' v_{\gamma j} = \delta_{ij}, \quad \delta_{ij} = \text{Kronecker delta}, \quad i, j = 1, \dots, N, \quad \gamma = b, t.$$

Form the matrices $\underline{V}_{\gamma, N \times N} = [v_{\gamma 1} \dots v_{\gamma N}]$, $\underline{\Lambda}_{\gamma, N \times N} = \text{diag}[\lambda_{\gamma 1} \dots \lambda_{\gamma N}]$, then it is apparent that

$$(\underline{\Psi}_w^{-1} + \underline{\Psi}_{s_\gamma}^{-1}) \underline{V}_\gamma = \underline{\Lambda}_\gamma^{-1} \underline{V}_\gamma, \quad (12)$$

$$\underline{V}_\gamma' \underline{V}_\gamma = \underline{V}_\gamma \underline{V}_\gamma' = \underline{I}, \quad \gamma = b, t. \quad (13)$$

Multiplying (12) by \underline{V}_γ' and applying (13), yields $\underline{V}_\gamma' (\underline{\Psi}_w^{-1} + \underline{\Psi}_{s_\gamma}^{-1}) \underline{V}_\gamma = \underline{\Lambda}_\gamma^{-1}$. Making use of the identity $(\underline{A} \underline{B} \underline{C})^{-1} = \underline{C}^{-1} \underline{B}^{-1} \underline{A}^{-1}$, the inverse is

$$\underline{V}_\gamma' (\underline{\Psi}_w^{-1} + \underline{\Psi}_{s_\gamma}^{-1})^{-1} \underline{V}_\gamma = \underline{\Lambda}_\gamma. \quad (14)$$

The symmetry and positive definiteness of $\underline{\Psi}_w^{-1} + \underline{\Psi}_{s_\gamma}^{-1}$ implies that elements of $\underline{\Lambda}_\gamma^{-1}$ are all real positive numbers, and, therefore, its square root $\underline{\Lambda}_\gamma^{-1/2}$ exists. Apply a linear operator $\underline{U}_\gamma = \underline{V}_\gamma \underline{\Lambda}_\gamma^{-1/2}$, then $\tilde{x}_\gamma = \underline{U}_\gamma' x$, $\tilde{s}_\gamma = \underline{U}_\gamma' s_\gamma$, $\mu_{\tilde{s}_\gamma} = \underline{U}_\gamma' \mu_{s_\gamma}$, $\tilde{w}_\gamma = \underline{U}_\gamma' w$, $\mu_{\tilde{w}_\gamma} = \underline{U}_\gamma' \mu_w$. Equivalently, since $\underline{U}_\gamma^{-1} = \underline{\Lambda}_\gamma^{1/2} \underline{V}_\gamma^{-1} = \underline{\Lambda}_\gamma^{1/2} \underline{V}_\gamma'$, we get $x_\gamma = \underline{V}_\gamma \underline{\Lambda}_\gamma^{1/2} \tilde{x}_\gamma$, $s_\gamma = \underline{V}_\gamma \underline{\Lambda}_\gamma^{1/2} \tilde{s}_\gamma$, $\mu_{s_\gamma} = \underline{V}_\gamma \underline{\Lambda}_\gamma^{1/2} \mu_{\tilde{s}_\gamma}$, $w = \underline{V}_\gamma \underline{\Lambda}_\gamma^{1/2} \tilde{w}_\gamma$, $\mu_w = \underline{V}_\gamma \underline{\Lambda}_\gamma^{1/2} \mu_{\tilde{w}_\gamma}$.

Rewrite (10) as

$$\begin{aligned} Q(\tilde{x}, \tilde{s}_\gamma) &= (\tilde{x}_\gamma - \mu_{\tilde{w}_\gamma})' \underline{\Lambda}_\gamma^{1/2} \underline{V}_\gamma' \underline{\Psi}_w^{-1} \underline{V}_\gamma \underline{\Lambda}_\gamma^{1/2} (\tilde{x}_\gamma - \mu_{\tilde{w}_\gamma}) + \mu_{\tilde{s}_\gamma}' \underline{\Lambda}_\gamma^{1/2} \underline{V}_\gamma' \underline{\Psi}_{s_\gamma}^{-1} \underline{V}_\gamma \underline{\Lambda}_\gamma^{1/2} \mu_{\tilde{s}_\gamma} \\ &\quad + \tilde{s}_\gamma' \underline{\Lambda}_\gamma^{1/2} \underline{V}_\gamma' \left(\underline{\Psi}_w^{-1} + \underline{\Psi}_{s_\gamma}^{-1} \right) \underline{V}_\gamma \underline{\Lambda}_\gamma^{1/2} \tilde{s}_\gamma - 2\tilde{s}_\gamma' \underline{\Lambda}_\gamma^{1/2} \underline{V}_\gamma' \left\{ \underline{\Psi}_w^{-1} \underline{V}_\gamma \underline{\Lambda}_\gamma^{1/2} (\tilde{x}_\gamma - \mu_{\tilde{w}_\gamma}) + \underline{\Psi}_{s_\gamma}^{-1} \underline{V}_\gamma \underline{\Lambda}_\gamma^{1/2} \mu_{\tilde{s}_\gamma} \right\} \\ &= (\tilde{x}_\gamma - \mu_{\tilde{w}_\gamma})' \underline{\Psi}_w^{-1} (\tilde{x}_\gamma - \mu_{\tilde{w}_\gamma}) + \mu_{\tilde{s}_\gamma}' \underline{\Psi}_{s_\gamma}^{-1} \mu_{\tilde{s}_\gamma} + \tilde{s}_\gamma' \tilde{s}_\gamma - 2\tilde{s}_\gamma' \left\{ \underline{\Psi}_w^{-1} (\tilde{x}_\gamma - \mu_{\tilde{w}_\gamma}) + \underline{\Psi}_{s_\gamma}^{-1} \mu_{\tilde{s}_\gamma} \right\} \end{aligned}$$

where

$$\underline{\Psi}_{\tilde{w}_\gamma}^{-1} = \underline{\Lambda}_\gamma^{1/2} \underline{V}_\gamma' \underline{\Psi}_w^{-1} \underline{V}_\gamma \underline{\Lambda}_\gamma^{1/2}, \quad \underline{\Psi}_{\tilde{s}_\gamma}^{-1} = \underline{\Lambda}_\gamma^{1/2} \underline{V}_\gamma' \underline{\Psi}_{s_\gamma}^{-1} \underline{V}_\gamma \underline{\Lambda}_\gamma^{1/2}. \quad (15)$$

We define $\tilde{\mathbf{A}}_\gamma = \underline{\Psi}_\gamma^{-1}(\tilde{\mathbf{x}}_\gamma - \mu_{w_\gamma}) + \underline{\Psi}_\gamma^{-1}\mu_{s_\gamma}$, and complete the matrix squares to obtain

$$\begin{aligned} Q(\tilde{\mathbf{x}}, \tilde{\mathbf{s}}_\gamma) &= \|\tilde{\mathbf{s}}_\gamma - \tilde{\mathbf{A}}_\gamma\|^2 + (\tilde{\mathbf{x}}_\gamma - \mu_{w_\gamma})' \underline{\Psi}_\gamma^{-1}(\tilde{\mathbf{x}}_\gamma - \mu_{w_\gamma}) + \mu_{s_\gamma}' \underline{\Psi}_\gamma^{-1}\mu_{s_\gamma} \\ &\quad - (\tilde{\mathbf{x}}_\gamma - \mu_{w_\gamma})' \underline{\Psi}_\gamma^{-1} \underline{\Psi}_\gamma^{-1}(\tilde{\mathbf{x}}_\gamma - \mu_{w_\gamma}) - \mu_{s_\gamma}' \underline{\Psi}_\gamma^{-1} \underline{\Psi}_\gamma^{-1}\mu_{s_\gamma} - 2(\tilde{\mathbf{x}}_\gamma - \mu_{w_\gamma})' \underline{\Psi}_\gamma^{-1} \underline{\Psi}_\gamma^{-1}\mu_{s_\gamma} \\ &= \|\tilde{\mathbf{s}}_\gamma - \tilde{\mathbf{A}}_\gamma\|^2 + (\tilde{\mathbf{x}}_\gamma - \mu_{w_\gamma})' (\underline{\Psi}_\gamma^{-1} - \underline{\Psi}_{w_\gamma}^{-2})(\tilde{\mathbf{x}}_\gamma - \mu_{w_\gamma}) + \mu_{s_\gamma}' (\underline{\Psi}_\gamma^{-1} - \underline{\Psi}_{s_\gamma}^{-2})\mu_{s_\gamma} \\ &\quad - 2(\tilde{\mathbf{x}}_\gamma - \mu_{w_\gamma})' \underline{\Psi}_\gamma^{-1} \underline{\Psi}_{s_\gamma}^{-1}\mu_{s_\gamma}. \end{aligned} \quad (16)$$

By the identity $|\underline{\mathbf{A}}_{N \times N} \underline{\mathbf{B}} \underline{\mathbf{C}}_{N \times N}| = |\underline{\mathbf{A}}| |\underline{\mathbf{B}}| |\underline{\mathbf{C}}|$, the determinant of $\underline{\Psi}_{s_\gamma}$ is

$$|\underline{\Psi}_{s_\gamma}| = |\underline{\Lambda}_\gamma^{-1/2} \underline{\mathbf{V}}_\gamma^{-1} \underline{\Psi}_\gamma (\underline{\mathbf{V}}_\gamma')^{-1} \underline{\Lambda}_\gamma^{-1/2}| = |\underline{\Lambda}_\gamma^{-1/2} \underline{\mathbf{V}}_\gamma' \underline{\Psi}_\gamma \underline{\mathbf{V}}_\gamma \underline{\Lambda}_\gamma^{-1/2}| = |\underline{\Lambda}_\gamma|^{-1} |\underline{\Psi}_\gamma|. \quad (17)$$

Applying (16) while taking into account the Jacobian $d\tilde{\mathbf{s}}_\gamma = |\underline{\mathbf{V}}_\gamma \underline{\Lambda}_\gamma^{1/2}| d\tilde{\mathbf{s}}_\gamma = |\underline{\Lambda}_\gamma|^{1/2} d\tilde{\mathbf{s}}_\gamma$ [14], each of the integrals (11) is evaluated

$$\begin{aligned} &\int \dots \int \left((2\pi)^{2N} |\underline{\Psi}_w| |\underline{\Psi}_{s_\gamma}| \right)^{-1/2} \exp\left\{ -1/2 Q_{(2)}(\tilde{\mathbf{x}}_\gamma, \tilde{\mathbf{s}}_\gamma) \right\} |\underline{\Lambda}_\gamma|^{1/2} d\tilde{\mathbf{s}}_\gamma \\ &= \left((2\pi)^N |\underline{\Psi}_w| \right)^{-1/2} \exp \left\{ -1/2 \left[(\tilde{\mathbf{x}}_\gamma - \mu_{w_\gamma})' (\underline{\Psi}_\gamma^{-1} - \underline{\Psi}_{w_\gamma}^{-2})(\tilde{\mathbf{x}}_\gamma - \mu_{w_\gamma}) + \mu_{s_\gamma}' (\underline{\Psi}_\gamma^{-1} - \underline{\Psi}_{s_\gamma}^{-2})\mu_{s_\gamma} \right. \right. \\ &\quad \left. \left. - 2(\tilde{\mathbf{x}}_\gamma - \mu_{w_\gamma})' \underline{\Psi}_\gamma^{-1} \underline{\Psi}_{s_\gamma}^{-1}\mu_{s_\gamma} \right] \right\}, \quad \gamma = b, t. \end{aligned} \quad (18)$$

The last line is due to (17) and the identity $\int \dots \int \left((2\pi)^N |\underline{\Psi}_{s_\gamma}| \right)^{-1/2} \exp\left\{ -1/2 \|\tilde{\mathbf{s}}_\gamma - \tilde{\mathbf{A}}_\gamma\|^2 \right\} d\tilde{\mathbf{s}}_\gamma = 1$.

Taking the logarithm of (18), transferring all normalized constants to the r.h.s., and simplifying, a sufficient statistics for the likelihood ratio detector in the form of (6) or (11) is

$$\mathcal{L}(\mathbf{x}) = Q(\tilde{\mathbf{x}}_b, \mu_{s_b}) - Q(\tilde{\mathbf{x}}_t, \mu_{s_t}) \underset{H_0}{>} \underset{H_1}{<} \tau \quad (19)$$

where

$$Q(\tilde{\mathbf{x}}_\gamma, \mu_{s_\gamma}) = (\tilde{\mathbf{x}}_\gamma - \mu_{w_\gamma})' (\underline{\Psi}_\gamma^{-1} - \underline{\Psi}_{w_\gamma}^{-2})(\tilde{\mathbf{x}}_\gamma - \mu_{w_\gamma}) + \mu_{s_\gamma}' (\underline{\Psi}_\gamma^{-1} - \underline{\Psi}_{s_\gamma}^{-2})\mu_{s_\gamma} - 2(\tilde{\mathbf{x}}_\gamma - \mu_{w_\gamma})' \underline{\Psi}_\gamma^{-1} \underline{\Psi}_{s_\gamma}^{-1}\mu_{s_\gamma}. \quad (20)$$

In general, it is preferable to work in the original \mathbb{R}^N space. Therefore, apply (12)-(14) together with the transformed vectors listed right after (14) to obtain

$$\begin{aligned} (\tilde{\mathbf{x}}_\gamma - \mu_{w_\gamma})' \underline{\Psi}_\gamma^{-1}(\tilde{\mathbf{x}}_\gamma - \mu_{w_\gamma}) &= (\mathbf{x} - \mu_w)' \underline{\mathbf{V}}_\gamma \underline{\Lambda}_\gamma^{-1/2} \underline{\Lambda}_\gamma^{1/2} \underline{\mathbf{V}}_\gamma' \underline{\Psi}_\gamma^{-1} \underline{\mathbf{V}}_\gamma \underline{\Lambda}_\gamma^{1/2} \underline{\Lambda}_\gamma^{-1/2} \underline{\mathbf{V}}_\gamma' (\mathbf{x} - \mu_w) \\ &= (\mathbf{x} - \mu_w)' \underline{\Psi}_w^{-1} (\mathbf{x} - \mu_w) \end{aligned}$$

$$\begin{aligned}
(\tilde{x}_\gamma - \mu_{\tilde{x}_\gamma})' \underline{\Psi}_{\tilde{x}_\gamma}^{-2} (\tilde{x}_\gamma - \mu_{\tilde{x}_\gamma}) &= (x - \mu_w)' \underline{V} \underline{\Lambda}^{-1/2} (\underline{\Lambda}^{1/2} \underline{V}' \underline{\Psi}_w^{-1} \underline{V} \underline{\Lambda}^{1/2}) (\underline{\Lambda}^{1/2} \underline{V}' \underline{\Psi}_w^{-1} \underline{V} \underline{\Lambda}^{1/2}) \underline{\Lambda}^{-1/2} \underline{V}' (x - \mu_w) \\
&= (x - \mu_w)' \underline{\Psi}_w^{-1} (\underline{\Psi}_w^{-1} + \underline{\Psi}_{s_\gamma}^{-1})^{-1} \underline{\Psi}_w^{-1} (x - \mu_w)
\end{aligned}$$

and

$$\begin{aligned}
(\tilde{x}_\gamma - \mu_{\tilde{x}_\gamma})' \underline{\Psi}_{\tilde{x}_\gamma}^{-1} \underline{\Psi}_{s_\gamma}^{-1} \tilde{s}_\gamma &= (x - \mu_w)' \underline{V} \underline{\Lambda}^{-1/2} (\underline{\Lambda}^{1/2} \underline{V}' \underline{\Psi}_w^{-1} \underline{V} \underline{\Lambda}^{1/2}) (\underline{\Lambda}^{1/2} \underline{V}' \underline{\Psi}_{s_\gamma}^{-1} \underline{V} \underline{\Lambda}^{1/2}) \underline{\Lambda}^{-1/2} \underline{V}' \mu_{s_\gamma} \\
&= (x - \mu_w)' \underline{\Psi}_w^{-1} (\underline{\Psi}_w^{-1} + \underline{\Psi}_{s_\gamma}^{-1})^{-1} \underline{\Psi}_{s_\gamma}^{-1} \mu_{s_\gamma}.
\end{aligned}$$

Thus, in the original (pretransformed) space the quadratic term (20) is

$$\begin{aligned}
Q(x, \mu_{s_\gamma}) &= (x - \mu_w)' \left(\underline{\Psi}_w^{-1} - \underline{\Psi}_w^{-1} (\underline{\Psi}_w^{-1} + \underline{\Psi}_{s_\gamma}^{-1})^{-1} \underline{\Psi}_w^{-1} \right) (x - \mu_w) + \mu_{s_\gamma}' \left(\underline{\Psi}_{s_\gamma}^{-1} - \underline{\Psi}_{s_\gamma}^{-1} (\underline{\Psi}_w^{-1} + \underline{\Psi}_{s_\gamma}^{-1})^{-1} \underline{\Psi}_{s_\gamma}^{-1} \right) \mu_{s_\gamma} \\
&\quad - 2 (x - \mu_w)' \underline{\Psi}_w^{-1} (\underline{\Psi}_w^{-1} + \underline{\Psi}_{s_\gamma}^{-1})^{-1} \underline{\Psi}_{s_\gamma}^{-1} \mu_{s_\gamma},
\end{aligned}$$

or, equivalently,

$$\begin{aligned}
Q(x, \mu_{s_\gamma}) &= \left[x - \mu_w - \frac{\underline{\Psi}_w^{-1} (\underline{\Psi}_w^{-1} + \underline{\Psi}_{s_\gamma}^{-1})^{-1} \underline{\Psi}_{s_\gamma}^{-1}}{\underline{\Psi}_w^{-1} - \underline{\Psi}_w^{-1} (\underline{\Psi}_w^{-1} + \underline{\Psi}_{s_\gamma}^{-1})^{-1} \underline{\Psi}_w^{-1}} \mu_{s_\gamma} \right]' \left(\underline{\Psi}_w^{-1} - \underline{\Psi}_w^{-1} (\underline{\Psi}_w^{-1} + \underline{\Psi}_{s_\gamma}^{-1})^{-1} \underline{\Psi}_w^{-1} \right) \\
&\quad \times \left[x - \mu_w - \frac{\underline{\Psi}_w^{-1} (\underline{\Psi}_w^{-1} + \underline{\Psi}_{s_\gamma}^{-1})^{-1} \underline{\Psi}_{s_\gamma}^{-1}}{\underline{\Psi}_w^{-1} - \underline{\Psi}_w^{-1} (\underline{\Psi}_w^{-1} + \underline{\Psi}_{s_\gamma}^{-1})^{-1} \underline{\Psi}_w^{-1}} \mu_{s_\gamma} \right] \\
&\quad + \mu_{s_\gamma}' \left[\underline{\Psi}_{s_\gamma}^{-1} - \underline{\Psi}_{s_\gamma}^{-1} (\underline{\Psi}_w^{-1} + \underline{\Psi}_{s_\gamma}^{-1})^{-1} \underline{\Psi}_{s_\gamma}^{-1} - \frac{\left(\underline{\Psi}_w^{-1} (\underline{\Psi}_w^{-1} + \underline{\Psi}_{s_\gamma}^{-1})^{-1} \underline{\Psi}_{s_\gamma}^{-1} \right)^2}{\underline{\Psi}_w^{-1} - \underline{\Psi}_w^{-1} (\underline{\Psi}_w^{-1} + \underline{\Psi}_{s_\gamma}^{-1})^{-1} \underline{\Psi}_w^{-1}} \right] \mu_{s_\gamma}.
\end{aligned}$$

The intermediate statistics $Q(x, \mu_{s_\gamma})$ measures the distance square of the decorrelated observation vector x to the vector sum of sensor noise mean μ_w and the scaled signal vector mean μ_{s_γ} , this is added by a bias $\mu_{s_\gamma}' \{ \dots \} \mu_{s_\gamma}$. In practice, the bias is merged with the threshold. Furthermore, simple algebra shows that $\underline{\Psi}_w^{-1} - \underline{\Psi}_w^{-1} (\underline{\Psi}_w^{-1} + \underline{\Psi}_{s_\gamma}^{-1})^{-1} \underline{\Psi}_w^{-1} = (\underline{\Psi}_w + \underline{\Psi}_{s_\gamma})^{-1}$ and $\underline{\Psi}_w^{-1} (\underline{\Psi}_w^{-1} + \underline{\Psi}_{s_\gamma}^{-1})^{-1} \underline{\Psi}_{s_\gamma}^{-1} = (\underline{\Psi}_w + \underline{\Psi}_{s_\gamma})^{-1}$, leading to a sufficient test statistic

$$\mathcal{L}(x) = Q(x, \mu_{s_\gamma}) - Q(x, \mu_{s_\gamma}) \stackrel{H_1}{>} \stackrel{H_0}{<} \tau \quad (21)$$

where

$$Q(x, \mu_{s_\gamma}) = \left(x - \mu_w - \mu_{s_\gamma} \right)' (\underline{\Psi}_w + \underline{\Psi}_{s_\gamma})^{-1} \left(x - \mu_w - \mu_{s_\gamma} \right). \quad (22)$$

Observe the simplicity of the quadratic term (22) as compare to that in (20). The primary reason for the intermediate statistics $Q(\tilde{x}_\gamma, \mu_{s_\gamma})$ is to orthogonally transform x (rotation and scaling) to \tilde{x}_γ by the linear operator U_γ , $\gamma = b, t$. This renders components of the signal field \tilde{s}_γ , which is a temperature-embedded emissivity vector, statistically independent of each other. This permits \tilde{s}_γ to be integrated with respect to its (*a posteriori*) multivariate pdf, yielding $Q(\tilde{x}_\gamma, \mu_{s_\gamma})$, which is subsequently transformed to $Q(x_\gamma, \mu_{s_\gamma})$ back in the original space. The detector $\mathcal{L}(x)$ (21) operates as follows: each intermediate statistic $Q(x_\gamma, \mu_{s_\gamma})$ prewhitens the zero-mean observation vector $x - \mu_w - \mu_{s_\gamma}$ and then square it. If $Q(x_b, \mu_{s_b})$ is greater than $Q(x_t, \mu_{s_t})$, then H_1 (target present) is selected, otherwise H_0 (target absent) is decided. The detector scheme is shown in Fig.1.

IV. SUBCLASSES

The generality of the optimal IR detector in the form of (21) will become clear when the sensor-noise field and/or emissivity field¹ ϵ_γ , $\gamma = b, t$, are subject to further regularity conditions:

a) Constant emissivity detector

Consider $s_\gamma = \mu_{s_\gamma}$, which implies that $\underline{\Psi}_{s_\gamma}$ is null. Eq.(22) becomes

$$Q_C(x, \mu_{s_\gamma}) = (x - \mu_w - \mu_{s_\gamma})' \underline{\Psi}_w^{-1} (x - \mu_w - \mu_{s_\gamma}). \quad (23)$$

The resulting test statistic

$$\mathcal{L}_C(x) = (x - \mu_w - \mu_{s_b})' \underline{\Psi}_w^{-1} (x - \mu_w - \mu_{s_b}) - (x - \mu_w - \mu_{s_t})' \underline{\Psi}_w^{-1} (x - \mu_w - \mu_{s_t}) \underset{H_0}{>} \underset{H_1}{<} \tau \quad (24)$$

is identical to the one given in the previous work [15].

For the insight into $\mathcal{L}_C(x)$, repeat the orthogonalization procedure in Section III to decorrelate the random field $x - \mu_w - \mu_{s_\gamma}$, $\gamma = b, t$: introduce a unitary matrix² \underline{V} such that $\underline{V}' \underline{V} = \underline{I}$, $\underline{V}' \underline{\Psi}_w^{-1} \underline{V} = \underline{\Lambda}^{-1}$, and apply a linear operator $\underline{U} = \underline{V} \underline{\Lambda}^{-1/2}$ to transform x , μ_w , μ_{s_γ} to $\tilde{x} = \underline{U}' x = \underline{\Lambda}^{-1/2} \underline{V}' x$, $\mu_w = \underline{\Lambda}^{-1/2} \underline{V}' \mu_w$, $\mu_{s_\gamma} = \underline{\Lambda}^{-1/2} \underline{V}' \mu_{s_\gamma}$, respectively. In the transformed space $Q_C(x, \mu_{s_\gamma})$ is

¹Because of the relation $\{s_{\gamma,i} = \epsilon_{\gamma,i} L_i(T_\gamma)\}$ and condition i), the terms emissivity and signal (radiance energy) are used interchangeably.

²Since signal field is no longer random, only one set of \underline{V} is required.

$$\begin{aligned}
Q_C(\tilde{\mathbf{x}}, \mu_{s_r}) &= (\tilde{\mathbf{x}} - \mu_w - \mu_{s_r})' \underline{\mathbf{V}} \underline{\mathbf{\Lambda}}^{1/2} \underline{\mathbf{\Psi}}_w^{-1} \underline{\mathbf{\Lambda}}^{1/2} \underline{\mathbf{V}}' (\tilde{\mathbf{x}} - \mu_w - \mu_{s_r}) \\
&= (\tilde{\mathbf{x}} - \mu_w - \mu_{s_r})' (\tilde{\mathbf{x}} - \mu_w - \mu_{s_r}) \\
&= \sum_{i=1}^N (\tilde{x}_i - \mu_{w,i} - \mu_{s_r,i})^2.
\end{aligned} \tag{25}$$

The transformation associated with $\underline{\mathbf{U}} \equiv \underline{\mathbf{V}} \underline{\mathbf{\Lambda}}^{-1/2}$ being a linear operation, the mean and the covariance of $\tilde{\mathbf{w}}$ are $E(\tilde{\mathbf{w}}) = E(\underline{\mathbf{\Lambda}}^{-1/2} \underline{\mathbf{V}}' \mathbf{w}) = \underline{\mathbf{\Lambda}}^{-1/2} \underline{\mathbf{V}}' \mu_w$, $\text{cov}(\tilde{\mathbf{w}}) = \text{cov}(\underline{\mathbf{\Lambda}}^{-1/2} \underline{\mathbf{V}}' \mathbf{w}) = \underline{\mathbf{\Lambda}}^{-1/2} \underline{\mathbf{V}}' \text{cov}(\mathbf{w}) \underline{\mathbf{V}} \underline{\mathbf{\Lambda}}^{-1/2} = \underline{\mathbf{I}}$, respectively.

Based on the signal model (5) and the general Gaussian assumptions i)-iv), under hypothesis H_0 , the mean and the covariance of $\tilde{\mathbf{x}} - \mu_w - \mu_{s_r}$ are

$$E(\tilde{\mathbf{x}} - \mu_w - \mu_{s_r} | H_0) = E((\mu_{s_s} + \tilde{\mathbf{w}}) - \mu_w - \mu_{s_r}) = \mu_{s_s} - \mu_{s_r} \tag{26a}$$

$$\text{cov}(\tilde{\mathbf{x}} - \mu_w - \mu_{s_r} | H_0) = \text{cov}((\mu_{s_s} + \tilde{\mathbf{w}}) - \mu_w - \mu_{s_r}) = \text{cov}(\tilde{\mathbf{w}}) = \underline{\mathbf{I}}. \tag{26b}$$

Similarly, under hypothesis H_1 , we have

$$E(\tilde{\mathbf{x}} - \mu_w - \mu_{s_r} | H_1) = \mu_{s_s} - \mu_{s_r} \tag{26c}$$

$$\text{cov}(\tilde{\mathbf{x}} - \mu_w - \mu_{s_r} | H_0) = \underline{\mathbf{I}}. \tag{26d}$$

Eqs.(26b,d) are due to the shift-invariance of covariance.

Evidently, under hypothesis H_j each intermediate statistics (23) is a noncentral chi-square variable with N d.f. (degrees of freedom) and the noncentrality parameter $\delta(\tau_1, \tau_2)$, $\delta^2(\tau_1, \tau_2) = \sum_{i=1}^N (\tau_{1,i} - \tau_{2,i})^2$, i.e.,

$$Q_C(\tilde{\mathbf{x}}, \mu_{s_r} | H_j) = \begin{cases} \chi_{N, \delta(\mu_{s_s}, \mu_{s_r})}^2, & H_j = H_0 \\ \chi_{N, \delta(\mu_{s_s}, \mu_{s_r})}^2, & H_j = H_1. \end{cases} \tag{27}$$

Divide (24) by $Q_C(\tilde{\mathbf{x}}, \mu_{s_r})$ to arrive at the test statistics

$$\mathcal{L}_C(\tilde{\mathbf{x}}) = \frac{Q_C(\tilde{\mathbf{x}}, \mu_{s_s})}{Q_C(\tilde{\mathbf{x}}, \mu_{s_r})} = \frac{\frac{1}{N} \chi_{N, \delta(\mu_{s_s}, \mu_{s_r})}^2}{\frac{1}{N} \chi_N^2} \underset{H_0}{>} \underset{H_1}{<} \tau. \tag{28}$$

Under hypothesis H_0 , the statistics $\mathcal{L}_C(\tilde{\mathbf{x}})$ has the noncentral F -distribution with N and N d.f. and noncentrality parameter $\delta^2(\mu_{s_s}, \mu_{s_r}) = \sum_{i=1}^N (\mu_{s_s,i} - \mu_{s_r,i})^2$. That is, given any significance level α of the test $\mathcal{L}_C(\tilde{\mathbf{x}})$, the threshold τ can be found from [16]

$$\alpha = \text{Prob} \left\{ \frac{\frac{1}{N} \chi_N^2}{\frac{1}{N} \chi_{N, \delta(\mu_s, \mu_b)}^2} > \tau \right\} = 1 - \text{Prob} \left\{ \frac{\frac{1}{N} \chi_{N, \delta(\mu_s, \mu_b)}^2}{\frac{1}{N} \chi_N^2} > \frac{1}{\tau} \right\} = 1 - \text{Prob} \left\{ F'_{N, N; \delta(\mu_s, \mu_b)} > \frac{1}{\tau} \right\}$$

which leads to

$$1 - \alpha = \text{Prob} \left\{ F'_{N, N; \delta(\mu_s, \mu_b)} > \frac{1}{\tau} = F'_{1-\alpha; N, N; \delta(\mu_s, \mu_b)} \right\}. \quad (29)$$

Also, the power of $\mathcal{L}_c(\tilde{x})$ under hypothesis H_1 is

$$\beta = \text{Prob} \left\{ \frac{\frac{1}{N} \chi_{N, \delta(\mu_s, \mu_b)}^2}{\frac{1}{N} \chi_N^2} > \tau = \frac{1}{F'_{\alpha; N, N; \delta(\mu_s, \mu_b)}} \right\}. \quad (30)$$

Therefore, for a specified significance of the test, one can refer to a F' -table to determine the threshold τ , $\tau = F'_{1-\alpha; N, N; \delta(\mu_s, \mu_b)}$, and $F'_{\gamma; N, N; \delta}$ represents the upper γ point of a F' random variable. The power β of the test is then evaluated using (30) (fixed τ). By the coincidence of the statistics $\mathcal{L}_c(\tilde{x})$ with the F' statistics, robustness is assured [16], [17] for small deviation from Gaussian distribution. In particular, based on the robustness of the constant-emissivity detector, we may infer loosely that the new detector will retain a high probability of detection for populations deviating from normal. We remark that in the case wherein components of the random noise field are pairwise statistically independent, then $\underline{\Psi}_x$ is a scaled identity matrix (equal variance over all color bands), and $\mathcal{Q}_c(\tilde{x}, \mu_s), \mathcal{Q}_c(x, \mu_s)$ equals one and the other, implying that the orthogonal transformation is not needed.

b) MAP emissivity detector

In the presence of the random emissivity field, the pdf of x given H_j , required in the implementation of Neyman-Pearson detector (6), is evaluated by the pdf of x given H_j and s_γ and integrated over the distribution of s_γ . This accounts for the multi-dimensional integration and is, generally speaking, formidable to implement in terms of computation time.³ One, however, may circumvent this difficulty by replacing the vector s_γ by a new vector \tilde{s}_γ that is free from the distribution of s_γ . Intuitively, one prefers to settle on an \tilde{s}_γ that maximizes the conditional *a posteriori* pdf $f_{x|H_j, s_\gamma}(x|H_j, s_\gamma)$, i.e., replacing $f_{x|H_j}(x|H_j)$ by $\max_{s_\gamma} f_{x|H_j, s_\gamma}(x|H_j, s_\gamma)$. In the general normal distribution

³The complexity can be appreciated by, trying to use a digital computer, approximating integration over a color band by 10^3 subintervals, then 3 color bands required 10^9 such actions. However, the complexity can be alleviated by *forcing* the independence of emissivity, probably not valid in reality, over the spectral bands.

setting (conditions i)-iv) in Section III), as conveyed in (9),(10), since $f_{X|H_j, s_\gamma}(x|H_j, s_\gamma) = ((2\pi)^N |\underline{\Psi}_w|)^{-1/2} \exp \{ -1/2 Q(x, s_\gamma) \}$, a particular s_γ that maximizes $f_{X|H_j, s_\gamma}(x|H_j, s_\gamma)$ also minimizes $Q(x, s_\gamma)$. Therefore, taking the derivative of $Q(x, s_\gamma)$ defined in (10) with respect to s_γ , using the formulas $(d/dA) A'B = B$ and $(d/dC) C'DC = 2DC$, yields $(d/ds_\gamma) Q(x, s_\gamma) = 2(\underline{\Psi}_w^{-1} + \underline{\Psi}_{s_\gamma}^{-1}) s_\gamma - 2\underline{\Psi}_w^{-1}(x - \mu_w) - 2\underline{\Psi}_{s_\gamma}^{-1} \mu_{s_\gamma}$. Setting it to zero, the maximum *a posteriori* (MAP) emissivity vector is

$$\check{s}_\gamma = s_\gamma = (\underline{\Psi}_w^{-1} + \underline{\Psi}_{s_\gamma}^{-1})^{-1} \{ \underline{\Psi}_w^{-1}(x - \mu_w) + \underline{\Psi}_{s_\gamma}^{-1} \mu_{s_\gamma} \}. \quad (31)$$

Taking the expectation, it is obvious that \check{s}_γ is an unbiased estimate of s_γ . Noting that $(d^2/ds_\gamma^2) Q(x, s_\gamma) = 2(\underline{\Psi}_w^{-1} + \underline{\Psi}_{s_\gamma}^{-1})$ is positive-definite, because both $\underline{\Psi}_w$, $\underline{\Psi}_{s_\gamma}$ are both positive definite, \check{s}_γ is a necessary and sufficient condition for the minimization of the intermediate statistics $Q(x, s_\gamma)$ and, therefore, the maximization of $f_{X|H_j, s_\gamma}(x|H_j, s_\gamma)$. The sufficient statistics for the generalized likelihood

detector [10],[15] $\frac{\max_{s_\gamma} f_{X|H_1, s_\gamma}(x|H_1, s_\gamma)}{\max_{s_\gamma} f_{X|H_0, s_\gamma}(x|H_0, s_\gamma)} = \frac{f_{X|H_1, \check{s}_\gamma}(x|H_1, \check{s}_\gamma)}{f_{X|H_0, \check{s}_\gamma}(x|H_0, \check{s}_\gamma)} \underset{H_0}{\overset{H_1}{> <}} \tau$ can be represented by

$$\mathcal{L}_M(x) = Q_M(x, \check{s}_b) - Q_M(x, \check{s}_t) \underset{H_0}{\overset{H_1}{> <}} \tau \quad (32)$$

where

$$Q_M(x, \check{s}_\gamma) = (x - \mu_w - \check{s}_\gamma)' (cov^{-1}(x - \mu_w - \check{s}_\gamma)) (x - \mu_w - \check{s}_\gamma). \quad (33)$$

Upon using \check{s}_γ evaluated before, the intermediate statistics (33) is

$$\begin{aligned} Q_M(x, \check{s}_\gamma) &= \left[\left(\underline{I} - (\underline{\Psi}_w^{-1} + \underline{\Psi}_{s_\gamma}^{-1})^{-1} \underline{\Psi}_w^{-1} \right) (x - \mu_w) - (\underline{\Psi}_w^{-1} + \underline{\Psi}_{s_\gamma}^{-1})^{-1} \underline{\Psi}_{s_\gamma}^{-1} \mu_{s_\gamma} \right]' cov^{-1}(x - \mu_w - \check{s}_\gamma) \\ &\quad \times \left[\left(\underline{I} - (\underline{\Psi}_w^{-1} + \underline{\Psi}_{s_\gamma}^{-1})^{-1} \underline{\Psi}_w^{-1} \right) (x - \mu_w) - (\underline{\Psi}_w^{-1} + \underline{\Psi}_{s_\gamma}^{-1})^{-1} \underline{\Psi}_{s_\gamma}^{-1} \mu_{s_\gamma} \right] \\ &= \left[x - \mu_w - \frac{(\underline{\Psi}_w^{-1} + \underline{\Psi}_{s_\gamma}^{-1})^{-1} \underline{\Psi}_{s_\gamma}^{-1}}{\underline{I} - (\underline{\Psi}_w^{-1} + \underline{\Psi}_{s_\gamma}^{-1})^{-1} \underline{\Psi}_w^{-1}} \mu_{s_\gamma} \right]' \left(\underline{I} - (\underline{\Psi}_w^{-1} + \underline{\Psi}_{s_\gamma}^{-1})^{-1} \underline{\Psi}_w^{-1} \right) cov^{-1}(x - \mu_w - \check{s}_\gamma) \\ &\quad \times \left(\underline{I} - (\underline{\Psi}_w^{-1} + \underline{\Psi}_{s_\gamma}^{-1})^{-1} \underline{\Psi}_w^{-1} \right) \left[x - \mu_w - \frac{(\underline{\Psi}_w^{-1} + \underline{\Psi}_{s_\gamma}^{-1})^{-1} \underline{\Psi}_{s_\gamma}^{-1}}{\underline{I} - (\underline{\Psi}_w^{-1} + \underline{\Psi}_{s_\gamma}^{-1})^{-1} \underline{\Psi}_w^{-1}} \mu_{s_\gamma} \right]. \end{aligned}$$

Making use of (31), the covariance of $\mathbf{x} - \mu_w - \check{\mathbf{s}}_\gamma$ is $\text{cov}(\mathbf{x} - \mu_w - \check{\mathbf{s}}_\gamma) = \text{cov}\left(\left(\mathbf{I} - (\underline{\Psi}_w^{-1} + \underline{\Psi}_{s_\gamma}^{-1})^{-1} \underline{\Psi}_w^{-1}\right)(\mathbf{x} - \mu_w) - (\underline{\Psi}_w^{-1} + \underline{\Psi}_{s_\gamma}^{-1})^{-1} \underline{\Psi}_{s_\gamma}^{-1} \mu_{s_\gamma}\right) = \left(\mathbf{I} - (\underline{\Psi}_w^{-1} + \underline{\Psi}_{s_\gamma}^{-1})^{-1} \underline{\Psi}_w^{-1}\right) \times \left(\text{cov}(\mathbf{x} - \mu_w)\right) \left(\mathbf{I} - (\underline{\Psi}_w^{-1} + \underline{\Psi}_{s_\gamma}^{-1})^{-1} \underline{\Psi}_w^{-1}\right)'$ and $\text{cov}(\mathbf{x} - \mu_w) = \text{cov}(s_\gamma + w - \mu_w) = \underline{\Psi}_w + \underline{\Psi}_{s_\gamma}$. Therefore, the intermediate statistic

$$\begin{aligned} Q_M(\mathbf{x}, \check{\mathbf{s}}_\gamma) = & \left[\mathbf{x} - \mu_w - \frac{\underline{\Psi}_w^{-1} (\underline{\Psi}_w^{-1} + \underline{\Psi}_{s_\gamma}^{-1})^{-1} \underline{\Psi}_{s_\gamma}^{-1}}{\underline{\Psi}_w^{-1} - \underline{\Psi}_w^{-1} (\underline{\Psi}_w^{-1} + \underline{\Psi}_{s_\gamma}^{-1})^{-1} \underline{\Psi}_w^{-1}} \mu_{s_\gamma} \right]' (\underline{\Psi}_w + \underline{\Psi}_{s_\gamma})^{-1} \\ & \times \left[\mathbf{x} - \mu_w - \frac{\underline{\Psi}_w^{-1} (\underline{\Psi}_w^{-1} + \underline{\Psi}_{s_\gamma}^{-1})^{-1} \underline{\Psi}_{s_\gamma}^{-1}}{\underline{\Psi}_w^{-1} - \underline{\Psi}_w^{-1} (\underline{\Psi}_w^{-1} + \underline{\Psi}_{s_\gamma}^{-1})^{-1} \underline{\Psi}_w^{-1}} \mu_{s_\gamma} \right] \end{aligned} \quad (34)$$

is identical to its counterpart (22). In short, the likelihood ratio detector and the MAP detector are the same under general Gaussian distributions. We remark that in general because the MAP detector does not use *full* information associated with the distribution of the signal field, it is suboptimum as compared to the likelihood ratio detector.

V. RESULTS OF EVALUATION

The detector $\mathcal{L}(\mathbf{x})$ in the form of (21) takes into consideration a random emissivity field, while $\mathcal{L}_c(\mathbf{x})$ in the form of (24) is designed on the assumption of a constant emissivity vector. It is then of interest to compare their performance in terms of power for the same type-I error. For ease of analysis, only a one-dimensional observation vector is assumed. This implies $\underline{\Psi}_w = \sigma_w^2$, $\underline{\Psi}_{s_\gamma} = \sigma_{s_\gamma}^2$, and orthogonal transformation is not needed. The detector $\mathcal{L}(\mathbf{x})$ in (21) is

$$\mathcal{L}(x) = (x - \mu_w - \mu_{s_\gamma})' (\sigma_w^2 + \sigma_{s_\gamma}^2)^{-1} (x - \mu_w - \mu_{s_\gamma}) - (x - \mu_w - \mu_{s_\gamma})' (\sigma_w^2 + \sigma_{s_\gamma}^2)^{-1} (x - \mu_w - \mu_{s_\gamma}) \stackrel{H_1}{>} \stackrel{H_0}{<} \tau.$$

Multiplying both sides by $\sigma_w^2 + \sigma_{s_\gamma}^2$, yields

$$\mathcal{L}(x) = (x - \mu_w - \mu_{s_\gamma})^2 - r^2 (x - \mu_w - \mu_{s_\gamma})^2 \stackrel{H_1}{>} \stackrel{H_0}{<} \tau, \quad (35)$$

where r , defined as $r = \{(\sigma_w^2 + \sigma_{s_\gamma}^2)/(\sigma_w^2 + \sigma_{s_\gamma}^2)\}^{1/2}$, is a measure of the ratio of the noisy background power to the desirable noisy target power. Similarly, the constant emissivity detector (24) is, after

dividing by Ψ_w^{-1} ,

$$\mathcal{L}_C(x) = (x - \mu_w - \mu_{s_i})^2 - (x - \mu_w - \mu_{s_i})^2 \underset{H_0}{>} \underset{H_1}{<} \tau_C. \quad (36)$$

Under hypothesis H_0 , $(x - \mu_w - \mu_{s_i})^2$ is $(\sigma_w^2 + \sigma_{s_i}^2)\chi_1^2$, while $(x - \mu_w - \mu_{s_i})^2$ is $(\sigma_w^2 + \sigma_{s_i}^2)\chi_{1,-\delta}^2$, $\delta = \mu_{s_i} - \mu_{s_i}$. Using the identity $\chi_{n,\delta}^2 = (\zeta + \delta)^2 + \chi_{n-1}^2$, where ζ is independent of χ_{n-1}^2 and is $N(0,1)$ [16], the false alarm encountered by $\mathcal{L}(x)$ and $\mathcal{L}_C(x)$ are

$$\alpha = \text{Prob} \left\{ (\sigma_w^2 + \sigma_{s_i}^2)U^2 - \{ (\sigma_w^2 + \sigma_{s_i}^2)^2 / (\sigma_w^2 + \sigma_{s_i}^2) \} (V - \delta)^2 > \tau \right\} \quad (37a)$$

$$\alpha_C = \text{Prob} \left\{ (\sigma_w^2 + \sigma_{s_i}^2)U^2 - (\sigma_w^2 + \sigma_{s_i}^2)(V - \delta)^2 > \tau_C \right\} \quad (37b)$$

respectively, and $U, V \sim N(0,1)$ and is independent of each other. For comparison, the condition $\alpha = \alpha_C$ is imposed, and can be satisfied through adjustment of the thresholds τ, τ_C .

By the same token, under hypothesis H_1 , $(x - \mu_w - \mu_{s_i})^2$ is $(\sigma_w^2 + \sigma_{s_i}^2)\chi_{1,\delta}^2$, while $(x - \mu_w - \mu_{s_i})^2$ is $(\sigma_w^2 + \sigma_{s_i}^2)\chi_1^2$. The power of detectors $\mathcal{L}(x)$, $\mathcal{L}_C(x)$ are, respectively,

$$\beta = \text{Prob} \left\{ (\sigma_w^2 + \sigma_{s_i}^2)(U + \delta)^2 - (\sigma_w^2 + \sigma_{s_i}^2)V^2 > \tau \right\} \quad (37c)$$

$$\beta_C = \text{Prob} \left\{ (\sigma_w^2 + \sigma_{s_i}^2)(U + \delta)^2 - (\sigma_w^2 + \sigma_{s_i}^2)V^2 > \tau_C \right\}. \quad (37d)$$

The lemma below is convenient for evaluating the α 's and β 's.

Lemma I. Suppose $U, V \sim N(0,1)$ and are statistically independent of each other. Suppose also δ_1, δ_2, ξ are scalar constants and, in particular, ξ is positive definite. Then the rv Y , $Y = \xi_1^2(U + \delta_1)^2 - \xi_2^2(V + \delta_2)^2$, has the pdf

$$f_Y(y) = \int_{\max(0,y)}^{\infty} \frac{1}{8\pi\xi_1\xi_2\sqrt{x(x-y)}} \left\{ \exp \left[-\frac{1}{2} \left(\frac{x^{1/2}}{\xi_1} - \delta_1 \right)^2 \right] + \exp \left[-\frac{1}{2} \left(\frac{x^{1/2}}{\xi_1} + \delta_1 \right)^2 \right] \right\} \\ \times \left\{ \exp \left[-\frac{1}{2} \left(\frac{(x-y)^{1/2}}{\xi_2} - \delta_2 \right)^2 \right] + \exp \left[-\frac{1}{2} \left(\frac{(x-y)^{1/2}}{\xi_2} + \delta_2 \right)^2 \right] \right\} dx.$$

Setting the rv $(\sigma_w^2 + \sigma_{s_i}^2)U^2 - \{ (\sigma_w^2 + \sigma_{s_i}^2)^2 / (\sigma_w^2 + \sigma_{s_i}^2) \} (V - \delta)^2$ equal to Y in Lemma I, the distribution of the former rv is identical to that of the latter with the parameters:

$\delta_1=0$, $\delta_2=-\delta$, $\xi_1=\sigma_w^2 + \sigma_s^2$, $\xi_2=(\sigma_w^2 + \sigma_s^2)^2/(\sigma_w^2 + \sigma_s^2)$. Therefore, given α , the threshold τ is selected by

$$\alpha = \int_{\tau}^{\infty} \int_{\max(0,y)}^{\infty} \frac{1}{4\pi\xi_1\xi_2\sqrt{x(x-y)}} \exp\left[-\frac{x}{2\xi_1^2}\right] \times \left\{ \exp\left[-\frac{1}{2}\left(\frac{(x-y)^{1/2}}{\xi_2} + \delta\right)^2\right] + \exp\left[-\frac{1}{2}\left(\frac{(x-y)^{1/2}}{\xi_2} - \delta\right)^2\right] \right\} dx dy. \quad (38a)$$

Similarly, given α_c , the threshold τ_c is selected from, with $\xi_1=\xi_2=\sigma_w^2 + \sigma_s^2$,

$$\alpha_c = \int_{\tau_c}^{\infty} \int_{\max(0,y)}^{\infty} \frac{1}{4\pi\xi_1\xi_2\sqrt{x(x-y)}} \exp\left[-\frac{x}{2\xi_1^2}\right] \times \left\{ \exp\left[-\frac{1}{2}\left(\frac{(x-y)^{1/2}}{\xi_2} + \delta\right)^2\right] + \exp\left[-\frac{1}{2}\left(\frac{(x-y)^{1/2}}{\xi_2} - \delta\right)^2\right] \right\} dx dy. \quad (38b)$$

The powers resulting from $\mathcal{L}(x)$, $\mathcal{L}_c(x)$ are then found by (τ , τ_c fixed)

$$\beta = \int_{\tau}^{\infty} \int_{\max(0,y)}^{\infty} \frac{1}{4\pi\xi_1\xi_2\sqrt{x(x-y)}} \left[e^{-\frac{x-y}{2\xi_1^2}} \right] \left\{ \exp\left[-\frac{1}{2}\left(\frac{x^{1/2}}{\xi_1} + \delta\right)^2\right] + \exp\left[-\frac{1}{2}\left(\frac{x^{1/2}}{\xi_1} - \delta\right)^2\right] \right\} dx dy \quad (38c)$$

with $\xi_1=\sigma_w^2 + \sigma_s^2$, $\xi_2=\sigma_w^2 + \sigma_s^2$;

$$\beta_c = \int_{\tau_c}^{\infty} \int_{\max(0,y)}^{\infty} \frac{1}{4\pi\xi_1\xi_2\sqrt{x(x-y)}} \left[e^{-\frac{(x-y)}{2\xi_1^2}} \right] \left\{ \exp\left[-\frac{1}{2}\left(\frac{x^{1/2}}{\xi_1} + \delta\right)^2\right] + \exp\left[-\frac{1}{2}\left(\frac{x^{1/2}}{\xi_1} - \delta\right)^2\right] \right\} dx dy \quad (38d)$$

with $\xi_1=\xi_2=\sigma_w^2 + \sigma_s^2$.

Since eqs.(38) cannot be expressed in a closed form, we resort to numerical computation. In particular, we consider the detector operating characteristics when $\mu_s = 0.5$, $\sigma_s^2 = 0.4$, $\mu_w = 0$, $\sigma_w^2 = 0.5$, $\sigma_s^2 = 0.3$, and μ_s varies from 0.05 to 0.30. Results are depicted in Fig.2. The superiority of $\mathcal{L}(x)$ over

$\mathcal{L}_c(x)$, even for a single color-band environment, is self-evident.

VI. CONCLUSIONS

We analyzed a detector on the basis of a model whereupon each signal component consists of the radiant thermal energy contributed by the emissivity and the blackbody radiation reference $L_i(T)$, at a particular bandwidth in the electromagnetic spectrum, of either the target or the background. Since $L_i(T)$ is a non-linear function of the unknown temperature, a low-order power series is employed for its approximation, using the integral square error (ISE) as a fidelity criterion and recognizing that the temperature *range* is usually known. An obvious advantage of this approach is that because the coefficients of the power series remain constant, the approximation of $L_i(T)$ can be easily computed for any varying temperature, provided it is within the temperature range for which the ISE was designed. More importantly, a reasonably good estimate of $L_i(T)$ may be obtained even if there is a mismatch between the actual temperature and its predicted counterpart. A less obvious advantage is that the power series approach permits evaluating statistics (e.g., mean and variance) of the underlying signal when the temperature is also random. However, the ISE method is pessimistic because it assumes that the variable temperature is uniformly distributed throughout the temperature range. If the probability distribution of temperature is known, a more appropriate criterion, i.e., the mean square error, should be applied instead. Note also that no approximation is required if the temperature is known.

A sufficient statistic $\mathcal{L}(x)$ in the form of (21) consisting of two intermediate statistics $Q(x, \mu_{\tau})$, $\tau=b, t$, when the underlying sensor noise and spectral emissivities are normally distributed, is derived. The new class of detectors exploits the spectral energy differences that exist between a desired target signature and the background over the wavelengths that make up the spectral bandwidth. To understand the mechanism of the new detector $\mathcal{L}(x)$ we proceed as follows: suppose H_0 is true, then $E\{Q(x, \mu_{\tau}) | H_0\}$ is zero and $E\{Q(x, \mu_{\tau}) | H_1\}$ is a negative quantity, implying that $E\{\mathcal{L}(x) | H_0\}$ is a negative quantity, with the resulting decision that H_0 is true (which is correct); similarly, if $E\{\mathcal{L}(x) | H_1\} = E\{Q(x, \mu_{\tau}) | H_1\} - E\{Q(x, \mu_{\tau}) | H_1\} = +ve$, again the correct decision that H_1 is true is reached. Therefore, the new detector yields a powerful design for enhancing the target and suppressing the clutter background and whitening the multispectral data prior to thresholding, on a pixel-by-pixel basis.

It is then shown that under more regular condition(s), the new detector represents other classes of detectors, including the constant emissivity detector and the MAP detector. This suggests that the new class of detectors performs at least as well as other classes of detectors and is better than the latter when the more restrictive condition(s) are not encountered in a given application.

The performance of the proposed detector is demonstrated by extensive numerical computations. Although only one pixel target is considered in the research, with slight modification the same detector can be applied for targets filling less than one pixel. On the other hand, if a target occupies more than one pixel, well-developed spatial filtering techniques [18] may provide additional information to allow discrimination between targets and backgrounds if their spatial frequency characteristics are different.

Finally, we remark that since the proposed detector exploits differences in the spectral energy content of target and background radiation, it may be more effective for combating targets in camouflage or using false coloring as compared to detectors based on emissivity alone.

REFERENCES

- [1] J.Y. Chen and I.S. Reed, "A detection algorithm for optical targets in clutter," *IEEE Trans. Aerospace and Electronic Systems*, vol.AES-23, no.9, pp.46-59, Jan. 1987.
- [2] I.S. Reed and X. Yu, "Adaptive multiple-band CFAR detection of an optical pattern with unknown spectral distribution," *IEEE Trans. Acoustics, Speech and Signal Proc.*, vol.38, no.10, Oct. 1990.
- [3] L.B. Stoots, E.M. Winter, L.E. Hoff and I.S. Reed, "Clutter rejection using multi-spectral processing," *SPIE* vol.1305, pp.2-10, April 1990.
- [4] D. Kryskowski and J.R. Maxwell, "Detection and estimation of spectral emissivity in the thermal infrared," *SPIE Small targets and backgrounds: Int. Sym. and Exhibitions on Optical Eng. and Photonics in Aerospace and Remote Sensing*, April 1993.
- [5] L.E. Hoff, J.R. Zeider and C.R. Yerkes, "Adaptive multispectral image processing for the detection of targets in terrain clutter," *SPIE* vol.1698, pp.100-114, 1992.
- [6] L.E. Hoff, J.R. Evans and L.E. Bunney, "Detection of targets in terrain clutter by using multispectral infrared image processing," *SPIE* vol.1481, pp.98-109, 1991.
- [7] W.L. Wolfe, *ed.*, Handbook of military infrared technology, Office of Naval Research, Dept. of the Navy, Washington, D.C., 1965.
- [8] S. Jaggi, D. Quattrochi and R. Baskin, "An algorithm for the estimation of upper and lower bounds of the emissivity and temperature of a target from thermal multispectral airborne remotely sensed data," *SPIE* Vol.1699, pp.420-431, 1992.
- [9] S. Jaggi, D. Quattrochi and R. Baskin, "An algorithm for the estimation of water temperatures from thermal multispectral airborne remotely sensed data," *SPIE* Vol.1700, pp.406-416, 1992.
- [10] H.L. Van Trees, Detection, estimation, and modulation theory, Part I, John Wiley, 1968.
- [11] J. Cheung and L. Kurz, "A class of memoryless robust detectors in dependent processes," *IEEE Trans. Signal Proc.*, vol.42, no.5, pp.1272-1275, May 1994.
- [12] J. Cheung and L. Kurz, "Asymptotically optimum finite memory detectors in ϕ -mixing dependent processes," *IEEE Trans. Signal Proc.*, vol.42, no.9, Sept. 1994.

- [13] S.R. Searle, Matrix algebra for the biological sciences, John Wiley, 1965.
- [14] A. Papoulois, Probability, random variables, and stochastic processes, second edition, McGraw Hill, 1984.
- [15] J.A. Richards, Remote sensing digital image analysis, Springer-Verlag, 1986.
- [16] H. Scheffé, The analysis of variance, John Wiley, 1959.
- [17] G.E.P. Box and S.L. Anderson, "Permutation theory in the deviation of robust criteria and study of departures from assumptions," J. Royal Soc., series B, vol.17, pp.1-34, 1955.
- [18] D. Behar, M. Hafeed Benteftifa and L. Kurz, "Directional line detection in correlated noisy environments," Pattern Recognition, *in review*.

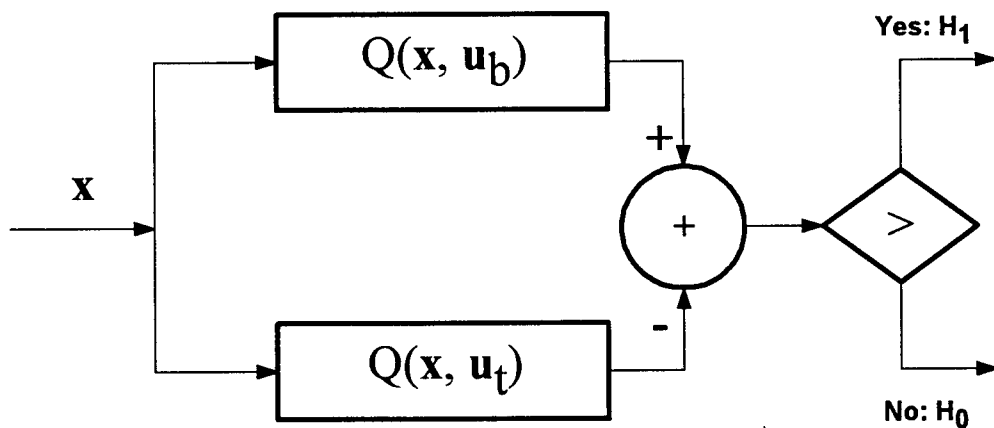


Fig.1 Optimum IR detector

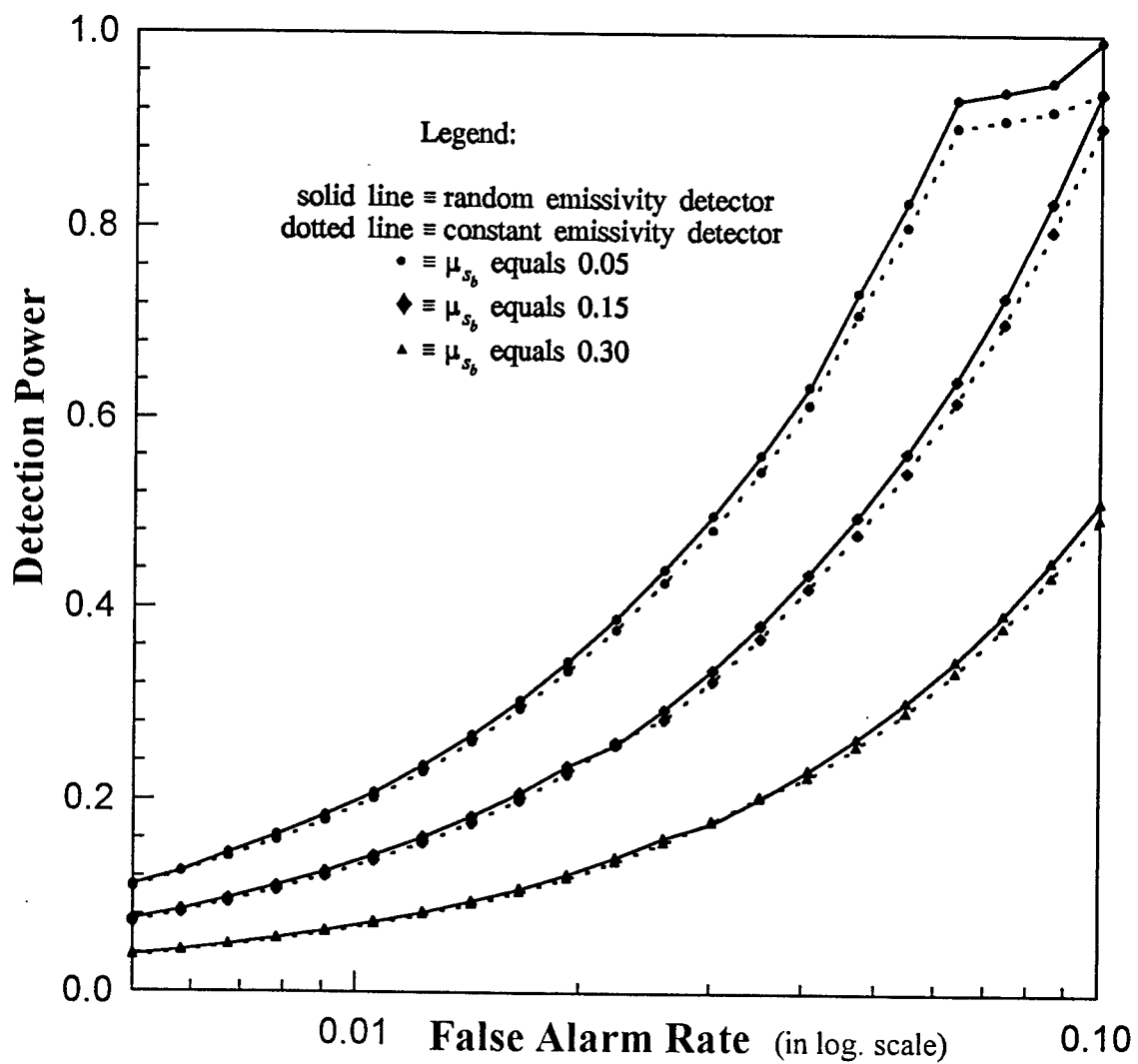


Fig.2 Performance comparison of random emissivity detector versus constant emissivity detector

**DETECTION PERFORMANCE OF OVER RESOLVED TARGETS WITH NON-UNIFORM
ENERGY DISTRIBUTION IN THE RANGE CELLS**

**Ajit K. Choudhury
Associate Professor
Department of Electrical Engineering**

**Howard University
2400 Sixth Street, NW
Washington, DC 20059**

**Final Report for
Summer Faculty Research Program
Armstrong Laboratory**

**Sponsored by
Air Force Office of Scientific Research
Bolling Air Force Base, DC**

and

**Rome Laboratory
Rome, New York**

August 1994

DETECTION PERFORMANCE OF OVER RESOLVED TARGETS WITH NON-UNIFORM ENERGY DISTRIBUTION IN THE RANGE CELLS

Ajit K. Choudhury
Associate Professor
Department of Electrical Engineering
Howard University

Abstract

Many formula involved in computation of radar detection performance, such as incomplete Toronto functions and modified bessel functions, have very bad numerical behaviors. This fact leads to errors of the results. Also, in the calculation of radar detection performance, it is generally assumed that the energy is uniformly distributed over the resolution cells. However, in practice the cells may have different energy. In these cases, modifications are necessary in computing the detection performance.

In this paper, we developed numerical methods to overcome the numerical difficulties and thus obtained much more accurate results. Also, we developed a realistic model of energy distribution, and found that the probability of detection generally tends to increase when the energy is not uniformly distributed. The phenomena are interpreted by the shape of the curves corresponding to uniformly-distributed energy.

DETECTION PERFORMANCE OF OVER RESOLVED TARGETS WITH NON-UNIFORM ENERGY DISTRIBUTION IN THE RANGE CELLS

Ajit K. Choudhury

Introduction

The formula to compute radar detection performance can be found in many literatures, such as [1]-[2]. A serious difficulty existing in radar detection performance calculation is that many formula involved have very bad numerical behaviors, and thus lead to significant errors of the results. Typical numerical error sources are truncation of numbers, subtraction of nearly equal numbers, truncation of series, numerical integration, overflow, underflow, and open-range integration. The overflows and underflows are mainly caused by two involved special functions - incomplete Toronto functions and modified Bessel functions.

The target models we have studied include:

- 1) single pulse, constant amplitude scatterers,
- 2) Single pulse, Rayleigh scatterers,
- 3) single pulse, dominant plus Rayleigh scatterers,
- 4) multi-pulses, constant amplitude scatterers,
- 5) multi-pulses, slow fluctuating targets, Rayleigh scatterers
- 6) multi-pulses, fast fluctuating targets, Rayleigh scatterers,
- 7) multi-pulses, slow fluctuating targets, dominant plus Rayleigh scatterers,
- 8) multi-pulses, fast fluctuating targets, dominant plus Rayleigh scatterers.

The target models with good numerical behaviors includes single-pulse Rayleigh scatterers and single-pulse dominant plus Rayleigh scatterers. The target models with bad numerical behaviors include single-pulse constant amplitude scatterers and multi-pulse constant amplitude scatterers. The target models with some numerical problems especially when the number of pulses is large and false alarm probability approaches zero include multi pulse Rayleigh scatterers (slow fluctuating or fast fluctuating targets) and multi-pulse Rayleigh scatterers (slow fluctuating or fast fluctuation targets).

Another problem associated with detection performance calculation is the energy model. In the existing works, it is generally assumed that the energy is uniformly distributed over the cells. However, in practical applications, the cells may have different energy: i.e., the energy is not uniformly distributed over the cells. In these cases, the actual probability of detection will differ from that with uniformly distributed energy and most of the formula involved in computing the probability must be modified.

A difficulty in studying the effects of energy distribution is caused by too many possible distribution patterns of the energy. To overcome this difficulty, we have developed a simple energy distribution model, pulse numbers and cell numbers. Based on those numerical methods and the new energy distribution model, we have also studied the effects of the energy distribution on detection performance for all the target models mentioned above. Large amount of figures were plotted. However, because of the space limitation, we will only use multi-pulse constant amplitude scatterers as the examples for both numerical problems and the energy model. For more results, please read Ref. [2].

Involved Formula for Uniformly Distributed Energy

The formula involved in computation of radar detection performance can be found in various literatures. The following formula are obtained from Ref. [1]. It is assumed that the energy is uniformly distributed over the resolution cells.

For multi-pulse cases, the relationship between false alarm probability, P_{fa} and threshold, Y_b , is given by

$$P_{fa} = 1 - [I(\frac{Y_b}{\sqrt{N}} N-1)]^M \quad (1)$$

where M is the total number of resolution cells: N is the number of pulses. $I(u, s)$ is the incomplete Gamma function expressed by

$$I(u, s) = \int_0^{u\sqrt{1+s}} \frac{c^{-1} t^s}{s!} dt \quad (2)$$

The probability of detection, P_d , is given by

$$P_d = 1 - (1 - P_{dm})^M \quad (3)$$

where P_{dm} is the probability of a single cell to across the threshold, and has different expressions for different target models. For multi-pulse constant amplitude scatterers:

$$P_{dm} = 1 - T_{\sqrt{E}} [2N-1, N-1, \sqrt{NP} (MN_B)] \quad (4)$$

where N is the number of the pulses, \bar{E} is the total signal energy. N_a is the total noise, and $T_B[m, n, r]$ is the incomplete Toronto function which has the following expression:

$$T_B(m, n, r) = 2r^{n-m+1} e^{-r^2} \int_0^R t^{m-n} e^{-t^2} B_n(2rt) dt \quad (5)$$

and $B_n(z)$ is the n th order modified Bessel function expressed by either

$$B_n(z) = \sum_{k=0}^{\infty} \frac{1}{k! (k+n)!} (z/2)^{n+2k} \quad (6a)$$

or

$$B_n(z) = \frac{(z/2)^n}{\Gamma(n+1/2) \Gamma(1/2)} \int_{-1}^1 (1-t^2)^{n-1/2} e^{zt} dt \quad (6b)$$

where $\Gamma(n)$ is the Gamma function.

The Numerical Difficulties

Most numerical difficulties are caused by the incomplete Toronto function, modified Bessel function and an open-range integral (for multi-pulse slow-fluctuating-target dominant plus Rayleigh scatterers).

The incomplete Toronto function and the Bessel function will generate large amount of overflows and underflows. The open-range integral converges very slowly; therefore, in order to obtain accurate results, we must use a large upper limit of the integral. However, when the limit becomes large, underflows and overflows may occur.

In the incomplete Toronto function (see Eq. (5)) following problems may appear.

1. The factor r^{n-m+1} may underflow when r is large and m is much greater than n .
2. The factor $\exp(-r^2)$ may underflow when r is large.
3. In the case m is much larger than n , the factor t^{m-n} may underflow or overflow when t is small or large respectively.
4. The factor $\exp(-t^2)$ may underflow when t is large.

In the modified Bessel function, if the series form (Eq. (6a)) is used and z is not small, we must sum up many terms in order to obtain accurate results. Then, the factors $(z/2)^{n+2k} \cdot k!$, and $(k+n)!$ may overflow. If the integral form (Eq. (6.b)) is used and n is zero, there are singular points at $t=-1$ and $t=1$. These singular points will seriously degrade the accuracy of the results.

The numerical difficulties of the open-range integral are discussed in Ref. [2]. The other numerical error sources include truncation of series, truncation of numbers, and numerical integration. Some series, such as the modified Bessel function, may decay slowly with the index. Then if the series are truncated too early, the results are not accurate: while if the series are not truncated early, overflows or underflows may occur.

The Numerical Methods

It is relatively easy to reduce the error caused by truncation of numbers and numerical integral. We can reduce the errors caused by truncation of numbers by using double precision variables which are generally sufficient. And we can reduce the errors caused by numerical integration by using the integration intervals finely. Also, if double precision variables are used, we find that the errors caused by subtraction of numbers are not serious.

To improve the behaviors of the modified Bessel function, we use the integral form when n is not zero and use the series form when n is zero. This method can reduce large numbers of overflows and underflows and to avoid the singular problems.

The remaining difficulties are overflows and underflows. To handle these problems, we classify the overflows into the following patterns:

1. $S \cdot t^{-n}$ when t and S are small and n is large. In this case the factor t^{-n} overflows. Generally, when a factor overflows, there should be another factor which is small, otherwise the problem can not be solved. In this pattern we can solve the problem by using an equivalent form of $t^{-n + 1/n} S^{1/n} t$.
2. $S \cdot r^{-n}$ when r and n are large, S is small. In this case, the factor r^{-n} overflows. We can solve the problem by using an equivalent form of $r^{-n + 1/n} S^{1/n} r$.
3. $S \cdot \sum t_i$ when some of t_i overflows and S is small. In this case, we can solve the

problem by using an equivalent form of $\sum (S \cdot t_i)$.

Similarly, we can classify underflows into the following patterns:

1. $B \cdot \exp(-t)$ when B and t are large. In this case, the factor $\exp(-t)$ underflows. Generally computer will assign zero to the under-flowed variables. This method will not introduce errors if no factor is large. Therefore, we only need to take care the cases with a large factor, B . In this pattern, we can solve the problem by using an equivalent form of $\exp(-1 + 1/nB)$. If the original form is used, the value of the expression is zero, but the equivalent form may give non-zero values.
2. $B \cdot t^{-n}$ when t is small, B and n are large. In this case, the factor t^{-n} underflows. We can solve the problem by using an equivalent form of $t^{-n + 1/n} B^{1/n} t$.
3. $B \cdot r^{-n}$ when r , n , and B are all large. In this case, the factor r^{-n} underflows, and we can solve the problem by using an equivalent form of $r^{-n + 1/n} B^{1/n} r$.
4. $B \cdot \sum t_i$ when some of t_i underflows and the sum is small. We can solve the problem by using an equivalent form of $\sum (B \cdot t_i)$. If the sum is not small, the

under-flowed term can be neglected without introducing errors.

By using these method, we can significantly improve the accuracy of the results. The methods can eliminate all the overflows. Although some underflows still exist, they will not introduce errors; e.g., all the factors are small, or a term in a series is neglectable compared with other terms in the series.

The Results for Uniformly-Distributed Energy

By using the numerical methods developed above, we plotted large amount of figures for various target models and pulse numbers. The figures shows the probability of detection vs. the signal to noise ratio for different cell numbers. We compared those figures with those in the literature, and found that our results are much more accurate than those in the literature.

Figures 1 shows our result of the detection probability for 16-pulse constant amplitude scatterers when false alarm probability is 1.1 S 1 or other cases and the comparison of the results, please read Ref. [2].

Formulation of Non-Uniformly Distributed Energy

To develop the energy distribution model, we assume that the total number of resolution cells M , is given and the energy of the cells is fallen into a preset number of energy levels. The energy of the second level is twice the energy of the 1st level, the energy of the 3rd level is three times the energy of the 1st level, and so on.

Generally, the energy of more cells is in the middle levels, and energy of only a few cells is in the upper levels and lower levels. Therefore, we assume that the number of the cells with specific energy is normally distributed over energy levels. The number of cells at energy level E_j is given by

$$M_j = S \exp \left(-\frac{(E_j - \bar{E})^2}{2\sigma^2} \right) \quad (j = 1, 2, \dots, N_p) \quad (7)$$

where N_p is the total number of energy levels. Since M_j is generally not an integer at an energy level, it has to rounded. In Eq. (7), \bar{E} and δ are free parameters to control the shape of the

distribution, and S is so selected that the total number of cells equals to the given number M. Figure 2 shows an example with 8 energy levels.

We should note the difference between energy distribution over cells and the distribution of the number of cells over the energy levels. When it is small, the number of cells is distributed nearby \bar{E} ; i.e., the number of cells is unevenly distributed over the energy levels. In this case, all the cells have almost the same energy, \bar{E} ; i.e., the energy is almost uniformly distributed over the cells.

When the energy is not uniformly distributed over the cells, most of the formula given in the literatures must be modified. The probability of detection is given by

$$P_d = 1 - \prod_{i=1}^{N_f} (1 - P_{dm_i})^{M_i} \quad (8)$$

where M_i is the number of cells at the i th energy level. Corresponding to different target models, the formula to compute P_{dm_i} are given in Ref. (2). For Multi-Pulses. Constant Amplitude Scatterers

$$P_{dm_i} = 1 - T_{\sqrt{Y_b}} [2N-1, N-1 \sqrt{NE_i M_i N_0}] \quad (9)$$

where N is the number of the pulses.

The threshold, Y_b is still related to false alarm probability. P_{fa} by Eq. (1). The total signal energy in a given energy level, \bar{E}_i is related to the total signal energy. \bar{E} by

$$\bar{E} = \sum_{i=1}^{N_f} E_i = \sum_{i=1}^{N_f} i M_i E_b \quad (10)$$

where M_i is the number of cells in the i th energy level. E_b is the base energy. Then

$$\bar{E}_i = i M_i E_b = i M_i \bar{E} / \sum_{i=1}^{N_f} j M_j \quad (11)$$

Results for Non-Uniformly Distributed Energy

Corresponding to different target models, different number of cells, different pulse numbers, and different energy levels, we have plotted numbers of figures in Ref. (2) which show the probability of detection vs the ratio of total energy to noise. Only a few of them will be shown in this paper.

Table 1 shows the distribution of the cells over energy levels for different values of σ when total number of cells is 10 and total number of energy level is 8 and $1 = 5$. We can see that when σ is small, the cells are distributed over a few energy levels nearby 1, i.e. the cells have nearly equal energy. This situation is similar as uniformly-distributed energy over the cells. When $\sigma = 0.1$ all the cells are in the energy level E; i.e. the energy is uniformly distributed over the cells.

Table 1. Distribution of the 10 Cells over 8 Energy Levels for Different Values of σ when $E = 5$

Energy Level σ	1	2	3	4	5	6	7	8
0.1	0	0	0	0	10	0	0	0
0.5	0	0	0	1	8	1	0	0
1.0	0	0	1	2	4	2	1	0
2.0	0	1	1	2	2	2	1	1
3.0	1	1	1	1	3	1	1	1

Figure 3 shows the comparison of detection performance between uniformly distributed energy and non-uniformly distributed energy for 4-pulse constant amplitude scatterers when $M=2$ and a false alarm probability of $1.E-8$. When energy is uniformly distributed over the cells, both cells have the same energy; when energy is non-uniformly distributed over the cells, the energy of one of the cells is twice that of the other.

Figure 4 shows the comparison of detection performance between different values of σ for 4-pulse constant amplitude scatterers when $N_s = 8$, $M=10$, $F=5$ and a false alarm probability of $1.E-8$.

In the figures, the horizontal axis denotes the ratio of total signal energy to total noise energy (E/N_0) in decible. the vertical axis denotes the probability of detection in percentage. Y_b is the threshold, M is the total number of cells. "I evel" is the total number of energy levels, "Mean" denotes E .

According to our study for different target models, number of pulses, energy levels, number of cells, average energy, σ values, and false alarm probabilities, we found the following common phenomenon for every target models:

When the false alarm probability is large (e.g. 0.01), the probability of detection is not significantly affected by energy distribution. When the false alarm probability become smaller, the effects of energy distribution become more significant.

In addition to this common phenomenon for every target mode, we have also found that the effects of energy distribution are also highly affected by target models. We found that multi-pulse constant amplitude scatterers are most seriously affected by energy distribution; single pulse constant amplitude scatterers are the second: then it comes in the order of multi-pulse fast-fluctuating-target dominant plus Rayleigh scatterers, multi pulse fast-fluctuating-target Rayleigh scatterers, multi-pulse slow-fluctuating-target dominant plus Rayleigh scatterers, multi-pulse slow-fluctuating-target Rayleigh scatterers, single pulse dominant plus Rayleigh scatterers, and finally single-pulse Rayleigh scatterers for constant amplitude scatterers (single-pulse or multi-pulse), the effects of the energy distribution are similar no matter the probability of detection is low or high. However, for other target models (Rayleigh scatterers and dominant plus Rayleigh scatterers), the effects of energy distribution is significant in some of the probability range and less significant in the other ranges. Generally, non-uniformly distributed energy will increase the probability of detection and the effects are more significant in low probability ranges. The reason is that the threshold is hard to across in that range and the non-uniformly distributed energy increases the chance to across the threshold significantly for the cells with higher energy.

To interpret the effects of the energy distribution, lets define the "cell probability of detection" as P_{dm_i} when the energy is uniformly distributed. Then the effects of the energy

distribution can be explained by the shape of the cell probability of detection. First, it is helpful to consider the problem with only two cells. The probability of detection of the first cell is p_1 , and the probability of detection of the second cell is p_2 . When the energy is uniformly distributed, $p_1=p_2=p$ (cell probability of detection). The total probability of detection is given by

$$P = 1 - (1-p_1)(1-p_2) = 2p - p^2 \quad (12)$$

Now, let's assume the energy is not uniformly distributed and the first cell has lower energy and the second cell has higher energy. Then p_1 becomes $(p-\delta p_1)$, and p_2 becomes $(p+\delta p_2)$. The total probability of detection becomes

$$P + \delta P = 1 - (1-p_1)(1-p_2) = P + (1-p)(\delta p_2 - \delta p_1) \quad (13)$$

therefore

$$\delta P = (1-p)(\delta p_2 - \delta p_1) \quad (14)$$

We can see the trends of δP from the plot of the p vs. signal to noise ratio in linear scales. When the curve is concave-up, $\delta p_2 > \delta p_1$ and the non-uniformly distributed energy will increase the probability of detection. When the curve is concave-down, $\delta p_1 > \delta p_2$, and the non-uniformly distributed energy will decrease the probability of detection. The increment of decrement will clearly depend on how large is the curvature of the curve of p , how the energy is distributed and how large p is.

As an example, figure 5 plots the cell probability of detection with different values of Y_b of 6.903 (large false alarm) and 20.72 (small false alarm) for single-pulse Rayleigh scatterers when $M=10$. The figure shows that below 23 db of signal to noise ratio the curve is relatively straight when $Y_b=6.903$; therefore, the probability of detection is not much affected by the energy distribution (see Ref. [2]). For $y_b=20.72$, figure 5 shows that the curvature of the curve is relatively large in certain ranges of signal to noise ratio. The curve changes from concave-up to concave-down at about 24 db. Therefore, the probability of detection is more significantly affected by energy distribution in low probability range and is not much affected by energy

distribution nearby 24 db. And when the signal to noise ratio is below 24 db non-uniformly distributed energy increases probability of detection and when the ratio is above 24 db, non-uniformly distributed energy decreases probability of detection (see Ref. [2]).

Conclusion

The formula involved in calculation of the radar detection performance have had numerical behaviors, and thus lead to errors of the results. Our numerical methods developed can overcome those difficulties, and give much more accurate results. Incomplete Toronto function, modified Bassel function and open-range integration are main sources of numerical problems.

For non-uniformly-distributed energy, we have found a common phenomena for every target model: the effect of energy distribution will become more significant when the false alarm probability approaches zero. However, the effect of energy distribution will also largely depend on the target models. Constant amplitude scatterers are more seriously affected by energy distribution, dominant plus Rayleigh scatterers are the next, and Rayleigh scatterers are least affected by energy distributions. Multi-pulse cases are more seriously affected by energy distribution than single-pulse cases. And fast fluctuating targets are more seriously affected by energy distribution than slow fluctuating targets.

The effect of energy distribution can be interpreted by a plot of so-called "cell probability of detection" vs. signal to noise ratio in linear scales. When the curve is concave-up, then non-uniformly distributed energy will increase the probability of detection. When the curve is concave-down, the non-uniformly distributed energy will decrease the probability of detection. The increment and decrement will depend on the curvature of the curve, the energy distribution and the cell probability of detection at the given energy to noise ratio. In most cases, non-uniformly distributed energy will increase the probability of detection.

References

- 1 Vincent C. Vannicola and Kenneth G. Hillman. "Detection Performance for Over Resolved Targets," ROME AIR DEVELOPMENT CENTER, RADC-TR-84-61, In-House Report, Sep. 1984.
2. Choudhury, A.K., and Ruan, M., "Radar Signal Processing for Over Resolved Targets," Final Report, Air Force contract #1 33615-90-C-1443, Nov. 1991.

3. Swerling, P., "Probability of Detection for Fluctuating Targets," IRE Trans. on Info. Theory, Vol. IT-6, No. 2, pp. 269-308. 1960.
4. Marcum, J.I., "A Statistical Theory of Target Detection by Pulsed Radar," IRE Trans. Info. Theory, Vol. IT-6, No. 2, pp.59-144, 1960.
5. DiFranco, J.V., and Rubin, W.I. *Radar Detection*. Prentice-Hall, Englewood Cliffs, New Jersey, 1968.
6. Nitzberg, R., "Effect of a Few Dominant Specular Reflectors Target Model upon Target Detection," IEEE Trans. Aerosp. and Electron. Sys., Nov. AFS-14, No. 4, pp. 670-673, 1978.
7. Hughes II, P.K., "A High-Resolution Radar Detection Strategy," IEEE Trans. Aerosp. and Electron. Sys., Vol. AES-19, No. 5, pp. 663-667, 1983.
8. Skolnik, M.I., *Introduction to Radar Systems*, McGraw-Hill, 1980.
9. Swerling, P., "Recent Developments in Target Models for Radar Detection Analysis," Presented at AGARD Avionics Technical Symposium on Advanced Radar Systems, May 1970.
10. Woodward, P.M., *Probability and Information Theory with Applications to Radar*, McGraw-Hill, New York, 1953.

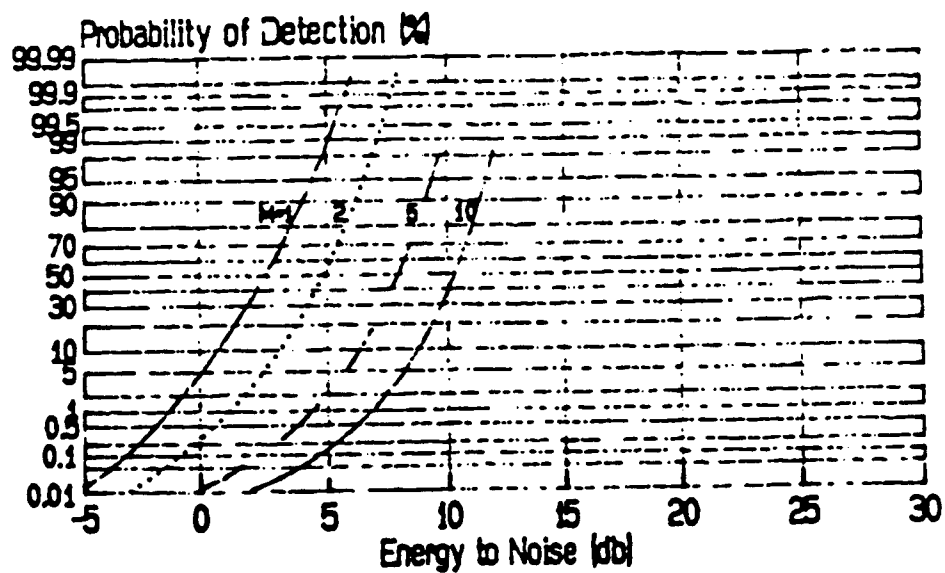


Figure 1. detection probability for uniformly-distributed energy. 16-pulse constant amplitude scatterers when false alarm probability is $1.E-8$.

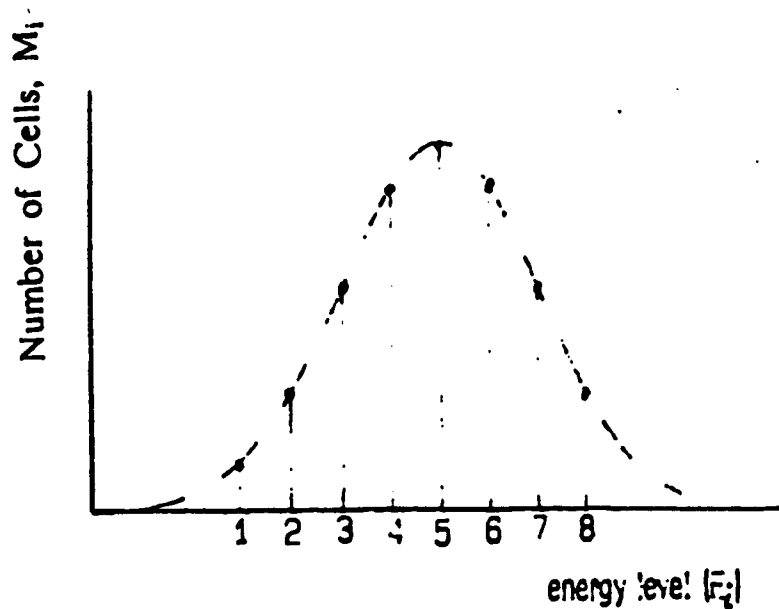


Figure 2. An Example of Energy Distribution over 8 Energy Levels.

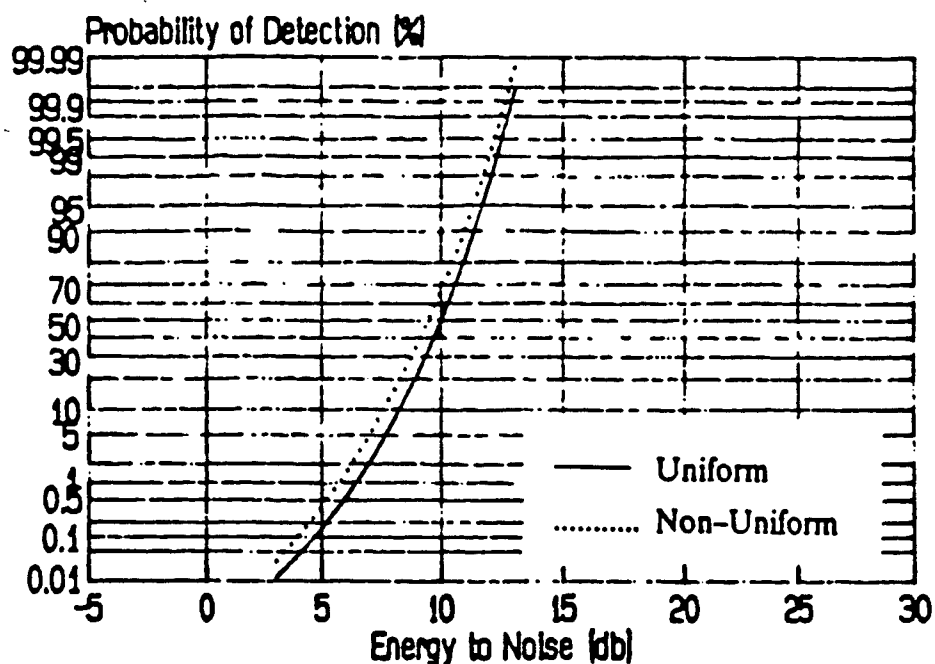


Figure 3. Comparison of Detection Performance between Uniformly Distributed Energy and Non-Uniformly Distributed Energy for 4-Pulse Constant Amplitude Scatterers when $M=2$ and False Alarm Probability = $1.E-8$.

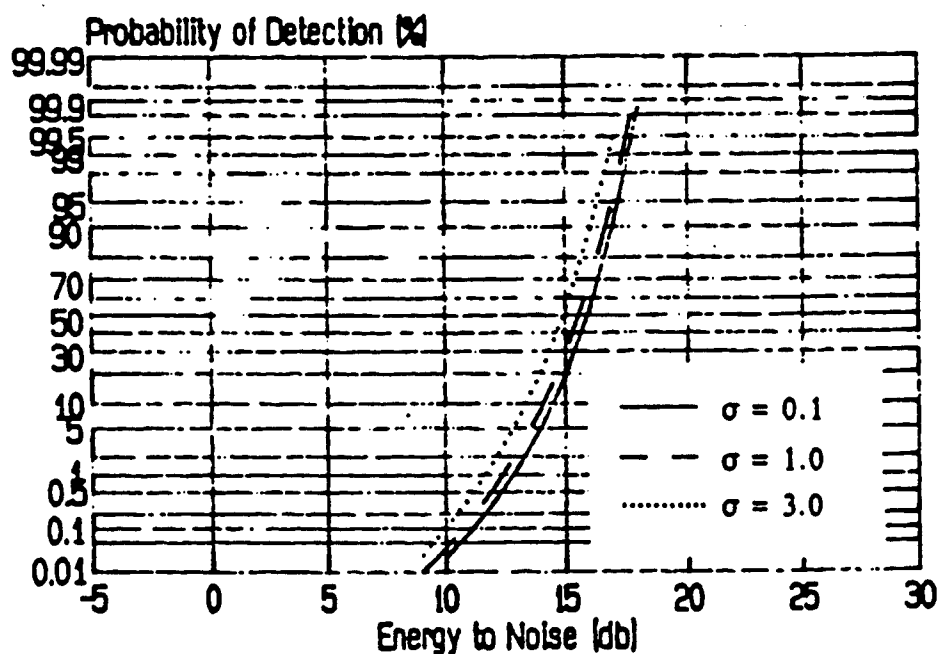


Figure 4. Comparison of Detection Performance between Different Values of σ for 4-Pulse Constant Amplitude Scatterers when $N_t=8$, $M=10$, $\bar{E}=5$ and False Alarm Probability = $1.E-8$.

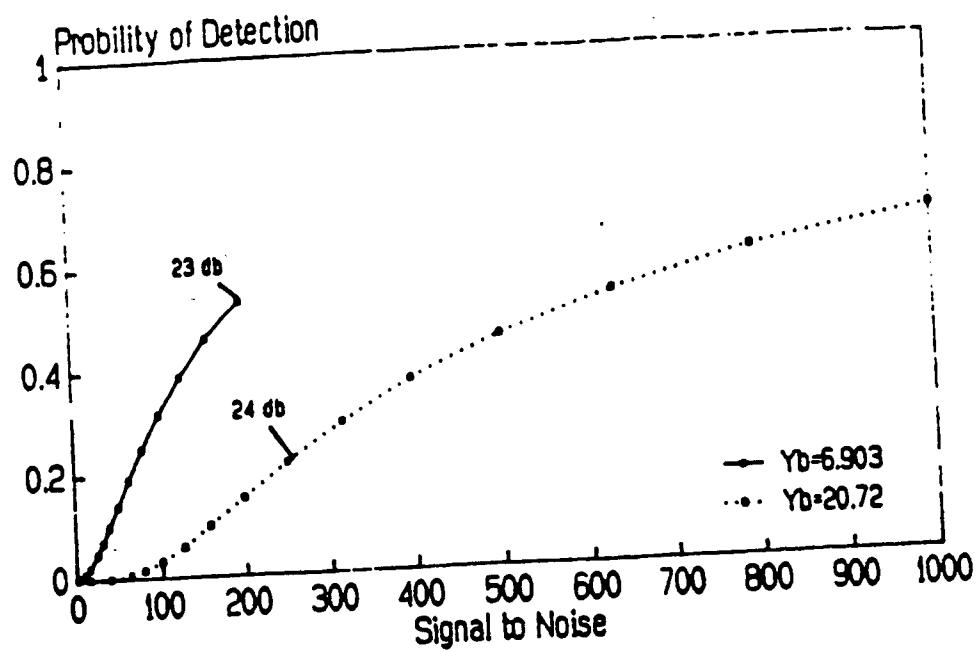


Figure 5. Cell Probability of Detection for Single-Pulse Rayleigh Scatterers when $M = 10$.

EXPERIMENTAL MEASUREMENT OF NONLINEAR EFFECTS IN FIBERS
BASED ON DEGENERATE TWO-WAVE INTERACTIONS.

Eric Donkor
Assistant Professor
Department of Electrical Engineering
University of Connecticut
Glenbrook Road
Storrs, CT. 06269-3157

Final Report For:
Summer Faculty Research Program
Rome Laboratory

Sponsored by:
Air Force Office Of Scientific Research
Bolling Air Force Base, DC

and Rome Laboratory

September 1994

**EXPERIMENTAL MEASUREMENT OF NONLINEAR EFFECTS IN FIBERS
BASED ON DEGENERATE TWO-WAVE INTERACTIONS.**

Eric Donkor
Assistant Professor
Department of Electrical Engineering
University of Connecticut
Glenbrook Road
Storrs, CT. 06269-3157

Abstract

We describe an experimental procedure to characterize optical nonlinearity and dynamic effects in fibers. The method is based on degenerate two wave mixing. In this method intensity dependent optical nonlinearity, such as the nonlinear refractive index, is induced by a high intensity laser beam in the fiber. The nonlinear effect is measured by probing with a weak probe signal time synchronized and having the same frequency as the pump. Effects such as pulse broadening and wavelength shift are also measured.

EXPERIMENTAL MEASUREMENT OF NONLINEAR EFFECTS IN FIBERS BASED ON DEGENERATE TWO-WAVE INTERACTIONS.

Eric Donkor

I. Introduction

Optical fiber and fiber-based devices are becoming increasingly important in applications including amplification, sensing, modulation and switching. Such applications are derived from a variety of nonlinear optical phenomena existing in fibers. In order to produce nonlinear fiber devices it is necessary to measure and characterize the nonlinear properties, and nonlinear effects in materials due to intensity induced or picosecond interactions. The material properties of interest have very small values. Also several dynamic effects including pulse broadening, wavelength shift, scattering e.t.c. can occur concurrently and are therefore not easily isolated for measurement.

Laser induced optical nonlinearity such as the optical Kerr effect and its related dynamics has been characterized extensively. Because, it is the basic mechanism underlying the operation of most all-optical devices. In principle an intense pump signal propagating in a Kerr medium, induces a third order polarization. Measurement of the induced nonlinearity can be obtained by probing with a weak signal. Optical probing methods for characterizing the nonlinear refractive index and related dynamic effects include the optical phase conjugate technique, modulation spectroscopy, hole burning spectroscopy, time resolved methods, photon-echo and magneto-optical techniques. Interferometric probing methods such as the time resolved technique measure the relative phase

change between probe and pump traversing different optical paths. Inherent fluctuations and instabilities in the different paths cause uncertainties in measurements.

The optical phase conjugate method, through degenerate four wave mixing, is another probing technique. It utilizes a single source and path for the probe and pump signals and is therefore less susceptible to external influence. However, special wave vector matching conditions must be satisfied. The difficulty of experimentally satisfying the wave-vector matching conditions makes this technique less flexible as a diagnostic method for analyzing optical nonlinearity and its dynamic effects in materials and devices.

We describe an experimental method for measuring the nonlinear refractive index and characterizing related dynamic effect in fibers. The methodology is based on degenerate two wave interactions. A theoretical model for the technique is described in Section II. The experimental method is discussed in section III.

II. Theoretical Model.

Consider two orthogonal polarized, pump and probe, signals copropagating in a Kerr medium. Let the peak pump power be P_p and the probe be P_s , the probe signal intensity being small compared with the pump. The intense pump signal induces a nonlinear refractive index change which can give rise to a shift in the wavelength of the probe signal¹

$$d\lambda_s = \frac{2n_2\lambda_s^2}{c\lambda_p A_{eff}} P_p \frac{L_w}{T_o} \cdot \left(e^{-\tau_d^2} - e^{-(\delta - \tau_d)^2} \right) \quad 1$$

¹ P. L. Baldeck, R. R. Alfano, G. P. Agrawal, "Induced-Frequency Shift of Copropagating Ultrafast Optical Pulses", Appl. Phys. Lett. 52 (23), pages 1939 - 1941, June 1988.

In the above equation n_2 is the nonlinear refractive index, c is the velocity of light in free space, A_{eff} is the effective cross-sectional area of the fiber core, λ_p and λ_s are the pump and probe wavelengths respectively. The bandwidth of the pump is T_O , and the parameter $\delta = L/L_W$ where L and L_W are the fiber length and the walk-off respectively. The delay between the pump and probe pulses is τ_d . Equation 1 suggests an indirect method for measuring fiber nonlinearity, that is through a measurement of the wavelength shift associated with the cross-phase modulation between probe and pump. If a single frequency source is used for the pump and probe the nonlinear refractive index simplifies to :

$$n_2 = \frac{d\lambda}{\lambda} \frac{cA_{eff}}{P_p} \frac{T_o}{L} \quad 2.$$

A temporal evolution of the nonlinear refractive index can be determined if there is a time delay between the pump and probe at the input of the fiber device.

III. Experimental Methods

The experimental setup for measuring the laser induced nonlinear effects in fibers is shown in fig. 1. A lightwave Electronics model 130 pulsed laser was used as the main laser source for our experiments. The laser outputs about 70mW with pulse repetition rate of 250 MHz and a pulse width of 10 pS. An INRAD MN5-14B autocorrelator was used to monitor the pulses for mode-locking. The output of the autocorrelator was connected to a Tetronix 2246 scope for display of the pulses.

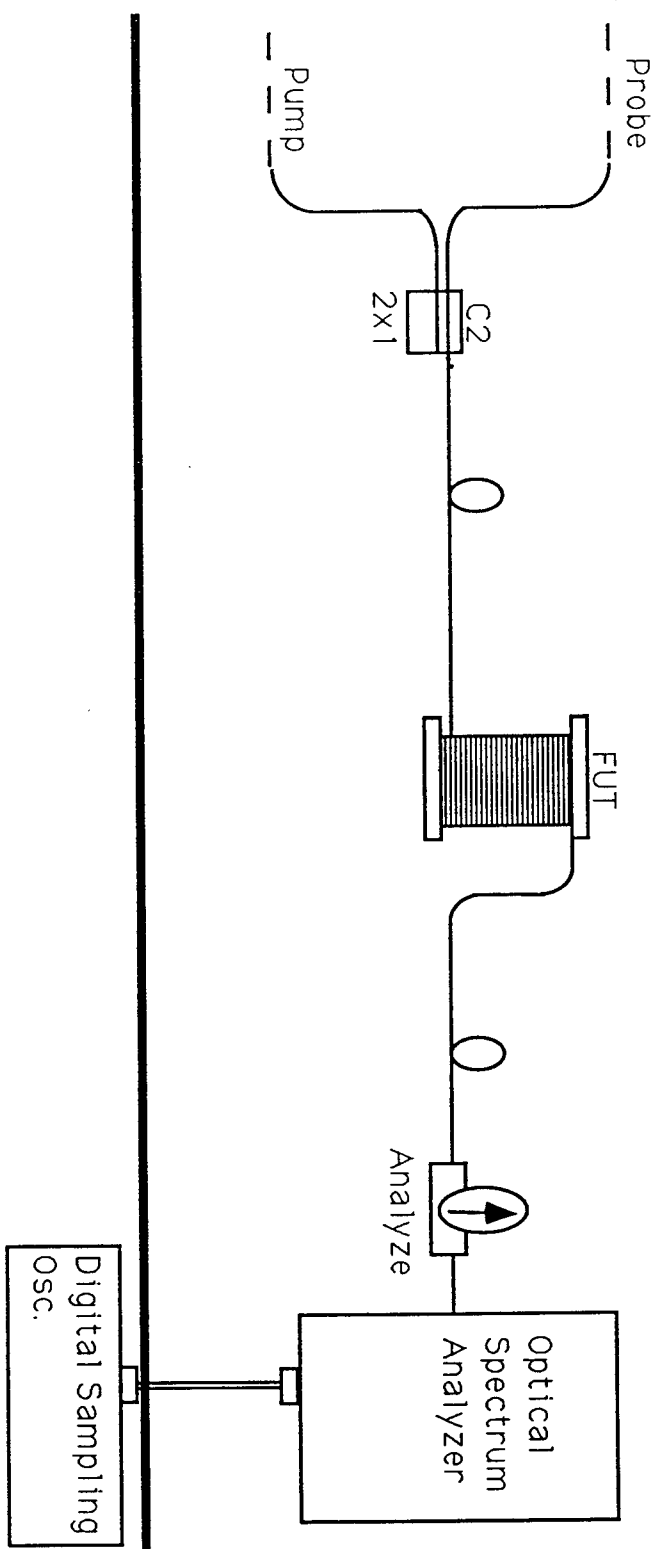


Fig. 2 Degenerate Two-Wave Measurement Continued

The subcircuit for tracking the pulses for mode-locking comprise the autocorrelator, the two infra-red coated mirrors M1 and M2, and the scope. M1 is fixed but M2 can be translated to reflected the laser beam to M1. M1 is positioned to reflected the beam a second time to enter into the autocorrelator. To observe or adjust the laser for mode-locking, set the time constant on the autocorrelator between 2 and 3. Move M2 and or adjust the tilt controls on M1 and M2 for a signal to register on the scope. Tune the laser cavity to obtain mode-locked pulses. The laser controller allows for tuning the cavity. A monitor connected to the laser controller displays the settings of the various laser parameters during tuning. The laser cavity is calibrated in picoseconds and can be tuned from 1200ps to 1700 ps. Mode-locking of the laser pulses occurred between 1320ps to 1370 ps. Once mode-locking is achieved M2 is removed to allow the laser source into the rest of the circuit.

A Gould 5:95 2x2 coupler was used to split the source into pump (95%) and probe (5%) signals. The fiber coupler, couples the source into the splitter C1. Approximately 20 mW of the source signal was coupled into the fiber. The probe was connected to a Laser Precision Corporation DB 2900 single mode variable attenuator. The output of the attenuator was connected to a polarization controller, PC1. The pump was connected to an electro-optic modulator through the polarization controller, PC2. The output of the modulator was also connected to a polarization controller, PC3. The 2x1 coupler, C2, was used to combine the probe and pump signals. A JDS FITEK SN 837 analyzer was used at the output for differentiating between the probe and pump. The fiber under test (FUT) was placed between the output of C2 and the analyzer. The fixed analyzer method

requires that the probe and pump signals be orthogonally polarized at both input and output ports of the FUT. This condition is verified in Experiment 1.

Experiment 1.

The variable attenuator was set to attenuate the probe signal, the modulator was then biased for maximum pump power. The controllers PC2 and PC3 were adjusted for minimum pump power reading on the meter, a record of the analyzer angle was taken. Without adjusting the polarizer the analyzer was rotated till the power meter registers a maximum again. The rotation of the analyzer for maximum pump power was approximately 90 degrees. The probe signal was then let through with the pump still off. The analyzer was rotated to the previous angle, and the probe power was recorded.

Results For Experiment 1.

Table 1: Orthogonal Polarization of Pump and Probe.

Analyzer Ang.	Probe Att.	Probe Power	Pump Power	Pump Volt.
270°	38 dB	2.0 μ W	0.5 μ W	2.9 V
180°	38 dB	2.0 μ W	4.4 mW	2.9 V
180°	38 dB	2.0 μ W	6.0 μ W	7.0 V
180°	38 dB	2.0 μ W	80.0 μ W	7.0 V
270°	3 dB	468.0 μ W	80.0 μ W	7.0 V

The extinction ratio of the pump and probe calculated from the above table were 39 dB for the pump and 23 dB for the probe. This results shows the two signals to be orthogonally polarized.

Experiment 2

In this experiment we studied the dynamic effects of copropagating pump and probe in a 2 kilometer Fiber. The FUT was connected between the 2x1 coupler, C2, and the input to the analyzer. The output of the analyzer was connected to an optical spectrum analyzer (Anritsu MS 90). The probe and pump signal were adjusted to be orthogonally polarized at the input of the fiber. The modulator bias voltage and the attenuator were adjusted to allow for the transmission of maximum pump and probe signals through the FUT. The spectra of the output signal was measured by the spectrum analyzer. The spectra of the probe only and the pump only signals were also measured.

Results For Experiment 2

The measured spectra are shown in fig 3a-3d. Fig. 3a represent the spectra of the probe, fig.3b is for the pump and two spectra of the modulated probe are shown in fig. 3c and fig. 3d. The peak of the probe-only and the pump-only signals are obtained from fig. 3a and 3b, and both occurred at a wavelength of $1.32170\mu\text{m}$, and the peak of the modulated probe signal occurred at $1.32166\mu\text{m}$. However the change was on the same order as the resolution of the scope and therefore regarded as insignificant. The available pump power was found to be rather small to induce any significant wavelength shift of the modulated probe signal.

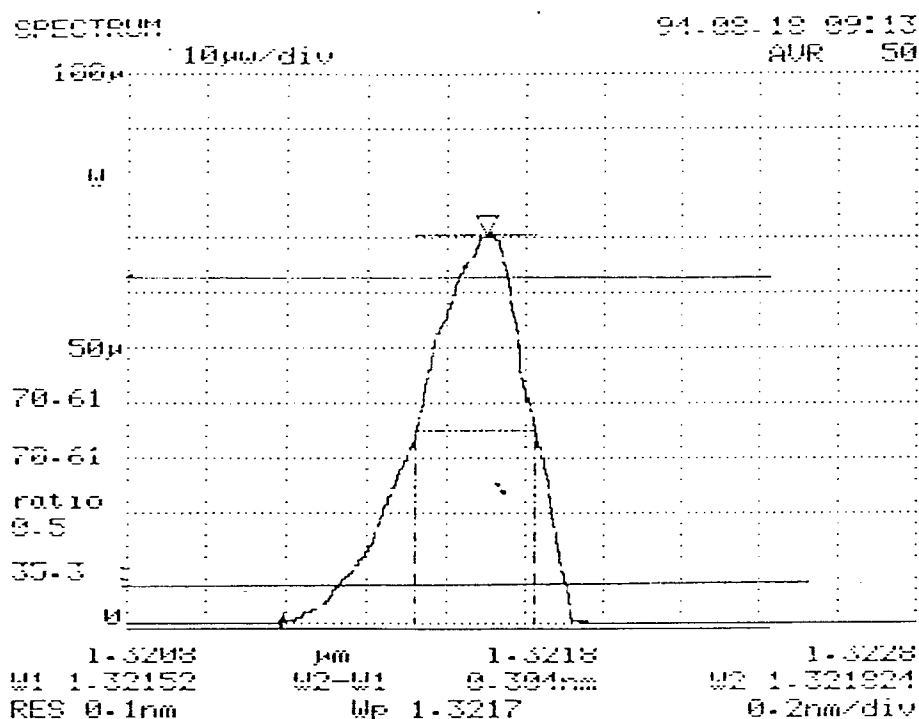


Fig. 3a Spectra of Probe-Only Signal

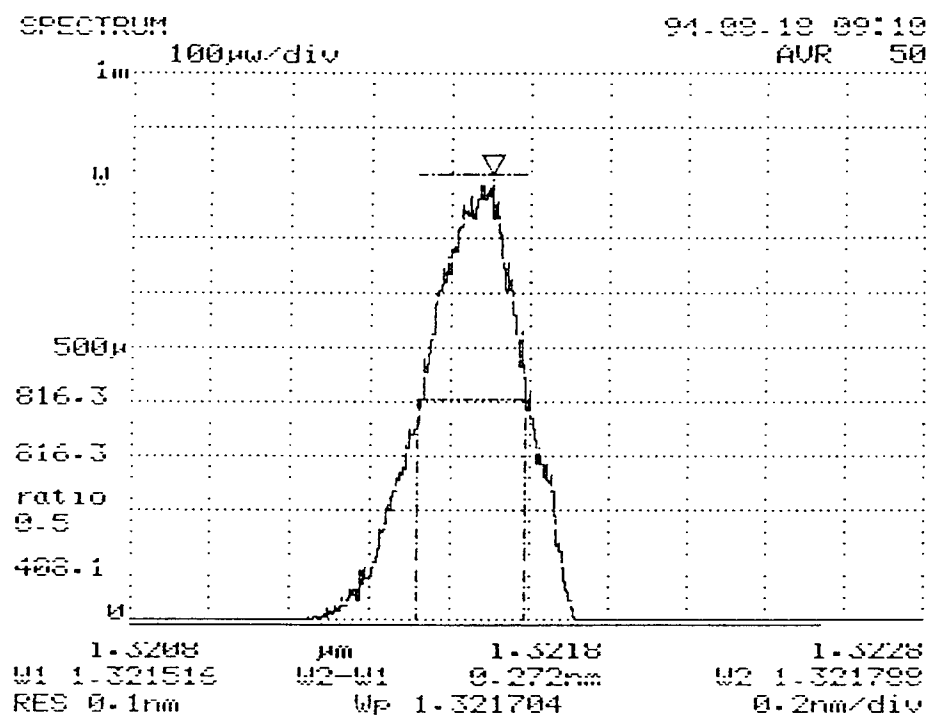


Fig. 3b Spectra of Pump-Only Signal

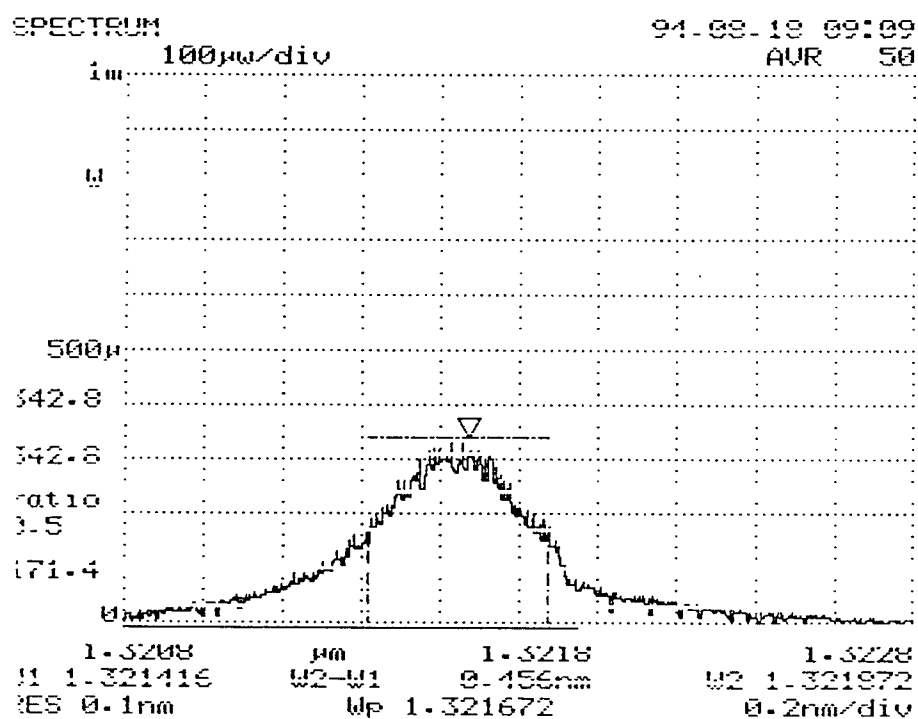
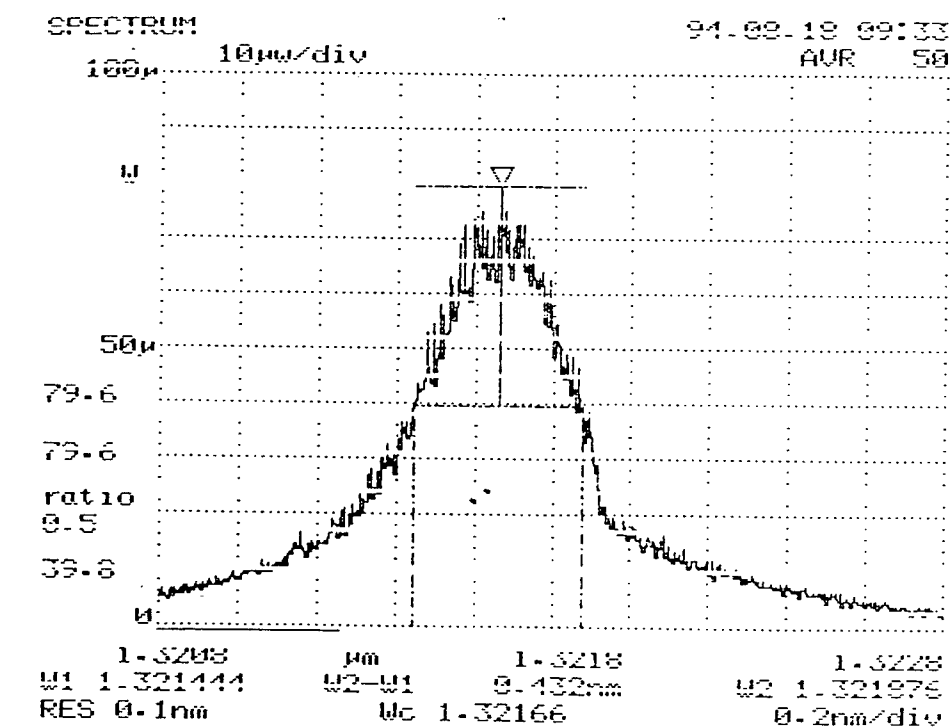


Fig 3c (Top) and 3d (Bottom). Spectra of Modulated Probe.

The probe-only and pump-only spectra are similar. In that they both depict similar rise and fall times. The bandwidth of the probe-only and the pump-only signals are 0.304 nm and 0.273 nm respectively. In contrast, the modulated probe signals depict remarkably slow rise and fall times. In addition, the fall times appear to be composed of two time constants, with the tail end much slower than the leading edge. The bandwidth of the modulated signal is 0.432 nm. This is 35% large than the pump-only signal and 28% higher than the probe-only signal.

The results indicate the occurrence of nonlinear effects in the fiber due to the degenerate interaction of copropagating signals. The results for the pulse broadening was significant although due to pump power limitations additional experiments, at higher power, could not be performed to identify the specific mechanisms involved.

CIRCULAR WAVEGUIDE TO MICROSTRIP LINE TRANSITION

Frances J. Harackiewicz
Assistant Professor
Department of Electrical Engineering

Southern Illinois University at Carbondale
Carbondale, IL 62901-6603

Final Report for:
Summer Faculty Research Program
Rome Laboratory
Hanscom AFB, MA

Sponsored by:
Air Force Office of Scientific Research
Bolling Air Force Base, DC

and

Rome Laboratory

September 1994

CIRCULAR WAVEGUIDE TO MICROSTRIP LINE TRANSITION

Frances J. Harackiewicz

Assistant Professor

Department of Electrical Engineering

Southern Illinois University at Carbondale

Abstract

A circular waveguide to microstrip line transition was analyzed with a spectral-domain Green function / method of moments technique. The goal of this work was to obtain the equations for the moment method matrices as they appear in Appendix D. These spectral integral expressions for the matrix elements take into account all the available symmetries in the spectral polar coordinates k_t and α . Beyond this goal, much of the analysis was written into numerical subroutines. When run together the subroutines will be a useful design tool. This written computer code will help engineers design a reliable transition through the cooling boundary layer to the rf circuitry in a high density microwave monolithic integrated circuit package.

The second goal of this work was to develop a postprocessing routine which will calculate the reflection coefficient on a microstrip line given sampled values of the current on that line. A fairly robust routine described in the text was developed.

CIRCULAR WAVEGUIDE TO MICROSTRIP LINE TRANSITION

Frances J. Harackiewicz

Introduction

Presently, multilayer microwave monolithic integrated circuits and their associated packaging use vertical conducting interconnects to couple the rf signal between layers. These vertical connectors may break and lose electrical contact. Such a break can be very difficult to fix if it is embedded in the circuitry. Solderless fuzball connections are sometimes used in an attempt to overcome this problem in high density packaging, but they are neither trustworthy nor satisfactorily simple to construct or to analyze.

Several geometries of layers electromagnetically coupled without vertical interconnects are also possible and some have been studied [1]. The general circular waveguide to microstripline (cwg2ms) transition is shown in Fig. 1. The special case with $y_s=0$, $\epsilon_2=\epsilon_3=\epsilon_0$ is studied here. This geometry was suggested by M. Davidovitz [2] who built and measured such a transition which had a good VSWR response over a promising frequency range. The cwg2ms transition should be useful in coupling to circuits with thick ground planes used as a heat sink or as a boundary between liquid N₂ cooled circuitry and the remaining circuitry at ambient temperature. A hole drilled in the thick metal ground plane is easily machined and becomes the circular waveguide.

The goal of this research is to do the analysis necessary prior to writing an efficient computer code to analyze the cwg2ms transition. The code should be fast enough to be used by engineers as an interactive design tool and accurate to within 1% to 3% of the experimental results. The code should be portable and independent of any non-public-domain libraries except for the programming language FORTRAN 77.

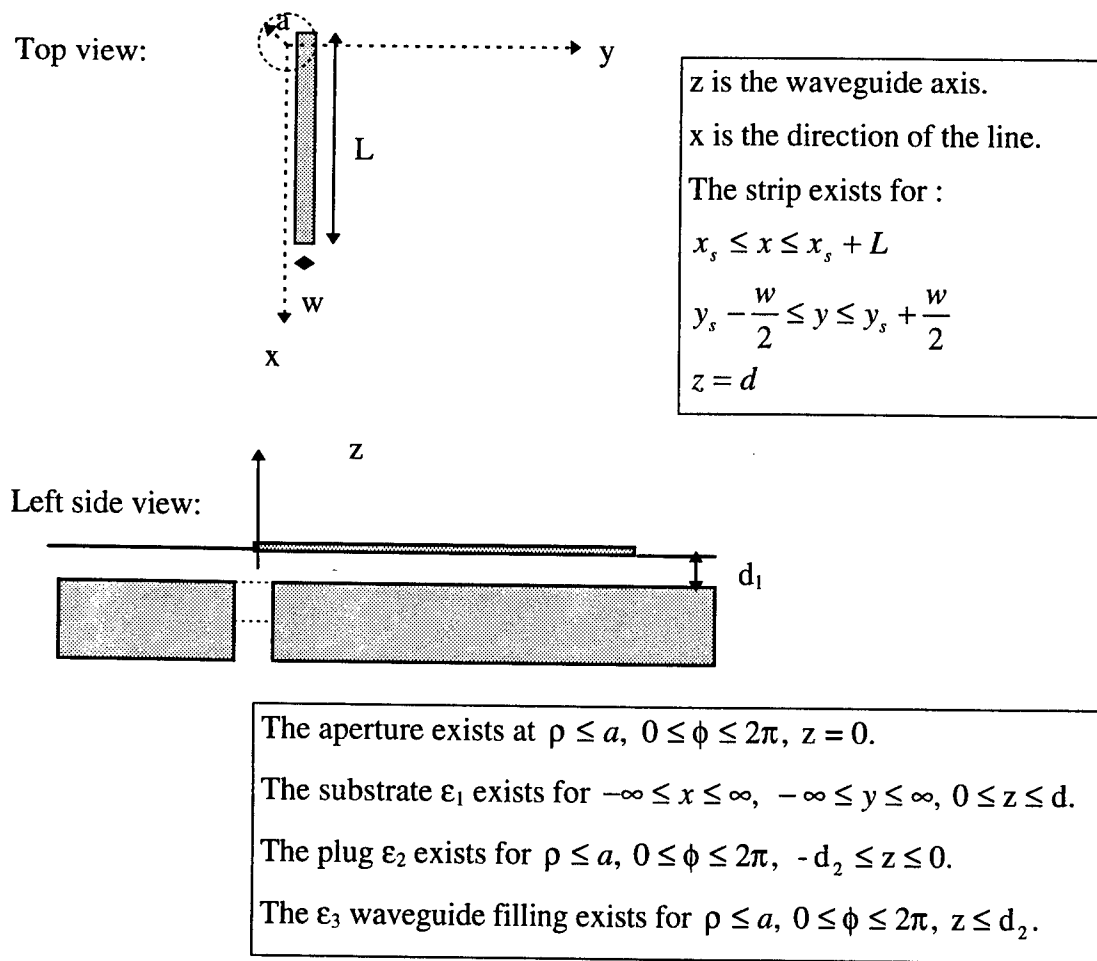


Figure 1 - Geometry of the Circular Waveguide to Microstrip line Transition

Methodology

The spectral-domain Green function / Method of Moments (MoM) is used to analyze the cwg2ms transition. Waveguide modes are used to expand the equivalent magnetic current over the ground plane at the waveguide aperture A, and overlapping triangular pulses (rooftop-modes) are used to expand the induced electric current on the microstrip line. The two-dimensional spectral integrals are done numerically using Chebyshev and Gaussian quadrature routines. The Green functions relate the vector fields and sources on the top and bottom boundaries of the dielectric substrate of the microstrip line. The integral equations and moment method matrix elements are defined in Appendix D.

After the MoM procedure is used to obtain the current on the strip S, some postprocessing is necessary to obtain the S parameters of the transition. A postprocessing

method similar to finding Fourier coefficients was developed for this purpose and is summarized in the next section. Since this technique involves numerical integration, one can assume that the method is more robust than one that has no “averaging” in it.

Summary of new Postprocessing Technique

The current on the strip is known as a series of weighted rooftop functions from the MoM, yet the true current is assumed to be of the form

$$I(x) = A^+ e^{-j\beta x} (1 + R e^{j\phi} e^{j2\beta x}).$$

The postprocessor must find the values of A^+ (magnitude and phase), R (real), and ϕ (real) while assuming that β is known by some other means such as

$$\beta = k_0 \sqrt{\epsilon_e} = \frac{2\pi}{\lambda_g}.$$

The rooftop sample points are spaced every $\frac{\lambda_g}{2N}$ from $x = 0$ to $x = \lambda_g / 2$ where N is an even number between 3 and 20. So, the sample points are

$$x_i = \frac{i\lambda_g}{2N} \text{ for } i = 0, 1, 2, \dots, N.$$

Three of the unknowns can be determined by first considering only the magnitude squared of the current

$$|I(x_i)|^2 = |A^+|^2 [1 + R^2 + 2R \cos(\phi + 2\pi i / N)] \text{ where the ranges of the unknowns are}$$

$$|I(x_i)| / \sqrt{2} \leq |A^+| \leq \infty, \quad 0 \leq R \leq 1, \quad 0 \leq \phi \leq 2\pi.$$

Three coefficients are defined and can be calculated from the current at the sample points by using Simpson's integration rule [4]:

$$\begin{aligned}
\alpha_1 &= 3N \frac{\beta}{\pi} \int_0^{\pi/\beta} |I(x)|^2 dx = 3N |A^+|^2 (1 + R^2) = 3N |A^+|^2 (1 + R^2) \\
&\equiv |I(x_0)|^2 + 4|I(x_1)|^2 + 2|I(x_2)|^2 + \dots + 4|I(x_{N-1})|^2 + |I(x_N)|^2 \\
\alpha_2 &= 3N \frac{\beta}{\pi} \int_0^{\pi/\beta} |I(x)|^2 \cos(2\beta x) dx = 3N |A^+|^2 R \cos \phi \\
&\equiv |I(x_0)|^2 \cos(2\beta x_0) + 4|I(x_1)|^2 \cos(2\beta x_1) + 2 \dots + 4|I(x_{N-1})|^2 \cos(2\beta x_{N-1}) + |I(x_N)|^2 \cos(2\beta x_N) \\
\alpha_3 &= 3N \frac{\beta}{\pi} \int_0^{\pi/\beta} |I(x)|^2 \sin(2\beta x) dx = -3N |A^+|^2 R \sin \phi \\
&\equiv |I(x_0)|^2 \sin(2\beta x_0) + 4|I(x_1)|^2 \sin(2\beta x_1) + 2 \dots + 4|I(x_{N-1})|^2 \sin(2\beta x_{N-1}) + |I(x_N)|^2 \sin(2\beta x_N)
\end{aligned}$$

Then solve for ϕ_0 , R_0 , and A_0 using the above α 's.

$$\phi \equiv \phi_0 = \arctan(-\alpha_3 / \alpha_2)$$

The atan function in FORTRAN returns a ϕ_0 between $-\pi/2$ and $\pi/2$. So, the following contingencies must be placed into the calculation:

$$\begin{aligned}
&\text{if } \phi_0 < 0 \text{ then} \\
&\quad \text{if } \alpha_2 < 0 \quad \phi_0 = \phi_0 + \pi \\
&\quad \text{if } \alpha_2 > 0 \quad \phi_0 = \phi_0 + 2\pi \\
&\text{else} \\
&\quad \text{if } \alpha_2 < 0 \quad \phi_0 = \phi_0 + \pi \\
&\text{end if}
\end{aligned}$$

To solve for R_0 define box \square as below which leads to a quadratic equation.

$$\square \equiv \frac{R^2}{(1 + R^2)^2} = \frac{\alpha_2^2 + \alpha_3^2}{\alpha_1^2} \text{ and note that } 0 \leq \square \leq \frac{1}{4}. \text{ So,}$$

$\square R^4 + (2\square - 1)R^2 + \square = 0$ which can be solved by letting $q=1$ and $p=1/(2\square)$. Note that $-\infty \leq p \leq -1$ so that $\text{sgn}(p)=-1$. Solving the quadratic leads to [5]

$$\begin{aligned}
R_1^2 &= -p - \text{sgn}(p) \sqrt{p^2 - q} \text{ if } p^2 \geq q \text{ and } p \neq 0 \\
R_2^2 &= q / R_1^2
\end{aligned}$$

Then, $R^2 \equiv R_0^2 = R_1^2$ but if $R_0^2 > 1$ then $R_0^2 = q / R_0^2$ and $R_0 = \sqrt{R_0^2}$.

The code calculating R_0 must also be written with contingencies to avoid two possible numerical problems. Notice that $p^2 \geq q = 1$ will always be true. A numerical problem arises if $p^2 - q$ should be zero, but is a small negative number instead due to roundoff error. Another numerical problem could arise if $\square = 0$ and then $p = -\infty$, $R = 0$. So, following is the corresponding code

```

q=1
if ( $\square=0$ ) then  $R_0=0$ 
else
if  $p^2 < q$  then  $R_0^2 = -p$ 
else  $R_0^2 = q / (-p + \sqrt{p^2 - q})$ 
end if
end if

```

To calculate the amplitude use $|A^+| \equiv A_0 = \sqrt{\frac{\alpha_1}{3N(1 + R_0^2)}}$.

By the Sampling theorem it seems that 4 sample points per λ_g should be OK, but after running several test cases it was found that at least 6 sample points were necessary. Perhaps these extra points are needed because we are using Simpson's Rule for integration rather than a trapezoidal rule. In Table 1 are examples of given $|A^+|$, R , and ϕ and the corresponding calculated A_0 , R_0 , and ϕ_0 for a given $2N$ number of samples per guide wavelength.

Table 1 - Examples of actual and approximated values from postprocessing routine.

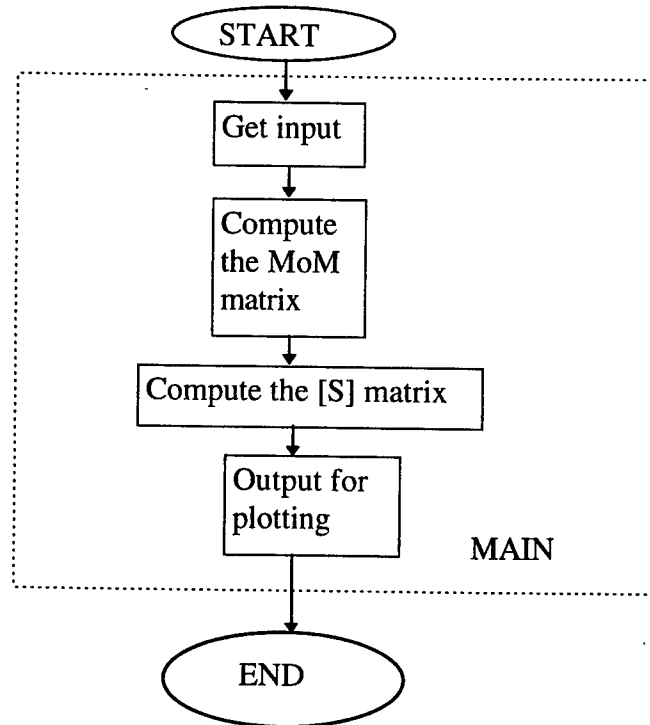
2N	$ A^+ $	R	ϕ	A_0	R_0	ϕ_0
20	1	1	1.8	1.00000	1.00000	1.80000
6	1	1	1.8	1.00017	0.999655	1.80000
4	1	1	1.8	1.08089	0.917337	3.14159

The phase of A^+ also needs to be calculated from a sample point of $I(x)$, which includes phase information.

$$e^{j\phi_A} = \frac{I(x_i)e^{j\beta x_i}}{|A^+|(1 + \operatorname{Re} e^{j\phi} e^{j2\beta x_i})}$$

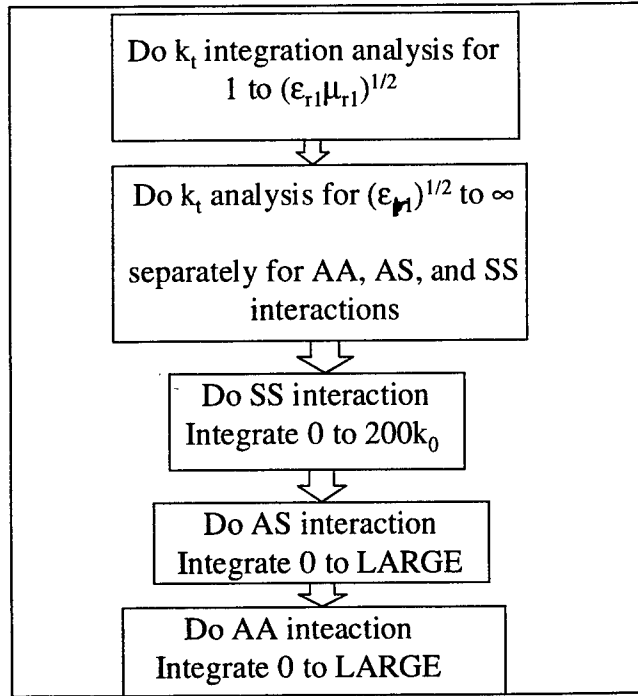
Planning the computer code

One way to construct the flowchart of the main program and some of its subroutines is sketched below.

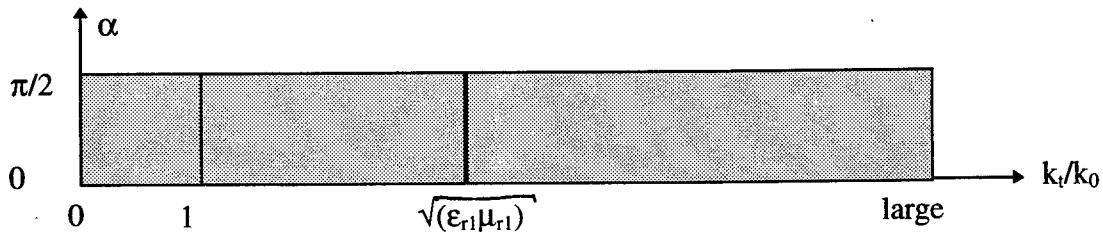


Filling the MoM matrix involves doing several two-dimensional, infinite, spectral integrals and is the most time-consuming part of the numerical calculation. The polar spectral variables are α and k_t and care must be taken so that integrating over them is accurate and efficient. On the k_t/k_0 axis between 1 and $\sqrt{\epsilon_{r1}\mu_{r1}}$ there will be poles of the Green functions if there is no loss in the substrate. If there is some loss in the substrate, then the poles will move into the complex plane but still be close enough to the real axis to cause some rapid changes in the integrands evaluated on the real axis. One must smartly choose

the sample points and integration method to best fit with this type of function. One possible way to construct the flowchart for the MoM matrix fill is shown below.



There are three interactions AA, AS, and SS which correspond to three different types of integrals which must be done over k_t and over α . The two-dimensional range of integration can be illustrated with the area of a rectangle shown below.



The α integration is done analytically for the AA interaction, but must be done numerically for the other interactions. The k_t integration from 0 to 1 can be done in one step with a 64 point Gaussian quadrature routine for all three interactions. The k_t integration from 1 to $\sqrt{\epsilon_{r1}\mu_{r1}}$ must be done in a number of steps using a grid that is sensitive to the regions where the Green functions have poles. All three interactions have poles at the same locations, but some Green function elements are worse behaved than others. To determine

the grid to use, a public library quadrature routine with an adaptive grid is first used to integrate over the worst behaved Green function. By testing it was found that the integrand for this preliminary integral should be the imaginary part of h_{mtm} if only one surface-wave pole exists and the imaginary part of h_{mtm} times the imaginary part of h_{mte} if more than one surface-wave pole exists. The value of $large$ is different for each interaction. Its value can be guessed at from the electrical dimensions between bases involved for each interaction. Then $large$ can be increased from those points until convergence of the final answer is achieved. For the AS and SS interactions, the α integrations must also be done numerically. A Chebyshev integration suitable for integrating over sinusoids is used in this dimension. The integration grid in the α direction is always found from the worst case (largest k_t and largest variation of the integrand) k_t point for each particular set of 64 k_t points. Much of this code and the MoM equations are similar to those in [3].

Conclusion

A computer-aided design tool for a transition reliable in high density feeds for phased array antennas is desired. The circular waveguide to microstripline transition can be analyzed with the spectral-domain / method of moments. All of analytical work necessary to implement this analysis method in a computer program has been done. This analytical work included deriving the moment method matrix element equations and developing a new post processing technique. The post processing technique was programmed and verified separately as were the routines calculating the Green function elements and the Fourier transforms of the basis functions. The individual pieces of code work well. A plan was well thought out of a good way to link the pieces of code together. Future work will include piecing together the code into one analysis program and comparing the results to the experimental data.

The following three figures show what the Green function elements and the basis functions look like in the spectral domain.

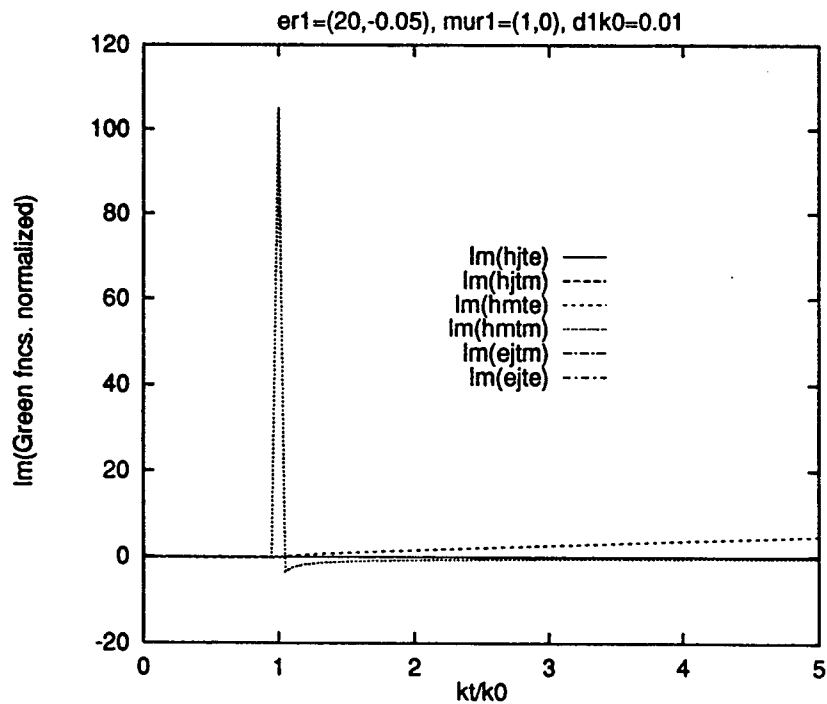
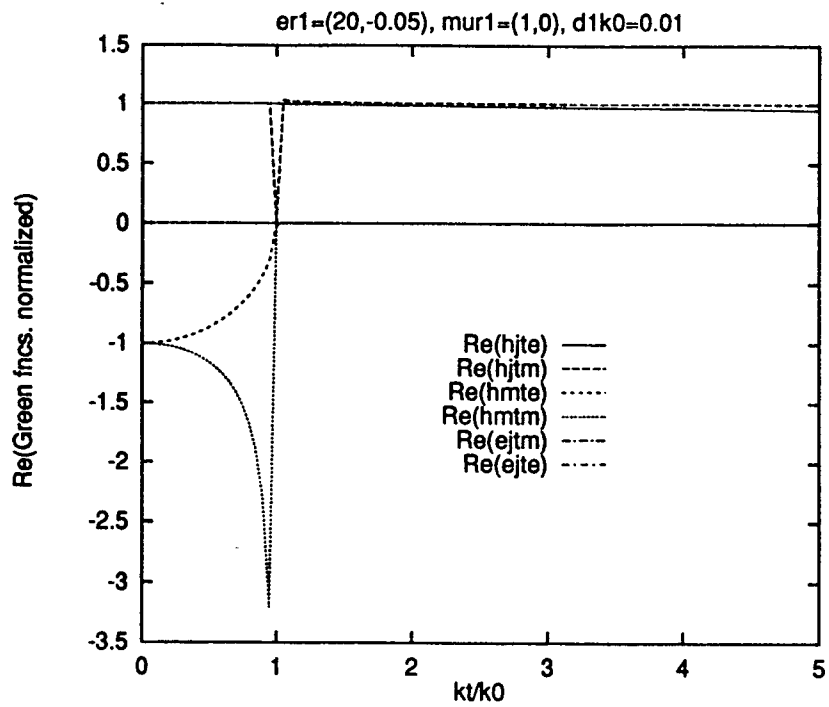


Figure 2 - Real and imaginary parts of the normalized Green function elements from Appendix A.

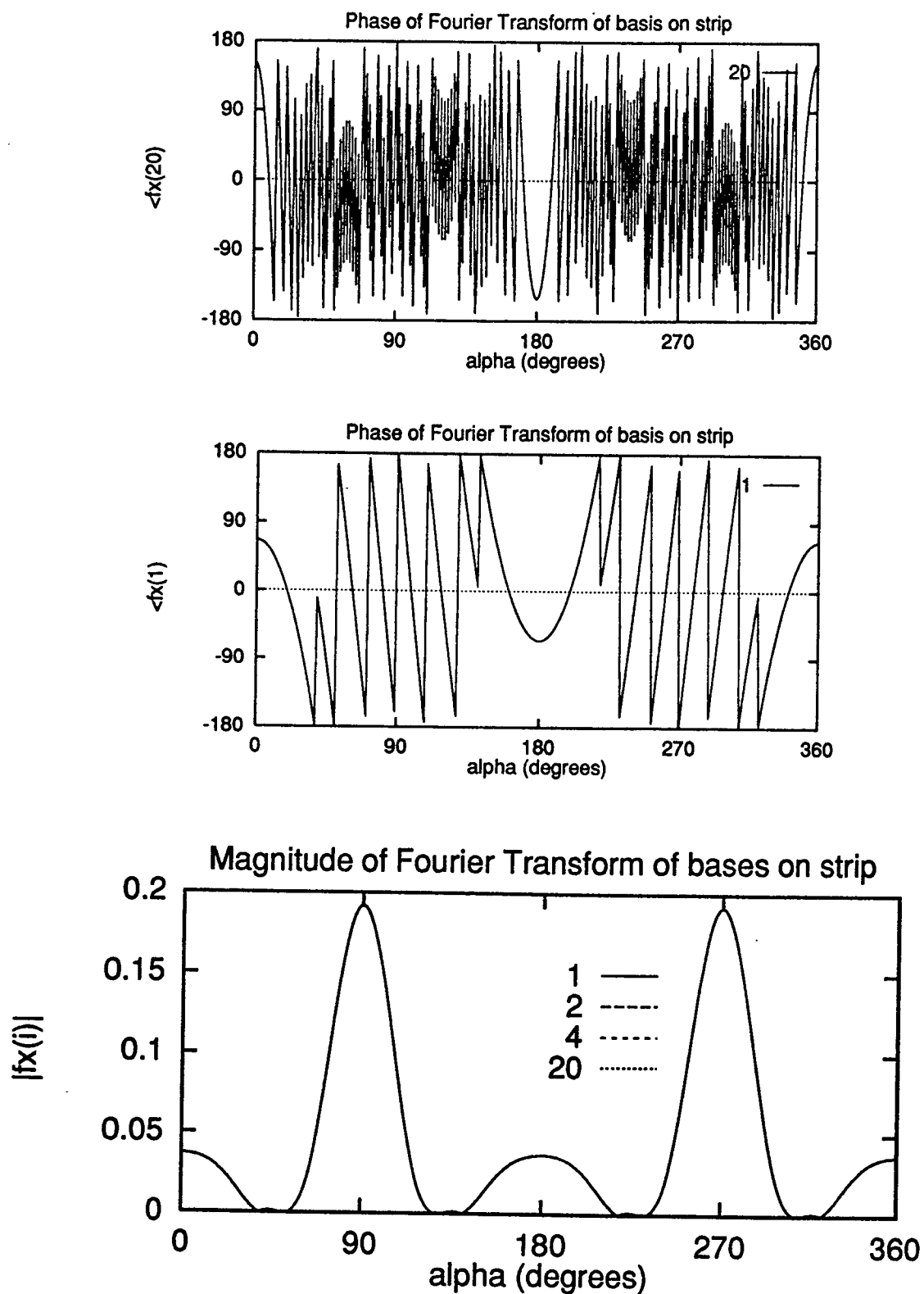


Figure 3 - Magnitude and phase of the Fourier transforms of a few of the 20 roof-top basis functions on the strip

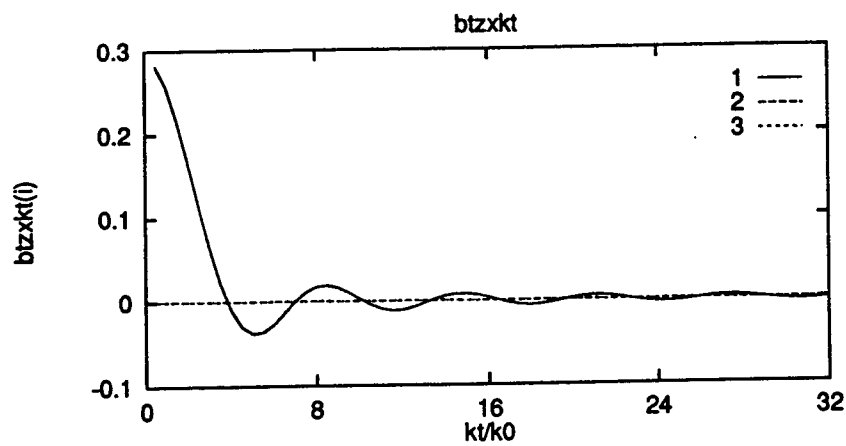
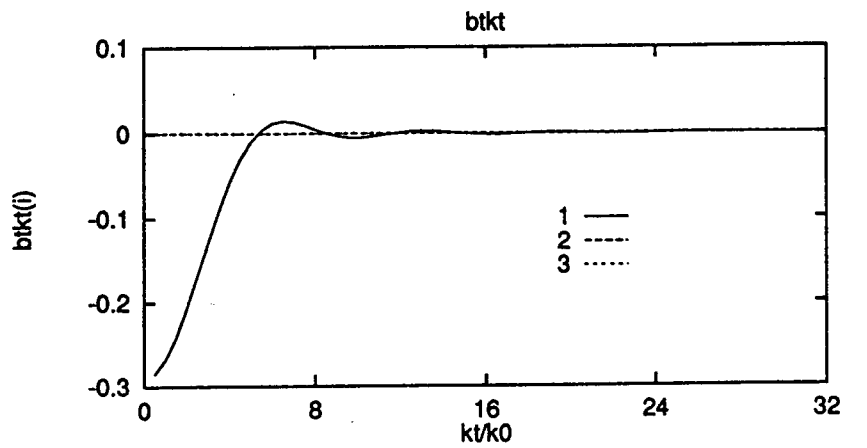


Figure 4 - Components of $\tilde{\tilde{b}}_i(k_i)$ for the first three modes of a circular waveguide. These functions are defined in Appendix B.

References

- [1] *Handbook of Microstrip Antennas*, edited by J. R. James & P. S. Hall, Peter Peregrinus Ltd., on behalf of the Institution of Electrical Engineers, London, UK, 1989.
- [2] Personal Communication with Marat Davidovitz May 18, 1994.
- [3] Marat Davidovitz and Yuen Tze Lo, "Rigorous Analysis of a Circular Patch Antenna Excited by a Microstrip Transmission Line," *IEEE Trans. Ant. and Propagat.*, vol. 37, no. 8, August 1989, pp. 949–958.
- [4] W. S. Dorn and D. D. McCracken, *Numerical Methods with FORTRAN IV Case Studies*, John Wiley & Sons, Inc., 1972.
- [5] J. Pachner, *Handbook of Numerical Analysis Applications (with programs for engineers and scientists)*, McGraw-Hill Book Co., New York, 1984.
- [6] D. M. Pozar, *Microwave Engineering*, Addison-Wesley Publishing Co., Reading, MA, 1990.
- [7] R. F. Harrington, *Time-Harmonic Electromagnetic Fields*, McGraw-Hill Inc., New York, 1961.
- [8] C. A. Balanis, *Antenna Theory analysis and design*, Harper & Row Publishers, New York, 1982.

Appendix A Green Functions

Listed below are the spectral-domain dyadic Green functions used in the program. The two superscripts above the G refer to the type of observation field and source current.

$$\overline{\overline{G}}^{HJ}(0, d_1) = \hat{k}_t(hjte)\hat{k}_t \times \hat{z} + \hat{z} \times \hat{k}_t(hjtm)\hat{k}_t$$

$$\eta_o \overline{\overline{G}}^{HM}(0, 0) = \hat{k}_t(hmte)\hat{k}_t + \hat{z} \times \hat{k}_t(hmtm)\hat{z} \times \hat{k}_t$$

$$\overline{\overline{G}}^{EM}(d_1, 0) = \hat{k}_t \times \hat{z}(emte)\hat{k}_t + \hat{k}_t(emptm)\hat{z} \times \hat{k}_t$$

$$\overline{\overline{G}}^{EJ}(d_1, d_1) / \eta_o = \hat{k}_t(ejtm)\hat{k}_t + \hat{k}_t \times \hat{z}(ejte)\hat{k}_t \times \hat{z}$$

$$hjte = -I^{TE}(0, d_1)$$

$$hjtm = -I^{TM}(0, d_1)$$

$$hmte = -\eta_o I_M^{TE}(0, 0)$$

$$hmtm = -\eta_o I_M^{TM}(0, 0)$$

$$emte = -hjte$$

$$emptm = -hjtm$$

$$ejtm = -V^{TM}(d_1, d_1) / \eta_o$$

$$ejte = -V^{TE}(d_1, d_1) / \eta_o$$

$$V(d_1, d_1) = 1 / (Y_o - jY_1 \cot(k_{z1}d_1))$$

$$I(0, d_1) = jY_1 V(d_1, d_1) / \sin(k_{z1}d_1)$$

$$I_M(0, 0) = -jY_1(Y_o \cot(k_{z1}d_1) + jY_1)V(d_1, d_1)$$

$$k_{z0} / k_0 = \pm \sqrt{1 - (k_t / k_0)^2} \quad \text{Im} < 0$$

$$k_{z1} / k_0 = \pm \sqrt{\epsilon_{r1}\mu_{r1} - (k_t / k_0)^2} \quad \text{Im} < 0$$

$$\eta_o Y_o^{TE} = (k_{z0} / k_0)$$

$$\eta_o Y_o^{TM} = (k_0 / k_{z0}) \text{ if } k_{z0} \neq 0$$

$$\eta_o Y_1^{TE} = (k_{z1} / \mu_{r1})(1 / k_0)$$

$$\eta_o Y_1^{TM} = (\epsilon_{r1} / k_{z1})(k_0)$$

Appendix B Basis Functions in the Aperture

The tangential electric field in the waveguide can be written as

$$\bar{E}_{TAN}(\rho, \phi) = \sum_{n=1}^M [V_n^i e^{-j\beta_n z} + V_n^r e^{j\beta_n z}] \bar{e}_n(\rho, \phi) \text{ (V / m)}, \text{ and}$$

the magnetic field in the aperture of the waveguide ($a \geq \rho$, $2\pi \geq \phi \geq 0$, $z=0$ aperture A) is

$$\bar{H}_{TAN} = \frac{1}{Z_n} \hat{z} \times \bar{E}_{TAN} = -\sum_{n=1}^M (V_n^i + V_n^r) \hat{z} \times \bar{e}_n = -\sum_{n=1}^M (V_n^i + V_n^r) \bar{h}_n \text{ (V / m)}$$

where the impedances of the waveguide modes are

$$Z_i^{TM} / \eta_o = \eta_r \sqrt{1 - \left(\frac{x_{nm}}{k_r a k_o} \right)^2} \quad \text{and} \quad Z_i^{TE} / \eta_o = \eta_r / \sqrt{1 - \left(\frac{x'_{nm}}{k_r a k_o} \right)^2}$$

where $k_r = \sqrt{\epsilon_r \mu_r}$ and $\eta_r = \sqrt{\mu_r / \epsilon_r}$

and the transformed waveguide modes are given by

$$k_o \tilde{\tilde{h}}_i^{TM} = \hat{z} \times \hat{k}_i c_{m_i}(\alpha) \tilde{\tilde{b}}_i^{TM}(k_i) \cdot \hat{z} \times \hat{k}_i$$

$$k_o \tilde{\tilde{h}}_i^{TE} = \hat{k}_i c_{m_i}(\alpha) \tilde{\tilde{b}}_i^{TE}(k_i) \cdot \hat{k}_i + \hat{z} \times \hat{k}_i d_{m_i}(\alpha) \tilde{\tilde{b}}_i^{TE}(k_i) \cdot \hat{z} \times \hat{k}_i$$

$$\tilde{\tilde{b}}_i^{TM} = x_{nm} J'_m(x_{nm}) J_m\left(\frac{k_i}{k_o} k_o a\right) \left[\frac{k_i / k_o}{\left(\frac{k_i}{k_o} \right)^2 - \left(\frac{x_{nm}}{k_o a} \right)^2} \right] \hat{z} \times \hat{k}_i$$

$$\tilde{\tilde{b}}_i^{TE} = (x'_{nm})^2 J_m(x'_{nm}) J'_m\left(\frac{k_i}{k_o} k_o a\right) \left[\frac{1}{k_o a \left(\left(\frac{k_i}{k_o} \right)^2 - \left(\frac{x_{nm}}{k_o a} \right)^2 \right)} \right] \hat{k}_i + m J_m(x'_{nm}) J_m\left(\frac{k_i}{k_o} k_o a\right) \frac{1}{(k_i / k_o)} \hat{z} \times \hat{k}_i$$

$$c_{m_i}(\alpha) = j^{m-1} 2\pi \begin{cases} \cos(m\alpha) \\ \sin(m\alpha) \end{cases} \sqrt{2 - \delta_{m0}} \text{ for } \begin{cases} \cos\phi \text{ dependence} \\ \sin\phi \text{ dependence} \end{cases}$$

$$d_{m_i}(\alpha) = j^{m-1} 2\pi \begin{cases} \sin(m\alpha) \\ -\cos(m\alpha) \end{cases} \sqrt{2 - \delta_{m0}} \text{ for } \begin{cases} \cos\phi \text{ dependence} \\ \sin\phi \text{ dependence} \end{cases}$$

Appendix C Basis Functions on the Strip

The microstrip line's left edge is centered at (x_s, y_s) . The line has width w and length L .

The electric surface current on the strip is expanded in triangular-pulse functions given by

$$\bar{J}_m(x, y) = \begin{cases} \frac{\hat{x}}{w} \left\{ 1 - \frac{|x - x_s - mhl|}{h} \right\} & \text{for } |x - x_s - mhl| < h \text{ and } |y - y_s| < w/2 \\ 0 & \text{else} \end{cases}$$

The Fourier transform of the pulses is

$$k_o \hat{J}_m = k_o F_x(k_x) F_y(k_y) \hat{x}$$

$$k_o F_x(k_x) = e^{jk_x x_s} e^{jk_x m h} h k_o \text{sinc}^2 \left(\frac{1}{2} \frac{k_x}{k_o} h k_o \right)$$

$$F_y(k_y) = e^{jk_y y_s} \text{sinc}(k_y w / 2)$$

$$k_x = k_t \cos \alpha, \quad k_y = k_t \sin \alpha$$

Appendix D Method of Moments Equations

The tangential fields in the waveguide and waveguide aperture are

$$\bar{E}_{TAN}(\rho, \phi, z) = \sum_{n=1}^M \left[V_n^i e^{-j\beta_n z} + V_n^r e^{j\beta_n z} \right] \bar{e}_n(\rho, \phi) \quad (\text{V / m})$$

$$\bar{H}_{TAN} = \frac{1}{Z_n} \hat{z} \times \bar{E}_{TAN}$$

$$\bar{M}_S(\rho, \phi, 0) = -\hat{z} \times \bar{E}_{TAN}(z=0) = -\sum_{n=1}^M (V_n^i + V_n^r) \hat{z} \times \bar{e}_n = -\sum_{n=1}^M (V_n^i + V_n^r) \bar{h}_n \quad (\text{V / m}).$$

$$\text{The current on the strip is } \bar{J}_S = \sum_{n=1}^N I_n \bar{J}_n(x, y, d) \quad (\text{A / m}).$$

The given coefficients V_n^i describe the incident field from the waveguide. The unknown coefficients V_n^r , I_n can be solved by using the spectral-domain Galerkin method on the boundary condition MFIE and EFIE

$$(*) \quad \bar{H}_{TAN}(z=0^+) = \bar{H}_{TAN}(z=0^-) \quad \text{in aperture A}$$

$$(**) \quad \bar{E}_{TAN}^{TOTAL}(z=d) = 0 \quad \text{on the strip S}$$

or

$$\text{FT}^* \quad \overline{\overline{G}}_{00}^{HM} \cdot \tilde{\tilde{M}} + \overline{\overline{G}}_{0d}^{HJ} \cdot \tilde{\tilde{J}}_S = \tilde{\tilde{H}}_{TAN}(z=0^-) = \sum_{n=1}^M (V_n^i - V_n^r) \frac{\tilde{\tilde{h}}_n}{Z_n}$$

$$\text{FT}^{**} \quad \overline{\overline{G}}_{d0}^{EM} \cdot \tilde{\tilde{M}}_S + \overline{\overline{G}}_{dd}^{EJ} \cdot \tilde{\tilde{J}}_S = 0$$

where \sim means Fourier Transform defined as $\tilde{f} = \iint f e^{j\bar{k}_t \cdot \bar{\rho}} d\bar{\rho}$.

After Galerkin weighting the MoM matrix equation showing units and dimensions is:

$$\underbrace{\begin{bmatrix} \eta_0 I_n \\ V_n^r \end{bmatrix}}_{\substack{(V) \\ (N \times M) \times 1}} = \underbrace{\begin{bmatrix} T^{AS} & \eta_0 \left(-Y^{AA} + \frac{\delta_{mn}}{Z_n} \right) \\ Z^{SS}/\eta_0 & -T^{SA} \end{bmatrix}^{-1}}_{\substack{(1) \\ (N+M) \times (M+N)}} \underbrace{\begin{bmatrix} \eta_0 \left(Y^{AA} + \frac{\delta_{mn}}{Z_n} \right) \\ T^{SA} \end{bmatrix}}_{M \times 1} \underbrace{\begin{bmatrix} V_n^i \end{bmatrix}}_{\substack{(V) \\ M \times 1}}$$

where the submatrices are defined as

$$\eta_0 Y_{mn}^{AA} = \frac{1}{4\pi^2} \iint d\left(\frac{\bar{k}_t}{k_0}\right) \left(\tilde{\tilde{h}}_m^* k_0 \right) \cdot \left(\overline{\overline{G}}_{00}^{HM} \eta_0 \right) \cdot \left(\tilde{\tilde{h}}_n k_0 \right) \quad (1) \text{ M} \times \text{M}$$

$$T_{mn}^{AS} = \frac{1}{4\pi^2} \iint d\left(\frac{\bar{k}_t}{k_0}\right) \left(\tilde{\tilde{h}}_m^* k_0 \right) \cdot \overline{\overline{G}}_{0d}^{HJ} \cdot \left(\tilde{\tilde{J}}_n k_0 \right) \quad (1) \text{ M} \times \text{N}$$

$$T_{mn}^{SA} = \frac{1}{4\pi^2} \iint d\left(\frac{\bar{k}_t}{k_0}\right) \left(\tilde{\tilde{J}}_m^* k_0 \right) \cdot \overline{\overline{G}}_{d0}^{EM} \cdot \left(\tilde{\tilde{h}}_n k_0 \right) \quad (1) \text{ N} \times \text{M}$$

$$= \frac{-1}{4\pi^2} \iint d\left(\frac{\bar{k}_t}{k_0}\right) \left(\tilde{\tilde{h}}_n k_0 \right) \cdot \overline{\overline{G}}_{0d}^{HJ} \cdot \left(\tilde{\tilde{J}}_m^* k_0 \right) \quad (1) \text{ N} \times \text{M}$$

$$Z_{mn}^{SS}/\eta_0 = \frac{1}{4\pi^2} \iint d\left(\frac{\bar{k}_t}{k_0}\right) \left(\tilde{\tilde{J}}_m^* k_0 \right) \left(\overline{\overline{G}}_{dd}^{EJ}/\eta_0 \right) \left(\tilde{\tilde{J}}_n k_0 \right) \quad (1) \text{ N} \times \text{N}.$$

Most terms are made dimensionless by dividing by either

$$k_0 = \omega \sqrt{\mu_0 \epsilon_0} \text{ or } \eta_0 = \sqrt{\mu_0 / \epsilon_0}.$$

The double infinite integrals can be done in polar spectral coordinates where

$$\hat{k}_i = \hat{x} \cos \alpha + \hat{y} \sin \alpha .$$

Using all the symmetries in the problem definition, the above submatrices can be calculated as follows.

The MxM matrix Y:

$$\eta_0 Y_{pq}^{AA} = \frac{1}{4\pi^2} \int_0^\infty \left(\frac{k_t}{k_0} \right) d\left(\frac{k_t}{k_0} \right) C_{mp}^* C_{mq} \left[\begin{array}{l} \tilde{\tilde{b}}_p(k_t) k_0 \cdot \hat{k}_i (hmte) \tilde{\tilde{b}}_q(k_t) k_0 \cdot \hat{k}_i Y_1 + \\ \tilde{\tilde{b}}_p(k_t) k_0 \cdot \hat{z} \times \hat{k}_i (hmtm) \tilde{\tilde{b}}_q(k_t) k_0 \cdot \hat{z} \times \hat{k}_i Y_2 \end{array} \right]$$

where

$$C_{mp}^* C_{mq} = 4\pi^2 j^{m_p+m_q-2} (-1)^{m_p-1} \sqrt{2-\delta_{0m_p}} \sqrt{2-\delta_{0m_q}}$$

and

$$Y_1 = \begin{cases} 0 & \text{if } m_p \neq m_q \\ & \text{or } \tau_p \neq TE \\ & \text{or } \tau_q \neq TE \\ & \text{or } p \cos \phi \neq q \cos \phi \\ \pi & \text{else} \end{cases}$$

$$Y_2 = \begin{cases} 0 & \text{if } m_p \neq m_q \text{ or} \\ & \text{if } \tau_p \neq \tau_q \text{ and } p \cos \phi = q \cos \phi \\ -\pi & \text{else if } \tau_p \neq \tau_q \text{ and } p \cos \phi \neq q \cos \phi \text{ and } p_{\cos \phi} = TE_q \\ \pi & \text{else} \end{cases}$$

Only the upper triangle of the matrix including the diagonal need be calculated since this matrix is symmetric:

$$\eta_0 Y_{qp}^{AA} = \eta_0 Y_{pq}^{AA} .$$

The MxN matrix T:

$$T_{pq}^{AS} = \frac{C_{m_p}}{4\pi^2} \int_0^\infty \left(\frac{k_t}{k_0} \right) d\left(\frac{k_t}{k_0} \right) \left[\begin{aligned} &\tilde{\bar{b}}_p(k_t) k_0 \cdot \hat{k}_t \left(\hat{k}_t \cdot \overline{\overline{G}}_{0d}^{HJ} \cdot \hat{k}_t \times \hat{z} \right) I_{pq}^1(k_t) \\ &+ \tilde{\bar{b}}_p(k_t) k_0 \cdot \hat{z} \times \hat{k}_t \left(\hat{z} \times \hat{k}_t \cdot \overline{\overline{G}}_{0d}^{HJ} \cdot \hat{k}_t \right) I_{pq}^2(k_t) \end{aligned} \right] \text{ and where}$$

$$\text{where } C_{m_p} = 2\pi j^{(m-1)} \sqrt{2 - \delta_{0m}}$$

$$I_{pq}^1 = (-1)^{m_p-1} \int_0^{2\pi} \left(\begin{array}{c} 0^{TM} \\ c_{mp}^{TE}(\alpha) \end{array} \right) F_x k_0 F_y \sin \alpha d\alpha$$

$$= \begin{cases} 0 & \text{if } p \text{ is TE and } \cos\phi \text{ harmonic} \\ 0 & \text{if } p \text{ is TM} \\ 4 \int_0^{\pi/2} \text{Re}\{F_{x_q} k_0\} F_{y_q} \sin(m_p \alpha) \sin \alpha d\alpha & \text{if } p \text{ is TE and } \sin\phi \text{ harmonic and } m_p \text{ is odd} \\ -4j \int_0^{\pi/2} \text{Im}\{F_{x_q} k_0\} F_{y_q} \sin(m_p \alpha) \sin \alpha d\alpha & \text{if } p \text{ is TE and } \sin\phi \text{ harmonic and } m_p \text{ is even} \end{cases}$$

$$I_{pq}^2 = (-1)^{m_p-1} \int_0^{2\pi} \left(\begin{array}{c} c_{mp}^{TM} \\ d_{mp}^{TE} \end{array} \right) F_x k_0 F_y \cos \alpha d\alpha$$

$$= \begin{cases} 0 & \text{if } p \text{ is TE and } \cos\phi \text{ harmonic} \\ 0 & \text{if } p \text{ is TM and } \sin\phi \text{ harmonic} \\ \pm 4 \int_0^{\pi/2} \text{Re}\{F_{x_q} k_0\} F_{y_q} \cos(m_p \alpha) \cos \alpha d\alpha & \begin{cases} +\text{if } p \text{ is TM, } \cos\phi \text{ harmonic and } m_p \text{ is odd} \\ -\text{if } p \text{ is TE and } \sin\phi \text{ harmonic and } m_p \text{ is odd} \end{cases} \\ \mp 4j \int_0^{\pi/2} \text{Im}\{F_{x_q} k_0\} F_{y_q} \cos(m_p \alpha) \cos \alpha d\alpha & \begin{cases} -\text{if } p \text{ is TM and } \cos\phi \text{ harmonic and } m_p \text{ is even} \\ +\text{if } p \text{ is TE and } \sin\phi \text{ harmonic and } m_p \text{ is even} \end{cases} \end{cases}$$

The two T matrices are related with a transpose and a minus sign $T_{pq}^{SA} = -T_{qp}^{AS}$ which

comes from the two Green functions being related $G^{EM} = (-G^{HJ})^T$.

The NxN matrix Z:

$$Z_{mn}^{SS} / \eta_0 = \frac{(hk_0)^2}{\pi^2} \int_0^\infty \left(\frac{k_t}{k_0} \right) d\left(\frac{k_t}{k_0} \right) \int_0^{\pi/2} d\alpha \left\{ \cos^2 \alpha (ejtm) + \sin^2 \alpha (ejte) \right\} \cos(k_0 h \cos \alpha (n-m)) \sin^4 \left(\frac{1}{2} \cos \alpha h k_0 \right) \sin^2 \left(k_0 \sin \alpha \frac{w}{2} \right)$$

Notice that Z has Toeplitz symmetry so that only the first row of elements need be calculated.

Simulation of Erbium-doped Fiber Lasers

J. W. Haus

Physics Dept.

Rensselaer Polytechnic Institute

Troy, NY 12180-3590

Final report for:

Summer Faculty Research Program

Rome Laboratory, Rome, NY

Sponsored by:

Air Force Office of Scientific Research

Bolling Air Force Base, DC

and

Rome Laboratory

August 1994

Simulation of Erbium-doped Fiber Lasers

J. W. Haus

Physics Dept.

Rensselaer Polytechnic Institute

Troy, NY 12180-3590

Abstract

Numerical simulation of pulse amplification in birefringent optical fibers has been examined with the goal of providing a realistic and accurate description of passive mode-locking. Emphasis of our studies was put on the evolution of the pulse's polarization. We found a complex polarization state of the amplified pulse; this has important implications for the operation of fiber lasers using a birefringent fiber amplifier mode locking element.

I. INTRODUCTION

Erbium-doped fiber lasers are a potential ultrashort pulse source for optical communications technologies [1]. They provide high repetition rates in the wavelength regime corresponding to the minimum loss of silica fibers. Such lasers have distinct advantages, for instance, they can be pumped using diode lasers and they are compatible with fiber technologies. However, they suffer from stability and reproducibility problems because of their complex dependence on the polarization of the light in the laser cavity [2,3]. Recently, this problem has been examined and new cavity designs have been proposed to operate with ultrashort pulses while being insensitive to environmental changes [5–12]. The new cavity designs incorporate birefringent fiber amplifiers as elements to control the polarization state of the light in the fiber. Polarization mode locking combines the uses of birefringent fibers with polarization elements to create fast saturable absorber-like action.

Generally, when a soliton pulse, which has a well defined polarization state, propagates through a birefringent fiber, then cross- and self-phase modulation effects act to rotate the polarization state of the pulse in addition to the linear birefringence of the fiber. When that fiber is an amplifier though, the perturbation of the pulse phase and amplitude can be large enough that the polarization varies across the pulse. In this situation, the mode-locking element no longer optimally functions as designed. The result will be a pulse that is distorted from its original shape.

II. MODEL AND SOLUTION METHOD

We simulated a model for erbium-doped, birefringent fibers and examined the evolution of the pulses in the amplifier. The simulation model incorporated features of the birefringent fibers [13] and amplification [14]. The simplest form of the evolution equations are expressed as:

$$i \left(\frac{\partial E_x}{\partial z} + \Delta \frac{\partial E_x}{\partial \tau} \right) + E_x (|E_x|^2 + \frac{2}{3} |E_y|^2) = i\Gamma E_x + i\mu \frac{\partial^2 E_x}{\partial \tau^2}, \quad (1)$$

$$i \left(\frac{\partial E_y}{\partial z} - \Delta \frac{\partial E_y}{\partial \tau} \right) + E_y(|E_y|^2 + \frac{2}{3}|E_x|^2) = i\Gamma E_y + i\mu \frac{\partial^2 E_y}{\partial \tau^2}. \quad (2)$$

E_x and E_y are the electric field vector components along the x - and y - axes, resp. ; propagation is along the z -axis. To simplify the expresions the equations have been scaled to soliton units throughout [15]. The time is scaled to a value T_0 , related to the initial pulse width; the length is scaled by the dispersion length $L_D = T_0^2/|\beta_2|$, where β_2 is the group velocity dispersion parameter. The field amplitude scaling corresponds to a fundamental soliton , $n_2|E_0|^2 = |\beta_2|^2 T_0^2$. The left hand side of Eqs. 1 and 2 includes the scaled inverse group velocity difference, 2Δ , between the two polarizations, and the effect of self- and cross-phase modulation [15,16]. We have neglected the four-wave mixing terms, which rapidly oscillate with propagation distance in a birefringent fiber and therefore average to zero.

On the right hand side the gain and gain dispersion coefficients are modeled after a two-level atom model for the medium with a rapid polarization relaxation time. The gain and gain dispersion parameters are Γ and μ . The equations were solved using a split-step Fast Fourier transform method, which was modified to take advantage of the vector nature of the equations [17]. The linear contributions are incorporated into a linear operator that can be solved in the frequency domain. The nonlinear contributions are treated in the time domain. We generally used 4096 FFT points, but runs have been made with 8192 FFT points to assure accuracy. The step size along the z - axis is 10^{-4} and our time window has varied from 80 to 160 units. Our results were tested against previous results for special cases. The input pulse shape, i.e. $z = 0$ is a fundamental soliton with, in general, unequal amplitudes along the x - and y - axes:

$$\begin{aligned} E_x(0, \tau) &= \cos \theta \text{sech}(\tau); \\ E_y(0, \tau) &= \sin \theta \text{sech}(\tau); \end{aligned} \quad (3)$$

thus, the starting pulse is linearly polarized with $\theta = \pi/4$ or $\pi/8$ with respect to the x -axis. To rotate the polarization of the pulse in a birefringent fiber, the input wave should be different amplitudes along each principal axis.

III. RESULTS

In this section some new results are illustrated; it should suffice to demonstrate the capabilities of the simulation. In Figure 1 a plot of the intensity along each polarization axis after 1 and 2 dispersion lengths for $\theta = \pi/4$; the group velocities are identical for this case. The pulse is amplified and compressed as it attempts to retain its fundamental soliton character during propagation; the pulse width is limited by the gain dispersion and eventually it breaks up as the energy develops higher order soliton effects. This behavior is analogous to that found by Agrawal for a single polarization [14]. The simulations without the polarization have not previously examined the phases of the fields. In the new simulations this property can now be examined; the phase of the pulses in Figure 2 is strongly modulated during the amplification process; before the pulse breaks up, the phase changes smoothly peaking at the position of the pulse maximum; after 2 dispersion lengths though, the phase is modulated with several local maxima. However, because there is no differential excitation of the axes and no group velocity difference, the polarization remains constant.

Now consider the situation with different group velocities and $\theta = \pi/8$ in Figure 3, which displays the two polarization intensity maxima walking off one another. After two dispersion lengths, the pulse have broken up displaying multiple maxima, as in Fig. 1, but the side peaks show a greater separation from the central peaks, which are still closely correlated. The state of polarization of a pulse is distorted and strongly so as the pulse phase is modulated and the polarizations walk off one another; the phase difference is displayed in Fig. 4 for two propagation distances. After one dispersion length ($z = 1$), the phases of the two polarizations are closely correlated, but after two dispersion lengths ($z = 2$), the phase differences are large; the central peaks are in phase, but the side peaks have large phase differences. This affects the operation of the birefringent fiber amplifier devices in erbium-doped fiber lasers. As a consequence, the operation of the lasers and the linear amplifier devices are going to be degraded by these effects.

Not only is there a limit imposed on the pulse width and intensity, but their polarization

state becomes distorted during propagation through the fibers. As the pulses walk off one another, the phase modulations at first remains locked, but the intensities are not so highly correlated, therefore, the polarization state varies across the pulse. We illustrate this in Figure 5, which shows the resultant pulse after passing through a polarizer which is either parallel or perpendicular to the input pulse polarization; the intensity polarized parallel to the input wave has structure and the orthogonal polarization has a broad structured intensity. The action of a birefringent amplifier and a polarizer can distort the pulse shape.

IV. SUMMARY AND FUTURE WORK

We made considerable progress toward a realistic simulation of a fiber laser. The amplifier and fiber characteristics were carefully examined including effects which will have a large effect on the operation of the laser. The fiber lasers can be developed as sources of ultrashort optical pulses for gigabit optical communications networks.

During the program a publication was prepared and submitted to Photonics Technology Letters. That paper details salient features of our simulations of a birefringent fiber amplifier.

Several future publications are planned and we will continue our collaboration; the fiber laser simulations will incorporate gain saturation, as well as stimulated Raman scattering, self-steepening, group velocity differences, and higher-order dispersion effects. Since we have both polarizations, we can examine the evolution of the pulses polarization in the fiber, as well as, studying the pulse in the time and frequency domains. The simulations here demonstrate a complicated evolution of the pulses, which ultimately impacts on the operation of birefringent amplifier devices in a laser cavity.

ACKNOWLEDGMENTS

JWH acknowledges the support and hospitality of the Photonics Laboratory in Rome, NY where this work was performed.

REFERENCES

- [1] E. Desurvire, *Erbium-doped Fiber Amplifiers: Principles and Applications*, Wiley, NY (1993).
- [2] A. B. Grudinen, D. J. Richardson and D. N. Payne, *Optical pulse propagation in doped fiber amplifiers*, Phys. Rev. A, vol. **44**, pp. 7493 - 7501 (1991).
- [3] W. Hodel, J. Schön and H. P. Weber, *Intensity discrimination of optical pulses with birefringent fibers*, Opt. Commun., vol. **88**, pp. 173-179 (1992).
- [4] M. Hofer, M. E. Fermann, F. Haberl, M. H. Ober and A. J. Schmidt, *Mode locking with cross-phase and self-phase modulation*, Opt. Lett., vol. **7**, pp. 502-504 (1991).
- [5] I. N. Duling III and R. D. Esman, *Single-polarization fiber amplifier*, Electron. Lett., vol. **28**, pp. 1126 - 1128 (1992).
- [6] M. E. Fermann, M. J. Andrejco, Y. Silberberg and A. M. Weiner, *Generation of pulses shorter than 200 fs from a passively mode-locked fiber laser*, Phys. Rev. A, vol. **48**, pp. 7493-7501 (1993).
- [7] M. E. Fermann, M. J. Andrejco, Y. Silberberg and M. L. Stock, *Passive mode locking by using nonlinear polarization evolution in a polarization-maintaining erbium-doped fiber*, Opt. Lett., vol. **18**, pp. 894 - 896 (1993).
- [8] M. E. Fermann, L.-M. Yang, M. L. Stock and M. J. Andrejco, *Environmentally stable Kerr type mode-locked erbium fiber laser producing 360 fs pulses*, Opt. Lett., vol. **19**, pp. 43-45 (1994).
- [9] V. J. Matsas, T. P. Newson and M. N. Zervas, *Self-starting passively mode-locked fibre ring laser exploiting nonlinear polarisation switching*, Opt. Commun., vol. **92**, pp. 61 - 66 (1992).
- [10] V. J. Matsas, D. J. Richardson, T. P. Newson and D. N. Payne, *Characterization of a*

- self-starting, passively mode-locked fiber ring laser that exploits nonlinear polarization evolution*, Opt. Lett., vol. **18**, pp. 358-360 (1993).
- [11] K. Tamura, H. A. Haus and E. P. Ippen, *Self-starting additive pulse mode-locked erbium fibre ring laser*, Electron. Lett., vol. **28**, pp. 2226 - 2228 (1992).
- [12] M. Y. Frankel, R. D. Esman and J. F. Weller, *Additive-pulse modelocking in fiber lasers*, IEEE J. Quant. Electron., vol. QE-30, pp. 200 - 208 (1994).
- [13] C. R. Menyuk, *Pulse Propagation in an elliptically birefringent Kerr medium*, IEEE J. Quantum Electron., vol. QE-25, pp. 2647-2682 (1989).
- [14] G. P. Agrawal, *Optical pulse propagation in doped fiber amplifiers*, Phys. Rev. A, vol. **44**, pp. 7493 - 7501 (1991).
- [15] G. P. Agrawal, *Nonlinear Fiber Optics*, Academic Press, San Diego (1989).
- [16] M. Islam, *Ultrafast Fiber Switching Devices and Systems*, Cambridge University Press, Cambridge (1992).
- [17] S. L. Doty, J. W. Haus, J. Oh and R. L. Fork, *Soliton interactions on dual core fibers*, Phys. Rev. E, submitted (1994).

FIGURES

FIG. 1. The intensity of the x - or y - polarization for two propagation distances $z = 1$ (solid line) and 2 (dashed line) for the case $\Delta = 0$ and $\theta = \pi/4$. The gain parameters are $\Gamma = 2.3$ and $\mu = 0.2$.

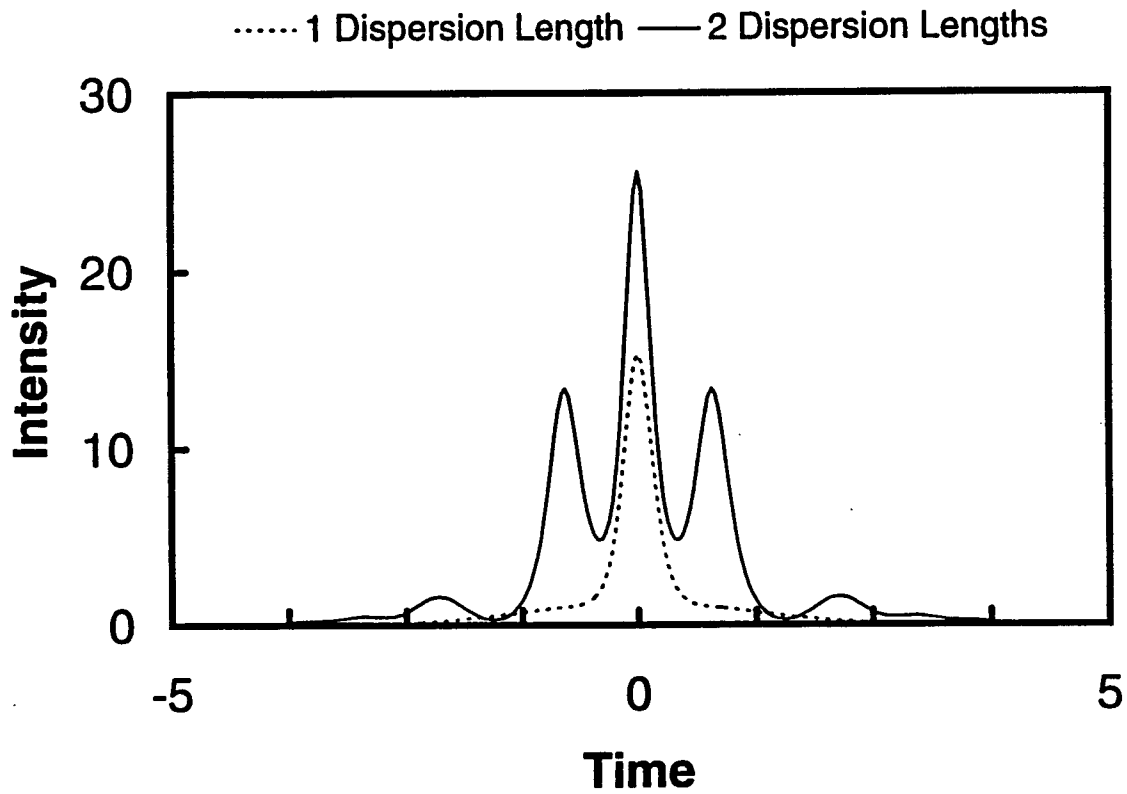


FIG. 2. The phase of the electric field corresponding to the intensity shown in Figure 1. For parameter values see the caption for Figure 1.

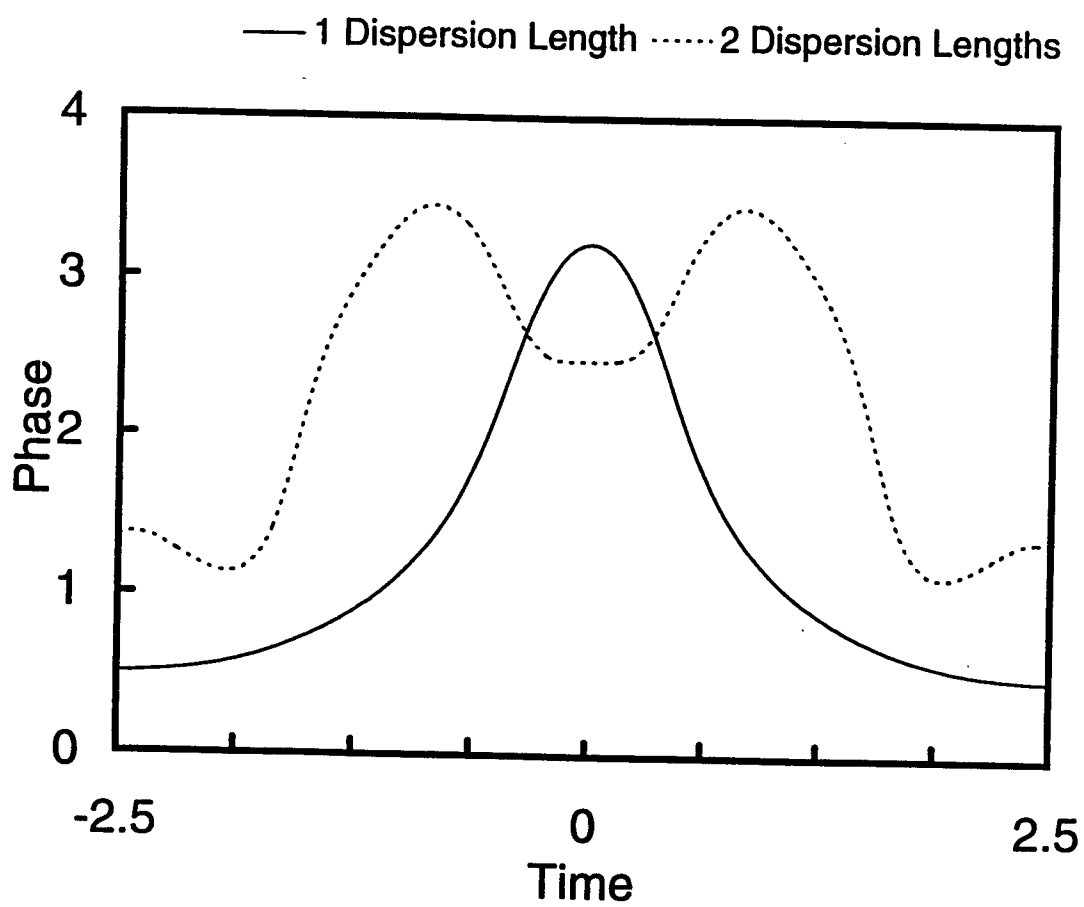


FIG. 3. The intensity of the x - and y - polarized components for the case $\Delta = 0.5$ and $\theta = \pi/8$. Two propagation distance is $z = 2$. The gain parameters are identical to the previous case.

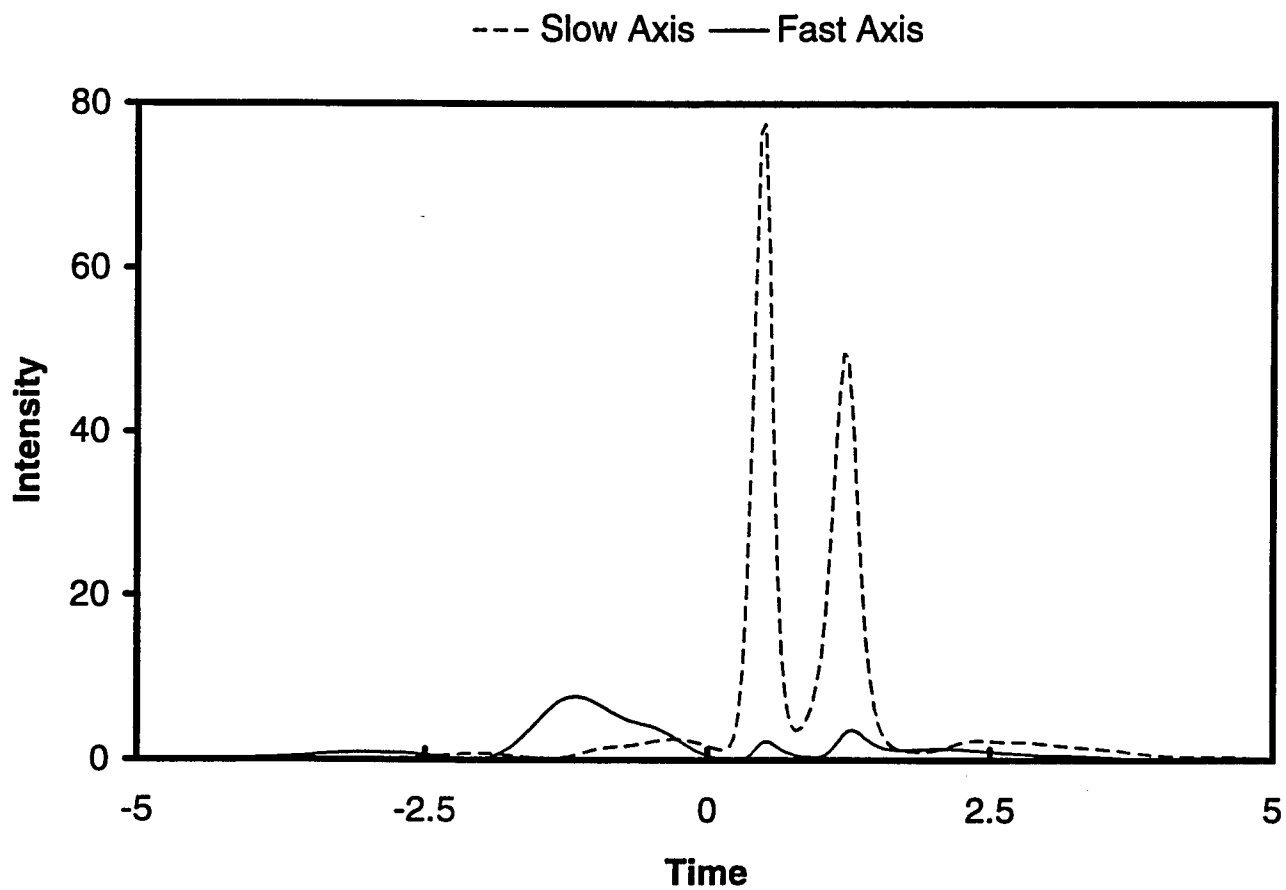


FIG. 4. Phase difference between the two polarizations for the intensity shown in Fig.3.

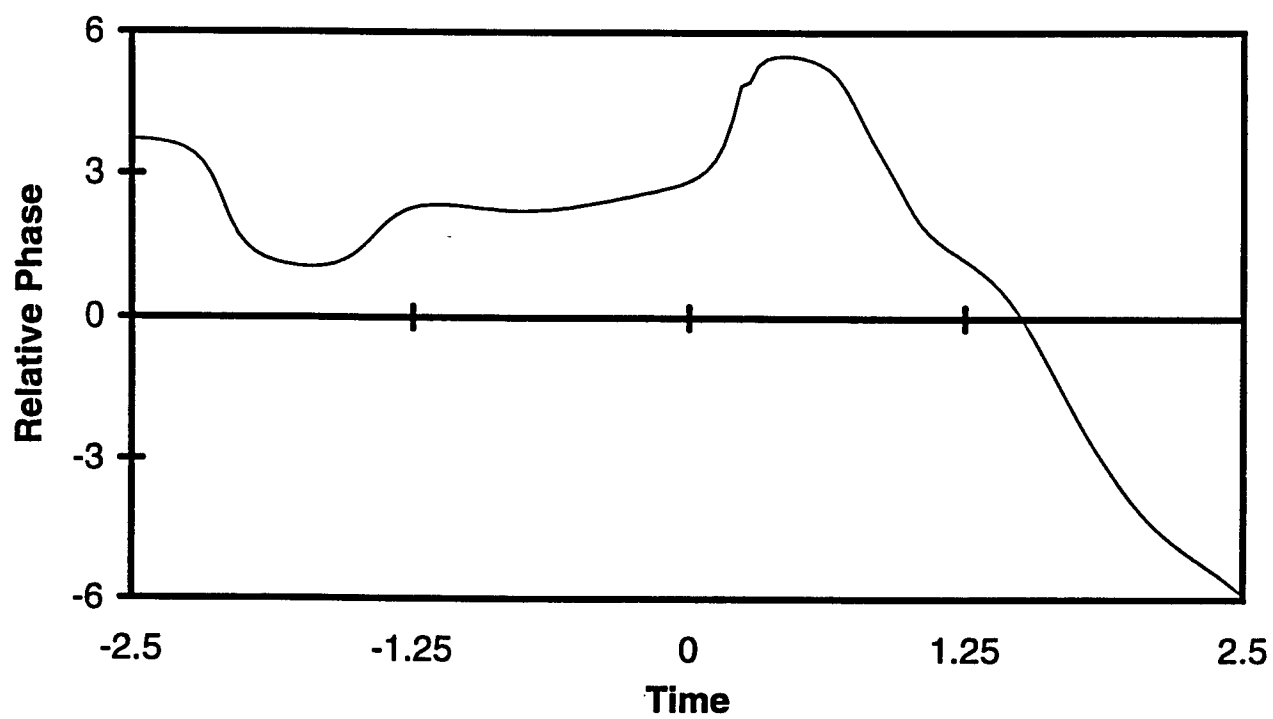
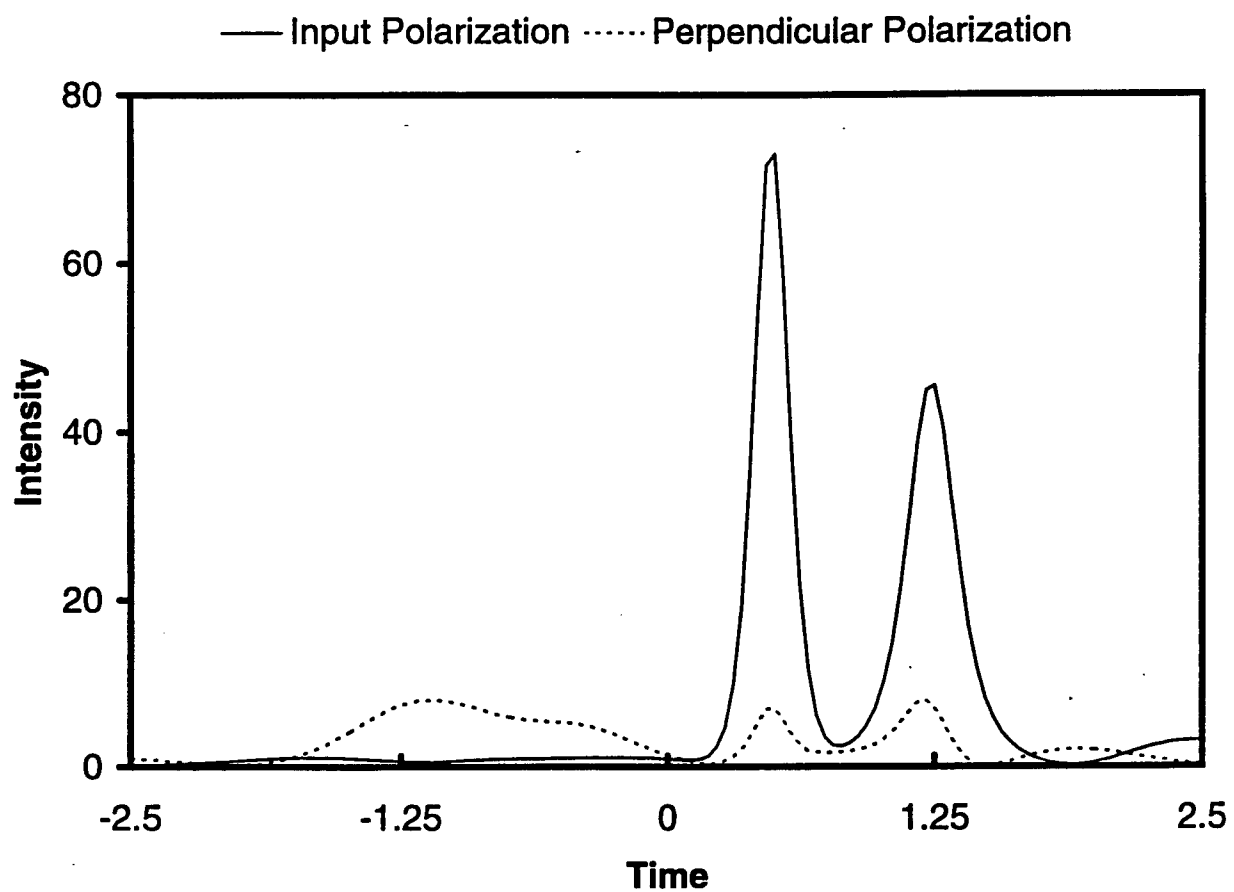


FIG. 5. The intensity of the pulse in Figure 4 as it passes through a polarizer parallel to the input polarization (solid line) and perpendicular to the input polarization (dashed line).



**A MACROSCOPIC MODEL OF ELECTROMIGRATION:
COMPARISON WITH EXPERIMENT**

Yolanda J. Kime
Assistant Professor
Physics Department

State University of New York: College at Cortland
P.O. Box 2000
Cortland, NY 13045-2000

Final Report for:
Summer Faculty Research Program
Rome Laboratory

Sponsored by:
Air Force Office of Scientific Research
Bolling Air Force Base, DC

and

Rome Laboratory

August 1994

A MACROSCOPIC MODEL OF ELECTROMIGRATION: COMPARISON WITH EXPERIMENT

Yolanda J. Kime
Assistant Professor
Physics Department
State University of New York: College at Cortland

Abstract

Comparison of theory and experiment is critical in microelectronic reliability. In this work, a model which has been previously used for electromigration time to failure predictions (developed by Harrison) is extended to include predictions for numbers of voids and void sizes. Predictions from the model are compared to experimental measurements. The model makes reasonable predictions for mean lifetimes, numbers of voids, and void areas with very few free parameters. The model, however, does *not* adequately reproduce the of lifetimes found in experiment.

A MACROSCOPIC MODEL OF ELECTROMIGRATION: COMPARISON WITH EXPERIMENT

Yolanda J. Kime

I. INTRODUCTION

In every area of science the continuous comparison between theory and experiment yields the growth and insight which drives scientific progress. This is no less true in microelectronic reliability. Much work has been done to understand, and hence to control, the damage and the ultimate failure of microelectronic parts due to electromigration in metal interconnects. From a pragmatic view, the characteristic of critical importance is the lifetime of the interconnect. Most of the theoretical work, and much of the experimental work as well, has focused primarily on lifetime measurements. However, other characteristics, such as the total area of electromigration voids on a stripe, can be measured, and our understanding of the electromigration process can only be complete when these other characteristics as well as the lifetimes can be predicted accurately.

The purpose of this work is test the extent to which characteristics of thin film electromigration damage such as void areas and the number of voids can be adequately simulated by a simple model [1] which has previously been used only to examine changes in the time to failure. The experimental results which are compared to the simulation results are discussed in detail elsewhere [2]. In brief, Al 1% Si meander test stripes, 1600 μ long, 3.4 μ wide, and 0.8 μ thick, were electromigrated to failure at a constant 2×10^6 A/cm². The test stripes were passivated with 0.4 μ of SiO₂. The test stripes were examined for void damage using a Scanning Electron Microscope (SEM). The void areas, perimeters, lengths, and widths were measured on thirty-eight of the stripes using a Cambridge SEM equipped with a Robinson backscatter detector in conjunction with an Optimas digital image analysis system.

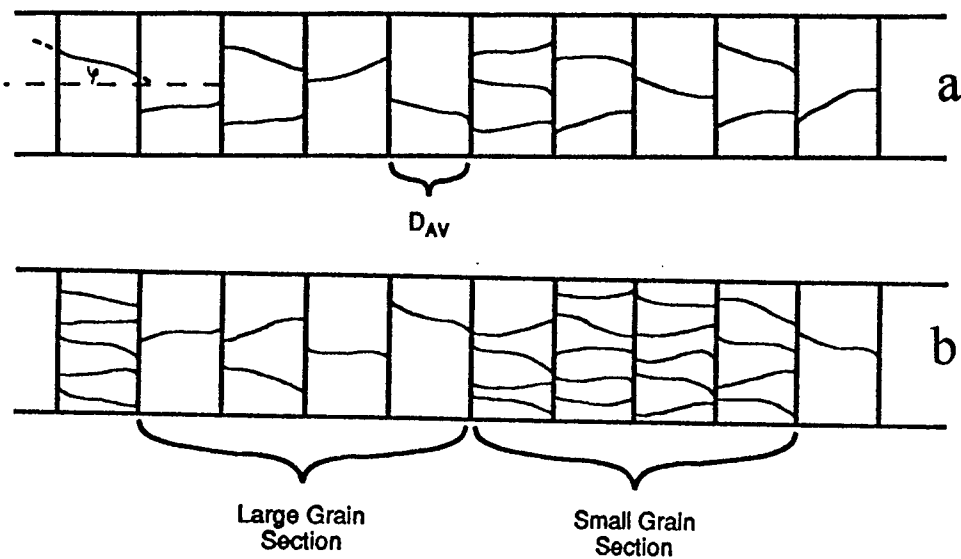
II. MODEL DEVELOPMENT

A. MICROSTRUCTURE

The microstructure and diffusion model adopted for this work is largely from the work of Harrison [1]. In this model, the metal grain sizes are assumed to be log normally distributed, with the peak of the distribution at D_{big} , full width half maximum of W_{big} , and a skew of ρ_{big} . If a bimodal distribution is used, the small grain distribution is described by D_{small} , W_{small} , and ρ_{small} . The stripe is divided up along its length into segments of width D_{av} , where D_{av} is the average of D_{big} and D_{small} . The grains are then placed into segments at random positions along the stripe, continuing to add grains to each segment (as it is randomly chosen) until the width of the stripe is reached (see Figure 1a). If a bimodal distribution is used it is assumed that the stripe consists of sections (a number of segments long) which are to be characterized by the large grain distribution, interspersed with sections which are characterized by the small grain distribution. The large grain sections are randomly scattered along the stripe, with the small grain sections filling the remaining length (see Figure 1b). This process determines the number of grain boundaries within the segment.

The interface between the metal stripe and the passivation at the sides of the stripes is also included as a grain boundary capable of passing material along the

Figure 1



stripe. This is a departure from Harrison's model. These interfaces are counted as grain boundaries primarily because of the experimental observation that, for the stripes I attempted to model, virtually all voids have an edge in common with this interface [2]. Since this is true even for the smallest voids, it seems likely that there is at least some material mobility along the interface.

Each grain boundary is assigned an angle ϕ with respect to the long axis of the stripe, and an angle θ which parameterizes the ion mobility along the grain boundary [3]. These angles are assigned randomly, within limits, except the boundaries at the interfaces, for which ϕ is zero. According to Attardo, et al [3], the mobility is proportional to $\sin(\theta/2)$ where $0^\circ < \theta < 37^\circ$, and proportional to $\sin(37^\circ/2)$ where $37^\circ < \theta < 60^\circ$.

It should be noted that, although the number of grains across the width of the stripe is determined, the model is still essentially one dimensional. The number of grain boundaries, and θ and ϕ for each boundary, are used to determine the flux divergence (the difference between the fractional mass flow into the segment boundary and the fractional mass flow out of the boundary), but the model does not monitor where across the width of the stripe the material actually flows.

Explicitly, the flux divergence, using Harrison's notation [1], is

$$\text{FLUXDIV} = \sum_i \sin(\theta_i/2)\cos\phi_i - \sum_j \sin(\theta_j/2)\cos\phi_j$$

where the summation on i is over the number of grains boundaries in the segment to the left of the segment boundary and the summation on j is over the number of grains in the segment to the right of the segment boundary, assuming mass flow from left to right.

B. DIFFUSION

The motion of material along the stripe, like the microstructure model, is largely from Harrison's work[1]. The diffusion of atoms in electromigration is assumed to obey the diffusion equation [4,5]

$$J_a = \left(\frac{ND}{kT} \right) (Force)$$

where

- J_a -- Atomic flux
- D -- Diffusion coefficient
- N -- Number density of metallic ions
- k -- Boltzmann's constant
- T -- Temperature

Following Harrison [1], let $Force = -grad(U)$ and

$$U = Z^* q V + \mu_o + kT \ln(N / N_o) + \Omega S_{nn}$$

where

- Z^* -- Effective mobile ion charge number
- q -- Electronic charge
- V -- Electrical potential
- μ_o -- Reference chemical potential
- N_o -- Equilibrium ion concentration
- Ω -- Atomic volume
- S_{nn} -- Mechanical (hydrostatic) stress

Combining these equations one gets

$$J_a = \left(\frac{ND}{kT} \right) \left[Z^* q E - (kT / N) grad(N) - \Omega grad(S_{nn}) \right]$$

where E is the local electric field strength.

It should be noted that there is no force term proportional to the local thermal gradient, which may be significant for the stripes I am trying to simulate [6]. Thermal effects are taken into account in the temperature dependence of the diffusion coefficient, the resistivity, and the thermal conductivity of the metal. Explicitly, it is assumed that

$$D = D_o \exp(-E_a / kT)$$

where

$$E_a = Q - V_a S_h$$

and

E_a -- Diffusion activation energy

Q -- Zero hydrostatic stress activation energy

V_a -- Activation volume

S_h -- Hydrostatic stress.

Likewise,

$$\rho = \rho_o [1 + \alpha(T - T_a)]$$

where

ρ -- Resistivity

ρ_o -- Resistivity at ambient temperature

α -- Temperature coefficient of resistivity

T_a -- Ambient temperature

Following Harrison [7], three sources of hydrostatic stress S_h are considered. First, there may be residual mechanical stress in the passivation. Second, there may be stresses due to the different thermal expansion rates of the various layers. Third, there may be stresses due to the local accumulation of metal.

The first, residual mechanical stress, depends on the manufacturing process of the stripes, and so must be included directly, rather than calculated. The stress due to differential thermal expansion is assumed to have the form [7]

$$S_{xx} = S_{yy} = \frac{E(\alpha' + \alpha'')\Delta T}{(1 + \nu)(1 - 2\nu)}$$

$$S_{zz} = \frac{E[(1 - \nu)\alpha'' + 2\nu\alpha']\Delta T}{(1 + \nu)(1 - 2\nu)}$$

where

$$\alpha' = \alpha_{\text{substrate}} - \alpha_{\text{metal}}$$

$$\alpha'' = \alpha_{\text{passivation}} - \alpha_{\text{metal}}$$

and

- E -- Young's Modulus of metal
- α -- Thermal expansion coefficient
- ν -- Poisson's ratio for the metal

Harrison [7] points out that if $\alpha'' \cong \alpha'$ then $S_{xx} = S_{yy} \cong S_{zz}$ and the stress is approximately hydrostatic. However, here I calculate stress due to differential thermal expansion from $S_h = (S_{xx} + S_{yy} + S_{zz})/3$, following Harrison.

The stress due to mass accumulation is assumed [7] to have the form

$$(S_h)_{mass\ accumulation} = K \left(\frac{\Delta V}{V_o} \right)$$

where K is the bulk modulus for the metal and V_o is the equilibrium volume.

For ease of computation, it is not the mass flow directly which is calculated at each step, but rather the fractional mass change -- the porosity change-- which is determined. The change in the porosity P with time is defined as

$$\frac{\partial P}{\partial t} = -\frac{1}{N} \frac{\partial N}{\partial t}$$

The negative assures that an increase in porosity corresponds to a loss of material and a decrease in porosity corresponds to a gain of material.

This can be related to the diffusion equation through the continuity equation

$$\frac{\partial N}{\partial t} = -\text{div}(J_a)$$

Combining, one gets

$$\frac{\partial P}{\partial t} = -\frac{1}{N} \left[\left(\frac{ND}{kT} \right) \text{grad}(U) \right]$$

The temperature at each time step is determined locally by assuming a steady state. The energy created by Joule heating is equal to the energy dissipated by thermal conduction. Thus, the temperature at the kth segment is determined by [1]

$$\begin{aligned} \rho J_e^2 = & \frac{K_m}{D_{av}^2} [T_k - T_{k-1}] \\ & + \frac{K_{ox}}{h_{ox} h_m} [T_k - T_a] \\ & + \frac{K_m}{D_{av}^2} [T_k - T_{k+1}] \end{aligned}$$

where

- J_e -- Local current density
- K_m -- Metal thermal conductivity
- K_{ox} -- Oxide thermal conductivity
- h_m -- Metal thickness
- h_{ox} -- Oxide thickness
- T_k -- Temperature at segment k
- T_a -- Ambient temperature

The metal thermal conductivity is assumed to follow the Wiedemann-Franz law. That is $K_m = LT/\rho$ where L is the Lorenz number, T is the local temperature and ρ is the resistivity. For aluminum I have used $2.45 \times 10^8 \text{ W}\Omega/\text{deg}^2$ for L.

For determining times to failure, it is sufficient to determine the porosity for each time step -- the easiest failure criteria to apply is simply that the stripe has failed when the porosity of any segment becomes 1.0. However, since one of the objectives of this work is to predict the distribution of void areas (which was not considered in Harrison's work), some method of turning porosities into void areas must be chosen. This has been done in two steps. First, a segment is not considered to have a void until the porosity has reached some critical porosity. The critical porosity thus becomes a free parameter. Second, once the critical

porosity has been reached, any *additional* porosity gain is correlated to a void area by

$$\frac{\Delta P}{\Delta t} = -\frac{1}{V_o} \frac{\Delta V}{\Delta t} = \frac{1}{A_o} \frac{\Delta A}{\Delta t}$$

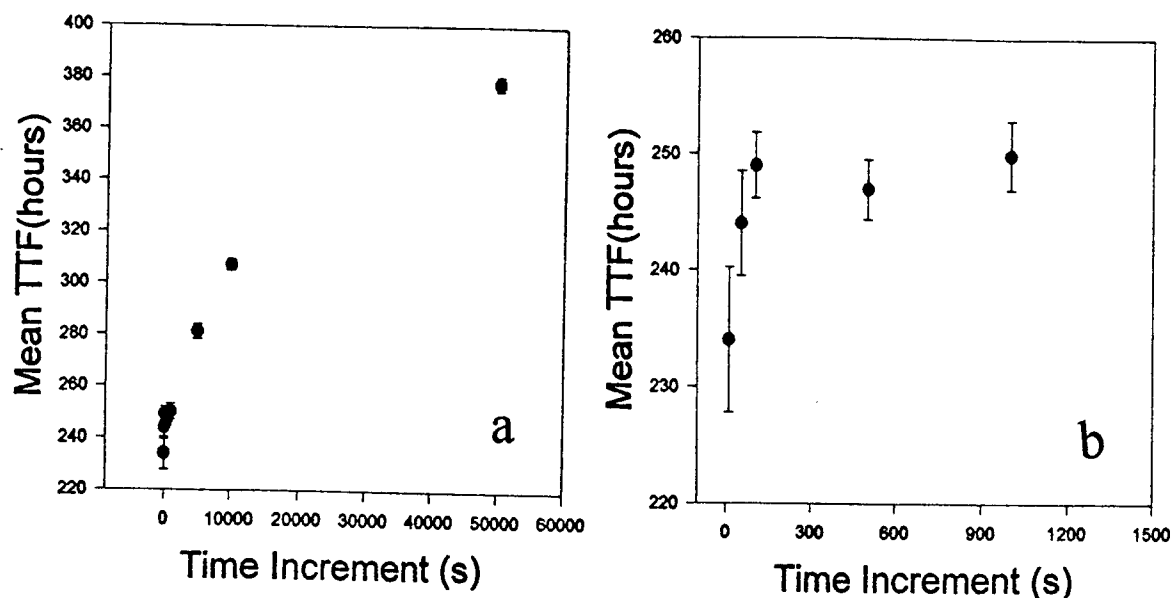
where A_o is the segment area and ΔA is the increase in the void area.

III. RESULTS

In any computer simulation it is important to verify that the results obtained are the result of the model being tested or explored, and are not artifacts of the way that the program makes the calculation. Results can vary dramatically, in particular, on the size of the time increment used in the simulation. For this model, I found that the mean times to failure varied sharply depending on the time increment (see figure 2a). The mean time to failure varies between 234 hrs at a 10 second time increment and 378 hrs at a time increment of 5×10^4 s (for a median grain size of 3.0μ and a residual stress of 100 MPa). Experimentally the mean time to failure for the stripes modeled is 200 ± 20 hrs.

The relationship between mean time to failure and the time increment used, however, is not strictly monotonic, especially at small time increments, as seen in figure 2b. This relationship may be due to two competing factors: at large

Figure 2



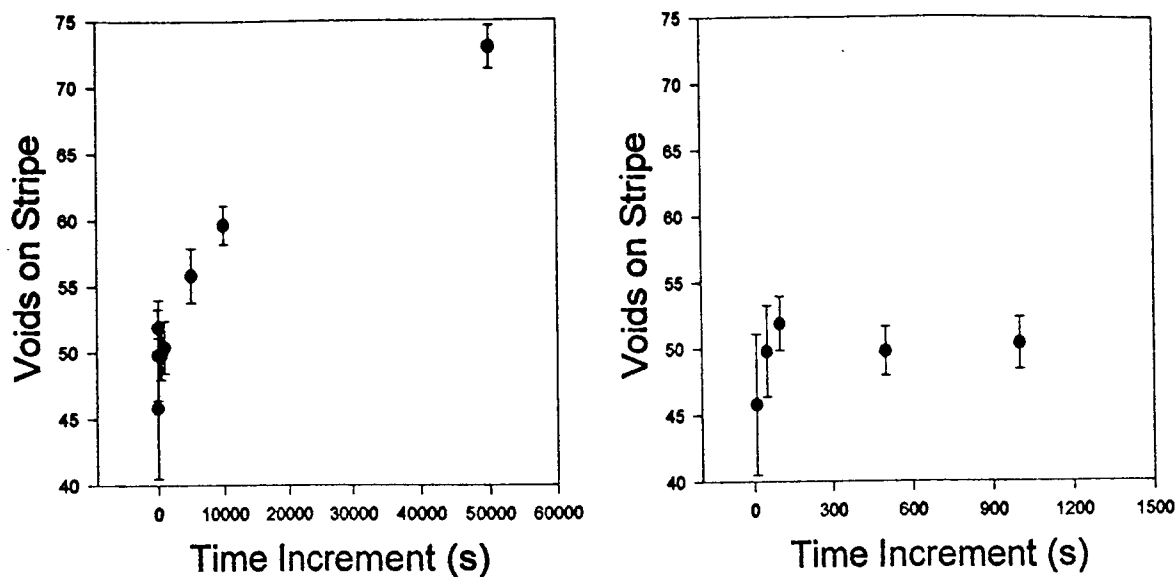
increments information is lost because one is essentially approximating the electromigration as linear in time, which it isn't. At small time increments, however, information may be lost because changes are smaller than the precision of the computer allows.

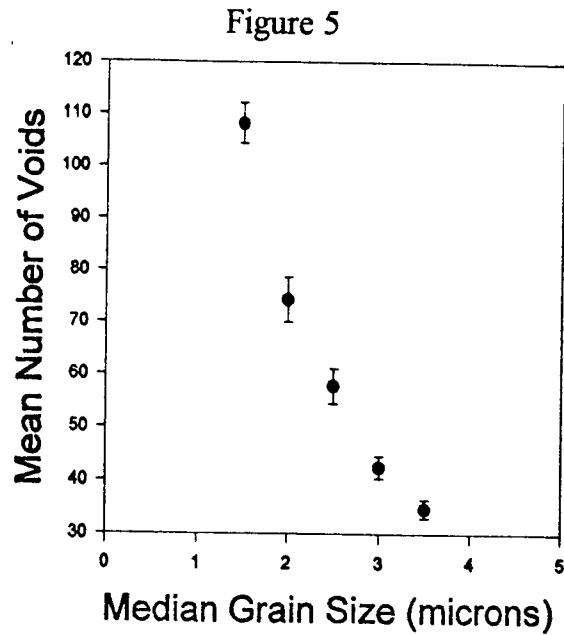
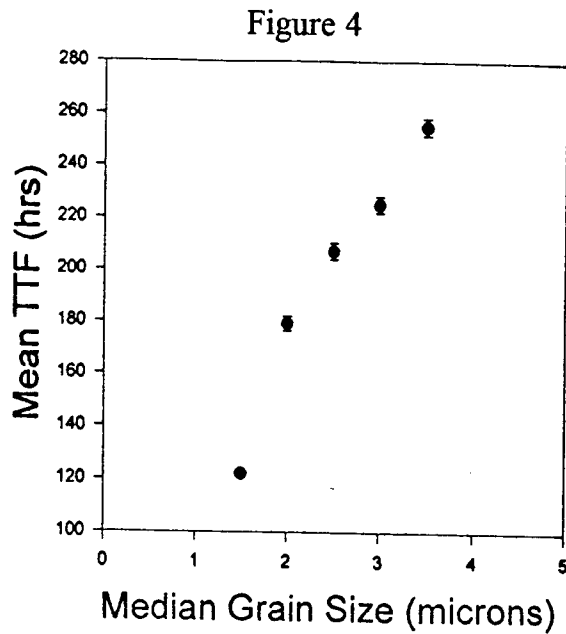
The number of voids on the stripe vary in a similar way with changing time increment, as show in figure 3 for a critical porosity of 0.30.

Reassuringly, the model predicts increasing lifetimes when the median grain size is increased, as shown in figure 4. This trend is well established experimentally by other authors. With a mean time to failure of 200 ± 20 hrs and a median grain size between 2.5 and 3.5μ , our experimental results lie close to the predicted values. Figure 5 shows that the number of voids (and also the total void area) decreased with increased grain size. The results plotted here are for a critical porosity of 0.30 at a time increment of 1×10^3 s.

It is interesting, also, to see how the plot of void area on the stripe as a function of time to failure changes with increasing grain size. These changes are shown in figure 6 (for a critical porosity of 0.30 and a time increment of 10^3 s). At larger grain sizes, the void area on the stripe does not grow as quickly with increasing time to failure. The range of times to failure also increases with greater

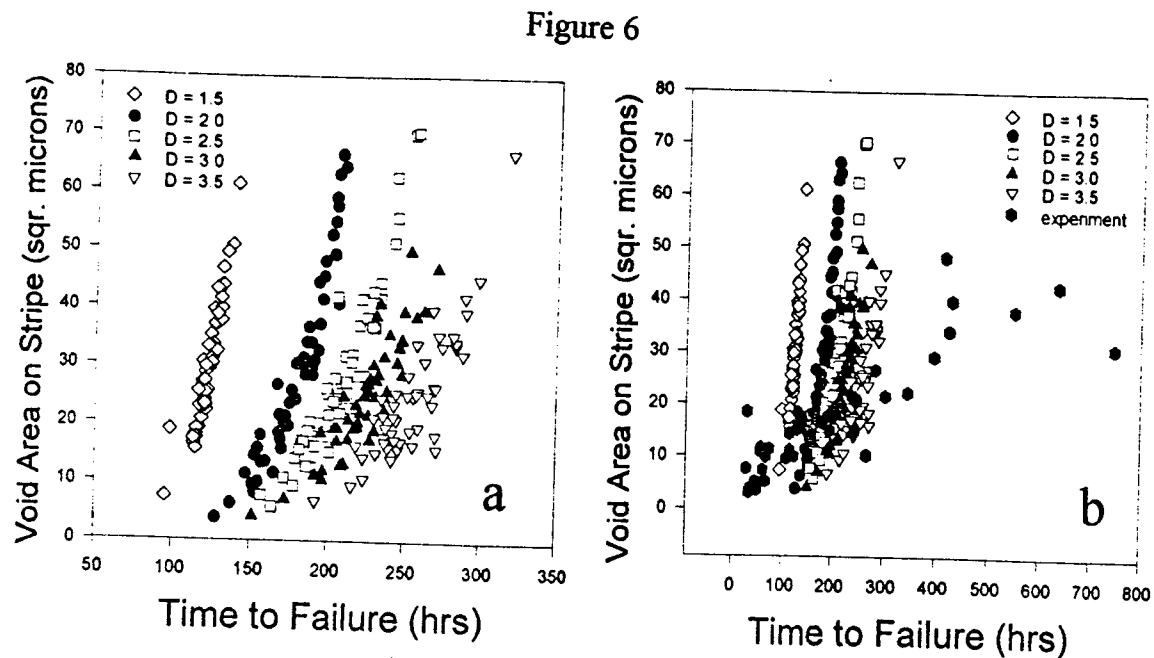
Figure 3





median grain size.

It is important to note, though, that even at the largest median grain size used the slope of the void area versus time to failure is *much* steeper than the slope found experimentally as shown in figure 6b. Although the range of the void areas is similar in experiment and simulation, the range of the time to failure is much



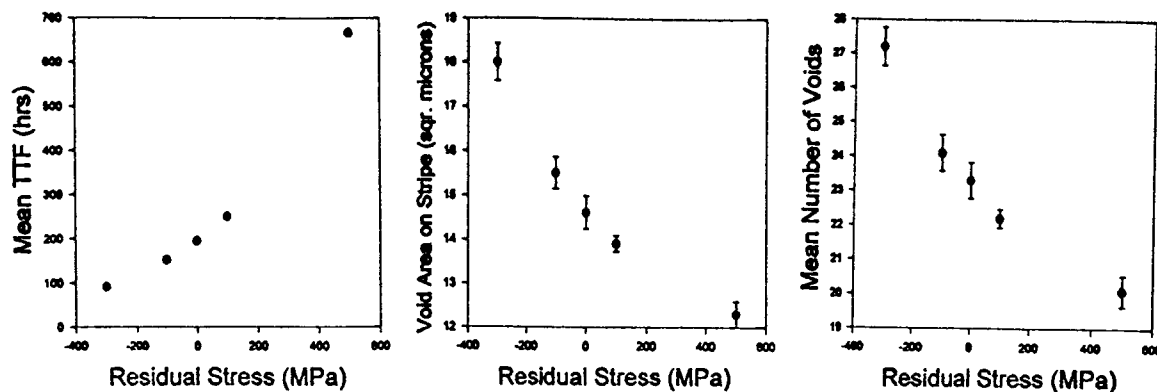
narrower in the simulation. This general result was true for *all* of the simulations run: the model simply does not predict as large a variation in time to failure as what is observed experimentally.

I also explored the changes in time to failure and number of voids with changes in the residual stress in the metallization, as shown in figure 7 (for a critical porosity of 0.45 and a time increment of 1×10^4 s). Not unexpectedly, the mean time to failure increases as the stress goes from tensile to compressive. And, correspondingly, the total void area and the mean number of voids decreases. With a residual stress of 200 MPa on the experimental stripes, a mean void area per stripe of $19 \pm 2 \mu^2$, and a mean number of voids of 28 ± 2 , the simulations appear to give results very different from the experimental. In this case, however, I think the difference is more due to the choice of critical porosity and time increment for these runs than due to a failure of the model itself.

As with increasing median grain size, increasing residual stress somewhat increases the range of the times to failure predicted and decreases the slope of the number of voids on the stripe versus the time to failure, as shown in figure 8. However, as before, the range of the times to failure of the experimental data is still much larger than the simulations, as shown in figure 8b.

One addition to the model which may make the microstructure more realistic is the possibility of flaws (in this case porosity) in the stripe before electromigration ever takes place. Here I have explored the effects both of

Figure 7



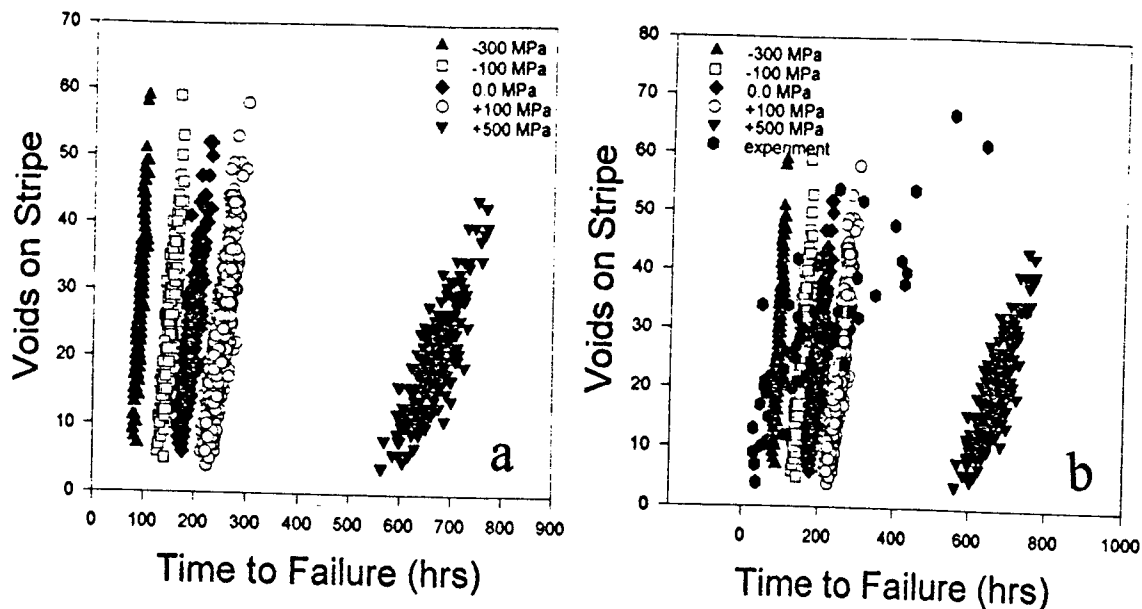


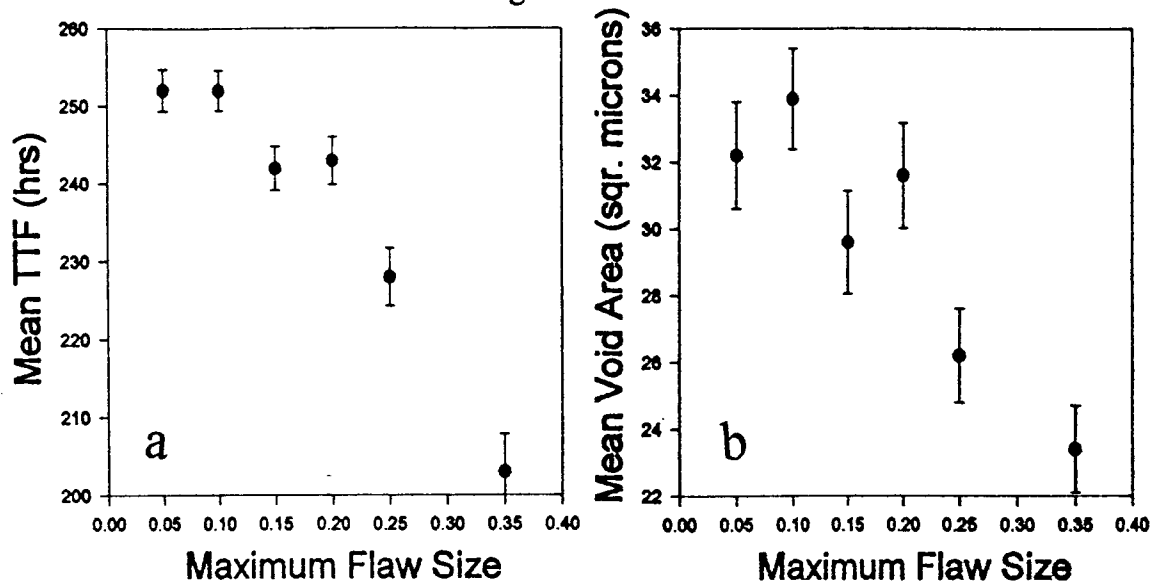
Figure 8

changing the size of the flaws and of changing the number of flaws. When flaws are included in the microstructure both the number of flaws on the stripe and the size of each flaw is chosen randomly, each up to a given limit. So changing the size of the flaws actually means changing the *maximum* size of the flaws, and likewise for the number of flaws. I found that for a maximum flaw size (porosity) of 0.05, increasing the maximum number of flaws on each stripe from 5 to one thousand resulted in only minimal changes in the mean time to failure (on the order of 5%). Changing the maximum size of the flaws had a larger influence on the times to failure.

It is important to note that even a flaw of 0.05 (ignoring critical porosity) corresponds to a void 10 times larger than the resolution limit of our experimental measurements. Furthermore, on all the 38 stripes measured, fewer than a dozen stress voids were observed on the guard stripes paralleling the electromigrated stripes. So even starting a simulation with 10 flaws of 0.05 size is probably more flawed than the experimental stripes were.

The mean time to failure and the total void area as functions of the maximum flaw size shown in figure 9. These simulations were run with a critical porosity of 0.3, a time increment of 1×10^3 s, and a maximum of 100 flaws per stripe. Not surprisingly, the mean time to failure drops with increasing flaw size. And,

Figure 9



primarily because the stripes fail sooner, the total void area on the stripe also decreases with increasing flaw size.

Whereas median grain size, residual stress, and maximum flaw size may be assessed experimentally, the critical porosity is truly a free parameter. Both the experimental value for mean number of voids per stripe (28 ± 2) and the mean void area per stripe ($19 \pm 2 \mu^2$) suggest a critical porosity between 0.35 and 0.40 (see figure 10). However, comparing the experimental distribution of void areas

Figure 10

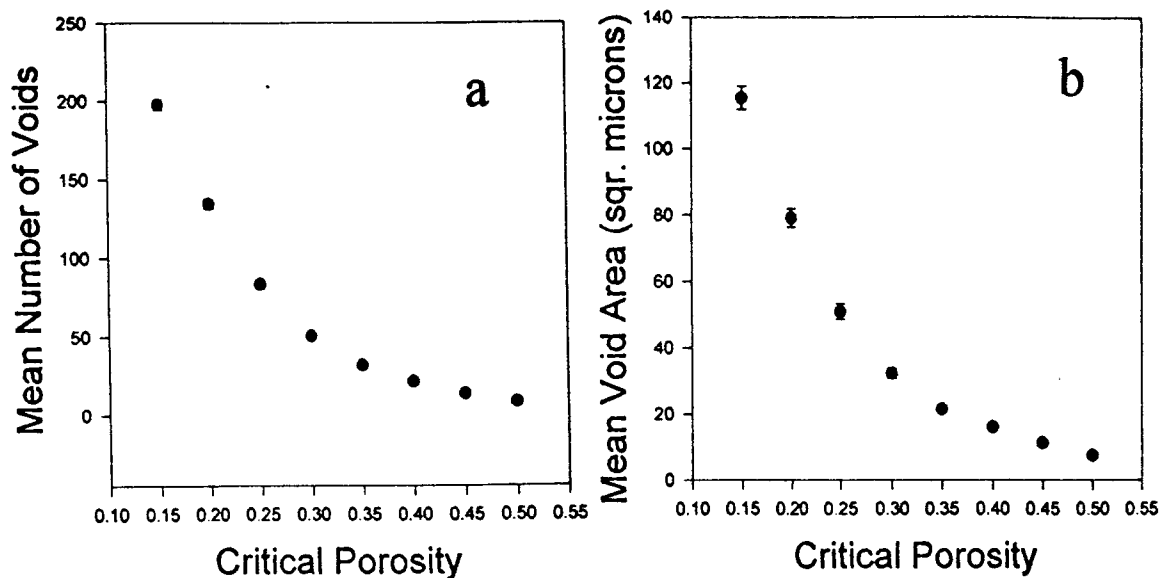
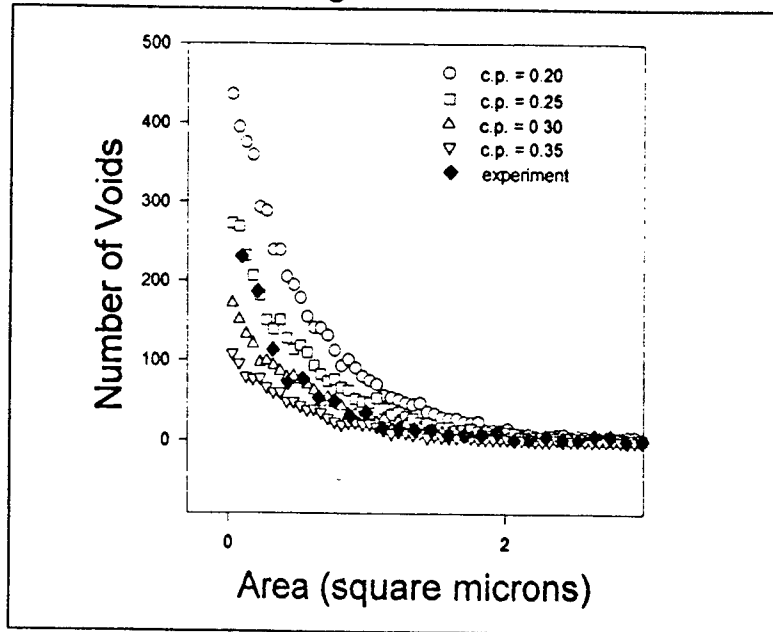


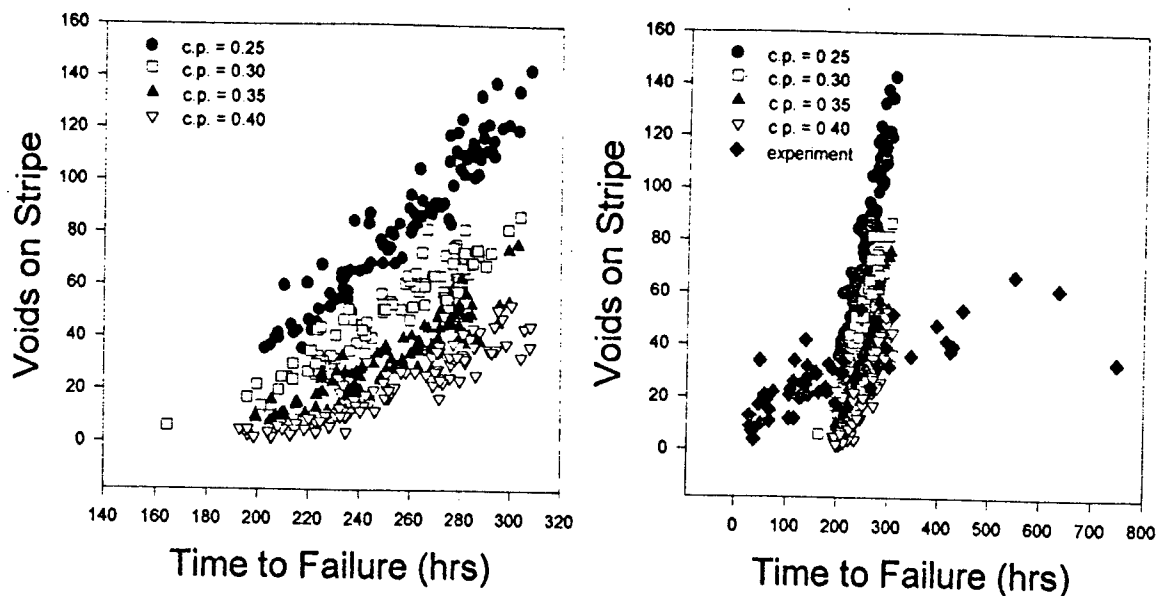
Figure 11



with simulations at different critical porosities (see figure 11) suggests a critical porosity between 0.25 and 0.30. It is actually rather surprising that the distribution of void areas (here normalized to the number of stripes simulated) can be fit as closely with only one truly free parameter.

Changing the critical porosity does not affect the mean time to failure, but it does affect the slope of the number of voids per stripe versus the time to failure, as seen in figure 12a. The slope decreases with increasing critical porosity. None the less, as with the median grain size and residual stress, all of the slopes are steeper than the experimental results, as seen in figure 12b. These simulations were done with a median grain size of 3.0μ and a time increment of 1×10^3 s.

Figure 12



IV. CONCLUSIONS

Although the agreement between the model predictions and the experimental results is by no means exact, the model does predict reasonable times to failure, numbers of voids, and void area distributions with very few free parameters. The model correctly predicts some well documented trends, such as increasing lifetimes with increasing grain sizes. The model does *not* adequately predict the *range* of times to failure. The range of times to failure from the simulations is consistently five to ten times smaller than the experimental range. A more sophisticated model for the microstructure may help provide more variability in the times to failure.

ACKNOWLEDGEMENTS

I would like to express my appreciation for the computer support, helpful conversations, and many insightful ideas which I've recieved from the generous people of the Reliability Physics Branch in the Electromagnetics Reliability Division of Rome Laboratory.

REFERENCES

- [1] James W. Harrison, Jr., IEEE Trans. on Electron Devices, **35** (1988) 2170.
- [2] Yolanda J. Kime and Peter Grach, Mat. Res. Soc. Symp. Proc. (1994) to be published.
- [3] M.J. Attardo, R. Rutledge, and R.C. Jack, J. Appl. Physics., **42** (1971) 4343.
- [4] R.V. Penney, J. Phys. Chem. Solids, **25** (1964) 335.
- [5] H.B. Huntington and A.R. Crone, J. Phys.Chem. Solids, **20** (1961) 76.
- [6] M.W. Levi and J.B. Mattila, Proceedings VMIC Santa Clara, June 1993, p258
- [7] James W. Harrison, *User's Manual for EMSIM*, (1991)

SEMICONDUCTOR CYLINDER FIBERS FOR FIBER LIGHT AMPLIFIER APPLICATIONS

by
Professor
Philipp Kornreich
DEPARTMENT OF ELECTRICAL AND COMPUTER ENGINEERING

Syracuse University
Syracuse, N. Y. 13244

Final report for:
Summer Faculty Research Program
Photonics Center of Rome Laboratories

Sponsored by:
Air Force Office of Scientific Research
Bolling Air Force Base, D. C.

and

Photonics Center of Rome Laboratories

August 1994

SEMICONDUCTOR CYLINDER FIBERS FOR FIBER LIGHT AMPLIFIER APPLICATIONS

Philipp Kornreich

Professor

DEPARTMENT OF ELECTRICAL AND COMPUTER ENGINEERING

Syracuse University

ABSTRACT.

We have measured the transmission spectrum of two type of Semiconductor Cylinder Fibers (SCyFs) at the Photonics Center of Rome Laboratories. These devices were fabricated by Syracuse University. The fiber preforms and SCyFs with CdTe and CdS semiconductor cylinders were tested. We have shown that the semiconductors survive the fabrication process. A number of fibers of each kind were tested with reproducible characteristics.

SEMICONDUCTOR CYLINDER FIBERS FOR FIBER LIGHT AMPLIFIER APPLICATIONS

Philipp Kornreich

INTRODUCTION

We have tested the transmission spectra of Semiconductor Cylinder Fibers (SCyFs) that were fabricated at Syracuse University. These results will be submitted for review for publication in "Photonics Letters" This report except for a modified introduction contains the text of the submitted publication. The SCyFs consist of a glass core surrounded by a thin semiconductor cylinder. The semiconductor cylinder, in turn, is surrounded by a glass cladding, see Fig. 1. A number of each type of fiber were fabricated by Syracuse University and tested at the Photonics Center of Rome Laboratories. To date we have used two semiconductors CdTe and CdS. Spectral measurements at the Photonics Center of Rome Laboratories showed that both types of semiconductors survived the fiber fabricating process. The fibers had reproducible characteristics.

Semiconductor Micro crystals¹ (SM) in glass are a predecessor of this technology. SMs have a large number of surface states at their interfaces with the host glass. These interface states are responsible for non radiative recombinations in SMs. There are techniques available to substantially reduces the non radiative recombination in SCyFs.

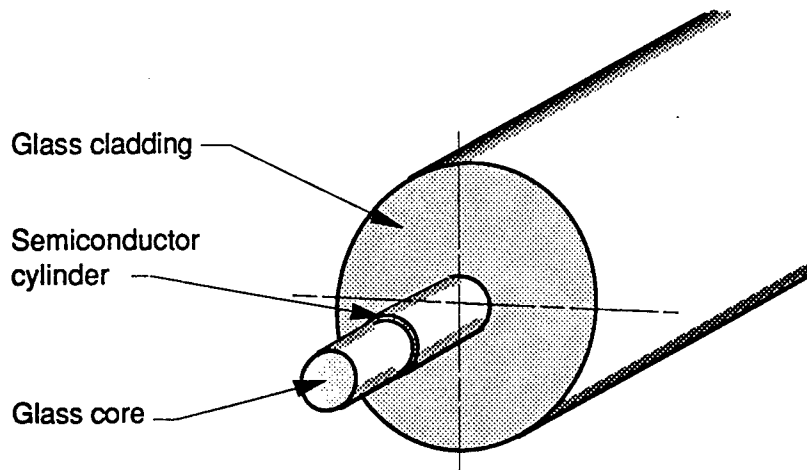


Fig. 1. Typical SCyF construction. The device consists of a glass core surrounded by a semiconductor cylinder. The semiconductor cylinder, in turn, is surrounded by a glass cladding.

An application of these devices is as Semiconductor Cylinder Fiber Light Amplifier (SCyFLA) for fiber optic communication. Another application is as non linear devices. An application that is probably much farther in the future is to develop fiber bundle plates consisting of SCyFLAs that operate in the visible spectrum and are electrically pumped. These devices could be used as true eye glass light amplifiers. The Micro Channel Plates that are used in current night vision devices are not true light amplifiers. The viewer observes a fluorescent screen rather than the actual amplified image.

A competing technology are Rare Earth doped glass Fiber Light Amplifiers² (REFLA). Since there are a great variety of semiconductors that can be used, SCyFLAs can be tailored to work at a large range of wavelengths. Unlike rare earth doped FLAs the SCyFLAs are broad band and thus capable of amplifying broad band Wavelength Division Multiplexed light signals.

SCyF FABRICATION

The SCyFs were fabricated by, first, vacuum depositing a direct band gap semiconductor, CdTe or CdS, film on a rotating Pyrex glass rod in a diffusion pumped vacuum system. The vacuum deposited semiconductor film was probably of poor quality since the glass rods could not be heated during deposition. A Pyrex glass was selected that has a softening temperature of 650 °C. This is lower than the melting points of 935 °C of the CdTe and 1400 °C of CdS semiconductors.

Next, the semiconductor coated glass rod was inserted into a Pyrex glass tube that has been closed at one end. This structure is evacuated and collapsed. N₂ is used as the residual gas in the evacuation process. Finally, a fiber is pulled from the resulting preform.

EXPERIMENTAL RESULTS

Several fibers with approximately 50 Å thick CdTe semiconductor cylinders and CdS semiconductor cylinders have been tested. These fibers had approximately 70 μm diameter Pyrex glass cores and 140 μm diameter Pyrex glass claddings. Material availability restricted us to use glass with the same index of refraction for both the core and cladding. Nevertheless, our test indicated that light was guided in the core by the semiconductor cylinder.

The CdS films were a yellowish gray when first deposited on the core glass rods of the preform indicating that they were Cd rich. However, when the cladding tube was collapsed onto the CdS cylinder at about 650 °C they turned bright yellow. Indeed, a spectrum analysis of the CdS preform showed that it had a sharp absorption edge at 514 nm exactly as predicted.

The transmission spectrum of CdTe fiber sections about 20 mm in length and CdS fiber sections about 150 mm in length have been measured. Samples were used from several fibers with identical results. Measurements were performed at the Photonics Center of Rome Laboratories using an Ando type AQ 1425 spectrum analyzer connected to an Apple "Power Book" computer. The computer used "Lab. Window" software to both control the spectrum analyzer and to record the data. The CdTe fibers exhibit an absorption edge at 830 nm, see Fig. 2. This corresponds to the absorption edge of bulk CdTe. The transmission spectrum of one of the preforms was also measured. It too exhibited an absorption edge at 830 nm. A small quantum size effect was predicted for the fibers. That is, we expected the fibers to have an absorption edge at a wavelength somewhat shorter than the absorption edge wavelength of bulk CdTe in the preforms. This was not observed. We suspect that surface

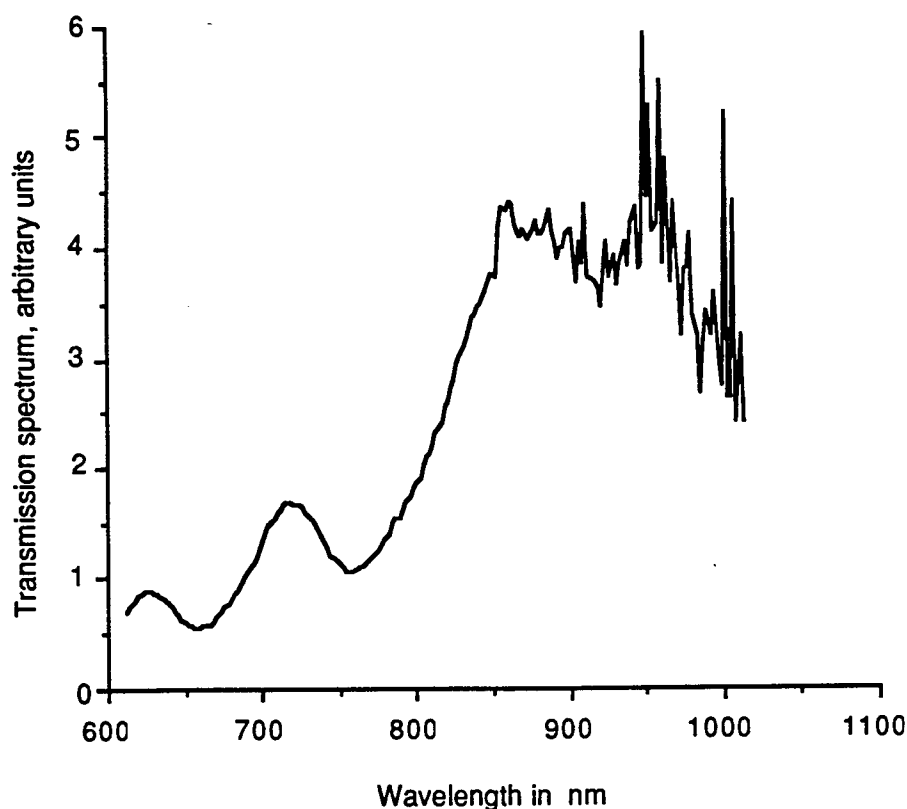


Fig. 2. Typical transmission spectrum of CdTe cylinder fiber with white light illumination. The data was normalized to a fiber without semiconductor cylinder. The spectrum was normalized using a Pyrex fiber with no semiconductor cylinder. A resolution of 10 nm was used.

states counteracted the quantum size effect. There is also considerable strain in the semiconductor film. The CdS fibers exhibit a steep absorption edge at 514 nm, see Fig. 3. This corresponds to the absorption edge of bulk CdS. The absorption spectrum of one of the preforms was also measured. It too exhibited an absorption edge at 514 nm. Again, a small quantum size effect was predicted for the fibers. This was, also, not observed. All measurements were performed at room temperature.

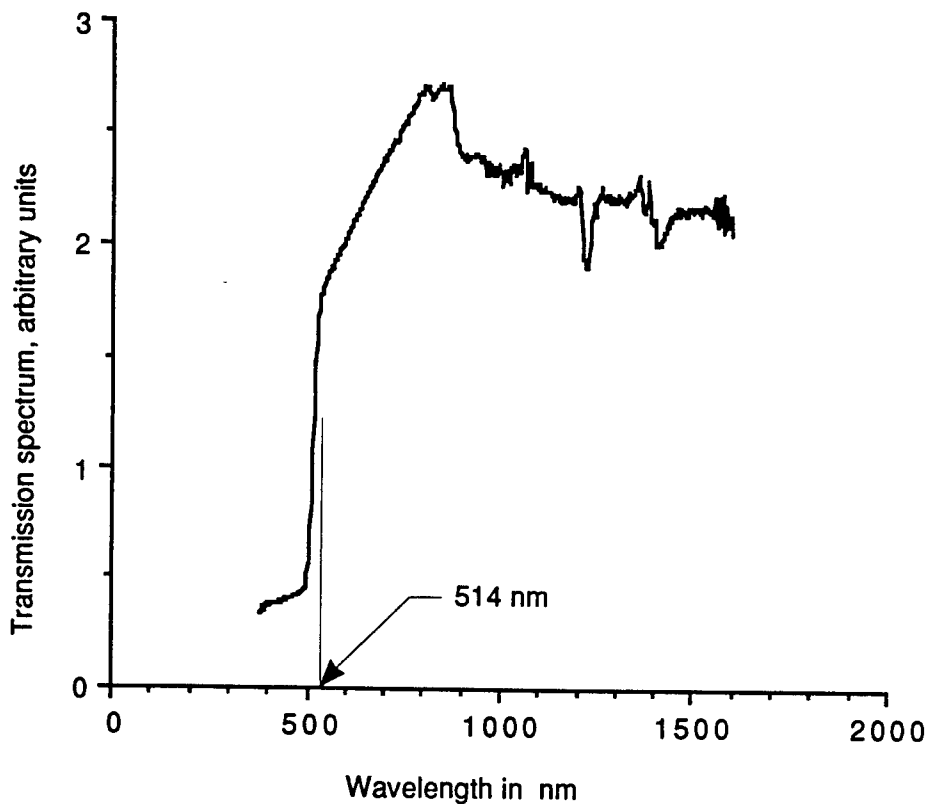


Fig. 3. Typical transmission spectrum of CdS cylinder fiber. A resolution of 10 nm was used to obtain this data.

From the above data we conclude that the semiconductors indeed survive the fiber fabricating process.

MECHANISM OF CHARGE CARRIER LIGHT INTERACTION

One can illustrate the interaction of the charge carriers in the semiconductor cylinder with the light electromagnetic field near the core cladding interface as follows: The transverse elec-

tric field of the light will induce a current with current density J in the thin semiconductor film see Fig. 4. The current depends on the charge carrier density in the semiconductor. This current density induces a discontinuity of the longitudinal magnetic flux density B at the core cladding interface. This requires that there be a mode propagating in the fiber with an electric field that does not go to zero at the core cladding interface.

The interaction between the light and the charge carriers in the semiconductor cylinder can be illustrated by an analysis of the propagation of the TE_{10} mode in a SCyF. Rather than performing the calculations in terms

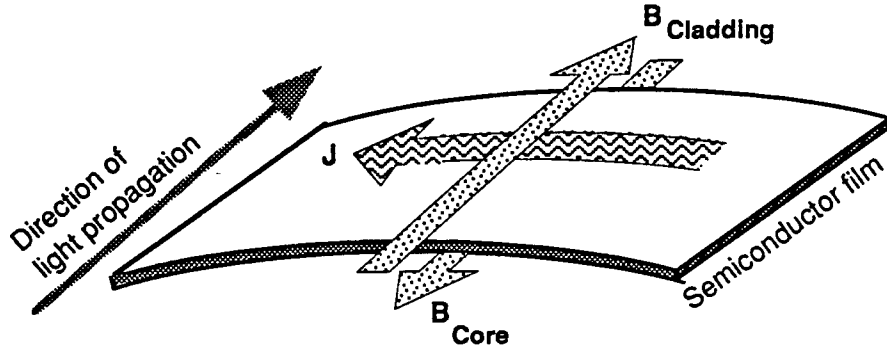


Fig. 4. The transverse light electric field induces a current with current density J in the thin semiconductor film. The current depends on the charge carrier density. The current density induces a discontinuity of the longitudinal magnetic flux density B at the core cladding interface.

of the conductivity at light frequencies of the semiconductor cylinder we use the imaginary part of the dielectric constant ϵ_I which is related to this conductivity. The dispersion relation of the TE_{10} mode of a step index fiber with a semiconductor cylinder having an imaginary (lossy) part of the dielectric constant ϵ_I can be obtained in a way similar to the derivation of the dispersion relation of the TE_{10} mode of a conventional step index fiber³.

$$\frac{uJ_0(ub)}{J_1(ub)} + j\frac{4\pi^2\epsilon_I a}{\lambda^2} + \frac{wK_0(wb)}{K_1(wb)} = 0 \quad (1)$$

where the solutions of the wave equations in the core and cladding yield:

$$\text{a) } k^2 + u^2 = \frac{4\pi^2 n_1^2}{\lambda^2} \quad \text{and} \quad \text{b) } k^2 - w^2 = \frac{4\pi^2 n_2^2}{\lambda^2} \quad (2)$$

k is the complex propagation constant of the TE_{10} mode, b is the core radius, a is the semiconductor cylinder thickness, and n_1 and n_2 are the indices of refraction of the core and cladding respectively.

By solving the dispersion relations for the real part β of the propagation constant k we obtain a result identical to the dispersion relation of the TE_{10} mode of a simple step index fiber as it appears in the literature³.

$$\frac{u_0 J_0(u_0 b)}{J_1(u_0 b)} + \frac{w_0 K_0(w_0 b)}{K_1(w_0 b)} = 0 \quad (3)$$

where u_0 and w_0 are the real parts of the transverse propagation constants u and w . The imaginary part α of the propagation constant k can be obtained by expanding equation 4.1 to first order in small quantities and making use of equations 4.2a, 4.2b, and 4.3. Here α is the gain coefficient.

$$\alpha = \frac{\beta^2 \frac{\lambda^2}{4\pi^2} - n_2^2}{\beta^2 \frac{\lambda^2}{4\pi^2} - \frac{n_1^2 + n_2^2}{2}} \frac{J_1^2(u_0 b)}{J_0^2(u_0 b)} \frac{2\pi^2 \epsilon_1 a}{\lambda^2 b} \quad (4)$$

Note that β and u_0 are wavelength dependent. Since both u_0 and w_0 must be real we observe from equations 4.2 that the real part of the propagation constant β must have values between two narrow limits:

$$n_2^2 \leq \beta^2 \frac{\lambda^2}{4\pi^2} \leq n_1^2 \quad (5)$$

In order for the gain coefficient to be non zero the first order Bessel functions $J_1(u_0 b)$ must be non zero at the core radius b for this mode.

The result obtained in equation 4.4 can not be directly compared to the experimental results since the fibers used in the experiments had 70 μm diameter cores through which a multitude of modes propagated.

REFERENCES

1. N. Peyghambarian, S. H. Park, S. W. Koch, A. Jeffery, J. E. Potts, and H. Ceng, Applied Physics Letters Vol. 52 pp 182, (1988).
2. B. J. Ainslie, S. P. Craig-Rayan, S. T. Davey, J. R. Armitage, C. G. Atkins, J. F. Massicott, and R. Wyatt "Erbium Doped Fibers for Effective Optical Amplifications" IEE Proceedings, Vol. 137 J pp. 205-208, (1990).
3. For example: "Optical Fiber Communications" by Gert Keiser, 2nd edition McGraw-Hill Book Co. Inc. ISBN 0-07-033617-2

SELF-PULSATION AND OPTOELECTRONIC FEEDBACK-SUSTAINED
PULSATION OF LASER DIODES AT 1300 NM

Guifang Li
Assistant Professor
Department of Electrical Engineering

Rochester Institute of Technology
1 Lomb Memorial Drive
Rochester, NY 14623

Final Report for:
Summer Faculty Research Program
Rome Laboratory

Sponsored by:
Air Force Office of Scientific Research
Bolling Air Force Base, DC

and

Rome Laboratory

August 1994

SELF-PULSATION AND OPTOELECTRONIC FEEDBACK-SUSTAINED PULSATION OF LASER DIODES AT 1300 NM

Guifang Li
Assistant Professor
Department of Electrical Engineering

Abstract

Transient self-pulsation has a lifetime of a few minutes with frequencies up to 7 GHz. The linewidth of self-pulsation is on the order of 0.5 GHz. With optoelectronic feedback, the transient self-pulsation can be stabilized and enhanced. The center frequency of feedback-sustained pulsation is dependent on the passband of the bandpass filter in the feedback loop. The linewidth of feedback-sustained pulsation is significantly reduced to about 20 kHz. The optical spectra of the laser diodes exhibit coherence collapse at weak optoelectronic feedback. The feedback sustained pulsation can be frequency modulated. Applications of the feedback-sustained pulsation include subcarrier multiplexing optical networks.

Self-sustained pulsation (SSP) is a well-known dynamic process in laser diodes [1]. It has been extensively studied both experimentally and theoretically [2,3,4]. The majority of these previous experiments has been conducted in 780 nm laser diodes. SSP was first considered to be a nuisance and there were efforts aimed at reducing or eliminating SSP. It was realized later on that SSP laser diodes have low relative intensity noise (RIN) because of short coherence length which reduced the effects of optical feedback into the laser diodes. SSP laser diodes have also been proposed for use in all-optical clock recovery [5]. Recently, a promising new application has emerged in which SSP would be used as subcarriers for lightwave communication networks [6]. Both analog (up to 1 GHz) [7] and digital (up to 800 Mb/s) [8,9] transmission using SSP subcarriers have been reported. Subcarrier-multiplexing (SCM) not only is compatible with wavelength-division multiplexing (WDM) but also can extend the capacity of WDM networks [10]. As a result, WDM-SCM networks are of particular interest for local area networks (LAN) where pure WDM may not be able to provide a large number of nodes. It is therefore important to generate microwave subcarriers in laser diodes at wavelengths other than 780 nm. This letter describes SSP, transient self-pulsation (TSP), and the generation and frequency modulation of feedback-sustained pulsations (FSP) in laser diodes at 1300 nm.

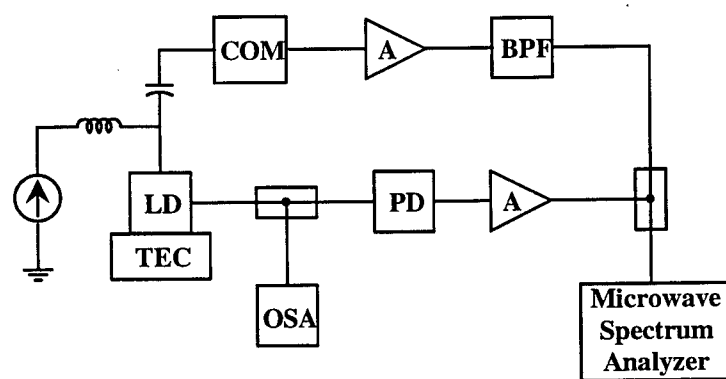
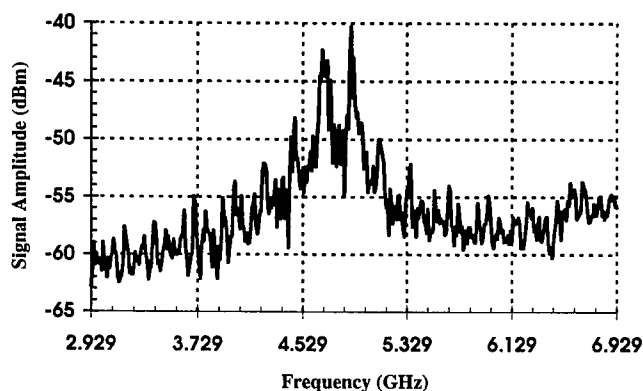
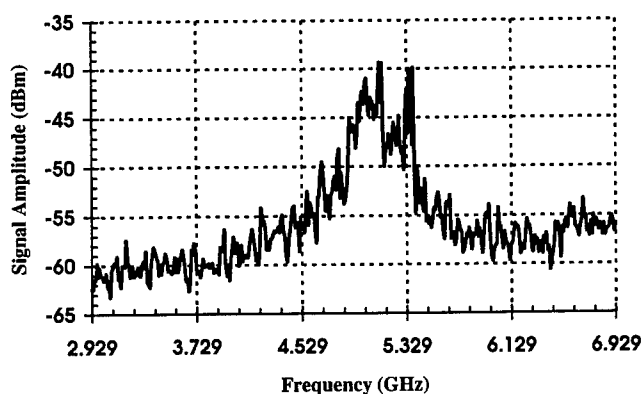


Fig. 1 Schematic of the experimental setup for studying SSP, TSP and FSP.

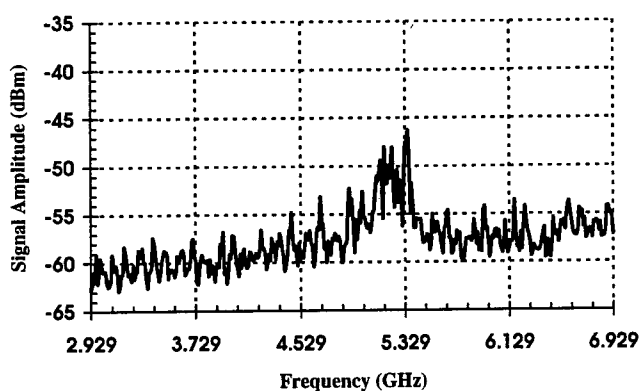
The schematic of the experimental setup is shown in Fig 1. The pulsations were observed in Mitsubishi Electric ML7011R InGaAsP single-mode (pigtailed) laser diodes (LD). The emission wavelength of these laser diodes is near 1300 nm with typical cw output powers of 5 mW. The laser diode is temperature stabilized to 20⁰ C using a thermal electric cooler (TEC). The pigtailed fiber from the laser diode is fusion spliced to a 3dB bi-directional fiber coupler. Half of the laser output was used for monitoring the optical spectrum using an Anritsu MS9001B1 optical spectrum analyzer (OSA). The other half of the laser output was used as a feedback into the laser diode through an optoelectronic feedback loop. The first component in the optoelectronic feedback loop is a photodetector (PD) which converts laser light pulsations into microwave oscillations. The microwave oscillation signal is pre-amplified using a Miteq 18-GHz wideband low-noise amplifier. The amplified signal is split into two parts using an rf power splitter. Half of the rf power was used for monitoring the spectrum of the microwave oscillations using a HP 8593E microwave spectrum analyzer. The second half of the pre-amplified signal was fed into the laser diode through the ac port of the bias tee via a bandpass filter (BPF), another wideband amplifier and a microwave power combiner (COM). The other input port of the COM was used for modulating signals.



(a)



(b)



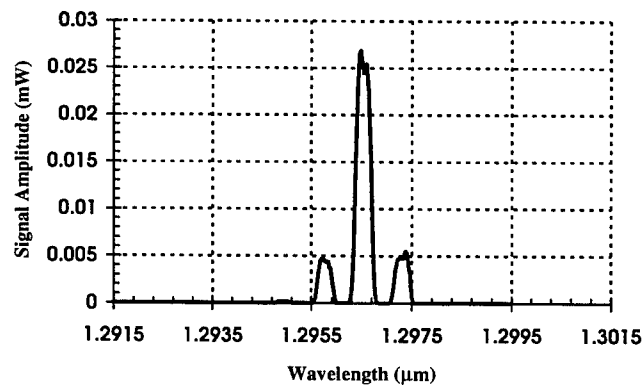
(c)

Figure 2 Microwave spectra of (a) SSP at a bias current of 20 mA, (b) TSP at a bias current of 21 mA immediately after turn on, and (c) same as (b) 35 seconds after turn on.

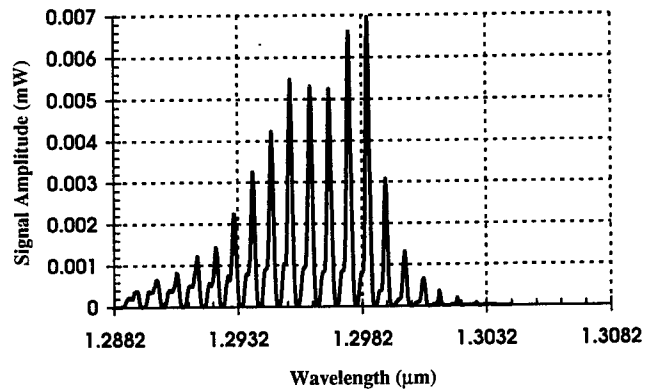
Self-pulsations in the laser diodes (with the feedback being turned off) fall into two categories, SSP and TSP. The laser intensity pulsations observed in this experiment are predominantly transient in nature. SSP only occurs within a very small range of bias current. The frequency range of the self-pulsation is between 2.0 GHz to 7.0 GHz. All laser diodes we have examined showed qualitatively similar pulsation behavior. For example, a particular laser diode exhibited self pulsation for bias currents

between 17.0 and 32.0 mA with pulsation frequencies ranging from 3.5 GHz to 6.5 GHz. However, self-sustained pulsation only occurs for bias current values near 20 mA. The microwave spectrum of the SSP at a bias current of 20 mA is shown in Fig. 2a. Self-pulsation for other bias current were transient, in which the intensity pulsation occurred as soon as the laser diode was turned on or turned to a different bias current. Transient self-pulsations typically only lasted for 1 to 3 minutes. Fig 2b shows the microwave spectrum of the TSP immediately after the laser diode was turned on with a bias current of 21.0 mA. The linewidth of the self-pulsation is very broad and is on the order of 0.5 GHz. The microwave spectrum 35 seconds after the laser was turned on is shown in Fig. 2c. The magnitude of the self-pulsation reduced significantly in 35 seconds. The TSP disappeared in about 45 seconds.

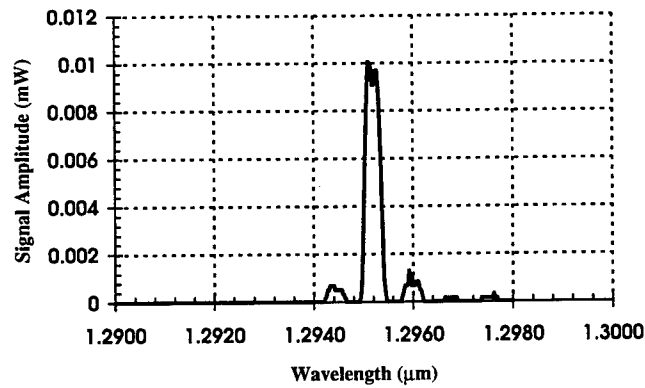
Optoelectronic feedback has been used previously work to reduce the linewidth of SSP [6,7]. In this experiment, optoelectronic feedback was used to stabilize the TSP. We found that optoelectronic feedback indeed stabilized the pulsations. Furthermore, the linewidth of FSP was also significantly reduced compared to that of the TSP. However, the center frequency of the FSP (nearly identical to that of the BPF) was mainly determined by the passband of the bandpass filter. The frequency of FSP can therefore be tuned by the BPF. In addition, the frequency of FSP with a fixed BPF can be fine tuned by laser diode bias current. This fine-tune range was about 45 MHz. Along with the generation of FSP with optoelectronic feedback were changes in the optical spectrum of the laser light.



(a)



(b)



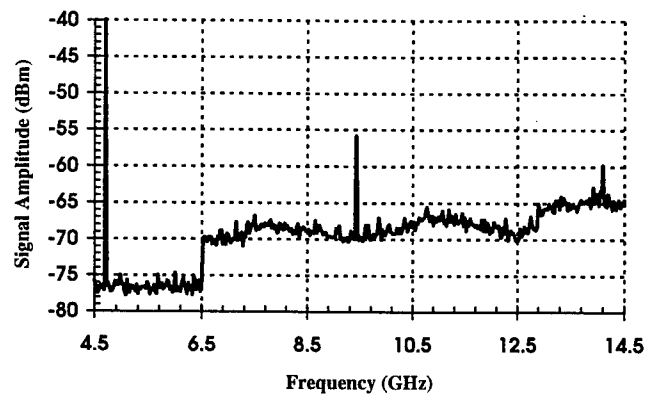
(c)

Figure 3 Optical spectra of laser output for (a) free running condition, (b) weak optoelectronic feedback, and (c) strong optoelectronic feedback.

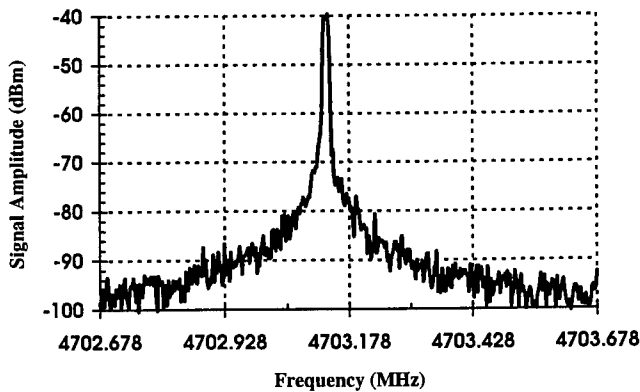
We first present the optical spectra of the laser output with and without feedback. The laser diodes used in this experiment is single mode. The spectrum of a free running laser diode in the TSP regime is shown in Fig. 3a. There existed occasional mode hopping. In this particular spectrum the two side modes were about 7dB down from the main mode. Almost all the optical power was contained in a wavelength span of about 2.0 nm. Optoelectronic feedback can significantly affect the optical spectrum of

the laser diode output. Figure 3b is the optical spectrum of the laser output when the feedback was slightly above a threshold value for stable FSP. Now the wavelength span is about 15 nm. This is very similar to the coherent collapse observed in laser diode with external optical feedback [11]. As the feedback was increased beyond a critical value, the optical spectrum, shown in Fig. 3c, switched into a form that more resembled that of the free running laser diode except for a few additional very weak side modes. It is worth mentioning that "strong" and "weak" feedback here are only qualitatively defined since the bias tee is not broadly matched to the laser diode and, as a result, it was not possible to easily estimate the extent of reflection of the feedback signal.

Now we present the electrical characteristics of the FSP. As mentioned earlier, the frequency of the FSP is predominantly determined by the passband of the bandpass filter. With a BPF of center frequency 4.68 GHz and 10% passband, the microwave spectrum of the FSP is shown in Fig. 4a. The fundamental frequency of the FSP is 4.70 GHz. High-order harmonics are also present in the FSP signal but are of lower amplitudes. The second harmonic is 20 dB below the fundamental harmonic. The linewidth of FSP is very narrow as can be seen in Fig. 4b which is a close-up look of the fundamental peak in the FSP signal.



(a)



(b)

Figure 4 Microwave spectra of FSP, (a) all harmonics and (b) fundamental harmonic only.

When a modulating signal is applied to the laser diode, the frequency of FSP is modulated by the applied modulating signal. Figure 5 shows the spectrum of the frequency modulated FSP signal. The carrier is the 4.70 GHz FSP and the modulating signal is a 200 MHz sinusoid. Eight sidebands are observed. The uneven first sidebands signifies residual amplitude modulation. This is expected because the laser output power is also dependent on the bias current. Frequency modulation of FSP by signals of frequencies exceeding 500 MHz have been demonstrated in the experiment. This FM signal can be demodulated using standard FM demodulators such as the delay line demodulator. We have achieved a signal-to-noise ratio of about 30 dB. The details of communication links and networks using FSP will be presented elsewhere.

In conclusion, we report the observation of self-sustained pulsation and transient self-pulsation in 1300 nm laser diodes. The mechanism for SSP is generally believed to be the formation of periodic orbits due to Hopf bifurcation in the laser diode nonlinear dynamics [6]. Transient self-pulsations have not been reported before. The origin of TSP is still under investigation. Although TSP is similar to the relaxation

oscillation [12], the transient time of minutes for TSP is much longer than typical relaxation oscillation time. With optoelectronic feedback, TSP and SSP turn into stable FSP which can be used as high-frequency tunable microwave subcarriers at 1300 nm. For WDM-SCM applications, it is important to provide sufficient optoelectronic feedback so that the optical spectrum of the laser output remains narrow. Even though FSP can be frequency modulated to very high frequencies (>500 MHz), the peak frequency deviation is within 45 MHz. We are currently investigating methods for achieving larger peak frequency deviation/modulation index for improved signal-to-noise ratios.

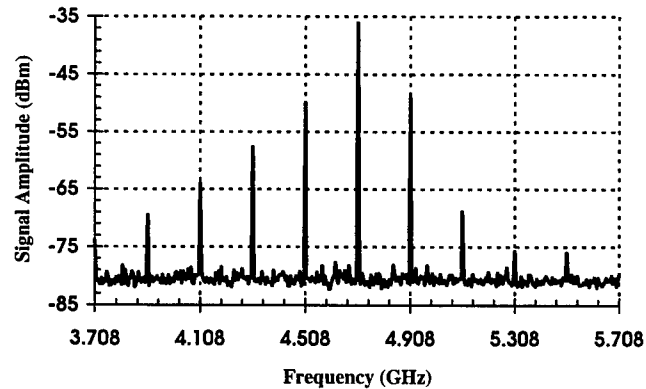


Figure 5 Microwave spectrum of a 4.7 GHz FSP frequency modulated by a 200 MHz sinusoidal signal.

Acknowledgment

I would like to thank Ray Boncek, Jim Cusack, and Andy Pirich of Rome Laboratory Photonics Center for their hospitality during the course of the summer research program. Technical support from Dave Grucza and Dave Sackett is greatly appreciated. Brimrose Corporation of America of Baltimore, MD provided some of the equipment for this project.

References

1. T. L. Paoli and J. Ripper, "Optical pulses from cw GaAs injection lasers," *Appl. Phys. Lett.* **15**, 105-107 (1969).
2. J. P. van der Aiel, J. L. Merz, and T. L. Paoli, "Study of intensity pulsations in proton-bombarded strip-geometry double-heterostructure $\text{Al}_x\text{Ga}_{1-x}\text{As}$ lasers," *J. Appl. Phys.* **50** (7), 4620-4637, (1979).
3. K. D. Chik, J. C. Dymont, and B. A. Richardson, "Self-sustained pulsations in semiconductor lasers: experimental results and theoretical confirmation," *J. Appl. Phys.* **51** (8), 4029-4037, (1980).
4. M. Ueno and R. Lang, "Conditions for self-sustained pulsation and bistability in semiconductor lasers," *J. Appl. Phys.* **58** (4), 1689-1692 (1985).
5. P. E. Barnsley, H. J. Wickes, G. E. Wickens, and D. M. Spirit, "All-optical clock recovery from 5 Gb/s RZ data using a self-pulsating 1.56 mm laser diode," *IEEE Photon. Technol. Lett.* **3**(10), 942-945 (1991).
6. X. Wang and Guifang Li, "Generating microwave/millimeter wave frequency modulation by laser diode self-sustained pulsation," *SPIE Proceeding*, vol. 1703, (1992).
7. X. Wang, Guifang Li and C. S. Ih, "Microwave/millimeter-wave frequency subcarrier lightwave modulations based on self-sustained pulsation of laser diodes," *IEEE J. Lightwave Technol.* **LT-11**(2), 309-315 (1993).
8. J. B. Georges and K. Y. Lau, "800 Mb/s microwave FSK using a self-pulsating compact disk laser diode," *IEEE Photon. Technol. Lett.* **4**(6), 662-665 (1992).
9. J. B. Georges and K. Y. Lau, "Self-pulsating laser diodes as fast-tunable (<1ns) FSK transmitters in subcarrier multiple-access networks," *IEEE Photon. Technol. Lett.* **5**(2), 242-245 (1993).
10. P. Hill and R. Olshansky, "Twenty channel FSK subcarrier multiplexed optical communication system for video distribution," *Electron. Lett.* Vol. **24**(14), 892-893 (1988).
11. D. Lenstra, B. H. Verbeek, and A. J. den Boef, "Coherence collapse in single-mode semiconductor lasers due to optical feedback," *IEEE J. Quantum Electron.* **QE-21** (6), 674-679 (1985).
12. H. A. Haus, "Parameter ranges for CW passive mode locking," *IEEE J. Quantum Electron.* **QE-12** (3), 169-176 (1976).

**PRELIMINARY REPORT ON THE FEASIBILITY OF MACHINE
SPANISH DIALECT IDENTIFICATION AND DESCRIPTION OF LATIN
AMERICAN DIALECT DATABASE (LADD) DEVELOPMENT**

**Beth L. Losiewicz
Experimental Psychology**

**The Colorado College
14 E. Cache La Poudre
Colorado Springs, CO 80903**

**Final Report for
Summer Faculty Research Program
Rome Labs/Speech Processing**

**Sponsored by Air Force Office of Scientific Research
Bolling Air Force Base
and
Rome Labs**

August 1994

**PRELIMINARY REPORT ON THE FEASIBILITY OF MACHINE
SPANISH DIALECT IDENTIFICATION AND DESCRIPTION OF LATIN
AMERICAN DIALECT DATABASE (LADD) DEVELOPMENT**

**Beth L. Losiewicz
Experimental Psychology
The Colorado College**

Abstract

The feasibility of machine Spanish dialect identification based on phonetic, lexical, syntactic or prosodic characteristics is investigated. It is concluded that prosody is a promising direction to pursue. The development of a digitized Latin American Dialect data base is described.

PRELIMINARY REPORT ON FEASIBILITY OF MACHINE SPANISH DIALECT IDENTIFICATION AND DESCRIPTION OF LATIN AMERICAN DIALECT (LADD) DATA BASE DEVELOPMENT

Beth L. Losiewicz

PART I: DIALECT IDENTIFICATION

A: TAXONOMY

One of the first problems that will arise in the deveopment of machine dialect identification of Spanish is the need for an adequate and agreed upon system of dialect classification. There is "not a single element of structure . . . considered one at a time and excluding vocabulary which would not be common to at least two different dialect regions in Spain or in America (Honsa, cited in Resnick, 1975). "Only a combination of two or more structural features, can be called characteristic of one dialect" (Resnick, 1975).

Henriquez Urena (cited by Resnick, 1975) based his Latin American (LA) dialect taxonomy on the indigenous language substrate, dividing LA into 5 regions based on Nahuatl, Caribe, Yarahuaca, Quechua and Guarani. Resnick claims that although this taxonomy is fairly adequate for delineating regions of lexical influences, it is wholly inadequate as a phonetic taxonomy.

The alternate approach is to divide the dialect zones by a combination of phonetic and morpho-syntactic features, but there appears to be little agreement among dialecticians as to which features should be used in such a classification system.

Rona (cited in Resnick, 1975) proposes a binary taxonomy based on phonetic and morphosyntactic features:

- (1) yeismo (phonemic leveling of /ll/ and /y/)
- (2) zeismo (phonetic rendition of palatalized /ll/ and/or /y/ as the voiced alveopalatal fricative [zh])
- (3) voseo (use of vos for second person singular)

(4) which verb form used with vos

Resnick (1975) has developed a region/dialect classification system, based on binary features, which is probably the most inclusive to date. As his most salient discriminator, Resnick chooses whether or not the /s/ is deleted, retained, or modified in certain contexts. Broadly speaking, in coastal areas which had extended periods of contact with Spain and were thus influenced by Peninsular language changes, word-final /s/ is aspirated or deleted. Word-final /s/ is likely to be retained in more isolated and mountainous areas of Latin America.

Resnick's second major distinction is the whether the fricative /x/ (as in *caja*, *jota*) has a pharyngeal or velar place of articulation. Northern hemisphere LA regions with Atlantic or Gulf of Mexico coasts, coastal Peru, Ecuador and the Western Texas-Mexican border, tend to use a pharyngeal [h], sometimes indistinguishable from an aspirated /s/. The velar /x/ is found in the rest of Mexico (except the Gulf coast and a few inland areas), and in all of Southern LA, in addition to the non-coastal parts of Peru and Ecuador. (Resnick, 1975). (The complexity of region-to-dialect feature mapping begins to appear!)

The third major feature in Resnick's scheme for LA dialect discrimination is the pronunciation of /r/. In standard Spanish /r/ is a voiced apicoalveolar trill, but appears as a voiced apicovelar sibilant in Chile, Paraguay, the interior of Argentina, and bordering areas of Peru and Bolivia. The same sibilant /r/, however, also appears in the geographically distant areas of highland Ecuador, parts of central Colombia, widely separated parts of Costa Rica, Guatemala, Mexico City, much of Central Mexico, and New Mexico.

Resnick (1975) proposes a dialect classification system based on a combination of binary features such as these, as illustrated below with two of his proposed features:

	/s/ = [h] or 0	/s/ = [s]
/x/ = [x]	Chile, Argentina, Uruguay, Paraguay, parts of Bolivia	Mountain regions of Peru, Bolivia, Ecuador and parts of Mexico

/x/ = [h]	Northern Countries	_____
-----------	--------------------	-------

The mapping, of course, becomes geometrically more complex as we add binary features to the classification system, but in Resnick's system this is done with only five additional features: presence or absence of "yeísmo" (phonemic leveling of palatalized /ll/ and /y/ as in *calló* vs. *cayó*), whether /b/ becomes /v/ after /l/ (*el bebe* => *el vebe*); whether or not word-final /n/ is velarized (*corazon* => *corazong* or *corazom*); presence or absence of leveling or confusion of /l/ and /r/ (*mar* => *mal*); and reduction or retention of unstressed vowels. This eight-feature classification system delimits 256 possible feature combinations. Once a general classification has been made on the basis of these binary distinctions, Resnick further classifies dialects on more fine grained distinctions (e.g., the manner of articulation of intervocalic stops; pronunciation of /c/; of /f/; details of the nature of the /ll/-/y/ and /l/-/r/ leveling; the nature of /r/, /s/ and /x/; and the leveling and/or devoicing of vowels).

Even if a classification scheme such as Resnick's proves useful for machine dialect identification, a further, and possibly insurmountable, difficulty still exists. Even within a given dialect or dialect region, great variability exists both within and between speakers. Social class, urbanicity, level of education, ethnic background, and speaking style (e.g., formal vs. informal) all contribute to large amounts of variability within any given dialect region. Further, dialectal features are more often graduated or probabilistic than binary phenomena, both in terms of how frequently, and how strongly the feature appears in any given speech segment. Especially since only limited information about frequency-of-occurrence and inter-speaker dialect variability exists, this variation could seriously complicate dialect identification efforts.

B: SOURCES OF DIALECTS

Contemporary dialects in LA derive from a complex interaction of a number of causes: the dialect of Peninsular Spanish spoken by the original immigrants to the region; the degree and length of contact maintained with Peninsular culture; the nature of the indigenous language of the area; patterns of commerce and interaction

with other areas; and degree of geographic and cultural isolation; in addition to any local pressures towards unique diachronic changes. **It cannot be too strongly stated that dialect boundaries in LA seldom, if ever, follow modern day political boundaries.** A more suitable delineator might be the identity and geographical boundaries of pre-European indigenous groups (e.g. Nahuatl; Mayan; Quechua; Arucana; to name a few) since modern day dialect boundaries *tend* to fall along those of the ancient language/cultural groups, although, as mentioned, this factor interacts with others such as duration of contact with Penninsular Spanish, and local regional topography. Highland dialects, for example, tend to differ fairly systematically from coastal dialects (at least in part because coastal areas tended to be much more open to continued Peninsular influence).

C. POSSIBLE SOURCES OF IDENTIFYING ELEMENTS

Dialectical differences in Spanish can appear at any linguistic level. Most studied are the phonetic and lexical differences, but differences have also been document at the levels of syntax, morphology, and, less extensively, in prosody. We will look at each in turn as possible candidates for use in machine dialect identification algorithms

C1: PHONETIC DIFFERENCES

Ideally what is needed is a handful of phonologically distinctive features that would successfully delineate clear geographic and/or social class variants of Spanish. However, it is doubtful whether such a map is possible, or, if it did exist, it might be too complex and indeterminate to be useful.

To further aggravate the problem, the phonetic differences, although clearly discernible (at least in their strongest forms) by the human ear, may be too subtle for machine discrimination. And, even if a recognition algorithm could pick out the differences, other serious problems stand in the way of easily using those phonetic features as indices of dialect. First of all, the phonetic variations are often phonologically mediated (i.e., they occur in certain phonological contexts and not in others) or even lexically mediated, or occur only in specific words. For example, /r/ - /l/ leveling may fail to occur, even in leveling dialects, in the case of infinitives (*hablar*) and/or object pronouns (*le, lo*). In Chile, as a further example, aspirated [h] appears only the lexical item *huir*. Conversely, coarticulatory phenomena can condition leveling even in dialects where leveling is not a dialectical feature, e.g., the coarticulatory leveling of /l/-/r/ in the word *arbol*. Dialect recognition based on

these features would thus require more than simple phonetic recognition. It would require processing at least at the lexical level, making the recognition process much more complex (assuming for the moment that even simple phoneme discrimination is possible without lexical-level information).

The second large problem, as mentioned above, arises from inter- and intra-speaker variation. Any given speaker, in a long passage of speech, will exhibit subtle allophonic variations in certain phonological contexts, (e.g., in the phoneme /s/), and the judgment of whether the variation is dialectal, co-articulatory, or random, would be a subtle one. Further, even if dialectically determined, any given phonetic variation may or may not be obligatory. Social status, discourse register (e.g., formal or informal speech) also impact phonetic dialectal variations. Add this to the allophonic variations across speakers, and the difficulties may be insurmountable.

C2: LEXICAL DIFFERENCES

Lexical differences may be the simplest dialect feature in terms of the relative simplicity of the region-to-lexicon mapping. Unique regional words characteristically derive either from the indigenous (Indian) language of the region, or from archaic Spanish words introduced through early Spanish influence, followed by lengthy periods of isolation from changing Peninsular Spanish. A substantial non-Hispanic European population in central LA (the Rio Plata region) has contributed some lexical items as well (e.g., the ubiquitous Italian *chiao*, meaning *adios*). Non-standard meanings for common lexical items are also common regional markers, but are probably too subtle to be exploited by any but the most sophisticated speech processor, if at all.

Lexical differences do have a certain advantage as a discriminator, however. Unlike phonetic dialectal features which can be found in isolated geographic pockets far removed from each other; regional lexical items are most likely to be wholly contained within a fairly circumscribed geographic region; although the size of the region can vary from a single city to a large region covering several countries.

The major problem with using dialect-unique lexical features as a dialect discriminator is the extent of the vocabulary that would be necessary to support such an algorithm, and the fact that fairly large samples of speech would likely be

necessary. A possible solution to this might be to use only high frequency words - greetings, exclamations and/or swear words.

Although, as mentioned, dialectical lexical variations tend not to appear in widely separated geographical regions, region-to-item mapping can nevertheless be fairly complex. The variation in regional ranges of lexical items was investigated using a dictionary of Chilean regionalisms. On a single page, chosen at random, were found words both of very limited, and of very wide distribution: some words listed were common to all Latin America; some common only to the Rio Plata region; others were common to Chile, Argentina, Mexico and Peru; still others found only in Chile and Mexico; some found in Chile, Ecuador and Costa Rica; still others confined to Chile and Argentina; and yet others found in Chile, Colombia, Honduras and Venezuela. While regional/lexical mapping may be somewhat simpler than regional/phonetic-feature mapping, it is by no means entirely simple.

C3: MORPHOLOGICAL AND SYNTACTIC DIFFERENCES

Dialects in LA also vary somewhat morphologically and syntactically. Slight differences in verb conjugations may appear in some regions, order of object pronouns is idiosyncratic in some regions, and a handful of distinctive suffixes or affixes are unique to a few circumscribed areas¹. One of the most common parameters of dialectical variation is the use or absence of the second person informal plural, *vosotros*; the alternation between *vos* and *tú*; and the choice of verb form used with *vos*. Use of the direct object pronoun *lo* can also vary regionally, the indirect object pronoun *le* taking its place, in some contexts, in many regions. Noun gender at a lexical level can also be idiosyncratic: e.g., *el llamado* in one region might be *la llamada* in another. Syntactic and morphological differences, although potentially exploitable by a trained Spanish dialectician are probably not good candidates on which to base machine dialect ID since the differences are often subtle, and are probably too rare in occurrence to be used in identification of short segments of speech. Further, radio communications commonly exhibit reduced syntactic patterns, making it even more unlikely that dialect-distinguishing syntactic cues would appear in radio transmissions.

C4: PROSODIC DIFFERENCES

¹E.g., the use of the affix *rete* in Mexico, the frequency of the augmentative affix *-azo* (*amigazo*, *buenazo*) in Argentina, the Quechua possessive *-y* in Peru; or the characteristic *-tico* (*momentico*, *ahoritica*) of the Carribean, etc.

"Intonation is perhaps the phonological feature most generally used by Latin Americans in characterizing and imitating the speech of other Latin American regions" (Resnick 1975; a similar comment is made by Navarro Tomas in his introduction to Canfield, 1962).

The existing literature on Spanish prosody does not shed much light on the issues of machine dialect identification. First of all, studies on Spanish prosody are sparse, and those addressing differences between dialects is even sparser. Most of the studies (many of which pre-date the spectrogram) rely on impressionistic judgments² rather than acoustic analysis of the data, and almost all focus on prosody as conditioned by linguistic and discourse factors: differences between declarative and interrogative sentences; rising or falling intonation as a marker of finality or continuation, etc. Further, most of the studies were conducted with quite small speaker samples (e.g., 1-4 speakers of each dialect). Kvavik and Olsen (1974) review the intonational literature. Those studies which contrasted dialects are summarized below.

C4.1 Mexican Spanish

Matluck (1965), found that Mexican Spanish is characterized by higher frequency on the accented syllable (than in "standard" Spanish), and by level, instead of falling, phrase-final intonation contours. Kvavik (1974) found that, contrary to the traditional claim that Mexican Spanish has a greater frequency range than Castilian Spanish, the frequency ranges of the two are quite similar. The largest difference she found was in the relationship between the average frequency of a phrase, and the frequency of the phrase-final segment. The phrase-final frequency of Mexican Spanish tends to be an average of 4 Hz *above* the phrase frequency average, whereas in Castilian Spanish it tends to be 4 Hz *below* the phrase average. She suggests, with Matluck (1965), that even when phrase-final intonation remains level, the listener's expectation (from standard Spanish) of hearing a falling tone leads to the *perception* of rising intonation.

C4.2 Argentinian Spanish

²Liberman (1965) found that impressionistic judgments about prosodic characteristics such as pitch level and terminal juncture type, even when done by trained linguists, are highly variable (between linguists), and thus relatively unreliable.

Malmberg (1950)³ noted that the Argentinian accent is characterized by a strong descending intonation; and both Malmberg (1948) and Alonso and Henriquez Urena (1939) noted Italian influences in the prosody of Buenos Aires Spanish.

Alvarez Puebla de Chavez (1948) noted intonational differences between Buenos Aires and Cordoba Argentinian Spanish, and Vidal de Battini (1949; 1954) delimited six different intonational regions in Argentina, and also mentioned intonational differences peculiar to certain social strata. Fontanella (1966) found a series of prosodic differences between the dialects of Tucumán and of Buenos Aires, Argentina:

- a difference in number of contrastive pitch levels in final stressed syllable
- Tucuman has a rising glide absent in Buenos Aires
- a difference in length and pitch of unstressed syllables in comparison with stressed syllables
- Buenos Aires has a falling phrase-final intonation option absent in Tucuman
- declarative sentences in Tucuman often have a high rise on final unstressed syllables (often mistaken by Buenos Aires speakers as interrogative intonation)

A further study by Fontanella (1971) describes the dialect of Cordoba which is characterized by an additional contrastive pitch level, and a lengthening and pitch change in last pretonic, tonic, or internal pretonic syllable.

C4.3 Chilean Spanish

Malmberg (1948) suggested that indigenous languages had an effect on Chilean Andean intonation. Gallardo (1953) described a regional intonation on a Chilean island. Oroz (1966) maintained that the prosody of Chilean Spanish is quite different from that of standard Spanish, and briefly described regional intonational differences which he ascribed to the influence of indigenous languages. He also found prosody to be alike in the two Chilean cities of Valparaiso and Santiago, and in neither were there prosodic differences based on social class.

C4.4 Conclusions

³All references in the paragraphs on Argentinian and on Chilean Spanish are cited in Kvavik & Olsen (1974). The reader is referred to that source for the full bibliographic references (i.e. they will not be duplicated in the bibliography of the present paper).

Although a handful of studies have been reported, the literature on prosodic differences between different dialects of Spanish is so sparse that machine dialect identification based on prosodic cues identified by linguists is probably not feasible at this point, without a large-scale study to fill in the large gaps in our knowledge. However, it is possible that more general, or global, prosodic differences could be identified, and directly investigated with current machine clustering algorithms such as those currently used for speaker or language identification. Since, anecdotally, native speakers of Spanish are fairly adept at identifying dialect based on prosodic cues, there is reason to believe that global prosodic characteristics may be adequate to discriminate between dialects.⁴

D: GENERAL CONCLUSIONS

Success of a dialect recognition algorithm is by no means certain. The **phonological** differences (e.g., /l/-/r/ confusions; aspiration or deletion of /s/; yeísmo; the presence or absence of the phoneme [zh]; assibilation of /r/) may well be too subtle to be utilized directly in a phoneme-based dialect recognition algorithm. **Lexical, morphological and syntactic** differences may well require more sophisticated processing than is currently available, or at least than is feasible in a "preliminary sorting by dialect" application, since large speech samples and complete language analysis at many linguistic levels would be necessary to disentangle dialects based on this information. Anecdotal evidence indicates that dialects may be **prosodically** distinguishable, but virtually no dialectal analysis has been done along these lines. Different dialects relatively systematically manipulate certain classes of phonemes (stops, liquids, aspirants), which could well leave a trace in **abstract acoustic representations** of the speech, such as Cepstra, making general acoustic analysis a possible route for analysis. Certain dialects (e.g., in the Quechua-influenced regions where vowel-leveling is common) may well be differentiable based on **formant characteristics**, although the question remains open whether these vowel-reducing dialects would even be identified as "Spanish" by formant-based language identification paradigms in the first place.

⁴Lieberman (1965), in fact, claims that even linguists do not use discrete cues to identify prosodic features like pitch level and terminal juncture type, but rely on more global characteristics such as amplitude and fundamental frequency changes over time.

Possible further directions for research include:

- Extraction of pitch contours of different dialects to investigate whether they have distinctive contours or ranges.
- Use dialect samples from LADD to investigate whether current speaker identification, or language identification algorithms can be used for dialect identification.
- Use dialect samples from LADD to test ability of current language identification algorithms to succeed in dialect recognition.
- Use dialect samples from LADD to investigate whether trained dialecticians can discriminate between dialects, either based on the full sample, or on extracted prosodic contours.

Part II: LADD (LATIN AMERICAN DIALECT)

DATA BASE DEVELOPMENT

A: INTRODUCTION AND DESCRIPTION OF LADD

No adequate Spanish database, labeled by dialect, currently exists. To remedy this, development of such a database was undertaken, using speech samples collected from several Spanish dialecticians in the United States (See "Sources" below). Their original ("source") recordings were made using a potpourri of analog audio recording equipment for which, for the most part, information is no longer available. However, since some educated guesses can be made about recording/recording conditions based on other evidence, whatever information was available (and this varied somewhat from sample to sample) was carefully documented: date of source recording; name of person making recording; name of dialectician in whose collection it was found; etc.

The problems arising from this characteristic of the database are not insurmountable, but does demand that care be taken in selecting samples for tests to ensure, for example, that proposed dialect ID algorithms are not in reality merely identifying the equipment used for the original recording. Alternately, samples

could be filtered before use to level the variations resulting from the variation in the original recording equipment.

The advantages of the data base, however, far outweigh the disadvantage of this variation in original recording equipment. First, this format allows the exploitation of large amounts of data that have already been collected by dialecticians across the U.S. Second, in a very real sense, it mimics the real-world data that dialect ID algorithms will be expected to cope with, in a way that a collection of studio-quality recordings cannot. Third, and probably most importantly, sample biases inherent in other databases are minimized: speakers, for the most part, have been solicited rather than self-selected (as in the OGI database); speakers range in education level from illiterates to holders of PhDs, and in occupation from army generals, Presidents and engineers, to sugar cane farmers and housewives; recordings have been made both in the U.S. and in Latin America, in both field and studio conditions; speech styles range from formal read speech to lectures, speeches, harangues, gossip, stories, monologues, interviews, and linguistic surveys. This information, whenever known, is carefully noted in the notes to the database. While these characteristics are not conducive to a thought-free, instant "add algorithm and run" approach, the database is exceedingly versatile, and with judicious use should have almost unlimited potential applications.

Speech samples were carefully screened for reliability of information about the speaker: samples were only collected for those speakers unambiguously documented as to country (or even city) of origin, and sex of speaker.

B: PROCEDURES

Audio recordings were borrowed from Spanish dialecticians (see "Sources"), and transferred to DAT tape using a Sony 670 High-Density Linear A/D D/A Converter. Source tapes were played on either a Sony Tape recorder TC755 Closed Loop Dual Capstan or a Sony Tape recorder TC645 3-Head reel-to-reel deck. If the source tape was a cassette, it was played on a Tascam Model 122 cassette recorder with Dolby.

From each 2-hour DAT tape, speech segments are transferred to computer hard disk, using Turtle Beach 56K SoundStage DSP hardware and software in sound files of 30 minutes or less duration. The speech files are currently being segmented as necessary to ensure that only the desired speaker is contained in the sound file. In some instances (e.g. interviews and conversations) this requires extensive cutting so that speech from only one speaker is present in any one file. In other instances

(e.g., reading, monologues and formal speeches) such segmentation is not necessary, and was only performed if there is a break in the audio recording, or a difference in speech style between one segment and another (e.g., the first part is a speech and the second part, for the same speaker, an interview). Cutting occurred at intonation boundaries whenever possible, and always respected word boundaries.

Each segment is then labeled with a unique identifier providing information about the dialect and the speaker. Data about each speaker, region of origin, speech style, quality of the sound file, the original audio source, etc. are maintained in a separate permanent data base (ORACLE) at Rome Labs IRAA/Speech Processing.

In the final phase digital binary sound files are archived both on magneto-optical disk and magnetic tape for exploitation by government and contractor agencies.

The data base on audio or on DAT tape, along with documentation is available at Rome Labs, IRAA, Speech Processing, Griffiss AFB, New York 13441, phone (315) 330-4024.

PART III: PARTIAL BIBLIOGRAPHY OF SPANISH DIALECTOLOGY

NOTE: Especially useful summaries of dialect regions/classification are in **bold print** and/or dialect maps are in **bold print**.

Aguero, A. (1962). El Espanol de America y Costa Rica. San Jose, Costa Rica: Libreria e Imprenta Atenea S. en C.

Besa-Oliva y L. Florez. (1954). El Atlas Linguistico-Etnografico de Colombia (ALEC).

Canfield, D. L. (1962). La Pronunciacion del Español en America. Bogota: Imprenta Patriotica del Instituto Caro y Cuervo.

Canfield, D. L. (1981). **Spanish Pronunciation in the Americas**.

Chicago: University of Chicago Press. (A different book from the 1962 book of similar name, in Spanish)

Cobos, R. (1983). A Dictionary of New Mexico and Southern Colorado Spanish. Santa Fe: Museum of New Mexico Press.

- Cotton, E. and J. Sharp. (1988). Spanish in the Americas. Washington, DC: Georgetown University Press.
- Delattre, P, C. Olsen and E. Poenack. (1962). A Comparative Study of Declarative Intonation in American English and Spanish. Hispania, 45. 233-241.
- Del Rosario, R. (1962). La lengua de Puerto Rico. NY: Las Americas Publishing Company.
- Garcia De Diego, V. (1978). Dialectologia Espanol. Madrid: Ediciones Cultura Hispanica del Centro Ibero-Americano de Cooperacion.
- Haden, E. and J. Matluck. (1973). El Habla Culta de la Habana. Anuario de Letras, 2, 5-33.
- Hammond, R. and M. Resnick (Eds). (1988). Studies in Carribean Spanish Dialectology. Washington, DC: Georgetown University Press.
- Henriquez Urena, P. (1976). Observaciones sobre el Espanol en America. Argentina: Academia Argentina de Letras.
- Hidalgo, M. (1990) The Emergence of Standard Spanish in the American Continent. Language Problems and Language Planning, 14. 47-63.
- Hutchins, S., A. Thyme and B. Haapa. (1993) . On the Use of Prosodic Parameters in Language Identification. Speaker Research Symposium XIII. Johns Hopkins.
- Kvavik, K. (1974). An Analysis of Sentence-Initial and Final Intonational Data in Two Spanish Dialects. Journal of Phonetics, 2, 351-361.
- Kvavik, K. & C. Olsen (1974). Theories and Methods in Spanish Intonational Studies. Phonetica, 30, 65-100.
- Lacayo (1954) Apuntes Sobre la Pronunciacion del Español en Nicaragua. Hispania, 37, 267-268.
- Lieberman, P. (1965). On the Acoustic Basis of the Perception of Intonation by Linguists. Word, 21, 40-54.
- Lipski, J. (1989). /S/ voicing in Ecuadoran Spanish. Lingua, 71. 49-71.
- Lope Blanch, J. (1987). Estudios Sobre el Espanol de Yucatan. Mexico: UNAM.
- Lope Blanch, J. (1972). Estudios Sobre el Espanol de Mexico. Mexico: UNAM.
- Lopez Morales, H. (n.d.). Estudio Sobre el Espanol de Cuba. NY: Las Americas.
- Matluck, J. (1965). Entonacion Hispanica. Anuario de Letras, 5, 5-32.
- Navarro Tomas, T. (1966) Manual de Entonacion Espanola. 3rd Ed. Mexico DF: Coleccion Malaga, S.A.

- Navarro Tomas, T. (1975). Capitulos de Geografia Linguistica de la Peninsula Iberica. Bogota: Instituto Caro y Cuervo.
- Olivier, C. (1971). De Nuestro Lenguaje y Costumbres. 2a Ed. Santo Domingo, Republica Dominicana: Impresora Arte y Cine C por A.
- Oroz, R. (1966). Lengua Castellana en Chile. Santiago: Univ. de Chile.
- Pascual Recuerdo, P. (1977). Diccionario Basico Ladino-Espanol. Barcelona: Ameller Ediciones.
- Resnick, M. (1975). Phonological Variants and Dialect Identification in Latin American Spanish. The Hague: Mouton.
- Robe, S. L. (1960). Spanish of Rural Panama. Berkley: Univ. of California Press.
- Rona. (1964). Presente y Futuro de la Lengua Espanola. 2 vols. Madrid: Oficina de Informacion y observacion del Espanol.
- Scavinicky, G. (Ed). (1980). Dialectologia Hispano-Americana. Washington: Georgetown Univ. Press.
- Wallis, E. (1951). Intonational Stress Patterns of Contemporary Spanish. Hispania, 34, 143-147.

**AUTOMATIC EXTRACTION OF DRAINAGE NETWORK FROM
DIGITAL TERRAIN ELEVATION DATA (DTED)**

Mohamad T. Musavi and Andrew J. Laffely
Associate Professor Graduate Student
Department of Electrical & Computer Engineering

University of Maine
5708 Barrows Hall
Orono, ME 04469-5708
Phone: (207) 581-2243
Fax: (207) 581-2220
E-mail: musavi@eece.maine.edu
E-mail: alaff@eece.maine.edu

Final report for:
Summer Faculty Research Program
Rome Laboratory

Sponsored by:
Air Force Office of Scientific Research
Bolling Air Force Base, Washington, DC
and
Rome Laboratory

July 1994

AUTOMATIC EXTRACTION OF DRAINAGE NETWORK FROM DIGITAL TERRAIN ELEVATION DATA

Mohamad T. Musavi and Andrew J. Laffely
Associate Professor Graduate Student
Department of Electrical & Computer Engineering
University of Maine

Abstract

In this report a straight forward approach for automatic extraction of drainage network from Digital Terrain Elevation Data (DTED) of the Defense Mapping Agency (DMA) is presented. The approach is based on common image processing methods such as frequency domain filtering, spatial domain histogram equalization, binarization, thinning and other techniques. The approach has been examined with several DTED files. The results obtained from this approach are as good as, or better than, other methods. The approach was developed using Khoros image processing system and C programming. Khoros has excellent visually based environment and its rather extensive library of functions helped avoid writing of commonly used codes.

AUTOMATIC EXTRACTION OF DRAINAGE NETWORK FROM DIGITAL TERRAIN ELEVATION DATA

Mohamad T. Musavi and Andrew J. Laffely

I. INTRODUCTION

A. Techniques

Digital elevation data files are important sources of information that have been used in many remote sensing applications such as geometric rectification [Wiesel, 85], terrain related radiometric correction [Colby, 91], image registration [Dubayah & Dozier, 86], topographic map update [Gugan & Dowman, 88], and extraction of such important features as drainage networks [Argialas, Rouge, & Mintzer, 88; Jenson & Domingue, 88; Hardipriono, Lyon, Li, & Argialas, 90].

Drainage networks have been applied in water resource assessment, hydrogeometric analysis, interpretation of soils and rocks, and segmentation of textures and structures. In principle the task is straight forward. Water drains from high to low elevation along channels that are connected to one another according to well-defined rules [Parvis, 50; Howard, 67; Argialas, 85]. Majority of the techniques used for extraction of water drainage are based on low level pixel (cell) labeling by using local operators and subsequent pixel grouping according to local criteria [O'Callaghan & Mark, 84; Jenson, 84]. Recently, Qian, Ehrich, & Campbell [90] applied both local operators and global reasoning to improve the performance of previous results. Water drainage extraction techniques normally assume one pixel wide networks that may cause difficulty in flat areas with flood patterns [Lee, Snyder, & Fisher, 92].

The technique presented here is based on two fundamental steps. In the first step, a complete and connected candidate for a possible drainage network is found. In the second step, the possible drainage network is pruned to remove unnecessary links that are not part of the drainage network. The first step is based on a set of image processing routines such as data preprocessing, frequency domain filtering, spatial domain histogram equalization, binarization, thinning and image blending. The Khoros image processing environment [The University of New Mexico, 1990] has been used in this study because its rather extensive library of functions helped avoid writing of common-used codes.

B. Databases

There are two common sources of elevation data, the Defense Mapping Agency (DMA) Digital Terrain Elevation Data (DTED) and the United States Geological Survey (USGS) Digital Elevation Model (DEM) data. While the experiments of the previous studies were all conducted on the DEM data, those of this study used DTED database. This database consists of many data files of digital terrain elevation data. Each data file is a cell defined by a matrix with longitude and latitude coordinates (x, y) and elevations (z). A cell covers a 1 degree by 1 degree geographical reference area. The sampling interval for elevation data is 3 seconds by 3 seconds. Absolute horizontal and vertical accuracy of DTED data are 50 and 30 meters respectively; while, relative accuracies within a cell are 30 and 20 meters [Military Specification, 86]. DTED data is available on CDROM and 9 track 1/2" magnetic tape.

II. METHODOLOGY

The following sections present a step-by-step description of the proposed methodology for automatic extraction of drainage network. A block diagram of the operations is shown in Figure 1. In order to show the result of each operation, a sample DMA data file has been selected. The file is a matrix of 128x128 elevation data. A three dimensional plot of this elevation file is shown in Figure 2. The elevation in this area changes from 420 to 4160 meters as indicated in the plot. For the sake of visual representation of the data and the future results, the elevation data is converted to gray level representations from 0, for the lowest elevation, to 255 for the highest elevation. The gray level representation of elevation data of Figure 2 is shown in Figure 3. Note that all future operations are performed on the original elevation data and only for demonstration purposes the results are converted to gray level images. In Figure 3 the lower elevations are almost featureless because of the great contrast of elevation present in this data.

A. Data Conversion

A DTED file supplied on CDROM is a 1201x1201 matrix of elevation data with the DMA data format. This data is first converted to the format accepted by Khoros image processing software and then is split into smaller matrices.

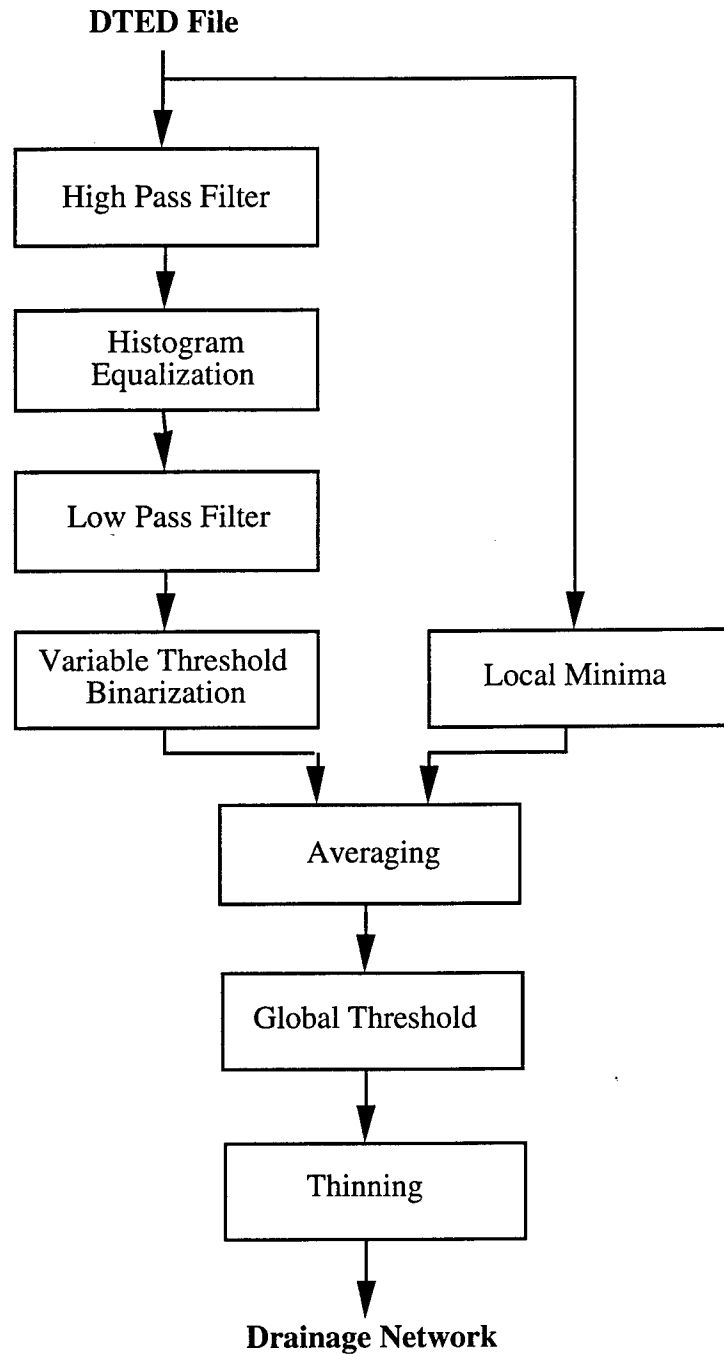


Figure 1. A block diagram for the automatic extraction of drainage networks.

B. High Pass Filter

The first step of the data processing is to bring up important features such as peaks and valleys that are necessary for identification of water drainage. A common tool is the application of a high pass filter (HPF). This can be performed both in spatial domain and frequency domain; however, frequency domain operation is more accurate and provides more flexibility for changing the cut-off frequency of the HPF. The cut-off frequency proves to be an important factor in handling different geographical areas. For example, in an area with high elevation changes the cut-off frequency can be quite low. While in an area with low elevation changes the cut-off frequency has to be higher in order to identify valleys with smooth changes that might be part of a drainage network or flood pattern.

To perform a HPF in frequency domain the data is first submitted to a Fast Fourier Transform (FFT) program to convert the spatial domain data to the frequency domain data. The data is then passed through the characteristic function of the HPF and then to an inverse FFT to recover the processed spatial data. Figure 4 shows the result of a high pass filter on the test data. The HPF was a first order exponential filter with a normalized cut-off frequency of 0.1.

C. Histogram Equalization

Although a possible drainage network might be recognizable by human eye in Figure 4, the data still poses difficulties in automatic extraction by computer. To further enhance the possible drainage network, the histogram of the data is equalized using a histogram equalization program. This step further enhances the drainage networks as shown in Figure 5. A comparison of Figure 5 and 3 shows the significance of the histogram equalization operation.

D. Low Pass Filter

Along with the enhancement of the high frequency and histogram information, the noise in the data is also enhanced. To suppress the noise, a low pass filter (LPF) is used. The result of LPF on the equalized data is shown in Figure 6. The filter used in this example was a second order Butterworth filter with the normalized cut-off frequency of 0.2. This provides an overall band-pass effect on the input data. Note that the process of implementing LPF is similar to that of HPF explained in section B above.

E. Binarization

The elevation data can now be segmented for isolation of the possible drainage area by a binarization process. Using a fixed threshold for the entire data file will cause either loss of drainage data or introduction of excessive points, depending on the value of the threshold. Therefore, a variable threshold binarization [Musavi, Shirvaikar, Ramanathan, & Nekovei, 88] was used. There are several sub-steps that are taken to accomplish this binarization. The threshold for an elevation data point n is defined as,

$$T_n = K_n * STDDEV_n + MEAN_n \quad n = 1, 2, \dots, M \quad (1)$$

M is the total number of data points in the file. K_n , $STDDEV_n$ (standard deviation), and $MEAN_n$ (mean) are defined as,

$$K_n = a * HIST(n) / M \quad (2)$$

$$MEAN_n = \sum P_i / (2*d + 1)^2, \quad i = 0, 1, 2, \dots, (2*d + 1)^2 - 1 \quad (3)$$

$$STDDEV_n = [\sum (P_i - MEAN_n)^2 / (2*d + 1)^2]^{1/2}, \quad (4)$$

Where a is a constant (3 in our experiments). $HIST(n)$ is the histogram element corresponding to the n -th data point, P_i is the value of the i -th data point in a local area around the n -th point, and d determines the size of the local area. For example, $d=1$ for a 3×3 area, $d=2$ for a 5×5 area, and so on. The result of the variable threshold binarization is shown in Figure 7. One option for drainage network extraction was to apply a thinning algorithm at this stage, the result of which was a fairly well connected set of paths. However, the thinning algorithm output might not accurately provide the drainage paths for all areas. This is especially true where a given path is bordered on one side by sharp elevation changes and on the other by more gradual ones.

F. Local Minima

The above binarization process provides a general area of the possible drainage network. The local minima in this general area provides a more accurate representation of the drainage network. One should note that the local minima alone will not be sufficient to provide a connected drainage network due to its local reach. The significance of the generalized drainage area is in its global nature, global in a sense that it provides a connected path for the network. Therefore, a merger between the general area and the local minima will provide a much better data set for extraction of the actual drainage network.

A simple routine is used to find the local minima in both the x, y, and both diagonal directions from the original data. Each data point in the original elevation file is compared to the four that precede it and the four that follow it (9 points in each local array). If the elevation of the test point is lower or equal to all the points of the local area, a corresponding point in a binary representation file is set to 1. If any one of the points in the local array is lower than the test point, then a 0 will be recorded for the test point. This process is repeated for all rows, columns and diagonals of the data file. As a result, any point in the output file can be set based on only one testing direction. This enables the extraction of drainage paths in the four connected neighbors of the test pixel. Figure 8 shows a binary file indicating the local minima of the original elevation data. Notice in Figure 8 that some points where the drainage paths seem to converge are not set. This is a direct result of the local minima algorithm and part of the reason that it alone is unable to extract a connected drainage path.

G. Local Blending and Global Thresholding

After the two binary files are created, the local minima and the variable threshold binarization outputs, they need to be combined in a manner that enhances the connectivity and reduces noise. First, a weighted sum of the two files is used to combine the information into a single image. The optimization of the weighting factor has not been extensively studied but adding one part variable threshold information and two parts local minima data, has given consistent results. In other words, after the summation a 4 level (0, 1, 2, and 3) data file, as shown in Figure 9, is created. Note that the local minima helps to identify the accurate location of the drainage network in the general area of drainage.

Considering only the local minimum points of Figure 8, one can identify a possible drainage network that is not completely connected. However, the information in the general drainage area can be used to create the appropriate connectivity. One way to do this is by a local blending or smoothing operator on the 4 level data file created above. In the experiments reported here two identical smoothing operators, 7x7 averaging masks, were applied in sequence to the 4 level data file. The result of this operation is shown in Figure 10. This operation closes small gaps in the local minima drainage network while reducing noise. After smoothing, a global thresholding, set at 1.5, is applied to successfully extract a possible drainage network, Figure 11.

H. Thinning

The output of section G above is a possible drainage network with more than one pixel in width. A thinning algorithm can be applied to find a one pixel wide network, Figure 12. At this

stage there might exist certain isolated pixels or segments that are created as the results of thinning algorithm. These sporadic pixels can be removed by a simple length thresholding filter. The thinned drainage network of Figure 12 has been overlaid on the original data in Figure 13.

I. Direction of Flow

With a nearly complete drainage network, several other steps of processing may be done to extract more information from the DTED file. One of these is the drainage flow direction. Some approaches to this have been investigated as part of this program, but complete methods and code have not been developed due to time limitation. The next several paragraphs contain this approach.

The input to this stage of processing could come from one of three different steps described earlier.

First, the thinned drainage network of part H could be used. This being the final result of the tested system thus far makes it the obvious choice, but the problems with the Khoros thinning algorithm especially the connectivity ones could create problems in finding the direction of flow. If a new thinning algorithm were developed this would be an excellent place to begin.

Second, the wide drainage network of part G could be used. To do this, the direction of flow algorithm could be given two tasks. One, to find the flow direction of each pixel in the wide network and two, to use this information to thin the resulting network where needed. The result of this may give much more insight than the one pixel drainage system of step H, by actually allowing rivers to have a width. This process will be discussed further.

Third, if a wide network can be used and then thinned based on direction of flow, it is conceivable to use the output of the variable threshold binarization as a starting point. This would cut several steps of processing including the time consuming smoothing steps.

At this point the direction of flow algorithm will be described in terms of the second input option, however the methods presented here could be transformed to meet the demands of the other two input cases. The input image in all three cases is binary with one level equal to the value 1, and the zero level is 0.

- 1) The first step of this approach is to multiply the binary drainage network file by the original DTED file pixel by pixel. This will weight each pixel in the drainage network by its elevation value.

- 2) Create a mask image consisting of the connectivity of the above network. In this file all non zero pixels contained in a connected drainage path will be assigned a numerated cluster. The number of clusters will be the number of individual drainage networks in the test area. This step is not too difficult to construct and is almost complete. It involves searching the input file pixel by pixel till a non-zero pixel is reached; the location of this is then stored. Once the first non-

zero pixel is reached all other non-zero pixels that are connected to it, be it directly as a neighbor pixel or through a complicated string of non-zero pixels are stored in the connection mask and assigned to a cluster. After all the pixels for that network have been identified, a file search for another non-zero pixel begins one pixel after the location of the first pixel in the last cluster. This time the search will not only look for non-zero pixels but also check whether the pixel has been assigned to a cluster to avoid repetition of clustering. The search will continue to the last pixel in the file assuring that all possible networks have been found.

3) With the clustering of networks a length threshold can easily be used to remove insignificant or error drainage paths.

4) Create a pixel by pixel direction mask by, comparing the elevation of each pixel with its immediate neighbors and selecting the neighbor pixel with the greatest absolute difference as the direction. A more elaborate method is to take a weighted average of all possible directions, but this is more complicate and may not be necessary.

5) Perform thinning and path check in one (iterative) step. Test each direction against the input file. If the direction of the test pixel points from a zero pixel on one side to a non-zero pixel on the other, delete it from the network. If the direction of the test pixel points from a non-zero pixel to a zero pixel, change the non-zero pixel to 1. If the direction of the test pixel points from one non-zero pixel to another, do nothing. This procedure will delete some of the network at the higher elevations, but in those regions the drainage network will not be visible in most other mapping media. Clustering and directions will need to be recalculated after each iteration. It is uncertain what number of iterations will be sufficient to obtain the correct network.

6) Use the pixel directions to obtain a global sense of drainage direction. This will be done by averaging the directions along each path.

This approach is untested and may need to be revised.

J. Drainage Vectorizatoin

A complete network or even a partial network can be represented as a set of connected or disconnected vectors. Each network, of sufficient length, can be simplified to a set of vectors that follow its path. The resulting set of vectors may be useful in registration of satellite imagery that has a perpendicular frame of reference. The relative vector lengths and angles should be similar in the DTED and imagery allowing the registration process to overcome rotational, translational and scaling problems.

III. CONCLUSION

A straight forward technique has been presented for automatic extraction of drainage network from Digital Terrain Elevation Data (DTED) of the DMA. It has been shown that an appropriately assembled set of commonly used image processing techniques is able to extract drainage networks from elevation data. However, there are other issues that need to be addressed before the proposed methodology can be adopted as a robust and reliable tool for the task. Among these issues are determination of direction of flow, test of the methodology with elevation data from different geographical areas, test of the accuracy by comparing the extracted drainage networks with ground truth data, and refinement and optimization of the parameters used in the methodology. A neural network approach could have also been investigated and devised for the task, however, due to lack of training data, the implementation was not feasible at this stage. In addition to many useful application of drainage networks, they can also be used for automatic registration of unregistered images because drainage networks are unique features of elevation data that can be used effectively for registration purposes. Expansion, modification, and utilization of the developed methodology will be addressed in future research proposals.

ACKNOWLEDGMENT

We would like to give our thanks and appreciation to all those who helped us in the completion of this research project.

First, we would like to thank our sponsors, the Air Force Office of Scientific Research and the Research and Development Laboratories. Special thanks go to Mr. Garry Barringer, Technical Director, Rome Laboratory Directorate of Intelligence and Reconnaissance (RL/IR), and Mr. Joseph Palermo, Chief, Image System Divisions, for providing us with the opportunity to work on a very interesting project.

We would especially like to thank Mr. James McNeely, our focal point, for providing the project and helping us to understand and conceptualize it. Without his efforts we would not have been able to successfully accomplish the goals of this research.

Our thanks are also extended to Mrs. Delores Spado for giving us administrative support, to Mr. Jeff Hanson for providing us with a Macintosh PowerBook for writing this report, and to Mr. James Siefert and Mr. Ron Woerner for the ADRI images and the DTED data files.

Finally, we would give our special thanks to Mr. John Pirog for providing us with a powerful computing facility and to Mr. Mike Scully for installing Khoros software and assisting us with many other miscellaneous computing tasks.

REFERENCES

- Argialas, D.P. (1985). A structural approach towards drainage pattern recognition, Ph.D. Dissertation, Dept. of Civil Engineering, The Ohio State University, Columbus, Ohio.
- Argialas, D.P., Lyon, J.C., & Mintzer, O.W. (1988). Quantitative description and classification of drainage patterns, *Photogrammetric Engineering and Remote Sensing*, vol. 54, no. 4, pp. 504-509.
- Colby, J.D. (1991). Topographic normalization in Rugged terrain, *Photogrammetric Engineering and Remote Sensing*, vol. 57, no.5, pp.531-37.
- Dubayah, R.O., & Dozier, J. (1986). Orthographic terrain views using data derived from digital terrain models, *Photogrammetric Engineering and Remote Sensing*, vol 52, no 4, pp.509-518.
- Hadipriono, F.C., Lyon, J.G., & Li W.H., T. (1990). The development of a knowledge-based expert system for analysis of drainage patterns, *Photogrammetric Engineering and Remote Sensing*, vol. 56, no. 6, pp. 905-909.
- Howard, A. (1967). Drainage analysis in geologic interpretation: a summation, *American Association of Petroleum Geologists*, vol. 51, pp. 2246-2259.
- Jenson, S.K (1985). Automated derivation of hydrologic basin characteristics from digital elevation model data, Proceedings of Auto-Carto 7, Washington, D.C., pp. 301-310.
- Jenson, S.K., & Domingue, J.O. (1988). Extracting topographic structure from digital elevation data for geographic information system analysis, *Photogrammetric Engineering and Remote Sensing*, vol. 54, no. 11, pp. 1593-1600.
- Lee, J., Snyder, P.K., & Fisher, P.F. (1992). Modeling the effect of data errors on feature extraction from digital elevation models, *Photogrammetric Engineering and Remote Sensing*, vol. 58, no. 10, pp. 1461-1467.
- Musavi, M.T., Shirvaikar, M.V., Ramanathan, E., & and Nekovei, A.R. (1988). A vision based method to automate map processing, *Pattern Recognition*, vol. 21, no. 4, pp. 319-326.
- O'Callaghan, J.F., & Mark, D.M. (1984). The extraction of drainage networks from digital elevation data, *Computer Vision, Graphics, and Image Processing*, vol. 28, pp. 323-344.
- Parvis, M. (1950). Drainage pattern significance in air photo identification of soils and bedrocks, *Photogrammetric Engineering*, vol. 16, pp. 387-409.
- Qian, J., Ehrich, R.W., Campbell, J.B. (1990). DNESYS - An expert system for automatic extraction of drainage networks from digital elevation data, *IEEE Transactions on Geoscience and Remote Sensing*, vol. 28, no. 1, pp. 29-44.
- Wiesel, J.W. (1985). Digital image processing for orthophotogeneration, *Photogrammetica*, Vol. 40, No. 2, pp. 69-76.

- Military Specification, Digital Terrain Elevation Data (DTED) Level 1, MIL-D-89000, Defense Mapping Agency, ATTN: PRS, 8613 Lee Highway, Fairfax, VA 22031-2137, April 1986.
- Khoros Image Processing Software, University of New Mexico, Department of Electrical and Computer Engineering, 1990.

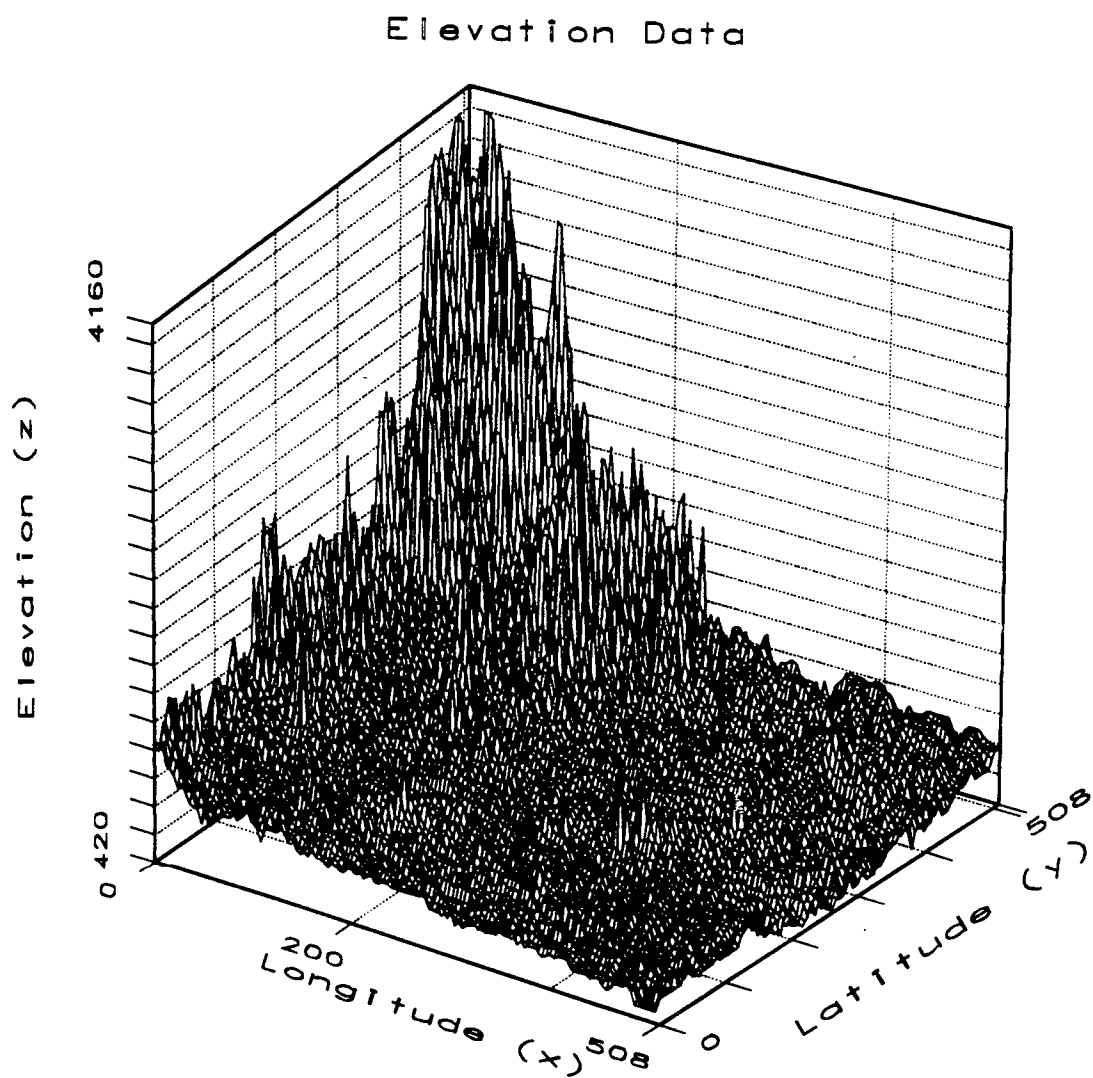


Figure 2. A three dimensional plot of a sample elevation data.



Figure 3. A gray level representation of the sample elevation data.

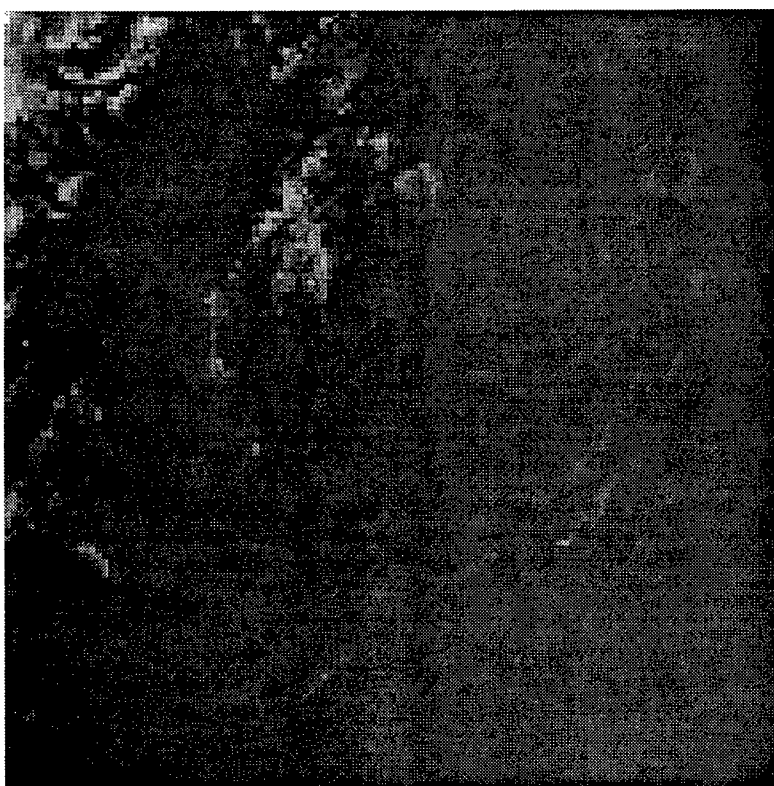


Figure 4. The result of a high pass filter on the sample elevation data.



Figure 5. The result of a histogram equalization on data of Figure 4.



Figure 6. The result of a low pass filter on the equalized image.



Figure 7. The result of a variable threshold binarization on the data of figure 6.

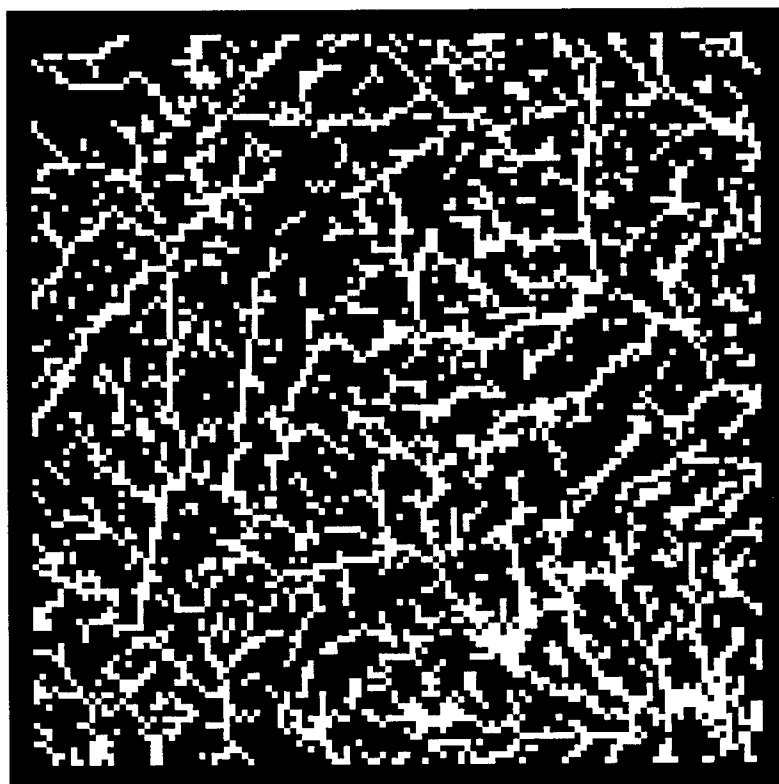


Figure 8. A binary representation of the local minima of the sample elevation data.

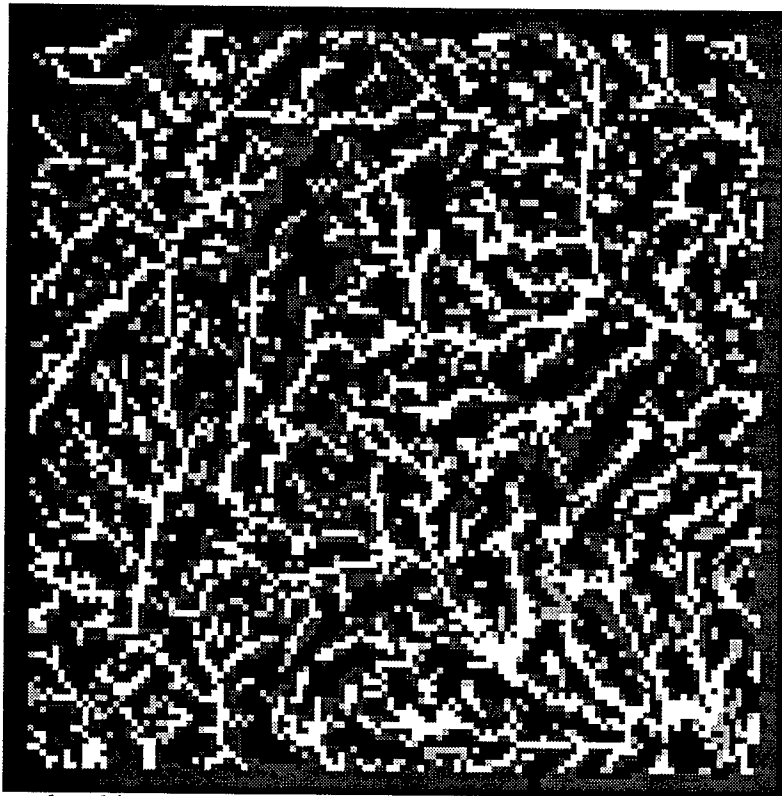


Figure 9. A four level image created from the general drainage area and the local minima.

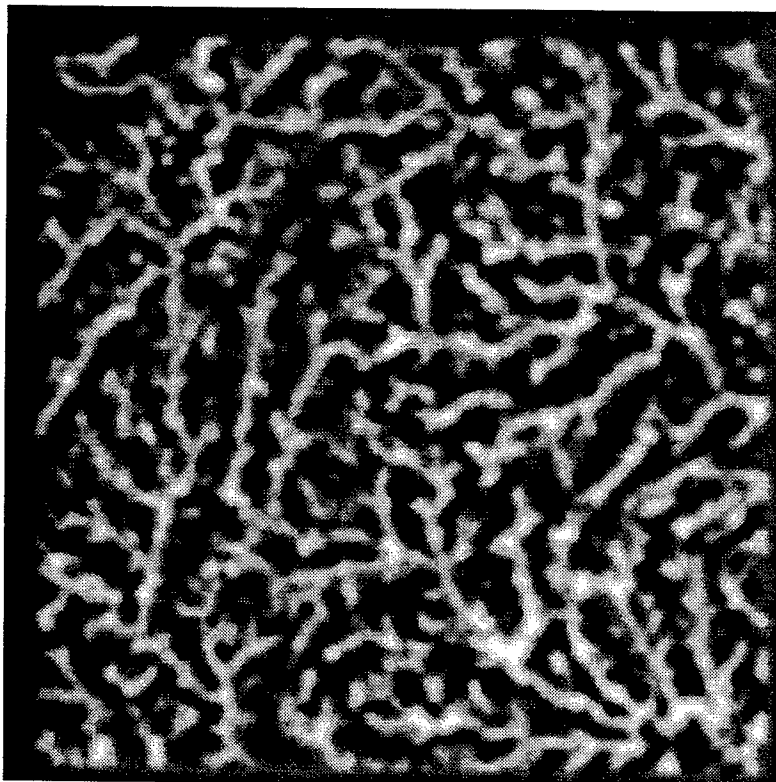


Figure 10. The result of smoothing operation on the four level data of Figure 9.

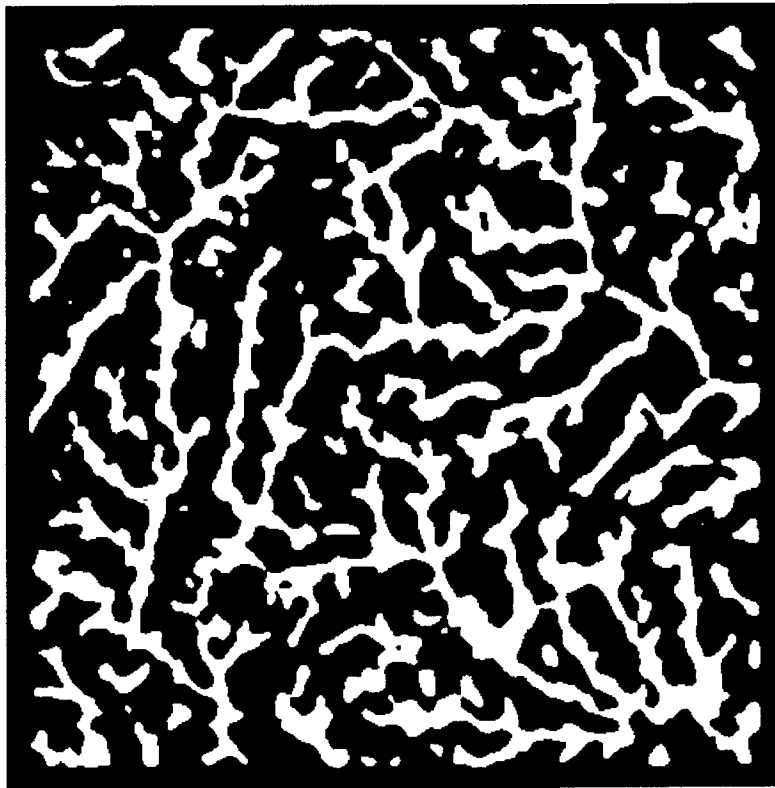


Figure 11. The result of a global thresholding on the data of Figure 10.

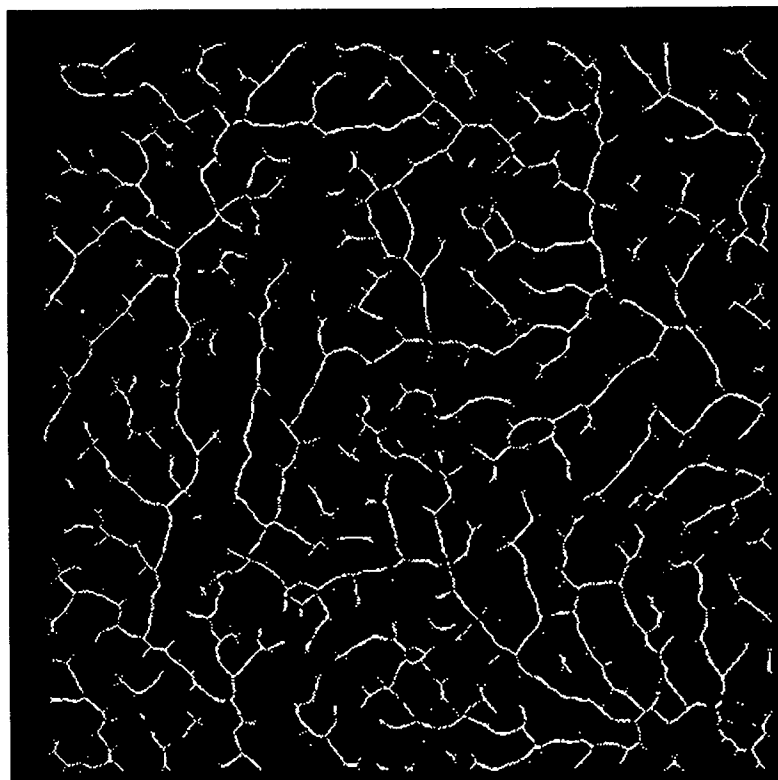


Figure 12. The result of thinning of the data of Figure 10, a possible drainage network.

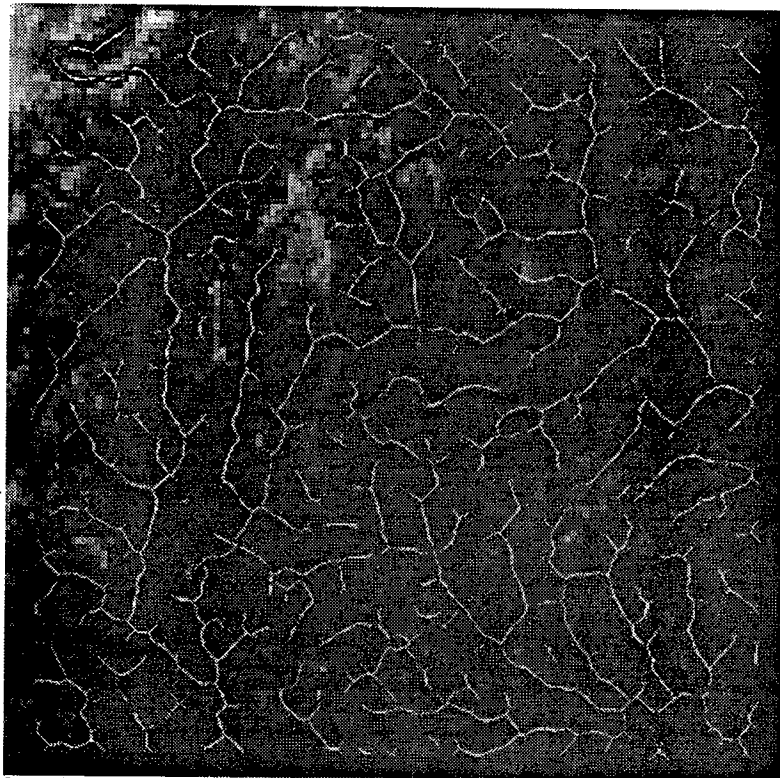


Figure 13. The overlay of a possible drainage network on the data of Figure 4.

INFRARED IMAGES OF ELECTROMAGNETIC FIELDS

John D. Norgard
Professor/ECE
Department of Electrical & Computer Engineering

University of Colorado
College of Engineering
1420 Austin Bluffs Parkway
Colorado Springs, CO 80917

Final Report for:
Summer Faculty Research Program

Rome Laboratory

Sponsored by:
Air Force Office of Scientific Research
Bolling AFB, Washington DC

September 1994

INFRARED IMAGES OF ELECTROMAGNETIC FIELDS

John D. Norgard
Professor/ECE
Department of Electrical & Computer Engineering
University of Colorado

Abstract

A new infrared (IR) imaging technique is being developed to measure two-dimensional electromagnetic (EM) field distributions near a radiator or a scattering body. Both electric and magnetic field intensities can be measured with this technique. Initial tests to prove the validity, accuracy and sensitivity of this new technique were performed this summer in the anechoic chamber at the Electromagnetic Vulnerability Analysis Facility (EMVAF) at Rome Laboratory (RL).

External radiation tests were performed on a conducting cylinder irradiated by an incident plane wave. E- and H- field patterns of the scattered/diffracted energy from the cylinder were measured. Tests were conducted at various microwave frequencies relative to the resonant frequencies associated with the cylinder and at numerous angles of incident (eg. end-on, broad-side, oblique-incidence) and at several different polarizations of the incident field relative to the axis of the cylinder (eg. horizontal, vertical, and skewed). Tests were performed in the near and far fields of the cylinder.

Internal coupling tests were performed to determine the induced energy coupled through long, thin slot apertures at various orientations in the side of the cylinder (eg. axial and longitudinal slots).

The scattering characteristics of several dielectric cylinders and spheres were also tested. Metallic and dielectric half-cylinders and half-spheres were tested for their scattering characteristics.

The radiation pattern of a standard gain horn (aperture antenna) was determined using the IR imaging technique. Radiation patterns in the E and H planes were taken in the near and far fields of the horn aperture. Several cross-sectional patterns were also taken in the near field of the horn and in the aperture plane.

These simple, canonical objects were tested to validate the accuracy of the IR technique. In all validation tests, the relative error was typically only 7 to 8 percent. Therefore, this new EM measurement technique, if further developed, has the potential to provide extremely accurate EM field measurements.

Three papers were presented at international IR and EM conferences this summer; three seminars were also presented on the technique. One paper has been submitted to an IR journal for publication; three new papers have been submitted for presentation at several IR conferences next year.

INFRARED IMAGES OF ELECTROMAGNETIC FIELDS

John D. Norgard

Table of Contents

1. Introduction
2. IR Measurement Technique (Overview)
 - 2.1 IR Experimental Setup
 - 2.1.1 Electromagnetic Parameters
 - 2.1.2 Thermal Parameters
 - 2.1.3 Thermal Equilibrium
 - 2.2 Approximate Solution
 - 2.3 IR Detector Screen
 - 2.3.1 Electric Field Detector Screen
 - 2.3.2 Magnetic Field Detector Screen
 - 2.4 IR Camera
 - 2.5 IR Images
 - 2.5.1 Spatial Resolution
 - 2.5.2 Thermal Resolution
 - 2.5.3 Polarization Dependence
 - 2.5.4 Thermogram Errors
 - 2.5.4.1 Lateral Conduction Effects
 - 2.5.4.2 Lateral Convection Effects
 - 2.5.5 IR Measurement Accuracy
 - 2.6 IR Advantages and Disadvantages
3. IR Thermograms ... Scattering from and Coupling into a Cylinder
4. Conclusions
5. Future Work
6. Publications
- Acknowledgement
- Figures
- Appendix

INFRARED IMAGES OF ELECTROMAGNETIC FIELDS

John D. Norgard

An infrared (IR) measurement technique is being developed to measure electromagnetic (EM) fields. This technique uses a minimally perturbing, thin, planar IR detection screen to produce a thermal map of the intensity of the EM energy over a two-dimensional region. EM fields near radiating microwave sources and scattering bodies can be measured with this technique. This technique also can be used to correlate theoretical data with experimental observations and to experimentally validate complicated numerical codes which predict electric field distributions inside waveguide cavities (E-Fields) and surface current distributions on metallic surfaces (H-Fields).

1. Introduction

A non-destructive, minimally perturbing IR measurement technique is being developed to observe EM fields. Metallic surface currents and charges also can be measured with this technique.

This IR measurement technique produces a two-dimensional IR thermogram of the electric or magnetic field being measured, i.e. a two-dimensional isothermal contour map or a gray scale of the intensity of the EM field.

Electric and magnetic fields can be measured separately. For example, electric field patterns radiated from microwave horn antennas, electric field intensities coupled through apertures in shielded enclosures, diffraction patterns of electric fields scattered from complicated metallic objects, and electric field modal distributions induced inside cylindrical waveguide cavities can be measured. Also, magnetic field distributions near conductive surfaces and induced surface currents on metallic surfaces can be determined.

The advantages and disadvantages of this new IR measurement technique are discussed later.

2. IR Measurement Technique (Overview)

The IR measurement technique is based on the Joule heating that occurs in a lossy material as an EM wave passes through the material. A thin, planar sheet of lossy carbon loaded paper can be used to map electric fields; a thin, planar sheet of lossy ferrite loaded epoxy can be used to map magnetic fields. In either situation, the absorbed heat energy is converted into conducted and convected heat energy and into re-radiated EM energy. The radiated EM energy is concentrated in the IR band. This "black body" energy can be detected with an IR (Scanning) Array or with an IR (Starring)

Focal Plane Array (FPA).

2.1. IR Experimental Setup

This technique involves placing a lossy non-perturbing IR detection screen in the plane over which the EM fields are to be measured.

2.1.1. Electromagnetic Parameters

The detector screen can be made from a thin sheet of linear, homogenous and isotropic but lossy material. From the complex form of Poynting's Theorem for a linear, homogeneous and isotropic material, the absorbed power P_{abs} within a given volume V of the lossy material is a function of the electric (E) and magnetic (H) field intensities inside the screen and is given by

$$P_{abs} = \int_V (\sigma E^2 + \omega \epsilon'' E^2 + \omega \mu'' H^2) dV \quad [W/m^2] \quad (1)$$

where σ is the conductivity of the detector screen, ϵ'' is the imaginary component of the permittivity of the detector screen, μ'' is the imaginary component of the permeability of the detector screen, and ω is the radian frequency of the incident field. The volume integral is over the illuminated portion of the detector screen. The spectral characteristics of the complex constitute parameters (μ, ϵ, σ) of the detector material must be known (or measured) over the entire frequency bandwidth to be measured.

The incident EM energy is absorbed by the lossy material and is converted into thermal heat energy which causes the temperature of the detector material to rise above the ambient temperature of the surrounding background environment by an amount which is proportional to the local electric and/or magnetic field intensity (energy) at each point (pixel) in the screen material. In regions where the fields are strong, the absorbed energy is large and the resulting pixel temperatures are high; in regions where the fields are weak, the absorbed energy is small and the resulting pixel temperatures are low. The resulting two-dimensional temperature distribution over the surface of the screen can be detected, digitized and stored in the memory of an IR camera. The temperature distribution on the surface of the screen without any EM energy incident on the screen also can be stored in the memory of the IR camera as a ambient background reference temperature distribution. The difference in the temperature distributions at each pixel (between the illuminated and the non-illuminated screen) is due to the effects of the electric or magnetic field incident on the screen at that pixel location.

The EM effects can be visualized by presenting the differenced two-dimensional temperature profile as a false color image, where cool colors (for example shades of blue) represent weak areas of

EM energy and hot colors (for example shades of red) represent strong areas of EM energy. The resulting two-dimensional false color image is called an IR thermogram, ie. an iso-temperature contour map, and is a representation of the electric and/or magnetic field distribution passing through the screen material.

2.1.2. Thermal Parameters

For a planar sheet of detector screen supported by a block of non-conducting material, eg. a styrofoam block, the thermal problem reduces to considering only the radiative and convective heat losses from the surface of the detector material.

The convective heat loss h_c is approximated by

$$h_c = h_o (T - T_{amb})^{1.25} \quad [W/m^2] \quad (2)$$

where h_o varies between 1.4 and 1.6. The radiative heat loss h_r is approximated by

$$h_r = \epsilon_{ir} \sigma_{ir} (T^4 - T_{amb}^4) \quad [W/m^2] \quad (3)$$

where ϵ_{ir} is the detector surface emissivity, σ_{ir} is the Stefan-Boltzman constant in $W/m^2 \cdot K^4$, and the temperatures are in degrees Kelvin. The conductive heat loss is negligibly small.

2.1.3. Thermal Equilibrium

The heat transfer problem in the detector material involves solving a non-linear, second order differential equation in both space and time, while considering radiative and convective heat losses from the surface of the material, conductive heat transfer within the material, and the EM power absorbed in the material as a function of distance into the material. For the case of the thin screens considered here, the temperature is initially considered to be constant in the direction normal to the surface of the material, so that the conductive term normal to the surface of the screen can be ignored and the power absorbed can be considered independent of the direction normal to the surface of the screen. Also, the time dependence of the absorbed heat energy is ignored for the steady-state solution.

Relating the convective and radiative heat losses in equations (2) and (3) to the absorbed power in equation (1), results in the following equation at thermal equilibrium:

$$P_{abs} = h_c + h_r \quad (4)$$

For a properly optimized detector screen, thermal equilibrium is achieved in just a few seconds.

This non-linear thermal/electrical equation can be solved for the electric or magnetic field, as a function of the material temperature T , using approximate techniques.

2.2. Approximate Solution

Equation (4) is highly non-linear for large temperature variations above ambient, due to the thermal processes of convection and radiation. However, for small temperature variations of only a few degrees above ambient, equation (4) can be linearized for small incremental temperature changes $\Delta T = T - T_{\text{amb}}$ above the ambient temperature T_{amb} .

This condition of small temperature variations above ambient is a desirable operational constraint, since this is also the requirement for small absorption of the EM energy passing through the screen, which equates to a small perturbation of the incident field when performing the measurement. For this minimally perturbing measurement case, an almost direct linear correlation exists between the incremental surface temperature ΔT and the absorbed electric or magnetic field intensity. The incident electric or magnetic field can then be determined from a solution of Maxwell's Equations (Fresnel's and Snell's laws) for an EM wave incident on a planar film of lossy material. Therefore, it is possible to correlate local surface temperature variations ΔT to E or H field intensities.

For the FPA camera available this summer at Rome Laboratory to make the IR thermograms, temperature differences ΔT as small as 0.01 °K could be detected.

Care is exercised, therefore, in the selection of the screen material not to significantly perturb the electric or magnetic field by the presence of the lossy material. The screen can be designed to absorb from 1% to 5% of the incident power and to produce a temperature change of less than a few degrees. The constitutive parameters of the IR detector screen can be optimized to produce a large temperature rise in the detector material for a small amount of absorbed energy.

Electric and magnetic fields produced by Continuous Wave (CW) sources operated in the sinusoidal steady-state mode are easy to measure because of the large amount of energy contained in the wave. Transients produced by high power microwave (HPM) pulsed sources, especially repetitively pulsed sources, also can be measured, if the average energy content in the pulse is high enough to raise the temperature of the detector screen material above the minimum temperature sensitivity of the IR camera. The thermal mass of the detector material should hold the absorbed heat energy long enough to capture the IR thermogram of the pulse.

2.3. IR Detector Screen

Referring to equation (1), the screen material can be tailored to respond to only one component

of the field, e.g. by optimizing the values of the electrical conductivity σ and the imaginary part of the permittivity ϵ'' of the material relative to the imaginary part of the permeability μ'' of the material, the detector screen can be made sensitive either to the tangential component of the electric field or to the tangential component of the magnetic field in the plane of the screen.

For example, an *electric* field detector screen can be constructed either

- i) from a lossy material with a high conductivity σ and a low imaginary permittivity ϵ'' and a low imaginary permeability μ''
- or ii) from an electrically polarizable material with a high imaginary permittivity ϵ'' and a low conductivity σ and a low imaginary permeability μ'' .

Alternatively, a *magnetic* field detector screen can be constructed from a magnetically polarizable (magnetizable) material with a high imaginary permeability μ'' and a low conductivity σ and a low imaginary permittivity ϵ'' .

The optimization of the thermal and electrical parameters of the detection screen material should be guided by a thermal/electrical computer code based on a plane wave normally incident on a planar interface between air and the lossy detector material. Other absorptive and re-emissive transducing materials have been studied for use as passive thermal screens for IR thermograms.

2.3.1 Electric Field Detector Screen

For the detection of electric fields, the IR detector screen can be made from a planar sheet of lossy thin-film material. Several different detector screens were used to make electric field thermograms. One was a carbon loaded thin film (eg. Teledeltos Paper) 80 μm thick with a conductivity of 8 mhos per meter. The other screens were made from carbon-loaded Kapton films. The films were loaded with different resistivities per square. These materials are non-polarizable and non-conducting; therefore, the imaginary components of the permittivity ϵ'' and the permeability μ'' are negligibly small. For these non-conducting, non-polarizable, non-magnetic screen materials, maximum heating occurs due to the electric field and negligible heating occurs due to the magnetic field.

For plane waves normally incident on this carbon loaded electric field detection screen and for an IR FPA with a temperature sensitivity of 0.01 $^{\circ}\text{K}$, electric fields with a magnitude on the order of 61.4 V/m (1 mW/cm² of incident power) could be detected. This result was obtained empirically from experimental data in which the incident power level was incrementally decreased until no electric field contour lines on the IR thermogram were discernable from the ambient background level.

2.3.2 Magnetic Field Detector Screen

For the detection of magnetic fields, an IR detection screen can be fabricated using a ferrite loaded epoxy. Several different ferrite powders have been tested, viz. Nickel Zinc Copper Ferrite, Iron Silicide Ferrite, Ferrite 50, etc. The best detector screen used to make magnetic field thermograms had an 80% by weight mixture of Ferrite 50 with a thickness of 0.5 mm and an imaginary relative permeability μ'' of approximately 2. The imaginary component of the permittivity ϵ'' and the conductivity σ were negligibly small. For this magnetic, non-conducting, non-electric screen material, maximum heating occurs due to the magnetic field and negligible heating occurs due to the electric field.

In the fabrication of a magnetic screen, it is difficult to keep the electric polarizability of the epoxy base material from contributing to the imaginary component of the permittivity ϵ'' of the composite and, thereby, introducing additional electric polarization losses. If the electric properties of the ferrite are not carefully controlled and minimized, the absorbed power will be due to both the electric and magnetic components of the EM field, as given by equation (1). In this case, it is difficult, if not impossible, to separate the two coupling mechanisms from each other and to calibrate the technique.

To detect surface currents on a metallic structure, the magnetic detection screen can be placed in direct contact with the surface of the metal. The thickness of the detector screen must be kept to a minimum, so that the magnetic field that is measured on the outer surface of the screen is a direct reflection of the magnetic field on the inner surface of the screen in contact with the surface of the metal. The material can be held flat against the surface of the metal using a non-conducting glue.

The surface current is related to the tangential component of the magnetic field intensity on the surface of the metal by the magnetic boundary condition on a perfect conductor:

$$\hat{n} \times \vec{H} |_s = \vec{J}_s$$

where \hat{n} is the normal to the surface S . The magnetic field is perpendicular to the direction of the surface current.

2.4 IR Camera

The temperature difference between the screen material and the background is detected, digitized, and can be stored in the memory of an IR camera on a pixel by pixel basis. The IR imaging system used to take the IR thermograms has approximately 200 by 100 pixels per frame of data. The detector is scanned over the image. The detector is a Mercury-Cadmium-Telluride (HgCdTe) IR photo detector operated in a photo voltaic mode. The detector operates at liquid Nitrogen temperatures. The

camera can detect temperature differences of approximately 0.01 °K, and has a relative accuracy of plus or minus 10% when detecting EM fields.

2.5 IR Images

The stored IR thermogram data represents the temperature distribution over the extent of the detector screen and is a map of the intensity of the electric or magnetic field distribution absorbed in the screen. For small temperature rises less than a few degrees above ambient, the electric and magnetic field intensities are nearly linearly proportional to the temperature change.

2.5.1 Spatial Resolution

The spatial resolution of the IR thermogram is a function of the number of pixel elements in the IR camera, and is fixed by the angular resolution of the telephoto, regular or wide angle lens used on the IR camera when making the IR image. A telephoto lens can be used to look at small details in the field structure on the detector screen; a wide angle lens can be used to look at large scale trends in the field structure in the detector screen.

The telephoto lens also has the added advantage for regular field mapping applications of allowing the IR camera to be located far away from the object under test and, thus, removing any perturbing effects that the metallic structure of the camera might have on the field distribution being measured.

2.5.2 Thermal Resolution

The thermal resolution of the IR thermogram is a function of the digitizer in the IR camera. The IR camera used to take the IR thermograms has a 12 bit digitizer. For a 12 bit digitizer, the temperature range seen by the IR camera is divided into 256 increments. Each digitized increment is assigned a unique color, resulting in a temperature resolution of 256 color levels.

2.5.3 Polarization Dependence

The magnitude of the total electric or magnetic field at each point on the detector screen can be measured by the IR technique, however, no phase information is available. Both polarizations in the plane of the screen are combined to produce the total magnitude of the field. One polarization can be measured if the detector screen is striated into a large number of thin, parallel strips of lossy material

each separated by a lossless material, eg. air. Only the component of the field in the direction of the stripes will be measured with this detector material configuration. The striated detector screen can be rotated 90° to pick-up both components of the field in the plane of the screen.

2.5.4 Thermogram Errors

The resulting IR image of an EM field depends on the combined EM and thermal properties of the detector material and is subject to several significant, but controllable, errors.

2.5.4.1 Lateral Conduction Effects

Conductive heating in the transverse direction within the screen material causes thermal "bleeding" from the hot spots on the screen to nearby cold spots. This thermal bleeding tends to fill in the nulls (minimums) somewhat, whereas, the areas of maximum heating (peaks) are not effected very much by this effect. This effect can be minimized by operating at small temperature variations above ambient.

2.5.4.2 Lateral Convective Effects

Convective heating of the top of the screen from heat rising from the bottom of the screen causes the top of the screen to appear slightly hotter than the bottom of the screen. This "blurring" of the image can be kept to a minimum by operating at small temperature variations above ambient.

This blurring effect can be eliminated completely by placing the IR detector screen in a horizontal position and observing the image with the IR camera looking down on the screen from above or from the side using an IR mirror.

2.5.5 IR Measurement Accuracy

The accuracy of the IR measurement technique can be demonstrated by performing two simple experiments with known theoretical solutions. In one experiment, as shown in *figure 1*, the diffraction pattern from a "Lloyd's Mirror" was measured. In the other experiment, as shown in *figure 2*, the diffraction pattern from an "knife edge" conducting half-plane was measured.

In the Lloyd's mirror experiment, the resulting diffraction pattern is due to the antenna interfering with its image in a large ground plane. The second peak in *figure 1* is smaller in magnitude than the first peak due to the fact that the radiation pattern of the horn antenna used in the experiment

decreases with angle from the bore sight direction of the horn. The near field (Fresnel Zone) antenna pattern of the horn antenna was used to obtain the theoretical results.

In both experiments, the screen material was optimized to measure only the tangential component of the electric field intensity in the plane of the screen.

These experiments were performed in an anechoic chamber, as shown in *figures 1a and 2a*. Good correlations between theory and experiment were obtained, as shown in *figures 1b and 2b*. The worst errors occurred in the minimums (deep nulls) of the diffraction patterns were thermal bleeding from the surrounding hot areas tended to obscure the real depth of the minimums. Some thermal bleeding out of the maximums into the surrounding areas also occurred, obscuring the real height of the maximums.

Even with conductive bleeding and convective blurring of the image, the measurement error is less than approximately 10% under controlled test conditions.

2.6 IR Advantages and Disadvantages

The IR measurement technique provides a quick and accurate method to observe EM fields in a two-dimensional plane. However, only the magnitude of the electric or magnetic field is measured; no phase information is detected. Also, since this technique is based on the thermal mass of the detector material, high energy is required to produce good thermal images of EM fields.

3. IR Thermograms ... *Scattering from and Coupling into a Cylinder*

As an example of the IR measurement of electric fields, a right circular cylinder, containing a long, thin slot aperture in its side, was irradiated with a plane EM wave. IR thermograms were made of the diffraction pattern of the EM field scattered from the cylinder and the cylindrical modes excited inside the cavity. The experimental setup is shown in *figures 3a and 3b*.

Measurements on a finite length cylinder (3D images) and theoretical predictions for an infinite length cylinder (2D cross-sectional analyses) were made and correlated.

The experimental cylinder is one meter in length and has an inner diameter of approximately 10 centimeters. The rectangular slot aperture is 64 millimeters in width and is 10 centimeters in length. The slot is located in the middle of the cylinder and is oriented parallel to the axis of the cylinder. The cylinder was irradiated with microwave energy at 3 GHz (10 centimeter wavelength) from a pyramidal horn antenna, polarized in the circumferential direction of the cylinder. Cylindrical TE modes were predominantly excited by the wave polarization inside the cavity.

A large IR detector screen of carbon paper was positioned in the radial plane that intersected

the middle of the slot aperture. Another IR disk was positioned inside the cylinder in the same cross-sectional plane.

Experimentally obtained IR thermograms of the results are shown in *figures 4 through 6*. The brightness of each color in the image corresponds to the intensity of the EM field.

Thermograms of the incident microwave field of a horn antenna are shown in *figure 4*. *Figure 4a* is an image of the electric field traveling wave in the longitudinal plane in front of the horn. *Figure 4b* is an image of the electric field in the transverse (cross-sectional) plane one meter in front of the aperture of the horn.

Thermograms of the field scattered from a cylinder are shown in *figure 5*. *Figure 5a* is an image of the electric field standing wave created between the horn and the cylinder. This thermogram shows the interference pattern between the incident wave and the scattered cylindrical wave. *Figure 5b* is an image of the electric field traveling wave in the shadow zone of the cylinder. The null behind the cylinder and the diffracted wave off the top and bottom of the cylinder can be seen in this thermogram.

Thermograms of the induced modes coupled into the cylindrical cavity are shown in *figure 6*. *Figure 6a* is an image of the electrical field coupled through the aperture for a frequency 10% below the cutoff frequency of the cylindrical waveguide. The EM energy coupled through the aperture is visible in this thermogram and, as expected, has the radiation pattern of an electric dipole. The dominant TE_{11} waveguide modal pattern is partially developed in the center of the waveguide. *Figure 6b* is an image of the electrical field coupled through the aperture for a frequency 10% above the cutoff frequency of the cylindrical waveguide. The dominant TE_{11} waveguide modal pattern is now fully developed in the center of the waveguide.

The diffraction patterns of the EM fields scattered from the cylinder and the modal patterns of the induced cylindrical cavity modes are clearly indicated in these figures.

4. Conclusion

The IR measurement technique is a viable method to aid in the determination of EM fields scattered from complex metallic objects and the EM energy coupled into complex cavity structures. This method is of particular importance in the study of scattering surfaces with complicated geometrical shapes, whose patterns of surface current distributions may not be found easily using theoretical methods.

The IR method allows for rapid observation of EM field activity and interference, resulting in an in-depth understanding of the EM scattering and coupling phenomena. Qualitative and quantitative comparisons can be made between the fields measured using the thermal radiation experimental

approach and the fields predicted using a theoretical/numerical approach. Experimental and theoretical data, therefore, can be easily correlated with this technique.

5. Future Work

The development of a suitable magnetic detection screen is in progress. The use of spin-on magnetic thin films is being investigated.

The calibration of the IR thermogram images to determine the absolute magnitude of the electric or magnetic field intensity is also in progress. Several empirical tests have been performed with a standard gain horn aperture antenna to correlate the intensity of the EM power of the radiated wave incident on the detector screen with the intensity of the measured temperature (color) of the screen on a pixel by pixel basis.

It may also be possible to estimate the phase of the incident wave by making a numerical model of the thermal/electromagnetic interaction in the detector screen material, and to use energy minimization techniques to estimate the phase of the incident wave. This work is being done in conjunction with Syracuse University (Prof. Tapan Sakar).

The imaging technique is also being used to map fields around a simple generic model of an aircraft. The IR thermograms of the scattered microwave energy will be used to verify the accuracy of the numerical code. The particular code being tested is the GEMAC code developed at Rome Laboratory.

6. Publications

The papers published on this project during the AFOSR Summer Research Program are listed in the Appendix.

Acknowledgement

The author would like to acknowledge the support of the AFOSR Summer Research Program on this IR project and the help of Michael Seifert at Rome Laboratory.

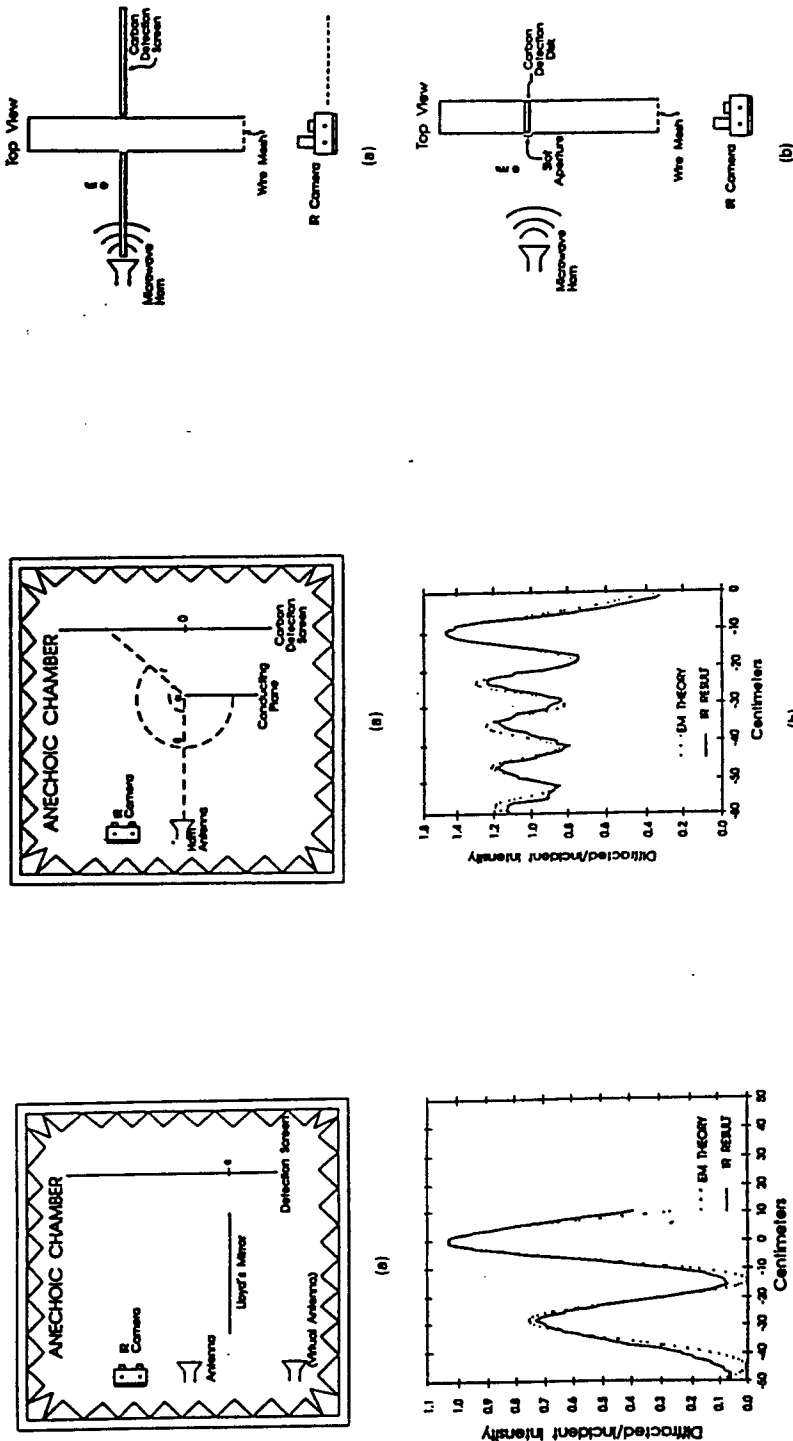


Fig. 3 Experimental arrangement for IR images of plane wave scattering from a finite-length cylinder and slot aperture coupling into a cylindrical waveguide cavity. (a) IR camera and detector screen setup for measuring exterior scattered fields. (The IR camera is positioned on either side of the cylinder). (b) IR camera and detector screen setup for measuring interior cylindrical waveguide cavity modes. (The IR camera is positioned on the axis of the cylinder and looks through a wire mesh screen simulating a microwave shield.)

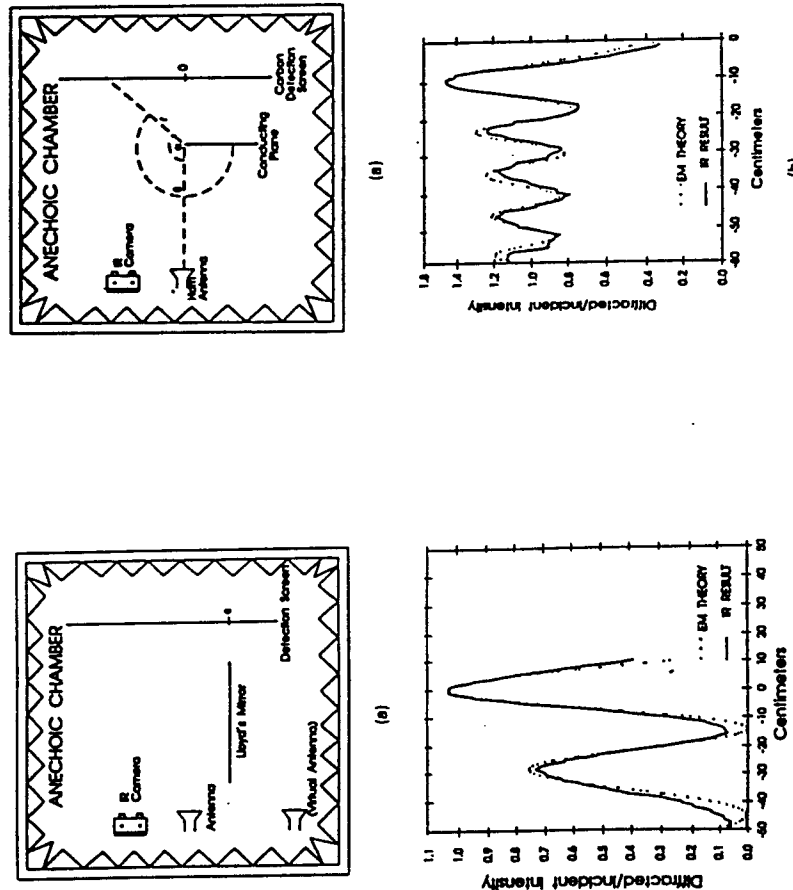


Fig. 2 Conducting half-plane experiment (an antenna in front of the edge of a half-plane)—correlation between theory and experiment: (a) IR experimental setup (looking down into the anechoic chamber) and (b) near-field diffraction pattern from a half-plane (along a horizontal line through the center of the IR detection screen).

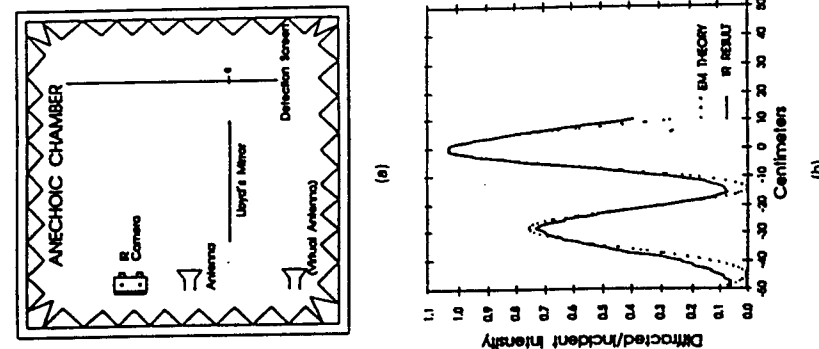
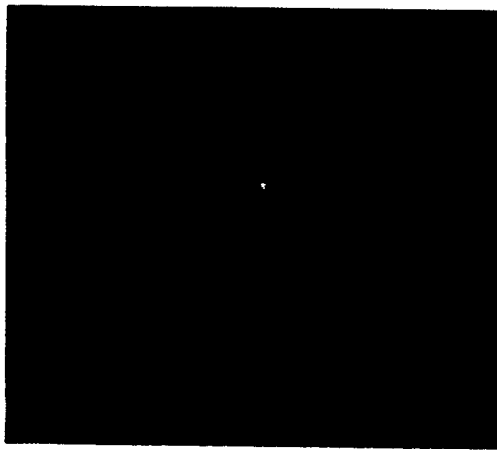


Fig. 1 Lloyd's mirror experiment (an antenna near a large ground plane)—correlation between theory and experiment: (a) IR experimental setup (looking down into the anechoic chamber) and (b) near-field diffraction pattern from a finite ground plane (along a horizontal line through the center of the IR detection screen).

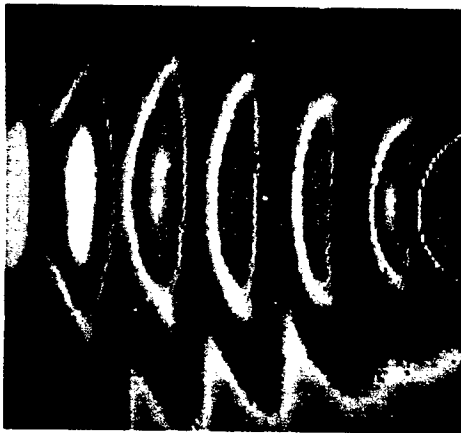


(a)

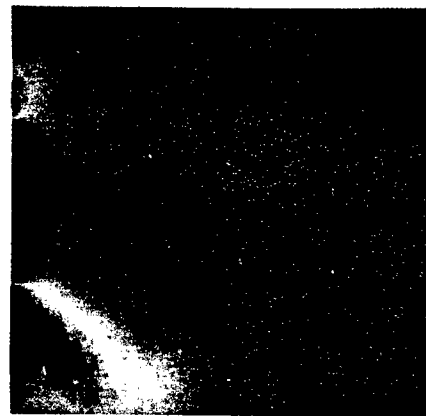


(b)

Fig. 4 IR thermogram of a microwave horn radiation pattern: (a) in the longitudinal plane (in a vertical plane through the center of the horn aperture) and (b) in the transverse plane (a cross-sectional cut of the microwave beam 1 m in front of the plane of the aperture).

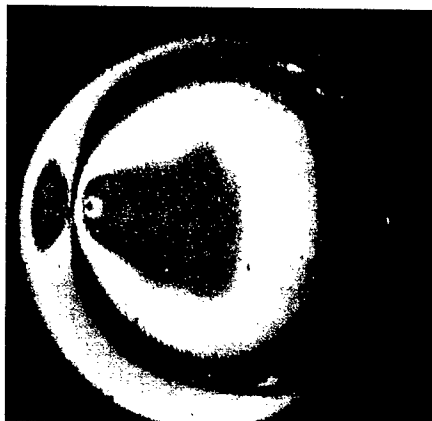


(a)

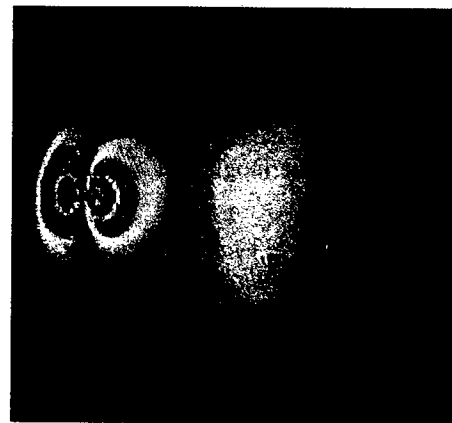


(b)

Fig. 5 Diffraction pattern of the scattered electric field from a finite cylinder: (a) standing wave between the horn and the cylinder (showing the constructive and destructive interference patterns between the incident and the reflected waves) and (b) traveling wave behind the cylinder (showing the shadow zone and the surface-diffracted waves).



(a)



(b)

Fig. 6 Excited cylindrical waveguide cavity modes. (The long, thin, horizontal slot aperture is centered on the left-hand side of the IR thermograms. A round IR detection screen is placed inside the cylinder. Note the reflection in the waveguide walls.) (a) excitation of an evanescent mode (at a frequency 10% below the cutoff frequency of the cylindrical waveguide) and (b) excitation of the dominant TE_{11} cylindrical waveguide mode (at a frequency 10% above the cutoff frequency of the cylindrical waveguide). Note the dipole pattern at the aperture predicted by Bethe hole coupling models.

APPENDIX

A. *Papers Presented:*

1. "Infrared Images of Electromagnetic Fields"
Dual-Use Technology Conference
SUNY/Utica, NY
May 1994
2. "Infrared Measurements of Waveguide Modes and Radiation Patterns of Beveled-Cut Shaped-End Microwave Antennas"
SPIE Symposium
Thermosense XVI
Orlando, FL
May 1994
3. "High Power Microwave (HPM) Antenna Design using Infrared Imaging Techniques"
QIRT Conference
Sorrento, Italy
June 1994

B. *Seminars Presented:*

1. "Infrared Images of External Radiated Electromagnetic Fields Scattered from a Finite Cylindrical Waveguide"
US Air Force Academy
Department of Electrical Engineering
Colorado Springs, CO
June 1994
2. "Infrared Images of Electromagnetic Fields"
Norwegian Defense Research Establishment (NDRE)
FFI/Geophysics
Kjeller, Norway
August 1994
3. Infrared Images of Internal Coupled Electromagnetic Field Modes in a Cylindrical Waveguide Cavity"
US Air Force Academy

Department of Electrical Engineering
Colorado Springs, CO
September 1994

C. Journal Articles Submitted:

1. "Measurement of Absolute Electromagnetic Field Magnitudes using Infrared Thermograms"

EuroTherm Quantitative Infrared Measurement Journal

D. Papers Submitted:

1. "Measurement of Absolute Electromagnetic Field Magnitudes using Infrared Thermograms"

URSI Winter Meeting
CU/Boulder, CO
January 1995

2. "Code Validation of Aircraft Scattering Parameters using IR Thermograms"

ACES Symposium
US NPS/Monterey, CA
March 1995

3. "Empirical Calibration of Infrared Images of Electromagnetic Fields"

SPIE Conference
Thermosense XVII
Orlando, FL
May 1995

ANYTIME INFERENCE AND DECISION METHODS

**Michael Pittarelli
Associate Professor
Computer Science Department**

**SUNY Institute of Technology
Utica, NY 13504-3050**

**Final Report for:
Summer Faculty Research Program
Rome Laboratory**

**Sponsored by:
Air Force Office of Scientific Research
Bolling Air Force Base, DC**

and

Rome Laboratory

August 1994

ANYTIME INFERENCE AND DECISION METHODS

Michael Pittarelli
Associate Professor
Computer Science Department
SUNY Institute of Technology

Abstract

We examine methods of decision making that are able to accommodate limitations on both the form in which uncertainty pertaining to a decision problem can be realistically represented and the amount of computing time available before a decision must be made. The methods are *anytime algorithms* in the sense of Boddy and Dean [1989]. An anytime adaptation of Nilsson's [1986] probabilistic logic is developed. Decision making techniques are presented for use with this system of logic, with Frisch and Haddawy's [1992] anytime deduction system, and with a probabilistic database model.

ANYTIME INFERENCE AND DECISION METHODS

Michael Pittarelli

1. Anytime Algorithms for Decision Making

An algorithm qualifies as an *anytime algorithm* [Boddy and Dean, 1989] if, minimally, it is interruptable in such a way that it provides usable output at any time it is interrupted and if the expected quality of the output improves in some sense with increasing execution time. (Additional properties are sometimes assumed, for example, that the marginal improvement in the quality of the output is nonincreasing.) For a decision problem under risk, where the probability of each of the conditions is known and is represented as a single real number, an anytime decision algorithm might consider the actions in some arbitrary sequence and output at each step the action with highest expected utility among those so far examined. The higher the expected utility of the action identified as best by a particular time, the better. Clearly, an action identified as best (among all those examined so far) at a later time will have higher expected utility than one identified as best at an earlier time. (However, the *improvement* in expected utility will not be a nonincreasing function of computing time.)

A more realistic representation of uncertainty is by means of intervals of real numbers [Kyburg, 1992]. A reasonable decision criterion interprets the intervals as linear inequality constraints determining a set of real-valued probability functions over the conditions and identifies an action as inadmissible if there does not exist an element of the set relative to which the action maximizes expected utility [Levi, 1980]. This may be determined for each action by checking for the existence of a feasible solution to a linear program [Pittarelli, 1991]. Any action not yet ruled out as inadmissible by some time may be classified (possibly incorrectly) as admissible relative to the current collection of probability intervals. At a higher level, the set of intervals may be iteratively refined (e.g., for confidence intervals, by decreasing the confidence level [Loui, 1986]) and the process of testing for inadmissibility repeated for each refinement, for the elements of the most recently computed admissible set.

With this sort of constraint on probabilities over conditions, the fewer actions identified as E-admissible, the better. As processing continues, tighter constraints reveal certain actions to be inadmissible. An action ruled out as inadmissible at one step will not be identified as admissible at any later step. Hence, at later stages, there are fewer actions among which choice using criteria other than E-admissibility (e.g., maximin, leximin, minimax regret, etc.) must be made. (Note that both the maximum and the minimum expected utility among actions in the admissible set decrease with additional computing time.)

A system for "anytime deduction" has been developed by Frisch and Haddawy [1992]. In this system, an interval of probability for a conclusion is determined from a collection of premises each of which itself has an associated probability interval. The interval of probability for the conclusion is initially [0,1] and is narrowed with each application of a rule of inference. This approach differs from [Nilsson, 1986] which requires the construction of a potentially very

large linear program for determining the endpoints of the probability interval for the entailed sentence. However, as explained in detail later in this report, it is straightforward to produce an anytime inference technique by an adaptation of Nilsson's methods that considers only subsets of the given set of premises. We will discuss methods of anytime decision making suitable for both forms of probabilistic inference.

Probabilistic databases [Pittarelli, 1994], that is, collections of contingency tables of joint frequencies or (real- or interval-valued) probabilities for finite variables, may also provide linear constraints relevant to a decision problem. There is again a tradeoff between the tightness of the constraint that can be inferred and the cost of doing the inference. We will discuss methods of anytime decision making utilizing probabilistic databases also.

2. Anytime Deduction and Decisions

Frisch and Haddawy [1992] have developed a system of deduction for probabilistic logic based on inference rules. The rules may be employed to compute increasingly narrow probability intervals for the conclusion of an argument. At any time, the currently computed interval is correct in the sense that it contains the narrowest interval computable from the probabilities associated with all of the premises. Thus, there is a tradeoff between the precision of an entailed probability interval and the time required to compute it. This feature makes anytime deduction especially suitable for use by "resource-bounded" systems [Horvitz *et al.*, 1989]; as Frisch and Haddawy point out, however, how to control the time/precision tradeoff depends on the particular decision situation in which the system finds itself.

Frisch and Haddawy's anytime deduction, Nilsson's probabilistic logic (unless maximum entropy or related techniques are used), and related systems, produce probability intervals for entailed sentences. A criterion applicable to decision problems in which probabilities are given as intervals and that reduces to standard maximization of expected utility when the intervals reduce to point values is Levi's *E-admissibility* criterion [Levi, 1980]: all and only those actions maximizing expected utility relative to some member of the set of (point valued) probability functions compatible with (or actually representing [Kyburg, 1992]) current beliefs are admissible. (Such actions are also referred to as *Bayes solutions*.)

We will consider decision problems consisting of a set of actions $A = \{a_1, \dots, a_m\}$ and a set of mutually exclusive and exhaustive conditions $C = \{c_1, \dots, c_n\}$ such that

$$p(c_j | a_i) = p(c_j), \text{ for all } i, j.$$

(Jeffrey [1976] shows how a problem in which conditions are not probabilistically independent of actions can be converted to an equivalent problem in which they are.)

A family D of subsets of the $(n-1)$ -dimensional simplex P_C of all probability distributions over C may be defined as

$$D = \{D(a_1), \dots, D(a_m)\},$$

where

$$D(a_i) = \{p \in P_C \mid \sum_{j=1}^n p(c_j) \times U(a_i, c_j) \geq \sum_{j=1}^n p(c_j) \times U(a_k, c_j), k=1, \dots, m\}.$$

$D(a_i)$ is the set of probability functions relative to each of which action a_i maximizes expected utility, and is referred to as the *domain* of a_i [Starr, 1966]. Each domain is convex; domains may intersect at faces; and $\bigcup_{a \in A} D(a) = P_C$.

Suppose the current belief state regarding probabilities of conditions is represented as $K \subseteq P_C$. An action a is E-admissible if and only if $K \cap D(a) \neq \emptyset$. The number of admissible actions decreases monotonically with the size of K :

$$K_1 \subseteq K_2 \rightarrow K_1 \cap D(a_i) \subseteq K_2 \cap D(a_i).$$

Thus, there will be a tradeoff between the quality of a decision — i.e., the number of admissible actions among which choice must be made using a criterion other than E-admissibility — and the computational expense of shrinking K . Reduction in the size of K may be achieved by applying additional inference rules; by adding premises, thereby enlarging the linear constraint system; by “extending” and “projecting” larger and larger portions of a probabilistic database; etc. (Of course, the *perceived* quality of a decision may be enhanced without this much work: invoke the maximum entropy principle. This approach will be criticized below.) Computing aimed at reducing the number of admissible actions may be interleaved with analysis of the type proposed by Horvitz et al. [1989] to determine whether the cost of such computation exceeds its expected value.

Consider a decision involving the two actions “Go to the beach” and “Do not go to the beach” the outcome of which is contingent on the truth or falsity of the probabilistically entailed sentence “It will rain this afternoon”. Utilities of the four possible outcomes are:

$$\begin{aligned} U(\text{Go, Rain}) &= 0, \\ U(\text{Go, No rain}) &= 1, \\ U(\text{Do not, Rain}) &= 0.8, \\ U(\text{Do not, No rain}) &= 0.2. \end{aligned}$$

The following propositions and associated probability intervals are available:

- (1) $p(\text{Temperature} > 85) \in [.95, 1]$
- (2) $p(\text{Humidity} > 80) \in [.95, 1]$
- (3) $p(\text{B. pressure} < 30) \in [.95, 1]$
- (4) $p((\text{B. pressure} < 30 \ \& \ \text{Humidity} > 80) \rightarrow \text{Rain}) \in [.65, .95]$
- (5) $p(\text{Temperature} > 85 \rightarrow \text{Rain}) \in [.4, .6]$
- (6) $p(\text{Cloudy} \ \& \ \text{Windy}) \in [.75, 1]$
- (7) $p(\text{Cloudy} \rightarrow \text{B. pressure} < 30) \in [.5, .8]$.

Both “Go to the beach” and “Do not go to the beach” have non-empty domains: “Go” maximizes expected utility when $p(\text{Rain}) \leq 0.5$; “Do not” does when $p(\text{Rain}) \geq 0.5$. Neither can be ruled out at this stage. However, Frisch and Haddawy’s probabilistic inference rules may be applied one-at-a-time to narrow the interval for $p(\text{Rain})$ until a single admissible action emerges, or it is no longer economical to continue refining (e.g., the last train to the beach is about to leave) and a choice among the admissible actions must be made using some other criterion (e.g., choose at random [Elster, 1989], use maximin, maximize expected utility relative to the midpoint of the probability interval, etc.).

A simple strategy for selecting portions of the database to which to apply the inference rules

suggests itself: Begin by applying the "Trivial derivation" rule,

$$\vdash p(\alpha|\delta) \in [0,1],$$

with α instantiated to each target proposition. Then add all sentences containing as a component one of the target propositions. If the target intervals are insufficiently narrow to eliminate all but one of the actions, add the sentences containing the other propositions contained in the first set of sentences, and so on. This can be refined to the addition of just one such sentence at each step.

In the example, there is one target proposition, and the trivial derivation rule gives

$$(8) p(\text{Rain}) \in [0,1].$$

Sentences (4) and (5) contain the statement "Rain". Trivial derivation can be applied to the antecedents, which in turn can be combined with (8) via "Forward implication propagation".

$$p(\beta|\delta) \in [x,y], p(\beta \rightarrow \alpha|\delta) \in [u,v] \vdash p(\alpha|\delta) \in [\max(0, x+u-1), v],$$

to yield two more intervals for $p(\text{Rain})$:

$$(9) p(\text{Rain}) \in [0, .95].$$

$$(10) p(\text{Rain}) \in [0, .6].$$

Sentence (10) is again produced when (8), (9), and (10) are combined using the "Multiple derivation" rule:

$$p(\alpha|\delta) \in [x,y], p(\alpha|\delta) \in [u,v] \vdash p(\alpha|\delta) \in [\max(x,u), \min(y,v)].$$

Use of this rule is necessary to maintain the tightest determinable interval at each step for the target sentence and is essentially what gives Frisch and Haddawy's system its anytime character.

Both actions remain admissible at this point.

There are no more sentences containing "Rain" as a component. We now look at those containing "Barometric pressure < 30", "Humidity > 30", and "Temperature > 85".

"Conjunction introduction",

$$p(\alpha|\delta) \in [x,y], p(\beta|\delta) \in [u,v] \vdash p(\alpha \& \beta|\delta) \in [\max(0, x+u-1), \min(y,v)]$$

may be applied to statements (2) and (3), resulting in

$$(11) p(\text{B. pressure} < 30 \& \text{Humidity} > 80) \in [.9,1].$$

Applying forward implication propagation to statements (4) and (11) gives

$$(12) p(\text{Rain}) \in [.55, .95]$$

Although combining statement (12) with statement (10) via the multiple derivation rule will further narrow the target interval, there is no need to do so; nor is there any need to consider statements (1), (6), and (7). "Do not go" has emerged as uniquely admissible:

$$D(\text{Do not go}) = \{p \in P_{\{\text{Rain, No rain}\}} \mid p(\text{Rain}) \geq .5\},$$

$$D(\text{Go}) = \{p \in P_{\{\text{Rain, No rain}\}} \mid p(\text{Rain}) \leq .5\},$$

$$D(\text{Go}) \cap \{p \in P_{\{\text{Rain, No rain}\}} \mid p(\text{Rain}) \in [.55, .95]\} = \emptyset.$$

$$D(\text{Do not go}) \cap \{p \in P_{\{\text{Rain, No rain}\}} \mid p(\text{Rain}) \in [.55, .95]\} \neq \emptyset.$$

3. Nilsson's Probabilistic Logic and Decision Making

Nilsson's methods may be modified to yield an anytime procedure for decision making. Rather than construct the linear system corresponding to the full set of sentences, increasingly larger

systems may be constructed by adding sentences to the subset currently in use until a uniquely admissible action emerges or it is necessary to choose among the currently admissible actions.

This may be illustrated with the sentences and decision problem above. Suppose sentences (2) and (4) are chosen for the first iteration. Using Nilsson's "semantic tree" method, five sets of possible worlds are identified for these sentences plus "Rain": those in which all three are true; those in which the implication is true, but "Rain" and "B. pressure < 30" are false; etc.

Both actions are E-admissible. "Go" is E-admissible because there exist feasible solutions to the system of linear inequalities below, where p_i is the probability of set w_i of possible worlds: "Rain" is true in sets w_3 and w_5 . "Humidity > 80" is true in sets w_1 , w_4 and w_5 , etc.:

$$p_1 + p_2 + p_3 + p_4 + p_5 = 1$$

$$p_2 + p_3 + p_4 + p_5 \geq 0.65$$

$$p_2 + p_3 + p_4 + p_5 \leq 0.95$$

$$p_1 + p_4 + p_5 \geq 0.95$$

$$(p_3 + p_5) \times 0 + (p_1 + p_2 + p_4) \times 1 \geq (p_3 + p_5) \times 0.8 + (p_1 + p_2 + p_4) \times 0.2$$

"Do not go" is also E-admissible, since the system resulting from reversing the direction of the final inequality also has feasible solutions.

Now add sentence (3). The resulting 8 sets of possible worlds may be determined by expanding only the "live" terminal nodes of the semantic tree constructed at the first iteration. (To eliminate the need for a row interchange, the root of the initial tree should represent the target sentence. One may proceed in this way until it is no longer necessary to continue, possible to continue, or worth continuing. If the number of sets of worlds generated becomes excessive, Snow's compression method [1991] may be attempted.) "Do not go" is now identified as uniquely E-admissible; there exist feasible solutions to the system below, but not to the corresponding system for "Go":

$$p_1 + p_2 + p_3 + p_4 + p_5 + p_6 + p_7 + p_8 = 1$$

$$p_1 + p_2 + p_3 + p_4 + p_5 + p_6 + p_7 \geq 0.65$$

$$p_1 + p_2 + p_3 + p_4 + p_5 + p_6 + p_7 \leq 0.95$$

$$p_1 + p_2 + p_6 + p_8 \geq 0.95$$

$$p_1 + p_3 + p_5 + p_8 \geq 0.95$$

$$(p_1 + p_2 + p_3 + p_4) \times 0.8 + (p_5 + p_6 + p_7 + p_8) \times 0.2 \geq (p_1 + p_2 + p_3 + p_4) \times 0 + (p_5 + p_6 + p_7)$$

4. Decisions with Multiple Conditions

Frisch and Haddawy's system is applicable to decision problems with an arbitrary number n of mutually exclusive conditions c_j . The $(\frac{1}{2}n(n-1)+1)$ statements

$$p(c_1 \vee \dots \vee c_n) \in [1,1]$$

$$p(c_1 \& c_2) \in [0,0]$$

.

.

.

$$p(c_{n-1} \& c_n) \in [0,0]$$

must be included. Intervals must be maintained for each of the conditions c_j . The soundness

of Frisch and Haddawy's inference rules guarantees that, at any time, the interval $[l_j, u_j]$ associated with any c_j is a superset of the tightest interval entailed (algebraically) by the full collection of sentences. Thus, the sharpest intervals available at any time yield a linear system from which it can be determined whether an action would not be E-admissible relative to the sharper probability bounds computable at any later time; action a_j is (ultimately) admissible only if there exist feasible solutions to

$$p(c_1) + \dots + p(c_n) = 1$$

$$p(c_1) \geq l_1$$

$$p(c_1) \leq u_1$$

.

.

.

$$p(c_n) \geq l_n$$

$$p(c_n) \leq u_n$$

$$p(c_1) \times U(a_j, c_1) + \dots + p(c_n) \times U(a_j, c_n) \geq p(c_1) \times U(a_1, c_1) + \dots + p(c_n) \times U(a_1, c_n)$$

.

.

.

$$p(c_1) \times U(a_j, c_1) + \dots + p(c_n) \times U(a_j, c_n) \geq p(c_1) \times U(a_m, c_1) + \dots + p(c_n) \times U(a_m, c_n),$$

where l_j and u_j are the current bounds on $p(c_j)$.

Information may be lost if probability intervals are computed separately for each of the conditions in a decision problem with more than two conditions. For a given set $K \subseteq P_C$ of probability distributions, let us refer to the solution set of the linear system obtained by combining the additivity constraint with the inequalities corresponding to the tightest probability bounds inferable from the constraints determining K as the *envelope* of K . There are naturally arising convex sets K of probability distributions over $n > 2$ conditions that are proper subsets of their envelopes. The intersection of the domain of an action with K may be empty, although its intersection with the envelope of K is not. Thus, actions that are not E-admissible may not be identified as such, resulting in unnecessary indeterminateness.

Nilsson's semantic tree method can be adapted to take into account the mutual exclusivity and exhaustiveness of multiple (i.e., more than two) conditions in a decision problem. The first n levels of the tree will correspond to the n conditions. (This facilitates the anytime adaptation of Nilsson's methods discussed above.) At level n there will be n live nodes, one for each of the assignments in which exactly one of the conditions is true. The remaining levels of the tree are constructed as usual. For example, with conditions c_1 , c_2 and c_3 , an arbitrary number $m \geq 2$ of actions a_j , and data $p(B \rightarrow c_1) \in [0.9, 1]$ and $p(B) \in [0.8, 1]$, there are 6 sets of possible worlds, corresponding to the matrix

1	1	0	0	0	0	(c_1)
0	0	1	1	0	0	(c_2)
0	0	0	0	1	1	(c_3)
1	1	1	0	1	0	$(B \rightarrow c_1)$
1	0	0	1	0	1	(B)

Action a_j is E-admissible iff there exist feasible solutions to the system of linear inequalities:

$$\begin{aligned}
p_1 + \dots + p_6 &= 1 \\
p_1 + p_2 + p_3 + p_5 &\geq 0.9 \\
p_1 + p_4 + p_6 &\geq 0.8 \\
(p_1 + p_2) \times U(a_j, c_1) + (p_3 + p_4) \times U(a_j, c_2) \\
&+ (p_5 + p_6) \times U(a_j, c_3) \geq \\
&(p_1 + p_2) \times U(a_1, c_1) + (p_3 + p_4) \times U(a_1, c_2) \\
&+ (p_5 + p_6) \times U(a_1, c_3) \\
&\vdots \\
&\vdots \\
&\vdots \\
(p_1 + p_2) \times U(a_j, c_1) + (p_3 + p_4) \times U(a_j, c_2) \\
&+ (p_5 + p_6) \times U(a_j, c_3) \geq \\
&(p_1 + p_2) \times U(a_m, c_1) + (p_3 + p_4) \times U(a_m, c_2) \\
&+ (p_5 + p_6) \times U(a_m, c_3)
\end{aligned}$$

5. Maximum Entropy and Probabilistic Logic

Nilsson [1986] shows how to maximize entropy within the set of probability distributions over the possible worlds in order to compute a point-valued probability for an entailed sentence. The maximum entropy estimate of the probability of the entailed sentence is the sum of the components of the maximum entropy distribution corresponding to the worlds in which the sentence is true. Point-valued probabilities for each of the conditions in a decision problem are computable also from the distribution over the possible worlds maximizing entropy.

If an action maximizes expected utility relative to the maximum entropy estimate, it is guaranteed to be E-admissible relative to any set K of distributions to which the estimate belongs. But, of course, the converse does not hold. E-admissible actions that, depending on one's philosophy of decision making, perhaps should be retained for further consideration, are eliminated. It may be that one of these actions uniquely maximizes expected utility relative to the (*pace, inter alios*, DeFinetti) "correct" element of K .

To illustrate, suppose that, after looking closely at the evidence, an expert comes finally to the conclusion that $p(P) = 0.2$ and $p(P \rightarrow Q) = 0.9$. Suppose that his conclusion is final also in the sense that he expires immediately upon recording it. Unfortunately, we wish to make a decision the outcome of which depends on the truth of the proposition Q . Suppose that $A = \{a_1, a_2\}$ and that

$$\begin{aligned}
U(a_1, Q) &= 1.0 \\
U(a_1, \bar{Q}) &= 0 \\
U(a_2, Q) &= 0.2 \\
U(a_2, \bar{Q}) &= 0.7
\end{aligned}$$

The range of probabilities for Q compatible with the expert's recorded opinions is

$$0.1 \leq p(Q) \leq 0.9.$$

The maximum entropy estimate (see below) is 0.5. Action a_1 has higher expected utility than a_2 does relative to this estimate. Suppose, however, that our expert was perfectly "calibrated" and that, had he survived long enough to arrive at an opinion on $p(Q)$ itself, it

would have been $p(Q) = 0.1$. Relative to this distribution, the expected utilities of a_1 and a_2 are 0.1 and 0.65 (utils), respectively; a_2 has by far the greater expected utility (expressed in utils). Retaining both actions as E-admissible relative to the available information and using, e.g., maximin to resolve the indeterminacy (or even performing a mixture giving any positive probability of selection to a_2) will result in higher expected utility than choosing action a_1 .

If the maximum entropy distribution at least tends to be *close*, on some metric, to the actual distribution over the worlds, then its projection will tend to be close to the actual probability distribution over the conditions. (But note that the result of marginalizing the maximum entropy element of a set K is not always the maximum entropy element of the set of marginals of elements of K .) The closer the estimate of the probabilities of the conditions is to the true distribution, the likelier it is that it will belong to one of the domains containing the true distribution. Thus, the likelier it is that an action maximizing utility relative to the true distribution will be selected.

How close can one expect the maximum entropy estimate to be to the true distribution over the possible worlds? If you accept Jaynes' *concentration theorem* [Jaynes, 1982], i.e., if probabilities are observed relative frequencies and sequences of observations are equiprobable *a priori* and the number of observations is infinite and if you accept difference in entropy as a distance measure, then the answer is "very". If you want to stick with metric distances and probabilities are allowed to be subjective, then it might be reasonable to ask how close the maximum entropy element is to the *centroid* of the set, which minimizes expected sum-of-squares error [MacQueen and Marschak, 1975], but is more expensive to calculate [Piepel, 1983].

When the set of distributions is either a singleton or the full probability simplex, the maximum entropy element is guaranteed to coincide with the centroid. It always coincides with the centroid for the *modus ponens* inference pattern: Let $x = p(P)$ and $y = p(P \rightarrow Q)$. There are four sets of possible worlds, the probabilities of which are the solutions to the system of equations:

$$p_1 + p_2 + p_3 + p_4 = 1$$

$$p_1 + p_2 = x$$

$$p_1 + p_3 + p_4 = y.$$

The solution set is either a single point (when $p(P)=1$) or a line segment in $[0,1]^4$ with vertices

$$(p_1, p_2, p_3, p_4) = (y - (1-x), (1-y), 1-x, 0)$$

$$(p_1, p_2, p_3, p_4) = (y - (1-x), (1-y), 0, 1-x).$$

The centroid of the line segment is the average of the vertices, which coincides with the maximum entropy distribution calculated by Nilsson.

This will not always be the case. It does not even appear that one can expect the maximum entropy estimate to be especially close to the centroid (which one cares about if one wishes to minimize expected squared error). Consider the *conjunction* pattern of inference: from A and B , infer $A \& B$. There are four sets of possible worlds: those in which $A \& B$ is true, those in which $A \& \bar{B}$ is true, etc. The set of solutions to the system is again either a single point or a

line segment in $[0,1]^4$. Let $l(A \& B)$ and $u(A \& B)$ denote, respectively, the greatest lower and least upper bounds on $p(A \& B)$. Ordering components as

$$(p(A \& B), p(A \& \bar{B}), p(\bar{A} \& B), p(\bar{A} \& \bar{B})).$$

the solution set has vertices

$$v^1 = (l(A \& B), p(A) - l(A \& B), p(B) - l(A \& B), (1 - (p(A) + p(B) - l(A \& B))))$$

$$v^2 = (u(A \& B), p(A) - u(A \& B), p(B) - u(A \& B), (1 - (p(A) + p(B) - u(A \& B)))).$$

The centroid is the average of the two vertices:

$$ce = (v^1 + v^2)/2.$$

The maximum entropy element coincides with the distribution computed under the assumption of probabilistic independence of A and B :

$$m = (p(A) \times p(B), p(A) \times p(\bar{B}), p(\bar{A}) \times p(B), p(\bar{A}) \times p(\bar{B})).$$

The *eccentricity* of an element of any non-unit solution set K is the ratio between its (Euclidean) distance from the centroid and the maximum distance of any element of the set from the centroid:

$$ecc(p, K) = d(p, ce) / \max_{p \in K} d(p, ce).$$

The eccentricity will have a minimum value of 0 (when $p = ce$) and a maximum value of 1 (when p is a vertex).

For conjunction entailment, it is possible for the value of $ecc(m, K)$ to be quite high. For example, when $p(A)=0.9$ and $p(B)=0.1$, $ecc(m, K)=0.8$. The expected value of $ecc(p, K)$ for a randomly selected element p of K is $1/2$. Letting $\langle p(A), p(B) \rangle$ range with uniform probability over $(0,1)^2$, the expected value of $ecc(m, K)$ is $1/3$. So, for conjunction entailment anyway, one cannot expect the maximum entropy approximation to be especially low-risk.

Kane [1990, 1991] has developed a method of computing the maximum entropy solution that is faster than that proposed by Nilsson. Deutsch-McLeish [1990] has determined conditions under which Nilsson's *projection approximation* (which is not, in general, the centroid of the solution set) coincides with the maximum entropy solution. These can be tested to determine whether the (much cheaper) projection approximation method can be substituted for direct maximization of entropy. But, as argued above, there is no need to compute *any* type of point-valued estimate of condition probabilities for a decision problem.

6. Anytime Decision Making with Probabilistic Databases

A *probabilistic database* [Cavallo and Pittarelli, 1987; Pittarelli, 1994; Barbara et al, 1993] generalizes a relational database by replacing the characteristic function of a relation with a probability distribution (or probability intervals). For example, the tables below represent estimates of probabilities for various (joint) events on a typical August day in a fictitious developing country:

Rain	No Phones	p^1
yes	true	0.4
yes	false	0.1
no	true	0.2
no	false	0.3

No Phones	Trains	p^2
true	yes	0.25
true	no	0.35
false	yes	0.25
false	no	0.15

No Phones	Temperature	p^3
true	high	0.45
true	med	0.1
true	low	0.05
false	high	0.25
false	med	0.1
false	low	0.05

Temperature	Humidity	p^4
high	high	0.6
high	low	0.1
med	high	0.15
med	low	0.05
low	high	0
low	low	0.1

Suppose, again, that it must be decided whether or not to go to the beach. It is believed that the only relevant conditions are whether or not it will rain and whether or not evening trains will run. Utilities this time are:

	Don't go	Go
(rain, train)	3/4	1/2
(rain, no train)	7/8	0
(no rain, train)	1/8	1
(no rain, no train)	1/2	5/8

Conditional independence relations that would permit calculation of a unique (maximum entropy) joint distribution over all of the attributes mentioned in the tables, and from which (by marginalization) a unique probability distribution over the four joint conditions for the decision problem could be calculated, are not assumed. Nonetheless, it can be determined from the database that exactly one of the actions is E-admissible. There are infinitely many distributions over the Cartesian product of the domains of the attributes in the database whose marginals coincide with the distributions in the database. Each of these is a solution to a system of 20 linear equations in 48 unknowns. (The solution set is referred to as the *extension* of the database, defined formally below.) The probabilities of any of the 4 rain/train conditions is the sum of 12 of the 48 unknowns. Thus, E-admissibility can be determined as in the previous examples.

However, we have seen that, for various systems of probabilistic logic, it is not necessary to take into account all of the available sentences (even those that are relevant in the sense of having an effect on the entailed probabilities of the conditions) in order to solve decision problems. Similarly, working with an entire database may introduce unnecessary expense. Anytime algorithms can be devised as well for decision making with probabilistic databases.

Let us introduce a bit of formalism.

The set of attributes over which a probability distribution p (i.e., element of a probabilistic database) is defined is referred to as its *scheme* and is denoted $s(p)$. The scheme of a database

$$P = \{p^1, \dots, p^k\}$$

is the set of schemes of its elements:

$$s(P) = \{s(p^1), \dots, s(p^k)\}.$$

The scheme of the database $\{p^1, p^2, p^3, p^4\}$ above is

$$\{\{\text{Rain, No Phones}\}, \{\text{No Phones, Trains}\}, \{\text{No Phones, Temp.}\}, \{\text{Temp., Humidity}\}\}.$$

Scheme S is a refinement of scheme S' , denoted

$$S \leq S'.$$

iff for each $V \in S$ there exists a $V' \in S'$ such that $V \subseteq V'$.

Each attribute v has a *domain*, its set of possible values, denoted $dom(v)$. In the example,

$$dom(\text{Temperature}) = \{\text{high, med, low}\}.$$

Where some arbitrary but fixed ordering is assumed over the attributes, the domain of a scheme is the Cartesian product of the domains of its elements:

$$dom(V) = \prod_{v \in V} dom(v).$$

So, with No Phones preceding Trains in the ordering,

$$dom(s(p^2)) = \{\langle \text{true, yes} \rangle, \langle \text{true, no} \rangle, \langle \text{false, yes} \rangle, \langle \text{false, no} \rangle\}.$$

The *projection* of a distribution p onto a set of attributes A such that $A \subseteq s(p)$, denoted

$$\pi_A(p),$$

is obtained by adding probabilities of tuples that agree on values for attributes in A :

$$\pi_A(p)(x) = \sum_{t \in dom(s(p)), t[A]=x} p(t),$$

where $t[A]$ denotes the *restriction* of tuple t to attributes contained in set A .

A database may be *projected* onto any scheme that is a refinement of its own. The result is a database whose elements are marginals of its own elements. For example, the projection of the database above onto the scheme $\{\{\text{Trains}\}, \{\text{Temperature}\}\}$,

$$\pi_{\{\{\text{Trains}\}, \{\text{Temperature}\}\}}(\{p^1, p^2, p^3, p^4\}),$$

is:

Trains	p^5	Temperature	p^6
yes	0.5	high	0.7
no	0.5	med	0.2
		low	0.1

An individual distribution may also be projected onto a database scheme. If

$$X \leq \{s(p)\},$$

then

$$\pi_X(p) = \{\pi_V(p) \mid V \in X\}.$$

Databases created in this way are guaranteed to exhibit various forms of consistency. For example, such databases are *locally consistent*. A database K is locally consistent iff, for any

p^i and p^j in K ,

$$\pi_A(p^i) = \pi_A(p^j),$$

for all $A \subseteq s(p^i) \cap s(p^j)$.

The *extension* of a distribution p to a set of attributes $V \supseteq s(p)$ is the set of all distributions over $\text{dom}(V)$ whose projection onto $s(p)$ equals p :

$$E^V(p) = \{p' \in P_V \mid \pi_{s(p)}(p') = p\}.$$

The extension of a database to set of attributes is the intersection of the extensions of its elements:

$$E^V(P) = \bigcap_{p \in P} E^V(p).$$

The superscript V may be omitted if

$$V = \bigcup_{p \in P} s(p)$$

A database P is *globally consistent* iff its extension $E(P)$ is non-empty.

Databases formed by projection are guaranteed to be both locally and globally consistent. So are databases whose schemes are partitions. Global consistency implies local consistency, regardless of the structure of the database scheme. However, local consistency implies global consistency only for databases whose schemes are α -acyclic [Fagin, 1983]. A polynomial-time test for α -acyclicity of a database scheme X is the following:

1. $W := X$.

Apply in any order until neither is applicable:

2. If v is an element appearing in only one $V \in W$,
then $W := (W - \{V\}) \cup (V - \{v\})$.
3. If $V_i \subseteq V_j$ for any $V_i, V_j \in W$, $i \neq j$,
then $W := W - \{V_i\}$.

X is α -acyclic iff the algorithm terminates with $W = \{\emptyset\}$.

The database algebra just sketched can be utilized to define various anytime decision-making algorithms. The key fact is that if database scheme S is a refinement of S' , then the extension (to any number of attributes) of the projection of a database onto S' is a subset of the extension of the projection onto S [Pittarelli, 1994]. Formally,

$$X \leq Y \text{ implies } E^V(\pi_Y(P)) \subseteq E^V(\pi_X(P)).$$

(This is due to the fact that the linear equations the solutions to which are the elements of $E^V(\pi_X(P))$ are linear combinations of the equations in the system corresponding to $E^V(\pi_Y(P))$.)

Thus, if an action is E-admissible relative to the set of probabilities over the conditions that can be calculated from a database, then it is E-admissible relative to the probabilities calculated from any projection of the database. Equivalently, if an action can be determined not to be E-admissible relative to a projection, it can be inferred that it is not E-admissible relative to the original database.

Since the number of E-admissible actions decreases monotonically as schemes become less refined, anytime decision methods are possible for problems in which the set of conditions is the Cartesian product of attribute domains from the database (or can be constructed from the

tuples in such a product). Let V_C denote this set of attributes.

This suggests the following anytime strategy: Starting with $W = \{\{v\} | v \in V_C\}$, the most refined scheme that is a cover of some $V' \supseteq V_C$, repeatedly aggregate W until there is a single admissible action relative to $\pi_{V_C}(E(\pi_W(K)))$, or $\pi_{V_C}(E(\pi_W(K)))$ happens to contain only one distribution, or $W = s(P)$, whichever comes first. However, if database schemes are replaced by immediate aggregation, very little progress toward sufficient reduction of the set $\pi_{V_C}(E(\pi_W(K)))$ is likely to be made at each step. Also, there will not be a unique immediate aggregate at each step. A reasonable alternative is the sequence of schemes:

$$(\{\{v\} | v \in V_C\}, \{V_i \cap V_C | V_i \in s(P), V_i \cap V_C \neq \emptyset\}, \{V_i | V_i \in s(P), V_i \cap V_C \neq \emptyset\}, s(P)).$$

Following this strategy, suppose that a single admissible action is identified with $W = \{\{v\} | v \in V_C\}$. Then, for m actions, linear programs with only $|dom(V_C)|$ unknowns and $m-1$ inequalities are sufficient.

For the beach decision problem, $V_C = \{\text{Rain}, \text{Trains}\}$. The projection of the database onto $\{\{v\} | v \in V_C\}$ is

Trains	p^5	Rain	p^7
yes	0.5	yes	0.5
no	0.5	no	0.5

Both actions are E-admissible relative to the set of joint probabilities compatible with this database.

For this problem,

$$\{V \cap V_C | V \in s(P), V \cap V_C \neq \emptyset\} = \{\{v\} | v \in V_C\}.$$

The projection onto $\{V | V \in s(P), V \cap V_C \neq \emptyset\}$ is the set of distributions $\{p^1, p^2\}$, above. "Don't go" is identified from this set of distributions as uniquely E-admissible. There exist feasible solutions to the system of inequalities below, but not to the corresponding system for "Go".

$$p(\text{Rain} = \text{yes}, \text{No Phones} = \text{true}, \text{Trains} = \text{yes}) + p(\text{yes}, \text{true}, \text{no}) = 0.4$$

$$p(\text{yes}, \text{false}, \text{yes}) + p(\text{yes}, \text{false}, \text{no}) = 0.1$$

$$p(\text{no}, \text{true}, \text{yes}) + p(\text{no}, \text{true}, \text{no}) = 0.2$$

$$p(\text{no}, \text{false}, \text{yes}) + p(\text{no}, \text{false}, \text{no}) = 0.3$$

$$p(\text{yes}, \text{true}, \text{yes}) + p(\text{no}, \text{true}, \text{yes}) = 0.25$$

$$p(\text{yes}, \text{true}, \text{no}) + p(\text{no}, \text{true}, \text{no}) = 0.35$$

$$p(\text{yes}, \text{false}, \text{yes}) + p(\text{no}, \text{false}, \text{yes}) = 0.25$$

$$p(\text{yes}, \text{false}, \text{no}) + p(\text{no}, \text{false}, \text{no}) = 0.15$$

$$\left(\frac{3}{4} - \frac{1}{2}\right) \times (p(\text{yes}, \text{true}, \text{yes}) + p(\text{yes}, \text{false}, \text{yes}))$$

$$+ \left(\frac{7}{8} - 0\right) \times (p(\text{yes}, \text{true}, \text{no}) + p(\text{yes}, \text{false}, \text{no})) +$$

$$\left(\frac{1}{8} - 1\right) \times (p(\text{no}, \text{true}, \text{yes}) + p(\text{no}, \text{false}, \text{yes}))$$

$$+ \left(\frac{1}{2} - \frac{5}{8}\right) \times (p(\text{no}, \text{true}, \text{no}) + p(\text{no}, \text{false}, \text{no})) \geq 0.$$

The set $|dom(V)|$ can be arbitrarily large, and many (or all) of the variables in $V - V_C$ may be irrelevant to the given problem. If the conjecture below is correct, then there exists a polynomial-time algorithm for eliminating irrelevant attributes from a connected α -acyclic database scheme. A database scheme $s(P)$ is connected iff there is no $V \in s(P)$ such that there does not exist a $V' \in s(P)$, $V \neq V'$ such that $V \cap V' \neq \emptyset$.

For $s(P)$ a cover of $V \supseteq V_C$, define a bipartite graph B with node set $V \cup s(P)$ and edge set $\{\{v, x\} \mid v \in V, x \in s(P), v \in x\}$.

Let

$$R = \{v \in V \mid v \in V_C \text{ or } v \text{ is on an acyclic path in } B \text{ between two elements of } V_C\}.$$

Let

$$Z = \{V_i \cap R \mid V_i \in s(P) \text{ and } V_i \cap R \not\subseteq V_j \cap R, \text{ for all } V_j \in s(P), i \neq j\}.$$

Conjecture: $\pi_{V_C}(E(\pi_Z(P))) = \pi_{V_C}(E(P))$. \square

If $s(P)$ is connected and α -acyclic then the following polynomial-time algorithm will produce the reduced structure Z [Maier and Ullman, 1982]:

1. $Z := s(P)$.
2. Repeat in any order until neither has any effect on the current value of Z :
 - a. If a variable $v \notin V_C$ appears in only one element of Z , remove v from that element.
 - b. If Z contains elements V_i and V_j such that $V_i \subset V_j$, then $Z := Z - \{V_i\}$. \square

In the unlikely event that the conjecture is proved false, it is still guaranteed to be the case that

$$\{V_i \mid V_i \in s(P), V_i \cap V_C \neq \emptyset\} \leq Z \leq s(P).$$

Therefore, Z can be inserted between these two schemes in the aggregation sequence suggested above.

It is difficult to achieve consistency for real-valued databases whose schemes are not partitions and for which probabilities are assessed on each element separately. Apart from the problem of consistency, it is also difficult to estimate real-valued probabilities with any degree of confidence.

To illustrate, imagine that data are generated via two coin tossing experiments. In the first experiment, coins c_1 and c_2 are tossed simultaneously 250 times with resulting frequency distribution

c_1	c_2	f^1
H	H	70
H	T	60
T	H	40
T	T	80

Coin c_2 is again tossed in the second experiment, this time with coin c_3 :

c_2	c_3	f^2
H	H	65
H	T	50
T	H	70
T	T	65

If probabilities are estimated as relative frequencies, we obtain the database:

c_1	c_2	p^8	c_2	c_3	p^9
H	H	0.28	H	H	0.26
H	T	0.24	H	T	0.20
T	H	0.16	T	H	0.28
T	T	0.32	T	T	0.26

Distributions p^8 and p^9 are inconsistent:

c_2	$\pi_{\{c_2\}}(p^8)$	\neq	c_2	$\pi_{\{c_2\}}(p^9)$
H	0.44		H	0.46
T	0.56		T	0.54

Just as interval-valued probabilities can be attached to statements in Nilsson's and Frisch and Haddawy's systems of probabilistic logic, we can assign probability intervals to the tuples in a database. The operations of projection and extension are easily modified to handle probability intervals (and in such a way that they reduce to the definitions given above for real-valued databases in the extreme case in which the intervals themselves reduce to real numbers).

For the coin experiments, we can report confidence intervals, instead of real-valued probabilities. 95% intervals for the data (based on 250 observations) are:

c_1	c_2	i^1	c_2	c_3	i^2
H	H	[0.22, 0.34]	H	H	[0.20, 0.32]
H	T	[0.18, 0.30]	H	T	[0.14, 0.26]
T	H	[0.10, 0.22]	T	H	[0.22, 0.34]
T	T	[0.26, 0.38]	T	T	[0.20, 0.32]

The interval distributions i^1 and i^2 are consistent. An interval-valued database $I = \{i^1, \dots, i^m\}$ is locally consistent iff

$$\pi_{s(i^j) \cap s(i^k)}(i^j)(t) \cap \pi_{s(i^j) \cap s(i^k)}(i^k)(t) \neq \emptyset,$$

for all $t \in \text{dom}(s(i^j) \cap s(i^k))$, where $j, k \in \{1, \dots, m\}$ and $s(i^j) \cap s(i^k) \neq \emptyset$.

The projection of an interval distribution onto any subset of its scheme is itself an interval distribution. The endpoints of a component of the projection are the minimum and maximum values of the components of the real-valued projections of the real-valued distributions enveloped by i . The endpoints can be determined by linear programming. For example, the projection $\pi_{\{c_2\}}(i^1)$ is determined from the system L of inequalities

$$p(HH) + p(TH) - p(H) = 0$$

$$p(HT) + p(TT) - p(T) = 0$$

$$p(HH) \geq 0.22$$

$$p(HH) \leq 0.34$$

.

$$p(TT) \geq 0.26$$

$$p(TT) \leq 0.38$$

$$p(H) + p(T) = 1$$

(which implies $p(HH) + \dots + p(TT) = 1$) as

$$\pi_{\{c_2\}}(i^1)(H) = [\min \{p(H) \mid p(H) \text{ satisfies } L\}, \max \{p(H) \mid p(H) \text{ satisfies } L\}]$$

and

$$\pi_{\{c_2\}}(i^1)(T) = [\min \{p(T) \mid p(T) \text{ satisfies } L\}, \max \{p(T) \mid p(T) \text{ satisfies } L\}]$$

The projections onto $\{c_2\}$ of i^1 and i^2 are:

c_2	$\pi_{\{c_2\}}(i^1)$	c_2	$\pi_{\{c_2\}}(i^2)$
H	[0.32,0.56]	H	[0.34,0.58]
T	[0.44,0.68]	T	[0.42,0.66]

Notice that, although they can in this case, in general, the endpoints of the marginals cannot be obtained simply by adding the endpoints of the corresponding joint intervals. Had $i^1(HT)$ been reported instead as [0.18,0.31], the value of $\max \pi_{\{c_2\}}(i^1)(T)$ would remain 0.68. $\max \pi_{\{c_2\}}(i^1)(T) = 0.69 (= 0.31 + 0.38)$ would imply the possibility that

$$p(HT) + p(TT) = 0.69,$$

which implies

$$p(HH) + p(TH) = 0.31,$$

which contradicts the constraints $p(HH) \geq 0.22$ and $p(TH) \geq 0.10$.

The real-valued extension of an interval distribution or database is the set of real-valued distributions (over the specified domain) satisfying the linear inequalities implied by the given intervals. An interval-valued extension can also be defined.

Let us say that i is *more informative than* i' , denoted

$$i \leq i',$$

iff

$$i(t) \subseteq i'(t),$$

for all tuples t . Where $E^V(I)$ denotes the real-valued extension of database I , and where $E^V(I)^*$ denotes the narrowest interval distribution enveloping $E^V(I)$, the interval-valued extension of I is the set of interval distributions

$$\{i \mid p \leq i \leq E^V(I)^*, \text{ for some } p \in E^V(I)\}.$$

where a real-valued distribution is regarded as a special type of interval distribution. This set

is partially ordered under ' \leq '; its structure is quite similar to that of solution sets for finite fuzzy relation equations [Higashi *et al.*, 1984].

For decision making, the same strategies used with real-valued databases are applicable in the interval-valued case. A series of decision problems is generated, using larger and larger portions of the database for each successive problem. The only difference is that E-admissibility is tested against a system of linear inequalities.

Note that even relative to the (projection of) the extension of an entire database there may be more than one E-admissible action. If this is so, then, if the database is interval-valued, Loui's methods [1986] may be applied to narrow them. If the intervals are confidence intervals, this amounts to merely reducing the confidence level in stages and checking at each step for the existence of a unique E-admissible action. Alternatives applicable to point-valued probabilistic databases are the variable and structural refinements discussed by Poh and Horvitz [1993] and "coarsenings" of the database scheme. The latter, which includes structural refinement as a special case (i.e. may, but needn't, introduce new variables) requires the assessment of joint probabilities over supersets of the sets of variables contained in the original database scheme. If the old database is a projection of the new database, then the new set of E-admissible actions is a subset of the old.

7. Conclusion

Anytime decision methods may be devised for use with probabilistic databases, Frisch and Haddawy's anytime deduction system, and Nilsson's probabilistic logic. Common to each of these methods is the generation of a system of linear inequalities the unknowns of which are probabilities of the conditions for a decision problem. Levi's E-admissibility criterion may be applied to the solution set of the system of inequalities. The size of the system of inequalities increases, and the set of admissible actions shrinks, as more of the knowledge base or database is taken into account.

Specific measures of the quality of a decision are not explored. It seems that, for a fixed set of actions under consideration, reasonable measures will be such that the quality of the decision based on a set E of admissible actions will be higher (ignoring the cost of computation) than that of any decision based on a superset of E . For each of the methods discussed, actions are eliminated from consideration as computation proceeds. Thus, the quality of a decision (made by choosing an action from the currently admissible set using some criterion other than E-admissibility) increases with time.

Determining which sentences, or projections of a database, will eliminate the greatest number of actions at the least cost, and whether it is worth the effort to consider additional sentences or projections at all, is a difficult problem which remains for future research.

References

- [Barbara *et al.*, 1993] D. Barbara, H. Garcia-Molina, and D. Porter. The management of probabilistic data. *IEEE Trans. on Knowledge and Data Engineering*, v. 4, pp. 387-402.
- [Boddy and Dean, 1989] M. Boddy and T. Dean. Solving time-dependent planning problems. *Proc. IJCAI-89*, Morgan Kaufmann, pp. 979-984.

- [Cavallo and Pittarelli, 1987] R. Cavallo and M. Pittarelli. The theory of probabilistic databases, *Proc. 13th Conf. on Very Large Databases*, Morgan Kaufmann, pp. 71-81.
- [Deutsch-McLeish, 1990] M. Deutsch-McLeish. An investigation of the general solution to entailment in probabilistic logic. *Int. J. of Intelligent Systems*, v. 5, pp. 477-486.
- [Elster, 1989] J. Elster. *Solomonic Judgements*. Cambridge University Press.
- [Fagin, 1983] R. Fagin. Degrees of acyclicity for hypergraphs and relational databases schemes. *JACM*, v. 30, pp. 514-550.
- [Frisch and Haddawy, 1992] A. Frisch and P. Haddawy. Anytime deduction for probabilistic logic. Technical Report UIUC-BI-AI-92-01, Beckman Institute, Univ. of Illinois, Urbana. To appear in *Artificial Intelligence*.
- [Groszof, 1986] B. Groszof. An inequality paradigm for probabilistic knowledge. In L. Kanal and J. Lemmer, Eds., *Uncertainty in Artificial Intelligence*, North-Holland.
- [Higashi et al., 1984] M. Higashi, G. Klir and M. Pittarelli. Reconstruction families of possibilistic structure systems. *Fuzzy Sets and Systems*, v. 12, pp. 37-60.
- [Horvitz et al., 1989] E. Horvitz, G. Cooper and D. Heckerman. Reflection and action under scarce resources: theoretical principles and empirical study. *Proc. IJCAI-89*, Morgan Kaufmann, pp. 1121-1127.
- [Jaynes, 1982] E. T. Jaynes. The rationale of maximum-entropy methods. *Proc. of the IEEE*, v. 70, pp. 939-952.
- [Jeffrey, 1976] R. Jeffrey. Savage's omelet. In F. Suppe and P. Asquith, Eds., *PSA 1976*, v. 2, Philosophy of Science Association.
- [Kane, 1990] T. Kane. Enhancing the inference mechanism of Nilsson's probabilistic logic. *Int. J. of Intelligent Systems*, v. 5, pp. 487-504.
- [Kane, 1991] T. Kane. Reasoning with maximum entropy in expert systems. In W. T. Grandy, Jr. and L. Schick, Eds., *Maximum Entropy and Bayesian Methods*, Kluwer.
- [Kyburg, 1992] H. E. Kyburg, Jr. Getting fancy with probability. *Synthese*, v. 90, pp. 189-203.
- [Levi, 1980] I. Levi. *The Enterprise of Knowledge*. MIT Press.
- [Loui, 1986] R. Loui. Decisions with indeterminate probabilities. *Theory and Decision*, v. 21, pp. 283-309.
- [MacQueen and Marschak, 1975] J. MacQueen and J. Marschak. Partial knowledge, entropy, and estimation. *Proc. Nat. Acad. Sci.*, v. 72, pp. 3819-3824.
- [Maier and Ullman, 1982] D. Maier and J. Ullman. Connections in acyclic hypergraphs. *Proc. ACM Symposium on Principles of Database Systems*, pp. 34-39.
- [Nilsson, 1986] N. Nilsson. Probabilistic logic. *Artificial Intelligence*, v. 28, pp. 71-87.
- [Piepel, 1983] F. Piepel. Calculating centroids in constrained mixture experiments. *Technometrics*, v. 25, pp. 279-283.
- [Pittarelli, 1991] M. Pittarelli. Decisions with probabilities over finite product spaces. *IEEE Trans. SMC*, v. 21, pp. 1238-1242.
- [Pittarelli, 1993] M. Pittarelli. Probabilistic databases and decision problems: results and a conjecture. *Kybernetika*, v. 29, pp. 149-165.
- [Pittarelli, 1994] M. Pittarelli. An algebra for probabilistic databases. *IEEE Trans. on Knowledge and Data Engineering*, v. 6, pp. 293-303.
- [Poh and Horvitz, 1993] K. L. Poh and E. Horvitz. Reasoning about the value of decision-model refinement: methods and application. *Proc. of the 9th Conf. on Uncertainty in Artificial Intelligence*, pp. 174-182.
- [Quinlan, 1983] R. Quinlan. Inferno: a cautious approach to uncertain inference. *The Computer Journal*, v. 26, pp. 255-269.
- [Snow, 1991] P. Snow. Compressed constraints in probabilistic logic and their revision. *Proc. 7th Conf. on Uncertainty in Artificial Intelligence*, Morgan Kaufmann, pp. 386-391.
- [Starr, 1966] M. Starr. A discussion of some normative criteria for decision-making under uncertainty. *Industrial Management Review*, v. 8, pp. 71-78.

**ULTRAFAST SPECTROSCOPY OF QUANTUM HETEROSTRUCTURES
FOR HIGH-SPEED OPTOELECTRONIC SWITCHING**

Dean Richardson
Assistant Professor and Photonics Program Coordinator
Department of Electrical Engineering Technology

State University of New York Institute of Technology at Utica/Rome
P.O. Box 3050
Utica, NY 13504-3050

Final Report for:
Summer Faculty Research Program
Rome Laboratory Photonics Center

Sponsored by:
Air Force Office of Scientific Research
Bolling Air Force Base, DC

and

Rome Laboratory Photonics Center

November 1994

ULTRAFAST SPECTROSCOPY OF QUANTUM HETEROSTRUCTURES FOR HIGH-SPEED OPTOELECTRONIC SWITCHING

Dean Richardson
Assistant Professor and Photonics Program Coordinator
Department of Electrical Engineering Technology
State University of New York Institute of Technology at Utica/Rome

Abstract

We have studied the ultrafast optical switching dynamics of type-II GaAs/AlAs superlattices, InGaAs asymmetric-coupled-quantum well (ACQW) materials and GaAs/AlGaAs vertical-cavity surface-emitting laser (VCSEL) structures, with an eye towards the development of high-speed optoelectronic modulators having unique operational advantages over current designs. To determine the absorption and refractive-index dynamics of these materials and to optimize device designs utilizing them, a flexible pump-probe characterization facility with femtosecond resolution in the visible, near IR, and 1.3-1.55 μm ranges is required. In this report we summarize our efforts to design and construct a suitable femtosecond pump-probe system, and outline preliminary attempts to exploit ultrafast switching mechanisms in type-II, ACQW and VCSEL materials for optical processing applications.

Background -- Materials and Devices for Optoelectronic Switching/Modulation

Asymmetric Fabry-Perot modulators (AFPMS) fabricated from multiple quantum well (MQW) materials have attracted considerable attention in recent years as potential elements in optical information processing, interconnection, and multiplexing/demultiplexing systems. Both electro-absorption¹⁻⁴ and all-optical⁵⁻⁶ devices have been demonstrated. Unfortunately, despite impressive performance characteristics, including 21 GHz modulation rates³ and 1000:1 contrast ratios⁴, AFPMS have yet to move from the university lab into the commercial marketplace.

Three key drawbacks of previously-studied material structures can be identified which have prevented AFPMS from finding their way into practical high-speed processing systems. First, the optical switching effect used in many of these devices is critically dependent on precise operating wavelengths. Second, the vast majority of the AFPM-based switching components demonstrated has been incompatible with the fiber-relevant 1.33 and 1.55 μm spectral regions. Finally, though the bulk of the AFPM concepts discussed in the literature display extremely rapid switch-on characteristics, their overall processing rates tend to be strongly limited by their recombination-time-dependent switch-off times, which are typically on the order of 1 ns or more.

Wavelength Sensitivity

Most of the electro-absorption modulators studied to date operate using the quantum-confined Stark effect (QCSE), while the all-optical AFPMS tend to rely on intensity-dependent bleaching of excitonic absorption. The QCSE and excitonic bleaching both utilize carrier-density-dependent shifting of excitonic resonances to bring about absorption and refractive-index changes. The relatively narrow linewidth of excitonic transitions leads to high contrast but makes the resulting devices extremely sensitive to operating wavelength. Thus a material which could undergo significant absorption and refractive-index changes at a wider range of operating wavelengths would contribute to device robustness and manufacturability. Tolerance to diode laser linewidth, process variation, temperature tuning, etc. could also be enhanced as a result.

Fiber Compatibility

Research concerning AFPMS has focused strongly on the GaAs/AlGaAs and strained GaAs/InGaAs material systems, producing operating wavelengths in the 860 and 980 nm regions. Though these wavelengths are compatible with inexpensive off-the-shelf diode laser sources, they fail to effectively exploit the well-established transmission "windows" in optical fiber. As a result, research groups have begun searching for high-performance modulators at the communications-relevant wavelengths of 1.3 and 1.55 μm , where significant commercial applications can be readily anticipated. Particularly promising are devices based on the InAlGaAs system, which can be lattice-matched to InP. As with earlier GaAs/AlGaAs work, both QCSE electro-absorption and all-optical AFPMS have

been successfully fabricated⁷⁻⁹. Perhaps the most encouraging result to date in this regard is the work of Krol et al.⁹, who reported 1000:1 contrast in an InAlGaAs/InAlAs MQW AFPM operating at 1.3 μm . The operating speed of this all-optical device was found to be limited by the 725 ps recovery time of the excitonic optical nonlinearities to just under 1 GHz.

Switching Recovery Time

Most optoelectronic and all-optical switching devices based on bandedge nonlinearities are limited in their switch-off speed by the recombination time τ_R of the electron-hole pairs created during the initial switch-on process. Typical values of τ_R for GaAs/AlGaAs-based material structures are between 1 and 10 ns. Though sub-nanosecond recovery times can be achieved through, e.g., enhanced-surface-recombination geometries or proton implantation, the resulting device operating frequencies are still limited to approximately 2-5 GHz. Since electronic systems routinely operate in the 1-10 GHz range, potential optoelectronic replacements will have to deliver significantly better performance if they are to be commercially viable. To raise potential operating frequencies of optical switching components to the range of 50 GHz, picosecond or subpicosecond recovery mechanisms are strongly desirable.

Enhancing AFPM Performance

My research this summer dealt with three different material/device structures with the potential to overcome the limitations of existing AFPM schemes: GaAs/AlAs Type-II superlattices, InGaAs/InAlAs asymmetric coupled quantum-wells (ACQWs) and vertical-cavity surface-emitting laser (VCSEL) structures.

Type-II Superlattices

A nonlinear electroabsorption effect is available in GaAs/AlAs heterostructures which is potentially more efficient and robust than the quantum-confined Stark effect at visible wavelengths and significantly less wavelength-sensitive. This mechanism utilizes so-called type-II superlattices, in which narrow GaAs wells and wider AlAs barriers lead to a band alignment which is indirect in both real and reciprocal space. Meynadier and co-workers have shown¹⁰ that under an applied electric field, such structures can be induced to switch their band alignment from type-II to type-I, i.e., from quasi-indirect to direct, albeit at low temperature. Since the nonlinear absorption characteristics of type-II and type-I materials differ considerably¹¹, it has been suggested that a nominally type-II material could exhibit strong absorption changes under an applied electric field. Because the switching mechanism involved depends on field-induced energy-level shifts (i.e., carrier redistribution among wells and barriers) rather than solely on carrier creation, switch-off speeds are a function of tunneling times instead of recombination rates. As a result, recovery times can be of the order of a few picoseconds. Type-II modulators could thus potentially operate at frequencies of the order of 50-100 GHz with significantly better tolerance to source

wavelength variation than QCSE-based devices.

We have designed and fabricated AFPM devices utilizing type-II superlattice spacer layers with the goal of demonstrating significant switching contrast utilizing the type-II->type-I transition. We have also studied type-II p-i-n structures with the goal of optimizing design of type-II materials for use at room temperature¹². Further measurements using photoluminescence and ultrafast pump-probe techniques in the 600-700 nm region are required before these goals can be achieved. The resulting devices should demonstrate robust wavelength response, femtosecond-on/picosecond-off switching, and room temperature operation. Though the 650-700 nm operating wavelength of these devices is incompatible with silica fiber, it provides an excellent match to transmission windows in rugged, low-cost plastic fiber.

InGaAs/InAlAs ACQWs

As mentioned above, the all-optical InAlGaAs/InAlAs MQW AFPM concept pioneered by Krol et al. operates at 1.3 μm but is limited by recombination to a 1 GHz modulation rate. Recent results from the same group imply that the recovery time could be lowered to about 20 ps through the use of asymmetric coupled quantum-well (ACQW) structures in the InGaAs/InAlAs spacer layer¹³. As of yet, this fast recovery mechanism is not well understood, and its device implications are still uncertain. Our research aims to pinpoint the relevant physical processes underlying the fast recovery, determine the corresponding absorption and refractive-index dynamics that accompany it, and design AFPM structures to utilize it for all-optical switching/routing functions in time-division-multiplexed network applications. The ideal tools for this effort are again photoluminescence and femtosecond pump-probe spectroscopy. In this case, however, tunable femtosecond pulses in the 1.3 μm region are required.

VCSELs operated as transmissive switching elements with gain

A third scheme for providing practical high-speed optoelectronic switching elements involves adapting vertical-cavity surface-emitting lasers for use as transmission-mode amplifying switches. When operated slightly below threshold, such devices should demonstrate rapid nonlinear switch-on and switch-off characteristics due to stimulated recombination within the gain region of the absorption spectrum¹⁴. Their amplification properties will allow for low-power addressing and cascability. We have designed such devices and performed preliminary theoretical modeling of their performance. Femtosecond pump-probe analysis of their optical response will allow experimental feedback to the modeling process and enable the optimization of cavity parameters, fabrication techniques, and device performance characteristics. Such measurements will once more require a tunable source of femtosecond pulses, this time in the near-IR portion of the spectrum between 750 and 900 nm.

Femtosecond Pump-Probe Spectroscopy

The design of asymmetric Fabry-Perot modulators requires understanding of both the absorption *and* refractive-index dynamics of the spacer material as a function of excited carrier density. The refractive index determination is crucial to the precise resonance-matching necessary to achieve very-low reflectivities and thus high contrast ratios. While differential transmission studies (whether with degenerate or non-degenerate pumping) can give ultrafast *absorption* response at one more isolated frequencies, they give no information on the time evolution of the index. Induced changes in the index spectrum $\Delta n(\omega, t)$ can be calculated using the Kramers-Kronig transformation applied to the dynamic absorption behavior $\Delta \alpha(\omega, t)$, but the absorption changes must be known at a wide range of closely-spaced frequencies for the calculated Δn values to be reliable. Thus the ideal experiment would extract the femtosecond-time-scale evolution of the entire near-bandedge absorption spectrum of the spacer material with high resolution in a series of "single shot" measurements, allowing accurate determination of the accompanying refractive-index spectrum using the Kramers-Kronig method. The α and Δn values could then be inserted into the standard transfer-matrix formalism for evaluating and optimizing AFPM reflectance/switching behavior.

The preferred method for performing simultaneous multiple-wavelength absorption spectroscopy is through the technique of femtosecond continuum generation¹⁵. In this approach, a femtosecond pulse is amplified many times until its energy is sufficient to generate a femtosecond broadband white-light continuum in a material such as ethylene glycol or quartz. Though the earliest continuum-generation set-ups relied on CPM lasers and multiple dye-jet amplifier stages, these have quickly given way to all-solid-state systems based on mode-locked Ti:Sapphire oscillators and Nd:YAG/YLF-pumped Ti:Sapphire regenerative amplifiers¹⁶. Microjoule fs pulses are readily achieved by both laboratory and commercial Ti:S regen systems, enabling the generation of white-light pulses containing 10's of nanojoules of energy. By taking a 10 nm "slice" out of the broadband signal using an interference filter, we can obtain a wavelength selectable fs pump pulse. The remainder of the continuum pulse provides the broadband probe signal we need to determine the absorption response to the pump radiation. Pump and probe are both focused on the sample under test, and the transmitted signals are input to an optical multichannel analyzer, which records the transmission spectrum as a function of delay between pump and probe, typically with 100 fs resolution. This technique has been successfully applied to a wide variety of organic and inorganic materials in the wavelength region from 500-900 nm, including CdSe microcrystallites in glass, and both type-I and type-II MQWs and superlattices.

These tools are only just now becoming applicable to the 1-2 μm region as well, through a technique known as optical parametric amplification. In an optical parametric amplifier (OPA), the broadband radiation from a white light continuum pulse (generated by a Ti:S regenerative amplifier) is mixed with a narrowband UV signal (obtained from frequency doubling a portion of the continuum) inside a nonlinear crystal such as BBO. By combining

the co-linear, coherent input beams, sum and difference-frequency signals can be generated. The lower frequency pulse is called the idler, while the sum frequency pulse is referred to as the signal. In a typical OPA, the idler signal can be tuned through the 1-2 μm region by simply adjusting the orientation of the BBO crystal. The idler pulse can then act as the pump, while the lower-frequency tail of the white-light continuum generated by the input regenerative amplifier acts as the broadband probe in the 1.3 μm spectral regime.

System to be Constructed

Commercially available systems generating tunable femtosecond pulses in the visible, IR and 1-2 μm regime range in cost from about \$100,000 to \$280,000, depending on whether or not the purchaser already owns a pump laser. A vastly more cost-effective option is to "home-build" a regen/OPA system of our own. This is the goal of our proposed follow-on project under the SREP program. The planned system will consist of the following components:

- (1) Coherent 310 10 watt CW Argon:Ion laser (already part of our lab).
- (2) Mode-locked Ti:Sapphire oscillator, pumped by the Coherent 310, producing 100 fs pulses at 780 nm (design and some component fabrication performed this last summer; alignment in progress.)
- (3) 50 watt Q-switched mode-locked frequency-doubled Nd:YLF laser operating at 30 kHz (under construction).
- (4) Ti:Sapphire regenerative amplifier, pumped by the Nd:YLF, including stretcher/compressor optics, a Pockels Cell/thin-film polarizer set-up with which to out-couple the amplified femtosecond pulses, and a quartz cell for continuum generation (components to be purchased).
- (5) Optical parametric amplifier, with one LBO crystal for frequency-doubling a portion of the continuum from the regen, and a second for generating the idler and signal pulses, tunable between 1-2 microns (components to be purchased).

Work performed this summer

In accordance with the areas of research emphasis discussed above, I performed the following tasks during my tenure as a research associate this last summer:

- Designed type-II p-i-n samples for temperature-dependent PL and electroabsorption measurements.

- Directed growth of the samples by Leavitt et al. of the Army Research Lab.
- Carried on preliminary conversations with Prof. Nan-Marie Jokerst of Georgia Tech to arrange for epitaxial lift-off of transmission-mode samples by her group.
- Reviewed earlier measurements for preparation of tech report summarizing moderate-temperature type-II->type-I transition results.
- Studied ACQWs in InAlGaAs material system; became familiar with Mark Krol's work on ultrafast recovery in such materials at low temperature; carried on extensive discussions with Mark concerning potential device design issues for AFPMs fabricated from such materials.
- Performed extensive literature review covering Ti:Sapphire-based regenerative amplifier systems, OPA technology and related OMA/cryogenic equipment for femtosecond pump-probe spectroscopy.
- Carried out vendor search for components for home-built regen/OPA system.
- Studied Ti:Sapphire Kerr-lens-mode-locked oscillator design; performed numerical simulations allowing optimization of cavity configuration for self-starting operation.
- Designed oscillator and custom components (crystal mount, etc.), ordered components and built; testing and alignment now underway.
- Conducted detailed literature search concerning recent VCSEL designs, including work of Raj et al.¹⁴ concerning VCSELs for modulation and switching.

Future Work

As is clear from the above summary, my efforts this summer have basically laid the groundwork for an aggressive experimental research program investigating three different semiconductor materials suitable for ultrafast switching, all centered around a tunable femtosecond pump-probe system. My immediate short-term goal is to build such a system and get it producing reliable data. To this end, I have submitted an SREP proposal to fund the work of a research associate who can assist me with exactly these tasks.

References

1. M. Whitehead et al., "Low-voltage multiple quantum well reflection modulator with on:off ratio > 100 ," *Electron. Lett.*, vol. 25, pp. 984-985, 1989.
2. R. H. Yan, R. J. Simes, and L. A. Coldren, "Extremely low-voltage Fabry-Perot reflection modulators," *IEEE Photon. Technol. Lett.*, vol. 2, pp. 118-120, 1990.
3. C. C. Barron et al., "K-Band Operation of Asymmetric Fabry-Perot Modulators," *IEEE Photon. Technol. Lett.*, vol. 4, pp. 459-461, 1992.
4. D. S. Gerber, R. Droopad, and G. N. Maracas, "A GaAs/AlGaAs Asymmetric Fabry-Perot Reflection Modulator with Very High Contrast Ratio," *IEEE Photon. Technol. Lett.*, vol. 5, pp. 55-58, 1993.
5. J. F. Heffernan et al., "All optical, high contrast absorptive modulation in an asymmetric Fabry-Perot etalon," *Appl. Phys. Lett.*, vol. 58, pp. 2877-2879, 1991.
6. R. Jin et al., "High contrast, submilliwatt power InGaAs/GaAs strained-layer multiple-quantum-well asymmetric reflection modulator," *Appl. Phys. Lett.*, vol. 59, pp. 3216-3218, 1991.
7. I. J. Fritz et al., "Vertical-cavity reflectance modulator for $1.3\ \mu\text{m}$ using (InAlGa)As multilayers," in Conference on Laser and Electro-Optics, 1993, vol. 11, OSA Technical Digest Series (Optical Society of America, Washington D.C., 1993), pp. 372-374.
8. S. M. Lord, et al., "Electroabsorption reflection modulators operating near $1.3\ \mu\text{m}$ on GaAs," in Conference on Laser and Electro-Optics, 1993, vol. 11, OSA Technical Digest Series (Optical Society of America, Washington D.C., 1993), pp. 12-13.
9. M. F. Krol et al., "All-optical, high contrast GaAlInAs multiple quantum well asymmetric reflection modulator at $1.3\ \mu\text{m}$," *Appl. Phys. Lett.* vol. 62, pp. 1550-1552, 1993.
10. M.-H. Meynadier, R. E. Nahory, J. M. Worlock, M. C. Tamargo, J. L. de Miguel, and M. D. Sturge, "Indirect-Direct Anticrossing in GaAs-AlAs Superlattices Induced by an Electric Field: Evidence of Γ -X Mixing," *Phys. Rev. Lett.* vol. 60, pp. 1338-1341, 1988.
11. K. Meissner, B. Fluegel, R. Binder, S. W. Koch, G. Khitrova, and N. Peyghambarian, "Comparison of optical nonlinearities of type II and type I quantum wells," *Appl. Phys. Lett.* vol. 59, pp. 259-261, 1991.

12. Richardson et al., in preparation.
13. M. F. Krol. et al., to be submitted to *Phys. Rev. Lett.*
14. R. Raj, J. A. Levenson, J. L. Oudar, and M. Bensoussan, "Vertical Microcavity Optical Amplifying Switch," *Electron. Lett.* vol. 29, pp. 167-169, 1993.
15. See, e.g., W. H. Knox et al., "Amplified femtosecond optical pulses and continuum generation at 5-kHz repetition rate," *Opt. Lett.* vol. 9, pp. 552-554, 1984.
16. J. Squier, G. Korn, G. Mourou, G. Vaillancourt, and M. Bouvier, "Amplification of femtosecond pulses at 10-kHz repetition rates in Ti:Al₂O₃," *Opt. Lett.* vol. 18, 625 (1993).

SYNTHESIS AND PROPERTIES
OF
 β -DIKETONATE-MODIFIED HETEROBIMETALLIC ALKOXIDES
(Single-Source MOCVD Precursors)

Daniel F. Ryder, Jr.
Associate Professor
Department of Chemical Engineering

Tufts University
Science and Technology Center
4 Colby Street
Medford, MA 02155

Final Report

USAF Summer Faculty Research Program
Rome Laboratory

Sponsored by

U.S. Air Force Office of Scientific Research
Bolling Air Force Base, DC

and

Rome Laboratory

September 1994

SYNTHESIS AND PROPERTIES
OF
 β -DIKETONATE-MODIFIED HETEROBIMETALLIC ALKOXIDES

(Single-Source MOCVD Precursors)

Daniel F. Ryder, Jr.
Associate Professor
Department of Chemical Engineering
Tufts University

Abstract

A study was initiated to investigate both the synthetic chemistry and properties of β -diketonate-modified heterobimetallic alkoxides of the alkaline earths and titanium. A number of single metal diketonates have been utilized as source compounds in the MOCVD processing of electronic oxides (e.g., BaTiO_3 , $\text{YBa}_2\text{Cu}_3\text{O}_x$, $\text{Pb}(\text{Zr,Ti})\text{O}_3$, etc.). It was proposed to extend this work by conducting an initial screening study to evaluate if such chelating and branching ligand systems may be used to develop new "single-source" compounds for bimetallic oxides (e.g., BaTiO_3). The synthesis and properties of a 2,2,6,6-tetramethyl-3,5-heptanedionate (thd) modified barium-titanium isopropoxide was specifically studied. The results of this initial study were inconclusive, but do provide a technological justification for further study.

SYNTHESIS AND PROPERTIES
OF
 β -DIKETONATE-MODIFIED HETEROBIMETALLIC ALKOXIDES
(Single-Source MOCVD Precursors)

Daniel F. Ryder, Jr.

Introduction

Metalorganic chemical vapor deposition (MOCVD) of multicomponent oxides has recently been the subject of extensive research study, particularly as related to the thin film processing of the cuprate superconductors (e.g., $\text{YBa}_2\text{Cu}_3\text{O}_x$, $\text{Bi}_2\text{Sr}_2\text{Ca}_2\text{Cu}_3\text{O}_y$) and the ferroelectric perovskites (e.g., BaTiO_3 , $(\text{Ba},\text{Sr})\text{TiO}_3$). Current commercial practise involves the controlled vaporization and transport of individual metal precursor compounds to achieve stoichiometric compositional control of the growing film. As an attractive processing alternative to the complicated operational strategies associated with conventional multi-source MOCVD processing, the use of single-source complexed-metal compounds which inherently possess the desired stoichiometric component ratio of the targeted oxide has been promoted. Chour *et.al.*¹ recently reported on the vapor deposition of LiTaO_3 from a single-source, volatile double metal alkoxide $(\text{LiTa}(\text{OBut}^n)_2)$. Likewise, Zhang *et.al.*² reported on the CVD growth of MgAl_2O_4 thin films from a flash-evaporated $\text{MgAl}_2(\text{OPri})_8$ precursor. A review of the definitive text Metal Alkoxides³ shows that there are a number of double metal alkoxides which possess the three properties required for a MOCVD single-source compound:

- 1) A stoichiometric composition consistent with the targeted product oxide.
- 2) Good thermal stability. Solid/liquid-phase thermal decomposition reactions to the individual metal alkoxides and/or other polymeric oxo-alkoxide intermediates would lead to nonstoichiometric deposition.
- 3) Sufficient volatility at normal processing conditions.

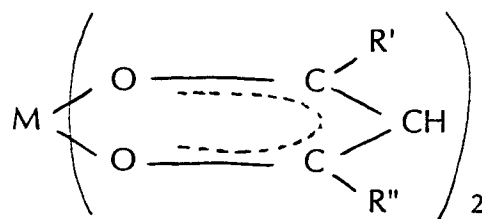
It is notable that no bimetallic alkoxide which contains an alkaline-earth (i.e., Ba, Sr, Ca) : Ti pair possesses adequate thermal stability for CVD applications. Furthermore,

and due to the propensity of the alkaline-earths to attain high coordination numbers, all of referenced alkaline-earth-based double metal alkoxides possess metallic stoichiometric ratios inconsistent with commercially significant oxide compositions. Given the current interest in thin film ferroelectric materials based on BaTiO₃, it would be of interest to investigate methods whereby the chemical composition, thermal stability, and volatility of Ba:Ti alkoxide-based systems may be modified/enhanced. In this study, the synthetic chemistry and properties of β -diketonate-modified Ba:Ti alkoxides were studied. As the basis for this choice, a brief summary of current work relating to the development of Group II source compounds is presented. In addition, background information relating to the synthesis of homo- and hetero- metal alkoxides and the reaction kinetics of metal alkoxides with β -diketones is briefly surveyed.

Precursor Development of Group II Source Compounds for CVD Applications

In order to ensure reasonable epitaxial growth rates at nominal substrate temperatures, source compounds should transport in the vapor phase at processing temperatures less than 200 °C and pressures greater than 5 torr.⁴ This constraint presents a significant problem for the case of the alkaline earth source compounds as their propensity to attain high coordination numbers, usually by forming multinuclear aggregates, severely limits their volatility.⁵ As such, only those alkaline earth compounds with multidentate, sterically encumbered anions have proven useful for MOCVD applications.

Recent synthetic chemical research has focused on both the fluorinated and fluorine-free β -diketonates which have the general structural form as shown below.^{5,6,7}



As illustrated, a monomeric alkaline earth β -diketonate would be coordinatively unsaturated with a coordination number (CN) of 4, where a CN of 6 to 10 is the thermodynamically-stabilized structural form. As such, intermolecular association takes place resulting in the formation of molecular clusters which adversely effects the volatility.

Volatility has been reported to increase with increased encapsulation of the metal ion through the utilization of bulky side-group ligands.⁵ Additionally, the use of fluorinated alkyl groups results in a decrease of intermolecular interactions which consequently increases volatility. For the case of fluorinated precursors, the resulting enhancement in volatility is at the expense of a more complicated decomposition reaction pathway to the oxide through the hydrolysis of a thermally stable fluoride salt. As such, more recent studies have concentrated on the non-fluorinated source compounds such as those based on 2,2,6,6-tetramethyl-3,5-heptanedionate (thd).

Ba(thd)₂ forms a tetrameric cluster in the solid state which is maintained in the transformation to the gas phase.^{5,8} While Ba(thd)₂ is air stable, significant decomposition through hydrolysis and carbonate formation preclude synthesis through the standard "wet" method⁹. Pure Ba(thd)₂ may be synthesized by direct reaction of the metal or metal hydride with 2 equivalents of the free β -diketone (Hthd). Based on nominal growth rate requirements, use of pure Ba(thd)₂ as a barium precursor requires sublimation temperatures in slight excess of 200 °C. Prolonged heating at these temperatures induces thermal decomposition processes which result in the significant deterioration of the vapor transport rate. Methods to induce dissociation of the tetrameric Ba(thd)₂ clusters to monomeric species would serve to enhance their volatility, and various methods to induce coordinative saturation through adduct addition have been reported. For example, evaporation of Ba(thd)₂ in the presence of oxygen (e.g., polyethers) or nitrogen (e.g., THF, HN₃, N(CH₃)₃) donor ligands has been reported to enhance the thermal stability and the volatility of the compound such that increased mass transport rates may be maintained at lower evaporation temperatures.⁶

Synthesis and Properties of Homo- and Hetero- Metal Alkoxides

The reader is referred to the text by Bradley et.al.³ for general information regarding the synthesis and properties of metal alkoxides, as the background information included herein is specific to the alkoxides of the alkaline earths and heterobimetallic alkoxides of the alkaline earths and titanium.

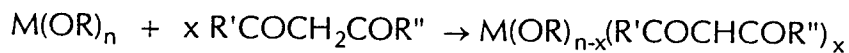
The alkaline earth alkoxides may be synthesized via the direct reaction of the metal and/or metal hydride with the alcohol. Simple [M(OR)₃]_n (R = Me, Et, Prⁿ, Prⁱ) alkoxides of group 2 metals are generally polymeric, insoluble in organic solvents, and non-volatile. Lowering the degree of association has been shown to increase the solubility and

volatility, and the role of steric factors on the extent of oligomerization has been actively studied. Recent strategies reported in the literature to induce dissociation include the utilization of sterically demanding ligands (e.g., 2,6-Bu^t₂C₆H₃O⁻, Et₃CO⁻, C(Me₃)₂CHO⁻; etc.) and chelating ligands (e.g., Me₂NCH₂CH₂O⁻, ROCH₂CH₂O⁻, CH₃(OCH₂CH₂)_nO⁻; etc.).¹⁰ Relative to the 2-methoxyethoxide chelating ligand, it is important to note that there is an additional trend for this ligand to act as a bridging ligand which may lead to the formation of large oligomers.¹¹ This property has been the basis for the use of 2-methoxyethoxide as an assembling ligand for the formation of heterometallic alkoxides.

As compared to associated homo-metallic alkoxides, the heterobimetallic alkoxides exhibit, in general, an enhanced stability probably resulting from the greater stability of the M(μ-OR)₂M' bridges between dissimilar metals. In addition, a number of heterobimetallic alkoxides containing an alkaline earth metal constituent are soluble, volatile, and monomeric - which contrasts sharply with the insoluble, polymeric, and non-volatile nature of the associated homo-metallic alkoxide. Bimetallic alkoxides containing an alkaline earth constituent have been synthesized by the Lewis acid-base interaction of the simple alkoxide of these metals with the alkoxides of less electropositive elements. D.A. Payne et.al.¹² recently reported on the synthesis of barium titanium methoxyethoxide [BaTi(OCH₂CH₂OCH₃)₆] via this method. In previous work¹³, the structure of a similar lead titanium alkoxide was reported to be consistent with that of a linear polymeric network with an empirical chemical formula of PbTi(OCH₂CH₂OCH₃)₆. This work highlights the fact that chelating ligands, such as 2-methoxyethoxide, not only act as bridging ligands conducive to the formation of a heterobimetallic alkoxide, but also induce the formation of large oligomers. The resulting polymeric structures are, in general, nonvolatile and as such bimetallic 2-methoxyethoxides are not suitable source compounds for CVD applications.

Chemical Reactions of Metal Alkoxides with β-Diketones

The enolic form of a β-diketone contains a reactive hydroxyl group and this molecule reacts very readily with metal alkoxides, which may be represented by the following general reaction³:



The reaction chemistry of titanium (IV) alkoxides with β -diketones has been well studied and the reader is referred to the literature^{14,15} for details.

Experimental Procedure

The following chemicals were used without further purification: titanium isopropoxide (Alfa/Johnson Matthey, MA), barium (Alfa/Johnson Matthey, MA), and 2,2,6,6-tetramethyl-3,5-heptanedione (Strem Chemical, MA). Isopropanol (Alfa/Johnson Matthey, MA) and thiophene-free benzene (Alfa/Johnson Matthey, MA) solvents were dried and purified by distillation over calcium hydride. All synthesis work was conducted in a controlled Ar-atmosphere glovebox.

Barium isopropoxide was prepared by reacting barium metal with excess isopropanol in benzene at room temperature. The diketone-modified alkoxide was prepared by adding 2,2,6,6-tetramethyl-3,5-heptanedione in a 1:1 molar ratio to barium and stirring for 12 hours at room temperature.

Titanium diisopropoxide di-2,2,6,6-tetramethyl-3,5-heptanedionate was prepared by reacting titanium (IV) isopropoxide with 2,2,6,6-tetramethyl-3,5-heptanedione in a 1:2 molar ratio in benzene at room temperature for 12 hours.

The Ba:Ti product complexes were prepared by reacting stoichiometric quantities of the barium precursor solution to the titanium precursor solution at the conditions of atmospheric reflux (T, 80 °C) for approximately 1 hour. Solvents were removed from product mixtures by vacuum distillation techniques. The resulting precipitates were analyzed by thermalgravimetric techniques.

Sublimation trials were conducted in a commercial vacuum sublimator (Aldrich Chemical Co., Milwaukee, WI). Chemical analysis of both sublimate and retentate samples was conducted by electron diffraction spectroscopy (EDS).

Results and Discussion

The reaction of barium isopropoxide and titanium isopropoxide with 2,2,6,6-tetramethyl-3,5-heptanedione exhibited a slight exotherm at the mild conditions employed in this study. All reaction products were soluble in benzene. Removal of the solvent benzene by room-temperature, vacuum distillation resulted in the dramatic precipitation

of a solid phase which was assumed to be the desired barium-titanium precursor compound.

The oxidative decomposition kinetics of the barium-titanium precursor were analyzed by thermalgravimetric techniques and compared to commercial $\text{Ba}(\text{THMD})_2$ and $\text{Ba}(\text{O}i\text{Pr})_2$. In general, the decomposition profiles (i.e., [wt. vs. T] and [d(wt.)/dT vs. T]) of the prepared Ba-Ti precursor were similar to the commercial $\text{Ba}(\text{THMD})_2$, and served to at least empirically confirm the successful complexation of diketone to the metal alkoxides.

Initial attempts to purify the precipitated product compound by vacuum sublimation resulted in deposition of two distinct solid phases - a white, needle-like, crystal structure and a fine, yellow powder. EDS analysis of a composite sample of the sublimate showed a molar Ba:Ti ratio of approximately 1:3 (note: target ratio, 1:1). By carefully controlling the sublimation rate (through T control), sublimate samples of essentially the pure needle-like crystal phase were isolated. EDS analysis of these samples indicated a molar Ba:Ti ratio of approximately 1:6. Attempts to re-purify this sublimate through a second vacuum sublimation process resulted in the deposition of a Ba-free sublimate. Given that these initial experiments were conducted at relatively high temperature (200-220 °C), it is surmised that thermal decomposition processes were a significant complicating factor to the overall process.

Conclusion

The results of this initial study were preliminary and incomplete, and as such, further work must be conducted in order to adequately assess the viability of the proposed approach. While samples from initial vacuum sublimations were found to contain both barium and titanium, re-sublimation of this purified material resulted in a sublimate which contained only titanium. Furthermore, we did not attempt to fully analyze the structural features of the synthesized products during this initial exploratory study, and as such, do not make any claim relative to the molecular structure of product compounds. It is notable, though, that the oxidative decomposition kinetics of the product samples were similar to commercial $\text{Ba}(\text{THMD})_2$ and dissimilar to commercial $\text{Ba}(\text{O}i\text{Pr})_2$.

In retrospect, and based on the subsequent detailed analysis of the current technical literature, the use of a starting alkoxide formula based on the utilization of a sterically

demanding ligand or a chelating ligand is preferred in order to enhance the formation of the initial heterobimetallic alkoxide. To this end, it is suggested that the chelating and bridging ligand 2-methoxyethoxide be utilized during the complexation of the barium and titanium alkoxides in future experimental studies.

Acknowledgment

The author wishes to acknowledge and thank the technical staff of Rome Laboratory (RL/ERX), particularly Mr. Michael Suscavage and Mr. Robert Andrews, for their encouragement, technical services, and cooperation over the course of this study.

References

- ¹ K. Chour, G. Wang, and R. Xu, "Vapor Deposition of Lithium Tantalate with Volatile Double alkoxide Precursors", in *Mat. Res. Soc. Symp. Proc. Vol. 335, Metal-Organic Chemical Vapor Deposition of Electronic Ceramics*, S.B. Desu, D.B. Beach, B.W. Wessels, and S. Gokoglu, Eds., Mat. Res. Soc., Pittsburgh, PA, 65, (1994).
- ² J. Zhang, G.T. Stauff, R. Gardiner, P. Van Buskirk, and J. Steinbeck, "Single Molecular Precursor Metal-Organic Chemical Vapor Deposition of $MgAl_2O_4$ Thin Films", *J. Mater. Res.*, **9**[6], 1333, (1994).
- ³ D.C. Bradley, R.C. Mehrotra, and D.P. Gaur, *Metal Alkoxides*, Academic Press, Orlando, FL, (1978).
- ⁴ G.B. Stringfellow, *Organometallic Vapor-Phase Epitaxy: Theory and Practice*, Academic Press, New York, (1989).
- ⁵ B.A. Vaartstra, R.A. Gardiner, D.C. Gordon, R.L. Ostrander, and A.L. Rheingold, "Advances in Precursor Development for CVD of Barium-Containing Materials", in *Mat. Res. Soc. Symp. Proc. Vol. 335, Metal-Organic Chemical Vapor Deposition of Electronic Ceramics*, S.B. Desu, D.B. Beach, B.W. Wessels, and S. Gokoglu, Eds., Mat. Res. Soc., Pittsburgh, PA, 203, (1994).
- ⁶ H.A. Meinema, K. Timmer, H.L. Linden, and C.I.M.A. Spee, "Synthetic Strategies for MOCVD Precursors for HTcS Thin Films", in *Mat. Res. Soc. Symp. Proc. Vol. 335, Metal-Organic Chemical Vapor Deposition of Electronic Ceramics*, S.B. Desu, D.B. Beach, B.W. Wessels, and S. Gokoglu, Eds., Mat. Res. Soc., Pittsburgh, PA, 193, (1994).
- ⁷ W.S. Rees Jr., H.A. Luten, M.W. Carris, C.R. Caballero, W. Hesse, and V.L. Goedken, "Current Status of Recent Results on Group 2 Source Compounds for Vapor Phase Epitaxy of Ferroelectric Thin Films", in *Mat. Res. Soc. Symp. Proc. Vol. 310, Ferroelectric Thin Films III*, E.R. Myers, B.A. Tuttle, S. Desu, and P.K. Larsen, Eds., Mat. Res. Soc., Pittsburgh, PA, 375, (1993).
- ⁸ J.E. Schwarberg, R.E. Sievers, and R.W. Moshier, "Gas Chromatographic and Related Properties of the Alkaline Earth Chelates with 2,2,6,6-Tetramethyl-3,5-Heptanedione", *Anal. Chem.*, **42**(14), 1828, (1970).
- ⁹ K.J. Eisentraut and R.E. Sievers, "Volatile Rare Earth Chelates", *J. Am. Chem. Soc.*, **87**(22), 5254, (1965).
- ¹⁰ R.C. Mehrotra, A. Singh, and S. Sogani, "Homo- and Hetero-metallic Alkoxides of Group 1,2, and 12 Metals", *Chem. Soc. Rev.*, pp 215-25, (1994).
- ¹¹ L.G. Hubert-Pfalzgraf, O. Poncelet, C. Sirio, and J.C. Daran, "Tailoring Metal Alkoxides Using Functional Alcolols: Aome Examples in Yttrium, Copper, and Main-Group Chemistry (Bismuth, Barium)", in *Chemical Processing of Advanced Materials*, L.L. Hench and J.K. West, Eds., John Wiley & Sons, Inc., New York, NY, 277, (1992).
- ¹² D.A. Payne, D.J. Eichorst, L.F. Francis, and J-F. Campion, "Molecular Precursors for the Chemical Processing of Advanced Electrical Ceramics", in *Chemical Processing of Advanced Materials*, L.L. Hench and J.K. West, Eds., John Wiley & Sons, Inc., New York, NY, 499, (1992).
- ¹³ S.D. Ramamurthi and D.A. Payne, "Structural Investigations of Prehydrolyzed Precursors Used in the Sol-Gel Processing of Lead Titanate", *J. Am. Ceram. Soc.*, **73**[8], 2547, (1990).

- 14 D.M. Puri and R.C. Mehrotra, "Derivatives of Titanium with Compounds Having Bidentate Ligands: II. Reactions of Titanium Alkoxides with Methyl Acetoacetate", *J. Less-Common Met.*, **3**, 253, (1961).
- 15 D.M. Puri, K.C. Pande, and R.C. Mehrotra, "Derivatives of Titanium with Compounds Having Bidentate Ligands: III. Reactions of Titanium Alkoxides with Acetylacetone", *J. Less-Common Met.*, **4**, 393, (1962).

**PHOTOREFRACTIVE DEVELOPMENT AND APPLICATIONS OF
InP AND BSO**

Gregory J. Salamo
Professor of Physics
Department of Physics

University of Arkansas
Physics Department
Fayetteville, AR 72701

Final Report for:
Summer Faculty Research Program
Rome Laboratory
Hanscom Air Force Base

Sponsored by:
Air Force Office of Scientific Research
Bolling Air Force Base, DC

and

Rome Laboratory
Hanscom Air Force Base

October 31, 1994

PHOTOREFRACTIVE DEVELOPMENT AND APPLICATIONS OF InP AND BSO

**Gregory J. Salamo
Professor of Physics
University of Arkansas**

Abstract

An investigation into the photorefractive properties of InP was initiated. Experimental apparatus for carrying out an investigation was built at Hanscom Air Force Base using a c. w. YAG laser for steady-state measurements while complimentary apparatus was built at the University of Arkansas using a picosecond tunable Ti-Sapphire laser for transient studies. Initial measurements on both energy exchange and diffraction efficiency were made indicating a high potential for InP as a photorefractor in the near infrared. Results also indicate that the photorefractive effect will be an effective diagnostic tool for characterization of InP. Because of this potential the collaboration between Arkansas and Hanscom will continue beyond the summer program period.

PHOTOREFRACTIVE DEVELOPMENT AND APPLICATIONS OF InP AND BSO

Gregory J. Salamo

I. INTRODUCTION

Over the last few years we have carried out experimental and theoretical investigations on the understanding and applications of the photorefractive effect in the ferroelectric oxides, such as, barium titanate (BaTiO_3) and strontium barium niobate (SBN). Our research has lead to an improved understanding of these materials and we have demonstrated several novel applications. For example, we have uncovered the affect of temperature, applied d.c. and a.c. electric fields, and the role of dopant concentration and type on the magnitude of the photorefractive index change and the speed with which it is produced. We have demonstrated the confinement or trapping of 30 micron diameter laser beams through 1 centimeter samples and a quasi-phase matching technique to produce real-time tunable second harmonic generation at any wavelength in a single crystal without temperature or angle tuning. Our research has produced a demonstration of a type of optical limiter which has the unique feature of limiting laser light while maintaining normal visibility. We have demonstrated a photorefractive spatial light modulator, image subtraction, addition, division, correlation, storage, color storage, contrast enhancement, phase conjugation, -all with spatial resolution exceeding a hundred lines per millimeter. Our most recent study has produced a real-time nondestructive material testing scheme using a holographic technique packaged in a small portable device.

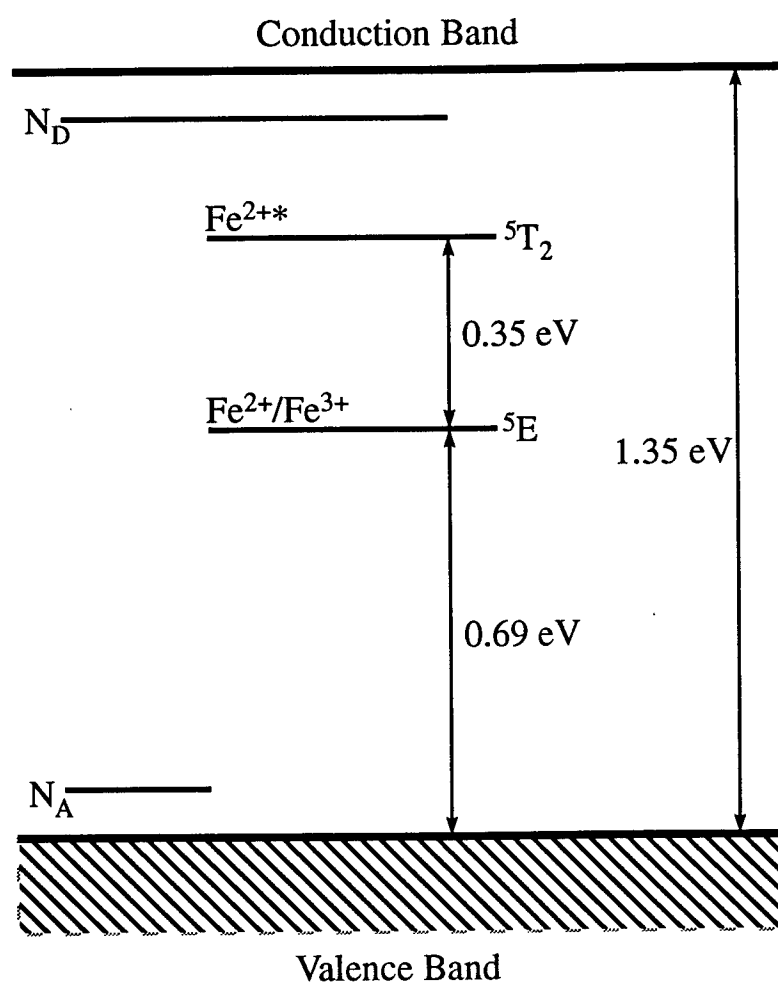
II. DISCUSSION OF THE PROBLEM

While each of these applications have been exciting to produce in the laboratory, all is not well with the field of photorefraction. The ferroelectric oxides are not striation-free, they have low carrier mobilities, and high dielectric constants. Moreover, it is difficult to control the acceptor and donor concentrations independently, and their ferroelectric nature produces unwanted effects with

applied d.c. or a.c. fields. For these reasons the sillenites, such as bismuth silicon oxide (BSO) and the III-V semiconductors, such as InP, are attractive materials for many of the applications we have investigated. BSO and InP, for example, have high mobilities, low dielectric constants, show no complications with applied d.c. and a.c. electric fields, and have the potential for independently controlled acceptor and donor concentrations. This is particularly true for InP where due to the importance of defects, the electronic and optoelectronic industry have developed techniques for controlling the acceptor and donor concentrations. Finally, both BSO and InP are produced with high optical quality. Rome Laboratory, for example, produces, if not perfect, near perfect BSO and InP. These materials, therefore, are an effective starting point for the development of controlled-high quality, photorefractives which in turn will lead to improved application potential.

This summer we began a collaboration with Rome Laboratory to architect these materials using measurements of their photorefractive properties and their performance in applications as a guide. The architecture of these materials involves experimenting with type and concentration of impurities. For example, for InP, (see figure on next page) the elements Ge, Si, Sn, S, Se might be typical species which would lead to shallow donor and acceptor levels while Ce, Cu, Cr, Fe, Ca, Zn, Mo, might be typical species leading to deep donor and acceptor levels. As impurity concentration of 10^{16} per cm^3 can give a resistivity as high as 10^9 ohm-cm and a dielectric relaxation below 1 ms. Deep traps reduce the free carrier lifetime of photoexcited carriers by providing a high probability of retrapping. Meanwhile, the density of deep traps gives rise to optical absorption at wavelengths above the band edge. Careful manipulation, therefore, of the dopant concentration can tailor the material response time, optical absorption, photo-carrier mobility and sensitive wavelength. For example, one interesting question we can answer about our samples is the relative importance of electron versus hole carriers. Due to the high mobility of electrons over holes, the two processes can be separated using femtosecond output optical pulses

from a Ti-sapphire mode-locked laser for time resolved measurements of the "writing" of a photorefractive grating. Another interesting point is that since InP substrates are used in electronic and opto-electronic devices the photorefractive effect can act as a non-contact probe for mapping



Energy Level Diagram for Fe^{2+}

out the optical and electrical behavior of the substrate. With high spatial and temporal resolution the resistivity, absorption, sign of photocarriers, drift length and diffusion length, could be mapped. Likewise BSO, is of intense interest. It is for example faster and more sensitive than lithium niobate LiNbO_3 and consequently would perform extremely well in the infrared spectral region for image processing applications.

III. PHOTOREFRACTIVE CONCEPT

In the photorefractive effect the index of refraction is changed by a spatially modulated light intensity pattern. Optically generated charge carriers migrate due to diffusion, drift, and the photovoltaic effect and produce a charge separation. The charge separation then results in a space charge field which changes the index of refraction via the electro-optic effect. In our model, the photorefractive material is doped with donor and acceptor traps. When photons of sufficient energy enter the crystal, donors are excited into the conduction band where they are transported until they are re-trapped. The process is modeled using the following transport equations:

$$\begin{aligned} \frac{dN_D^+}{dt} = & s_e I (N_D - N_D^+) - \gamma_e n_e N_D^+ - s_h I N_D^+ \\ & + \gamma_h n_h (N_D - N_D^+) \end{aligned} \quad (1a)$$

$$j_e = en_e \mu_e E + \mu_e k_B T \nabla n_e \quad (1b)$$

$$\frac{dn_e}{dt} = \frac{1}{e} \nabla j_e + s_e I (N_D - N_D^+) - \gamma_e n_e N_D^+ \quad (1c)$$

$$\nabla E = -\frac{e}{\epsilon} (n_e + N_A - N_D^+ - n_h) \quad (1d)$$

$$j_h = en_h \mu_e E - \mu_h k_B T \nabla n_h \quad (1e)$$

$$\frac{dn_h}{dt} = \frac{-1}{e} \nabla j_h + s_h N_D^+ I - \gamma_h n_h (N_D - N_D^+) \quad (1f)$$

In these expressions N_D is the total number of donor species and N_D^+ the number of ionized donors available for electron recombination and hole photoexcitation, j_e and j_h are the electron and hole current densities and E the total internal field. n_e and n_h are the densities of free holes and electrons and s_e and s_h their excitation cross sections. γ_e and γ_h are the recombination rates and μ_e and μ_h the carrier mobilities. The density of compensative acceptors is N_A and is equal to the density of ionized donors in the dark.

These equations describe the formation of the space charge field which is then responsible for the change in index of refraction via the electro-optic effect described by

$$\Delta\left(\frac{1}{n^2}\right)_{ij} = \sum r_{ijk} E_k$$

where r_{ijk} is the electro-optic coefficient.

IV. TWO BEAM COUPLING OR METHODOLOGY

An important character of two-beam coupling in a photorefractive material is the energy exchange from one laser beam to the other. The steady-state value of the energy transfer signal (ETS) and the diffraction signal (DS) due to the grating inside the crystal, can provide interesting information about a photorefractive material. The origin of energy exchange in two-beam coupling is the phase shift between the grating and the intensity fringe pattern.

The phase shift between the grating and the fringe pattern can be determined by measuring the energy exchange signal and the diffraction signal. The phase shift measurement can be a technique for determining photorefractive constants of a crystal. One important application of this technique is to measure the crystal trap number density by applying a DC field to a crystal and determining the resulted phase shift between the grating and the fringe pattern as a function of the magnitude of the DC field.

A. Basic Theory For Phase Shift Measurement

In a photorefractive material, the two light waves which are expressed as

$$E_1(x,z) = E_{10} \exp[i(k_x x + k_z z)] \quad (2a)$$

$$E_2(x,z) = E_{20} \exp[i(-k_x x + k_z z)] \quad (2b)$$

interact at an angle 2θ in the volume phase grating, where k_x and k_z are components of the wave vector. If ϕ is the phase shift between the grating and the interference pattern the output waves will become

$$E_1(d) = E_{10} \cos(\kappa d) - iE_{20} e^{+i\phi} \sin(\kappa d) \quad (3a)$$

$$E_2(d) = E_{20} e^{-i\phi} \cos(\kappa d) - iE_{10} \sin(\kappa d) \quad (3b)$$

where κ is the coupling constant and d is the thickness of the crystal.

Using these two equations the optical intensities after passing through a crystal are given by

$$\begin{aligned} I_T(d) &= E_1(d) E_1^*(d) \\ &= I_1 \cos^2(\kappa d) + I_d \sin^2(\kappa d) - (I_T I_D)^{1/2} \sin(2\kappa d) \sin \phi \end{aligned} \quad (4a)$$

$$\begin{aligned} I_D(d) &= E_2(d) E_2^*(d) \\ &= I_d \cos^2(\kappa d) + I_1 \sin^2(\kappa d) + (I_T I_D)^{1/2} \sin(2\kappa d) \sin \phi \end{aligned} \quad (4b)$$

where $I_T = E_{10}^2$ and $I_D = E_{20}^2$ are incident intensities of two beam. In this expression the first term corresponds to the transmitted component, the second term is the diffracted component due to the grating, and the third term is the energy-exchange component between two beams. These terms are depicted in the following figures. As a result, the diffraction efficiency η will be given as

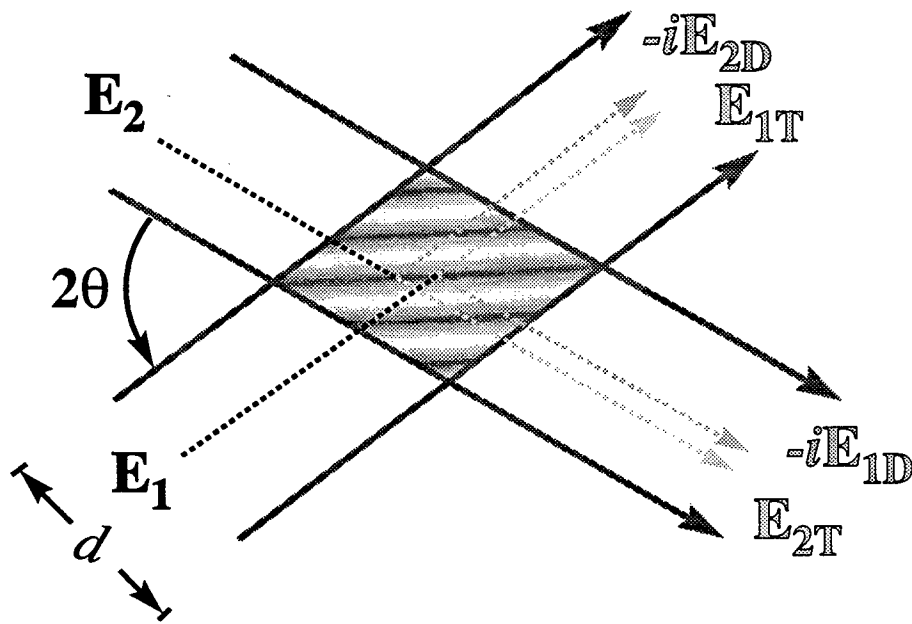
$$\eta = \sin^2(\kappa d) \quad (5)$$

If the incident intensities of both beams are equal we can get the energy-exchange efficiency ϵ in terms of diffraction efficiency η as

$$\epsilon = 2[\eta(1-\eta)]^{1/2} \sin \phi \quad (6)$$

$$\text{Then} \quad \sin \phi = \epsilon / \{2[\eta(1-\eta)]^{1/2}\} \quad (7)$$

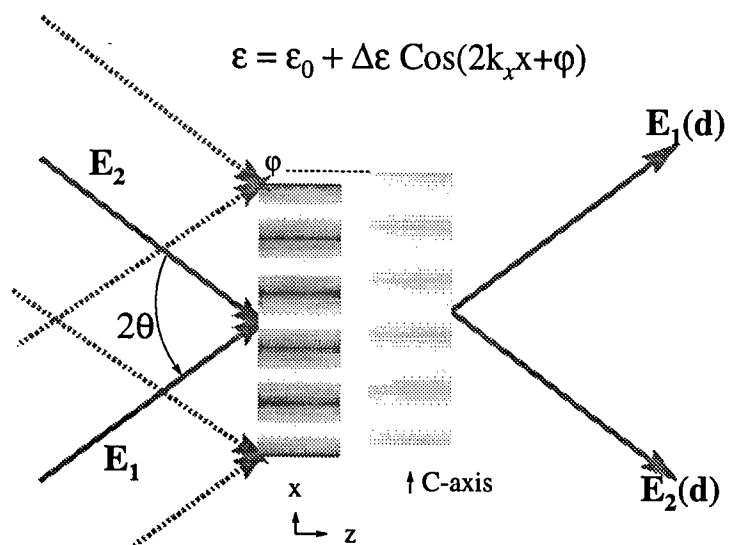
$$\text{or} \quad \sin \phi = I_e / \{2[I_d(I_0 - I_d)]^{1/2}\} \quad (8)$$



$$\mathbf{E}_1(d) = \mathbf{E}_{1T} - i\mathbf{E}_{2D}$$

$$\mathbf{E}_2(d) = \mathbf{E}_{2T} - i\mathbf{E}_{1D}$$

Two Wave Coupling 1



$$E_1 = E_{10} \text{Exp}[i(k_x x + k_z z)] \quad E_1(d) = E_{10} \cos(\kappa d) - i E_{20} e^{-i\phi} \sin(\kappa d)$$

$$E_2 = E_{20} \text{Exp}[i(-k_x x + k_z z)] \quad E_2(d) = E_{20} e^{-i\phi} \cos(\kappa d) - i E_{10} \sin(\kappa d)$$

$$\text{Coupling Coefficient } \kappa = \pi \Delta\epsilon / 2(\epsilon)^{1/2} \lambda \cos \theta$$

Two Wave Coupling 2

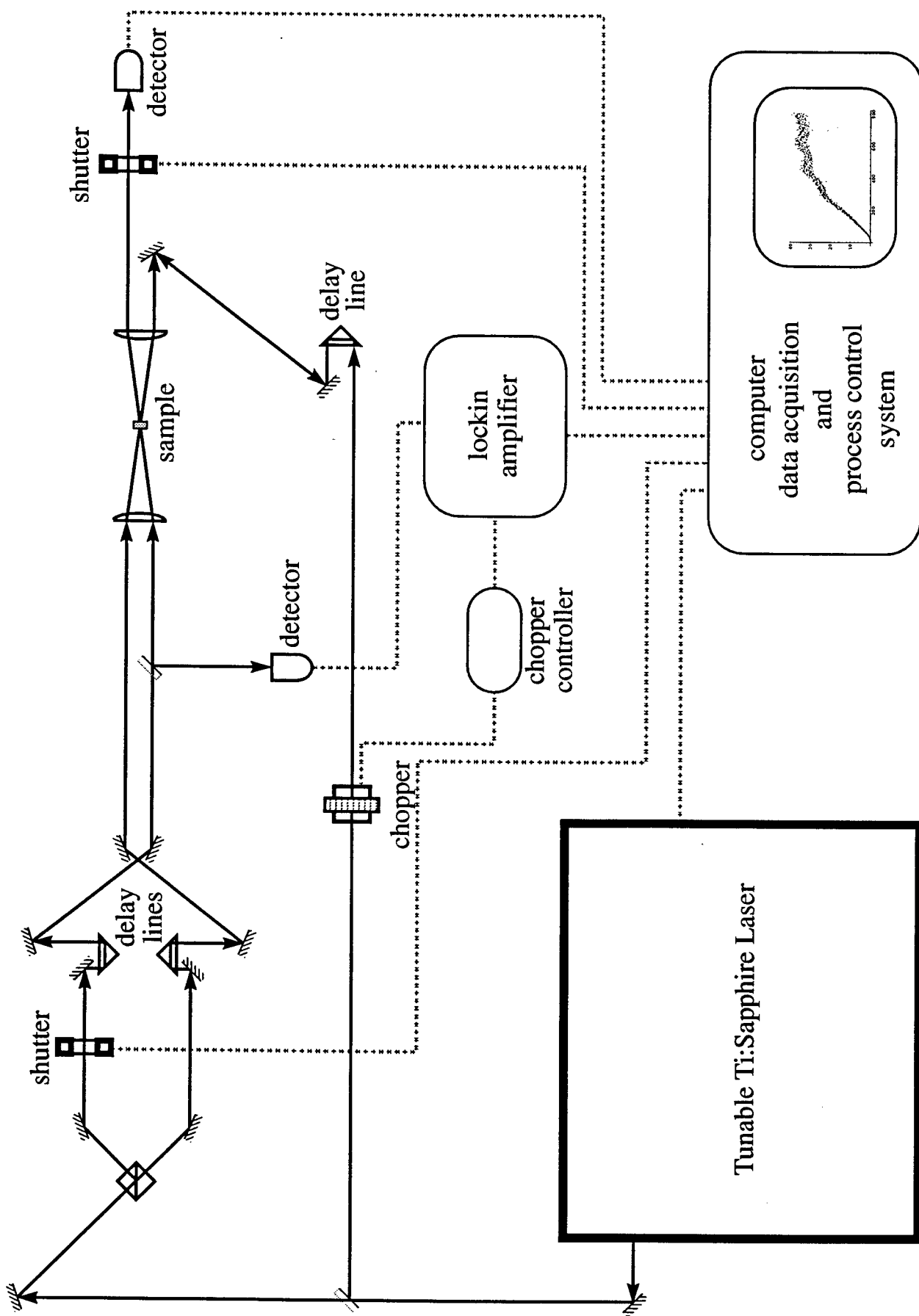
where I_e is the energy exchange signal, which is the intensity change of the detected beam after two beams are turned on; I_d is the diffraction signal, which is the intensity measured of the detected beam immediately after the incident detected beam is blocked; and I_0 is the intensity of the detected beam without coupling.

B. Energy-Transfer Measurement And Determination Of The Phase Shift Between The Grating And The Fringe Pattern

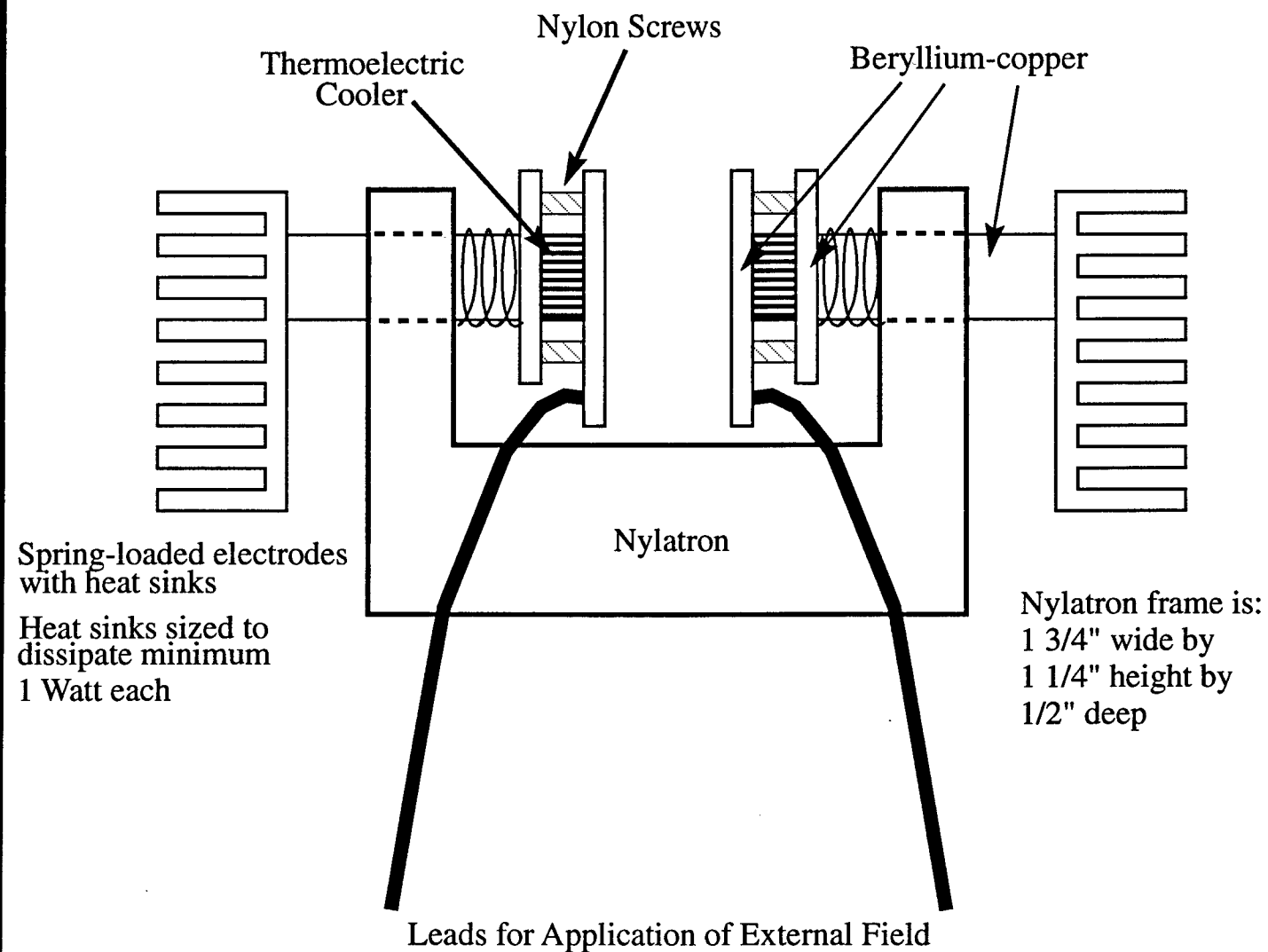
The experimental set up for two beam coupling is shown in the following figure. The YAG or Ti-Sapphire laser beam is split into two beams I_T and I_D that intersect inside a thin sample (held at constant temperature) such that the grating vector is parallel to the c-axis and the applied field (see crystal holder on next page). The beam is split 50% to 50% to make the beam I_T having the same intensity as I_D . The angle 2θ between the two beams is about 10° . The beam $I_T(d)$ is detected with a photodiode. For all our observed intensity values the photodiode was linear. To avoid the observation of multi-exponential growth and decay times, the detected beam is expanded with a beam expander so that only the uniform portion of the beam is detected by the photodiode. The output of the diode is fed into the 602A Digitizing Signal Analyzer or a Computer Data Acquisition System. After turning on both beams a growth curve is recorded and the energy exchange signal I_e can be measured. When the grating reaches a steady state we then block the detected beam. The transmitted beam immediately went to zero, and the diffraction signal I_d was detected. Finally, the intensity of the transmitted beam I_0 was measured. Using I_0 , I_e , and I_d into Eq. (8) we can then calculate the phase shift between the grating and the interference pattern in the crystal.

C. Determination of Trap Number Density By Phase Shift Measurement

The trap number density N_A of a crystal plays a key role in the photorefractive response time. Therefore, measuring N_A accurately becomes an important topic in the research on photorefractive phenomena. We have developed a new technique for the measurement of N_A by



Experimental Apparatus for Simultaneously Monitoring Energy Exchange and Diffraction Efficiency



Sample Holder for Stabilizing Temperature While Applying External Field

applying a DC field across a crystal and determining the resulting phase shift between the grating and the fringe pattern.

After applying a DC field across a crystal and measuring I_0 , I_e and I_d , we can calculate both the $\sin \phi$ and the $\tan \phi$. In order to get accurate results we can vary the magnitude of DC field and measured I_0 , I_e and I_d for each DC field value E_0 .

A second method for measuring N_A is to measure the two-beam coupling on a weak beam I_1 . The intensity along its propagation direction is given by

$$\frac{I_{1c}}{I_1} = \frac{(1+m)e^{\gamma L_{eff}}}{1+me^{\gamma L_{eff}}} \quad (9)$$

where $m = I_{01}/I_{02}$, a ratio of the weak beam intensity to the strong beam intensity. Experimentally, we measured I_{1c} , I_1 and m , and then calculated γL_{eff} , where

$$\gamma L_{eff} = R \frac{2\pi R_{eff} K_B T}{\lambda n \cos \theta e} \frac{K_g}{1 + (K_g / K_0)^2} \quad (10)$$

and $R_{eff} = n_e^4 r_{33} \cos^2 \theta - n_0^4 r_{13} \sin^2 \theta$ for an extraordinary ray, K_g is grating constant and

$$K_0^2 = \frac{4\pi e^2}{K_B T} \left(\frac{N_{eff}}{\epsilon} \right) = C \left(\frac{N_{eff}}{\epsilon} \right) \text{ provided } C = 4\pi e^2 / K_B T, \text{ and } R \text{ is the measure of the electro-hole}$$

competition in the formation of the space-charged field.

By defining $f(\theta) = \cos \theta - \frac{n_0^4 r_{13}}{n_e^4 r_{33}} \sin^2 \theta$ we will have

$$\gamma L_{eff} f(\theta) \propto \frac{K_g}{1 + \frac{K_g^2}{c} \frac{1}{N_{eff}/\epsilon}} \quad (11)$$

By plotting the data of $\gamma L_{eff} f(\theta)$ vs K_g and fitting the data, we can then obtain a value of N_{eff}/ϵ .

If electrons and holes occur simultaneously in the charge transport process, there will be a electron-hole competition in the formation of the space-charge field which will lead to a reduction in

strength of the photorefractive effect. Suppose both electrons and holes can be excited from (and to) a single impurity band, then by employing band-transport model a first-order differential equation for the time evolution of the space-charge field can be derived. When there is no voltage applied to the crystal the amplitude of the steady-state space-charge field is

$$E_{sc} = -\frac{imk_B T}{e} \frac{k}{1+k^2/k_0^2} R \quad (12)$$

where $R = (1-C)/(1+C)$

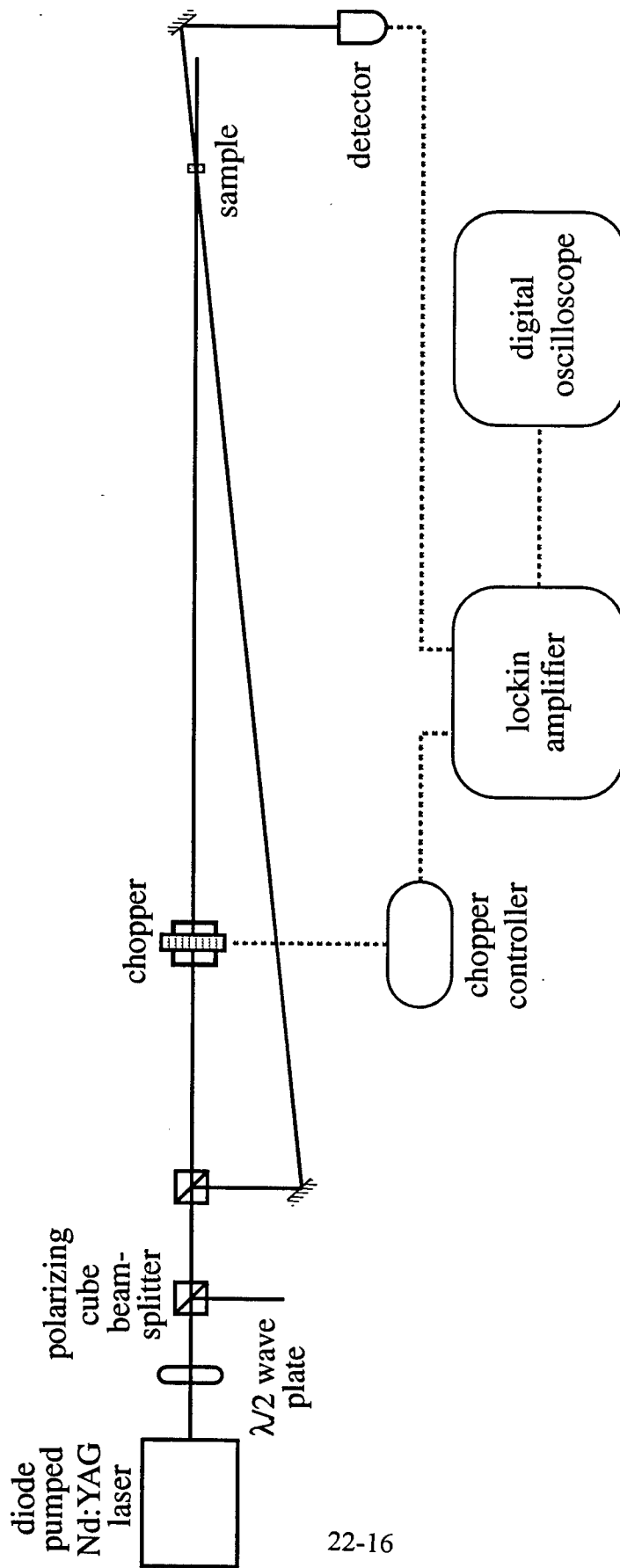
with $C = s_h N_A (k_g^2 + k_e^2) / [s_e (N_D - N_A) (k_g^2 + K_h^2)]$

If the charge carrier is only electron $C=0$, $R=1$, and if the charge carrier is only hole $C \rightarrow \infty$, $R = -1$. Therefore, $R=1$ or -1 indicates no electro-hole competition. A plot of K_g/γ vs K_g^2 gives us a straight line. The slope and the y-intercept of the line enable us to determine the electro-hole competition R .

RESULTS

During the summer we have

- (i) Set-up beam coupling apparatus at Hanscom Air Force Base and taken initial data on several samples.
- (ii) Set-up two-beam coupling and 4-wave mixing apparatus at Arkansas. This system is capable of continuous wave and picosecond investigations from $.88\mu$ to 1μ .
- (iii) Set-up a c.w. two-beam coupling system operating at 1.3μ at Arkansas.
- (iv) Obtained two-beam coupling and 4-wave mixing data at Arkansas. Typical Data is shown below.
- (v) Carried out an extensive review of the literature in order to take advantage of all previous studies on InP.
- (vi) Constructed Computerized Data Acquisition System.



22-16

Two-Wave Mixing Apparatus Set Up at Rome Laboratories, Hanscom Air Force Base

Using initial results we obtained gains on the order of $.3\text{cm}^{-1}$ for applied fields of 5kv/cm .

Using the parameters of

$$n = 3.29$$

$$\epsilon = 12.1$$

$$\Gamma_{41} = -1.53 \text{ pm/v}$$

$$\sigma_n = 4 \times 10^{-18} \text{ cm}^2$$

$$\sigma_p = 3 \times 10^{-16} \text{ cm}^2$$

we are now in a position to make measurements on

- (i) electron-hole competition
- (ii) charge of major carrier
- (iii) response time
- (iv) gain versus intensity and applied field
- (v) diffraction efficiency
- (vi) phase of grating
- (vii) donor and acceptor concentrations

CONCLUSIONS

We are now in the process of making these measurements and developing modeling for comparison. As soon as we develop an understanding of the photorefractive properties of InP which is comparable to our understanding of the ferroelectrics we will focus attention on exploring some novel ideas and applications. These will be explored with dr. David Bliss of Rome Lab, Hanscom Air Force Base during the next year.

The TkWWW Robot: Beyond Browsing

Scott Spetka
Assistant Professor
Department of Computer Science

State University of New York
Institute of Technology at Utica/Rome
Route 12 North
Utica, New York 13504

Final Report for:
Summer Faculty Research Program
Rome Laboratory

Sponsored by:
Air Force Office of Scientific Research
Bolling Air Force Base, Washington, D.C.

September 1994

The TkWWW Robot: Beyond Browsing

Scott Spetka

Assistant Professor

Department of Computer Science

State University of New York

Institute of Technology at Utica/Rome

Abstract

The TkWWW Robot extends the functionality of the TkWWW browser. It can also be used as a standalone agent that processes queries on the WWW. In either case, the robot traverses the web according to functions described using Tcl extensions developed for the TkWWW browser and the TkWWW robot. Tcl language extensions allow novice users to direct a search based on key words and HTML data types or to invoke predefined queries. Expert users can add their own Tcl extensions for use in more sophisticated searches. The system can be quickly adapted to support new resource types that may become available on the WWW, such as live audio/video connections for interaction with experts.

When TkWWW robots are dispatched from the TkWWW browser, their results can be used to guide further browsing. Robots can also be run in the background to build HTML indexes, compile WWW statistics, collect a portfolios of pictures, or perform any other function that can be described by the TkWWW Tcl extensions. Searches can be restricted according to URL names, limits on search path lengths, etc. The TkWWW robot can interact with its master by popping up windows to request input according to a Tcl query description. The main advantage that the TkWWW robot has over existing web spiders and robots is its flexibility in adapting to virtually any criteria possible to guide its search path and control selection of data for retrieval.

The paper presents the architecture and implementation of the TkWWW robot. It describes Tcl extensions implemented to support TkWWW robot queries. The TkWWW Robot is being developed over the summer at the Air Force Rome Laboratory with funding from the Air Force Office of Scientific Research.

The TkWWW Robot: Beyond Browsing

Scott Spetka

Introduction

The global distributed WWW database is growing dramatically, as is the Internet itself. If the WWW follows a growth pattern similar to the Internet, we can expect an explosion of information and commercial applications in the near future. The quantity of data available has already aided the development of techniques for building indexes to help users direct their search. Many of the index-building applications require exhaustive search of the net, taking significant time.

Most access to WWW resources today is through interactive *browsers*. In these systems, a WWW *query* is limited to the use of a single pointer to reference a page. The page is retrieved and the user determines whether further references can provide additional information. WWW public databases are hierarchically structured. The only dynamically created state information associated with a search is a stack of branch points that can be used to move forward and backward through a history of pages to effectively search a hierarchically structured information server.

WWW database structures and the tools used for their access must be enhanced in order to provide effective access to an information database that is growing rapidly. The terms *robot* and *spider* (<http://web.nexor.co.uk/mak/doc/robots/robots.html>) are used in reference to automated browsing tools for access to publicly accessible databases on the internet. A simple robot is described in this paper that is flexible enough to implement many query processing techniques. The robot is analogous to the access methods of a classical database, but it provides a much higher level interface which simplifies the implementation of new query processing techniques in a heterogeneous WWW environment. The paper also discusses the changes in database structure that may

be expected as the current structuring techniques become overloaded by the increasing size of the database.

The first section of the paper discusses the issues that were considered in deciding to build a robot. The second section describes the rationale for basing the robot on Tcl/Tk and describes its implementation. The third section examines issues related to whether servers should provide additional functionality. Section 4 discusses research directions for further experimentation with the TkWWW Robot. The paper concludes with some general comments from the experience gained in implementing a robot.

Issues for Consideration

Locality of Reference

Robots exploit the *locality of reference* inherent in the natural organization of the WWW data. Home pages reflect the main interests of their maintainers. While there is nothing to prevent random links and disorganized information hierarchies, links are most often used to present sub-topics in accordance with the underlying storage structure. The notion of locality of reference suggests that a *logical neighborhood* of a node would have a good chance of referencing the major sites that store related data. Pages found in browsing the WWW are often linked to pages presenting related topics. Links can be used to revisit pages that may be changing dynamically.

Improved storage organization would help to reduce the search radius needed to find most of the related data. Although a dynamic robot search does not guarantee that all desired data is retrieved, there is no way that any query processor can make that guarantee on today's WWW. The increasingly dynamic nature of WWW servers, storing information like live video (<http://tms-www.lcs.mit.edu/vs/demos.html>) and weather information (xmosaic <http://rs560.cl.msu.edu/weather/>) affects the ability of indexes to be properly maintained. Autonomous operation of servers and reliability considerations make it impossible to deliver all possible responses to a query.

Resource Requirements

There is some concern that automated browsing will either be too slow to be effective or will overload existing Internet communication channels. These are the same concerns that characterize the development of any advanced research system. Software must be developed on today's systems to be developed in time to service the next generation of computers. The rate of development of Internet resources and the drop in cost of computer processors, memory and disk all support the assertion that robots will be able to operate at reasonable levels of resource consumption within a short time.

The main questions for resource consumption are how far it is worth searching for a result and whether the result is worth the expenditure of resources needed for the search. In a single machine environment, a database scheduler can determine priorities for processing to provide for balanced and efficient operation. Distributed database systems cooperate to provide similar scheduling functionality. The growth of the WWW has placed the same type of unpredictable resource requirements on computer server implementations that have characterized the Internet communications processors for years.

Client/Server Architecture: Parallelism

The current client/server architecture implemented in the WWW is based on full autonomy of the server. Client applications, like Mosaic, TkWWW, and Gopher, request pages from the server which are then processed locally. This architecture minimizes the degree of parallel processing that can occur because of the synchronous nature of the *read* function. A client may have just a single request outstanding, even if it is waiting on a very slow server.

There are two approaches to developing increased parallelism. In the first, servers do local processing to

minimize the amount of data that is transmitted. This approach requires that a *filter* be sent to the server. A natural extension would be for a more complex query to be sent to the server and for additional steps in the processing to take place there. A second approach can improve parallelism while having less impact on autonomy. Several machines in a local network can cooperate to share the I/O burden associated with a query. This approach suffers from the need to share a common network connection, limiting the degree of parallelism that can be accomplished.

TkWWW Robot - Using Robots on Today's WWW

The prototype TkWWW Robot is the first step in developing a general purpose robot that can be programmed to provide a query processing interface to users. Users will, in general be interested in finding particular types of HTML objects (similar to *projection* in relational databases), finding HTML objects that satisfy a specific search criteria (relational database *selection*), and looking for logical relationships between HTML objects scattered over the WWW database (relational database *join*). The initial TkWWW Robot implementation *projects* all *links* found within a set of WWW pages.

Figure 1 shows the TkWWW Robot browsing interface after a search for links within a radius of 2 hops is selected from the robot pull-down menu. Notice that the links on the robot home page (shown in the background) are labeled to show the links that can be expected to be found on the corresponding page. The pop-up dialog box contains all links found on the pages referenced by the home page in addition to all links found on the home page. Any of these links can be selected directly for further browsing.

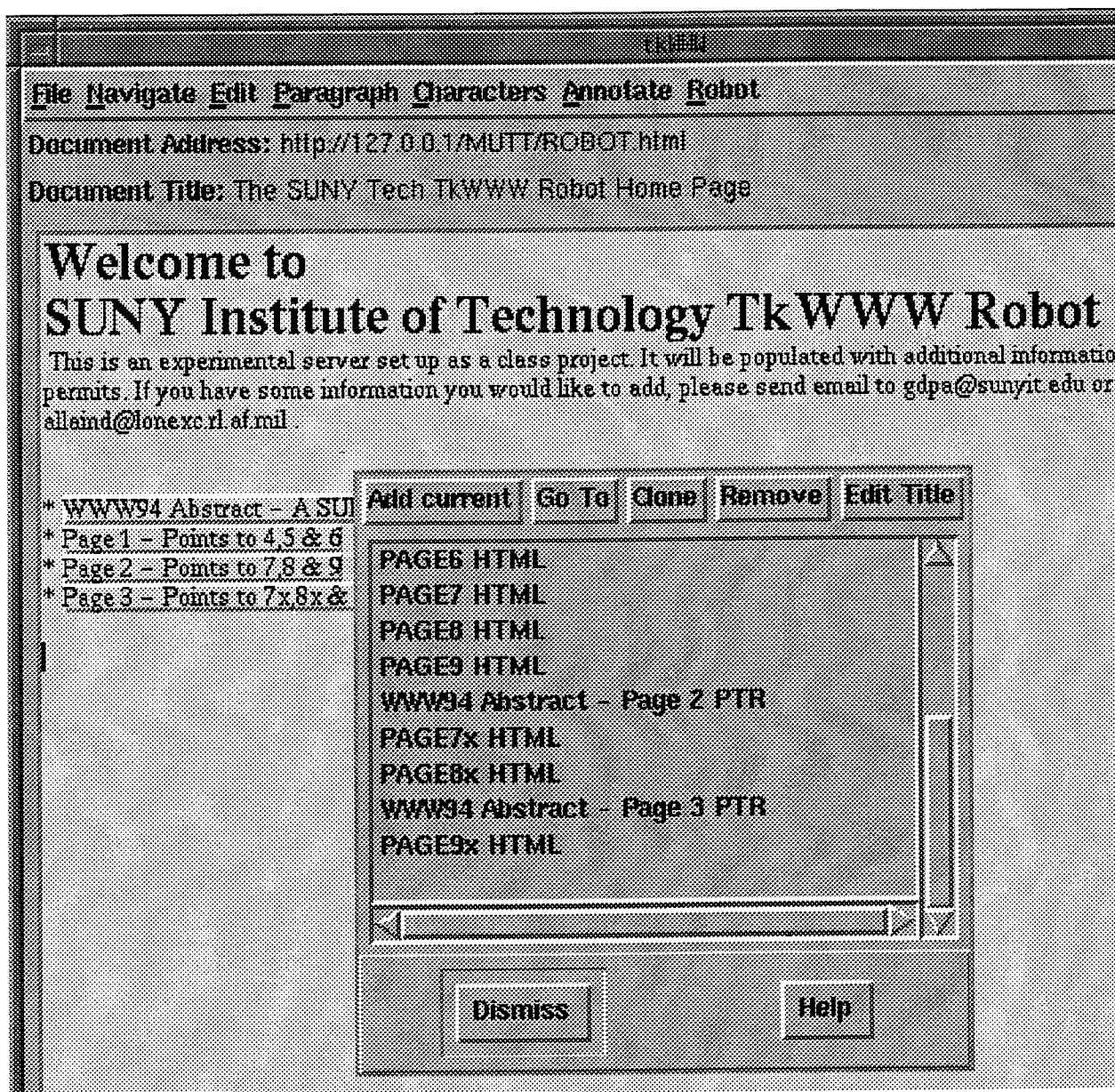


Figure 1 - TkWWW Robot Browsing Interface

Design and Implementation

The TkWWW Robot is an extension of the TkWWW browser which is written in Tcl/Tk (URL ref). The TkWWW browser implements commands in the C language which augment the base Tcl/Tk command language to provide a convenient interface which can be used to access WWW resources. The TkWWW Robot uses TkWWW commands along with additional commands that are specifically designed to support the implementation of autonomous agent data retrieval. The diagram below shows the layering of the TkWWW Robot implementation. Commands at all levels of the system are used in developing query processing algorithms and automated browsing tools.

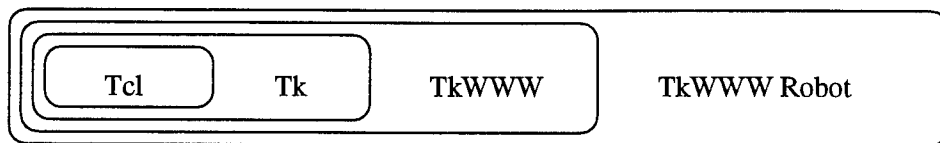


Figure 2 - TkWWW Robot System Structure

In order to provide maximum flexibility in implementing additional robot functionality, the additional commands added for TkWWW Robot should be as simple as possible. The interface implemented in the prototype robot operates on a URL (WWW page address). It returns all *links* stored on the page. The links are returned as a character stream which is easily processed using the powerful string handling commands of Tcl. Figure 3 shows the call to the HtRobot function which returns a list of pairs of <URL (page address), hypertext identifier> to the higher-level Tcl/Tk functions the HtRobot function is written in the C language. The \$page_value parameter specifies the address of a page to search for links.

```
set RobotList [HtRobot $page_value]
```

Figure 3 - The HtRobot Function Interface

Higher level Tcl functions loop through the addresses/identifier pairs and produce an display display of the identifiers with appropriate *callbacks* defined to invoke WWW page access commands when one of the identifiers is selected. The tkW3RobotDialog function, implemented in the prototype TkWWW Robot is designed to provide access to all links within a radius of 1 hop from the current page (another similar function implements the 2 hop access shown in figure 1 above). The implementation, shown in figure 4 is simplified by the use of the tkW3NavigateRobot function which uses the HtRobot interface described above to access the links on the specified page. The list is then processed to display the links and set up appropriate callbacks for their access. This simple loop builds the pop-up menu shown in figure 1 above.

```

proc tkW3RobotDialog {} {
    global tkW3Robot

    set parent .

    set w .robot

    # tkW3NavigateRobot returns a list of links, using HtRobot
    tkW3NavigateRobot

    # Set up the pop-up dialog window (some buttons not shown)

    DLG:toplevel $parent $w

    tkW3OutputMakeButtons $w.button_frame {
        {current "Add current" "tkW3RobotAdd"}
        ... {edit "Edit Title" "tkW3RobotEditTitle"}
    }

    # Draw box and set up bindings

    pack append $w $w.button_frame top

    DLG:draw_listbox $w {}

    DLG:draw_buttons $w [list "Dismiss" "Help"]

    DLG:bind_button $w 1 "DLG:hide $w"

    DLG:bind_button $w 2 "tkW3HelpNoHelp"

    # Loop through list of page address/description pairs
    # and add them to pop-up dialog box

    set Rcnt 0

    set Rlen [llength $tkW3Robot(list)]

```

```

while { $Rcnt < $Rlen } {

    $w.list insert end

        [lindex $tkW3Robot(list) [expr $Rcnt + 1 ] ]

    incr Rcnt 2

}

# Display the pop-up box

DLG:show $parent $w }

```

Figure 4 - Tcl/Tk/TkWWW Processing for a List of Links

Implementation Problems

The current structure of the system made it somewhat difficult to isolate the links that were found on each HTML page. The functions for parsing and generation of the bitmap display are integrated rather than being performed separately. The current implementation identifies links during the parsing process and copies them into a global list structure for use in the HtRobot interface function. The call to the parser is implemented in the same way as a call to display a page. Page display functions accept the URL address of a page as a parameter but default to the current page when none is given.

The TkWWW Robot: a Distributed Database Query Processor

Eventually, WWW will support distributed query processing with parallel execution of server functions to support queries generated by client programs that provide the parameters for a dynamic search of the WWW. Today's concern over limited processing resources and bandwidth will be reduced as the resources become available in the Internet, or its successor, to support the ideas and software being developed in research laboratories today. Addition of resources to local processing resources to provide adequate query processing support will be driven by the need for companies to compete commercially. Providing convenient query processing support will be comparable to providing a facility where people can shop. In addition to ordering products from on-line hypertext catalogs, the WWW provides a market for research ideas where the acceptance of ideas may depend on how easily they can be located.

Database Structure

If we assume that the WWW is moving in a commercial direction, then the perspective of the WWW database designer should be oriented toward a structure that is general enough to provide the information that would be expected, in a standard format, rather than supporting a totally unstructured information system. The hypertext *page* is analogous to the *tuple* in relational database systems. Pages could be linked together to form an IMS-like database system. A more appropriate model for WWW databases is an object-oriented database structure. The WWW access methods (page retrieval) are already designed to access pages of varying formats. Additional structure is required to support identification of attributes from *base classes* which define the basic structures which can be used in *sub-classes* that use them in their definition. Such a definition could be used for accessing an *personal URL* type page. Each page should provide a core of information (in this case the name, company, and email address) associated with the individual.

Access Methods

Data that is made available on the WWW will be more efficiently retrieved through robots which implement parallel exploration of access paths to the data required. A search for a product will be successful if data is readily accessible (see above) and if an appropriate search engine or robot is in use. In the case of the TkWWW Robot prototype, described above, the support for distributed processing would retrieve lists of <address, title> pairs for the links known to the server. Either all links or only those at a particular hop count from the entry point would be retrieved. The server would, with a minor increase in local processing, significantly reduce network traffic.

The TkWWW browser operates on the HTML retrieved from remote servers and performs all operations locally. It would seem reasonable that simple search functions be added to servers that would allow search operations to use remote processing resources in order to reduce the impact on the network at a server. A server-based search capability would allow a robot or browser to return all links stored at a site, rather than retrieving all pages, then throwing away all data except the links.

Indexing

Indexing techniques are commonly used in database systems that are highly structured. Many static indexes have been developed for access to WWW resources. They are mainly produced through exhaustive search techniques. The indexes are not updated upon changes to the objects they point to, as they would be in a standard database system. This is due in part to an effort to maintain the autonomy of servers. Robots, like the W4 Worm can not insist that the objects that they put into their indices report back to them upon changes in their status. Increasing the frequency of exhaustive search would be a large burden to the network in order to avoid a few missed references. Good indexes exist on the WWW for convenient search of many resources, by name, subject, etc.

The only mechanism that supports user controlled static index construction for today's browsers requires manually inserting pointers to pages into a *bookmark* list. In most cases, bookmarks are unrelated and are used as starting points for independent searches.

Future Robots: Using Robots on Tomorrow's WWW

Eventually, the WWW must move away from a model where all decisions regarding WWW navigation are made by the local browser/client/robot, based on remote information retrieval. Current robots have no choice but to retrieve links from remote sites as a basis for their navigation. The TkWWW, with its flexible implementation is poised to change as the WWW moves in the direction of increased intelligence in database servers. This section describes some of the changes that will force WWW designers to address the issues involved in increasing the functionality in WWW servers and clients.

Real-Time Video Communication

Much of what has driven the evolution of the WWW involves integration of multimedia databases through a high-level object-oriented interface. Many systems of the future will have real-time constraints and will include videotelecommunications as an integral component. The TkWWW robot is poised to meet the challenges of these new environments. In addition to having real-time constraint requirements, future servers will be characterized by increasingly dynamic behavior. Servers may offer buttons to initiate dynamic videoconferences based on the instantaneous availability of an appropriate research expert or salesman, depending on the organization offering the connection.

Searching for sources of live video provides the WWW analog of a channel scanner where each WWW page may provide a source of live video. Robot starting points, similar to the "bookmark" capability in today's

browsers gives a robot a set of initial starting points for a search. This functionality is already implemented in the TkWWW Robot. A robot may find all experts in an area that are prepared for a videoconference. In a similar way, real-time video may be used for talking to sales and technical representatives. Information services, analogous to touchtone hierarchy traversal for telephone-based systems already exist, without the ability to establish a direct videoconference connection.

A typical TkWWW Robot query of the future (with a natural language interface):

"Go find someone to talk to and negotiate
a price of less than \$X for the conversation"

Individual Databases and Servers

Robots are useful to support the flexibility of personal data representation and communication, helping people communicate by integrating network, video, and multimedia databases into modern information systems. They can perform automated answering, filtering and customizing messages received through a communication system, depending on the authorization of a caller. A robot can actively pursue information on behalf of its master by finding servers that have answers to questions and retrieving the appropriate data.

Advanced Functionality

The use of a Tcl-based robot offers the potential for communication and cooperation with distribution robots, by client-agent robots. EXPECT extensions to the basic Tcl command set allow discrimination of requests and can be used to enhance both the TkWWW browser and the TkHttpd. Security would not be a problem since the browser would control interaction with the server. A server (httpd) robot may query the client database to determine areas where a search could provide additional information and avoid unnecessary overhead needed to return data that

is already available. This suggests that data should be structured as HTML in a hierarchic database that is understood by the httpd.

Future Research

The TkWWW prototype demonstrated the feasibility of implementing a robot. Extensions will be needed to develop support for additional capabilities described in the paper. In addition to handling the basic link objects, the robot will be upgraded to retrieve other types of HTML objects will be implemented. New TkWWW Robot commands to search for objects independent of type, perhaps based on size or some other attribute would also be interesting. A command that searches for a logical combination of given parameters can search pages that satisfy expressions like (mpeg or jpeg or gif).

More complex commands may search pages based on the relationship of objects on a page. A low-level TkWWW Robot command to return the next object on a page would allow queries like "get the addresses of all pages that have mpegs immediately followed by audios", ie. queries where the ordering of objects is important. In general the Tcl functions will determine the characteristics that are sought on the objects. For example "find pages that have an mpeg followed by at least 3 audio files where the sizes of audio files are increasing" would indicate how many WWW database managers sort their files.

There are several other research issues related to the operation of WWW servers that should be addressed to improve the general efficiency of Internet robots. Other issues involve commercializing the WWW. Robots must be able to avoid servers that would charge for their access. The current approach to limiting robot access, through the installation of an advisory file which requests that robots refrain from access can be amplified to provide them with the equivalent of a toll booth where desired by the server operator. Some of the appropriate structure may depend on the rate structure that develops as NSFnet is turned over to commercial providers.

Conclusion

The TkWWW robot can be programmed to perform most of the functions of other robots that are in common use. The work being done on the robot is focused on providing additional low level functionality and developing techniques to implement indexes based on the current content of databases of interest. It seems likely that additional types of data will be continue to be integrated into the WWW framework. The TkWWW can adapt quickly to changes in the environment, making it a reasonable target for future development.

The ability to develop advanced robot functionality depends on whether server functions can be developed to help robots do their work efficiently. If initial experimentation with robots is successful, additional server functionality seems inevitable. Servers that do not support robot access will be overlooked, causing a great deal of effort invested in their development and maintenance to be of limited value.

Acknowledgment

The TkWWW Browser is GNU General Public License software. It is available through the Internet.

Author Biography

Scott Spetka received his Ph.D. degree in computer science from UCLA in 1989. He is currently an Assistant Professor in the Computer Science Department at the State University of New York Institute of Technology at Utica/Rome. His research interests are in the areas of distributed databases, operating systems and networks. During the last year, Scott has been developing a network of PCs running the Unix operating system. Before becoming involved in WWW research, Scott was developing SUNY Nodes, a Network Oriented Data Engineering System. The system is used to experiment with query processing techniques.

POLARIMETRIC RADAR SCATTERING FROM A
VEGETATION CANOPY

James C. West
Associate Professor
Department of Electrical Engineering

Oklahoma State University
202 ES
Stillwater, OK 74074

Final Report for:
Summer Faculty Research Program
Rome Laboratory

Sponsored by:
Air Force Office of Scientific Research
Bolling Air Force Base, DC

and

Rome Laboratory
Hanscom AFB, MA

August 1994

POLARIMETRIC RADAR SCATTERING FROM A VEGATATION CANOPY

James C. West
Associate Professor
Department of Electrical Engineering
Oklahoma State University
202 ES
Stillwater, OK 74074

Abstract

Experimental measurements of the bistatic radar scattering from a wall of deciduous trees have been performed. The coherent like- and cross-polarization scattered fields were measured for both vertical and horizontal transmit polarization, allowing the calculation of the full Mueller scattering matrix. The transmitter location was fixed throughout the experiment, while the receive position was varied approximately along an arc around the illuminated section of trees. The illumination elevation angle was downward at 6 degrees while the measured receive elevation angles varied from approximately 0 degrees to 6 degrees downward.

I. INTRODUCTION

The ability of a radar to detect a target is often limited by the clutter returns from vegetation canopies. One method to improve the detection of a target in a clutter background is to use polarimetric target-clutter discrimination techniques (Eaves and Reedy, 1987). These techniques use both the like- and cross-polarized scattering characteristics of the target and clutter, thereby yielding more information for the detection algorithm. Another method is the use of bistatic radar systems, where the transmitter and receiver are not co-located. This method is particularly useful in detecting targets that are designed to minimize the scatter in the backscatter direction. For these techniques to be used most effectively the bistatic polarimetric scattering characteristics of the clutter as well as the target must be well described.

Experimental measurement of the bistatic scattering from a wall of deciduous trees has been performed. Full polarimetric scattering was measured and the effects of the Stokes vectors of the radar antennas were calibrated, allowing determination of the full Mueller scattering matrix of the tree clutter patch. The experiment was performed at the Rome Laboratory-Hanscom AFB Ipswich test site with William Stevens (Rome Laboratory) and David McLaughlin (Northeastern University).

II. EXPERIMENTAL HARDWARE

A. Radar system

The radar system used is described by Rao et al. (1991). The operating frequency was 3.2 GHz, and the CW transmitted power was 3 W. Range resolution was obtained using a 1023 bit binary phase code modulated at 200 Mbits/sec, yielding a 1.5 m one-way range resolution. All signals within the transmitting unit were derived from the same stable 5 MHz crystal oscillator. The transmitter provides a single channel, so transmitted polarization was controlled by an external switch.

The receiver unit was completely independent of the transmitter, and is therefore clocked to different stable crystal oscillator. Coherence was maintained by phase-locking the receiver to the direct feed-through signal from the transmitter. The receiver generates a binary phase code that is identical to the transmitted code. Range compression of the received signal is performed using a Costas-loop processor (Holmes, 1990). The range side-lobes resulting from this technique limit the system signal-to-noise ratio to 30 dB. The equivalent output pulse repetition period (PRP) of the Costas loop was 20 mS (pulse repetition frequency of 50 Hz), indicating that clutter fluctuations of up to 50 Hz can be measured. The range cells were output from the Costas-loop at a 615.66498 KHz clock rate. The receiver included two channels that were configured for simultaneous measurement of the vertical and horizontal polarization scattered field. Each channel provided the inphase, quadrature, and magnitude signals after range compression, and full coherence was maintained so the relative phase between the two scattered polarizations was conserved.

The receiver includes an automatic gain control (AGC) circuit that sets the peak received signal to a safe level below the receiver saturation point. The radar was calibrated for full measurement of the target Mueller scattering matrix using the technique of Mead and McIntosh (1990).

C. Antennas

The transmitting antenna was a Seavey Engineering Associates Model AS48-33NA dual polarized feed 4 foot dish antenna. The measured gain at both polarizations was 28.6 dB over isotropic with 3-dB beamwidths of 5.5 degrees in both planes. The highest sidelobe level (-19.3 dB) occurred in the vertical polarization, H-plane pattern. Cross-polarization isolation was better than -30 dB. The transmitted signal was switched between the two feed ports using an external ferrite switch.

The transmit antenna was positioned on a tripod that included a calibrated elevation-over-azimuth positioner. The tripod was placed on a level Worthington positioner that

is located on the roof of a building at the Rome Laboratory's Ipswich test site, as shown in Figure 1. As configured, The antenna center was 45 feet above ground level. The Worthington positioner was not moved throughout the experiment. A narrow-view video camera was attached to the transmitting antenna for bore-sighting. The camera was aligned at the beginning of the experiment by maximizing the direct feed-through to the receiver antenna. Alignment was reconfirmed at the end of the experiment.

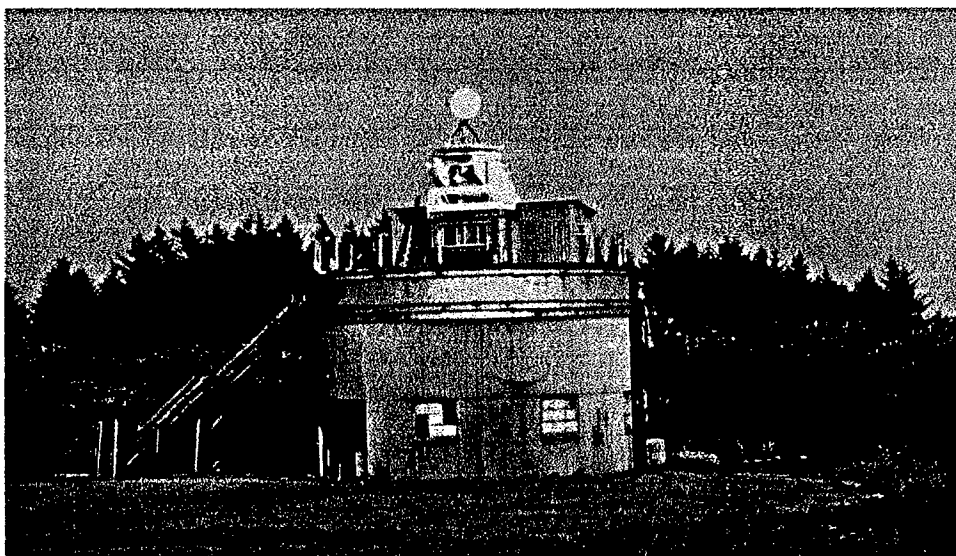


Figure 1. Transmitting antenna at Rome Laboratory Ipswich test site.

The receiver antenna was a dual polarized, wide band conical horn. Calibrated measurements of the gain, beamwidth, and cross-polarization characteristics were not completed at the end of the summer fellowship; however, simple field measurements of the direct feed-through signal and comparison with a standard gain horn receive antenna indicated the cross-polarization isolation was better than 20 dB and the gain and beamwidths were consistent with that expected from the 5 1/2 inch antenna aperture.

The receive antenna was mounted directly to an uncalibrated elevation over azimuth positioner. The positioner was mounted directly to two levels of scaffolding, which were in turn placed on the roof of a site truck, as shown in Figures 2 and 3. The antenna was

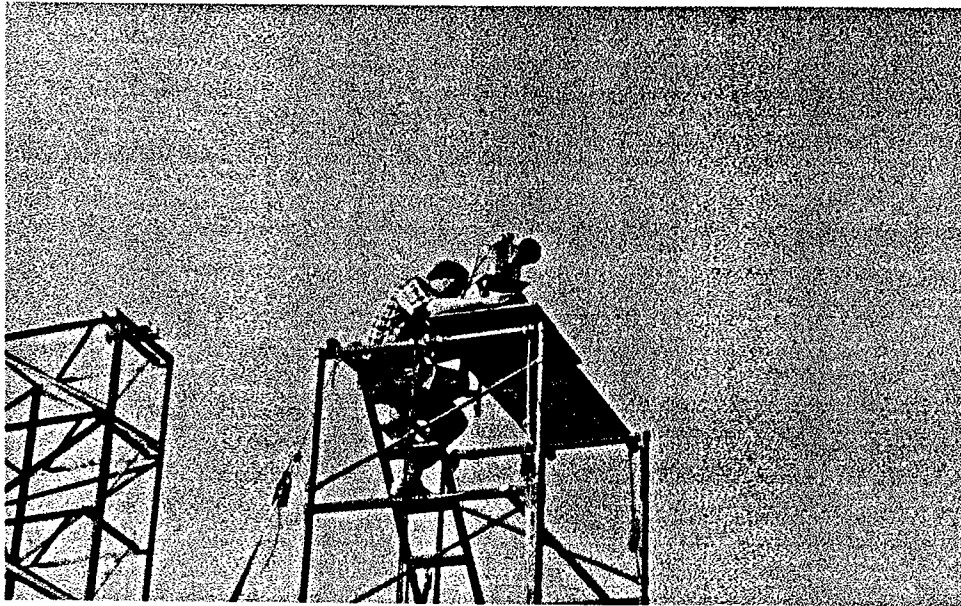


Figure 2. Receive horn antenna mounted on scaffolding.

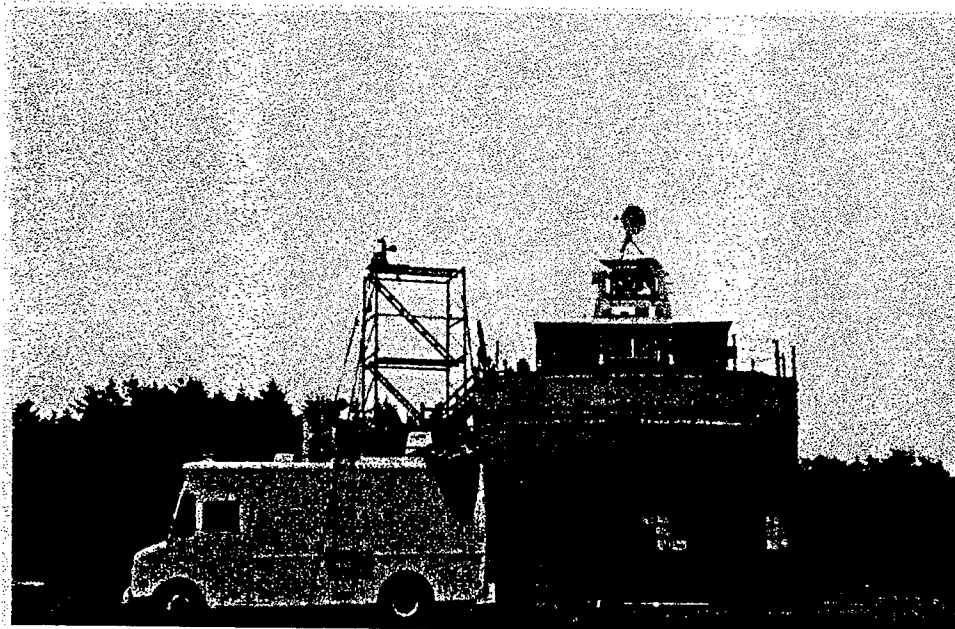


Figure 3. Receive and transmitting antennas.

approximately 23 feet above ground level. The truck was moved to each measurement position and was stabilized with four hydraulic jacks. The positioner was then leveled and visually boresighted at the target area along a straight edge that was parallel to the peak

of the antenna beam.

D. Data Acquisition

The inphase, quadrature, and magnitude signals at both polarizations were digitized and stored directly to a hard disk. The AGC setting of the receiver was also digitized and recorded. The signals were recorded continuously for 30 s at each receiver position and transmitter polarization. At least two redundant data acquisition runs were made for each unique transmitter/receiver configuration. Because of the short sample time, runs that were made during low wind speed periods were repeated, thereby maximizing the number of independent samples available for estimating the scattering coefficients.

III. EXPERIMENTAL LAYOUT

The positions of the transmitter antenna, target clutter patch, and the receiver locations are shown in Figure 4. The target clutter patch was a small outcropping of trees, shown in Figure 5. The antennas were boresighted at a point 6 m above the ground at the edge of the outcropping and about 8 m below the tree tops. (The boresight point was marked by a ribbon that is not visible in the Figure.) The distances from the target clutter patch to the individual receiver positions and the angular position of the receiver locations (with respect to the transmitter locations) are given in Table 1. Because of the unevenness and general slope of the terrain (roughly 3 degrees, with the lowest point near lower left of Figure 4 and the highest point at the upper right), the absolute receiver antenna height varied with position. Thus, the elevation look angle of the receiver antenna is different at each position (also summarized in Table 1).

The transmitting antenna was 63.7 m from the target clutter patch and pointed down in elevation at 6° when boresighted on the target point.

IV. RESULTS

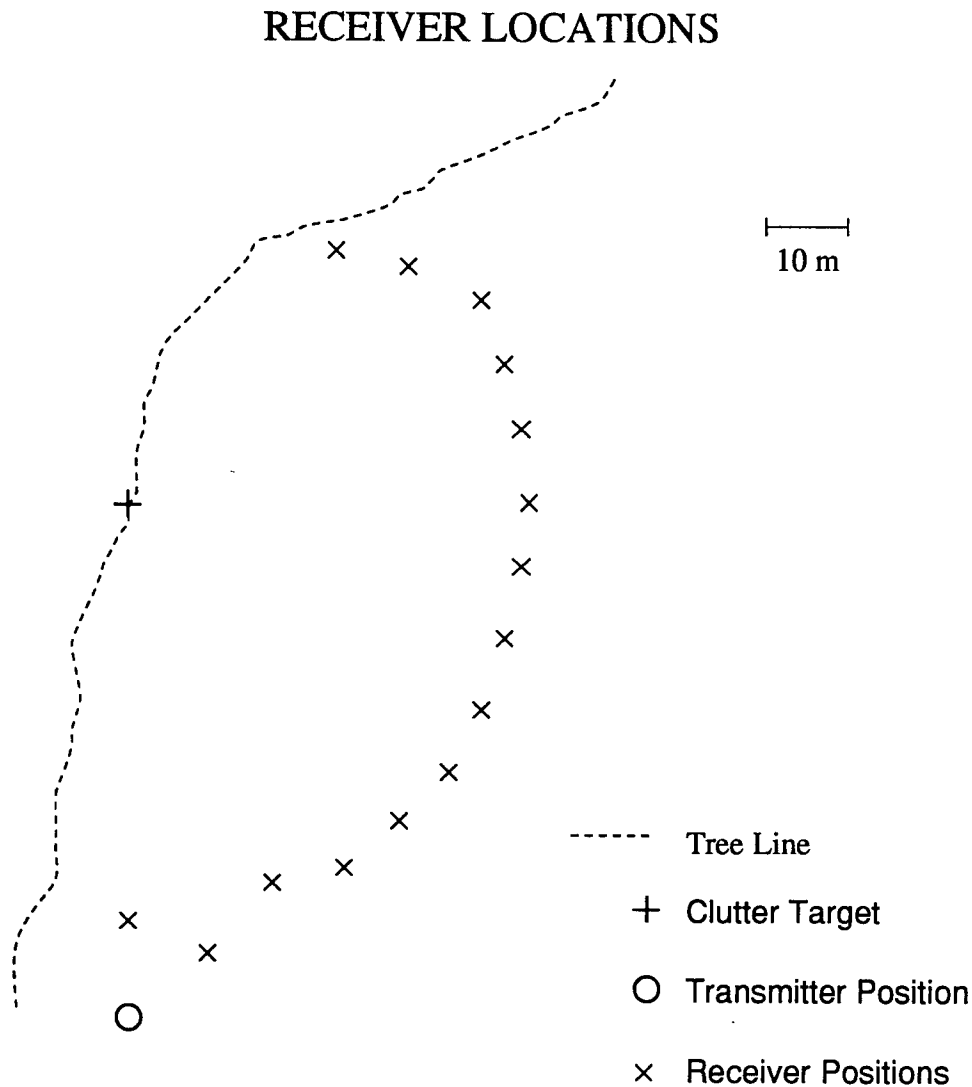


Figure 4. Receiver, transmitter, and clutter patch positions.

Data collection efforts were just being completed during the last week of the summer fellowship. Data reduction and preparation for analysis is currently being performed by Rome Laboratory personnel so no results available for this report.

V. REFERENCES

- Eaves, J. L. and E. K. Reedy, *Principles of Modern Radar*, Van Nostrand Reinhold, 621-645.
- Holmes, J. K., 1990, *Coherent Spread Spectrum Systems*, Kreiger, 129-135.



Figure 5. Target clutter patch.

Mead, J. B. and R. E. McIntosh, 1990, "A 225 GHz polarimetric radar," *IEEE Trans. Micro. Theory Tech.*, **38**, 1252-1258.

Rao, K. V. N., W. G. Stevens, J. Mendonca, 1991, "Bistatic scattering statistics of deciduous trees," AGARD Conference Proceedings 501, Target and Clutter Scattering and their Effects on Military Radar Performance, 5-1-5-12.

Receiver Position Number	Azimuth Angle From Transmitter (degrees)	Distance From Target Area (m)	Elevation Look Angle (degrees)
1	0	51.8	-0.6
2	10	56.4	-0.4
3	20	49.7	-1.0
4	30	52.1	-1.3
5	40	51.5	-1.9
6	50	50.6	-2.1
7	60	49.1	-2.5
8	70	49.1	-3.5
9	80	48.5	-4.0
10	90	48.9	-5.0
11	100	48.8	-5.0
12	110	49.1	-5.5
13	120	50.3	-6.0
14	130	44.2	-5.6
15	140	39.6	-5.7

Table 1. Receiver positions used. The angular position is given as the angle between the line from the transmitter to the clutter target and the line from the receiver to the clutter target.

TRANSFERRING TECHNOLOGY VIA THE INTERNET

**Rolf T. Wigand, Ph. D.
Professor**

**Slawomir J. Marcinkowski
Ph. D. Student**

**John Carlo Bertot
Ph. D. Student**

**School of Information Studies
4-293 Center for Science and Technology
Syracuse University
Syracuse, NY 13244-4100**

**Final Report for:
Summer Faculty Research Program
Rome Laboratory**

**Sponsored by:
Air Force Office of Scientific Research
Bolling Air Force Base, DC**

and

Rome Laboratory

September 1994

TRANSFERRING TECHNOLOGY VIA THE INTERNET

**Rolf T. Wigand, Slawomir J. Marcinkowski and John Carlo Bertot
School of Information Studies
Syracuse University**

Abstract

The current global economic climate is such that a nation acquires and maintains its wealth, prosperity, and strength predominantly through trade. It is necessary, but no longer sufficient, for a nation to possess a strong military function in a global marketplace. This new emphasis on national competitiveness in trade places Rome Laboratory, as well as other federal laboratories, at an important crossroads. On the one hand, a military advantage requires continual technological superiority. On the other hand, Rome Laboratory needs to facilitate national economic development through the transfer of its technologies into the marketplace. These developments serve to highlight the importance of a proactive technology transfer process within Rome Laboratory. However, a proactive operation is difficult to put into action without forthcoming budgetary and personpower increases. This study focuses on a low-cost alternative: to use MOSAIC on the Internet and the World Wide Web to promote the transfer and commercialization of technology. An electronic system was developed allowing access on various technology transfer information and databases to the private sector, as well as Rome Laboratory and other Air Force and public sector users. This report describes these efforts, underlying reconceptualizations, design and implications of the electronic system.

TRANSFERRING TECHNOLOGY VIA THE INTERNET

Rolf T. Wigand, Slawomir J. Marcinkowski and John Carlo Bertot

Introduction

The current global economic climate is such that a nation acquires and maintains its wealth, prosperity, and strength predominantly through trade. It is necessary, but no longer sufficient, for a nation to possess a strong military function in a global marketplace. This new emphasis on national competitiveness in trade places Rome Laboratory (RL), as well as other federal laboratories, at an important crossroads. On the one hand, a military advantage requires continual technological superiority. On the other hand, RL needs to facilitate national economic development through the transfer of its technologies into the marketplace. These developments serve to highlight the importance of a proactive technology transfer operation within RL. However, a proactive operation is difficult to put into action without forthcoming budgetary and personpower increases. This study attempts to identify a low-cost alternative: to use the Internet to promote the transfer of technology.

RL is currently positioning itself to meet the challenges precipitated by the emphasis on the technology transfer process. This process, if viewed as a life cycle, minimally contains the following components:

Technology research

Technology development

Technology announcement

Technology marketing

Fulfilling technology information requests

Making the technology available for outside use

Technology utilization, and

Technology commercialization.

In addition, technology transfer occurs within political and social climates that may impose certain constraints. The overriding condition in all of these considerations is, of course, first of all the Air Force mission. In that sense technology transition within the Air Force is of primary importance, followed by

technology transfer to the private sector, hopefully resulting in technology commercialization. The latter term incorporates such desirable events as successful technology transfer, technology utilization, profitability of the technology when marketed by a firm, hopefully resulting in the creation of jobs, adding value, contributing to the regional and national economies, and adding overall to the Gross Domestic Product.

Many of these technology transfer tasks are mandates and specified by legislation such as the Stephenson-Wydler Act, the Technology Transfer Act, and others. There are also certain limitations and constraints on the technology transfer process such as export control regulations intended to help only U. S.-owned companies.

Technology transfer deliverables could be classified as: products, knowledge, advice, know-how, and facilities use. These deliverables are not unique to RL, but can be envisioned to apply to all federal laboratories. They can be broken down into a set of specific and clearly definable technology transfer activities may include the following:

- Cooperative Research and Development Agreements (CRDAs)

- Educational Partnerships

- Exhibits

- Conferences

- Presentations (by the Technology Transfer Office or scientists and engineers)

- White papers

- Information exchange

- Inquiries (face-to-face, by phone, written)

- Publications

- Advertising

- Public relations

- Communication with company representatives

- Electronic dissemination

Others.

The present focus for this study is on just one of the above activities, electronic dissemination of information about technology.

The authors reviewed the technology transfer process at RL and revisited this process by reconceptualizing the underlying assumptions pertaining to basic principles of marketing, diffusion, information retrieval and networking. The key driver of this reconceptualization was that of a user or target audience orientation. From this perspective a model was developed that provides the desired electronic linkage between RL and targeted private sector firms.

Reconceptualization

Four different approaches to a reconceptualization of the technology transfer process, especially when this process occurs electronically, were advanced. Each is described below:

A. Marketing. All marketing efforts are based on the basic premise that there is a specific audience of consumers. This is a set of specific firms within an industry or the private sector, which have needs that can be filled by firms operating within a specific market. In the this case, RL constitutes such a firm that can fill the demand for specific technologies that can be marketed and commercialized by private sector firms.

One can identify three main policies of orientation within the marketing effort: customer orientation, product orientation and profit orientation. The latter orientation is not an appropriate orientation for RL. A product orientation is predicated on the view that consumers will recognize and appreciate products for superior merit and bestow their patronage on firms--in this case the product is research and development. In the present case though, it must be realized that, in general, this product is not designed by RL having private sector firms in mind foremost. Rather, the key customer is the Air Force and the product and the product orientation are determined by the Air Force mission. An exclusive product orientation effort is therefore not wise for RL, but the product certainly determines a potential market that can be tapped within the private sector. It is therefore apparent that an appropriate focus for RL in terms of marketing orientation is a customer orientation.

In this setting, a customer orientation denotes (a) an attitude and a pattern of conduct, as well as (b) the extent to which RL tries to determine what its customers want and then gives them what they want. Granted, it is often difficult and complex to discover what the customer wants. For example, in such efforts one recognizes that customer preferences vary widely and that customers want something only once they are given concrete choices, i. e. they are incapable of conceiving possible new products. Potential customers often also request features that are incompatible with product capabilities. The basic challenge faced by RL is to identify those needs and provide a linkage between RL and the customer, i. e. a firm interested in a specific RL technology. To maximize this linkage and relationship to customers, RL needs to form hypotheses and understanding about these present and future potential customers. Included should be questions such as:

What kinds of things affect customer behavior?

Through which channels (advertising, face-to-face contacts, publications, etc.) can customers be reached by RL?

What is the degree or strength of need or desire for the product?

What are the appropriate appeals (or arguments) to which customers are most responsive?

What is the customer's responsiveness to different types of sales devices, i. e. their ability to be influenced by technology transfer discussions by the Technology Transfer staff, engineers and scientists?

After these questions have been answered, the marketing dimension entails five general activities:

1. Identifying and selecting the type of customer that RL chooses to cultivate and learning that set of firms' needs and desires.
2. Designing products, know-how and services, to include facilities, that RL can transfer in conformity with customer desires.
3. Persuading customers to acquire and adopt RL's products, know-how and services.
4. Displaying, moving and to some extent storing products, know-how and services after they have been developed at RL.

5. Identifying dual use technologies and applications.

In designing its products, acquiring and developing know-how, and deciding how much and what specific services to offer, RL will unquestionably benefit from having a clear picture of its *target customer*. The present project attempts to provide a linkage, an *electronic marketing channel*, between these target customers and RL.

B. Diffusion. Diffusion is another conceptualization that guided the study. Diffusion is the social process by which an innovation is communicated through certain channels over time among members of a social system (Rogers, 1983). This process clearly resembles the task at hand for RL in the technology transfer process: i. e. a technology or an innovation within RL, needs to be communicated to a set of firms (members of a social system) within a particular industry. The communication channel chosen for the present study is that of electronic messaging via the Internet. The authors view such electronic diffusion means as timely, cost-effective, quick and targeting specific means to reach the target customer described above.

Many other dimensions could be addressed here that determine the speed with which such diffusion occurs. Obviously the quicker the target audience can be reached and the significance of the technology to be transferred can be communicated, the more effective the diffusion process. The rate of diffusion or adoption of that technology is, however, determined by the characteristics of the innovation (e. g., the relative advantage, compatibility, complexity, trialability and observability).

The communication channel chosen, electronic messaging via the Internet, determines in part the success of making a successful linkage with the target customer. General diffusion principles posit that, ideally, successful communication occurs in a face-to-face setting with the target audience or customer. This, however, is often impracticable or too expensive. Substitutes to face-to-face settings are chosen and the mass media come into play. The use of mass media in such efforts, as in advertising, is often a vague undertaking, as one cannot be sure that one's message truly reaches the intended target. Often a compromise between the two extremes is desirable, e. g., the use of mass media, followed up by face-to-face meetings with smaller groups, etc. Electronic messaging via the Internet comes close to this ideal,

i. e. using a cost-effective mass medium and still reaching specific individuals. Moreover, the Internet's use makes it possible to be interactive with specific individuals within the target group and thus allowing *almost* face-to-face interaction. This potential for interactivity certainly makes the medium highly attractive as requests, needs, etc. certainly can be customized. Moreover, such interactivity makes possible the often missing *feedback* in the technology transfer process. Such feedback allows us to shape and additionally customize the very next step in the diffusion and communication process. Such customization is almost impossible when viewing the diffusion process via advertising as a communication channel.

C. Information Retrieval. In an electronic system, such as using the Internet, it is obvious that the users can readily retrieve information once the information is stored on the system. There are many data bases available at RL that could be accessed through the Internet, and many of those pertain to technology transfer and related issues. The authors made every effort to identify such data bases and make them available in a format conducive to outside users, hopefully firms that might acquire a particular product, know-how or service. The design of such information, data bases, etc. often determines their successful use. In this sense, a customer or *end-user* orientation was applied in the design of the system. Unless such design is inviting, encouraging, timely, informative and user-friendly, the success of the system is highly questionable (Taylor, 1986).

D. Networking. The topic of networking as a conceptualization embeds all three of the above topics, i. e. marketing, diffusion and information retrieval. Without these three, networking would be impossible. Networking in this sense goes beyond the traditional means of reaching a target customer. George Kozmetsky, director of the IC2 Institute, Austin, Texas, stated at a recent conference on commercialization of technology from federal laboratories that, "The secret to successful commercialization of technology developed in the federal labs is networking, networking, networking (Kozmetsky, 1993)." This importance was already demonstrated in an empirical NSF-funded study by Wigand focusing on technology transfer issues within the microelectronic industry and the role of industry, government and universities (Wigand and Frankwick, 1989).

Networking denotes interaction, feedback, customizing and creating a dialogue to a degree that otherwise would not exist. In that sense and in this particular case, RL may conceive of transferring technology, at

least in the beginning stages, as a partially cooperative means with potential target customers within industry. Networking would suggest the creation of Listservs, electronic bulletin boards (discussion groups), direct electronic inquiries that might be shared with the rest of likewise interested individuals/firms around a particular product, know-how or technology. Such individuals within firms appear to be quite interested in such dialogue as a technology emerges, although it is understandable that such dialogue would be reduced or cease entirely once the technology becomes highly marketable or commercializable due to competitive reasons. But even if RL could speed up the development and diffusion of a technology to such a point and if interaction would then discontinue, RL still would have provided a most valuable service to the development of that technology and industry. Typically, such networks do not come about by themselves. Such interaction must be fostered, encouraged, managed and nurtured by knowledgeable professionals within RL, perhaps among the Technology Transfer staff or the Directorate's Technology Transfer Focal Points. Networking, in this sense, is conceived as the highest level of technology transfer along the electronic medium of using the Internet. Lastly, networking as envisioned here, is characterized as rating high in terms of customer interaction, as well as high in terms of information content, implying that RL has the means to get closer to the customer. Moreover, it is interactive, multifaceted, customized, and on demand with time delay and time zone shifts playing merely a minor role.

Methodology

Various methods were employed to investigate and research the task at hand. The authors conducted interviews with numerous individuals within RL and with non-RL employees. Interviews were conducted with the members of the RL Technology Transfer Office staff, including RL elements at Hanscomb AFB, as well as several engineers and scientists. One engineer was interviewed in greater depth, as his ACT technology was highlighted for demonstration purposes on the Internet, i. e. the World Wide Web (WWW) at RL. This particular technology was demonstrated to show the various capabilities and cross-linkages possible using MOSAIC as the software to navigate on the WWW. In addition, several branch chiefs were interviewed as well as several area company representatives (Kaman, TRW and Booze, Allen & Hamilton). Moreover, in-depth interviews were conducted with the officers of the Photonics Development Corporation

in Rome, NY, as well as members of the RL Library. The authors interviewed appropriate, selected private sector firms in terms of their willingness, availability and readiness to enter the Internet and WWW world. The effects of the interviews were surprising to some extent as we saw a *snowball effect* emerging. That is the discussion of our interests in the electronic transfer process generated numerous additional suggestions, existing and potential services, as well as data bases. All in all, a surprising synergy was created between the research team and RL members engaged in research and technology transfer.

The Internet and the World Wide Web

The Internet is a very fast growing organization over the last several years. No one knows for sure the exact number of users, as the Internet itself is an organization of loosely coupled networks. An August 4, 1994 report of the Internet Society, the organizing body representing the Internet, reports dramatic growth in 1994. The latest Internet Society measurements reveal that there are worldwide 3.2 million reachable machines. This is an increase of 81 percent for the past year and represents an even steeper than normal increase over the past six months. Indeed, one million new hosts were added during the first six months of 1994. Of the world-wide total, the U. S. connections account for 63 percent (Internet Society, 1994). The fastest currently growing segment on the Internet are businesses, again demonstrating the potential to reach the private sector via the Internet. Although it is difficult to specify a threshold at which a critical mass of business Internet users has been reached, it is possible today to reach most major firms via the Internet. Small and medium sized firms are representative of the vast majority of firms signing on the Internet (Cf., e. g., with "Going *I-way?*," 1994; McBride, 1994).

An important caveat needs to be expressed here: Just getting a presence on the Internet is not enough. Just putting one's server on the Internet is analogous to hanging a shingle on a rural road. If one is selling something and has something important to offer that is intended to reach a large audience, it is important to have not just a shingle, but a major advertising board on the *main drag*, i. e. a major highway.

The Internet's rapid proliferation suggests that organizations in the public and private sectors want to take advantage of the Internet's interactive or two-way capabilities. In turn, this suggests the establishment and exploitation of visible and invisible social and physical networks linking and bridging public and private

sector organizations.

The appropriate use of the Internet may result in such desirable outcomes as: obtaining support from vendors, participating in joint development, collaborative research projects, providing customer support, marketing and product/service/know-how distribution. Due to space limitations it is impossible here to highlight various features of a value chain derived from appropriate Internet use. This value chain can be segmented into internal operations, inputs from suppliers, and customer relations. The Internet in conjunction with other appropriate technology and software, such as the World Wide Web and MOSAIC, lends itself ideally to provide an effective, quick and responsive interactive linkage between RL and its customers, i. e. various private sector firms (Cf., e. g., with Blattberg et al., 1994; Dallaire, 1993). Having a home page on the World Wide Web is not sufficient; the information content must reflect the potential user's information need. The authors have incorporated into the technology transfer home page the information that is most sought after by potential adopters of RL's technologies. The nature of this linkage is ideal in terms of cost-effectiveness and time-based considerations. Moreover, it provides the potential for feedback, the essential component in any effective communication effort.

Data Bases and Electronic Features Available Via the Internet and WWW

During the summer months of 1994 the authors designed, built and applied various data bases and services of interest in the technology transfer process. As mentioned initially, our efforts were driven by an overall customer/user orientation. The designed system uses MOSAIC on the WWW, is fully accessible to outside, i. e. non-RL, users, as well as RL users and features the following:

- What's Happening in Tech Transfer at Rome Lab?

- Technology Transfer at Rome Laboratory

- Hot Products

- Technology Transfer Inquiries

- A Model CRDA

- CRDA Data Base

- Educational Partnerships

Fact Sheets of Directorates

Facilities

Skills at Rome Laboratory Database

Rome Laboratory Staff Directory

The Reliability Engineer's Tool Kit

Patents Granted at Rome Laboratory

The management, use and ownership of these databases poses an intriguing question. It is very important that data bases are kept up-to- date and various current features such as *Hot Products* and *What's Happening in Tech Transfer at Rome Laboratory* feature products and information that truly is current. Otherwise, the system designed will be of little use to the outside, and RL users will recognize quickly that it is not a timely device to find out information about RL and its technologies.

The authors suggest that the ownership of this system resides with the Rome Laboratory Technology Transfer Office. Access to various features should be categorized such that it is available to all users (including the private sector) or only the Rome Laboratory Technology Transfer staff or only the RL Technology Transfer staff and all RL scientists and engineers. We recommend that the gatekeepers of information as well as the implementors of information into the system are the various Technology Transfer Focal Points within each directorate.

Implications

The system designed clearly demonstrates that the technology transfer capabilities can be achieved via electronic means. This elegant design derives value for Rome Laboratory through the timely and appropriate alignment of information technology already in place (personal computers, high-speed networks, software such as MOSAIC, and access to the Internet and WWW), Rome Laboratory's goals and strategies with regard to technology transfer and its larger role within the Armed Forces and society, as well as the appropriate alignment with existing *business processes*, especially with regard to technology transfer. Through the appropriate alignment and organizational fit, it is possible to generate added value for Rome Laboratory. It is of considerable importance, though, to realize that this designed process

occurring electronically cannot be arrested by peripheral traditional processes that might be paper-based, and still assume that the value chain continues delivering the same value. Appropriate electronic alignment must occur in such peripheral processes as well.

One must realize also that implementing this effort, even though highly cost-effective when compared to more traditional means, e.g., advertising, does not come cheaply. The system as conceived must be taken on by an individual or a team of individuals knowledgeable of the technology transfer process, RL, private sector operating practices, and probably some technology background and competence would be helpful as well. The task at hand is not just the mounting of the system on the WWW, but the effort must be nurtured, customized and *mothered*. Especially, the involvement of key individuals in private sector firms with an interest in technology transfer in such electronic organizational forms as Bulletin Boards, Listservs, etc. requires sensitivity, understanding and a sense of managing groups from a group dynamics perspective. This is time-consuming and requires patience in real life, but especially when done electronically. Numerous examples, however, abound demonstrating success in such efforts.

References

- Blattberg, Robert C., Glazer, Rashi, and Little, John D. C. (Eds.). *The Marketing Information Revolution*. Boston, MA: Harvard Business School Press, 1994.
- Dallaire, Rene M. Data-Based Marketing for Competitive Advantage. *Data Resource Management*, Spring, 1993, pp. 46-50.
- Going *I-way*? [Cover Story]. *PC Computing*, September, 1994, pp. 120-169.
- Internet Society Press Release, August 4, 1994.
- Kozmetsky, George. "Commercialization of Technology" (Keynote Address). Presented at the Conference on Commercialization of Technology within Federal Laboratories, Santa Fe, New Mexico, March, 1993.
- McBride, James. Marketing MOSAIC: The War Has Begun. *Internet World*, October, 1994, pp. 40-43.
- Rogers, Everett M. *Diffusion of Innovations* (Third Edition). New York: Free Press, 1983.

Taylor, Robert S. *Value-Added Processes in Information Systems*. Norwood, NJ: Ablex, 1986.

Wigand, Rolf T. and Frankwick, Gary L. Inter-Organizational Communication and Technology Transfer: Industry-Government-University Linkages. *International Journal of Technology Management*, 1989, 4(1), pp. 63-76.

Temperature Dependence of THz Emission from <111>
GaAs via Trans-Resonant Excitation

X.-C. Zhang
Associate Professor
Department of Physics

Rensselaer Polytechnic Institute
Troy, NY 12180-3590

Final Report for:
Summer Faculty Research Program
Rome Laboratory

Sponsored by:
Air Force Office of Scientific Research
Bolling Air Force Base, DC

and

Rome Laboratory

July 1994

Temperature Dependence of THz Emission from <111> GaAs via Trans-Resonant Excitation

X.-C. Zhang

Associate Professor
Physics Department
Rensselaer Polytechnic Institute
Troy, NY 12180-3590

Abstract

We have measured and compared the temperature dependence of THz radiation induced by ultrafast photocarrier transport and optical rectification via trans-bandgap femtosecond optical excitation from a single <111> oriented GaAs crystal. We report our extended measurement of the temperature dependence of THz emission from a single <111> oriented semi-insulating GaAs crystal under femtosecond trans-resonant optical excitation. Specifically, we report on the temperature effects in the THz radiation resulting separately from optical rectification or ultrafast photocarrier transport, as a function of the incident excitation wavelength. In particular, we observed enhanced THz emission from both radiation mechanisms when the incident excitation wavelength was tuned above the temperature dependent optical absorption bandedge.

Temperature Dependence of THz Emission from $\langle 111 \rangle$ GaAs via Trans-Resonant Excitation

X.-C. Zhang

Introduction

Previously, an initial time-resolved measurement of the temperature dependence of optically induced femtosecond electromagnetic radiation from several bulk semiconductors was performed, in which a significant increase in the peak radiated field was observed when the sample temperature was reduced [1]. Since, at modest incident optical fluence, photocarrier mobility in bulk semiconductors depends on temperature, the increase in THz radiation was attributed to temperature dependent carrier mobility effects. However, due to the off-normal incidence of the laser excitation used therein, the detected signal was a superposition of radiation produced via both optical rectification and ultrafast photocarrier transport. Furthermore, due to the limited tunability of the previous laser source, a balanced colliding pulse mode-locked dye laser, a measurement of the dispersion in THz emission as a function of temperature was not provided. Currently, it is a critical lack of information about the temperature dependence in the radiation produced by optical rectification and ultrafast photocarrier transport which limits our understanding of the mechanisms underlying these phenomena. A very recent study of infrared wavelength and temperature dependence of optically induced THz radiation from InSb demonstrated a substantial change in the THz emission spectra between doped and undoped InSb at low temperatures [2]; an effect attributed to impurity scattering in the doped sample.

Experimental Set up

Our experimental set up for the temperature dependent measurement has been fully described previously [1]. The important differences between the experimental arrangement used previously and the one here, are that here we used: (1) a single $\langle 111 \rangle$ oriented GaAs crystal for both the optical rectification and ultrafast photocarrier transport measurements, (2) a tunable Ti:sapphire laser, and

(3) normal sample illumination. This allowed us to make consistent and separate measurements of the two radiation effects, thus eliminating systematic errors resulting from using different sample crystals. Fig. 1 schematically illustrates the relative sample orientations used during the two experiments. Normal optical incidence was maintained during both measurements, and the incident laser polarization was fixed parallel to the dipole axis of the detecting antenna.

Experimental Results

THz radiation can be optically induced when certain materials are illuminated by ultrashort laser pulses. The two major radiation mechanisms which have been widely studied recently are (1) ultrafast photocarrier transport in bulk semiconductors and (2) THz optical rectification in non-centrosymmetric crystals. THz optical rectification is a special case of nearly degenerate difference-frequency-generation where the beating frequency ranges from near DC to several THz. Normal illumination of a $\langle 111 \rangle$ oriented zincblende crystal can be used to distinguish THz emission resulting from ultrafast photocarrier transport from that due to optical rectification [3]. Under this arrangement, in the absence of an applied magnetic field, the forward emitted THz radiation results only from optical rectification. However, when a magnetic field is applied, the path of the transient photocarriers is bent via the Lorentz force, so that a component of the THz radiation produced in this way propagates in the forward direction. Thus, by rotating the azimuthal angle of the crystal to eliminate THz emission via optical rectification, we may separately observe the THz emission resulting solely from ultrafast photocarrier transport. In addition, very recently the two contributions to the THz radiation induced by 10 fs laser pulses were also resolved in the time-domain [4]. This was possible because whereas THz optical rectification results from an instantaneous virtual excitation, ultrafast photocarrier transport extends over several hundreds of femtoseconds.

For the optical rectification measurement, as shown in Fig. 1(a), the $\langle 111 \rangle$ oriented crystal was aligned with its $[11\bar{2}]$ axis parallel to the direction of the laser beam polarization. This geometry maximizes THz radiation via optical rectification in the forward direction, while as discussed above, normal optical incidence in the absence of an applied magnetic field prevents THz radiation via ultrafast photocarrier transport from propagating in the forward direction.

Fig. 1(b) shows the sample rotation used for the transient photocurrent portion of the measurement. The $[11\bar{2}]$ axis was rotated 30 degrees with respect to the incident optical polarization, whereby following crystal symmetry, the THz optical rectification signal to nominally zero. To produce THz radiation via ultrafast photocarrier transport in the forward direction, an external magnetic field of approximately 0.1 Tesla was applied on the sample. This imposed a Lorentz force on the photocarriers which produced a transverse component of the THz signal which propagated in the forward direction [5]. This ensured the THz signal detected in this manner resulted solely from transient photocurrents. Overall, using such an arrangement, as shown in Fig. 1(a) and (b), we could directly determine and separately measure the THz radiation resulting from each radiation mechanism.

To test the symmetry of our $\langle 111 \rangle$ GaAs crystal, we first measured the peak value of THz optical rectification signal versus azimuthal angle and incident excitation wavelength. Fig. 2 displays the trans-resonant dispersion in the peak THz optical rectification as a function of azimuthal angle at room temperature. A three-fold rotation symmetry in the signal clearly indicates that THz optical rectification via a bulk $\chi^{(2)}$ process is the dominant radiation mechanism. The trans-resonant flip in polarity of the signal, as the incident excitation wavelength is tuned through the optical absorption bandedge, at a constant azimuthal angle, is a result of the optical resonance contribution in $\text{Re}[\chi^{(2)}]$. This measurement is consistent with our separate previous measurement of the effects of either crystal symmetry or incident trans-resonant optical wavelength on THz emission by optical rectification [2], but now includes both. We also measured the angular dependence of THz radiation emitted by ultrafast photocarrier transport. To within our instrument resolution, we confirmed that this component of the THz radiation, at moderate optical fluence, is independent of azimuthal angle. This result is consistent with the spherical symmetry, in reciprocal space, of the resonant electronic states near the Γ point in zincblende crystals.

Figs. 3 and 4 show the temporal waveforms radiated via THz optical rectification and by ultrafast photocarrier transport, respectively, versus trans-resonant optical excitation at 90 K. In Fig. 3, we further observe that the entire time-resolved THz optical rectification signal undergoes a polarity flip as the incident excitation wavelength is tuned through the optical absorption bandedge. In contrast, since THz emission via ultrafast photocarrier transport can only occur

under resonant optical excitation, in Fig. 4, no trans-resonant polarity flip can be observed.

Fig. 5 displays the peak radiation signal via THz optical rectification versus incident excitation wavelength and sample temperature. The measurement was performed at normal incidence, in the absence of an applied magnetic field to eliminate THz emission from ultrafast photocarrier transport, and at a fixed azimuthal angle which oriented the crystal symmetry to maximize THz optical rectification. The resonance feature shifts with the temperature dependent optical absorption edge, and the rising edge of the resonance peak is sharper at lower temperatures. Similarly to Fig. 5, Fig. 6 plots the THz radiation from ultrafast photocarrier transport. In this plot, no THz radiation was measured when the incident photon energy was tuned below the optical absorption bandedge.

Currently, there is a considerable interest in measuring the radiation efficiency between ultrafast photocarrier transport and THz optical rectification. Previously, most comparisons of radiation efficiency from the two mechanisms were made using different samples. However, this ratio is extremely sensitive to the sample preparation as it depends both on the surface condition as well as the strength of the applied magnetic field. Therefore, our single crystal approach provides a much more reliable comparison between the radiation efficiency of the two mechanisms. In this experiment, at an incident excitation wavelength of 820 nm (1.51 eV) and a magnetic field strength of 0.1 Tesla, we found that from our single $\langle 111 \rangle$ SI-GaAs crystal, the magnitude of THz emission due to ultrafast photocarrier transport increased from 3 to 30 times larger than that due to optical rectification as the sample temperature was decreased from 300 to 90 K. This room temperature ratio is consistent with a measurement made previously [5].

Conclusion

We present a detailed measurement of the trans-resonant dispersion and temperature dependence, from 300 to 90 K, of THz emission via both optical rectification and ultrafast photocarrier transport from a single $\langle 111 \rangle$ GaAs crystal. Our results indicate that there is both an enhancement of the resonant second-order nonlinear susceptibility near the optical absorption bandedge and a significant increase in photocarrier mobility at low temperatures.

Acknowledgment

We would like to thank M.N. Alexander, J.J. Larkin, M.T. Harris, B.S. Ahern, D. Bliss, and D.W. Weybume for their support during the 1994 AFOSR Summer Faculty Research Program.

References:

- [1] B.B. Hu, X.-C. Zhang, and D.H. Auston, Appl. Phys. Lett., **57**, 2629 (1990)
- [2] S.C. Howells, S.D. Herrera, and L.A. Schlie, unpublished, (1994)
- [3] X.-C. Zhang, Y. Jin, K. Yang and L.J. Schowalter, Phys. Rev. Lett., **69**, 2303 (1992); X.-C. Zhang, Y. Jin, K. Ware, X.F. Ma, A. Rice, D. Bliss, J. Larkin and M. Alexander, Appl. Phys. Lett., **64**, 622 (1994)
- [4] B.B. Hu, E.A. DeSouza, W.H. Knox, M.C. Nuss, and J.E. Cunningham, Proceeding of Ultrafast Phenomena Topical Meeting, Optical Society of America, PD-12, (1994)
- [5] X.-C. Zhang, Y. Jin, T.D. Hewitt, T. Sangsiri, L.E. Kingsley, and M. Weiner, Appl. Phys. Lett., **62**, 2003, (1993)

Figure Captions:

- Fig. 1. Schematic illustration of sample geometry for forward THz emission via: (a) THz optical rectification and (b) ultrafast photocarrier transport under an applied magnetic field. The direction of $[11\bar{2}]$ axis was rotated 30 degrees between (a) and (b).
- Fig. 2. Peak value of THz optical rectification versus incident excitation wavelength and azimuthal angle. The surface gray-level, ranging from black to white, corresponds to a normalized signal magnitude ranging from zero to the extremum value, respectively.
- Fig. 3. Temporal waveform of THz emission via optical rectification versus incident excitation wavelength at 90 K.
- Fig. 4. Temporal waveform of THz emission via ultrafast photocarrier transport versus incident excitation wavelength at 90 K.
- Fig. 5. Peak value of THz emission via optical rectification versus incident excitation wavelength and sample temperature. Note: the sign of the data has been reversed, with respect to Fig. 3, to improve clarity.
- Fig. 6. Peak value of THz emission via ultrafast photocarrier transport versus incident excitation wavelength and sample temperature. Note: the sign of the data has been reversed, with respect to Fig. 4, to improve clarity.

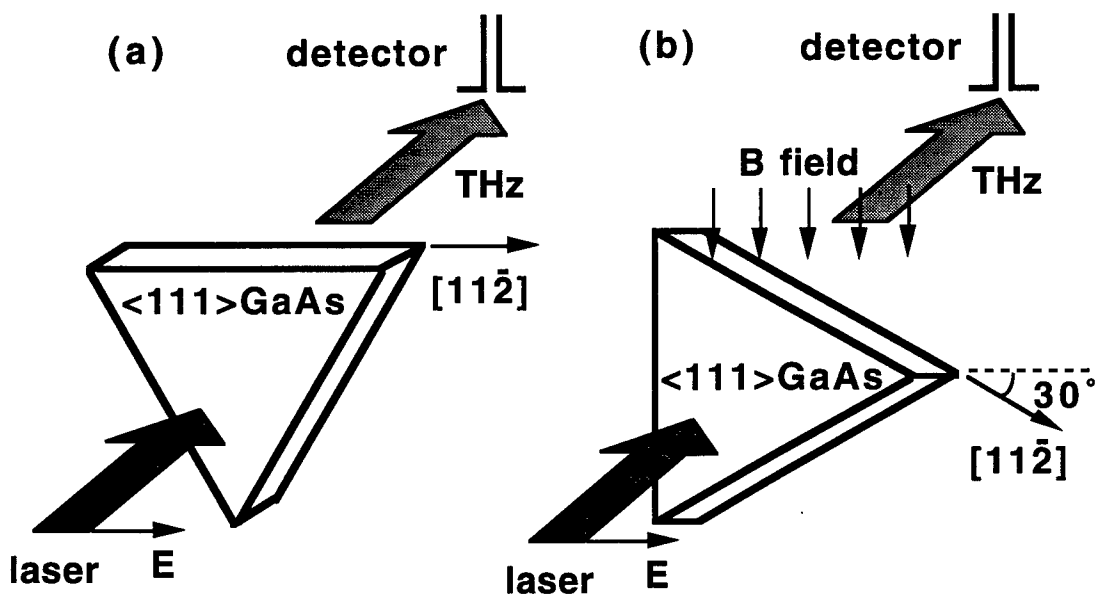


Fig. 1

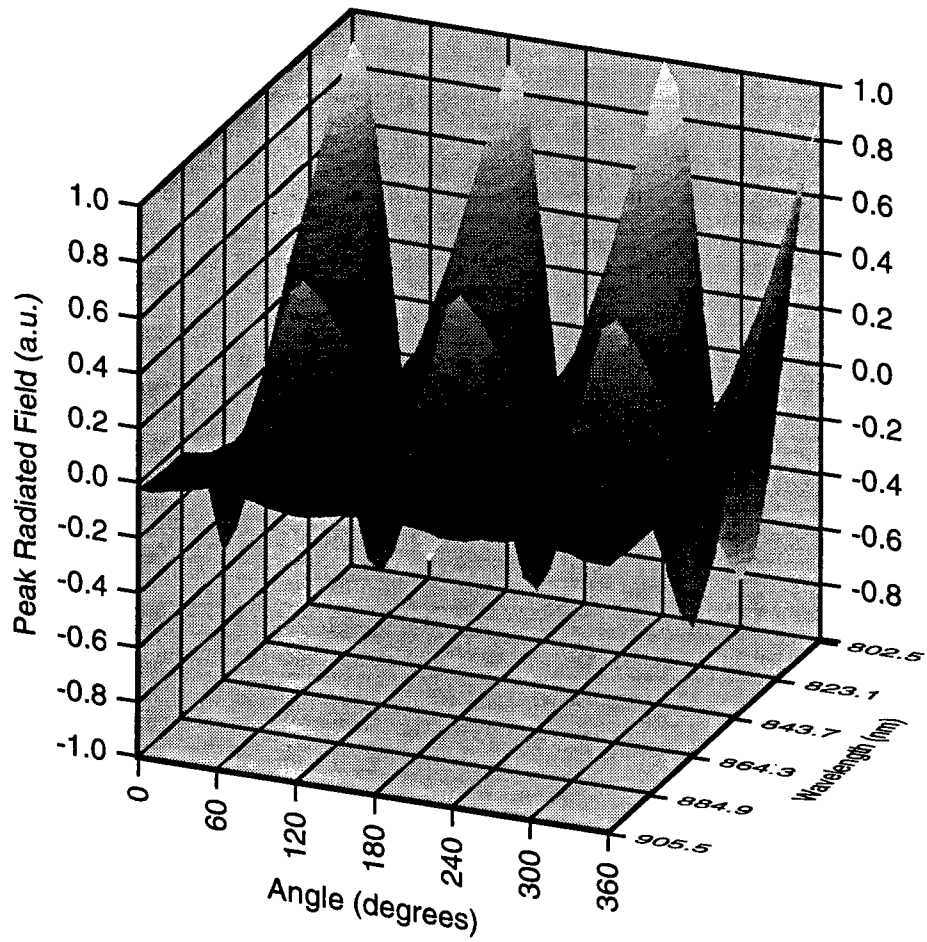


Fig 2

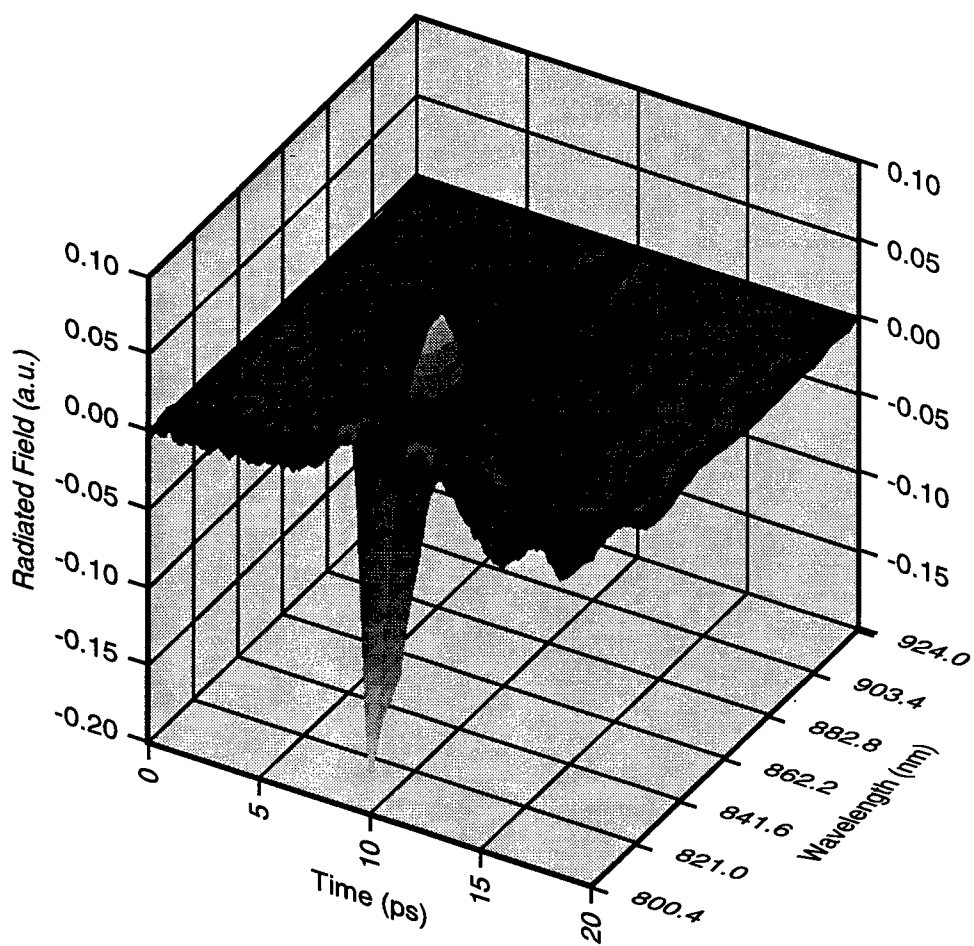


Fig 3

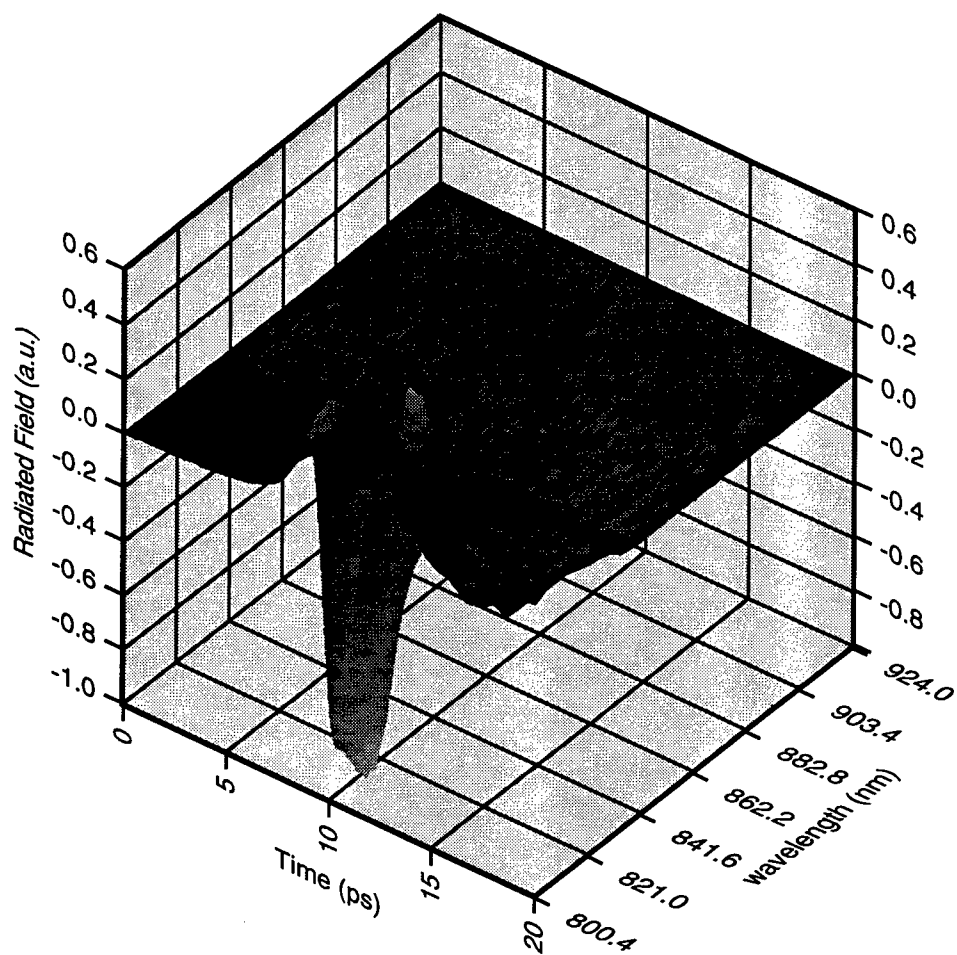


Fig 4

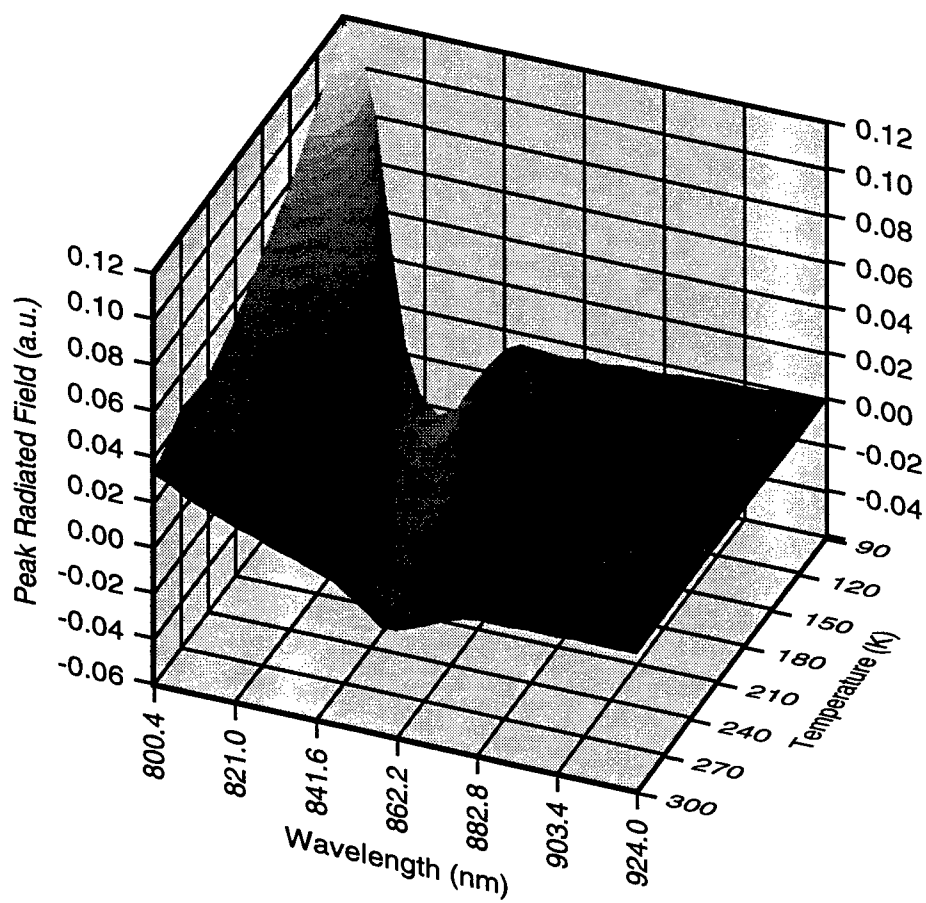


Fig 5

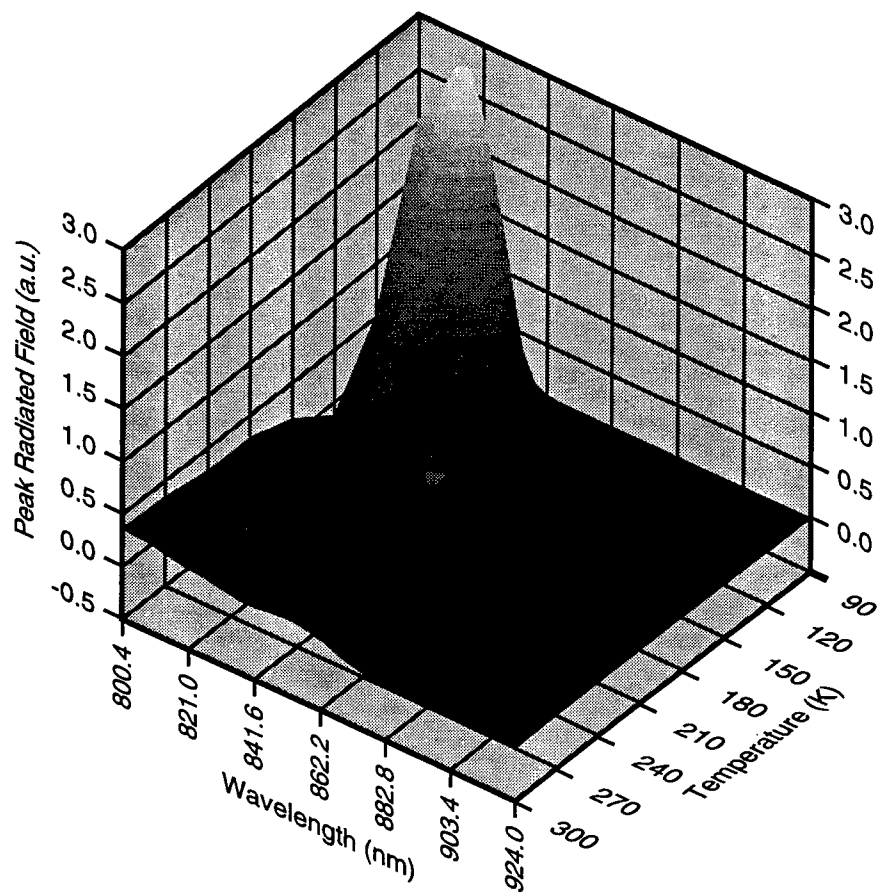


Fig 6